Core Collapse Supernovae Neutrino Detection in XENONnT

Layos Daniel García

École doctorale des Sciences de la Terre et de l'environnement
et Physique de l'Univers, Paris - ED 560

Laboratoire de Physique Nucléaire et de Hautes Énergies - UMR 7585

Core Collapse Supernovae Neutrino Detection in XENONnT

Presented by
Layos DANIEL GARCIA

Supervised by Dr. **Luca SCOTTO LAVINA**

Defended on 1st October 2024 in front of the committee:

Dr.	Olivier	DRAPIER	Reviewer
Dr.	Pascal	PRALAVORIO	Reviewer
Dr. Prof.	Laura	BAUDIS	Member
Dr. Prof.	Eli	BEN-HAIM	Member
Dr.	Maria Cristina	VOLPE	Member
Dr.	Jacques	DUMARCHEZ	Invited
Dr.	Luca	SCOTTO LAVINA	Supervisor

Remerciements

Je voudrais remercier premièrement le laboratoire LPNHE de m'avoir accueilli pour cette thèse et à son directeur Marco Zito. En extension, au groupe XENON de ce laboratoire, et aussi à celui du laboratoire Subatech à Nantes qui m'acceuilli pendant deux mois cette dernière de thèse.
Deuxièmement, je voudrais remercier à la collaboration XENON, en particulier au petit groupe de travail pour l'étude des neutrino de Supernovae; à Kara Melhi, Sayan Gosh, Ricardo Peres, Andrea Molinario et Amanda Baxter pour leur soutien et leur écoute. Je tiens aussi à remercier Diego Ramirez, pour sa dédication et ses efforts à répondre à mes nombreuses questions. Je remercie également Frederic Girard pour ces corrections précises et pointilleuses.
Troixièmement, je voudrais remercier à Irena Nikolic et Jacques Dumarchez pour leur regard attentionnée et intelligent.
Quatrièmement, à Jean Philippe Zoupounoudis, pour son encadrement lors de mon stage de M1 au groupe XENON au LPNHE, élément déclancheur de cette thèse. Aussi, pour nos conversations qui finissaient d'une manière ou d'une autre par aborder la physique, et avec lesquelles j'ai énormément appris.
En dernier, je voudrais remercier Luca Scotto Lavina, de m'avoir encadré dans cette thèse avec un rare mélange d'intélligence et bienveillance, comprenant toujours ce qu'il y avait dans ma tête. Aussi, par la physique et par l'humanité qu'il m'a transmis.

A Capucine et Lucio

Abstract

Core Collapse supernovae (CCSNs) emit more light than all the stars in the galaxy from which their progenitor star was born. The remnants of the core collapse supernovae will be visible for centuries. However, information about what occurred in the core is transmitted via a neutrino burst that is emitted ten seconds only after the core bounces. While telescopes have time to point out supernova remnants, particle detectors on Earth expect to see half of the neutrino burst events in the first second after the collapse. The first and only CCSN neutrino signal has been detected in 1987 (SN1987A). Since then, we are still searching for the next one. Detecting a future, new CCSN neutrino burst presents a challenge for particle detectors, necessitating precise timing and energy resolution. Direct dark matter detectors provide a unique environment for investigating the CCSN signal, through mechanisms that are different from what large volume water cerenkov or liquid scintillator detectors are capable to provide. Dark matter detectors are often located underground, protected from cosmic radiation and exhibit ultra-low backgrounds, allowing them to potentially observe cosmic neutrinos, such as those from our Sun, which present around 10^4 times lower fluxes than a CCSN neutrino burst from the Milky Way center. The XENONnT detector is based on a xenon dual phase time projection chamber (TPC), surrounded by a water cerenkov volume that acts as a muon or neutron veto. XENONnT presents then two detection volumes sensitive to CCSN neutrinos: the 5.9 tonnes of liquid xenon in the TPC, where neutrinos are expected to interact via coherent elastic scattering with xenon nuclei (CEνNS); and the water tank with 700 tonnes of ultrapure water doped with Gd salt, compounding the neutron (56 tonnes) and muon (644 tonnes) vetoes, in which neutrinos are expected to induce an inverse beta decay (IBD) reaction. The goal of this thesis is to investigate the CCSN signal in all available detection volumes, with a particular focus on the expected neutrino interactions in the water tank.

The thesis manuscript is organized as follows. Chapter 1 covers the physics of the core collapse, while Chapter 2 focuses on neutrinos emission and their propagation that will result in the final detectable neutrino flux at the Earth. This second chapter presents as well the state of the art of CCSN modeling, culminating in the selection of one of the available models that will be used in the CCSN analysis in the next chapters. Chapter 3 opens with a small review of CCSN neutrino detection, then moves to the description of the XENONnT TPC detector. The chapter ends with an original work where the CEνNS are simulated in the TPC. The next two chapters are devoted to the investigation of the CCSN signal in the water tank. In particular, chapter 4 describes the two sensitive volumes, including the micro-physics of the Cerenkov light induced by the CCSN signal. In addition, the predicted IBD rates used for CCSN

signal simulation in the water tank are discussed. Chapter 5 addresses the CCSN simulation chain, with an original work on the digitalization of the IBD process in the muon and neutron veto, included in the full GEANT4 simulation chain of the experiment. To test the reliability of the data digitalization, a comparison with data from AmBe calibrations have been used.

Finally, this manuscript ends with a conclusion chapter in which the simulation results from CEνNS in the LXe TPC and IBD in the water tank will be summarized. This work has been thought as well to provide precise guidelines for scientists who intend to perform new and updated projections on CCSN detectability for future and larger dark matter detectors.

Résumé

Les supernovae à effondrement de coeur (CCSN en anglais) émettent plus de lumière que toutes les étoiles de la galaxie dans laquelle leur étoile est née. Les restes de ces supernovae seront visibles pendant des siècles. Cependant, les informations sur les processus physiques dans le cœur de l'étoile sont transmises via un jet de neutrinos émis dix secondes seulement après le rebondissement du cœur. Alors que les télescopes ont le temps de détecter les rémanents de supernovae, les détecteurs de particules sur Terre s'attendent à voir la moitié des événements du flux de neutrinos dans la première seconde après l'effondrement du coeur. Le premier et unique signal de neutrinos provenant de CCSN a été détecté en 1987 (SN1987A). Depuis, nous cherchons toujours le prochain. Les neutrinos CCSN présentent un défi pour les détecteurs de particules, nécessitant sont observation d'une résolution en temps et en énergie très précises. Les détecteurs directs de matière noire fournissent un environnement unique pour étudier ce signal, à travers des mécanismes différents de ceux utilisés par les détecteurs à eau cerenkov ou à scintillateur liquide de grand volume. Les détecteurs de matière noire sont souvent situés sous terre, protégés du rayonnement cosmique et présentent un bruit de fond ultra-faible, ce qui leur permet d'observer potentiellement des neutrinos cosmiques, comme ceux provenant de notre Soleil. Ces derniers présentent un flux environ 10^4 inférieur à celui d'un flux de neutrinos CCSN au centre de la Voie Lactée. Le détecteur XENONnT est composé par une chambre de projection temporelle (TPC) à double phase remplie de xénon liqude, entourée d'un volume d'eau qui agit comme veto pour les muons ou les neutrons. XENONnT présente alors deux volumes de détection sensibles aux neutrinos CCSN : les 5,9 tonnes de xénon liquide dans le TPC, où les neutrinos devraient interagir via diffusion élastique cohérente avec les noyaux de xénon (CEνNS) ; et le réservoir d'eau avec 700 tonnes d'eau ultrapure dopée au sel de Gd, contenant le neutron veto (56 tonnes) et les muon veto (644 tonnes), dans lesquels les neutrinos devraient induire une réaction de désintégration bêta inverse (IBD). L'objectif de cette thèse est d'étudier le signal CCSN dans tous les volumes de détection disponibles, avec un accent particulier sur les interactions attendues des neutrinos dans le réservoir d'eau. Le manuscrit de la thèse est organisé comme suit. Le chapitre 1 couvre la physique des CCSNs, tandis que le chapitre 2 se concentre sur l'émission de neutrinos et leur propagation dans le milieu. L'état de l'art de la modélisation du flux de neutrinos CCSN, aboutissant à la sélection de l'un des modèles disponibles sera aussi présenté dans ce chapitre 2. Le chapitre 3 s'ouvre avec un aperçu des techniques de détection des neutrinos CCSN, incluant XENONnT. Le chapitre se termine par une simulation du signal CEνNS induit par le flux des neutrinos CCSN dans la TPC. Les deux derniers chapitres 4 et 5 sont consacrés à l'étude du signal CCSN dans le réservoir d'eau. En particulier, le chapitre 4 décrit les deux volumes sensibles,

dont la micro-physique de la lumière Cerenkov induite par le signal des neutrinos CCSN. De plus, les taux d'éventments de IBD et les spectres qui seront utilisés pour la simulation du signal CCSN dans le réservoir d'eau sont discutés. Le chapitre 5 aborde la chaîne de simulation de neutrino CCSN, incluant le travail de digitalisation du signal IBD dans le vetos. Finalement, ce manuscrit se termine par un chapitre de conclusion dans lequel les résultats de simulation de CEνNS dans le LXe TPC et IBD dans le réservoir d'eau seront synthétisés. Ce travail a également été pensé pour fournir des lignes directrices précises aux scientifiques qui ont l'intention d'effectuer des projections nouvelles et mises à jour sur la détectabilité des neutrinos CCSN pour les futurs détecteurs de matière noire de plus grande envergure.

Contents

Chapter 1

Core Collapse Supernovae Neutrinos

Introduction

[February 23rd, 1987], astro-particle physicists of KAMIOKANDE-II, Irvine-Michigan-Brookhaven, and Baksan experiments recorded a neutrino signal consisting of a few events, 11, 8, and 5, respectively [1, 2, 3]. This signal arrived one day before light from a supernova at 50 kpc, in the Large Magellanic Cloud, finally reached telescopes at the Earth, after traveling through the intergalactic space around 163 050 years. The event was named supernova 1987 A (or SN 1987 A), and the neutrino emission associated with his explosion is the only one confirmed to this days. This neutrino signal was particularly fast and energetic; the neutrino burst was estimated to have a duration of twelve seconds and emit a total energy of 8 10^{52} ergs for the $\bar{\nu}_e$ flavor, which represent only a $\sim$1/6 of supernova neutrino flux [1]. Efforts to understand supernova explosions, core collapse mechanisms, and star evolution of supernova progenitors, including neutrino physics, have been multiplied during the last decades. Also, the sensitivity of astro-neutrino detectors has been increased with the improvement of the detection techniques and their scaling to larger volumes. The search for supernova neutrino signal is now being considered, not only in neutrino-dedicated detectors, but in the majority of particle detectors sensitive to neutrinos, including direct dark matter experiments. In this first chapter, the different types of supernovae and basics of core collapse will be introduced, in order to understand the role of neutrinos as messengers of the physics inside the progenitor star core, as well as their implications for triggering the supernova explosion after the core bounce. Types of supernovae with different mechanisms of collapse, that could cause a detectable neutrino flux at the Earth will be detailed. Finally, the history of supernovae observation, going all the way back to documented astronomy, will be summarised in order to understand the actual context of these observations and determine what are the chances to observe a supernova in the next few decades.

1.1 Supernovae Types

Supernovae types correspond to a spectroscopic classification. Types I have lost their hydrogen (H) layers and are divided in three subcategories: Type Ia, Ib and Ic. Type Ia supernovae can be distinguished from Types Ib and Ic by the lack in the last of an absorption line of singly ionized silicon at a wavelength of 635.5 nm [4], while Type Ic distinguish from Type Ib having lost, plus to the H, his helium (He) layers. In a second order of subcategories we distinguish Type b(n), with narrow He lines [5] and Type c-BL characterised by very broad spectroscopic features (BL-broad line) and often associated to a gamma ray burst [6]. Types II present H-lines in their light emission spectrum, and they are also classified into subcategories, depending on the shape of their H-line spectrum and light curves. Types II-L/P refers to the evolution of luminosity in time: linear (L) or presenting a *Plateau* (P). Also, Type IIn and b describes the width of these H-lines: Type IIb (weak) — the case of 1993J [7] — and Type IIn (narrow or intermediate width). **Figure 1.1** represent light curves of this supernova different types. A special mention goes to the supernova1987A classified as a Type II, the only one where a neutrino signal was detected (see **Section 3**), but presents a very particular light curve (see **figure 1.1**). Its brightness increased very fast, decreasing in the same way along the first few days, when Types II typically reach their peak after gradually increasing their luminosity for around ten days. SN1987A did not reach its maximum luminosity until 3 months after its collapse; therefore it's represent itself as a new category of Supernova, the named *SN1987A-like* due to his particular light curve [8].

The importance of the local environment of supernovae imposes these spectroscopic distinctions between the types of supernovae core collapse. This immediate local environment will affect the early stage of the core collapse process and the evolution of the progenitor star before this one. As it will be explained in **Section 2.5**, this will also affect neutrino propagation through the core to the outer layers.

These are the supernova Types distinguished today, some of them are the result of a core collapse. Astrophysicists have studied supernovae phenomenology during the last century, distinguishing two principal production pictures. The first one involves a binary system of stars with at least one white dwarf. The latter is a remnant of a massive progenitor star that has burned all its H, becoming an electron-degenerate system composed mostly of He, oxygen, and carbon. White dwarf hydro-stability is constraint by the compensation between the electron degeneracy pressure and gravitational one, described by a critical mass, known as the Chandrasekhar limit $\approx 1,44 M_{\odot}$[1]. This mass can be exceeded by the matter accretion of the companion star. The scenario for carbon-oxygen white dwarfs is that this gradual accretion of mass leads to reaching temperatures of carbon fusion slightly before the Chandrasekhar limit [2]. At this point, a cascade of thermonuclear explosions burns the star material, leaving no remnant, producing a Type Ia supernova [11]. In the same way, a fusion of two white dwarfs with a resulting mass in the Chandrasekhar limit will produce a Type Ia supernova.

The other mechanism is the core collapse of a star, which involves stars with masses between $\approx 8 - 40 M_{\odot}$

[1] Our Sun mass $1.98855 \pm 0.00025 \times 10^{30}$kg.

This is the unit of mass for supernova progenitors and it will be represented by the symbol $M_{\odot}$ to refer to this value.

[2] This carbon fusion occurs when the core mass $\geq$ 99% of Chandrasekhar limit[10]

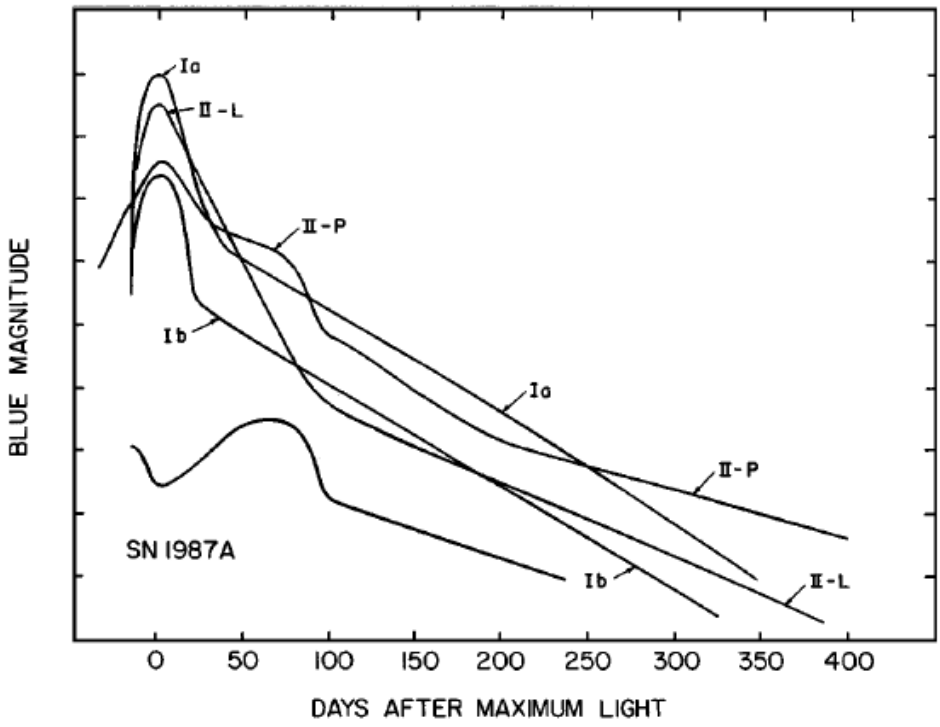

Figure 1.1: Evolution of luminosity of th SN after the explosion for the mentioned types of SN: Ia, Ib , II-P/L including the SN1987A[9]

— or limitless depending on their metallicity [12]. The hydrostatic stability of the star breaks down when the maximum binding energy per nucleon is reached $\sim$ 8 MeV in the region of iron [13]. The internal energy will be not enough to maintain the energy gain from fusion beyond iron. As a consequence of the drop on radiation pressure, electron degeneracy pressure supports almost alone the gravitational one. This will not be enough when the mass of the core exceeds the Chandrasekhar limit, leading to a gravitational collapse with the ejection of $\approx 95\%$ of the mass of the star [13]. This second group, core collapse supernovae CCSN, includes Types II, Ib, and Ic supernovae, in which core collapse leads to the neutrino burst of interest. Before focusing on CCSN, it has to be said that a neutrino burst from a Type Ia supernovae explosion is also expected, but the flux of these neutrinos is approximately four orders of magnitude lower than the CCSN one, and the energy spectrum is around 3 MeV rather than the 10–20 MeV for the neutrino spectrum from CCSN [14, 15].

1.2 CCSN Explosion Mechanism

Speculations about the apparition of life on Earth place it around 4.2 billions years ago [16]. Since then, each form of life has been heated by the same energy; the same gamma rays originating from the nuclear H burning process that leads to He production. Those high energy photons cross the core of the Sun,

being absorbed and re-emitted. After a million years of travel, they reach the outer layers, now divided into millions of low energy photons that compose visible light [3]. This process will continue, and those photons filtered by our atmosphere, become the pale yellowish light[4] that will surround us for at least 5 billion years. The H $\rightarrow$ He nuclear fusion, is indeed the result of a chain of proton reactions called the pp-chain. In these consecutive reactions leading to He, not only photons are released but also neutrinos, which, on the contrary, reach the outer Sun layers instantaneously (nearly at the speed of light). They therefore retain the information about the actual state of the core.

Also, more massive stars than the Sun burn H to make He most of their lives, during $\mathcal{O}(10^7)$ years in the

Mass Fraction	**T (C°)**	**Density** (kg/m^3)	**Reactions**	**Time for 25 $M_\odot$**	**Composition**	**Cooling process**
0.6	10^7	10	H $\rightarrow^4$ He	7×10^6y	^{1}H, ^{4}He	Photons, Neutrinos
0.1	2×10^8	10^6	^{4}He $\rightarrow^{12}$ C,^{16} O	5×10^5y	^{4}He	Photons
0.05	5×10^8	6×10^6	^{12}C $\rightarrow^{20}$ Ne,^{24} Mg	600 y	^{12}C,^{16} O	Neutrinos
0.15	8×10^8	3×10^7	^{20}Ne $\rightarrow^{16}$ O,^{24} Mg	1 y	^{16}O,^{20} Ne,^{24} Mg	Neutrinos
0.02	3×10^9	2×10^9	^{16}O $\rightarrow^{28}$ Si	180 d	^{16}O,^{24} Mg,^{28} Si	Neutrinos
0.08	8×10^9	4×10^{12}	^{28}Si $\rightarrow^{56}$ Fe,^{56} Ni	1d	^{28}Si,^{32} S	Neutrinos

Table 1.1: Description of layer structure formation during burning process. The values summarized are obtained from this works [20][21]

case of the CCSN progenitors, leading also to a neutrino emission in the subsequent chain of reactions. This H burning phase is crucial for the stability of the star, and his future stellar evolution. At this time the star joins the Zero Age Main Sequence (ZAMS) on the Hertzsprung-Russell diagram [22] (see **figure 1.2**). After this time the star enters a phase of stellar evolution that is quite stable, and steadily processes H into higher elements.

The life of CCSN progenitors is shorter — in comparison of the Sun — due to gravitational pressure that makes denser cores[5]. This greater pressure results in higher temperature at the core and accelerates the burning process. As the HR of **figure 1.2** shows, luminosities is expected to increase with mass, as well with temperature (star can be assumed as a black body emitter), in the ZAMS (solid black line). Regarding this luminosity behaviour, massive stars are expected to be between 10^3 to 10^6 brighter than the Sun. Due to this high core temperature, CCSN progenitors don't burn H via the pp-chain but via CNO cycle, which is strongly dependent on temperature and domains in temperatures $> 2\times10^7$ K (see **table 1.1**). In this sense, the CNO cycle produces also early neutrinos during H burning process. These neutrino have different energy spectrum and higher flux at MeV energy than pp-chain solar neutrinos[24]. For example, for the He-burning neutrino luminosities are $>10^6 L_{\nu,\odot}$ [25][6].

[3]The spectrum of sun is larger than visible light, covering the UV to the IR in a wavelenght range of ($\sim 300-2500$ nm [17])

[4]Sun light spectrum arriving at the earth appears to us white or yellow most of the time, because of Rayleigh scattering of blue and green parts of visible spectrum with atmospheric particles [18]. The latter scattering depends on angle of the incident light, explaining the red in sunrise and sunset[19]

[5]Star life is also related to the H and He abundances as there represent the most significant fusion process

[6]$L_{\nu,\odot}$ correspond to solar neutrino luminosity. $L_{\nu,\odot} = 0.02398$ $L_{\gamma,\odot} = 9.1795\times10^{31}$ erg s^{-1} [26]

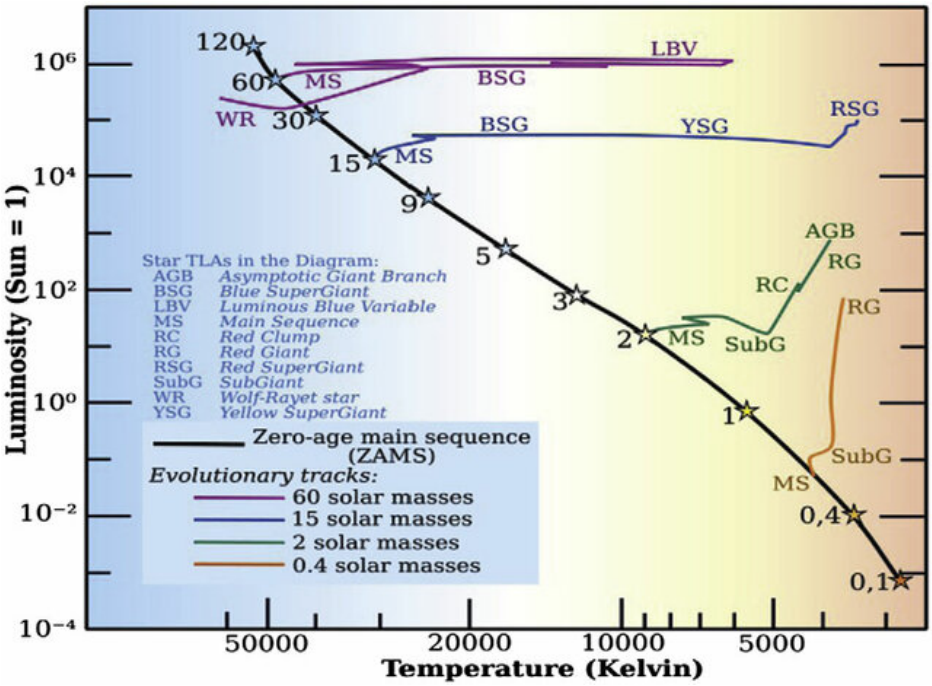

Figure 1.2: Hertzsprung-Russell diagram showing luminosity-temperature relation of stars at their evolutionary phases as function of main sequence initial mass. The potential stellar sources of cosmic dust are marked with circles. The final fate of the RSG (red super giant) phase as shown in the diagram, is the core-collapse supernova. [23]

The **figure 1.3** represents the pp-chain and CNO cycle energy curves from neutrino emission as a function of temperature. At the expected temperature of supernovae progenitors, the strongly exponential dependence in temperature of the CNO cycle ($\sim T^{17}$) domains this neutrino emission[27].
Regrettably, the distance between these massive stars and our Sun prevents the detection of their neutrino emission at this early stage of their star life on Earth. Only around 10 million years later, these star cores will collapse, and neutrino emission will be $\simeq 10^{10}$ more luminous[25], including neutrino with higher energy in the ten of MeV range. At this juncture, the core of these stars has undergone evolution, transforming into a composition of heavy nuclei. In the next paragraphs, the evolution of these massive stars, CCSN progenitors, from the H burning process to this heavy nuclei dense core formation just before collapse.

1.2.1 Star evolution to collapse

When most of the H is burned, the pressure (P) related to the internal energy release from its combustion is no longer able to compensate for the gravitational pressure, and the star contracts instead of reducing radiation energy. This contraction leads to a pressure increase, which in turn causes a temperature (T) increase. Assuming that the equation state of the star is that of a non-degenerate ideal gas, $P \propto \rho T$, with

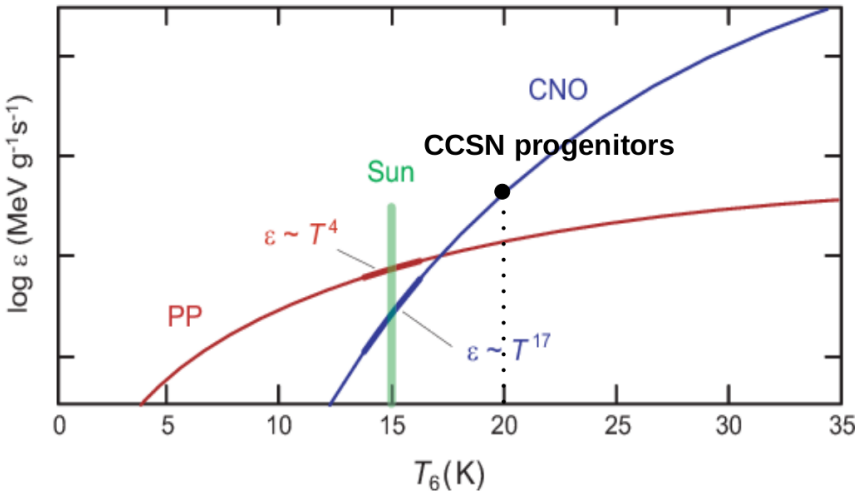

Figure 1.3: Energy released in neutrino emission as a function of temperature for the pp-chain (red) and CNO cycle (blue). We see that in SN progenitor region, CNO cycle domains, strongly dependent in temperature[28].

ρ the density in the star. This assumption is based on the relative low densities at this early stage of core collapse, as it can be seen in **table 1.1**. The hydrostatic equilibrium before contraction reveals the relationship between this pressure and the gravitational one:

$$\vec{\nabla}\mathrm{P} = -\rho(\tilde{\mathrm{r}})\tilde{\mathrm{g}}(\tilde{\mathrm{r}}) \tag{1.1}$$

with $\rho(\vec{r})$ the matter density on a sphere of radius r and $\vec{g}(\vec{r})$ the gravitational local field. This expression can be derived into an only r dependence, assuming spherical symmetry:

$$\frac{\mathrm{dP}}{\mathrm{d}r} = -\frac{\mathrm{GM(r)}}{r^2}\rho(r) \tag{1.2}$$

It can be assumed, that the star is engaged in an adiabatic process as only H burning is considered for instance. Taking into account these variables, in order to understand the role of energy from the burning process, internal energy per volume (u) can be expressed in terms of pressure using the adiabatic coefficient γ:

$$u = \frac{\mathrm{P}}{\gamma - 1} \tag{1.3}$$

As a consequence the gravitational potential energy for a mass $dm(r)$ as:

$$E_p = -\int_0^R \frac{\mathrm{GM_r}}{r} dm(r) \tag{1.4}$$

With values of E_p and $\mathrm{M_r}$ defined explicitly in **Appendix A.1**.
Integrating by $4\pi r^3 dr$ the expressions (1.2 1.3) the potential E_p as a function of the thermal (internal) energy U can be written as:

$$-\int_0^R \frac{\mathrm{GM(r)}}{r^2} r\rho(r) 4\pi r^2 dr = -\int_0^R \frac{\mathrm{GM}}{r} dM(r) = E_p \tag{1.5}$$
$$= -3\int_0^R 4\pi r^2 \mathrm{P} dr = -3(\gamma-1)\int_0^R u 4\pi r^2 dr = -3(\gamma-1)U = -2U$$

In the last calculation, the Virial theorem derivation was applied. Replacing for a non-relativistic ideal gas $\gamma = 5/3$, the resulting potential energy is the double of kinetic energy (internal energy in this case). Taking into consideration the energy conservation of an ideal gas, the temperature dependence of the internal energy can be characterized as follows:

$$E = E_p + U = -2U + U = -U = -\frac{3}{2}\langle N\rangle KT \tag{1.6}$$

Equation 1.6 shows that contraction of the core has as a consequence a dissipation of half of the potential energy. The immediate implication of this is the creation of a layer structure with different temperatures that can associate to each burning process. It can be concluded that the energy losses lead to a temperature increase. This implies, thermodynamically, that the star has a negative heat capacity. This contraction process will repeat at the end of any burning process, making this mechanism the most effective solution to maintain stability (until the core degenerates). However, increasing the temperature in the core accelerates nuclear reactions. This marks the start of the star's decline.

After the H→ He phase physic process accelerates, contraction continues until the core reaches a high temperature enough to start the fusion of He. This is a critical stage in the star's evolution. Respective masses of the core and the H envelope, determine the final explosion mechanism, as well as the spectrum and light curves (see **figure 1.1**)[7], in other words, the final supernova type[29]. Another consideration is how fast the burning process occurs, which depends on the star's mass. For example, regarding the supernova progenitors, the He ignition can happen relatively softly in comparison to low-star masses (0.5–2) $M_\odot$[8]. The He core can degenerate before burning out, and the pressure of this degeneracy, carried by electrons, prevents the core from expanding during the nuclear burning process, thereby increasing the burning rate. This will cause a delay in the gravitational contraction process, which restarts once the majority of the He burns. The star core is then composed of carbon, oxygen, and nitrogen, that heats again from the contraction process, and interacts with the outer H-layer. During the He burning process, no neutrino is directly produced, and the photon emission became the energy loss mechanism (see **table 1.1**). In the fusion of heavy elements since ^{12}C neutrino emission becomes the dominant mechanism of energy loss. As explained for the H-burning process, this sequence of burning and contraction creates a disruption in the core, forming an onion-like structure, with temperature dependent layers associated with a predominant nuclear burning process (see **figure 1.4**). In other words, the transport of thermal energy, conduction, convection, and radiation depends on the star's temperature gradient.

Figure 1.4 describes the external layer formation due to this contraction-burning cycle. The number of external layers depends on the mass of the star; if the star is massive enough ($\geq 10M_\odot$), this cycle keeps going, forming a core of iron. In this case, the star evolution follows the main CCSN mechanism through collapse. For lower mass progenitors, this is not the only mechanism leading to core collapse and neutrino burst. Instabilities in the core can appear after the He or Carbon production phases in lower-mass

[7]This H envelope only determines the spectrum and light curves of Type II, as Type I has lost all of this H

[8]During the burning process, a high enough temperature can enable the production of ^{12}C through the triple alpha process. This induces a rapid thermonuclear sequence of reactions called **helium flash** [31], that can lead to inflation and the production of a red giant (future evolution of our Sun)

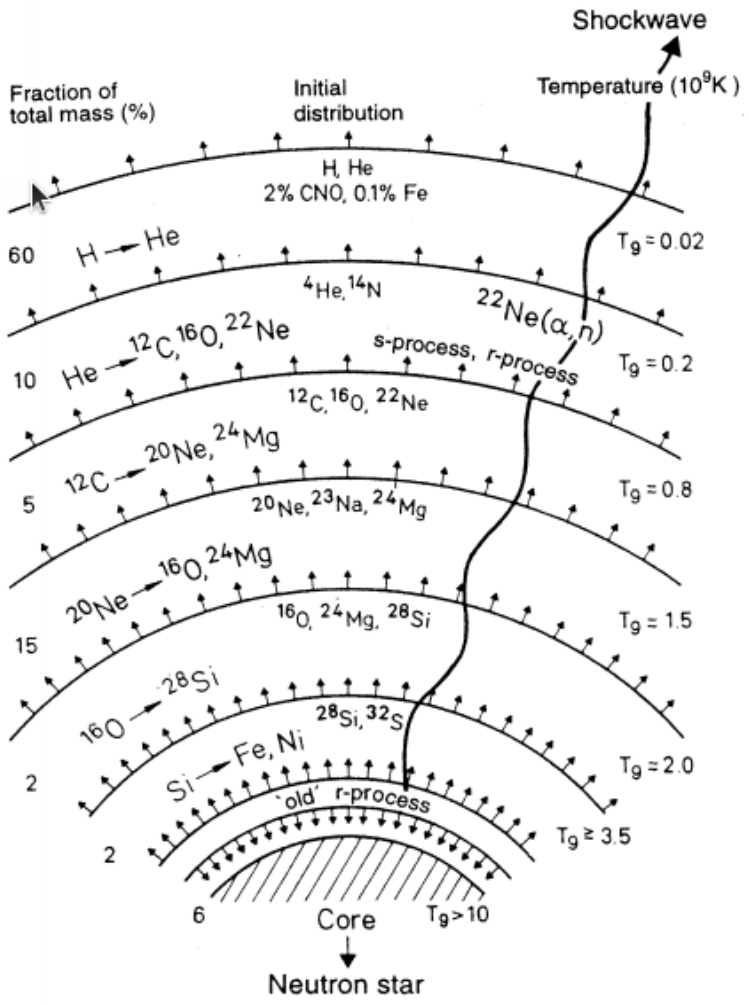

Figure 1.4: Chemical structure of a massive star about 25 $M_\odot$before core collapse and became a proto-neutron star [13]. The different layers correspond to the different hydro-static burning phases of elements of higher atomic number, up to a maximum of Fe and Ni forming iron Core.[30]

progenitors, stopping the evolution of the burning chain to iron. In the case of stars $\sim$ 8-10 $M_\odot$, electron capture core collapse (ECSN) is the principal path leading to collapse.

Figure 1.5 schematizes that said in this section concerning the evolution of the progenitors stars, through the different types of supernovae, complementing this outline of the two principal mechanisms of core collapse. In the next sections, a brief description of these two different CCSN mechanisms related to two different formation cores will be approached.

1.2.2 Iron Core Collapse

The burning cycle of stars with masses higher than $12M_\odot$ described above leads to an iron core, as/ shown in **figure 1.5**. The core is then an electron-degenerate gas, and there is not enough energy per nucleon to continue the nuclear fusion further than iron. With just the pressure of the degenerate electrons to

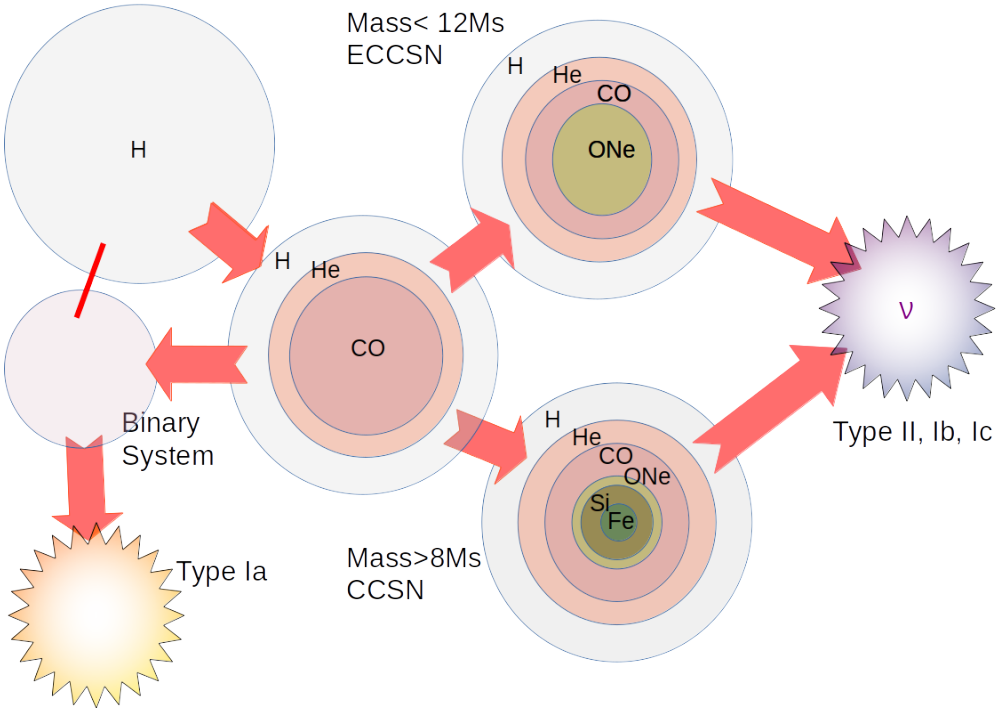

Figure 1.5: Schema of evolution for supernovae spectroscopic classification

compensate for gravitational attraction, the core collapses. This is the simplified schema of the CCSN mechanism, but from the point of view of neutrino emission bursts, the nuclear and particle physics processes that strongly link this CCSN thermodynamic description to neutrinos, must be described in order to understand the importance of their role as carriers of energy.

At temperatures around 10^{10}K [32], i.e., very high densities in the core, the Pauli exclusion principle has to be taken into account. Pressure does not depend anymore on temperature but on Fermi energy and so on the density ρ_e of relativistic electrons in the core.

$$P = \begin{cases} \text{non-relativistic} & \frac{1}{5m_e}(3\pi^2)^{2/3}\rho_e^{5/3} \\ \text{relativistic} & (1/4)(3\pi^2)^{1/3}\rho_e^{4/3} \end{cases} \tag{1.7}$$

With m_e the electron mass.

Using the equations (1.2, 1.3 and 1.6) and $\gamma = \frac{\partial \ln P}{\partial \ln \rho}$, the condition for hydro-static equilibrium is:

$$E = \frac{(3\gamma - 4)\mathrm{GM}^2}{(5\gamma - 6)} \tag{1.8}$$

For relativistic degenerate gas, the adiabatic coefficient γ is 4/3, which implies that the energy of the equation (1.6)$\approx$ 0. The system is very sensitive to energy fluctuations, associated to instabilities in temperature and density. We can relate this condition for this case, in the ultra-relativistic limit, to a critical mass of the core [33].

$$M_c = 5.72\mu_e \mathrm{M}_\odot \tag{1.9}$$

This is the so-called Chandrasekhar critical mass, expressed here as a function of the electron/nucleon fraction μ_e, that shows the horizon of collapse when the pressure of the electron degeneracy is no longer enough to contain gravitation. In the case of white dwarfs, the star becomes a neutron star when this critical mass is reached. In this ultra-relativistic limit, the critical mass does not depend anymore on the radius of the core but only on the electron density (see **figure 1.6**).

This iron core collapse phase is characterized by two main processes. The first is the photo-disintegration

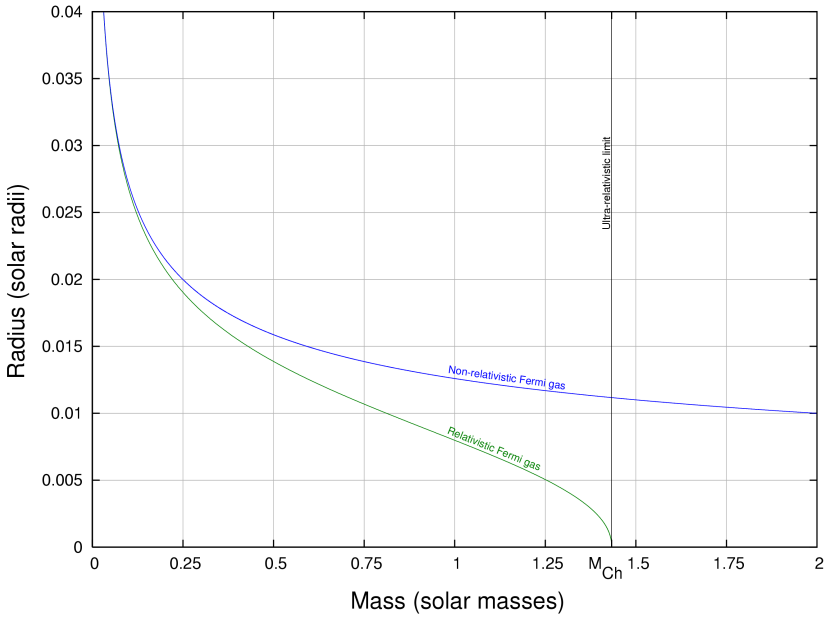

Figure 1.6: radius of the core as a function of critical mass [34]

of iron nuclei, which increases the number of neutrons. $^{56}Fe \rightarrow 13^4He + 4n - Q$. These neutrons will trap neutrinos by coherent scattering, preventing the neutrino energy from escaping the shock wave to the outer layers. The second process is the electron capture from free protons, or atom nucleus, if the Fermi energy is high enough: $e^- + p \rightarrow n + \nu_e$ and $e^- + N^z \rightarrow \nu_e + N^{z-1}$. This process reduces the electron population and, therefore, the degeneracy pressure that opposes gravity, accelerating the collapse. It is also a source of ν_e that will dominate the first milliseconds before and after the bounce of the core. Both processes are also strong sources of neutrons that *neutronize* the core, playing an important role in neutrino energy loss.

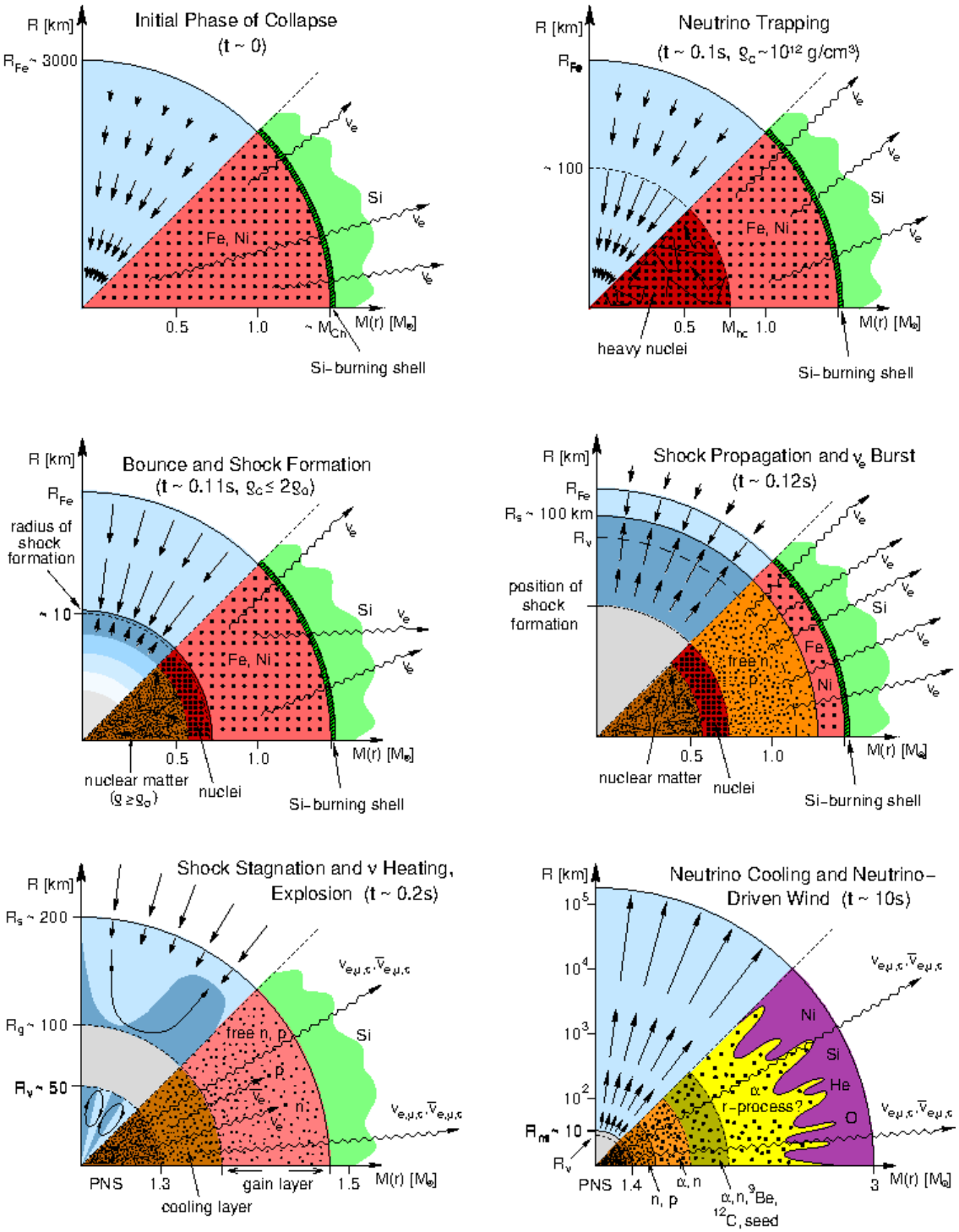

Figure 1.7: Schema of the CCSN of a massive star forming an iron core. Times represented are referenced at the time of the collapse. In the top half of the fourth part of the sphere representing the progenitor, shadowed blue region represents the motion of matter described by the arrows. The shadowed grey region correspond to the shock wave. In the other half part of the bottom layer structure as well as neutrino emission are represented. Center figures show the role of neutrinos triggering the supernova explosion [35]. Figure from [32]

After the collapse, heavy nuclei in the core continue to be produced. These nuclei are rich in neutrons, trapping neutrinos by coherent scattering, and preventing them from reaching outer layers that do not *notice* the collapse. The core is a degenerate, hot, dense gas composed of neutrons, nuclei, neutrinos, and electrons, whose degeneracy pressure drives the stability of the system. When densities in the core reach the atomic ones ($\approx 10^{14}$g/cm^3), strong nuclear force becomes repulsive, and compression of matter is no longer possible. The core bounces back, producing a shock wave moving outwards, in the opposite motion of the collapse, i.e., in the accreted matter direction, creating a shock region. The bounce energy released in the core is able to dissociate heavy nuclei, which are partially responsible for neutrino trapping. Free neutrons and protons contribute to that stage often called *neutronization*. Protons interact via electron capture, creating a huge amount of neutrinos behind the shock. The later are almost trapped by scattering with nuclei and neutrons, but also some of them, leave the core (removing their energy from the bounce shock). In summary, shock bounce looses energy by dissociating heavy nuclei, but at the same time increases the pressure inside the core.

However, this assumption of the shock leaving the core depends on the energy contained in it — most of it is kept by neutrinos – and, at the same time, depends on the equation of state of high-compressed nuclear matter in the core, which is not well known. Supernova core collapse simulations don't provide a clear answer, and in most of the cases in the supernova progenitor mass range of interest, the shock is stalled in the core, because it needs not only enough energy to stop the collapse, but also to leave the core. The core exhibits an extreme high-density, increasing energy loss of the bounced shock wave through interactions with the former matter. If the shock has enough energy to escape and produce a supernova explosion, this scenario is referred to as *prompt supernova explosion*. When this occurs, the neutrino sphere, where neutrinos are trapped, moves to the outer layers and decouples from neutrons and nuclei, leading to the first neutrinos burst. But this scenario seems to be the case only for progenitors, whose collapse leads to very small cores [36], and does not happen, when larger mass cores (> 0.5 M$_\odot$) are produced, which is the case in the 12-30 M$_\odot$progenitor mass range. Improvement of simulation for CCSN collapse, basically implementing spatial resolution of shock wave modeling, and further explosion (2D and 3D [37]) may clarify the role of neutrinos reviving the stalled shock and also have a better accuracy for the simulation of this neutrino-driven physics at this collapse phase. Particularly, capturing neutrino-driven turbulence that could push out the stalled shock wave is an important aspect of these simulations [38].

This is the main picture of the CCSN, beyond the neutrino role reviving the stalled shock, robust predictions about progenitor star evolution during collapse can be made for ones with masses above 12 M$_\odot$ forming and iron core. The last, constituting up 60% of the total CCSNe. **Figure 1.7** resumes this standard CCSN schema in the 10 seconds after the core bounce of the core and the role of the neutrino to trigger the explosion after the shock stallation. These figures emphasize the opposite motion of neutrinos and the shock wave before the bounce during the neutrino trapping. The blue shadowed regions show the motion of the shock during the 10 s neutrino burst. In the two top figures, representing times <0.1s after the collapse, the formed shock wave moves downwards. The figures in the center, represent the change of direction of the bounced matter (dark blue shadowed region) close to the core and the shock creation

at the front. The shock moves outwards, and after a few hundred milliseconds, CCSN explosions take place. Final structure of the external layers and the core of the future proto-neutron star (PNS) are formed.

1.2.3 Low mass range progenitors Core Collapse

At this point, it is convenient to describe what happens during the evolution to the collapse in stars with masses between 8-10 $M_\odot$, because this mass range is expected to be the more abundant for CCSN considering the last decades of observations [39]. Indeed, the progenitor mass distribution profile decreases as a power law [40] and considering the CCSN mass threshold of $8M_\odot$, this low progenitor mass range deserves to be regarded more in detail. In this mass range, ECSN and iron CCSN mechanisms coexist. Furthermore, this mass range is not only significant for the CCSN rate and the CCSN mechanism; in fact, it is considered a critical mass range for two primary reasons. First, in this range, the collapse can lead to a supernova explosion or directly to a white dwarf, with no explosion, if the mass of the core is not high enough (regarding the relation (1.9)) . Second, if the explosion takes place, it can happen without the formation of an iron core, but as an ECSN as mentioned before. The top part of the **figure 1.5** represents the scenario of supernovae produced in this low-mass range without an iron core but a degenerate O-Ne-Mg core, resulting from the H-He double shell burning process that becomes quickly unstable partially due to the fast electron capture from free protons and nuclei.
Ne and Mg capture electrons, releasing heat in the core, increasing its temperature, and initiating the oxygen burning process that produces heavy nuclei, Ni and Fe, and free protons, both increasing the electron capture rate and accelerating more and more the collapse. The balance between oxygen burning radiation pressure and decreasing degeneracy electron pressure due to electron capture, is crucial to attenuate the acceleration of the collapse and preserve enough energy in the shock wave, driven now by neutrinos, to make a supernova explosion happen. If density in the core is high enough due to the quick production of iron nuclei and free protons that rapidly absorb electrons, the core collapses, forming a neutron star [41]. On the contrary, if thermonuclear radiation, produced by oxygen-burning, dominates, it induces a partial explosion of the O-Ne-Mg core, leading to an ECSN [42]. O-Ne-Mg core evolution depends not only on the electron capture rate but also on the initial population of ^{24}Mg and residual ^{12}C, and the treatment of the criterion for the convective stability in supernova collapse modeling [43]. It is important to consider this mechanism, as it could represent around 30% of the supernovae population [44, 45], and on the contrary of CCSN simulations, explosions in ECSN simulations happen even in 1D [46]. However, this ECSN explosion is only partial, while 95% of the matter of the star is supposed to be released in the CCSN explosion by the standard collapse mechanism. In addition, lower neutrino profile luminosities and energies during the burst, are expected compared to a CCSN forming an iron core.
CCSN forming an iron core and ECSN will have different evolutions related to the burning process, which will lead to different evolution of temperature and density. **Figure** 1.8 shows the stage in terms of temperature and density of the different burning processes that were detailed before for three different mass ranges of iron CCSN, 12,15 and 20 $M_\odot$ and a 9 $M_\odot$ ECSN [47]. It can be remarked that the correlation

between temperature and density is always almost linear while for the ECSN it degenerates around the C burning process, finally producing collapse in a lower density region.

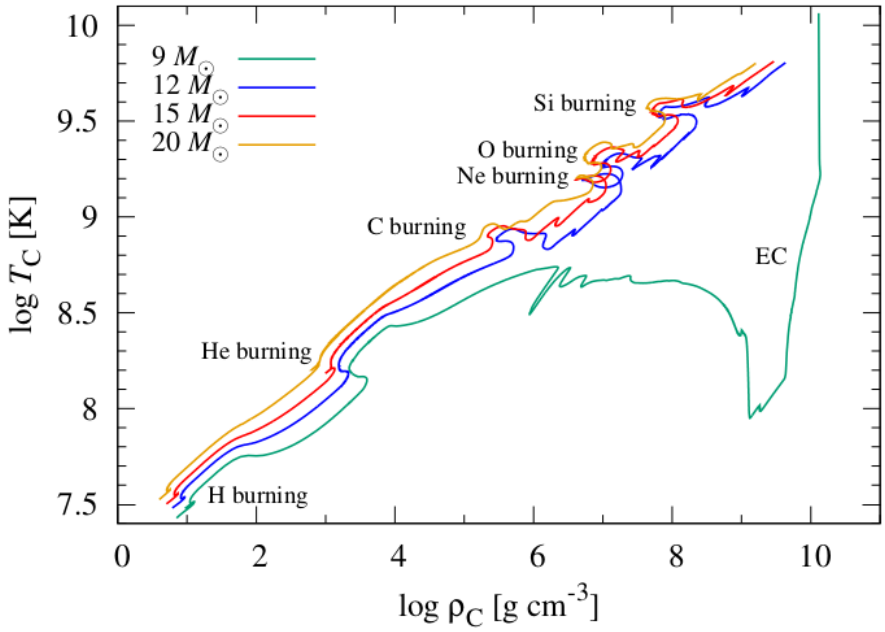

Figure 1.8: Evolutionary paths in the central density (ρ_c) and temperature (T_c) plane. The figure shows 12 (blue), 15 (red) and 20 $M_\odot$(orange) progenitors of iron CCSN and a 9 $M_\odot$progenitor (green) of ECSN[47]

1.2.4 Neutrino emission in ECSN and iron CCSN

Neutrino light curves for the ECSN and low-mass iron CCSN collapse mechanisms, can be compared to better understand their implications in the analysis of neutrino signals. **Figure 1.9** shows light curves comparing three types of core collapse supernovae in the mass range of interest: ECSN model *n8.8* (8.8 $M_\odot$) progenitor from Nomoto [48], the ECSN-like models (with an iron core formation) *u8.1* (8.1 $M_\odot$) and *z9.6* (9.6 $M_\odot$) progenitors [49], and the 9, 10,and 11$M_\odot$ solar-metallicity iron CCSN low-mass progenitors from Sukhbold et al. [50]. These curves also consider an implementation of neutrino-matter interaction simulation, including many-body corrections for the neutrino-nucleus scattering cross section [51], in dashed lines, for each model. These corrections are particularly concerned with heavy flavor luminosities, as shown in the bottom left panel. This is due to the fact that neutral current neutrino nucleus scattering is an important source of opacity for μ and τ neutrino flavors, being forbidden charged current interaction at these supernova neutrino energies. In this sense, many-body corrections decrease neutral current interactions, increasing the mean energy.

Back to the differences between the ECSN and CCSN neutrino emissions, luminosities and mean neutrino energies (especially ν_e and $\bar{\nu}_e$) are lower for ECSN during the first second after the bounce. The first milliseconds do not make too much difference in terms of mean energy, but later, star presenting differences

particle remarkables for ν_e flavor during the first tenth of a second, compared to the mean energy of lowest mass CCSN model (9.0 $M_\odot$). For ν_e flavor and iron CCSN low-mass comparison, luminosities are around 25% lower in the same period, even compared with ECSN-like models. The same behavior is found for the $\bar{\nu}_e$ flavor. For heavy flavors, luminosity differences are around 10% lower, compared to the iron CCSN low-mass model, while energies have only significant differences for the 10 and 11 $M_\odot$ progenitors of iron CCSN low mass models.

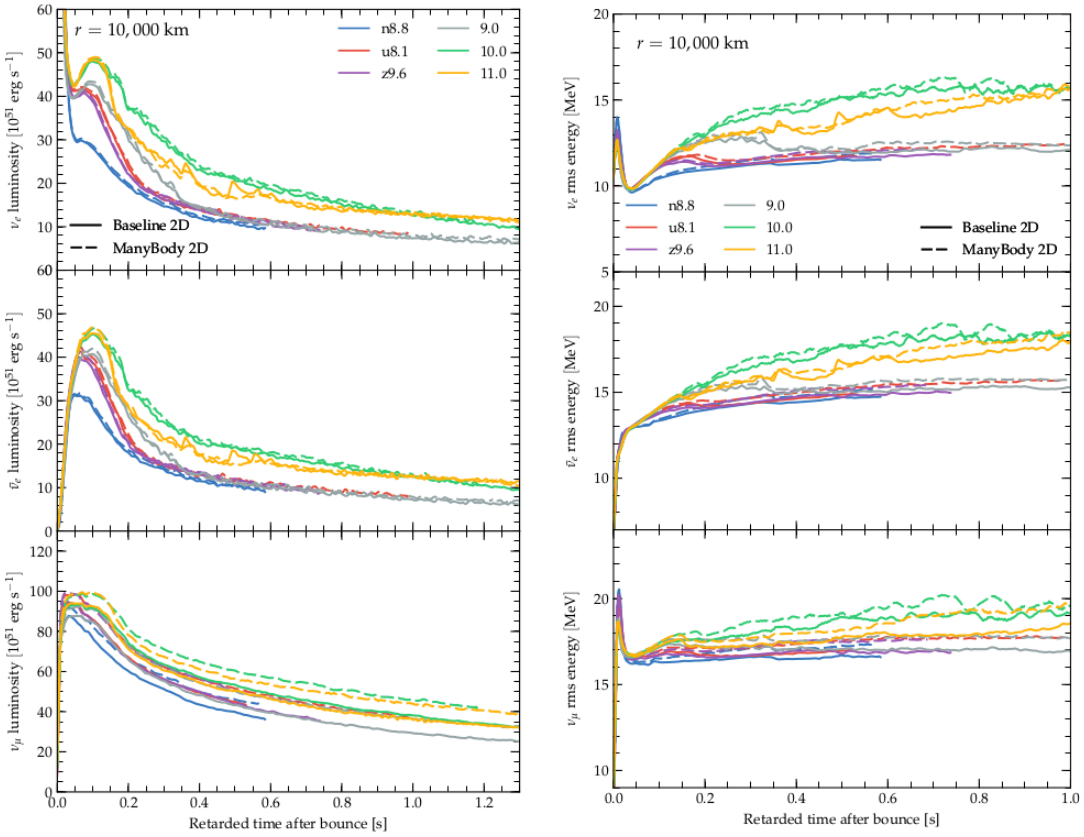

Figure 1.9: Neutrino luminosity (left panel) and rms energies (right panel) at 10^4 km as a function of the retarded time for all progenitors, for the ECSN n8.8 progenitor, the ECSN-like u8.1 and z9.6 progenitors, and the 9, 10 and 11 $M_\odot$solar-metallicity standard iron-core collapse progenitors. Here, ν_μ denotes the sum of all heavy-lepton (anti)neutrino species [46].

1.2.5 High mass range progenitors Core Collapse

Finally, considering ECSN as a substitute for the core collapse mechanism in front of an iron core does not rule out the possibility of other scenarios leading to core collapse. Beyond 25 $M_\odot$ mass progenitors, the scenario of a weak SN explosion has to be considered. In this high mass range, the form of the final remnant, as well as the likelihood of a successful CCSN explosion, depend on the metallicity of the progenitor. A critical region barely independent of metallicities, is the one between 25 and 40 $M_\odot$. Here is

expected the formation of a BH due to *fallback*, when the stalled shock is not able to escape and produce an supernova explosion. When this occurs, the shock wave front moves backward, reducing the PNS's radius. Accretion of mass continues increasing the mass of PNS, leading to a small relation between radius and PNS mass [52]. As a consequence, the formation of NS is above its maximum mass (2-3 $M_{\odot}$) [53], neutron degeneracy pressure can stand gravitational pressure and NS collapseslimit [54, 29]. This leads in this mass range, to a weak or failing neutrino-driven supernovae explosion[55, 56].

Figure 1.10 shows the possible scenarios leading to a neutron star NS including a supernova explosion,

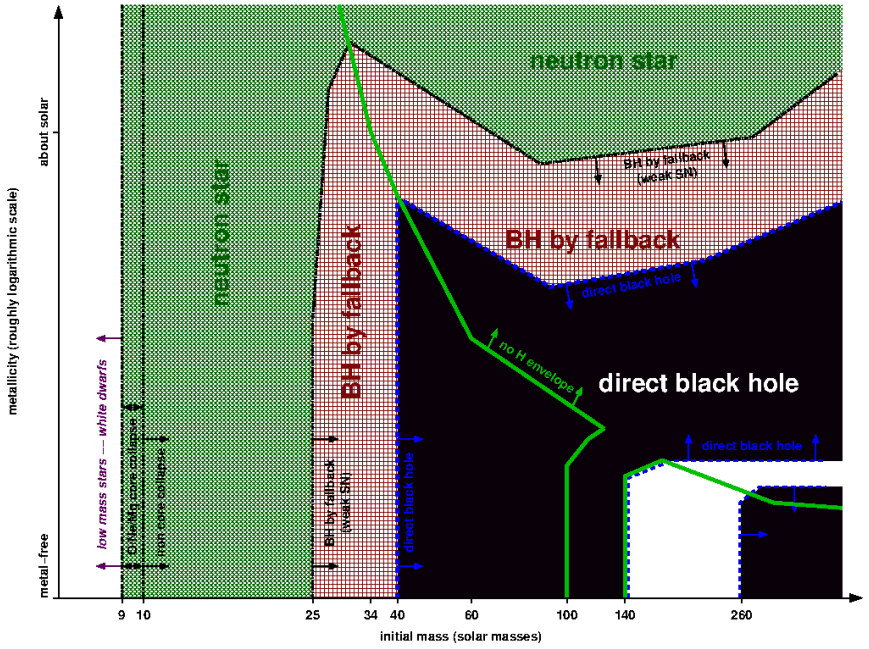

Figure 1.10: Remnants of massive single stars as a function of initial metalicity and initial mass (0-300) $M_{\odot}$. In the regions above the thick green line (for the higher initial metalicity), the H envelope is stripped during its evolution due to the active mass loss processes. The dashed blue line indicates the border of the regime of direct black hole formation. The white strip near the right lower corner indicates the occurrence of the pair-instability supernovae. In the white region on the left side at lower mass, the stellar cores do not collapse and end their lives as white dwarfs. This figure is taken from [29].

or a black hole BH including or not this explosion, in terms of metallicity as a function of the supernovae progenitors mass [57]. At first, in the low mass range progenitors, ECSN (ONeMg) and iron core collapse, limits for the mechanism that starts dominating are represented by a black doted line at 9 and 10 $M_{\odot}$respectively, with arrows that extend those limits to the range, that has been assumed in the last section 8 to 12 $M_{\odot}$. For metallicities close to the solar one ($ZM_{\odot}$=0.02), the supernova explosion can also be produced leaving a neutron star remnant in the mass range 9-25 $M_{\odot}$. Regarding the evolution of remnants for progenitors with metalicities greater than solar, chances of NS are dominant in front of BH. The large green line crosses this high metallicity region, defining the limits of the H-envelope. This implies that

this line is also the boundary between SN-Type II and SN-Type-I, having the Type II his H-enveloppe, as explained in **Section 1.1**. It is expected that the explosion of Types Ib/Ic around solar metallicities to be unsuccessful, resulting in the formation of a black hole. At least that Type Ib/Ic have metallicities more large than solar they not produce a supernova explosion, producing a NS, out of the weak fealing supernovae (pink shadowed region). However, recent studies, e.g. [58], suggest that no conclusive direct relation between ZAMS mass and metallicity of the progenitor exist, remaining the fate of the CCSN a debated issue.

Finally, supernovae from progenitors with masses larger than $40M_{\odot}$are expected to lead directly to a BH formation. CCSN from progenitors of $40M_{\odot}$ and $ZM_{\odot}$[59] simulations were performed leading to a partial neutrino-driven supernova explosion, releasing about a half of the energy of the iron CCSN predicted one. However, the power of this neutrino burst is higher, as it's duration is around 1s, which is almost the duration of BH formation, but can be extended, presenting an emission tail of 15 ms [60]. **Figure 1.11** shows the neutrino light curves for this $40M_{\odot}$ progenitors. The duration of the burst is around 500 ms, this makes the emission rates very intense, and it's dominated by the ν_e flavor in the first mili-seconds. In comparison to the iron CCSN, neutrino mean energies (see **Section 2.2**), this massive progenitor present higher values: $\sim$ 17, 22 and 25 MeV for the $\nu_e, \bar{\nu}_e$ and ν_x respectively (with x$\equiv \mu, \bar{\mu}, \tau, \bar{\tau}$).

For more massive stars finally producing a black hole remnant *gamma ray burst supernova, or Hypernova*

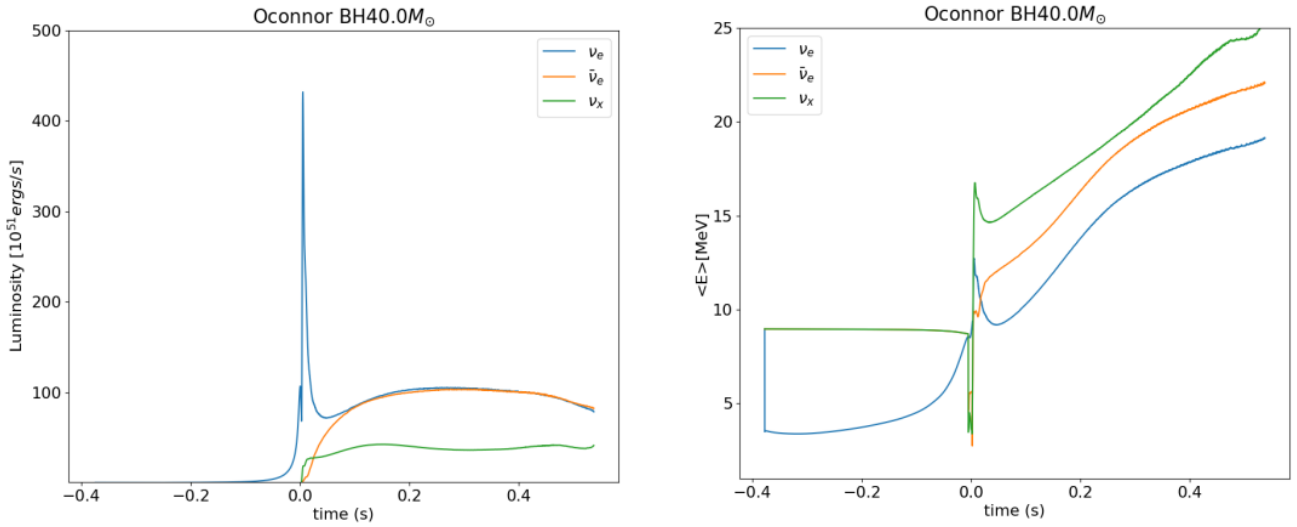

Figure 1.11: Luminosities(left) and Mean Energies(right) for a BH fallback progenitor with solar metalicity and 40 $M_{\odot}$from [61]. The heavy flavor are normalized and x$\equiv \mu, \bar{\mu}, \tau\bar{\tau}$.

HN [62] and a *pair instability supernova* ($>100M_{\odot}$)[63] are also subjects of study, implying considerable differences in the core evolution, collapse sequence, and final explosion. However, these last ones are less abundant, representing less than a 1%, as it is expected, from the last CCSNe observations, that their population decreases following a power law relative to the progenitor mass [64, 39].

1.3 Supernova Core Collapse Observations

Across centuries and civilizations, ancient astronomers have observed supernova explosions with their naked eyes. Recent studies suggest the existence of astronomical observatories during the Stone Age [65], emphasizing the role of astronomy for ancient humans, which included celestial objects in their *cosmos*. However, records of these observations date back only thousands of years. It is known that the sky has been surveyed in the last two millennials by Chinese astronomers, and two confirmed CCSN observations have been reported, at least in the last 13 centuries, by astronomer Yi Xing [66]. But older ones occurred during the 4th century AC, supernova185 and supernova 393, which could also be classified as CCSN [67]. The two last ancient observations of supernovae correspond to the Type Ia SN 1572 and SN 1604 observed by Tycho Brahe (in 1572) and Johannes Kepler (in 1604) respectively, which have also been reported by Arabs and Chinese astronomers. Cassiopeia A remnant of a Type II supernova can also be included, as its light should have arrived to the earth around 1667 [68]. However, no trace of these observations has been found yet. An inverse exercise than for Cassiopea A can be done using ancient supernova observation reports, in order to look for the supernova remnants. In this sense, these observations are precious, as having an estimation of the location of these supernova events in the sky, their context, and the further evolution of their supernova remnants can actually be better understood. Pointing to this ancient supernova observation region with our telescopes post-supernova systems can be studied and compared with similar more recent observations, inferring on other non-reported supernovae that happened in the past, complementing a study of thousands of years. Also, these reports are crucial to anticipate next supernova observations, enhancing the observation time exposure and allowing the estimation of the supernova rate on a larger time scale (per century), as it will be explained in the next section. A timeline of the mentioned supernovae observations with their respective spectroscopic classification, is represented in **figure 1.12**.

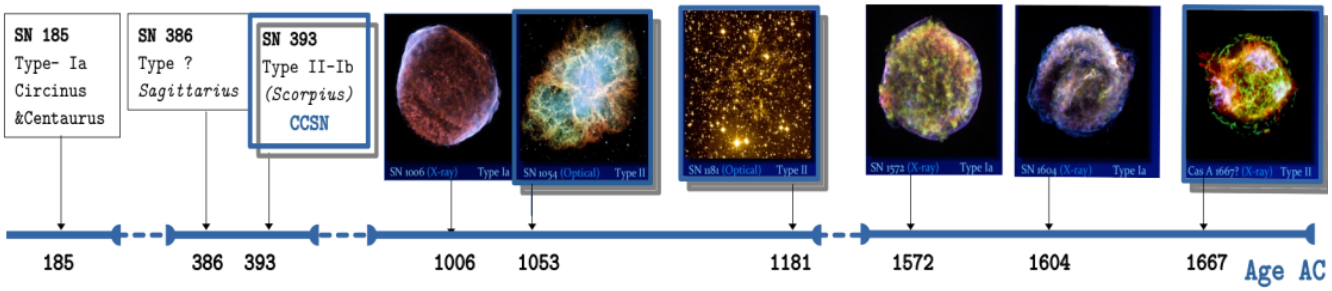

Figure 1.12: Historical reports of supernova observations: Name, Type (*Constellation*). Observations classified as CCSN are highlighted in blue and are: SN 1006, Type Ia; SN 1054, Type II;SN 1181, Type II; SN 1572, Type Ia; SN 1604, Type Ia and Cassiopea A 1667, Type II.

The likelihood of these observations depends not only on the supernovae distance and the progenitor mass, proportional to its luminosity, but also on the position of the observer. Prior to the 19th century, the majority of reports on SNe observations came from the northern hemisphere. With the development of terrestrial telescopes in sky-clean and remote observatories around the world at the beginning of the last

century and spatial telescopes, and in addition particle detectors in the last decades, complete supernova sky map observations have been performed, and their number is increasing today exponentially with the deployment of new generation of telescopes. However, the numerous observations and spectroscopic classifications of these supernovae are not enough to understand the physics that led to their generation. Not only in the microscopic process into the core before Supernova, but also macroscopic — or thermodynamic — parameters that could be crucial for the progenitor evolution.

1.3.1 On the next CCSN

CCSN Neutrino detection can complement other neutrino studies at MeV-scale, with information derived from their transformation during their travel to the Earth, such as matter effects in the high density supernova medium (Mikheyev-Smirnov-Wolfenstein MSW effect, see e.g. [70]), leading to observable effects on the neutrino mass hierarchy, see e.g. [71], or some more exotic physics, like neutrino magnetic moment, see e.g. [72]. But also, the detection of neutrinos from CSSN, among this cited neutrino physics, could contribute to the understanding of paramaters, such as metallicity or nuclear reaction chains for massive stars (nucleo-synthesis). Particularly, these neutrinos have useful information to study the Equation of State (EoS) inside high-density progenitors core in the last instants of their lives, which is dominated by weak nuclear interactions. Finally, as already mentioned in **Section 1.2.2** they play an important role in the CCSN collapse, reviving the stalled in the named *neutrino-heat-mechanism*. To study them, it would be desirable to have a high rate of this supernova neutrino signal, but unfortunately, the estimation of CCSN rates turns out to be roughly one or two per century. This approximation is, of course, constrained by how far our detectors can see a supernova neutrino burst.

According to the actual state of CCSN neutrino detection techniques, *to see further* implies scaling detection volumes, or target masses [9] as the arriving neutrino flux is scaled by the inverse of the square of the supernova distance (see **Section 2.6**). Considering historical reports of SN393 and SN1053, the rate of CCSN in our *Local Group*[10] have been estimated thanks to the more prolific supernova detections of the last century 1.63 ± 0.46 [66] and $3.2^{+7.3}_{-2.6}$ [73] per century in the Milky way (MW). Since the last local group Supernova, the SN1987A, was 37 years ago, neutrino experiments are therefore optimistic about detecting a CCSN neutrino burst signal in the next few decades. These experiments expect to constrain, in terms of supernova distance, a region with enough high rates to reconstruct the neutrino energy spectrum and luminosity curves. In this sense, it is important to determine the most probable distance to detect the next CCSN to better understand and improve the detection capacities. It's difficult to find in the literature a clear answer to this most probable distance value, and detection sensibility is often expressed in a large range of 1 kpc to 1 Mpc[11] (for larger neutrino detection volumes). The Sun is around 8.3 kpc from the center of the MW, where massive star populations and binary star systems should be more abundant

[9] For the Cherenkov light detectors or neutrino coherent scattering ones, cross section and rate exposure are proportional to detector target mass

[10] Local group is refereed to the Milky Way and Andromeda Galaxies

[11] Interstellar distance is often measured in *parsecs* pc = $3.085\ 677\ 581 \times 10^{16}$ m

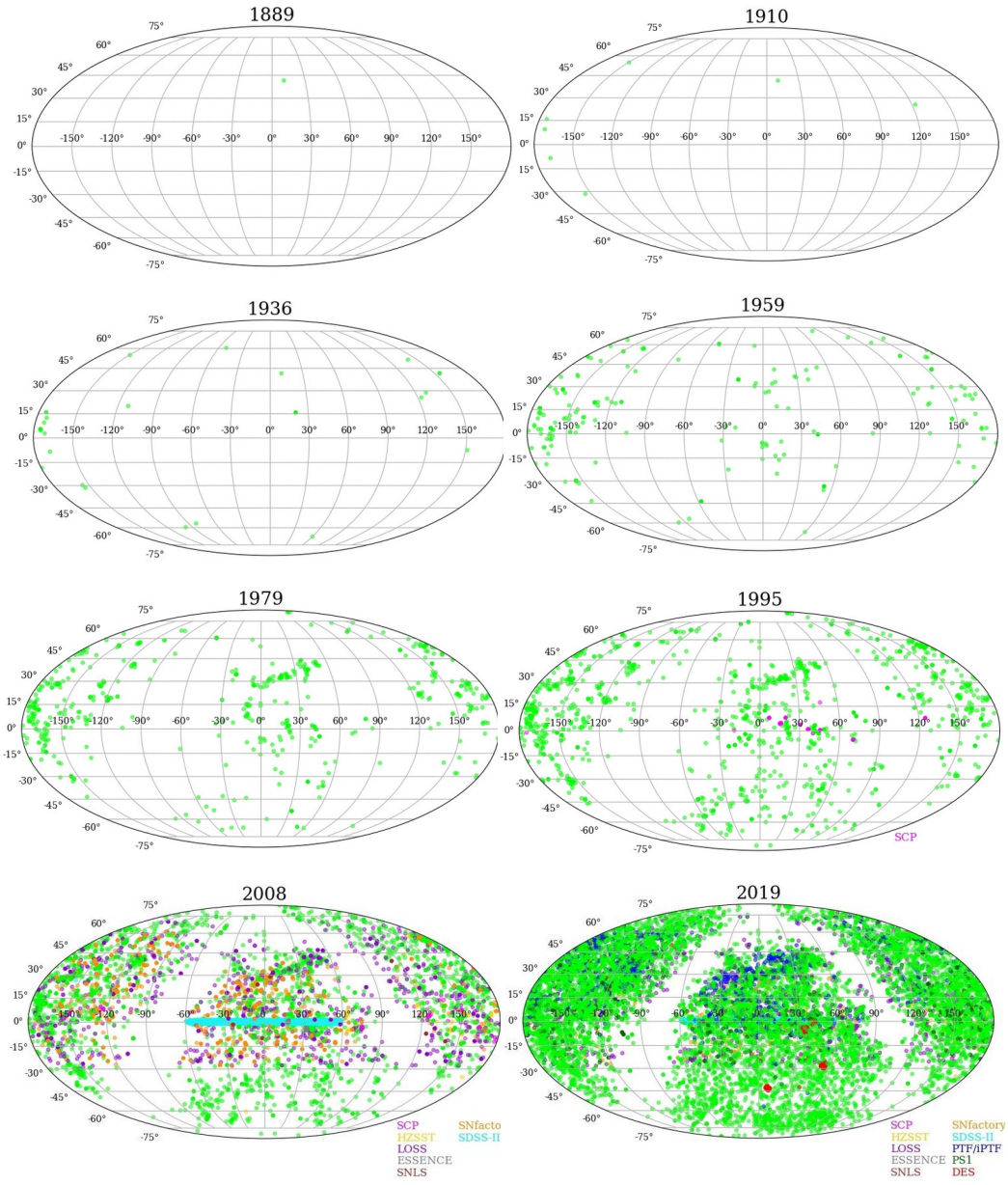

Figure 1.13: Sky map of supernova observations between 1889 and 2019[69]

[74]. Failing to find enough explicit studies regarding CCSN probability as a function of the distance [12], it seems to be some consensus in recent CCSN neutrino detection literature, that the next galactic supernova probably will happen close to the center of the MW. In order to scale the detection signal of the CCSN

[12] As an exception recent study (2013)[73], based on a Monte Carlo simulation of the positions of Galactic supernovae and their corresponding dust extinctions.

neutrinos, is convenient to estimate a *typical* distance and MW center is often rounded to 10 kpc [75, 76].

1.4 Summary

CCSN progenitor stellar evolution until collapse and final supernova explosion forming a neutron star (or black hole), have been described, emphasizing the role of neutrinos as carriers of gravitational energy, but also their importance in reviving the stalled shock during the core collapse after the core bounces. However, simulations do not give a complete description to this explosion mechanism. The standard iron CCSN mechanism leading to a detectable neutrino burst at the Earth was described, showing that there is a critical mass range between 8-12 $M_\odot$representing a significant population of supernovae where a different mechanism, ECSN, is able to generate a similar explosion with a consequent neutrino burst. Indeed, based on recent simulations, this mechanism appears to be more effective in triggering the explosion, as it doesn't require 2D spatial simulation to account for convective effects in the neutrino-matter interaction energy transfer. It's interesting to take into account the ECSN mechanism regarding these simulation results; furthermore, they are supposed to happen in a progenitor mass range where the CCSN are more abundant. However, it has also to be accounted for that the neutrino emission is expected to be lower. As this work is focused on the CCSN neutrino detection in ton-scale dark matter detectors, beyond **Chapter 2** only iron CCSN will be accounted for in this low mass range. In addition, this work also reduces the mass range of the progenitors to the range of 11–27 $M_\odot$; with 11 $M_\odot$representing an approximation of the required minimum progenitor mass to produce an iron CCSN; and 27 $M_\odot$a more arbitrary maximum progenitor mass leading to a CCSN neutron star remnant, assuming that, at this mass, the fraction for failing collapse leading to a Black Hole formation is not relevant [55][12]. This $27M_\odot$value is also justified by the choice of the majority of CCSN models, as it will be shown in **Section 2.4**. It can be added that iron CCSN from massive progenitors is expected to be significantly less abundant, as mentioned before (see [55, 39, 40]). Finally, in **Section 1.4** the historical supernova observations are overviewed in order to understand when and where the next CCSN will be, concluding that its most probable detection should happen in the next decades (in this century) around our galactic center. Consequently, the next chapters will often represent 10 kpc in the supernova neutrino flux, interaction rate, and simulation results plots.

Chapter 2

CCSN Neutrino emission

2.1 Introduction

This chapter shows the state of the art on our knowledge on neutrino emission from a Core Collapse Supernova (CCSN). Among the many models presented, a special attention is done on few of them that will be used later on, in the next chapters, to perform the studies on the detectability of CCSN with XENON.

Upon the completion of a collapse process, the remaining core material either forms a black hole or a neutron star The binding energy of a neutron star is the amount of energy needed to bring together a finite number (N) of baryons to create a stable star. Supernova neutrino bursts are a useful tool for measuring the remnant gravitational binding energy, since it carries 99% of this energy [77]. Over the course of about ten seconds, neutrinos with energies greater than 10 MeV unleash this enormous quantity of energy. Unlike photons, which are confined in an absorption-re-emission cycle, neutrinos interact only weakly and can readily escape. Therefore, when a star collapses, neutrinos are predicted to arrive hours or days before the first photons can be seen.

This chapter will go into extensive detail about those $\sim$ 10-second neutrino burst. In particular, it will explain the physics of the many processes that result in the creation of neutrinos in the proto-neutron star (PNS) environment. The CCSN neutrino signal is time-dependent, and flux evolution is expected to present peaks even if it has a short duration. As it will be shown, the time evolution of this neutrino flux may be used to identify three main phases of a neutrino burst: *neutronization, acretion*, and *cooling*. These phases differ in terms of neutrino flavor composition, energy, and luminosity. The *supernova neutrino light curves* (**Section 2.2**) are commonly used to display these three parameters, which describe the neutrino initial spectra that will be detailled in (**Section 2.3**).

Only one neutrino signal was found with sufficient statistics to reconstruct the neutrino energy spectrum, as stated in **Chapter 1** [1]. Therefore, simulations are commonly used to model the neutrino flux, which can lead to a significant degree of uncertainty. A summary of the current state of CCSN neutrino models will be presented in **Section 2.4**, focusing specifically on the mass range that is of interest (10-30 $M_{\odot}$). One of the causes of these uncertainties arises from the propagation of neutrinos within the CCSN

environment. To understand this, it is conducted in **Section 2.5** a comprehensive examination of the factors that specifically impact the transport of neutrino flavors. Finally, the **Section 2.6** shows the observable flux of CCSN neutrinos at the Earth.

In the rest of the manuscript, the *natural units* will be adopted: $\hbar \equiv c \equiv 1$. This implies no distinction between mass, frequency and energy, as well as [Energy]≡[1/length] [1].

2.2 CCSN Neutrino burst

The primary mechanism for neutrino generation in a star is the electron capture (EC), that occurs long before the core collapses. As stated in **Section 2.3**, the production of neutrinos, which are predominantly composed of the ν_e flavor, plays a crucial part in the collapse process as one of the primary mechanism for energy loss. EC neutrinos can interact with atomic nuclei, particularly with neutrons. These neutrinos are confined in the more condensed region, which has a density of approximately 10^{11}g/cm^3, and are unable to reach the outer layers. At this density the neutrino mean free path λ_ν falls below the core radius $\lambda_\nu > R_{CORE}$ and the core becomes opaque for neutrinos, leading to the apparition of the named "neutrinosphere" [79]. The neutrinosphere can also be defined as the region in which neutrino start free streaming, as its density is lower than the core region which will reach higher densities. Neutrinos retain the internal radiation energy around the core and in the shock wavefront after the core collapses. The thermal energy carried out by neutrinos is essential for reinvigorating the stagnant shock, in the event that the shock wave becomes stale, propelling it towards the outer layers and ultimately resulting in a supernova explosion. Neutrino scattering with heavy nuclei in a high-density region is commonly referred to as "Neutrino trapping". Nevertheless, low-energy neutrinos can penetrate (or may have already penetrated, prior to collapse) the outer layers due to the fact that their interaction with atomic nuclei is influenced by their energy, denoted as E_ν, as demonstrated by equation (2.3). This leads to a pre-supernova neutrino flux, primarily consisting of ν_e with a lesser contribution of $\bar{\nu}_e$[2], with energies lower than CCSN neutrinos ($<$ few MeV) but with similar luminosities[3] [81].

The shock wave reaches a sufficient level of energy to exit the core and neutrinos are able to escape and reach the outer layers. This results in the initial emission peak in the flux of supernova neutrinos, occurring within the first few milliseconds after the core bounces[4]. The neutrino flux possesses an overall energy that is approximately 99% of the difference between the binding energy of the PNS and the gravitational energy contained within the initial core, which will eventually transform into a neutron star [82]. Thus, the ultimate binding energy of a neutron star can be described as [13]:

[1] Otherwise we would have $\hbar$ c = 197 MeV fm[78]

[2] Since the hydrogen burning stage, pair annihilation production $e^- + e^+ \rightarrow \nu_e + \bar{\nu}_e$ dominates as neutrino production interaction in low core densities before heavier nuclei are produced [80]

[3] The luminosity of ν_e population is estimated around 10^{55} s^{-1} (10^{57} s^{-1}) before the core collapses (bounces) for a 15 $M_\odot$ progenitor.

[4] All time scales and time ranges are measured relative to the moment when the core of the progenitor star undergoes a rebound. In **Section 2.4**, certain models display negative timings (prior to bounces) to account for the first electron capture neutrinos that successfully evade the neutrino-sphere

$$\Delta E = GM_{core}^2(\frac{1}{R_{PNS}} - \frac{1}{R_{core}}) \approx \frac{3}{5}\frac{GM_{NS}}{R} = 3 \times 10^{53} erg \frac{(10\ km)M_{NS}^2}{R_{NS}(1.4\ M_\odot)^2}. \quad (2.1)$$

This provides the magnitude of the energy released based on the ultimate mass and radius of the neutron star. The value of $\mathcal{O}(10^{53}$ erg) is 100 times greater than the energy required for a CCSN explosion, which is $\mathcal{O}(10^{51}$ erg), as discussed in **Section 2.3**. Essentially, this means that only a small fraction, specifically 0.1-1.0%, of the binding energy needs to be converted into neutrinos in order to heat up the stalled shock and resuscitate it, thereby initiating the supernova explosion. This is a critical issue in the simulation of neutrinos in supernovae, namely the delayed explosion mechanism caused by the stalling of the collapsing shock wave (see **Section 2.3.1**). This topic will be revisited in **Section 2.4**.

Another crucial factor to consider is its temporal profile or shape. The temporal progression of the flux is connected to the moments preceding the rebound and following the detonation, encompassing a duration of around one-tenth of a second during which various interactions leading to neutrino generation occur. The next sections will outline the distinct stages of this neutrino emission and the corresponding mechanisms responsible for neutrino generation. **Figure 2.1** displays the temporal evolution of neutrino emission for several flavors, utilizing the simulation from the *Bollig 2016* Model [75]. It is important to note that the evolution of time in this context might result in variations between models due to the influence of many simulation parameters, specifically the equation of state (EoS), supernova explosion process, and neutrino-matter interaction physics. Nevertheless, certain resilient characteristics of core collapse theory can result in a common temporal shape and a prevailing production process for each of the three described phases. The neutrino emission during the processes of neutronization, accretion, and cooling, is linked to the population hierarchy based on neutrino flavor: $N_{\nu_e} > N_{\bar{\nu}_e} > N_{\nu_x \equiv \nu_\mu, \bar{\nu}_\mu, \nu_\tau, \bar{\nu}_\tau}$. Electron neutrino flavor dominates during neutrinosation, while electron antineutrino flavor appears to be significant during the last moments of this neutronization phase (see **figure 2.1**). Finally, it is expected that the emission of heavy-flavor neutrinos[5] happens during the accretion phase before supernova explosion, as its production requires a region with very high density of energy.

2.2.1 Neutronisation phase

The neutronization phase occurs within about 0.05 seconds after the bounce [86]. This period, in the context of neutrino observation, is linked to the initial peak of neutrino emission. This does not imply that the supernova explosion occurs during neutronization. In fact, the collapse shock wave does not have enough energy to reach the outer core region yet, adhering to the delayed explosion process. Neutronisation occurs when the center of a collapsing core achieves densities higher than those of atomic nuclei, causing the nuclear force to become repulsive, pushing matter back. The matter motion is reverted due to the bounce, causing the dissociation of heavy nuclei. This nuclei are mainly responsible for neutrino trapping

[5]Heavy-flavor neutrino refers to ν_μ,$\bar{\nu}_\mu$,ν_τ,$\bar{\nu}_\tau$, due to their associated leptons μ and τ that are heavier than electrons. As their contribution to the CCSN neutrino initial spectra is equivalent, there are often designed by an x, see e.g. [83, 84, 85]. Furthermore, their respective masses m_{ν_μ} and m_{ν_τ} are expected to be heavier than m_{ν_e} in the normal mass ordering (see **Section 2.5**)

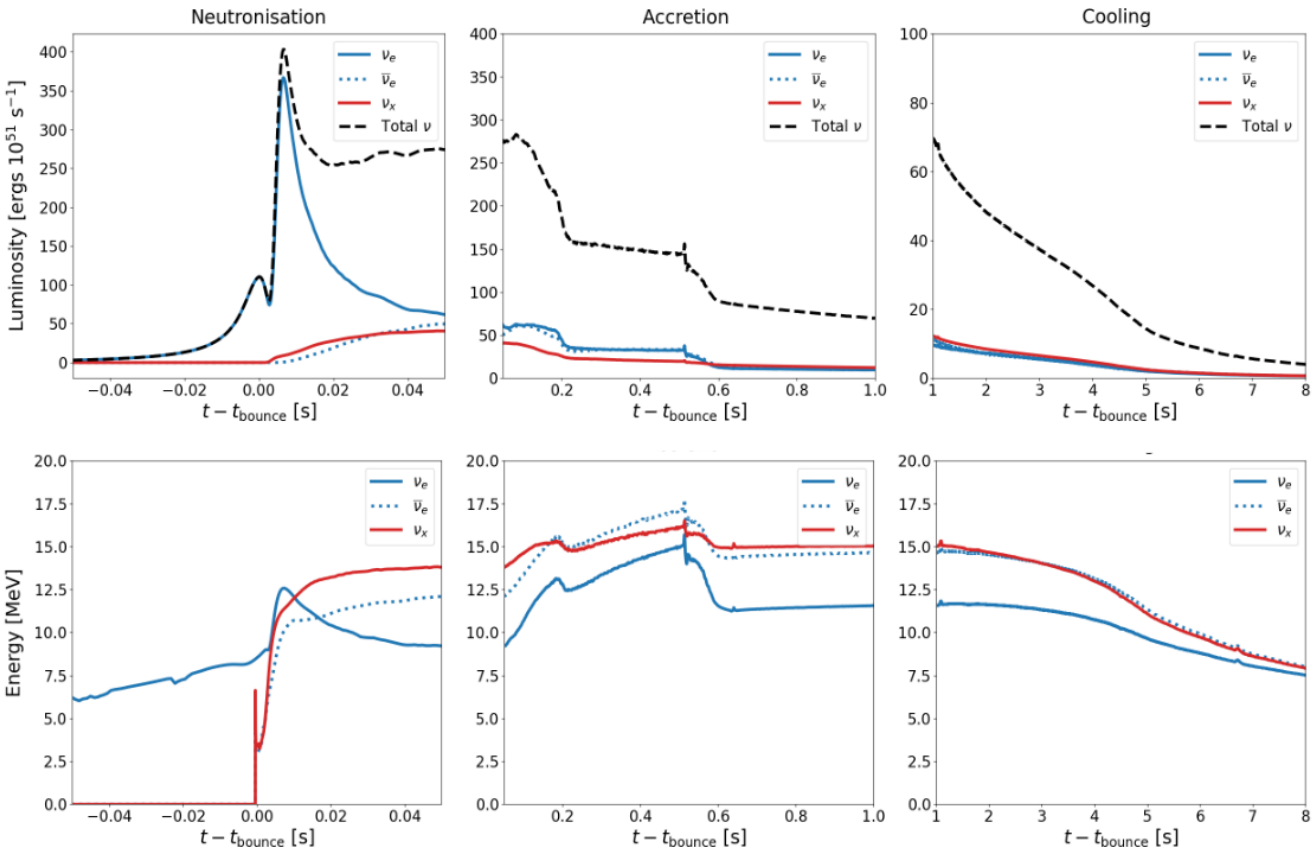

Figure 2.1: The upper and lower panels show the neutrino luminosity L_{ν_β} and mean energy $\langle E_{\nu_\beta} \rangle$, respectively, as a function of the post-bounce time $t_{\rm pb}$ for the Bollig Model $27M_\odot$[75] supernova progenitors with the LS220 EoS for ν_e (blue continuous lines), $\bar{\nu}_e$ (blue dot lines) and ν_x (red continuous lines). The total neutrino luminosity is represented by a black continuous line, here it is assumed that luminosities of all heavy-flavor have an equal contribution $\sum_{i=\mu,\tau,\bar{\mu},\bar{\tau}} L_i = 4L_x$. The panels on the left show the neutrino properties during the neutronization burst phase, the middle panes refer to the accretion phase, and panels on the right describe the Kelvin-Helmholtz cooling phase. Figure taken from reference [86].

through coherent scattering, as the scattering cross-section is proportional to the square of the atomic number (denoted by A) of the heavy nuclei:

$$\nu_e + A \Longrightarrow \nu_e + A. \tag{2.2}$$

Neutrinos start free streaming at the neutrinosphere. Free protons and nuclei contribute to the neutronization process as they interact with electrons through electron capture, resulting in the generation of neutrons and respective electron neutrinos (see equation (1.4)). This results in the prompt neutrino burst removing the lepton content from the core and acquiring the binding energy of dissociated nuclei, which accounts for approximately 10% of the mass of the iron core. The initial burst of electron neutrinos

from electron capture is mostly unaffected by the specific model and is considered a reliable forecast of supernova neutrino emission.

The energy of the neutrinos from the neutronization burst is around 10 MeV. This low energy is a consequence of the trapping of high-energy neutrinos, primarily through coherent scattering with neutrons. The preference for neutron-neutrino interaction arises from the reduction of neutral current (NC) interactions with protons by a factor of $1 - 4sin^2(\theta)$, where θ represents the Weinberg angle. This preference becomes significant in the core, which contains an abundance of free neutrons and neutron-rich nuclei resulting from electron capture. The coherent scattering cross-section can be approximated as stated in reference [13]:

$$\sigma \approx 10^{-44} cm^2 N^2 (\frac{E_\nu}{MeV})^2, \tag{2.3}$$

where N is the neutron number in the nuclei, as interaction with protons in nuclei is reduced. This trapping process also contributes to the conservation of lepton number, compensating electron losses through EC.

During the neutronization phase, approximately 5% of the total neutrino flux is emitted during a time span of around 0.01 seconds. This emission mostly releases trapped electron neutrinos by electron capture. The light curves depicted in **figure 2.1** illustrate the temporal changes in luminosity (top) and average energy (bottom), differentiating the aforementioned classification into three flavors. Prior to its collapse, the core was already a significant emitter of ν_e. Therefore, the brightness immediately following the core bounce reaches around 10^{53} erg/s, primarily due to the low-energy neutrinos that manage to escape from the trapping process. The energy of ν_e intensifies as the shock wave infiltrates the neutronisphere for approximately 0.01 seconds, thereby liberating confined neutrinos. As depicted in **figure 2.1**, this phenomenon results in the emission of a burst of ν_e neutrinos, with a brightness peak of $3.5 \cdot 10^{53}$ erg/s. The luminosity of ν_e decreases until the end of neutronization, at which point the luminosities of all flavors converge to a similar magnitude. This phenomenon is also found in the evolution of neutrino energy. This occurrence is a result of the initiation of $\bar{\nu}_e$ production through charged current interactions, namely an increase in the abundance of positrons that are subsequently caught by neutrons. Additionally, ν_x production occurs through bremsstrahlung and neutrino pair conversion. For further details, see **Section 2.2.2**.

Finally, the main neutrino production mechanism in this neutronization phase can be summarized:

$$\text{Charged current interactions} \qquad e^- + p \implies \nu_e + n \tag{2.4}$$

$$e^+ + n \implies \bar{\nu}_e + p \qquad \text{from} \quad (\gamma + \gamma \Longrightarrow e^+ + e^-) \tag{2.5}$$

$$e^- + A \implies \nu_e + A^* \tag{2.6}$$

$$\text{Bremsstrahlung} \qquad N + N \implies N + N + \nu_{e,x} + \bar{\nu}_{e,x} \tag{2.7}$$

$$\text{Pair annhilation} \qquad e^+ + e^- \implies \nu_{e,x} + \bar{\nu}_{e,x} \tag{2.8}$$

$$\nu - \nu \text{ interaction} \qquad \nu_e + \bar{\nu}_e \implies \nu_x + \bar{\nu}_x \tag{2.9}$$

$$\nu_e + \bar{\nu}_x \implies \nu_x + \bar{\nu}_e \tag{2.10}$$

2.2.2 Accretion phase

The accretion phase is marked by a rise in temperature, leading to the thermal generation of neutrinos and antineutrinos of various flavors. This is primarily caused by pair annihilation and nucleon bremsstrahlung. Nevertheless, the emission of electron and heavy-flavor neutrinos flavors has distinct characteristics throughout this period. As a result, the neutrino flux can be divided into two components. The first is related to a diffusive thermal emission of neutrinos. It calls for accounting for interactions at the surface of the PNS. This flux component impacts all neutrino flavors and can be characterized by a black body emission law, employing a deviation factor ϕ [87]:

$$L_{diff} = 4\pi\phi\sigma_{fermi}R^2T^4, \tag{2.11}$$

where $\sigma_{\text{fermi}} = 4.5 \times 10^{35}\,\text{erg MeV}^{-4}\ \text{s}^{-1}\ \text{cm}^{-2}$. The second component of the neutrino flux, out of the PNS, is more intricate and is connected to the micro-physics, impacting electron and heavy flavors in distinct ways. This difference mostly arises from the diminished interaction of the heavy flavors with nucleons through charged current (CC) interactions at the expected neutrino energies (<100 MeV). In addition, it is worth noting that the emission of heavy-flavor neutrinos occurs in a region with a lower density outside the PNS. This is because a density of around $10^{13}g/cm^3$ is necessary for the generation of heavy flavor neutrinos by nucleon bremsstrahlung and neutrino pair annihilation, as mentioned in reference [13]. The convergence of all these factors leads to a predominant contribution of neutrino electron flavors, ν_e and $\bar{\nu}_e$, in comparison to the $\nu_\mu(\bar{\nu}_\mu)$ and $\nu_\tau(\bar{\nu}_\tau)$ heavy flavors. **Figure 2.2** depicts the initial structure of the progenitor during the phase of accretion prior to the occurrence of a supernova explosion. The PNS core achieved densities equal to or more than $10^{14}g/cm^3$ following the immediate release of neutrinos [13]. This is a result of the core contracting due to the loss of radioactive energy carried by the expelled neutrinos. In the Mantle region immediately surrounding the PNS as depicted in the **figure 2.2**, energy transfer from all flavors with the PNS is mostly driven by convection. This energy transfer also occurs between the neutrinosphere, where ν_e and $\bar{\nu}_e$ constitute the main flavor, and the exterior layers. In these locations, the interactions of ν_e and $\bar{\nu}_e$ with matter help maintain hydrostatic equilibrium, as seen by the "radiative equilibrium" zone in **figure 2.2**. This image depicts the radial position of two emission flux components: the thermal diffuse component near the PNS core in the Mantle and the other in the radiative equilibrium region. The shock wave gathers matter from regions of low density and comes to a halt outside the PNS due to the loss of energy as it traverses the core. As previously mentioned, neutrinos are believed to transfer a portion of their energy by heating up the shock wave and pushing it towards the outer layers. CC interactions involving ν_e and $\bar{\nu}_e$ with unbound nucleons can be included in nucleon

scattering to enhance energy transfer and reignite the shock wave.

$$\text{Main heat transfer charged current interactions} \quad \nu_e + n \implies e^- + p \tag{2.12}$$

$$\bar{\nu}_e + p \implies e^+ + n \tag{2.13}$$

$$\text{Other neutrino-nucleons interactions} \quad \nu, \bar{\nu} + p, n \implies \nu, \bar{\nu} + p, n \tag{2.14}$$

Neutrinos interact with fermions, especially in the PNS region where the fermion density is larger. Such interactions lead to a difference in the potential between heavy and electron neutrino flavors, since the CC interactions are diminished for the heavy-flavor neutrinos. Neutrino-shock heat exchange can be influenced by flavor transformation, which in turn may contribute to instabilities and turbulence effects, ultimately affecting the efficiency of the neutrino-heat mechanism as discussed **Section 2.4.1**:

Other neutrino-fermions interactions

$$\text{Charged Current} \quad \nu_e(\bar{\nu}_e) + e^-(e^+) \Longrightarrow \nu_e(\bar{\nu}_e) + e^-(e^+) \tag{2.15}$$

$$\text{Neutral Current} \quad \nu(\bar{\nu}) + e^-(e^+) \Longrightarrow \nu(\bar{\nu}) + e^-(e^+) \tag{2.16}$$

$$\nu(\bar{\nu}) + x(\bar{x}) \Longrightarrow \nu(\bar{\nu}) + x(\bar{x}). \tag{2.17}$$

The transfer of energy between neutrinos and the accretion shock wave is intensified when they are moving in different directions, resulting in convection instabilities in the region immediately after the shock. The implementation of convection instabilities is an object of interest in the multi-dimensional SN Models [88]. The convective heat transfer process can cease when the accumulated material rapidly reaches the zone of energy gain, as shown in **figure 2.2** [89]. By this stage, the accretion shock has reached its maximum expansion and the transmission of energy is driven by hydrodynamic instabilities. The standing accretion shock instabilities (SASI) are examined in the context of this study, as referenced by [90][91]. These instabilities are also considered in supernova modeling, as discussed in **Section 2.4**. A successful supernova explosion occurs in the early stages of the accretion phase, around 100 milliseconds, when there is energy transfer between the neutrino heat process and hydrodynamical instabilities. Concerning the evolution of the light curves during this phase, the absorption of neutrinos by nucleons causes a decrease in the luminosity of ν_e and $\bar{\nu}_e$. However, this process also generates electrons and positrons, which are then captured by free nucleons, resulting in another burst of ν_e and $\bar{\nu}_e$ with an energy of approximately 0.6×10^{53}erg/s at around 0.1 seconds, as depicted in the center panel of **figure 2.1**. Furthermore, there is a noticeable rise in the average energy of these two neutrino flavors. This can be attributed to the neutrino generation by pair annihilation occurring after 0.1 seconds.

Conversely, the creation of heavy-flavor neutrinos is amplified by an increase in temperature and the accumulation of nuclear matter from the shock wave. Consequently, these neutrinos become degenerate, resulting in an increase of the averaged energy which is around 16 MeV. In addition, they solely engage in NC interactions with nuclei, which reduces their absorption and results in a gradual drop in their luminosity relative to ν_e and $\bar{\nu}_e$. After a time interval of 500 milliseconds, the luminosities of all neutrino flavors reach a state of convergence, with an approximate value of 10^{52} erg/s. At the same time, the mean

energies of the flavors remain stable within a range of 12 to 14 MeV.

In this phase of the neutrino observation, detectors using CEνNS interaction signal, that is sensitive of all flavors — as direct dark matter ones —, or to both electron-flavored neutrinos through charge current interactions are expected observe a significant number of CCSN events as detailed in **Section 3.1**. In this context, we anticipate a reduced neutrino flux intensity compared to the neutronization burst, approximately 2×10^{53} ergs/s, but with higher energy.

From the perspective of core evolution, the PNS becomes separated from the expelled material and regions with low density. The PNS is enriched with degenerate neutrons due to the accretion of neutrons from fragmented nuclei in low-density regions. PNS contracts due to a significant loss of radiative energy caused by the emission of neutrinos following the explosion. The PNS is unable to further adjust for the gravitational potential energy, therefore it decreases its radius to approximately 10 km [87]. The generation of neutrinos within a PNS is heavily influenced by the temperature, which has risen due to the process of contraction. This temperature is intimately linked to the binding energy of the PNS, a significant portion of which remains in its core.

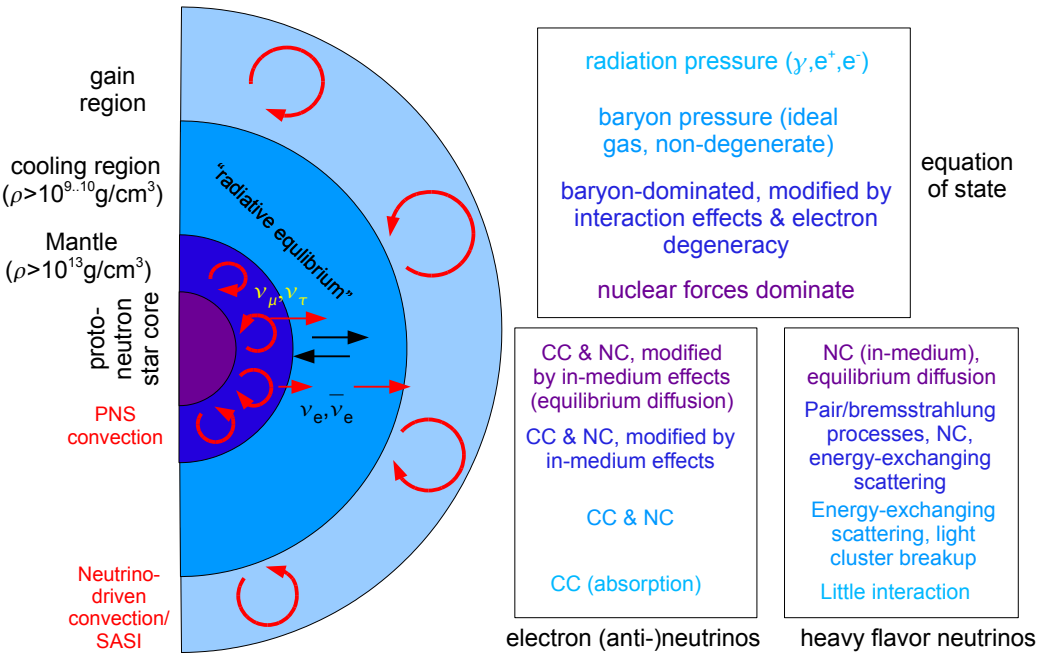

Figure 2.2: Sketch of the various regions in the supernova core before explosion. Abbreviations: CC, charged-current; NC, neutral-current; PNS, proto-neutron star; SASI, standing accretion-shock instability [87].

The accretion period lasts for around 1 second. Time range estimations serve as a mean to categorize the various neutrino emissions. Following the accretion phase, the CCSN transitions smoothly into the cooling phase, that is the object of the next section.

2.2.3 Cooling phase

Instead of a sudden reduction, accretion reduces gradually, and it is closely linked to the cooling process of the PNS. In this section, the process of transitioning from accretion to cooling is detailed.

The revival of stalled shock is accompanied by a decrease in neutrino emission. Thermal diffusion is the primary mechanism for neutrino production as a consequence of the reduction of the accretion shock energy. Nevertheless, the thermal energy, which starts at a range of 50 to 100 MeV [92] in the innermost region of the core, diminishes as the neutrinos lose energy. Thermal neutrinos exit the PNS when scattering enables them to release sufficient energy to break out. The energy losses of neutrinos causes the SN to enter into the Kelvin-Helmholtz cooling phase.

The main factor affecting the rate of neutrino emission during the cooling phase is the binding energy. Its majority is released following the explosion. Unlike the emission during neutronization, all flavors of neutrinos carry the same amount of energy. As previously stated and demonstrated by equation (2.1), the binding energy is directly linked to the PNS and its radius, namely through the EoS. Valuable insights into the EoS can be obtained from this phase, which is determined by the binding energy. This is particularly significant because the binding energy can be inferred without any uncertainties related to flavor conversion.

Concerning light curves, the luminosities of all types fall and return to their previous values before rebounding in around 1 second. The right panel of **figure 2.1** displays a linear decrease in luminosities that impacts all flavors equally. This decrease is associated with the diffuse component of the flux (described in equation (2.11)). The luminosities five seconds after the bounce are lowered by a factor of 100 compared to the luminosities in the first second. The mean energy of neutrinos likewise decreases without any differentiation in flavor evolution. This is due to the fact that the high energy component of the neutrino spectrum has already left the supernova environment, and the interaction rate of neutrinos with matter is steadily diminishing. The average energy of electron and heavy flavors neutrinos decrease to 6 MeV and 8 MeV, respectively. Neutrinos at those energies can still being detected by large detectors on Earth through electron elastic scattering and charged current by Cerenkov detectors, depending on their energy threshold (see **Section 3.1**).

This phase involves the production of a supernova remnant, which can result in either a neutron star or a black hole depending on many criteria such as the initial mass and metallicity of the progenitor, as discussed in **Section 1.2**. Additionally, the explosion mechanism and instabilities in the PNS during the accretion phase can also play a role.

2.3 CCSN Neutrino Initial Spectra

Due to the properties discussed in the previous section regarding the neutrino emission flux and its evolution over time during the burst, it is anticipated that there will be challenges in accurately describing the overall shape of the neutrino emission spectrum from CCSN. This, consequently, leads to complex uncertainties associated with it. The production of neutrinos is contingent upon certain progenitor properties,

such as metallicity, mass, and initial chemical composition. The final star evolution before collapse can be determined by examining the layers of H, He, C, Si, etc. that surround the core, as shown in **figure 1.4**. This structure plays a crucial role regarding the transportation of neutrinos that are generated in denser regions. These neutrinos have the ability to interact with the outer layers before finally exiting. This immediately prompts the consideration of matter effects in the examination of the neutrino spectrum, as well as changes in neutrino flavor oscillations from their creation until they exit the supernova environment. This section solely focuses on describing the neutrino spectrum emitted by supernovae in their immediate surroundings. The subsequent section, namely **Section 2.5**, will delve into the neutrino flavor transformations in the supernova environment, while **Section 2.6** will describe the final observable spectrum reaching the Earth.

The collapse process and subsequent evolution of the PNS leading to the neutrino burst are directly influenced by the EoS, once the characteristics of the zero-age main sequence (ZAMS) progenitors are determined. Here we delve into the extensive realm of supernova simulations, which encompass various methodologies [75][93][94]. The EoS cannot be accurately determined, and there are uncertainties and selections regarding the neutrino physics list used to consider their interactions with matter. The complexity of neutrino spectrum modeling will be addressed in a comprehensive manner (refer to **Section 2.4**). The overall context of physics about the neutrino burst discussed in the previous sections leads to conclude that neutrino emission is primarily made up of two distinct production mechanisms. The first impacts all the flavors and is thermal diffusive, resulting in the emission of neutrinos exhibiting a thermal spectrum (see equation 2.11). This mechanism presents dominance following the supernova explosion, namely during the accretion and cooling stages. The second mechanism is more complex and impacts the flavors of electron (anti)neutrinos, mostly based on their interaction through charged current and neutral current scattering with atomic nuclei.

Given this, the neutrino emission spectra take on the form of a quasi-thermal spectrum, specifically a thermal spectrum resulting in a "pinched Fermi-Dirac distribution". The latter includes adjustments to accommodate the various mechanisms of neutrino production and their time development as documented in previous studies (mentioned already in **Section 2.2**). In addition, energy spectra can also be described by a power law distribution as shown in the following works [95][96]. This image is widely recognized as the most often used representation of the neutrino spectrum. The output neutrino spectrum from the majority of supernova simulation models, including SN 1987A, can be accurately fitted to this Fermi-Dirac-like spectrum with high energy resolution. This has been demonstrated in several studies, such as [75, 93, 97, 98]. The convenient fit of SN 1987A does not exclude other approaches or improvements to constrain the neutrino spectrum [99, 95, 100, 101]. Some of these approaches include new perspectives such as radiation-hydrodynamics [59], the impact of the magnetic field [102], or the assumption of black hole formation [103, 104]. Those studies aim to comprehensively investigate the complex physics and various mechanisms involved in core collapse, with a specific focus on understanding the properties of stellar evolution such as progenitor layer structure and core equation of state. All those analyses are limited by the availability of only one scientific dataset from SN1987A.

2.3.1 Initial neutrino differential flux

The light curves depicted in **figure 2.1** illustrate the temporal evolution of neutrino luminosity and mean energy during the burst from the *Bollig 2016* Model [75] progenitor with a mass of 27 $M_{\odot}$and EoS LS220 [105]. It is necessary to include the time-dependent parameters $L_{\nu_\beta}(t_{\rm pb})$ and $\langle E_{\nu_\beta}\rangle(t_{\rm pb})$ for each flavor β when describing the initial spectra of neutrinos emitted from the supernova. The first one governs the progression of the intensity of the neutrino burst, while the second one indicates the temporal change of the neutrino energy. It is important to note that the term "neutrino initial spectra" specifically refers to the flux of neutrinos that leave the surface of supernovae, and any interactions or changes that occur during their journey are already taken into consideration. In this initial analysis of the spectra, which will be further described in the following paragraphs, flavor transformations of the neutrino flux will be disregarded. This topic will be addressed in **Section 2.5**. The description of the formalism of the two dimension (time and energy) differential spectrum, in which flavor transformations probability factors will be further applied, is the main goal of this section.

Considering a quasi-thermal spectrum implies the assumption that the average energy is dependent on an effective temperature. Consequently, the emission of neutrinos must be exponentially scaled by this temperature. However, in order to consider the non-thermal component of the flux, it is necessary to adjust the form of the pinched Fermi-dirac spectrum, especially during the later stages of accretion and cooling. This is because the emission tail at high energy levels is suppressed in the case of ν_e and $\bar{\nu}_e$, due to their scattering with nuclei. The assimilation of this suppression can be described by a time-dependent spectrum pinching parameter for each flavor. This parameter $\alpha_{\beta(t_{\rm pb})}$ is flavor β and it time $t_{\rm pb}$ dependent.

The three parameters required to characterize the early spectra of neutrinos are the values of $L_{\nu_\beta}(t_{\rm pb})$, $\langle E_{\nu_\beta}\rangle(t_{\rm pb})$ and $\alpha_\beta(t_{\rm pb})$, being the luminosity directly proportional to the number of emitted neutrinos. This number depends on time, on the evolution of the collapse and on the energy present in the shock wave. Additionally, the energy of the produced neutrinos also plays a role, as most of their interactions depend on it. However, only the average energy $\langle E_{\nu_\beta}\rangle(t_{\rm pb})$ and the parameter $\alpha_\beta(t_{\rm pb})$ are required to characterize the energy distribution at a specific time $t_{\rm pb}$ after the bounce. Thus, in the next section, the neutrino energy distribution will be delineated.

2.3.1.1 Energy distribution of initial spectra

The mean energy of heavy flavors, denoted as $\langle E_{\nu_x}\rangle$, can be estimated by utilizing an effective temperature, denoted as T, which has energy units[6], as is described in equation (2.18). This is the outcome of thermal pair creation in the PNS, which is analogous to a black body emitter. Electron flavor (anti)neutrinos $\langle E_{\nu_e,\bar{\nu}_e}\rangle$ are influenced by both temperature and matter interactions. In this context, the term "mean energy" can be linked to an effective chemical potential denoted as μ^*_β. This also entails making the assumption that μ_x follows a normal distribution with a mean of zero [106]:

[6]Sometimes it is pertinent to assume *natural units*, setting the Boltzmann constant K_B (normally equal, in the International System of Units, to $1.380649\times\ 10^{-23}$ J K^{-1}) to 1, to better put in evidence in this case the relation between temperature T and energy E: [K_B T(K)]= [E(J)] in the context of Fermi-Dirac spectrum.

$$\langle E_{\nu_x} \rangle \sim \pi T \qquad \text{and} \qquad \langle E_{\nu_e, \bar{\nu}_e} \rangle = \frac{3}{4} \mu_\beta * . \tag{2.18}$$

With the temperature and the chemical potential, we can use a Fermi-Dirac spectrum to describe energy distribution as follows:

$$f(E_\beta) \propto \frac{E_\beta^2}{1 + e^{\frac{E_\beta - \mu}{T}}}. \tag{2.19}$$

As previously stated in **Section 1.2**, degeneracy pressure is a significant factor in the collapse process. It is closely linked to the evolution of the density and, consequently, of the temperature. The neutrino energy distribution is influenced by the degeneracy, which takes into consideration the interaction of neutrinos with the medium. This is especially important for neutrinos of the electron flavor. The chemical potential can be expressed using the degeneracy parameter $\eta = \frac{\mu}{T}$. This allows one to characterize the neutrino spectrum as a function of neutrino energy, as proposed in the approach put forward by [107] and [108]:

$$f(E_\beta) = \frac{\phi_{\nu_\beta}}{T^3 f_2(\eta_\beta)} \frac{E_\beta^2}{1 + e^{\frac{E_\beta}{T} - \eta}} \qquad \text{with} \qquad f_2(\eta_\beta) = \int \frac{x^2}{e^{x - \eta_\beta} + 1} dx, \tag{2.20}$$

where ϕ_{ν_β} is the number of total neutrino emitted.

In order to correct this spectrum, assuming it has a thermal behavior, with a "pinching parameter" the following relation can be defined through an energy moment k :

$$l = \frac{\langle E^k \rangle}{\langle E \rangle^k} \tag{2.21}$$

The value $k = 2$ has been considered adequate to accurately characterize the spectrum [108]. For a Fermi-Dirac spectrum with a null chemical potential, the value of parameter l is around 1.309 [95], which is close to that of a Maxwell-Boltzmann distribution $4/3$ [7]. Based on this conclusion, we can establish a threshold value p to determine pinching for this second moment:

$$p = \frac{1}{l} \frac{\langle E^2 \rangle}{\langle E \rangle^2} \tag{2.22}$$

This signifies that a *pinched spectra* with the suppression of the high energy tail is expected to be $p < 1$ and, on the contrary, an *anti-pinched spectra* increasing this high energy tail requires $p > 1$. The value $p = 1$ corresponds to a thermal spectra with $\eta = 0$.

The final goal is to obtain an energy distribution depending only on the mean energy $\langle E \rangle \equiv T$, and so include p into equation (2.20). It is therefore useful to establish an analytic approximation of p and $\langle E/T \rangle$ in terms of η:

[7] The Maxwell-Boltzmann distribution is commonly employed to characterize a system of particles that do not interact with their surroundings (with a chemical potential $\mu = 0$). In this distribution, the kinetic energy K of the particles is dependent on the temperature, and is described by the equation $f_{M-B} \propto e^{-\frac{K}{K_B T}}$.

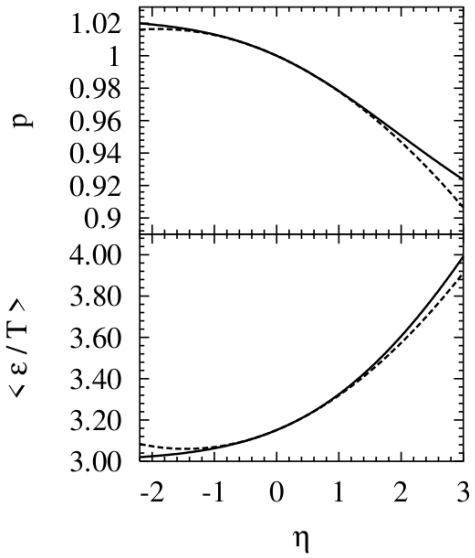

Figure 2.3: Mean energy $\langle \epsilon/T \rangle$ (corresponding to $\langle E/T \rangle$ in the text) and pinching parameter p as a function of the degeneracy parameter η for a Fermi-Dirac distribution (solid lines). Dashed lines correspond to the approximation of equation (2.23).

$$\langle \frac{E}{T} \rangle \sim \pi + \frac{1}{8}\eta + 0.0429\eta^2 \qquad \text{and} \qquad p \sim 1 - 0.0174\eta - 0.0046\eta^2. \tag{2.23}$$

Those dependencies are represented in **figure 2.3** [95]: the solid lines show the non-approximated ones, while the dashed ones correspond to their analytic approximation. The parabolic behavior of p has its center located at negative values of the degeneracy parameter η (about -2 according to equation (2.23) and approximately -3 based on the Fermi-Dirac spectrum). This phenomenon is driven by the fact that, when neutrinos interact with nuclei, their energy is reduced through the transfer of part of their momentum, enabling them to exit from locations where they were previously trapped, due to the square energy dependence of the coherent scattering. However, the change in $\langle E/T \rangle$ is inversely related to p as a function of η, reaching a minimum at around $\eta = -2$. This is in accordance with the observation that *anti-pinched spectra* amplify the high energy distribution at a specific t_{pb}. It is noticeable that the minimal ratio $\langle E/T \rangle$ is approximately equal to 3, indicating that the maximum suppression of high energy tails results in this relationship.

To achieve a distinct separation of energy distribution in the expression of the neutrino spectrum (2.20), an alternative formalism can be employed. This formalism is associated with the value of p in terms of the previously described pinching parameter α_{ν_β} [86]:

$$\frac{\langle E_{\nu_\beta}(t_{\rm pb})^k \rangle}{\langle E_{\nu_\beta}^{k-1}(t_{\rm pb}) \rangle} = \frac{k + \alpha_\beta(t_{\rm pb})}{1 + \alpha_\beta(t_{\rm pb})} \langle E_{\nu_\beta}(t_{\rm pb}) \rangle \qquad \text{with} \qquad p = \frac{\alpha + 2}{\alpha + 1} \qquad , \qquad k = 2 \tag{2.24}$$

Limit values for *pinched* and *anti-pinched spectra* become $\alpha > 2.3$ and $\alpha < 2.3$ respectively, while

$\alpha = 2.3$ represents the Fermi-Dirac distribution (equations 2.19 and 2.20) with $\eta = 0$.

Using the pinching parameter, it can be finally defined the energy distribution as in reference [93]:

$$f(E_{\nu_\beta})_\alpha = \xi_\beta(t_{\rm pb}) \left(\frac{E}{\langle E_{\nu_\beta}(t_{\rm pb})\rangle} \right)^{\alpha_\beta(t_{\rm pb})} e^{-\frac{(\alpha_\beta(t_{\rm pb})+1)E}{\langle E_{\nu_\beta}(t_{\rm pb})\rangle}}, \tag{2.25}$$

where $\xi_\beta(t_{\rm pb})$ is a normalization factor defined such that $\int dE\, f(E_{\nu_\beta})_\alpha = 1$.

At this point, it is important to notice that the pinching parameter $\alpha_\beta(t_{\rm pb})$ and the mean energy $\langle E_{\nu_\beta}(t_{\rm pb})\rangle$ are strongly correlated, and characterize $f(E_{\nu_\beta})_\alpha$. Also, the squared mean energy $\langle E_{\nu_\beta}(t_{\rm pb})\rangle^2$ and the respective variance $\omega(t_{\rm pb})$ are also correlated by $\alpha_\beta(t_{\rm pb})$. These values can be defined for a given time t_{pb} as:

$$\begin{aligned} \langle E_{\nu_\beta}(t_{\rm pb})\rangle &= \int_{-\infty}^{+\infty} E_{\nu_\beta} f(E_{\nu_\beta})_\alpha dE_{\nu_\beta}, \\ \omega(t_{\rm pb}) &= \int_{-\infty}^{+\infty} E_{\nu_\beta}^2 f(E_{\nu_\beta})_\alpha dE_{\nu_\beta} - \langle E_{\nu_\beta}(t_{\rm pb})\rangle^2, \\ \alpha_\beta(t_{\rm pb}) &= \frac{\langle E_{\nu_\beta}(t_{\rm pb})\rangle^2 - \omega(t_{\rm pb})^2}{\omega(t_{\rm pb})^2}. \end{aligned} \tag{2.26}$$

The correlation between energy and $\alpha_\beta(t_{\rm pb})$ indicates that since $\langle E_{\nu_\beta}(t_{\rm pb})\rangle$ can be considered as an observable, $\alpha_\beta(t_{\rm pb})$ serves as an adjustment or fitting parameter that matches the neutrino spectrum for a specific time [75, 86, 92, 93].

Figure 2.4 illustrates the change in $\alpha_\beta(t_{\rm pb})$ during the three stages of the neutrino burst. During the process of neutronization, the spectrum for the electron flavor is highly pinched, with a α_e value of more than 6 before the time $t = 0$ seconds. This suggests that there is trapping of ν_e by nuclei and nucleons prior to the core bounce. Neutrinos ν_e that were previously trapped are suddenly released due to a shock bounce. These neutrinos have high energy and their $\alpha_e(t = 0.05s)$ values start to drop, eventually reaching values of around 3.8. During the initial phase of the bounce, the energy distribution of $\bar{\nu}_e$ and ν_x, which are produced in the core through interactions with dissociated nuclei, becomes pinched and the value of $\alpha_{\bar{e},x}$(0-0.01s) rises rapidly. The interaction of $\bar{\nu}_e$ with nucleons suggest that $\alpha_{\bar{e}}(0.02 - 0.05s)$ is similar to that of ν_e, while $\alpha_x(0.05s) \sim 3$ and therefore the energy spectrum of ν_x is less pinched. It is important to note that the absence of α null values before the bounce does not have any physical significance. This is simply because the contributions of $\bar{\nu}_e$ and ν_x are not expected to be produced during this period [109].

During the initial hundred milliseconds of the accretion phase, neutrinos are emitted from the heating process in the PNS region. In all flavors, the energy drops, resulting in spectra that are less pinched. The accretion shock is halted due to the predominant heating from electron neutrinos. In addition, during the initial accretion phase it can be observed that the spectra of ν_e and $\bar{\nu}_e$ exhibit a pinched shape. However, this pinching gradually decreases over time. At the same time, the distribution of heavy flavor approaches a Maxwell Boltzmann distribution with an $\alpha_x(0.2s - 0.5s) \sim 2$. Prior to the explosion, the heat exchange between the accretion shock and neutrinos reaches its maximum at approximately 500

milliseconds, resulting in an increase in all $\alpha_\nu(0.5s)$ values. Following the explosion, there is a cessation of electron flavor trapping, resulting in a narrowing of the electron spectrum, with $\alpha_{\bar{e},e}(0.5s-1s) \sim 3$. Heavy flavors experience a lower interaction rate with the medium, causing their spectrum to quickly approach a thermal distribution. Specifically, the value of α_x for heavy flavor is almost equal to 2.3. This thermal-like behavior remains consistent even during the cooling phase.

During the cooling phase, the $\bar{\nu}_e$ spectrum reaches thermal equilibrium, and the interactions between charged currents and protons decrease. Additionally, the $\alpha_{\bar{e}}(> 4s)$ converges to the heavy flavor ones $\alpha_x(>0.75$ s). However, the ν_e spectrum stays compressed with nearly identical α_e values following the explosion.

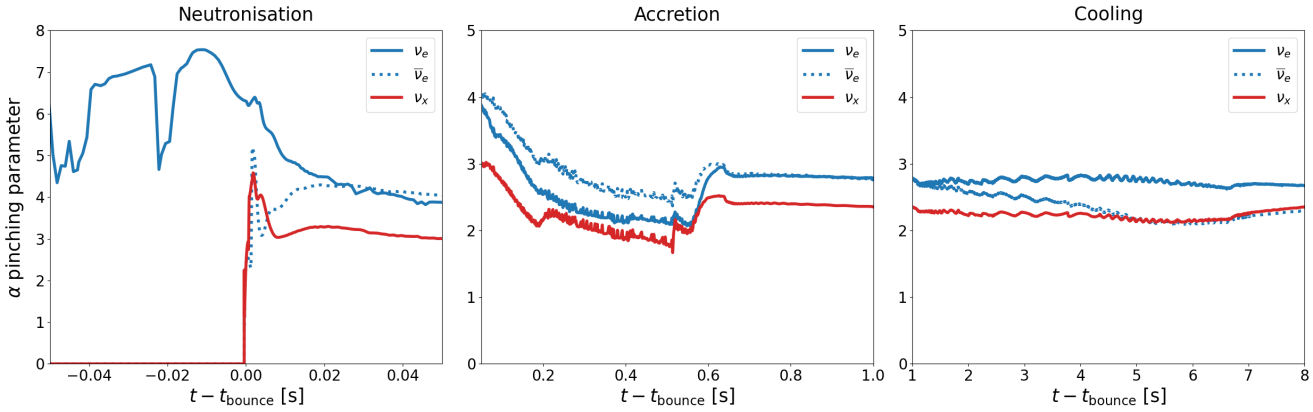

Figure 2.4: Pinching parameter $\alpha_\beta(t_{\text{pb}})$ as a function of the post-bounce time t_{pb} for the Bollig Model $27M_\odot$ supernova progenitors with the LS220 EoS for ν_e (blue continuous lines), $\bar{\nu}_e$ (blue dot lines) and ν_x (red continuous lines). The panel on the left show the neutrino properties during the neutronization burst phase, the middle panel refers to the accretion phase, and panel on the right describe the Kelvin-Helmholtz cooling phase

It is now possible to include the energy distribution $f_{\nu_\beta}(E, t_{\text{pb}})_\alpha$ in the 2-dimensional differential supernova neutrino spectrum:

$$\frac{dN}{dE_{\nu_\beta}dt}(E, t_{\text{pb}}) = \frac{L_{\nu_\beta}(t_{\text{pb}})}{\langle E_{\nu_\beta}(t_{\text{pb}})\rangle}\ f_{\nu_\beta}(E, t_{\text{pb}})_\alpha, \tag{2.27}$$

where $L_{\nu_\beta}(t_{\text{pb}})$ is the ν_β luminosity, $\langle E_{\nu_\beta}(t_{\text{pb}})\rangle$ is the mean energy, and $f_{\nu_\beta}(E, t_{\text{pb}})_\alpha$ is the neutrino energy distribution. The luminosity is related to the number of neutrinos, each one carrying a given amount of energy at a given time, the sum of which is the total energy released during the burst:

$$E_T = \sum_\beta \int_{ti}^{tf} L_{\nu_\beta}(t_{\text{pb}})dt. \tag{2.28}$$

Figure 2.5 shows some representative values for the three phases of the supernova neutrino differential spectrum, at 0.07 s, 0.3 s and 1s for the neutronization, accretion and cooling respectively. Clear differences between the tree phases are present in the spectra of all flavors. These are the consequence of what was

discussed in figures 2.1 and 2.3, regarding the three main parameters of the spectra $L_{\nu_\beta}(t_{\rm pb})$, $\langle E_{\nu_\beta}(t_{\rm pb})\rangle$ and $\alpha_\beta(t_{\rm pb})$, and also discussed in the description of the burst in **Section 2.2**.

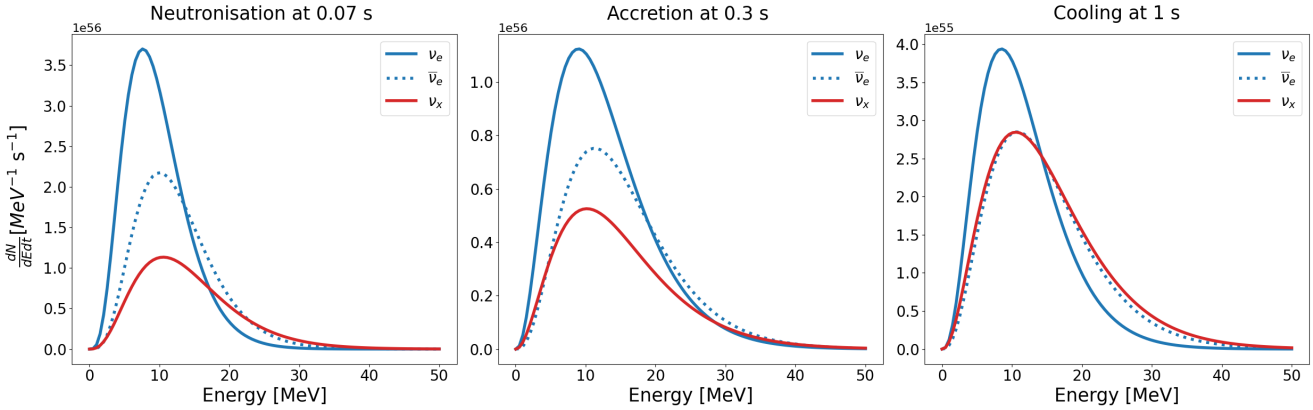

Figure 2.5: 2-dimension differential (time and energy) non-transformed neutrino initial spectra (without considering matter effects) for Bollig Model 2016 LS220 EoS 27 $M_\odot$. All neutrino flavors are represented: ν_e (blue continuous lines), $\bar{\nu}_e$ (blue dot lines) and ν_x (red continuous lines). The panel on the left shows the neutrino spectrum during the neutronization burst phase at 0.07s, coinciding with ν_e bursts; the middle pane refers to the accretion phase at 0.3s during the supernova explosion, and the panel on the right describe the spectrum during the Kelvin-Helmholtz cooling phase at 1s.

Given that supernova neutrino detection can yield anywhere from a few to a thousand events per kton scale detectors, the primary objective is to reconstruct the overall time-integrated energy spectrum. This is the main achievable goal of detectors willing to detect supernova neutrinos, as will be discussed in **Chapter 3**. Additionally, the time evolution of the neutrino energy distribution is also of interest. By integrating the expression of equation (2.27) over time, we can derive the whole spectrum for each flavor, as well as a combined spectrum for all flavors. The latter is specially interesting for non-neutrino flavor sensible detection volumes.

$$\frac{dN}{dE_{\nu_\beta}}(E_{\nu_\beta}) = \int_0^{t_f} \frac{L_{\nu_\beta}(t_{\rm pb})}{\langle E_{\nu_\beta}(t_{\rm pb})\rangle}\, f_{\nu_\beta}(E, t_{\rm pb})_\alpha dt \quad , \qquad \frac{dN}{dE_\nu}(E_\nu) = \sum_\beta \frac{dN}{dE_{\nu_\beta}}(E_{\nu_\beta}) \tag{2.29}$$

2.3.1.2 Time evolution of initial spectra

This section describes the time structure of the neutrino spectrum, through the continuity of the three phases, that can be actually reduced in terms of neutrino emission to only two: the early spectrum, that is derived by the shock wave and its matter accretion; and the one after the accretion phase, describing the cooling physics leading to the PNS formation. As the luminosity is scaled by the mean energy at a given time, one can obtain the number of emitted neutrinos $\frac{dN}{dt}$, integrating the normalized energy distribution:

$$\frac{dN_{\nu_\beta}}{dt}(t) = \int \frac{L_{\nu_\beta}(t_{\rm pb})}{\langle E_{\nu_\beta}(t_{\rm pb})\rangle}\, f_{\nu_\beta}(E, t_{\rm pb})_\alpha dE = \frac{L_{\nu_\beta}(t_{\rm pb})}{\langle E_{\nu_\beta}(t_{\rm pb})\rangle} \tag{2.30}$$

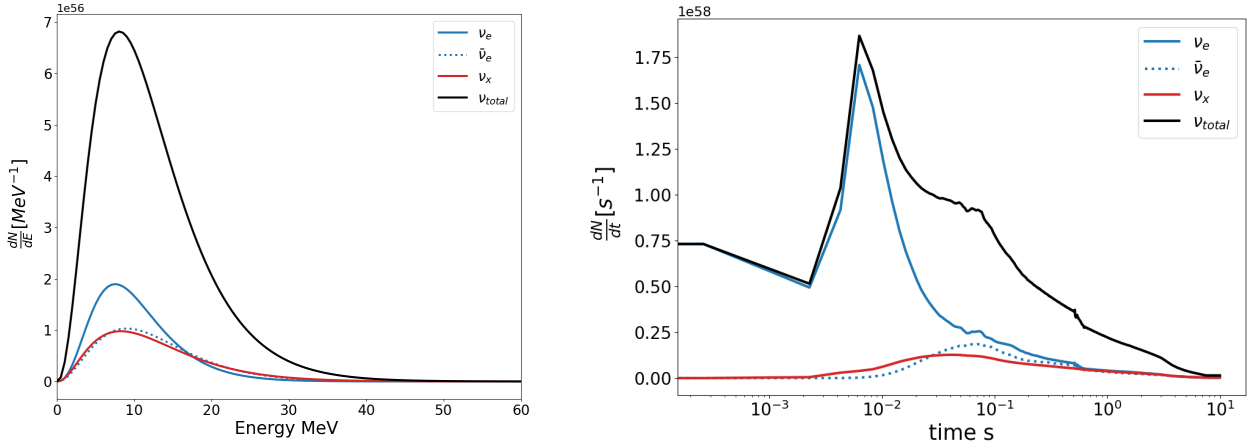

Figure 2.6: **Left.**Energy differential neutrino initial spectra (non-transformed) for Bollig Model 2016 LS220 EoS 27 $M_\odot$. All neutrinos flavors are represented: ν_e (blue continuous lines), $\bar{\nu}_e$ (blue dot lines) and ν_x (red continuous lines). The total neutrino energy spectrum is represented with a solid black line. **Right.**Time differential neutrino initial spectra (non transformed) for Bollig Model 2016 LS220 EoS 27 $M_\odot$. All neutrinos flavors are represented: ν_e (blue continuous lines), $\bar{\nu}_e$ (blue dot lines) and ν_x (red continuous lines). The total neutrino time evolution spectrum is represented with a solid black line

.

The left panel of **figure 2.6** presents the neutrino emission evolution for the different flavors for the *Bollig 2016* model, stated in (2.30). The final spectrum is strongly linked to the luminosity evolution presented in the equation **figure 2.1**. The ν_e neutronization burst in the first milliseconds will represent the maximum rate of the burst. The drop in the ν_e emission during the accretion phase is only interrupted during the explosion, where all the flavors exhibit an increase. The $\bar{\nu}_e$ appears to be significant during the accretion phase, reaching the values of ν_e, while the neutrino heavy flavors become dominant during the early cooling phase.

However, to understand better the distributions of the populations and the physics involved, the *Nakazato* (2013) model can be referenced. It is a one-dimensional (1D) model that incorporates several EoS, mass ranges, final progenitor remnants, and different revival times t_{rev}. Simulation data is stocked in the database [110], and its physics is explained in references [111, 94]. This model is intriguing to report here because it artificially triggers the supernova explosion. In 1D models, an explosion does not occur unless a 1D approximation of the neutrino heat transfer mechanism is accounted to revive the stalled shock. The *Nakazato 2013* model is built by linearly interpolating two fluxes constrained by t_{rev}. The first flux represents the development of neutrino emission during the neutronization and accretion phase, handled by the neutrino radiation hydrodynamics νRHD model [112, 113], indicated as $\frac{dN}{dtdE}^{\nu\text{RHD}}$. The other part of the interpolated flux concerns the hydrodynamics of the PNS cooling phase, represented as $\frac{dN}{dtdE}^{\text{PNSC}}$. Those dynamics are discussed in detail in references [114] and [115]. The flux can be written as:

$$\frac{dN}{dtdE}_{\nu_\beta}(E, t_{\rm pb}) = \frac{dN}{dtdE}^{\rm acc}_{\nu_\beta}(E, t) + \frac{dN}{dtdE}^{\rm cool}_{\nu_\beta}(E, t). \tag{2.31}$$

Those two different dynamics also have implications into the flavor population. While the first therm involves the dynamics of the neutrino-sphere mainly affecting the ν_e and $\bar{\nu}_e$ flavors, the PNS dynamics leads to a thermal diffuse flux involving all the neutrino flavors.

Finally, from the time and the energy spectra from the *Bollig 2016* model, two important quantities are summarized in **table 2.1**: the total energy released, as from the equation (2.28), and the average energy, which can be determined from equation (2.30), for each neutrino flavor. These quantities represent the weight of each phase in terms of energy released, and also give the first predictions involving the CCSN neutrino detection for each phase of the burst.

***Neutronisation* (∼ 0.05s)**	ν_e	$\bar{\nu}_e$	ν_x	Total
Total Energy [10^{51} ergs]	6.49	1.28	1.40	13.38
Mean Energy [MeV]	10.02	8.22	9.52	9.39
Accretion (0.05-1s)	ν_e	$\bar{\nu}_e$	ν_x	Total
Total Energy [10^{51} ergs]	25.33	25.66	18.85	126.33
Mean Energy [MeV]	9.75	15.35	15.28	14.87
Cooling (1-10 s)	ν_e	$\bar{\nu}_e$	ν_x	Total
Total Energy [10^{51} ergs]	25.79	27.45	30.83	176.58
Mean Energy [MeV]	12.76	11.52	11.45	11.18

Table 2.1: Total energy released via neutrino emission; as the time integral (2.28) during the *neutronization, accretion* and *cooling* phases , as well as Mean Energy for each phase. Values are taking from a $27M_\odot$ progenitor from *Bollig 2016* model.

In this section, light curves from the *Bollig 2016* model were selected because it incorporates convection effects that seem crucial to revive the stalled shock wave and result in a supernova explosion without external forcing. At first glance, this appears to be a valid criterion for qualitatively assessing a supernova model. However, there exist more approaches and to in under to understand the implication of this choice, several CCSN modeling approaches will be thoroughly explained in the following section.

2.4 CCSN Modeling

CCSN encompasses the convergence of multiple fields of physics, including star evolution, chemical structure, strong and weak interaction physics, electromagnetic radiation, neutrino physics, (magneto-)hydrodynamics, statistical and kinetic physics, and general relativity. The scope of the CCSN simulation is then extensive. Thanks to the rich CCSN Model library provided by the Garching Group archive [116], a wide range of progenitor masses, equations of state (EoS), metallicities, alternative core collapse mechanisms, and physics that drive neutrino burst simulations are accessible. This discussion is not an exhaustive description of all potential ways to simulate CCSN. Instead, it focuses on a specific range of progenitor

masses, namely 10-30 $M_\odot$, which result in the formation of a neutron star as the remnant. Within this range, the developers of the package *SNEWPY* [117] have already made a prior selection, by including twenty-one CCSN models, the majority of which will be discussed in the next paragraphs. The models referred to before, namely *Bollig 2016* and *Nakazato 2013*, are included and designated by their respective names as they appear in the Python code[8] from the SNEWPY package [9]. The Python programming language has been used for the analysis of simulation results of CCSN in XENONnT, which will be presented in Chapters 3-5.

The objective of this section is to categorize the current models that incorporate CCSN simulations for our progenitor selection, with the aim of drawing qualitative conclusions about them. Furthermore, this allows to go deeper into certain features of the CCSN mechanism and neutrino burst that have already been discussed in **Sections 2.2** and **1.2**. Due to the extensive and intricate nature of the physics of CCSN, which goes beyond the scope of this thesis, a focus is given on the modeling parameters that directly impact the following aspects: the neutrino-heat mechanism, the time and energy resolution of the neutrino burst, the population of neutrino flavor, and the transport of neutrinos within the stellar envelope (matter effects, approached in **Section 2.5**).

The impact of spatial dimension on simulations of CCSN will be the starting point. This directly influences the neutrino-heat process, shock revival, and the neutrino burst that occurs during the accretion phase.

2.4.1 Spatial Dimension in CCSN Simulation

Simulations in 2D and 3D are actually able to reproduce the basics of the CCSN mechanism in the mass progenitor range of interest, with consistent results regarding neutrino bursts, and particularly a good description of the iron CCSN low mass range [118][119], while 1D simulations are consistent for describing ECCSN [120]. The latter ECCSN or *ECCSN-like* 8-10 $M_\odot$ ZAMS progenitor modeling presents excellent results in 1D (spherical) simulations, leading to a supernova explosion after the bounce [121][44]. On the other hand, for more massive progenitors $> 12M_\odot$, a multidimensional approach is required to trigger the explosion through the neutrino heat mechanism [93][122][123]. A complete overview of CCSN simulations in 2016 has been done in reference [124], with valid statements for 1D and 2D, while new approaches in 3D [125][109][102] have since been implemented.

1D Models

Supernova explosions are of course not unidimensional, and it can be also anticipated that the ejection of matter occurs in an asymmetric manner in multidimensional space [126]. Nevertheless, in order to incorporate the maximum amount of physics processes described in **Chapter 1** and at the beginning of the present chapter, in CCSN neutrino multi-dimensional simulations it is often necessary to perform approx-

[8] Python is a programming language that comes with a vast library of packages for data analysis. You may find more information about Python at this URL: https://www.python.org/

[9] https://github.com/SNEWS2

imations that remove one or two dimensions, to improve computation time. This results in at least two collateral consequences. The first is the challenge of eliminating the spatial dimensions, needed, a priori, to accurately describe the heat convection transfer between neutrinos and the stalled shock wave, as well as the SASI phenomenon, both of which are essential for initiating a supernova explosion. The second is that 1D modeling frequently imposes the spherical symmetry description of EoS. Historically the majority of 1D simulations are incapable of triggering a supernova explosion using neutrino-driven mechanisms for progenitors with masses higher than 10 $M_{\odot}$. In the case of low mass ECCSN, 1D simulations are able to initiate the supernova explosion [46]. However, for these models the explosion triggering mechanism relies on the effects of violent SASI [127].

The spherical approximation does not rule out the ability to consider convective effects, as demonstrated by the successful explosion achieved in the model proposed by *Bollig 2016*. It is interesting to compare this model with *Nakazato 2013*, which does not take into account convection and SASI effects during the accretion phase. Instead, it artificially triggers a supernova explosion for three different revival times of the stalled shock (100, 200, and 300 ms) [111]. One notable feature of the *Nakazato 2013* model is that it necessitates higher luminosities during the accretion phase, surpassing the maximum luminosity observed during the neutronization ν_e burst. The shift from accretion to an expansion shock wave is anticipated to occur when the luminosity reaches a critical value, named critical luminosity [128]. Incorporating convection and SASI into a multidimensional simulation results in a reduction of around 30% in the critical luminosity, compared to 1D models [129]. It is observed a significant decrease in luminosities for all flavors, approximately 40-50%, from the *Bollig 2016* model (top panel of **figure 2.1**) which employs a 1D1D symmetric approach that takes into account convection effects. Convection is addressed in the PNS region, rather than in the neutrino-heat zone immediately beyond the accretion shock boundaries. In this region, convection or other instabilities, such as the SASI require an aspherical modeling approach. Quasi-stationary convection in the PNS can be incorporated into a 1D simulation using a mixing-length approximation, as described in detail in reference [75]. This approximation shows excellent agreement with the results obtained from the hydrodynamical treatment of convection in 2D simulations.

In1D simulations, the intensity of neutrino bursts is primarily influenced by the density profile, namely the mass of the progenitor [124], more so than in multidimensional simulations. The absence of instability or shock turbulence in the outer regions of the PNS results in a direct relationship between the mass accretion rate, temperature, and luminosity, as well as the star's density profile. This density profile is determined by the ZAMS progenitor mass and not solely by the collapse core mass. The *Sukhbold 2015*[130] model is interesting because it looks at the effect of progenitor mass by simulating a wide range of 9 to 120 $M_{\odot}$ ZAMS with solar mass metallicities. A most recent addition to the 1D model in *SNEWPY*, based on *Sukhbold 2015* CCSN progenitors, is designated as *Warren 2020*. This model incorporates the effects of turbulence using the Supernova Turbulence in Reduced-Dimensionality (STIR) model, as described in reference [131]. Additionally, it includes convection to mimic 3D simulation results for this wide range of progenitor masses, and it will be discussed in the next section. The *Warren 2020* model examines the relationship between neutrino emission and gravitational waves (GW). Precisely, it

compares both emissions in a successful CCSN in front of an unsuccessful and black hole formation. This comparison is interesting because, even if there is an emerging consensus on the astrophysical community about the explosion mechanism dependence on neutrino heating, neutrino-driven convection, turbulences and dynamical instabilities (see e.g. [132]), the "reviving stalled-shock mechanism" is not fully understood [133, 131, 134]. In addition, it can be noted that failed CCSN explosions represent a significant portion of massive progenitors (see [135, 55]), which is confirmed recent 3D simulations have confirmed these findings [136, 137].

2D and 3D Models

Introducing an additional dimension into CCSN simulations is expected to directly impact light curves reducing luminosities, and improve the modeling of the revival of the neutrino-heat mechanism and the treatment of instabilities, which require a multidimensional treatment. A study conducted in 2018 [127] contrasted convection-driven 1D models (as described in *Bollig 2016*) with 2D asymmetric models, including a successful supernova explosion. That study compares computational aspects, which we are not interested in, with a detailed description of neutrino physics lists, as well as EoS and density profiles. From a theoretical standpoint, the 1D approximations for convection effects, results in a convection-dominated model, providing a satisfactory explanation for the predicted neutrino light curves, especially when considering a high critical luminosity. However, this spherical model fails to account for the non-spherical aspects of the CCSN mechanism and does not offer any comprehensive information about the explosion mechanism itself, as outlined in reference [61].

When it comes to the mechanism of CCSN collapse and the evolution of the PNS after the initial collapse, especially during the phase of accretion, additional approximations are still required in 2D models to address asymmetries that give rise to hydrodynamical instabilities. While the majority of 2D asymmetric models successfully address the issue of initiating CCSN explosions within the desired range of progenitor masses, their primary challenge lies in their inability to accurately replicate the characteristic attributes of these explosions. Following the shock revival, detailed analysis of 2D asymmetric models reveals an erratic and limited progression of the neutrino energy profile throughout the explosion. In this context, the last have decreased energy levels following the revival of the shock, and their critical brightness is likewise reduced by approximately 20%. Furthermore, a significant proportion of 2D models in the ZAMS low-mass range do not experience explosions, as stated by reference [124].

The analysis of 2D CCSN models provides valuable insights into the behaviors of convection and SASI, revealing instabilities that may not be evident in 1D models [138]. SASI dominant models in the 2D approach exhibit prominent large-scale structures with high entropy, referred to as *bubbles*. These bubbles persist for a significant duration by receiving heat from neutrinos and pressure from turbulence, which in turn triggers the explosion [139]. On the other hand, convection may happen in non-spherical, symmetric areas outside the PNS, where the impact of energy transfers within the gain region behind the shock is significant enough to revive the latter. Convection results in the formation of bubbles, which occur rapidly and create anisotropies in the pressure gradient. These anisotropies further intensify pressure turbulence.

Generally, a 2D model is expected to provide a more accurate description of theoretical instabilities in the PNS and gain area represented in **figure 2.2**, as well as shock turbulence and neutrino interactions with matter, such as neutrino-electron scattering, which often exhibit angle dependency. From a broader perspective, 2D simulations decrease the radius of the PNS and as the process of neutronization removes free electrons. Despite improving computer performances, it can be argued that 3D models are the most reliable and preferred option for analyzing the neutrino emission. However, it seems arduous to converge towards a consistent approach for 3D CCSN modelling. The simulation of a ten-second burst in 3D, that includes all the abovementioned physics, is still a challenge with regard to computing capabilities, which makes the validation of the 3D treatment difficult. 3D models are anticipated to address the issue of low-energy during the accretion phase, while maintaining the typical ratio of successful explosions of 2D simulations, and ideally improving it in the ZAMS low-mass range. In the context of the low-energy problem, a significant parameter of interest is the critical luminosity. It has been observed that the accretion phase of most 3D simulations corroborate that of 2D simulations. This value serves as an indicator, albeit uncertain, of the effectiveness of an explosion. However, it is not concluded that they exhibit similar levels of explosive success in ZAMS stars with a mass less than 12 $M_{\odot}$when compared to 2D models [134]. Nevertheless, there appears to be consistency in terms of large progenitors [109].

Based on the established CCSN mechanism physics, and assuming the absence of rapid rotational effects, strong magnetic fields, or other unconventional physics, the SNEWPY package encompasses a representative spectrum of 1D models *Nakazato 2013, Bollig 2016, Sukhbold 2015, O'Connor 2013, 2015*, and the more recent study by *Warren 2020*. Regarding 2D models, the package also contains *Fornax 2021* as well as 3D models: *Fornax 2019* [125], *Tamborra 2014* [140][93]. That said, some conclusions can be drawn regarding the **figure 2.7**. The energy spectra obtained from the 1D simulations conducted by *Bollig 2016* and *Sukbold 2015* exhibit remarkable similarity, approximating both neutrino-shock convection effects in 1D. However, the model referred to as *Warren 2020* includes approximations for convection and SASI, and it additionally drives the effects of turbulence using a turbulence parameter α_{turb} [141]. This model exhibits a high rate of neutrino emission and has a similar overall energy spectrum as the other two models, except for electronic flavors. It is worth noting that the high energy tail of the ν_e is slightly less suppressed, and practically not suppressed at all for the $\bar{\nu}_e$ component.

On the other hand, the energy spectrum of *Fornax 2021* exhibits the highest rate, but it appears to have a limited energy resolution, especially for the high energy range. However, it is the only 2D model that is able to simulate the 10 seconds neutrino burst.

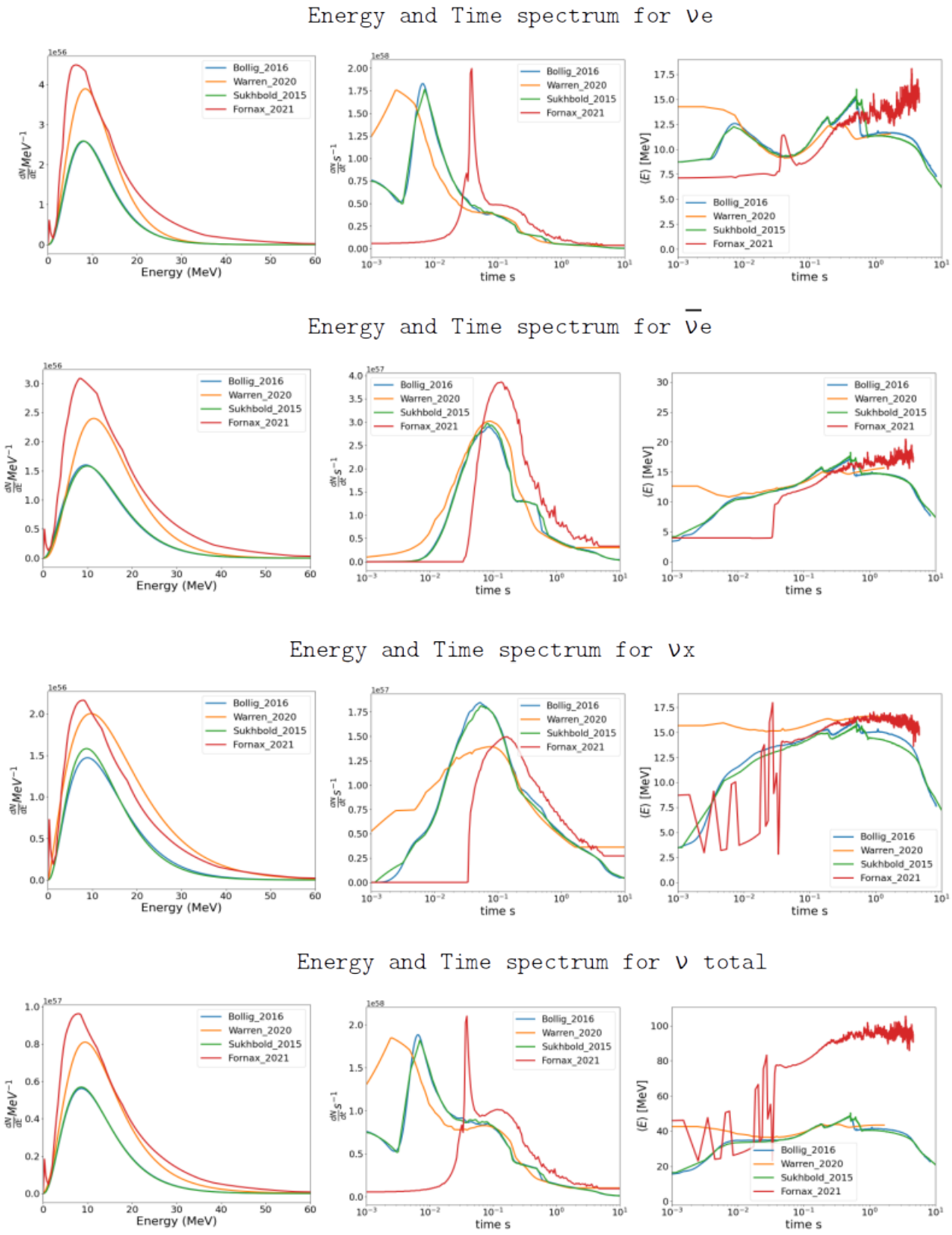

Figure 2.7: Energy spectra (left) and time evolution of the rate (right) of neutrinos for different progenitors of 27 $M_\odot$from *Bollig 2016*, *Sukhbold 2015*, *Fornax 2021* and *Warren 2020* (using $\alpha_{turb} = 1.25$). From top to bottom: ν_e, $\bar{\nu}_e$, ν_x and the total one calculated as $\nu_e + \bar{\nu}_e + 4\ \nu_x$.

It can be noted that its ancestor, *Fornax 2019*, that incorporates a spatial 3D simulation, is not represented in the figure because its energy spectrum exhibits comparable features and is only simulated up to a time of around 0.6 seconds, providing no information about the later stages of accretion and cooling. Additionally, the *Nakazato 2013* Model is not displayed, as it has already been compared to the *Bollig 2016*, showing discrepancies in the emission spectrum during the accretion phase, while presenting a limited time resolution ($\sim$ 300 points) and not taking into account convection effects.

Regarding the temporal evolution of the neutrino burst, the explosion in *Fornax 2021* occurs later. As anticipated, multi-dimensional modeling can account for factors that may delay the revival of the shock wave. Additionally, the collapse of *Fornax 2021* happens at a later time, accompanied by a burst of *neutronization* occurring approximately 20-30 milliseconds later. The time evolution of the other 1D models is similar, although there are some subtle differences, especially in the case of the *Warren 2020* model. The increased emission rates of neutrinos, namely for $\bar{\nu}_e$ and heavy flavors ν_x, during the late accretion and cooling stages are mostly attributed to the presence of turbulence. This effect is observed in the 1D models, although it is more pronounced in the 2D *Fornax 2021* model. Additionally, it undergoes collapse prior to the neutronization burst, occurring a few milliseconds earlier than *Bollig 2016* and *Sukhbold 2015* models.

To have a complete view of the different models, it is necessary to include the temporal evolution of the average energy throughout the burst. This clue serves to further assess whether the model more accurately represents the physics of CCSN mentioned in the preceding sections. Considering the main picture of a neutrino burst, it can be anticipated that the mean energy will rise rapidly prior to the explosion, followed by minor fluctuations but a slow decline during the later stages of accretion and cooling. It is also expected to observe a significant reduction in the high-energy tail as a result of the (anti)neutrino electron scattering with nucleons, especially during the neutronization burst. As mentioned before, *Warren 2020* does not fulfill this last aspect, demonstrating markedly elevated average energies of around 14 MeV. Furthermore, the behavior exhibited by *Fornax 2021* deviates from this high-tail suppression pattern during neutronization as well as during accretion, when the average energy level rises and persists throughout the cooling phase. Regarding the mean energy distribution, this model is not able to accurately represent its projected evolution.
Once again, the studies conducted by *Bollig 2016* and *Sukhbold 2015* demonstrate a striking similarity in their average energy distribution. However, Sukhbold's model appears to provide a somewhat better fit for energy variations following the explosion. This includes a significant fall in energy before the explosion, followed by a sudden drop and subsequent oscillations. The selected progenitor from the study conducted by R.Bollig in 2016 initiates the explosion prior to the one described by Sukhbold in 2015. Consequently, the energy drop occurs earlier. Nevertheless, both observations align with the anticipated characteristics of the neutrino burst, and the discrepancies between them are not substantial.

2.4.2 CCSN Model Physics list

As described in the **Section 2.2** neutrino burst is strongly correlated to the CCSN time evolution and physic process derived of it. It is anticipated that the majority of models will utilize a *CCSN Physics list* that covers both neutrino generation and subsequent neutrino-matter interaction during the collapse. The EoS is responsible for this physics list, as it determines the principal factors such as star structure, temperature, density, baryonic (specifically neutron concentration), and leptonic numbers. Neutrino-matter interactions can be optimized depending on the handling of the neutrino-heat mechanism, which includes convection, SASI and turbulence. These factors have already been detailed and can affect the rate of the interactions. In addition, certain initial conditions, such as the mass, metallicity, and chemical composition (specifically the H/He fraction) of the progenitor, will influence the subsequent dynamics of the EoS and thus affect the emission of neutrinos.

Equation of State

The Equation of State (EoS) for hot, dense matter in star cores is not well understood. This results for our inability to reproduce such extreme conditions in the laboratory. Despite having estimations of the necessary parameters to compose the EoS, it is challenging to confine correlations and inter-dependencies inside a dynamic equation that encompasses the micro-physics of the weak, strong, and electromagnetic interactions, including the frame of general relativity, crucial to model radiation hydrodynamics, such as the *GR1D* model[10] [59]. CCSN simulations serve as a virtual laboratory for simulating the physics at high densities, where specific parameters cannot be directly retrieved or tested, but can only be indirectly validated by accessible astronomical data. The EoS is one of the sources of uncertainty in the flux of neutrinos from CCSN.

The following quantities and features are all determined by the EoS: the density and timing of the core bounce, the rate at which matter is accreted, the timing and mechanism of reviving a stalled shock, the production of thermal neutrinos (which is determined by the contraction, radius, mass, temperature, and density evolution of the PNS), the success of the explosion, the cooling process, the formation and characteristics of the resulting remnant. The evolution of the neutrino differential spectra (equation 2.27) and its exact flavor composition depend as well on the EoS.

Acknowledging the inherent uncertainties in the EoS resulting from the limited availability of scientific data on CCSN — or insufficient self-consistent experimental data on CCSN core conditions in the laboratory —, it can be noted that the level of convergence achieved in the physics incorporated in most of the EoS, makes the latter less significant compared to the spatial dimension of the simulation. Regarding the detection of neutrinos, the application of dimensionality to the EoS has a significant impact on the reconstruction of the temporal and energy spectrum of the detected signal. These approximations have a particularly strong effect on light curves and the success of explosions.

[10]This is the main neutrino transport model used for *SNEWPY* Models `https://github.com/evanoconnor/GR1D`

Neutrino-Matter interaction

In this section, a concise overview of the primary interactions that impact the transportation and generation of neutrinos in the context of CCSN modeling will be provided. The majority of these interactions have already been discussed in **Section 2.2**. There is a python library called NuLib that has summarized information about neutrino interactions. It can be found at this URL: https://github.com/evanoconnor/NuLib.

- **Charged Current neutrino absorption/emission**

  The absorption of neutrinos by free nucleons (and nuclei) is the primary cause of neutrino opacities, and at the same time of neutrino emission. This process mainly involves the production of neutrinos of the electron flavor through electron captures on free nucleons, or nuclei.

- **Neutral Current Neutrino-Heavy Nuclei scattering**

  As mentioned in **Section 2.2.1**, neutrino-nuclei coherent scattering [142] (equation 2.2) is responsible for the neutrino trapping before the bounce. It is also the main process for energy transfer, from neutrinos to matter, during the accretion phase, susceptible to reviving the stalled shock. In this sense it is worth to mention here some corrections often applied that can have an impact on the efficiency of this transfer:

  - Many-body corrections can increase the neutrino-matter heating rates in the gain region and, hence, facilitate explosion. [143, 144]
  - Strangeness corrections in cross-sections can also balance in favor of the explosion [145, 146]

- **Thermal production**

  Pair annihilation (equation 2.8) [142] and Bremsstrahlung (equation 2.7) [147], are the main interactions for the heavy flavor neutrino production, and dominates the thermal part of the flux, i.e. heavy flavor luminosities. Those reactions will increase the neutrino density in PNS, allowing self-neutrino interactions to increase secondary heavy flavor production.

- **$\nu - \nu$ interaction**

  Neutrino-neutrino interaction (equation 2.9) plays a significant role in the transportation of neutrinos into the CCSN medium. It is the primary source, beyond matter effects, for the alteration of neutrino flavor [70] (refer to Section 2.5). The potential describing $\nu - \nu$ interaction is influenced by the density of neutrinos which are considered to be prominent in the PNS and denser regions, such as the neutrino-sphere, during the accretion phase. When it comes to the production of neutrinos, a significant fraction of heavy flavors results from the induced flavor oscillation of electron flavor

neutrino-neutrino coherent scattering. This production mechanism turns out to be more important than electron-positron annihilation (equation 2.8) [148].

Recent studies indicate that considering a strong self-interaction potential increases the duration of the neutrino burst, which is consistent with the SN 1987 time evolution of the burst [149]. Furthermore, the efficiency of the neutrino heat mechanism can be significantly lowered by the interaction between neutrinos, $\nu - \nu$ coherent scattering. In the gain region, this interaction can lead to a reduction of around 40% in the energy transfer efficiency, as shown in the reference [85]. Finally, regarding the simulation of $\nu - \nu$ interaction, it has a strong angular dependence, as it is basically governed by neutrino coherent scattering. This implies the necessity of an accurate multi-dimensional approach, as neutrino trajectories need to be modeled. Flavor transformation and neutrino self-potential interaction will be introduced in **Section 2.5.3**.

- **Electron Scattering**

  The scattering of electrons by neutrinos:

$$e^{-(+)} + \nu(\bar{\nu}) \quad \Longrightarrow \quad e^{-(+)} + \nu'(\bar{\nu}') \tag{2.32}$$

  occurs approximately 100 times less likely compared to the scattering of nucleons, at a typical neutrino energy of around 10 MeV [143]. Nevertheless, its energy transfer is highly efficient and substantial, resembling to a Compton-like scattering. The inelastic interaction, on the other hand, mostly changes the electron flavor of (anti)neutrinos by scattering electrons, which makes their average energy go down. This significantly impacts the efficiency of heat transfer to the accretion shock. Note, that in the case of electron scattering only neutral current involves neutrino heavy-flavor.

2.4.3 Other CCSN Physics

Not all the CCSN simulations result in a successful explosion. Alternatives to the primary *neutrino-heat-mechanism* are investigated in order to elucidate the revival of the shock. In addition to the uncertainty surrounding the explosion mechanism, there are also undetermined physics processes responsible for the eventual rotation of the NS remnant. Astronomical measurements indicate that neutron stars exhibit rapid rotational speeds on the order of approximately 1000 km/s [150, 56, 151]. Stellar evolution theories suggest that the cores of massive stars rotate rapidly. However, measurements on low-mass stars have shown that this rotation is actually slower than predicted. Nevertheless, the rotation speed increases during the collapse of the star. The asymmetries resulting from the SASI might impart angular momentum to the cores of proto-neutron stars [152]. These instabilities can cause asymmetry in the matter ejection following the explosion, leading to spatial variations in the flux of neutrino emissions. This phenomenon has been treated in many studies [153, 154, 122, 155].

The effects of this rotation can be examined by studying neutrino emission [156], as SASI instabilities produced quasi-periodic time modulation that can be characterized [157, 158, 159]. In this context, a recent study [156] suggests that the *IceCube* detector is expected to be sensitive to them, along with other future detectors such as *Hyper-Kamiokande* and *DUNE* (those experiments are introduced in **Section 3.1.3**).

In addition, the rotational motion can be intensified if the transfer of heat by neutrinos penetrates the PNS without dissipating, hence increasing its rotation. The Lepton-Number Emission Self-sustained asymmetry (LESA), as described in [157], has the ability to propel the PNS to velocities ranging from 100 to 200 km/s, as reported by [160]. If considering the impact of strong magnetic field, this kick has the potential to reach a velocity of 3000 km/s[161].

The angular momentum can enhance the magnetic field, resulting in intense fields exceeding 10^{12} G. They can influence the explosion process and subsequent asymmetries in the ejection of materials, including neutrinos. The "magneto-rotational CCSN mechanism" [162, 163], offers an alternative explanation for the explosion of core-collapse supernovae (CCSN). A strong magnetic field can generate asymmetries in neutrino emissions, therefore increasing the efficiency of energy transfer from neutrino-shock interactions. This, along with other instabilities, can contribute to the explosion process [164, 165].

Rotation and magnetic field are strongly coupled and have both an impact on the stellar nucleosynthesis and path of the progenitor through collapse [166]. The magneto-rotational mechanism requires a sufficiently rapid rotation of the PNS core in order to enhance the existing magnetic field [167, 163, 168, 162]. It is expected to exhibit a bipolar structure aligned with the rotational axis, with a preference for expelling matter in the direction of this axis. This amplification also proves to be more energy efficient than the neutrino-heat mechanism, leading to one order of magnitude larger explosions $\sim$ 10 Bethe[11] [169]. The magneto-rotational mechanism is considered as a potential explanation for the core collapse of Hypernovae HNe, as discussed in references [170, 171]. In the context of neutrino detection, less interesting occurrences are expected, as they are more rare [12]. However, such a mechanism enables the exploration of parity-violation caused by the existence of a magnetic field. The model proposed by *Kuroda 2021* [102] simulates the effects of magnetic fields at three different levels of intensity. The simulation demonstrates the successful occurrence of an explosion for two of these intensity levels.

CCSN Models: Summary and Conclusions

At this point, an evaluation of the models integrated in SNEWPY can be done. It should be emphasized that the following conclusions only regard models in SNEWPY in the version cited in the reference [117], corresponding to the one used in the CCSN neutrino signal simulation in this thesis. That said, it is unlikely that recent eventual updates of the package might have a relevant impact on the assumptions that will be stated in the next sections. Other approaches and updates can be found, particularly in the garching group database[116].

[11] 1 Bethe = 10^{51} ergs

[12] The estimated galactic rate is approximately 10^{-5}-10^{-6}/year [172]

As a conclusion, *Bollig 2016* and *Sukhbold 2015* accounts for the expected picture of the neutrino burst. No substantial differences between them are present regarding CCSN neutrino initial spectra. However, *Bollig 2016* has a better time resolution with more than 10 000 points. This is illustrated in **figure 2.7**, in the first two panels related to the (anti)neutrino electron spectra. During the neutronization, in the first tens of milliseconds, the *Bollig 2016* is smoother than *Sukhbold 2015* because it uses a cubic energy interpolation. This mainly affects the resolution of ν_e neutronization burst. A priori, in the XENONnT dual-phase xenon time projection chamber (TPC) in which neutrino coherent elastic scattering with Xe nucleus (CEνNS) is sensitive to all neutrino flavors, this can enhance the detection uncertainty for the intense rate during neutronization burst. On the other hand, CCSN ν_e events are not expected to be observed in the water tank, being the flavor of interest $\bar{\nu}_e$, detectable via IBD interaction. However, the flux represented **figure 2.7** is the initial spectra, applying no flavor transformation, but it is expected that flavor oscillation significantly impacts both ν_e and $\bar{\nu}_e$ spectra. This transformation during the transport of neutrinos in the CCSN medium will be explored in the next section. For the simulation of CCSN neutrino signal in water tank and the dual-phase xenon TPC, *Bollig 2016* will be the chosen model in the context of this thesis.

2.5 Neutrino Transport in CCSN

The local medium of supernovae has an impact on the survival probability of a neutrino flavor. This section will focus on two primary factors that influence the transportation of neutrinos and their interplay with flavor oscillations. The first is the Mikheyev–Smirnov–Wolfenstein (MSW) effect. As described in reference [173], this effect is influenced by the non-contribution of ν_x to the CC interaction, while ν_e and $\bar{\nu}_e$ scatter with electrons and nuclei through this channel. This difference in neutrino-matter interaction between electron and non-electron neutrino, is dependent on the electron number density (n_e). Secondly, $\nu - \nu$ interactions can induce a high rate of flavor transformations. In this case, the neutrino number density, denoted as n_ν, is the main factor that regulates this process, as demonstrated in studies presented in references [174, 175, 176, 177]. Both effects can be associated to the $\mathcal{V}_{matter}(\mathrm{t})$ and the $\mathcal{V}_{\nu\nu}(\mathrm{t})$ potentials, respectively. These may be incorporated into the dynamics of the neutrino Hamiltonian $\mathcal{H}(\mathrm{t})$. In the CCSN medium, the two type of densities, electron and neutrino, depend on time. However, it can be anticipated that the evolution of the electron density can be considered as adiabatic, after some assumptions that will be described later in this section.

The mixing of neutrino flavors leading to the transformed final flux leaving the CCSN medium is determined by the interactions with the surrounding matter and its varying density. To understand the role of the CCSN medium in neutrino oscillations, it is necessary to establish first the concept of neutrino oscillations in a vacuum. This involves defining the Hamiltonian $\mathcal{H}_0$, which describes the dynamics of neutrinos in a vacuum. Subsequently, it can be examined how this Hamiltonian changes when the neutrinos interact with high-density media and the associated potentials. The time dependent Hamiltonian can be splitted in tree terms: vacuum $\mathcal{H}_0$, matter (or MSW) $\mathcal{V}_{matter}(t)$ and $\nu - \nu$ interaction $\mathcal{V}_{\nu\nu}(t)$ potentials.

Summarizing, the total neutrino Hamiltonian $\mathcal{H}(t)$ can be written as:

$$\mathcal{H}(t) = \mathcal{H}_0 + \mathcal{V}_{matter}(t) + \mathcal{V}_{\nu\nu}(t) \tag{2.33}$$

The rest of the section will introduce both three terms of this equation.

2.5.1 Neutrino Flavor Oscillations in Vacuum

Neutrino oscillations were postulated in 1957 by Bruno Pontecorvo, under the condition that neutrinos possess non-zero masses, which was not initially considered in the Standard Model (SM) of particle physics. Several neutrino experiments have shown evidence for the phenomenon of neutrino oscillations. One of the important implications of this oscillation mechanism is its ability to explain the shortfall of neutrinos observed in the named *solar neutrino problem* [178, 179, 180], emerging in 1967 by R.Davis observations [181]. Estimates of the neutrino flux originating from the solar pp-chain indicate a shortfall, especially in the electronic flavor component observed on Earth. Finally, the evidence of neutrino oscillation in atmospheric neutrinos observations by Kamiokande in 1998 [182], lead to the extension of SM to include massive neutrinos.

Neutrino only interact via the weak interaction which depends on the flavor. To produce vacuum oscillations the neutrino flavor states have to be represented in the mass basis, using a unitary transformation given by [78]:

$$|\nu_\beta\rangle = \sum_{i=1,2,3} U^*_{\beta i} |\nu_i\rangle \,, \tag{2.34}$$

with i the index corresponding to each mass state and the unitary matrix $UU^\dagger$=1 defined as:

$$U = \begin{bmatrix} c_{12}c_{13} & s_{12}c_{13} & s_{13}e^{-i\delta_{CP}} \\ -c_{23}s_{12} - s_{23}c_{12}s_{13}e^{i\delta_{CP}} & (c_{23}c_{12} - s_{23}s_{12}s_{13}e^{i\delta_{CP}})e^{i\phi_2/2} & s_{23}c_{13} \\ s_{23}s_{12} - c_{23}c_{12}s_{13}e^{i\delta_{CP}} & -s_{23}c_{12} - c_{23}s_{12}s_{13}e^{i\delta_{CP}} & c_{23}c_{13}e^{i\phi_3/2} \end{bmatrix}. \tag{2.35}$$

Here $c_{ij} = \cos\theta_{ij}$, $s_{ij} = \sin\theta_{ij}$, θ_{ij} represent the ν_i-ν_j mixing angles (i, j=1,2,3), $e^{i\phi_2/2}$, $e^{i\phi_3/2}$ are the Majorana phases [183]. The parameter δ_{CP} as well as Majorama phase, represents a possible CP-violating phase. The eigenenergies of the mass neutrino eigenstates of the diagonal vacuum Hamiltonian $\mathcal{H}_{\rm m0} = {\rm diag}(E_i)$ can be defined as:

$$E_i = \sqrt{\mathbf{p}_i^2 + m_i^2} \,, \tag{2.36}$$

with the neutrino momentum $\mathbf{p}_i$ and the mass m_i. Assuming that neutrinos are ultra-relativistic, their energy can be approximated as:

$$E_i \approx E + \frac{m_i^2}{2E} \,, \tag{2.37}$$

where $p_i \sim p_j = |\mathbf{p}| = E$.

Finally, in the flavor basis, the vacuum Hamiltonian can be so described through the following relation:

$$\mathcal{H}_0 = U\mathcal{H}_{\mathrm{m0}}U^* = U \begin{bmatrix} 0 & 0 & 0 \\ 0 & \frac{\Delta m^2_{21}}{2E} & 0 \\ 0 & 0 & \frac{\Delta m^2_{31}}{2E} \end{bmatrix} U^\dagger \tag{2.38}$$

At this point, it is convenient to express the probability of flavor $\beta \to \alpha$ transformation as $P_{\beta\to\alpha}(t)$, at an instant t. For that, the plane wave solution to the Schrödinger equation of motion for mass eigenstates $|\nu_i(t)\rangle$ in vacuum has to be defined:

$$i\hbar\frac{d}{dt}|\nu_i(t)\rangle = \mathcal{H}_{\mathrm{m0}}|\nu_i(t)\rangle \qquad |\nu_i(t)\rangle = e^{-iE_it}|\nu_i(0)\rangle\,. \tag{2.39}$$

$|\nu_i(0)\rangle$ the initial condition for the mass eigenstates, and $|\nu_\beta\rangle \equiv |\nu_\beta(0)\rangle$ refers to the initial condition of the flavor state in equation (2.34). Using this result, the probability for a $\beta \to \alpha$ oscillation reads as:

$$P_{\beta\to\alpha}(t) = |\,\langle\nu_\alpha|\nu_\beta(t)\rangle\,|^2 = \sum_{i,j=1,2,3} U^*_{\beta i}U_{\alpha j}U_{\beta j}U^*_{\alpha i}\underbrace{|\,\langle\nu_j|\nu_i\rangle\,|^2}_{=1}e^{-i(E_j-E_i)t}\,. \tag{2.40}$$

An analytic solution of the equation (2.40), assuming the possibility of three flavor mixing, can be expressed as [184, 78]:

$$P_{\beta\to\alpha}(t) = \delta_{\beta\alpha} - 4\sum_{i<j} Re[U_{\alpha j}U^*_{\beta j}U^*_{\alpha i}U_{\beta i}]sin^2X_{ij} + 2\sum_{i<j} Im[U_{\alpha j}U^*_{\beta j}U^*_{\alpha i}U_{\beta i}]sin2X_{ij} \tag{2.41}$$

$$X_{ij} = \frac{(m_i^2 - m_j^2)L}{4E} = \Delta m^2_{ij}\frac{L}{4E}, \qquad \Delta m^2_{ij} = m_i^2 - m_j^2 \tag{2.42}$$

When neutrino oscillations were predicted, the relative weights of these three mass states were unknown. The mass relations between these three states are called *mass ordering*. Today, experiments measuring the two mass differences $\Delta m^2_{2,3}$ and $\Delta m^2_{2,1}$ are so precise that the inference of those quantities start to differ with the two possible mass ordering scenarios: the normal mass ordering (NMO), where $m_3 > m_2 > m_1$, and the inverted mass ordering (IMO), where $m_2 > m_1 > m_3$ [78]. This hierarchy affects also the transformation described in equation (2.34) as it impacts the neutrino mixing matrix U. Below, recent results for the parameters of U, required to estimate neutrino flavor oscillations probabilities (equation (2.40)), are summarized [185, 186] [13].

[13] Concerning the squared mass difference parameters, the best fit ordering with a 1σ significance is represented. These values are from reference [187]

$$
\begin{aligned}
\sin^2\theta_{12} &= 0.304^{+0.013}_{-0.012} \quad (\text{ NMO or IMO }),\\
\sin^2\theta_{23} &= 0.452^{+0.052}_{-0.028} \quad (\text{NMO}), \quad 0.579^{+0.025}_{-0.037} \quad (\text{IMO}),\\
\sin^2\theta_{13} &= 0.0218^{+0.0010}_{-0.0010} \quad (\text{NMO}), \quad 0.0219^{+0.0011}_{-0.0010} \quad (\text{IMO}),\\
\delta_{CP}[^\circ] &= 306^{+39}_{-70} \quad (\text{NMO}), \quad 254^{+63}_{-62} \quad (\text{IMO}),\\
\Delta m^2_{3l} &= 2.507^{+0.026}_{-0.027}10^{-3}\times \text{eV}^2(\text{NMO}), \quad -2.486^{+0.025}_{-0.028}\times 10^{-3}\times \text{eV}^2(\text{IMO}),\\
\Delta m^2_{21} &= 7.39^{+0.21}_{-0.20}10^{-5}\times \text{eV}^2(\text{NMO or IMO}).
\end{aligned}
\tag{2.43}
$$

with $l = 1, 2$ and $\Delta m^2_{31} > 0$ in NMO and $\Delta m^2_{32} < 0$ in IMO. The values reported neglect the Majorana phases, as they do not affect the flavor transformation probability. As concluded in **Section 1.4**, the next CCSN neutrino burst is expected to come from the center of the galaxy, from a SN progenitor at a distance of around 10 kpc from us. At this distance, for neutrino energies of $\mathcal{O}(10$ MeV), the phase terms X_{ij}, also called oscillatory terms, vanish as they average out [188, 189]. This leads to averaged transformation probabilities from neutrinos arriving at the earth only depending on mixing parameters, i.e. the $U_{\alpha i}$ terms [78]:

$$P_{\beta\to\alpha}(t) = \sum_i |U_{\beta i}|^2 |U_{\alpha i}|^2. \tag{2.44}$$

Another cause for the vanishing of the oscillatory term is the loss of coherence. A significant decoherence occurs when neutrinos traverse the CCSN medium, due to the high density of the latter medium. Hence, flavor transformation probability will be no more dependent on the ratio L/E [188].

2.5.2 Neutrino in CCSN dense matter

The objective of this section is to examine the flavor transformations that occur when neutrinos are transported through dense matter. The presence of dense matter will have an impact on oscillations as different neutrino flavors do not interact with matter in the same manner, as previously discussed in **Sections 2.2** and **2.4.2**. A starting point may be to incorporate the matter potential $\mathcal{V}_{matter}(\text{t})$ into the Hamiltonian, equation (2.38). The unitary matrix U_m describes now the transformation of U matrix (2.34) between flavor and mass basis, acting into the matter Hamiltonian $\mathcal{H}_\text{m}$, which is the corresponding representation of the Hamiltonian in the mass basis [184, 190, 191]:

$$\mathcal{H} = U\mathcal{H}_{\text{m}0}U^\dagger + V_{matter} = U_m\mathcal{H}_\text{m}U_m^\dagger. \tag{2.45}$$

The projection of flavor states in this new basis becomes:

$$|\nu_\beta\rangle = U_m\,|\nu_{im}\rangle\,. \tag{2.46}$$

The interaction of neutrinos with matter can be divided in two channels: neutral current and charged current, affecting differently electron and heavy flavors. Hence, let be the $\mathcal{V}_{matter}$ equal to the sum of these two contributions:

$$\mathcal{V}_{matter} = \mathcal{V}_{NC} + \mathcal{V}_{CC} \tag{2.47}$$

The charged current contribution is dominated by the scattering of (anti)neutrinos and (positron) electrons, as described in equation (2.4), and is predominantly influenced by the fermion density. The neutral current on the other hand is characterized by the neutrino-nuclei scattering (2.2), particularly in neutron rich nuclei as stated in **Section 2.2.1**, and so mainly depends on neutron number density n_n. The important quantity of fermion density arises from the electron number density n_e. The density of positrons is irrelevant, primarily due to pair annihilation. However, it is worth noting that the muon density number, denoted as n_μ, can increase during the accretion phase, contributing to the fermion density, enhancing neutral current interactions [192]. It appears that muons in the PNS can contribute to increase the heat transfer to the stalled shock and potentially assist in initiating the explosion.

Muons interact with neutrinos through neutral current and charged current. However this and the neutral current neutrino-neutron contribution are equal for all flavors, and do not contribute to flavor evolution because they give a term proportional to the identity matrix. Electrons and protons are also engaged in interactions through neutral current. Considering that the CCSN is neutral in charge, it can be inferred that electron and muon numbers compensate for protons, positrons, and anti-muons, implying that their respective contributions to the neutral current are compensated. This means that the neutral current potential is driven by the neutron contribution, and while n_μ is significantly smaller than n_n, which contribution as the same time can be neglected for the detection purposes of this thesis [193]. This finally leads to approximate matter effects, considering neutrino-electron charged current interactions.

After these assumptions, matter Hamiltonian (2.33) can be described by the mean-field approximation, which is detailed in the references [194, 195]. Representation of the matter potential in the flavor basis leads to the following expression from [196, 190]:

$$\mathcal{V}_{matter} = \begin{bmatrix} \sqrt{2}G_{\mathrm{F}}n_e & 0 & 0 \\ 0 & 0 & 0 \\ 0 & 0 & 0 \end{bmatrix} + \begin{bmatrix} -\frac{G_F}{\sqrt{2}}n_n & 0 & 0 \\ 0 & -\frac{G_F}{\sqrt{2}}n_n & 0 \\ 0 & 0 & -\frac{G_F}{\sqrt{2}}n_n \end{bmatrix}. \tag{2.48}$$

The neutral current contribution is diagonal in the flavor space, as it does not distinguish between neutrino flavors. Contrarily, charged current interactions only impact the dynamics of ν_e and $\bar{\nu}_e$. This is the primary factor contributing to the MSW effect in the CCSN medium. One final point to note is that charged current potential therm, $\mathrm{V_{CC}} = \sqrt{2}G_{\mathrm{F}}n_e$ for the ν_e has an opposite sign for $\bar{\nu}_e$, $\bar{\mathrm{V}}_{\mathrm{CC}} = -\mathrm{V_{CC}}$.

MSW Effect

To study the matter effects of transformation between electron and heavy flavors, the matter Hamiltonian can be written explicitly using equations (2.38) and (2.46):

$$\mathcal{H} = U \begin{bmatrix} 0 & 0 & 0 \\ 0 & \frac{\Delta m^2_{21}}{2E} & 0 \\ 0 & 0 & \frac{\Delta m^2_{31}}{2E} \end{bmatrix} U^\dagger + \begin{bmatrix} \sqrt{2}G_{\rm F}(n_e - \frac{n_n}{2}) & 0 & 0 \\ 0 & -\frac{G_F}{\sqrt{2}}n_n & 0 \\ 0 & 0 & -\frac{G_F}{\sqrt{2}}n_n \end{bmatrix}. \tag{2.49}$$

The Mikheyev-Smirnov-Wolfenstein (MSW) effect describes the dependency on the evolution of the electron density, which can result in adiabatic or partially adiabatic flavor transformations [70, 173]. The MSW is the result of two main contributions. The first is the work of Wolfenstein in a series of articles between 1978 and 1984, studying matter effects in neutrino oscillations [197, 198]. The second is an extension to these studies carried out regarding extreme density varying conditions, leading to the theorization of the Mikheyev-Smirnov mechanism in 1985-86[199, 200, 201]. The whole effect ultimately leads to adiabatic neutrino flavor transformation as a consequence of these density variations. The MSW effect is necessary to properly describe neutrino flavor evolution in the Sun. Its formulation aided to understand the 1/3 reduction for the ^{8}B neutrinos in comparison to the SM prediction[202]. On the contrary, in CCSN medium, a small impact of MSW induced mixing flavor is expected, driven by the 1–3 transformation [203]. To investigate oscillations in the dense CCSN environment, it is necessary to express the potential of matter in the matter state basis, referred to as $|\nu_m\rangle$. This can be achieved by utilizing the Schrödinger equation and equation (2.46), while also ensuring that the unitary condition $U_m^\dagger U_m = \mathbf{1}$ is satisfied. The resonant condition for the MSW effect[202] can be written as:

$$\frac{\Delta m^2}{2E} cos2\theta = \sqrt{2}G_F n_e. \tag{2.50}$$

This solution is obtained in the case the term sin $2\tilde{\theta}$, associated to the effective mixing angle $\tilde{\theta}$ in matter, is maximum (sin $2\tilde{\theta} \rightarrow$1). $\tilde{\theta}$ is related with the mixing angle θ through the following relation:

$$\sin 2\tilde{\theta} = \frac{\sin 2\theta}{\sqrt{(\cos 2\theta - \frac{\rm V_{cc}}{k})^2 + \sin^2 2\theta}} \tag{2.51}$$

Adiabaticity for flavor oscillations implies that density variations are slow, and by this fact, negligible compared to k. In this sense, the adiabaticity condition is related to the mixing angles $\tilde{\theta}$ in matter and the $\Delta\epsilon$ evolution, that depends on n_e. In order to study the MSW resonance within the CCSN environment, the adiabaticity condition (γ_R) can be expressed as [190, 204]:

$$\gamma_R^{-1} = k\frac{\sin^2 2\theta n_e}{\cos 2\theta |\dot{n}_e|}, \qquad k = \frac{\Delta m^2}{E} \tag{2.52}$$

with $\dot{n_e} \equiv \frac{dn_e}{dt}$. To understand implication of this equation one can examine the standard values of n_e and $\rm V_{cc}$ in relation to k . Intentionally, the equation (2.51) was written into this form, in order to be evaluated based on their dependence on the relation $\rm V_{cc}$/k. The CCSN medium during the phases of neutronization and accretion is characterized by a dense matter profile, as explained in Sections 2.2.1 and 2.2.2. At high densities $\frac{\rm V_{cc}}{k} \gg 1$, assuming that the electron density number n_e depend on matter densities (ρ_{SN}(x)) and the electron fraction (Y_e) as: $\rm Y_e\rho_{SN}(x)$.

At high densities $\sin 2\tilde{\theta} \to 0$ (from equation (2.51)). This large densities can appear in the vicinity of the PNS and the neutrino-sphere. In addition, it can be noted that as $\sin 2\tilde{\theta}$ depends on the $Y_e\ \rho_{SN}(\mathrm{x})$ product, Y_e diminution at some time after the bounce may compensate the large $\rho_{SN}(\mathrm{x})$. However, as shown in the bottom panel of **figure 2.8**, Y_e remains stable, and is not expected to present significant modifications, able to affect the electron density. However, the density profile of matter undergoes variations due to the formation of low-density zones in outer layers.

It is possible to find specific areas and times in which resonances caused by the MSW effect may have a significant effect by using the term (2.50). There are three potential resonances that might occur: $\nu_2 \to \nu_1$, $\nu_1 \to \nu_3$, and $\nu_2 \to \nu_3$. The last resonance indicates a transformation from ν_μ to ν_τ [205]. The effects of the late transition cannot be observed through the flux of a CCSN supernova, since the assumption of neutrino population: $x \equiv \mu \equiv \tau$. The problem can be simplified to the remaining two resonances. Considering the significant difference between the values of the neutrino mass eigenstates (2.43), a distinct and noteworthy disparity in the effects of the two resonances can be expected. In this sense, high-resonance, which is associated with the neutrino oscillation frequency $k_H = \frac{\Delta m^2_{31}}{2E}$, and low-resonance, associated with $k_L = \frac{\Delta m^2_{21}}{2E}$, can be differentiated. At the same time, its respective density resonances are:

$$n_H = k_H \frac{Y_e cos2\theta}{\sqrt{2} G_F}, \qquad n_L = k_L \frac{Y_e cos2\theta}{\sqrt{2} G_F} \tag{2.53}$$

Likewise, in the vacuum scenario, the probability of flavor transitions in matter is driven by the mixing angles. Those are re-defined in matter, but still depending on vacuum mixing parameters $\tilde{\theta}_{ij}(\theta_{ij}, \Delta m^2_{ij})$ (see equation (2.51)). The probability of resonances, namely the high (H) and low (L) resonances, denoted as $P_H(\theta_{31}, \Delta m^2_{31})$ and $P_L(\theta_{21}, \Delta m^2_{21})$ respectively, finally depends on the vacuum mixing parameters.

The transition probabilities are sensitive upon the density profile of the CCSN at a particular time. This density profile influences the makeup of regions inside the onion-like structure of the CCSN medium, and potentially gives emergence to regions of MSW resonance density. **Figure 2.8** illustrates the variation in density with respect to the radius of the CCSN. Regions where the two density resonances ($\rho_H \equiv n_H$ and $\rho_L \equiv n_L$ from (2.53)) occur, are highlighted by yellow and cyan bands for the normal mass ordering (NMO). The width of the band corresponds to the energies for which the MSW resonance condition is fulfilled. The matter profile intersects these bands during the cooling phase at a time $t_{pb} \geq 2$s. The average energy of neutrinos decreases gradually over this period of cooling, and the average energy range for ν_e is between 7 and 12 MeV (refer to **figure 2.1**). This values give resonance densities bands of $\sim$0.47-0.8 10^4 g/cm^3 for H and $\sim$0.55-0.94 10^2 g/cm^3 for L resonances, considering once again that $Y_e = 0.5$. Since the variable $n_{H,L}$ are inversely proportional to the energy E, the impact of these resonances will be greater for neutrino energies below 10 MeV (see equation (2.53)).

The evolution through the MSW H and L resonances, are adiabatic for typical CCSN profiles, in absence of shock waves; whereas shock waves can produce non-adiabatic evolution. These effects can produce neutrino spectral swapping or spectral modifications [176, 208, 209, 210].

The probability of MSW resonance for both the H and L-resonances can be stated using the linear

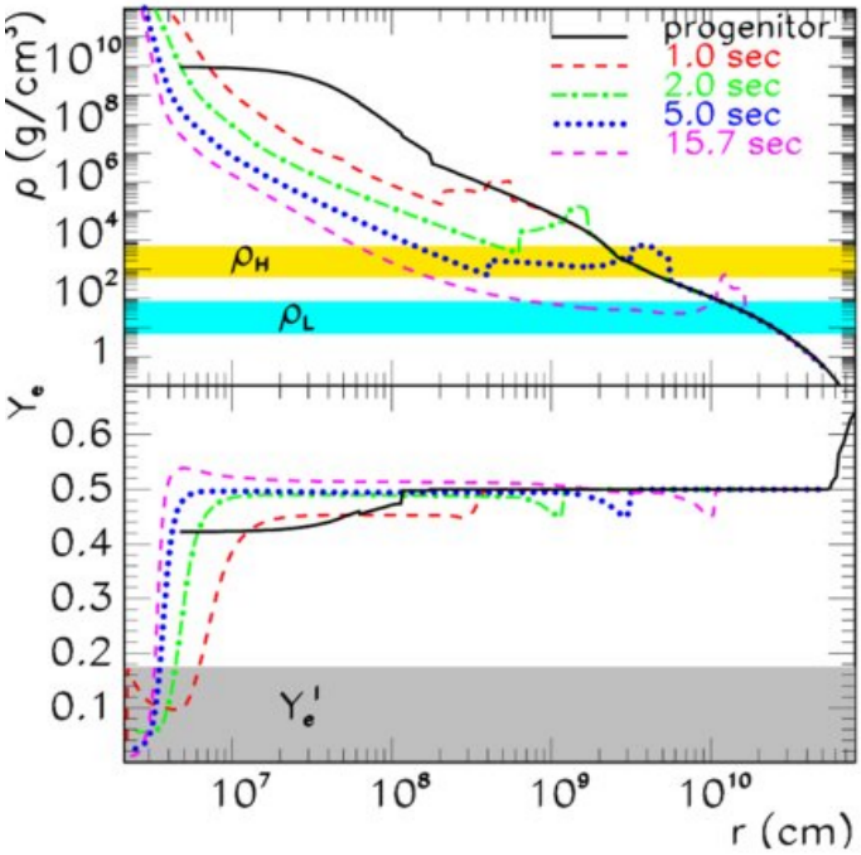

Figure 2.8: **Top**. SN matter density profiles, at different post-bounce times, as a function of distance in an exploding CCSN model. Front and reverse shocks are visible. Bands corresponds to density resonance for High (yellow) and Low (cyan) resonances from expression (2.50) [206]. **Bottom**. Electron fraction Y_e evolution as a function of the radius for several times after the bounce. The gray zone can be ignored present resonance region for non standard neutrino interactions. Figure from [207].

transformation $U \to U_m$. Survival probabilities for electronic flavors turns out to be equivalent in the two flavor approximation $P^m_{ee} \equiv \bar{P}^m_{ee}$ [211]. The last can be expressed in terms of probability transformations between two mass eigenstates i,j denoted as P^m_{ij} [212]:

$$P^m_{ee}(\nu) = \begin{pmatrix} 1\,, & 0 \end{pmatrix} \begin{pmatrix} \cos^2\theta & \sin^2\theta \\ \sin^2\theta & \cos^2\theta \end{pmatrix} \begin{pmatrix} 1-P^m_{ij} & P^m_{ij} \\ P^m_{ij} & 1-P^m_{ij} \end{pmatrix} \begin{pmatrix} \cos^2\tilde{\theta} & \sin^2\tilde{\theta} \\ \sin^2\tilde{\theta} & \cos^2\tilde{\theta} \end{pmatrix} \begin{pmatrix} 1 \\ 0 \end{pmatrix}, \tag{2.54}$$

in the case of high density profile in which $\sin 2\tilde{\theta} \to 0$ and $\cos 2\tilde{\theta} \to -1$. From $U \to U_m$ flavor survival probabilities in matter for the electronic flavor, $P^m_{ee} \equiv \bar{P}^m_{ee}$ can be expressed as a function of the mass state transformation probability in matter P^m_{ij} [213] as follows:

$$P^m_{ee} \equiv \bar{P}^m_{ee} = \cos^2\theta_{ij}\, P^m_{ij} + \sin^2\theta_{ij}\,[1 - P^m_{ij}] = U^2_{ei}\, P^m_{ij} + U^2_{ej}\,[1 - P^m_{ij}]\,, \tag{2.55}$$

It is worth to note that the equivalence between $P^m_{ee} \equiv \bar{P}^m_{ee}$ is only true under the consideration of P_H

and not P_L. In this case, P_H depends on θ_{31} which can be replaced in (2.55) as $P_{31}^m \equiv P_H$. Finally, the unitary matrix for these two flavor scenario transformation is written as:

$$\begin{pmatrix} U_{ei} & U_{ej} \\ U_{xi} & U_{xj} \end{pmatrix} = \begin{pmatrix} \cos\theta & \sin\theta \\ -\sin\theta & \cos\theta \end{pmatrix}. \tag{2.56}$$

Deriving the analytical expression for transformation probabilities P_{ij}^m is a challenging task. The time dependence of the system is influenced by the evolution of the density profile and is also affected by the neutrino energy spectrum. In an adiabatic regime when $P_H \to 0$ the expression can be approximated as $P_{ee}^m \approx sin^2\theta$ [75, 213, 214, 117, 215].

Non Adiabatic Transformations

The probability of flavor surviving depends on the adiabaticity, which fluctuates over time (see equation (2.52)). One way to achieve this was obtained by approximating the convolution between P_H(E) and the neutrino initial spectra at a given time after the bounce, in which the H-resonance is expected to fluctuate in adiabatic and non-adiabatic regimes. This may occur because evolution of the CCSN during the neutrino burst can alter the adiabatic condition, particularly the presence of the shock wave, or turbulences and instabilities mentioned in **Sections 2.2.2, 2.2.3** and **2.4.1**, resulting in a non-adiabatic MSW effect [216, 191]. These non-adiabatic density profiles may alter particularly the H-resonance [206]. In contrast, based on the magnitude of the oscillation frequency k_L, it appears that L-resonance can be approximated consistently, through its value in the adiabatic scenario, in the absence of shock waves [190].

The MSW resonance probability $P_{ij}^m(\Delta m_{ij}, \theta_{ij}, k_{L,H}(r))$ takes a new form, and incorporates the radius dependence r. The reader can find the explicit expression of this probability and the potential profile dependent on the radius in the following works [213, 211]. It is worth to notice that this probability is influenced by the neutrino energy, as its phase is determined by the ratio r/k. **Figure 2.9** top panel shows the evolution in H-resonance probability with respect to neutrino energy in the 5 seconds H-resonance gap, as described in reference [75]. The normalized neutrinos initial spectra given in **figure 2.9** illustrates the neutrino emission probability as a function of energy, during the cooling at 5 seconds after the bounce. The probability H resonance following passes from a pure adiabatic regime when $P_H \to 0$, to an extremely non-adiabatic forward shock-front ($P_H \to 1$) [75]. It is noticeable that, at this 5-seconds time, P_H(E) has a significant influence to a large part of the ν_e and the $\bar{\nu}_e$ spectra.

H-resonance can be affected by the presence of the shock wave, that strongly modifies density matter profile, as well as the electron fraction Y_e. The shock wave after the explosion expands to the external layers, modifying the structure of matter profile during the cooling phase through its passage. Its presence in the MSW H-resonance region can create multi MSW resonances and non-adiabatic density evolution. This can lead to energy drops that will affect final interaction rates at the Earth [190]. This effect turns important particularly for $\bar{\nu}_e$ in the IMO hierarchy case when the detection channel is the Inverse Beta Decay in water [217], which is the case of XENONnT muon and neutron vetoes (as it will be seen in **Section 4.3**). **Figure 2.10** shows this energy drop for the expected IBD rates. The CCSN matter profile,

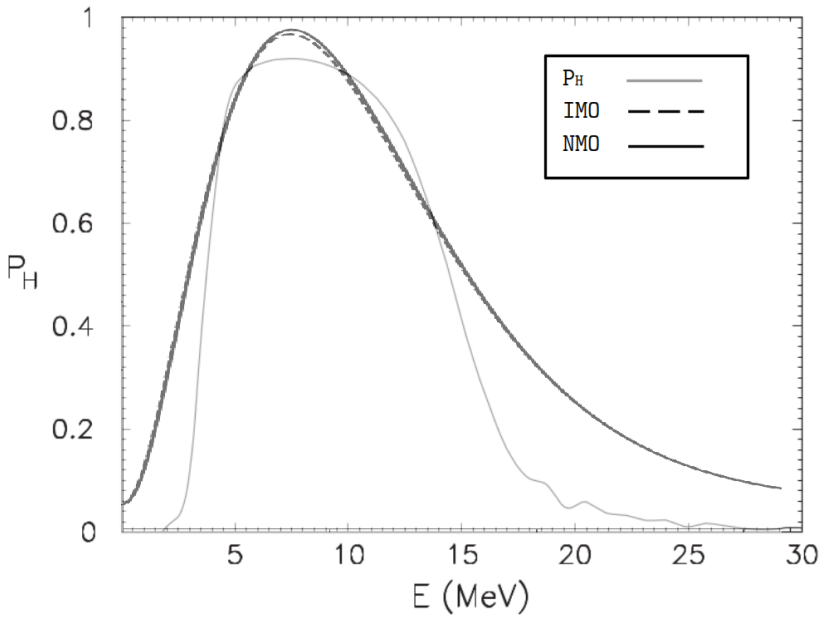

Figure 2.9: P_H (E) at t = 5s, for *large* value of $\sin^2\theta_{13}$.A scaled(not normalized) neutrino energy spectrum at t=5 s is added in black lines for IMO (dashed) and NMO (solid) mass orderings, in order to understand better the implications of the MSW high-resonance transformations. Figure adapted from the original [75]

as well as neutrino energy spectra, depend on the relative position of the shock wave. The blue dotted line includes the case of a forward plus reverse shock waves, which can produce multi MSW resonances. It is worth to notice particularly that the effect of the shock wave crossing the H-resonance region is more significant between 2-10 s. Matter profile behind and forward of the shock, as well as its probabilities regarding H and L resonances, are discussed in more the detail in the following works [206, 190, 211].

The impact on the adiabatic evolution in the MSW effect can be evaluated in the 3 flavor mixing scenario. In this case, it is not necessarily accurate to approximate P_{ee} as $\bar{P}_{ee}$. On the other hand, the contribution of the L-resonance, even in the presence of the shock wave, remains small [75, 190, 117, 216] and it will be neglected. However, a connection may be established between the survival probabilities of ν_e and $\bar{\nu}_e$ in matter, specifically in relation to $P_{\nu_{ee}}$ and the mass ordering, taking into consideration a non-adiabatic H-resonance. This relationship is discussed in references [211, 191], where similar approximations have been done, as in the case of the 2-flavor scenario. The survival probability in matter, denoted as $P^{3\nu}_{ee}$, can be expressed using the PMNS matrix terms from equation (2.35), while ignoring the terms from $_{2\to3}$ this time (as already mentioned, no observable effects result associated to the $\mu \to \tau$ flavor transformation):

$$P^{3\nu}_{ee} = |U_{e1}|^2 \, P_L \, P_H + |U_{e2}|^2 \, (1 - P_L) \, P_H + |U_{e3}|^2 \, (1 - P_H) \tag{2.57}$$

where P_L and P_H are the probabilities related to the L and H resonance, analogous to P^m in the 2ν flavor mixing case. Neglecting the P_L terms, we can include the $\bar{\nu}_e$ probability in NMO and IMO cases as [71, 149]:

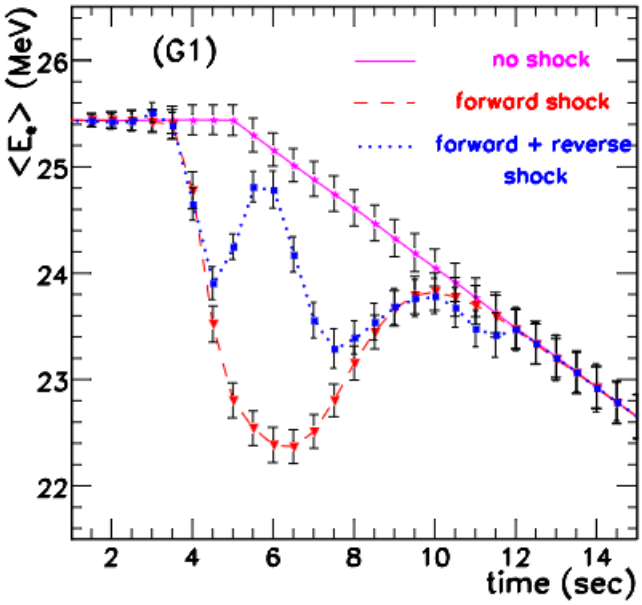

Figure 2.10: The average energy of inverse beta decay ($\bar{\nu}_e + p \rightarrow n + e^+$) events binned in time for a static density profile, a profile with only a forward shock and with forward and reverse shocks. Forward and forward-reverse corresponding impact on the shock lead to an only one or to a second transformation between the V^+ to the V^- sub-states described in [206]. Figure from [218].

NMO

$$P_{ee}^{3\nu} = |U_{e2}|^2 P_H + |U_{e3}|^2 (1 - P_H), \qquad \bar{P}_{ee}^{3\nu} = |U_{e1}|^2 \tag{2.58}$$

IMO

$$P_{ee}^{3\nu} = |U_{e2}|^2, \qquad \bar{P}_{ee}^{3\nu} = |U_{e1}|^2 P_H + |U_{e3}|^2 (1 - P_H) \tag{2.59}$$

Under a strong adiabatic scenario, the NMO and IMO values for survival probability at the H-resonance are the same. In addition to the shock wave, there are other phenomena, such as turbulences and/or instabilities, that may affect the MSW resonance and flavor evolution of neutrinos in matter. These phenomena are discussed in greater detail in references [190, 211, 219].

2.5.3 Flavor transformations induced by $\nu - \nu$ interaction

After dealing with the MSW effect, $\nu - \nu$ interactions can also be considered in neutrino flavor dynamics. Both effects can be treated separately in terms of dynamics, because they are expected to be significant in different regions of the CCSN medium and at distinct times. Flavor transformations induced by $\nu - \nu$ interaction requires high densities, that are expected to appear around the PNS and neutrinosphere. Such transformations are likely to occur before neutrino flux reaches the MSW H-resonance areas. In this scenario, $\nu - \nu$ interaction produces spectral modifications before the neutrinos reach the MSW resonance region.

Neutrino-neutrino scattering, described in **Section 2.4.2**, can induce neutrino flavor transformations during accretion and cooling phases (but can also be observed from neutronization burst [149]). Regarding neutrino flux, these transformations will mainly impact the neutrino emission, which is dominant in the PNS (see **Section2.2.2**).
The description of this interaction through a potential is more sophisticated than the matter effects discussed in the preceding section, resulting in a many-body problem in a dense medium. The contribution of $\mathcal{V}_{\nu\nu}$ in the Hamiltonian (equation 2.33) is predominantly off-diagonal due to the non-linear nature of this many-body potential. The high neutrino density number n_ν ($\sim 10^{32}$ cm^{-3} [208]) enhances scattering rate, causing mainly by the dispersion of neutrino trajectories. This phenomenon is known as the coherent scattering multi-angle effect [210, 220]. To consider an effective Hamiltonian [221, 75, 190, 177], a multidimensional approach of the CCSN simulation model is required. In early works $\nu - \nu$ scattering was implemented by assuming spherical or radial symmetry, in the neutrino emission in the so called *bulb model* [222, 223].

The modeling of this $\nu - \nu$ interaction potential, requires accurate spatial and time resolution, which will require enormous computing efforts, for the simulation of the entire 10 seconds neutrino burst. Furthermore, the effects induced by the neutrino-neutrino interaction on flavor transformations are not yet fully understood. However, as the modeling of CCSN is expected to be significantly improved in the next few years due to the exponential increase in computing capabilities, the implications of $\nu - \nu$ transformations will be thoroughly reviewed in view of future analyses.
To estimate the magnitude of the frequency of flavor transformations induced by $\nu - \nu$, an approximation through an effective potential $\mathrm{V}_{\nu\nu}$ depending on neutrino density number as $\mathrm{V}_{\nu\nu} \sim \sqrt{2} G_F n_\nu$ can be done [149, 190]. The reader can find the explicit form of this potential in the following works [221, 75] for the bulb model scenario. As proceeded for the MSW effect, the mentioned approximation for the potential may lead to some resonant conditions. So far, there are two types of modes induced by the neutrino-neutrino interaction that have been identified: the slow and the fast modes. The first happens at typical distances of $l_S \sim 10^2 - 10^3$ km from neutrino-sphere [190]. The most notable impact is associated to the $\nu_e, \bar{\nu}_e \to \nu_x, \bar{\nu}_x$ channel, which is expected to occur with a frequency $\omega_{col} \sim \sqrt{\frac{\Delta m^2_{ij}}{2E} V_{\nu\nu}}$[224]. On the other hand, the fast mode has typical length $l_F \sim \mathrm{V}_{\nu\nu}$ [225, 223, 176], that can also be expressed in natural units as frequency $\omega_F \sim \mathrm{V}_{\nu\nu}$.

The principal signature of slow modes in the bulb model are depicted in **figure B.1**, mainly affecting ν_e population in benefit of ν_x at energies ≥ 9 MeV [176, 208, 209, 210]. Regarding the fast mode, the latter presents typical frequencies $\mathcal{O}(\mathrm{ns}^{-1})$ in regions where the relation $2G_F(n_{\nu_e} - n_{\bar{\nu}_e}) \gg \frac{\Delta^2 m_{31}}{2E}$ is satisfied [226, 227]. This makes the fast mode dependent on the ratio $\alpha = \frac{n_{\nu_e}}{n_{\bar{\nu}_e}}$. When this ratio is less than 1, the potential switches its sign. This occurs when the angular distribution within a specific region or along a particular axis is sufficiently distinct to infer an intersection between the ν_e and $\bar{\nu}_e$ trajectories. This is known as the *crossing* into the angular Electron Lepton Number (ELN) distribution [228, 229]. These variations can lead to the instability required to enhance the fast mode conversion [230, 231]. **Figure B.2** depicts polar maps of the α distribution at various CCSN radii during the explosion. However, if the

difference between ν_e and $\bar{\nu}_e$ is too large, the fast mode is suppressed; hence, the former should happen when $\alpha \sim 1$ [232].

The MSW effect and the $\nu - \nu$ interactions impact transformation probabilities that can be evaluated as a function of the distance from the NS surface. **Figure 2.11** represent the evolution of $P_{\bar{\nu}_e \to \bar{\nu}_\alpha}$ in the IMO case as a function of the radius, in the bulb model, within the region influenced by $\nu - \nu$ induced flavor transformations. It can be remembered that $\bar{\nu}_e$ is the main target for CCSN interactions in water through IBD, and the MSW effect has a major impact on $\bar{\nu}_e$ in IMO . As seen from 2.11 the $\bar{\nu}_e$ survival probabilities $P_{\bar{\nu}_e \to \bar{\nu}_e}$ vanish between the 100-200 km region from the NS surface and $P_{\bar{\nu}_e \to \bar{\nu}_e} \to 0$ beyond 300 km. This suggests that the $\bar{\nu}_e$ flux undergoes complete transformation due to the collective oscillations upon reaching the adiabatic MSW zone. Conversely, at a distance of less than 80 km, the probability of $\bar{\nu}_e$ surviving as $\bar{\nu}_e$ approaches 1. In regions close to the PNS, fast modes are expected to dominate, being their influence particularly enhanced at 50-100 km as shown in **figure B.2**, which are not considered in this case.

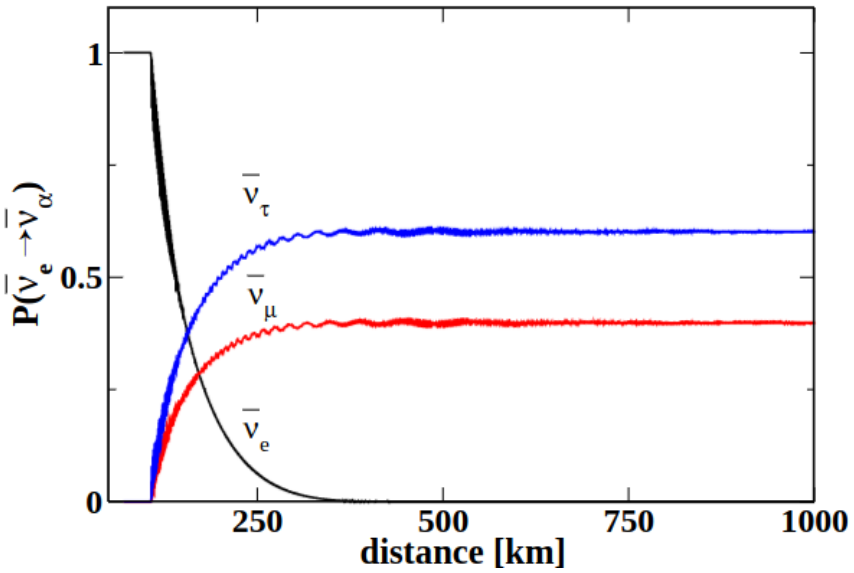

Figure 2.11: Antineutrino oscillation probabilities, as a function of the distance from the neutron-star surface, including the $\nu - \nu$ interaction and the $\bar{\nu}_\alpha = \nu, \tau$. The curves correspond to antineutrinos having 15 MeV energy, the hierarchy is inverted and θ_{31} is large[217]

2.6 Observable CCSN Neutrino flux at the Earth

The previous section allowed to draw few conclusions on neutrino transport in CCSN, that are important for the final detection of the CCSN signal in XENONnT. The first is that flavor transformations mainly affect the IBD signal in the water tank induced by $\bar{\nu}_e$. In IMO the MSW effect impacts mainly the $\bar{\nu}_e$ fluxes, while in NMO it influences the ν_e flux, considering the H-resonance, as shown in equation (2.59).The transformations caused by these MSW resonances can be influenced by the non-adiabatic changes in density

that occur during the passage of the shockwave. In this scenario, the probability of H-resonance might converge to $P_H \to 1$.

Additionally, $\nu-\nu$ interactions can generate flavor transformations, which occur in two distinct modes: fast and slow. Both primarily impact neutrinos that are generated or interact within the PNS and the neutrino-sphere. The occurrence of $\nu - \nu$ induced flavor conversions is contingent upon the neutrino trajectories modifications in these regions due to the $\nu - \nu$ scattering. The fast mode is primarily determined by the ratio between ν_e and $\bar{\nu}_e$, and exhibits an exceptionally high oscillation frequency of $\mathcal{O}$(ns). The presence of slow mode, on the opposite side, resulted in the occurrence of oscillations primarily caused by the annihilation process of $\nu_e + \bar{\nu}_e \to v_{\mu,\tau} + \bar{\nu}_{\mu,\tau}$, with an oscillation length of approximately $\sim 10^2 - 10^3$ km as shown in **figure 2.11**. Estimating the probabilities of $\nu - \nu$ induced flavor conversions in both fast and slow modes is extremely difficult. The simulation of these interactions requires a 4D (temporal and 3D spatial) approach with precise resolution to manage them effectively. Identifying fast and slow modes in the current 3D models, is challenging, and the simulation of a complete 10-second neutrino burst necessitates enormous computational resources. However, there are different approaches to handle $\nu - \nu$ interaction modeling, in which the emergence of signatures of the fast and slow modes is expected[233, 234]. In the end, the account for the MSW adiabatic transformation, will be the only observable considered. The corresponding probabilities stated in equations (2.58,2.59), will describe the final observable flux at the earth. In the non-adiabatic case, substituting the estimated value of P_H into the previously mentioned expression, the survival probability for $\bar{\nu}_e$ in both IMO and NMO turns out to be the same, as proposed in the reference [117], during strong non-adiabatic H-resonance approximation. Moreover, without access to a CCSN model with the temporal and spatial resolution required to genuinely account for $\nu - \nu$ induced flavor transformations, its effect cannot be accounted.

Finally, the adiabatic MSW H-resonance will be the main transformation affecting the flavor transport in the CCSN. This is done a posteri through an analytic and simplified transformation of the flux. Using the averaged probabilities from (2.58,2.59), the final spectrum arriving to our detectors at the earth, $\frac{dN_{\bar{e}}}{dtdE_{\bar{e}}}_{\oplus}$ neglecting earth matter effects is[214, 235]:

$$\text{NMO} \qquad P_{\nu_e\nu_e} = sin^2\theta_{13}, \qquad P_{\bar{\nu}_e\bar{\nu}_e} = cos^2\theta_{12}cos^2\theta_{13} \tag{2.60}$$

$$\text{IMO} \qquad P_{\nu_e\nu_e} = sin^2\theta_{12}cos^2\theta_{13}, \qquad P_{\bar{\nu}_e\bar{\nu}_e} = sin^2\theta_{13} \tag{2.61}$$

For NMO and IMO the rest of flavor transformations can be writted as:

$$P_{\nu_x\nu_x(\bar{\nu}_x\bar{\nu}_x)} = \frac{1}{2}(1 + P_{\nu_e\nu_e(\bar{\nu}_e\bar{\nu}_e)}), \quad P_{\nu_e\nu_x(\bar{\nu}_e\bar{\nu}_x)} = 1 - P_{\nu_e\nu_e(\bar{\nu}_e\bar{\nu}_e)},$$
$$P_{\nu_x\nu_e(\bar{\nu}_x\bar{\nu}_e)} = \frac{1}{2}(1 - P_{\nu_e\nu_e(\bar{\nu}_e\bar{\nu}_e)}) \tag{2.62}$$

The final observable spectrum can be written as:

$$\frac{dN_{\nu_e(\bar{\nu}_e)}}{dtdE_{\nu_e(\bar{\nu}_e)}}_{\oplus} = \frac{1}{4\pi d^2}\left(P_{\nu_e\nu_e(\bar{\nu}_e\bar{\nu}_e)}\frac{dN_{\nu_e(\bar{\nu}_e)}}{dtdE_{\nu_e(\bar{\nu}_e)}} + P_{\nu_x\nu_e(\bar{\nu}_x\bar{\nu}_e)}\frac{dN_{\nu_x(\bar{\nu}_x)}}{dtdE_{\nu_x(\bar{\nu}_x)}}\right) \tag{2.63}$$

Figure 2.12 illustrates the spectrum of (2.63) for *Bollig 2016* model for the NMO (dashed lines) and IMO (dot line) orderings for a 27 $M_{\odot}$at 10 kpc. It is noticeable that flavor oscillations strongly impact ν_e (blue) flavor as expected, which is is reduced in favor of ν_x flavors. On the side of $\bar{\nu}_e$ (green) in the IMO case its spectrum is reduced appearing overlapped with the ν_x one without flavor transformation (solid red line). In the NMO case $\bar{\nu}_e$ (green dashed line) spectrum is slightly reduced around 10 MeV by flavor transformation, but increased at low energies. Concerning the total spectrum, regarding its detection in the liquid Xenon TPC, not suffer any modification with neutrino flavor transformation being its shape equal to the un-oscillated spectra.

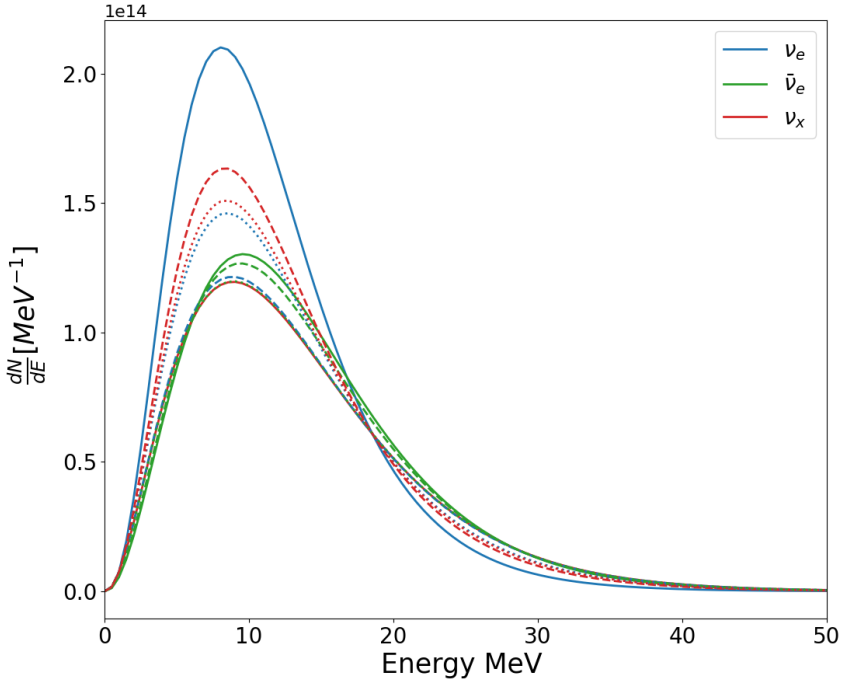

Figure 2.12: Neutrino flavor energy spectrum of (2.63) for *Bollig 2016* model for the NMO (dashed lines) and IMO (dot line) orderings for a 27 $M_{\odot}$ at 10 kpc. The ν_e (red), $\bar{\nu}_e$ (green) and the ν_x(red). Solid lines represent the spectrum with no flavor transformation.

2.7 Summary

This chapter had three main purposes. The first was describing the intricate physics underlying the neutrino signal by CCSN, which introduces uncertainties in its detection on Earth. This signal is characterized by three distinct phases: *neutronization* with a dominant ν_e burst in the first tenths of seconds, the *accretion* phase with approximately the emission of half of the total neutrinos, this time involving similarly all neutrino flavors, and finally the *cooling* phase when the neutrino emission rate and energies gradually decrease. This occurs within around 10 seconds, resulting in the release of $\sim 3\times10^{53}$ erg. Furthermore, a

vital role of neutrinos during the accretion phase, reviving the stagnant shock by convection heat transfer in the neutrinosphere, a phenomenon known as the *neutrino-heat-mechanism*, was described. According to the presented models, the SASI (Standing Accretion Shock Instability) and turbulence also contribute to improve the efficiency of heat transfer between neutrinos and the stalled shock. It is necessary to accurately simulate the time evolution of the neutrino signal, since approximately half of the neutrinos are expected to be detected within the first second after the bounce.

The second objective of this chapter was to evaluate the CCSN models available for simulating the neutrino signal and select one to perform the signal simulation for the XENONnT detecting volumes. It is desirable that the simulation model takes into consideration convection, SASI and turbulences triggered by accretion shock, which are significant aspects of the CCSN physics. This neutrino physics needs, a priori, a multidimensional approach rather than a 1D dimension approximation. However, the modeling of the CCSN mechanism requires the inclusion of a vast number of physics processes, leading to the use of a significant amount of simulation parameters. This generates an important computing cost, which is why 1D approximations are important to consider the main physics of CCSN. Elements of CCSN simulations, such as the Equation of State (EoS) and the neutrino physics list, were overviewed. The neutrino physics list in particular is crucial for the generation of neutrinos, mostly through the interaction of electrons/positrons with nucleons. It also plays a significant role in the transport of neutrinos throughout the CCSN medium, emphasizing the importance of $\nu - \nu$ coherent scattering. After considering all these factors, the *SNEWPY* models have been discussed and the *Bollig 2016* model has been chosen. This model represents consistently the main picture of the neutrino burst, as well as takes into account convection and SASI instabilities, successfully leading to explosions in ZAMS progenitor mass range of interest.

The third objective of this chapter was to determine the observable neutrino spectrum at Earth by studying the evolution of the composition of neutrino flavors in CCSN high-density medium. Two factors that influence the transformation of neutrino flavor are considered: the MSW effect and $\nu - \nu$ interaction. The two effects are denoted by two potentials in the neutrino Hamiltonian, and their influence on neutrino flavor transformation can be assessed separately. This approximation is valid because both MSW and self-neutrino interactions become prominent across different spatial and temporal regions. The occurrence of the MSW effect is contingent upon the presence of regions with low densities. This effect takes place during the tree phases of the CCSN explosion, as adiabatic, unless the presence of shock wave (or turbulences) effects when it exhibit a non-adiabatic behavior. In contrast, self-induced transformations take place in regions with high density, and are particularly notable during the accretion and the cooling phases. It was concluded that the transition of interest is the conversion of ν_e and $\bar{\nu}_e$ into ν_x and $\bar{\nu}_x$.

Because of limitations of the SNEWPY pre-selected 1D models, it can be concluded that one needs to incorporate MSW adiabatic neutrino flavor conversions to the neutrino spectrum, while excluding non-adiabatic effects. Self-induced alterations, while significant, cannot be accounted explicitly. The reason for this is the challenge of directly incorporating them into the examined simulation models.

Upon exiting the CCSN medium, the neutrinos undergo vacuum oscillations, during which the terms, proportional to L/E, are averaged out, given a typical CCSN distance of 10 kpc. The probabilities of

these oscillations rely solely on the mixing parameters. In addition, the CCSN flux flavor population ν_x is equivalent to ν_τ and ν_μ, inferring that the transformation of mass states $\nu_2 - \nu_3$ is not observable. As a consequence of this, the probabilities are solely dependent on the mixing values of 1-2 and 1-3.

Finally, the expression of the flux at the Earth was given for antineutrinos $\bar{\nu}_e$, that is of interest for the XENONnT water tank. This flux contains uncertainties arising from the CCSN mechanism itself, as well as from the simulation and flavor transformation occurring within the CCSN. As a result, the uncertainties from the neutrino flux will be greater than those that contribute to their detection.

Neutrinos have been emitted from regions near the PNS and the neutrino-sphere, traversed the dense and hot CCSN environment, transforming their flavor flux, and finally propagate freely through interstellar space to reach the Earth. It is now the time to see how we can aim to observe them, that is the subject covered by next chapters.

Chapter 3

CCSN neutrino detection

Introduction

This chapter focuses on how neutrinos emitted by Core Collapse Supernovae (CCSN) can be observed by particles detectors. In **Section 3.1**, an overview on different detection techniques will be performed: Cerenkov detectors (**Section 3.1.1**), large liquid scintillators (**Section 3.1.2**), as well as time projection chambers designed for direct dark matter discovery (**Section 3.1.3**), which is the core of this manuscript. Each of these detection techniques are sensitive to well specific neutrino interaction channels with different levels of performance. **Section** 3.2 presents the SuperNova Early Warning System (SNEWS), a global network of experiments sensitive to supernova neutrinos, whose goal is to provide the astronomical community with a prompt alert of an imminent Galactic CCSN. The XENONnT experiment is part of this network. **Section** 3.3 focuses specifically on XENONnT. After a quick introduction on the experiment and its primary mission to detect dark matter, the study of the CCSN neutrino signal is presented. Such a study can be conducted on two different sensitive volumes: the dual-phase xenon Time Projection Chamber (Xe TPC) and the two water-based vetos (originally designed to actively suppress the background for dark matter search). This chapter is focused on the TPC only, delegating to the next two chapters the work on the vetoes. For a better understanding of the observables of neutrino detection in a Xe TPC, a few sections are dedicated to detail the microphysics of interactions in LXe. In a Xe TPC, coherent neutrino scattering with Xe atoms, often referred to as CEνNS, is the main interaction channel. **Section** 3.4 discusses interaction parameters and expected rates for CCSN neutrinos. The Chapter ends with the presentation of a full simulation of CCSN neutrinos interacting via CEνNS in the XENONnT TPC. This simulation includes the state-of-the-art of our knowledge on the SN models, the LXe microphysics, and the geometry of the detector. The outcome of this simulation is the detection efficiency for the CCSN CEνNS signal, where we learn how important it is to use uniquely the ionization signal to boost our sensitivity to low energy events. We present as well the study of the background of the detector in the same Region of Interest (ROI) of the signature of SN neutrinos. For this purpose, the XENONnT Science Run 1 data have been studied. Thanks to the good detector sensitivity and the background study, the Chapter ends by presenting the discovery potential of a future CCSN CEνSN signal as a function of the SN distance.

3.1 Introduction to neutrino detection

The primary methods employed for neutrino detection in recent decades include radio chemical detection, Cerenkov light detectors, liquid scintillators, calorimeters, and TPCs [236]. There are various sources of neutrinos that can reach a detector on Earth, including reactors, the solar pp chain, atmospheric cosmic events, and accelerators. These neutrinos span a wide range of energies, from eV to PeV. Neutrinos interact only via weak interaction processes, typically requiring large volumes or low detection thresholds, depending on their energy level. Also, neutrino properties, their extreme low mass, and its flavor transformations handled by mixing parameters (see **Section 2.5** expression (2.43)) are objects of study, as this makes their measurement difficult. These intrinsic neutrino characteristics are a significant source of uncertainties, affecting their detection through interaction with matter. This presents a challenge for detectors, which have been adapted to handle larger volumes and to improve their procedures and choice of materials to increase their detection sensitivity.

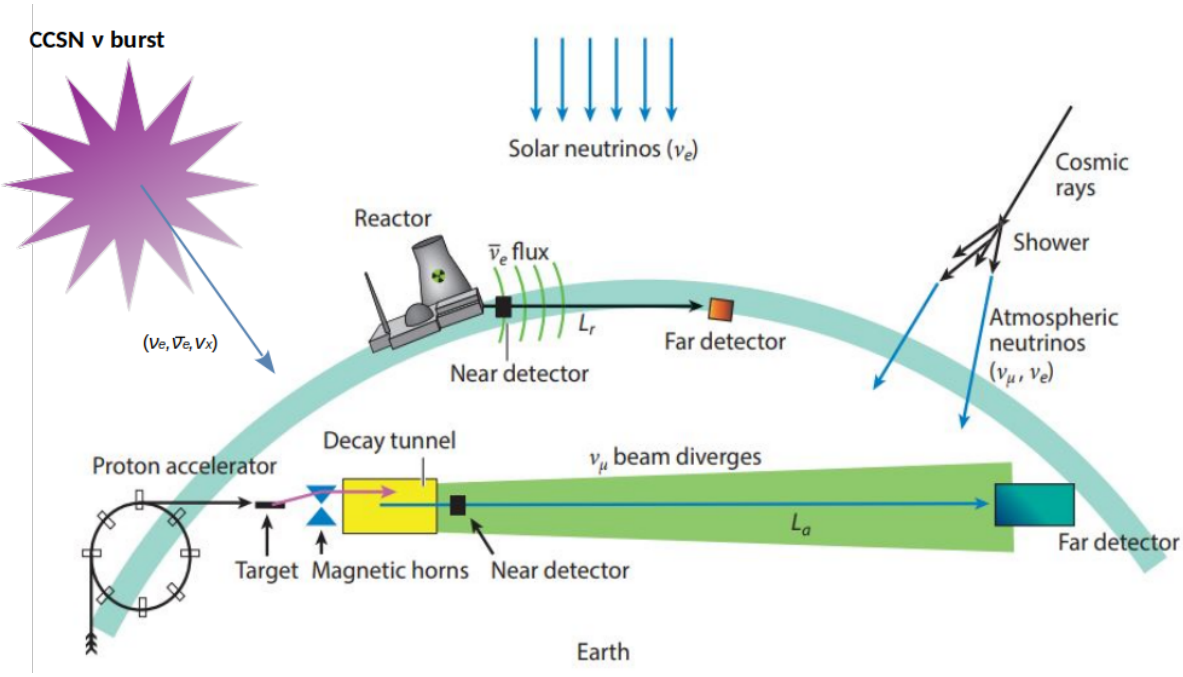

Figure 3.1: Schematic illustrating neutrino sources that have contributed to the current understanding of neutrino properties through neutrino oscillation experiments. Top: the Sun produces electron neutrinos (ν_e). Right: neutrinos of two types, ν_μ and ν_e, and their antiparticles are produced by collisions of high energy cosmic rays with atoms in the atmosphere of the Earth. Middle: nuclear reactors emit electron antineutrinos ($\bar{\nu}_e$) isotropically. Bottom: high energy proton accelerators produce a beam of neutrinos, predominantly ν_μ or $\bar{\nu}_\mu$ that is directed through the Earth [237]. In the top left corner, to the original figure, the CCSN neutrino burst composed by all neutrino flavors has been added: $\nu_e, \bar{\nu}_e$ and $\nu_x (x \equiv \mu, \bar{\mu}, \tau, \bar{\tau})$

Figure 3.1 shows, in a single image, all the possible sources of neutrinos, including the ones coming from the CCSN. In **Chapter 2**, it was explained that the CCSN signal detection presents several challenges.

Firstly, this signal is very fast, with a duration of approximately 10 seconds. Secondly, it is affected by flavor transformations in both matter and vacuum, as discussed in **Section 2.5**. Then, CCSN neutrinos have energies of around 10 MeV, which means that a very low energy threshold is needed to detect them through coherent scattering. For charged current interactions, detectors also need dense photosensitive coverage and detection volume transparency. The Water Cerenkov Kamiokande II and IMB, as well as the liquid scintillator Baksan BUST, discovered the neutrino burst from SN 1987A, as previously mentioned in Chapter 1. They both observed these neutrinos through IBD. The next sections will provide a summary of the many particle detectors capable of detecting a CCSN neutrino burst. Many of these detectors already estimated their sensitivity to the CCSN signal.

3.1.1 Water Cerenkov detectors

Cerenkov radiation refers to the prompt emission of blue, or near-blue, light when a charged particle moves through a dielectric medium, at a speed higher than the phase velocity of light in that medium [238]. The charged particle will polarize the molecules in the medium, leading to the emission of radiation upon their relaxation. This will generate a cone of light, as depicted in **figure 3.2**, by means of the excitation that propagates outward from the immediate vicinity of the moving particle. In order to employ Cerenkov radiation for detection purposes, it is necessary to have a transparent dielectric medium such as ultrapure water, preferably in a significant quantity [239]. Secondly, sensitive devices capable of detecting blue light, such as PMTs, are required [240]. The primary approach employed by Cerenkov detectors is now described. The cross-section of Cerenkov radiation is inversely proportional to the square of the wavelength ($\propto 1/\lambda^2$),

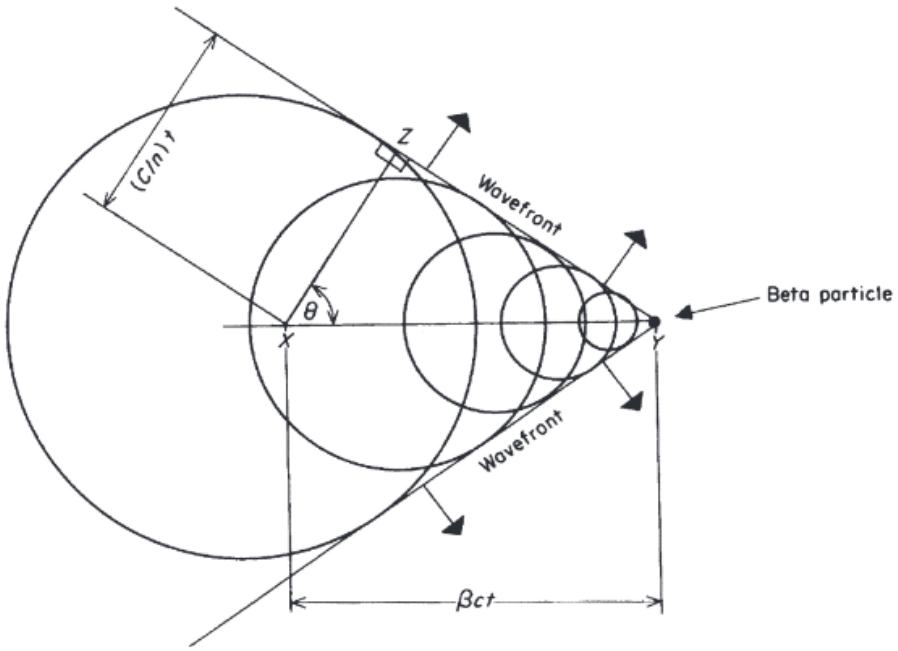

Figure 3.2: Production of a conical Cerenkov wave front. The particle travels the distance βct in a time t. θ is the angle of photon emission relative to the axis of the particle motion. Figure from reference [241].

which is responsible for its blue color [242]. The aperture of the cone, denoted as θ_c, is contingent upon both the velocity of the particle and the refractive index of the medium, represented as n_r. The Cerenkov energy threshold E_{th} is determined by the minimal aperture of a cone, which can be calculated by setting the aperture angle to zero:

$$cos(\theta_c) = \frac{1}{\beta n_r} \quad \longrightarrow \quad 1, \qquad E_{th} = \gamma m \quad \longrightarrow \quad \frac{m}{\sqrt{1-(\frac{1}{n_r})^2}}, \tag{3.1}$$

where m is the mass of the particle and $\gamma = E/m = 1/\sqrt{1-\beta^2}$. The primary detection channel is the IBD: $\bar{\nu}_e + p \rightarrow n + e^+$, where the observables are a neutron and a positron. The cross-section as a function of the incident neutrino energy is depicted in **figure 3.3**. According to its kinematics, the positron retains almost all the kinetic energy of the antineutrino, resulting in the formation of the Cerenkov light cone upon its emission in water. Due to the relativistic nature of the positron, in the case of CCSN $\bar{\nu}_e$ energies, the aperture of the cone reaches its greatest value when β approaches 1, and the angle θ_c is around 41.5° (assuming a refractive index of approximately 1.33 for water [243]). On the other hand, the Cerenkov threshold for positron energy is E_{th}= 0.772 MeV. Additionally, the IBD-$\bar{\nu}_e$ threshold (1.806 MeV), necessary from the difference in mass between the products (neutron + electron) and the reactants (proton and neutrino), does not affect the detectable CCSN $\bar{\nu}_e$ spectrum, as this energy range represents a negligible part of the $\bar{\nu}_e$ spectrum. Super-Kamiokande, along with other Cerenkov detectors, utilizes gadolinium salt as a dopant substance. This material significantly improves the effectiveness of neutron capture, achieving a capture efficiency of around 90%, allowing for the combination of neutron and positron IBD signals for CCSN detection purposes [244]. **Section 4.3** will provide a thorough analysis of the IBD interaction related to CCSN neutrinos detection in XENONnT vetoes.

Moreover, large volumes of water are sensitive to neutrino elastic scattering (ES): $\nu + e^- \rightarrow \nu + e^-$, via neutral and charged current for neutrino electron flavors and neutral current for heavy flavors. This channel is particularly interesting as it may be used for determining the direction of the incoming neutrino flux [245]. Additionally, the scattering of neutrinos with oxygen molecules, both in neutral and charged states, can be taken into account to study the high energy neutrino spectrum. However, for this last channel, there are considerable associated uncertainties [101].

The table presented in **figure 3.4** provides a comprehensive overview of water Cerenkov detectors, based on large volumes of ultrapure water [239]. The previously mentioned Cerenkov Water IBM-I-II[2] and Kamiokande I-II [1], which have a capacity of kton scale, were involved in the discovery of the neutrino burst from the SN1987A event. The Kamiokande detector has been surpassed by the subsequent generation of detectors, such as Super-K I-(II-III+) which is 22.5 kton of water [249, 250, 251]. This has resulted in a more than twenty-fold increase in the possibility of detecting a neutrino burst from a CCSN. **Figure 3.5 (left)** displays the anticipated event count as a function of distance for several CCSN models. It is worth noting that over 1000 events are projected at a distance of 10 kpc. The addition of gadolinium (Gd) to the water volume of the Super-K detector increases its ability to detect and identify neutron captures resulting from IBD induced by CCSN $\bar{\nu}_e$. This enhancement also improves the capability of the detector to determine the direction of the neutrino source [252]. Finally, the SNO experiment [253], conceived to solve

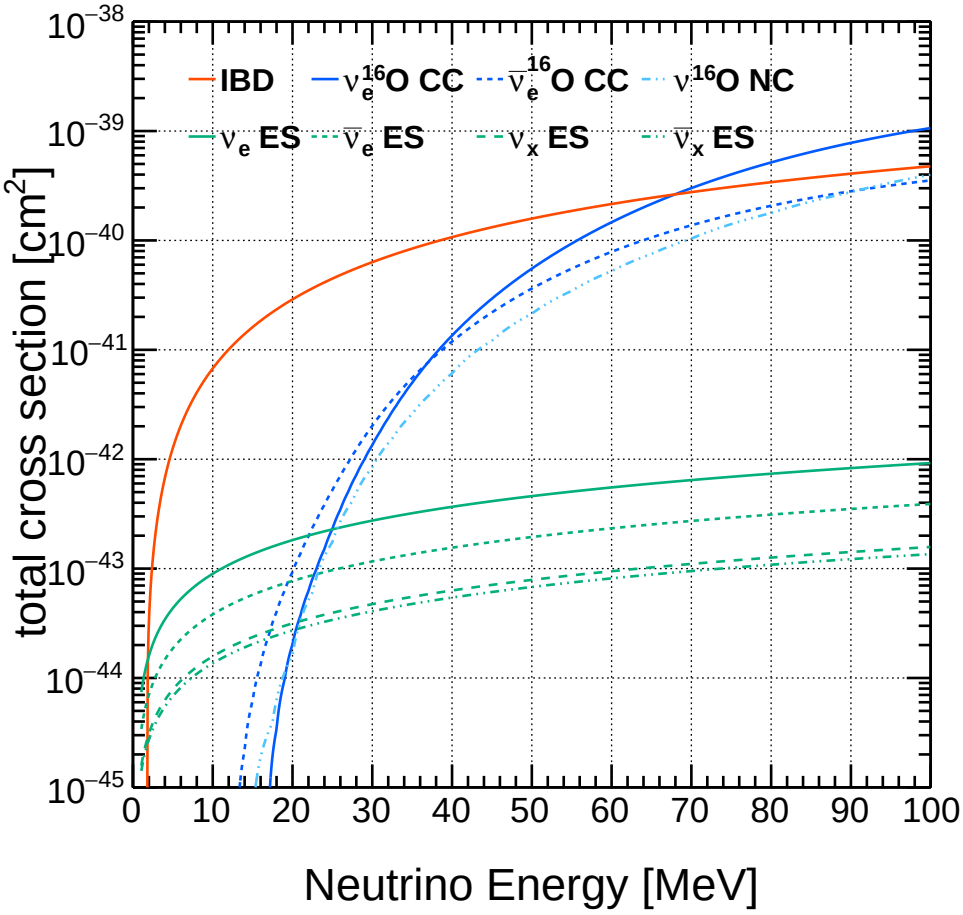

Figure 3.3: Total cross-sections of neutrinos with water as a function of neutrino energy. The solid red line indicates IBD, and the green lines represent ES with a neutrino flavor: ν_e (solid), $\bar{\nu}_e$ (dotted), ν_x (dashed), and $\bar{\nu}_x$ (dot-dashed). The solid and dashed blue lines represent ^{16}O CC ν_e and $\bar{\nu}_e$ respectively. The dot-dashed light blue line indicates ^{16}O NC interaction. The cross-sections are calculated according to [246] for IBD, for ES [247], for ^{16}O CC interaction [111], and [248] and [245] for ^{16}O NC interaction.

the *solar neutrino problem* [254] with 1 kton of deuterium and 1.7 kton of water, is as well sensitive to a CCSN burst. Regarding the upcoming generation of Cerenkov detectors, Hyper-Kamiokande is anticipated to have the ability to detect CCSN neutrino bursts within a range of 100 kpc. Additionally, it is predicted to be able to distinguish between different CCSN models.

Long baseline neutrino oscillation detectors have incorporated Cerenkov detection in recent years. This group includes the IceCube [255], ANTARES [256, 257] and KM3net [258] experiments. These detectors are specifically built to detect neutrinos with an energy ≥ 1 TeV. They are not capable of seeing individual neutrino events from CCSN, but they can detect the sudden release of energy from a supernova by the diffuse glow emission of Cerenkov photons caused by the IBD [259]. The IceCube project consists in a vertical array of 86 strings, embedded 1-2 km beneath the surface of the Antarctic ice [260]. Each string is equipped with 60 digital optical modules (DOMs). A DOM consists of a ten-inch PMT and associated

Detector	Location	Fiducial Mass (kton)	PMTs (diameter, cm)	Effective coverage	pe/MeV	Live dates
IMB-1	US	3.3	2048 (12.5)	1%	0.25	1982-1985
IMB-2	US	3.3	2048 (20)	4.5%	1.1	1987-1990
Kamiokande I	Japan	0.88	1000/948 (50)	20%	3.4	1983-1985
Kamiokande II	Japan	1.04	1000/948 (50)	20%	3.4	1986-1990+
Super-K I	Japan	22.5	11146 (50)	39%	6	1996-2001
Super-K II	Japan	22.5	5182 (50)	19%	3	2002-2005
Super-K III+	Japan	22.5	11129 (50)	39%	6	2006-
SNO	Canada	1/1.7 (D_2O/H_2O)	9438 (20)	54%	9	1999-2006

Figure 3.4: Cerenkov Detector list: the participants of SN 1987A detection IMB-1-2[2] and Kamiokande I-II[1], its update Super-Kamiokande I(II,III+)[249, 250, 251] and the SNO experiment [253]

electronics. It has been formerly equipped with a supernova trigger and has shown the ability to detect supernovae within the Milky Way [261]. The KM3net experiment uses the Mediterranean Sea to create its array of 6 200 optical modules, equipping a total of 200 000 PMTs. As depicted in **Figure 3.5** (right), KM3NeT will achieve a remarkable level of sensitivity by merging its two detectors, ORCA and ARCA. This sensitivity will allow for the detection of massive progenitors at a distance of 10 kpc and a significance level exceeding 5σ at a distance of 30 kpc beyond the outer edge of the Milky Way.

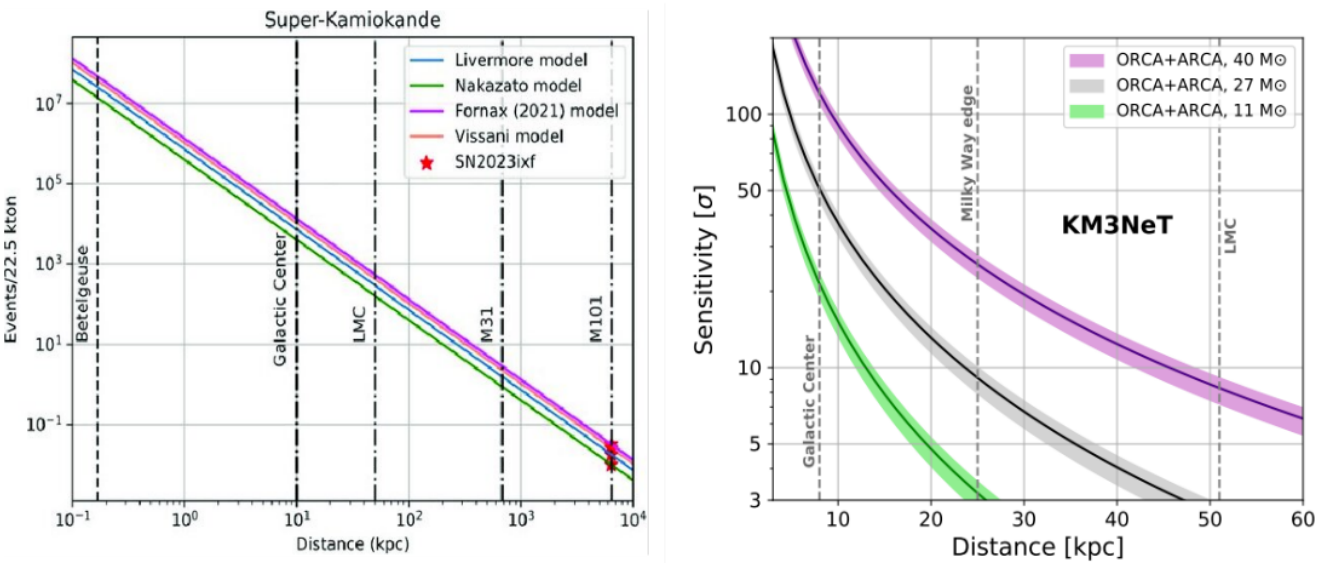

Figure 3.5: **Left.** Number of expected IBD events in Super-Kamiokande as a function of distance for supernovae based on different models. The number of events is calculated considering the fiducial volume (FV) of the detector (22.5 kton). The black dashed lines correspond to "typical" distances within the Milky Way and in the Local Group up to M101, the host galaxy of SN 2023ixf [262]. **Right**. KM3NeT detection sensitivity as a function of the distance to the CCSN for the three progenitors considered: 11 $M_\odot$ (green), 27 $M_\odot$ (black) and 40 $M_\odot$ (purple). Figure from [263].

3.1.2 Large liquid scintillators

Large-mass scintillators ($>$ 100 tons) are made up of uniform volumes of liquid scintillators coated by a dense array of PMTs, which allows for great energy resolution and low energy thresholds. These volumes may also be divided into smaller ones. The scintillation detection technique relies on the capture of light from the de-excitation of molecular energy levels. When a particle enters the liquid scintillation volume, it deposits energy, which is released during de-excitation processes, resulting in the production of photons in the ultraviolet or visible spectrum. This process is known as luminescence [264]. At the same time, energy losses from light can cause ionization and non-radiative de-excitations in scintillator atoms, a process known as *quenching* [265]. The incident particle's energy loss is proportional to the total number of photons collected. As a result, an accurate knowledge of quenching is required, especially for low energy recoils. Energy resolution correlates with time resolution, as interaction vertices can be rebuilt using photon time-of-arrival information [266].

Liquid scintillation detectors use transparent liquid hydrocarbons (C_nH_{2n}). These liquids, as well as Cerenkov detectors, are rich in protons, and the main CCSN burst detection channel is the IBD, sensitive to the $\bar{\nu}_e$ flavor. Some of the liquid hydrocarbon scintillators operated during the last 40 years are the Baksan observatory [267], LVD [268], Borexino [269], KamLAND [270], and MiniBooNE [271]. Baskan is one of three detectors that recorded the SN1987A. Since 2014, the segmented NOvA detector has operated with a total of 8.8 kton of liquid scintillator [272, 273, 274]. SNO+ replaced ultrapure water with liquid scintillator linear alkylbenzene (LAB) [275].

CCSN ν_e and ν_x flavors are expected to interact with electrons via ES, as well as through charged-current interaction with the ^{12}C nucleus. The latter requires a bigger detection volume, $\mathcal{O}$(10-kton) [276]. This is the mass scale of the JUNO experiment [277]. The JUNO detector consists of 20 kton of LAB, with 2,5-diphenyloxazole (PPO) as the fluoride and bis-MSB as the wavelength shifter [278]. The liquid scintillator is located in a spherical volume covered by 17 612 20-inch PMTs and 25 600 3-inch PMTs. JUNO is expected to be sensitive to all the CCSN flavor flux [279]. The table in **Figure 3.6** summarizes the CCSN neutrino interaction channel and their respective expected number of events. The JUNO project has made efforts to monitor the CCSN signal online and explore sensitivities for pre-SN neutrino bursts. As a result, an online trigger has been implemented, intending to cover pre-SN neutrinos $\sim$ 1 kpc and CCSN beyond 350 kpc [282]. JUNO also expects to use ES neutrino interaction to gain directional information.

Other methods for detection through scintillation include liquids based on deuterium, known as deuterated liquid scintillators (DLS). A CCSN at 10 kpc with 1 kton of DLS is projected to exhibit $\sim$ 435 neutrino-nucleus neutral current interactions, as well as 170 and 108 charged current interactions with deuterium for ν_e and $\bar{\nu}_e$, respectively[283]. The future detector THEIA combines Cerenkov detection and liquid scintillators in a water-based liquid scintillator (WBLS) [284]. Neutrinos interacting with liquid scintillators produce Cerenkov photons through a secondary process, with a significant part of these photons in the UV/blue range absorbed. This renders Cerenkov photons indistinguishable from scintillation ones. WBLS can reduce the attenuation length of Cerenkov photons by about 20m, making it suitable for large liquid scintillators [285]. For a 100 kton of WBLS, 19 800 IBD CCSN neutrino events are expected

Channel	Type	Number of SN Neutrino Events at JUNO		
		No Oscillations	Normal Ordering	Inverted Ordering
$\overline{\nu}_e + p \rightarrow e^+ + n$	CC	4573	4775	5185
$\nu + p \rightarrow \nu + p$	ES	1544	1544	1544
$\nu + e \rightarrow \nu + e$	ES	313	315	315
$\nu + {}^{12}\mathrm{C} \rightarrow \nu + {}^{12}\mathrm{C}^*$	NC	352	352	352
$\nu_e + {}^{12}\mathrm{C} \rightarrow e^- + {}^{12}\mathrm{N}$	CC	43	134	106
$\overline{\nu}_e + {}^{12}\mathrm{C} \rightarrow e^+ + {}^{12}\mathrm{B}$	CC	86	98	126

Figure 3.6: Numbers of neutrino events at JUNO for a CCSN at a typical distance of 10 kpc, for different interaction channels, considering No oscillations, NMO and IMO [280]. For the elastic proton and electron scattering, a threshold of 0.2 MeV for the recoil energy is chosen[281].

at 10 kpc [286].

3.1.3 Time Projection Chambers

When an incoming neutrino enters a liquid scintillator, it interacts with target atoms, resulting in secondary charged particles and scintillation photons. Some time projection chambers (TPC) are built with the purpose to reconstruct the trajectory of these charged particles. As a result of this reconstruction, the incident particle is recognized, as well as its interaction vertex, and the primary incident particle's 4-momentum is measured. Along its path, secondary charged particles ionize and excite the atoms. Ionization electrons can be drifted using an electric field; however, this requires liquids that do not absorb these electrons to ensure their survival as they drift to sensitive volumes where they are recorded as signals. De-excitation of atoms can also produce scintillation photons [287], which can be detected with PMTs if the liquid is sufficiently transparent in the range of spectra of the emitted photons. Drifted electrons can either be detected directly (with wires for instance, in that case we speak about a single phase TPC), or they can be extracted in the gaseous phase of the scintillator, with the purpose of accelerating them and producing an avalanche of secondary scintillation photons, called secondary scintillation light [288] (detectors using this technique are called dual-phase TPCs). **Figure 3.7** shows those two primary detection methods for noble liquid (argon in this example) scintillators [289, 290].

Two types of TPCs sensitive to CCSN neutrinos will be discussed: large scale $\mathcal{O}$(kton) with Liquid Argon (LAr) and ton-scale with LAr or Liquid Xenon (LXe). Argon is more than a half less dense than xenon (see **table** in **figure 3.9**). For kton-scale liquid Argon detectors, CC interactions with Argon nuclei are expected to be the dominant channel for ν_e and $\bar{\nu}_e$. ES is also considered sensitive to all neutrino species and sometimes paired with CC interactions with nuclei, particularly in order to extract directional information [292].

To the kton experiments we can cite ICARUS T600 [293] that, with its 0.6 kton, operated at the LNGS laboratory from 2010 to 2013. DUNE [294, 295] can be seen as a successor of ICARUS, with 4 segmented

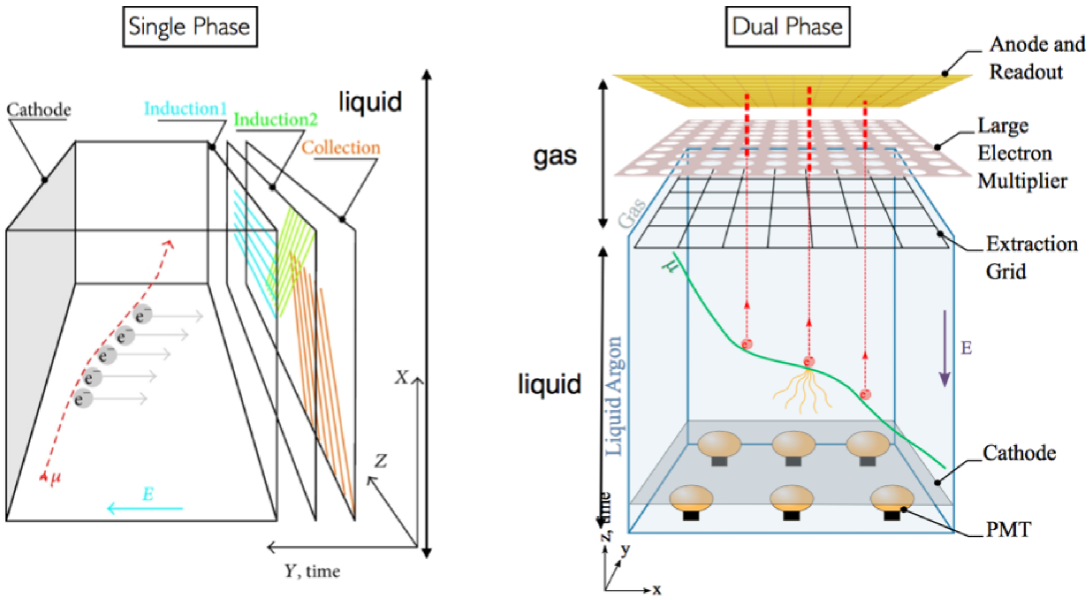

Figure 3.7: **Left**. Single phase detectors: the single phase using a homogeneous liquid volume, in this case recording the drifted electron signal and/or prompt scintillation signal. **Right**. The double phase, which combines prompt and secondary scintillation signal for vertex reconstruction with both liquid and gas phases. Figure from [291].

detectors of 10 kton each that will be constructed at SURF, in South Dakota, USA. It is expected to be significantly sensitive to the next CCSN neutrino burst, combining ES and CC-$\nu_e(\bar{\nu}_e)$ interaction signals in argon. The DUNE TPC detects both ionization electrons and de-exitation photons. This can be done utilizing two different strategies: single phase alone with LAr or double phase with an argon gas interface [294] (see **figure 3.7**). Incoming neutrinos are predicted to produce charged particles through LAr interactions, leaving traces of electrons and photons along their path. The latter can be observed by both the single-phase and the dual-phase techniques. In the dual phase arrangement, CEνNS in LAr has to be considered. CEνNS is the most interesting channel in terms of cross-section (see **figure** 3.11) but requires extremely low thresholds. The study of the requirements for neutrino detection via coherent scattering is an occasion to prospect the DUNE experiment sensitivity to Weak Interacting Massive Particles (WIMPs) [289]. **Figure 3.8** depicts the expected number of CCSN neutrino interactions combining ES and CC interactions for the single phase configuration in DUNE [296]. At 10 kpc, each 10 kton module should be able to collect more than 200 CCSN interactions. Combining the four modules, a CCSN in the Large Magellanic Cloud LMC is predicted to be detected with more than 40 interactions.

The other category of TPCs corresponds to the ton-scale and frequently uses the dual-phase configuration, as they are designed for direct dark matter detection. This arrangement enables the detectors to explore the CEνNS interaction, requiring a lower threshold from the nucleus recoil energy: $\nu + \mathrm{A(Z,N)} \rightarrow \nu + \mathrm{A(Z,N)}^*$. Ionization and scintillation result from the de-excitation of the atomic nuclei. If the extraction of electrons from the liquid/gas interaction is efficient enough, a significant number of secondary scintillation photons are created, which is proportional to the number of extracted electrons;

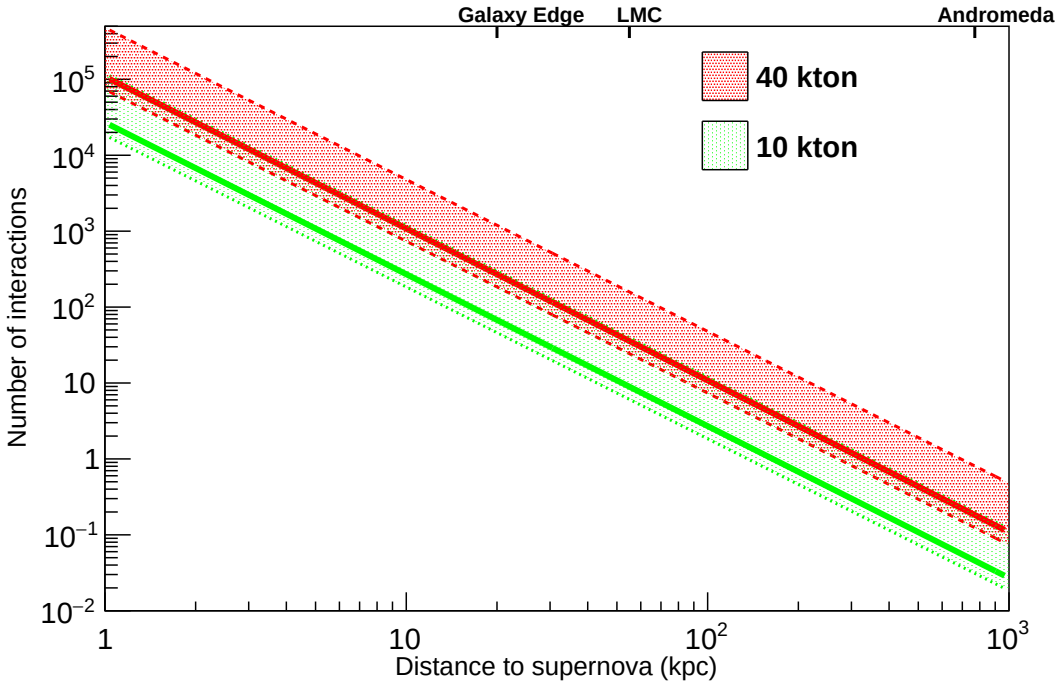

Figure 3.8: Estimated number of total supernova neutrino interactions in DUNE as a function of the distance to the supernova, for 40-kton (red band) and 10-kton (green band). The extent of the bands corresponds to the use of different CCSN models. Figure from [297].

this is known as delayed electro-luminescence[298]. In **Sections 3.3**, the combination of the prompt and secondary scintillation signals will be detailed, since this corresponds to how the XENONnT Xe dual-phase TPC works.

In argon, CEνNS cross-section is 50 times higher than the cross-section for charged current interactions [266], and it is insensitive to neutrino flavour, i.e., the integrates detected spectrum is a priori not affected by flavour composition uncertainties from neutrino transport to the Earth (see **Section 2.5**). A large number of nucleons is preferable for the target liquid scintillator, as the cross-section of CEνNS depends on the square of the number of nucleons in the atom. However, the cross-section decreases exponentially with the recoil energy of the nucleus. In this regard, heavier nuclei are expected to be less sensitive to lower energy recoils. Only liquid argon and xenon TPCs will be mentioned here, as they are the most representative liquid scintillators used for direct DM detection in the ton-scale masse range. Both present a low CEνNS recoil energy threshold covering the range of CCSN neutrinos induced nuclear recoils < 20 keV. Similarities between these two noble liquids in their detection properties by coherent scattering are summarized in the table in **figure 3.9 (right)**. One major distinction between Ar and Xe atoms is the characteristic peak of wavelenght of their scintillation spectra at 128 and 175 nm, respectively. It is usual to utilize a wavelength shifter in LAr to improve the detection efficiency of commercially available PMTs. The adopted photosensors are built for wavelengths closer to the vacuum ultraviolet VUV; for the LAr

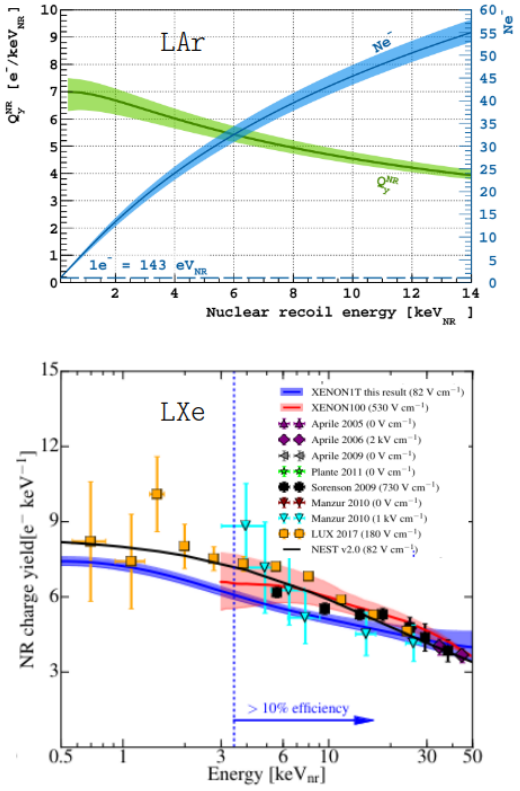

Property	*Argon*	*Xenon*
Atomic No. (Z)	18	54
Atomic weight (A)	39.95	131.3
Maximum recoil energy (% of incident n energy)	9.5	3.0
Boiling point (K°)	87.3	165
Density (g/cc)	1.4	3.0
Electron mobility (cm2/v*s)	400	2200
Ion drift velocity at 1kV/cm (mm/μs)	2.2	2.4
Energy resolution (FWHM @ 662 keV) scint. only (%)	8%	8%
Scintillation wave length (nm) and PMT used	128 (w/λ shifter, fast PMT)	175 (quartz window PMT)
Scintillation yield (# scintillation photons/MeV)	40000	42000
Fast decay time (ns)	7 (25% light)	4.3
Slow decay time (ns)	1500 (75% light)	22(100% in $\leqslant$22ns)
(n,γ) propensity	medium	high
Neutron activation	medium	high

Figure 3.9: **Left**. Charge Yield for LAr (top) and LXe(bottom). For LAr, charge yield nuclear recoil Q_y^{NR}[e$^-$/keV] corresponds to the green solid line, and the number of extracted electrons N_e corresponds to the blue line. These curves are obtained using DarkSide-50 ^{241}AmBe Calibration data [299]. This experiment uses a drift field of E = 200 V/cm. On the bottom for LXe, Q_y^{NR}[e$^-$/keV] from XENON1T ^{241}AmBe calibration data in blue (E= 82 V/cm), and XENON100 [300] (E= 530 V/cm) in red and different values of drift field [301]. **Right**. Table proprieties for LAr and LXe scintillators from [302]. Values of the scintillation yield are related to atom excitations for fast neutrons (with energies above 1 MeV) like for ^{241}AmBe neutron spectrum [303] .

scintillation spectrum, their efficiencies are often quite poor, reaching at most 15% [304]. To detect VUV light using normal blue-sensitive PMTs, an efficient wavelength shifter is required to absorb it and re-emit it isotropically at a longer wavelength [305]. Moreover, a longer photon wavelength benefits from a modest impact of Rayleigh scattering due to the reliance of this interaction on the former as $1/\lambda^4$. For these reasons, protoDUNE suggests doping the LAr with xenon [306]. Argon and xenon liquid scintillators excel at extracting information about the energy deposition of incident particles in liquids, specifically the light yield (number of photons per unit of deposited energy) and charge yield (number of extracted electrons per unit of deposited energy) [307, 308, 309]. This number depends on the type of recoil, nuclear or electronic, the energy of the incident particle, and, most importantly, the intensity of the drift field. **Figure 3.9** (left) displays the charge yield Q_y^{NR}[e$^-$/keV] for a nuclear recoil based on ^{241}AmBe calibrations, which

yields a fast neutron spectrum with energies between $\sim 1 - 11$ MeV [303]. The charge yield distributions for LAr and LXe are comparable, with the latter somewhat higher. In terms of scintillation yield, LXe is 42 photons per keV, whereas LAr is 40 photons per keV.

Another important property is the decay of the two main distinct excited argon states, which are separated sufficiently in time to perform a pulse shape discrimination to distinguish nuclear recoils from electron recoils [304]. Xe dual phase TPCs are constrained to the use of the prompt and secondary scintillation signals to do this discrimination between nuclear and electron recoils.

For LAr DM detectors, ArDM [310] is no more operative, and DarkSide-20k [311] uses 20 tons argon, which expects high statistics for CCSN burst [312]. The latter collaboration made efforts to study its sensitivity to the CCSN bursts in terms of energy and the time evolution of the signal. **Table 3.1** shows the expected events per ton for DarkSide-20k and the future update ARGO with 360 ton of LAr for the three different phases of the CCSN neutrino burst (see **section 2.2**).

	11-$M_\odot$ SN	27-$M_\odot$ SN
SN phase	[1/t]	[1/t]
Burst	0.08	0.09
Accretion	1.83	3.30
Cooling	1.96	3.76

Table 3.1: Number of events per ton for the DarkSide-20k and ARGO TPCs from 11-$M_\odot$ and 27-$M_\odot$ CCSN at 10 kpc. Table adapted from [312].

Finally, for these LAr ton-scale TPCs, the resulting significance for a neutrino burst from a CCSN in the Milky Way is expected to be high. Also, good significance is expected for the neutronization burst (see **section 2.2.1**) composed by almost only ν_e. Both results are presented in **figure 3.10**. This result was obtained assuming a nuclear recoil threshold of 0.46 keV [312]. This value will be compared in the next paragraphs with the LXe one for a similar CCSN neutrino analysis. Ton-scale LAr TPCs using CEνNS obtain sensitivity to CCSN neutrino signals similar to large LAr detectors such as DUNE, which are three orders of magnitude larger. The high CEνNS cross-section compensates for the detection volume difference, while giving sensitivity for all neutrino flavors that allows to normalize CCSN neutrino flux. This is not the case of CC interactions used in kton-scale LAr detectors, which are not equally sensitive to all neutrino flavors.

For the case of LXe TPCs, XMASS [314], PANDAX-4T [315], Lux-Zeplin (LZ) [316] and XENONnT [317] (XENON1T [318]) are (were) also sensitive to a CCSN burst through CEνNS. A general approach of their sensitivity to CCSN will be introduced in this section, while the specific characteristic of Xe TPCs will be detailled for the XENONnT direct DM detector in **Section 3.3** , as well as the CEνNS interaction in this detector, object of this Thesis in **Section 3.4**. The energy threshold for recoils in LXe may be slightly higher than for Ar atoms, $\sim$ 1 keV when combining prompt and secondary scintillation signals, and $\sim$ 0.7 keV for secondary only [86]. In **Section 3.4**, we will see that CCSN signal due to this specific time evolution rate allows studying neutrino signal with only this secondary scintillation. On the other

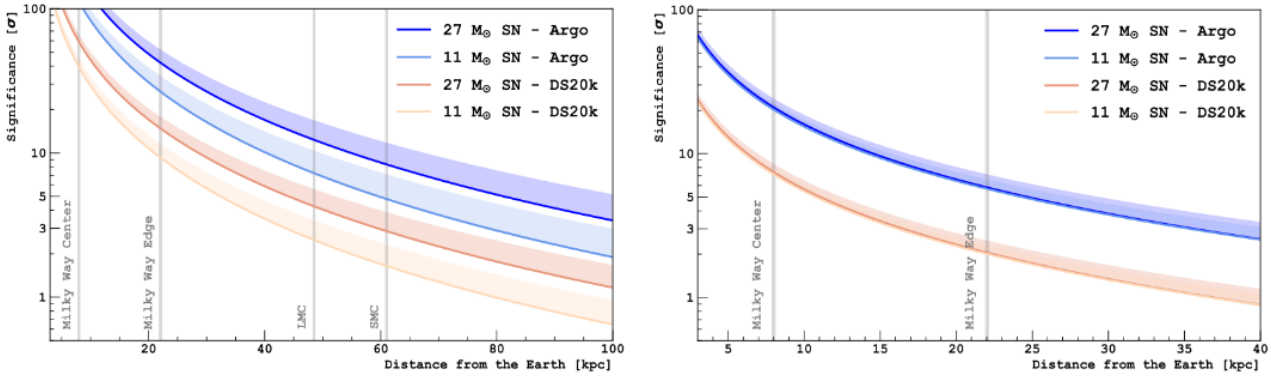

Figure 3.10: **Left**. DarkSide-20k and ARGO significance to 11-$M_\odot$ and 27-$M_\odot$ CCSN progenitors SNe as a function of the distance. **Right**. Same than right plot but only for the neutronization burst. Vertical lines represent the distance from the Earth to the Milky Way center and farthest edge, and of Large (LMC) and Small (SMC) Magellanic Clouds. Figure from [312].

hand, the interaction rate in LXe is enhanced by the high atomic number of Xe by one order of magnitude compared to LAr at low energy recoils (see **figure 3.11**). The CEνNS interaction rate also decreases exponentially with the energy recoil of target nuclei, and in this sense, the rate in LXe decreases faster than LAr, making the detection of neutrino $\mathcal{O}$(10 MeV) inefficient around 15 keV [319] (see **figure** 3.12). Some recent reviews have explored the potential of Xe dual phase TPCs, with optimistic expectations in energy recoil rates and time evolution sensitivities [320, 86, 319, 321]. In the next paragraphs, we will highlight results of three of them.

LZ is the largest of the operating direct detection Xe DM detectors, with 7 tons of LXe as active target. As anticipated in the **Section 2.2**, more than half of the neutrino signal is expected to be detected within the first second. More exactly, for LZ 184 of 357 total contacts occur in the first second, assuming an energy recoil of 0.5 keV [319]. **Figure 3.13** depicts a time distribution histogram of the CEνNS signal using 10-ms time bins. During the ν_e burst induced by the neutronization phase, the interaction rate t_{pb} <50 ms reaches a maximum of ∼350 Hz, but before the explosion, t_{pb} <150 ms, this rate is greater than 300 Hz. These frequencies are indicative of the CCSN CEνNS interaction, and may be troublesome in terms of temporal sensitivity. The high rate of the latter may cause pile-up for the secondary scintillation signal (see **Section** 3.4).

A recent CCSN study (2024) corresponds to the PandaX-4T experiment with 3.7 tons (2.67 tons of effective mass) of LXe, the smallest TPC for direct DM currently operating. Among the CCSN neutrino burst rate estimations and a sensitivity study, PandaX-4T extracted an upper limit for the occurrence of CCSN explosions in the Milky Way. This is estimated to be equivalent to 678.2 per century of CCSN in our galaxy 10 kpc away [321]. In the context of CCSN neutrino detection, this upper limit can be interpreted as the maximum of CCSN that can be detected for a given experiment, with a *confidence level* of 90% (the statistical treatment used comes from reference [322]). The result depends on specific instrumental parameters of the detector, the background, and the time exposure, but also on the discrimination between

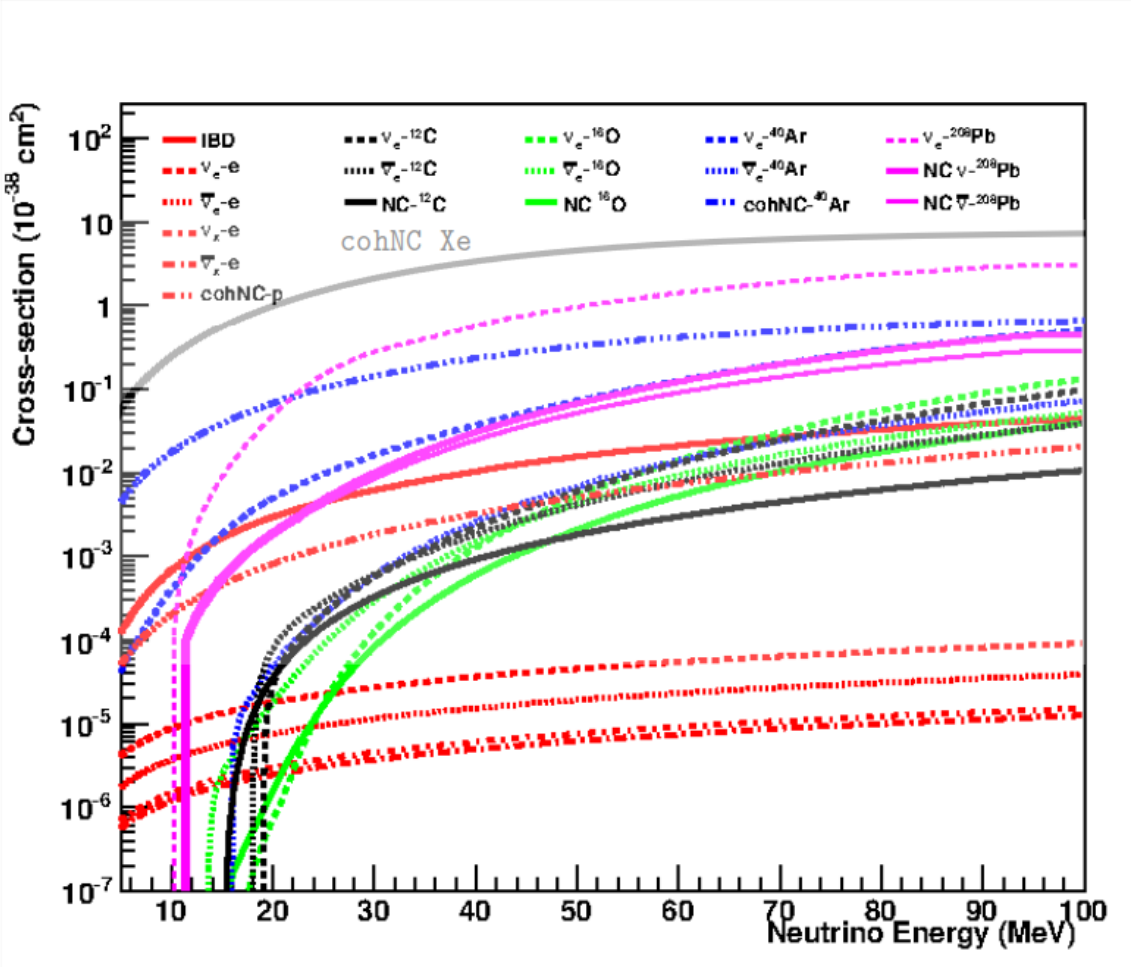

Figure 3.11: Cross-sections of all the CCSN neutrinos detection channels, corresponding to the different experiments mentioned in **Section 3.1**. To be noted that relevant lead (Pb) interactions in the 79 tons of the HALO experiment are also accounted for [313]. The CEνNS for ^{131}Xe from equation 3.28 has been added to the original figure, taken from [266].

false burst and a *real* CCSN burst. As **figure 3.14** shows, the probability to observe a CCSN neutrino signal, meaning at least one CCSN event, in the Milky Way, is close to 100%. For this probability calculation, PandaX uses the requirements of the *Supernova Early Warning System* SNEWS [76] to define a CCSN signal. XENONnT also participates actively to the SNEWS network of detectors sensitive to CCSN neutrinos, most of whom are already mentioned in the **Section 3.1**.

3.2 The Supernova Neutrino Early Warning System

When the collapse shockwave reaches the surface of the supernova, it breaks out, creating the first photons visible to telescopes sensitive to this electromagnetic radiation [73, 323]. This shock breakout (SBO) occurs hours or days after particle detectors on Earth discover the CCSN neutrino signal (see **figure 3.15**). This

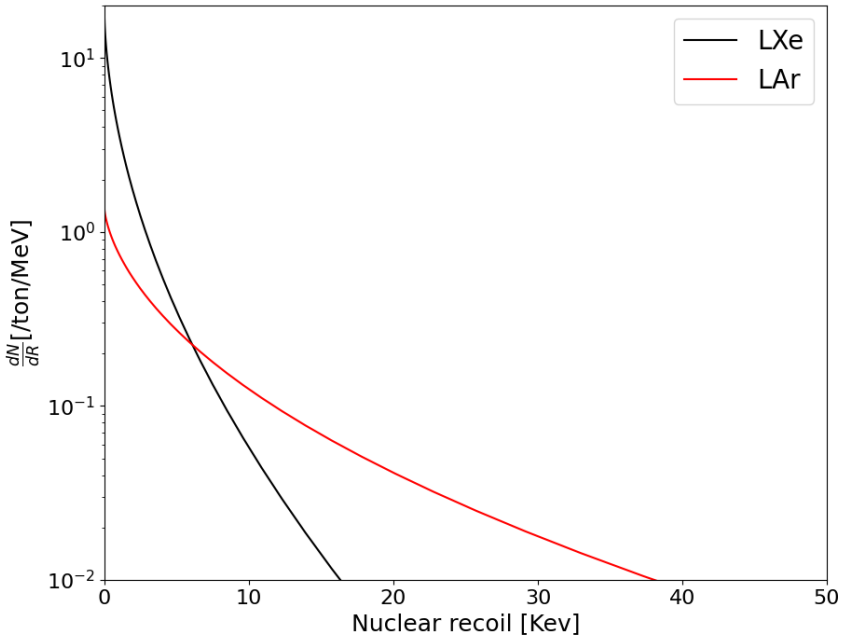

Figure 3.12: Simulated recoil energy spectrum for CEνNS interactions induced by CCSN neutrinos for a 27M$_\odot$ progenitor at 10 kpc.

neutrino burst signal can serve as a warning for telescopes to pinpoint the next CCSN [1]. This is the main idea behind the global network SNEWS. The SNEWS network began in 2005 with SNEWS 1.0 [324], which was a simple coincidence between neutrino experiments: SuperKamiokande, LVD, and SNO. Since then, other experiments have been added to the charter, including AMANDA [325], IceCube, KamLAND, Borexino, Mini-BooNE, ICARUS, OMNIS [326], and the gravitational wave detector LIGO [327]. In SNEWS 2.0 [76], the CCSN experiment network evolved, accounting for multi-messenger astronomy [323], including dark matter detectors: Panda-4X, DarkSide-20k, LZ, and XENONnT, as well as gravitational wave alarms for SN astrophysical events. The next generation of water scintillator detectors, Hyper-K, Km3net, the large scintillators JUNO and DUNE, and the hybrid helium-lead experiment HALO-1kt [328] all participate at different levels. This adds up to 19 experiments, which will improve multiplicity and sensitivity to the following CCSN.

3.2.1 Detection Multiplicity and Multi-messenger CCSN

The significant number of contributing experiments enables a reduction in the detection threshold, particularly due to the direct DM detectors that utilize the CEνNS interaction. This last detection channel permits a priori the detection of pre-SN [81, 47] and Type Ia SN neutrinos [15], which have typical energies

[1] A priori, directional information can be provided for large volumes of Water Cerenkov or liquid scintillator experiments [252, 323]

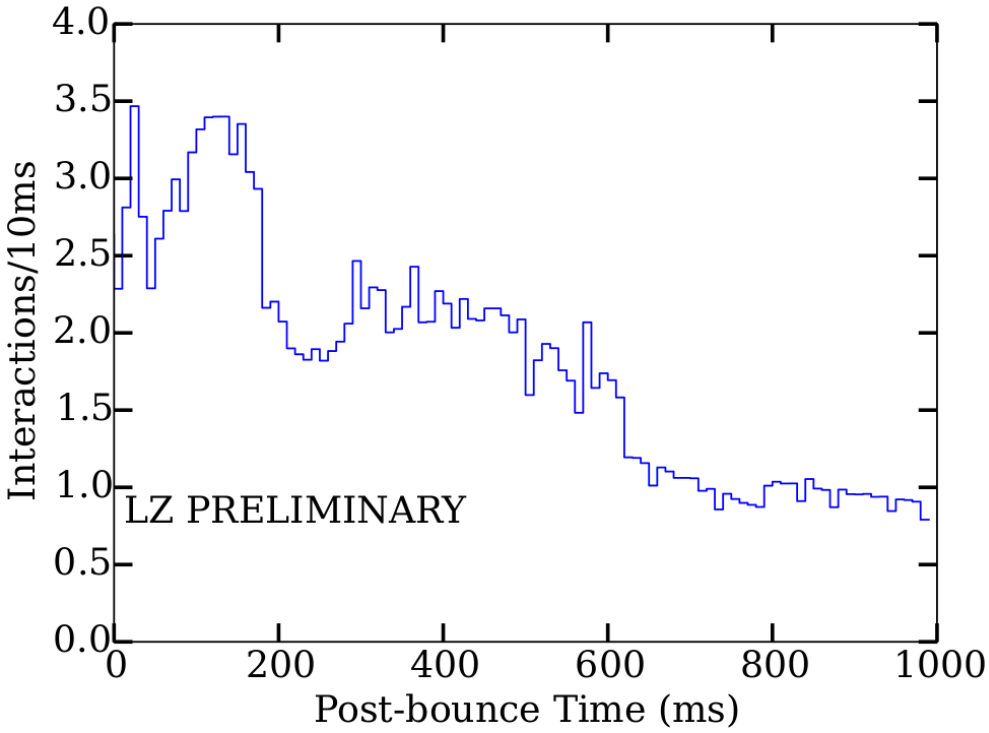

Figure 3.13: Histogram of the expected CEνNS interaction rate in time for the first second after the bounce of the core in LZ from a 27 $M_\odot$ CCSN at 10 kpc, assuming a detection energy threshold of 0.5 keV. Figure from reference[319].

of $\sim$ 5 MeV and $\sim$ 3 MeV, respectively, and have also been included in the SN event range of SNEWS. However, their flux is smaller than CCSN, so it is most reasonable to wait for the next 10 ton-scale of direct DM detectors for LXe, such as DARWIN [329], and 100 ton-scale for LAr, such as ARGO[330]. Signals from pair-instability supernova ray bursts, CCSN-like neutrino bursts from merging neutron stars [331], and black hole-neutron star mergers [332] are also accounted for. The GWs detection signal from LIGO-VIRGO is also an active part of SNEWS and expects to receive SNEWS neutrino alerts. GW are projected to arrive in the same time-scale as neutrinos, as seen in **figure 3.15**, with maxima occurring during collapse, core bounce, and explosion. The GW signal shape is characterized by several short-time pulses, *burst-like* signals that are difficult to fit [333]. Furthermore, the amplitude of a GW signal is connected to the asymmetries of the CCSN collapse, including the core bounce, collapse, and shock breakout [334]. The asymmetric collapse behavior is anticipated in most multidimensional CCSN models and plays an essential role in the *neutrino heat mechanism* (see **Sections 2.2, 2.4.1, 2.4.2**). Spherical symmetry breaking is required to explore the GW CCSN signal [335], but GW signal shape makes detection challenging. In this regard, the CCSN neutrino can function as a GW trigger. Another factor to consider is the delay between the neutrino and the GW signal, as neutrinos have tiny masses. The $\mathcal{O}$(10 MeV)

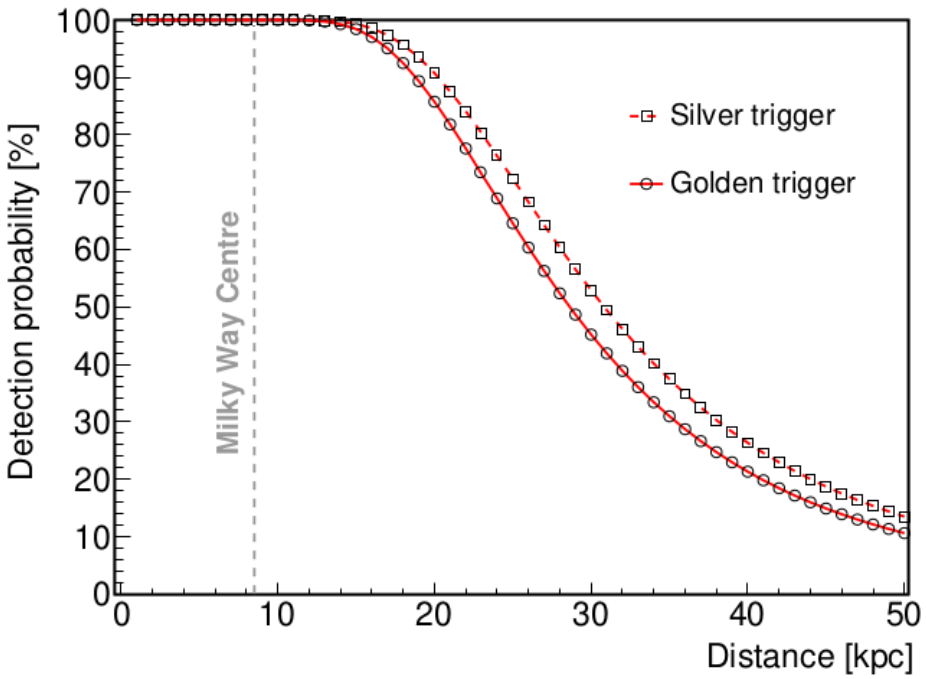

Figure 3.14: The detection probability of the SN explosion as a function of distance from the SN to the Earth. The Garching model is used with 27 $M_{\odot}$. Figure from reference [321].

neutrinos travel at $\sim$ 99.9999999999995 % of the speed of light[2], while GWs travel at the speed of light. This difference propagates along the travel to Earth and becomes substantial enough for detectors to be sensitive to it at the typical 10 kpc CCSN distance, where the delay is $\sim$ 0.5 s [337]. Finally, electromagnetic radiation (EM) is expected to have a delay of $\mathcal{O}$(10 hours) with neutrinos. This is then the transient time to send the neutrino alarms to telescopes. **Figure 3.15** depicts the EM signal SBO plateau and subsequent degradation, which can last for months depending on the SN type [76]. The total energy emitted after the bounce in the form of $\bar{\nu}_e$, photons, and GW is $\sim 6 \times 10^{52}$ ergs, $\sim 4 \times 10^{49}$ erg, and $\sim 7 \times 10^{46}$ erg, respectively.

3.2.2 Direction

SNEWS network detectors, which are situated at different locations, allow pointing the right direction of the SN by using the different signal arrival times. A simple technique to point the right direction is to estimate the relative delay between the timings of the signals, starting with the first one that recorded an SN event. The first experiment among the 19 provides preliminary information regarding the placement of the CCSN in the sky. **Figure 3.16** depicts a schematic of this method, which benefits from prior knowledge of potential neighboring CCSN candidates. These candidates are depicted by white spheres,

[2]For this speed neutrino estimation, an upper mass limit of 1 eV/c^2 was used. Recent measurements give a lower value for this upper limit of 0.8 eV/c^2 [336].

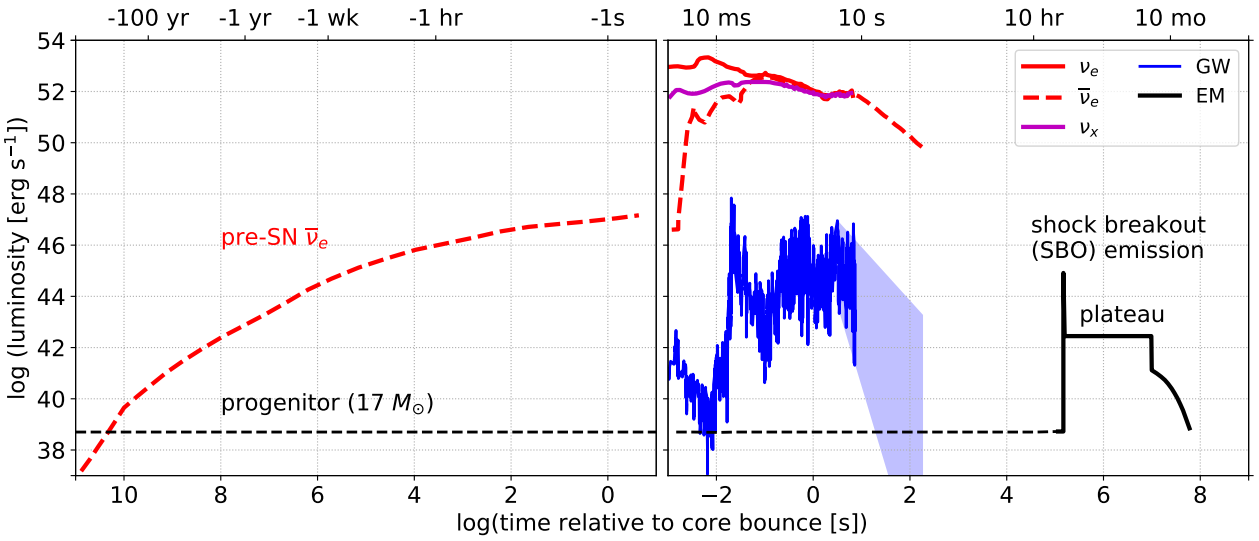

Figure 3.15: Time sequence for multi-messenger signals pre- (left panel) and post- (right panel) core collapse of a non-rotating 17 $M_\odot$ progenitor star. Neutrinos (ν_e , $\bar{\nu}_e$, and ν_x are shown by red, thick red, and magenta lines, respectively, where ν_x represents heavy-lepton neutrinos: ν_μ , ν_τ ,$\bar{\nu}_\mu$ and $\bar{\nu}_\tau$), GW (blue line), and electromagnetic signals (black line) are shown [323].

the earth by a cyan sphere, and the red crosses represent the detectors that observed the signal. The table on the left side of the picture displays the delay in seconds since the first experiment that detected the burst, in this case, Km3net.

This pointing can be accomplished using triangulation techniques and/or including more precise directional information for each experiment. Not all detectors respond to the same components of the neutrino flavor spectrum. For example, Cerenkov and large liquid scintillators are more sensitive to $\nu_e, \bar{\nu}_e$ flavors, while TPCs are sensitive to all flavors. For the latter, no information regarding the direction of the CCSN can be obtained. However, in detectors sensitive to ES, information about the direction of the incident neutrino can be extracted, because the scattered electron is always emitted forward and has a strong correlation with the incoming neutrino direction [338, 339, 340] (see **Section 4.4**). At CCSN neutrino energies, the positron released from IBD in water is nearly isotropic; the only directional information is saved by the neutron, which is difficult to exploit due to the weak correlation between the neutron and the neutrino directions (see **Section 4.3**). As Cerenkov detectors use the signature of the PMT pattern to identify particles, IBD positrons and ES electrons are difficult to differentiate. In this regard, Gd dopage in Water Cerenkov detectors may boost the detection efficiency of the IBD neutron capture while reducing the neutron capture time, and improving the precision of the discriminating between positron and electron [341]. In large liquid scintillators, the IBD neutron direction can be used for pointing, as it is always released forward, thus emission patterns can be predicted a priori based on neutrino direction. This information can be mixed with or without ES.

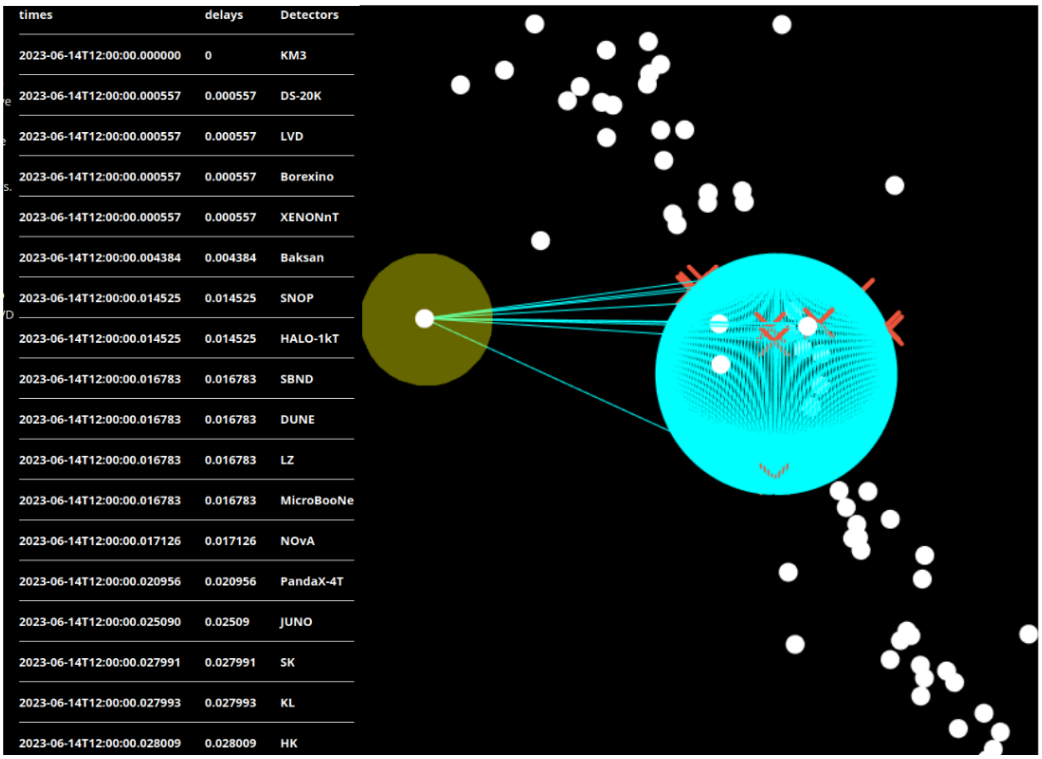

Figure 3.16: Scheme of the time delay from the SNEWS2.0 web site: `https://snews2.org`. Detectors at the Earth (cyan sphere) are represented by red crosses, CCSN candidates as white spheres, the one selected in this figure geing NSV-166 09-2. The table on the left shows the delay in seconds from the first experiment that observed the burst, in this the case KM3 (the Km3net experiment).

3.2.3 Alarms

Signal alarms are based on three notions, two of which have already been mentioned: they need to be prompt, as the neutrino alarm transient has to be short enough to be useful for EM telescopes and eventually GW experiments; they must provide pointing capabilities, or they must be added a posteriori to the neutrino alarm, in this case the analysis has to be performed as quickly as possible; finally they have to be able to provide *positive* signals, i.e. they have to contribute on discriminating fake from real CCSN alarms. The first two factors concern experimental CCSN trigger capability and hardware-software development. The third one is more complex.

One of the aims of SNEWS is to reduce the number of false alarms. Some requirements are necessary to evaluate the quality of a CCSN alarm and label it as a positive one. For each particular experiment, poissonian and non-poissonian signals can be differentiated. The first type is supposed to be known, and its source is frequently tied to detector components, as well as constant flux background sources, depending on the timescale considered. Reducing this is an experiment-specific task. On the other hand, individual estimates of the non-poissonian component are possible, and they also vary in time scale. Predicting this component is more challenging due to its multiple origins. However, coincidences between the other experiments can help to lessen it.

Connecting many detectors has advantages, but it also requires accounting for unintentional coincidences between their *false* background alarms within a 10-second interval. To avoid this, the total number of false alarms is limited to one per week if only three experiments are operating and online during this time [324]. This rate limit, however, is expected to increase as the number of running experiments increases. For instance, non-astrophysical correlations might appear, particularly for detectors operating in the same place, such as LNGS, which hosts XENONnT, LVD, DarkSide, and Borexino. In principle, most TPCs

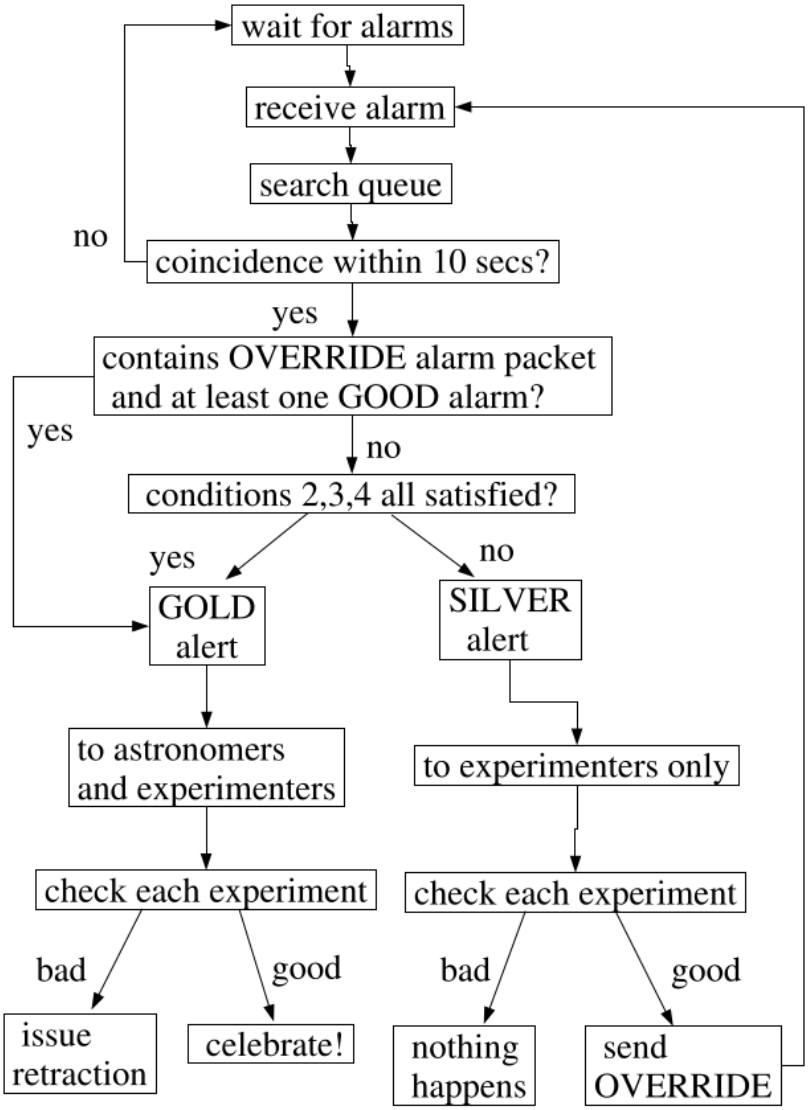

Figure 3.17: Flowchart of the trigger alarm scheme from SNEWS 1.0 [324], summarizing the sequence of events and decisions that determine whether an alert is GOLD or SILVER.

for direct DM detection meet these background requirements because they have low backgrounds, and the majority of them have cosmic background vetoes, as well as radiogenic neutron background vetoes, such as XENONnT.

Figure 3.17 depicts the SNEWS trigger structure. The coincidence trigger generates two different alerts: GOLD and SILVER. The four conditions for the GOLD criteria are detailed in reference [324], with the alert raised to SILVER if any of the four conditions is not met. Another distinction is that GOLD alarms will be sent to all astronomers, including amateurs, as well as SNEWS experiments, whereas SILVER alarms will only be sent to experiment members. Indeed, it is a unique objective of SNEWS to incorporate not just experiments but also the whole astronomy community, including amateurs who can contribute with their observations.

Finally, data gathering is a crucial consideration. This needs to be as fast as possible and capable of performing a preliminary CCSN analysis online. Each experiment must have its own trigger for CCSN and send data to the SNEWS trigger coincidences. This requires continuous online data collection and an online report on the state of the detector (operating or not). SNEWS members must modify or build their trigger, as well as their data gathering hardware, before they can transmit alarms. Meanwhile, they can receive alarms from other studies and send *heart-beats* to update the detector state. This is exactly the standing of XENONnT, which makes efforts to implement the CCSN-specific trigger and the online CCSN analysis in the TPC while also including the vetoes in the CCSN detection via IBD.

3.3 The XENONnT Dark Matter Detector

The XENONnT experiment is located underground at LNGS. A 1.5 km thick layer of rock protects the dual phase TPC, carrying the LXe target from cosmic radiation. However, due to the huge flux of this radiation, primarily constituted of cosmic muons ($\sim 1/\mathrm{cm}^2/\mathrm{s}$ [342]), a volume of 700 tons of water surrounds the detector. This water tank vetoes muons at 92%, and vetoes neutrons at 8% with the whole total water volume. The latter is one of the upgrades of XENONnT compared to XENON1T, created to reduce the radiogenic background (primarily produced by nuclear recoils generated by radiogenic neutrons) from 0.04 to 0.02 events per tonne-year [343]. These are the three volumes that comprise the XENONnT experiment [344], which all are sensitive to CCSN neutrinos: in the TPC via CEνNS (see **Section 3.4**), and in the neutron and muon vetos via IBD.

3.3.1 XENONnT Xe TPC

The TPC is the main volume of the XENONnT experiment, built to be sensitive to nuclear recoils produced by WIMPs of masses ranging from few $\mathrm{GeV/c}^2$ to 10 $\mathrm{TeV/c}^2$ [344, 343]. An almost cylindrical volume filled with 5.9 tonnes of LXe at -96 °C, composes the active volume, which is hosted by a double-walled stainless steel vacuum-insulated cryostat in which more LXe is installed for a total of 8.5 tonnes. The main body of the TPC is made of polytetrafluoroethylene (PTFE, also known as Teflon®), a radio-pure material utilized as reflector panels to limit the loss of prompt scintillation photons. The internal cylinder has dimensions of 148 cm in height and 134 cm in diameter, resulting in a diameter/height ratio close to one. This design maximizes the target detection volume while reducing the electron drift length and the losses associated with it. Furthermore, this diameter reduces the sagging of wires of the electrodes. The

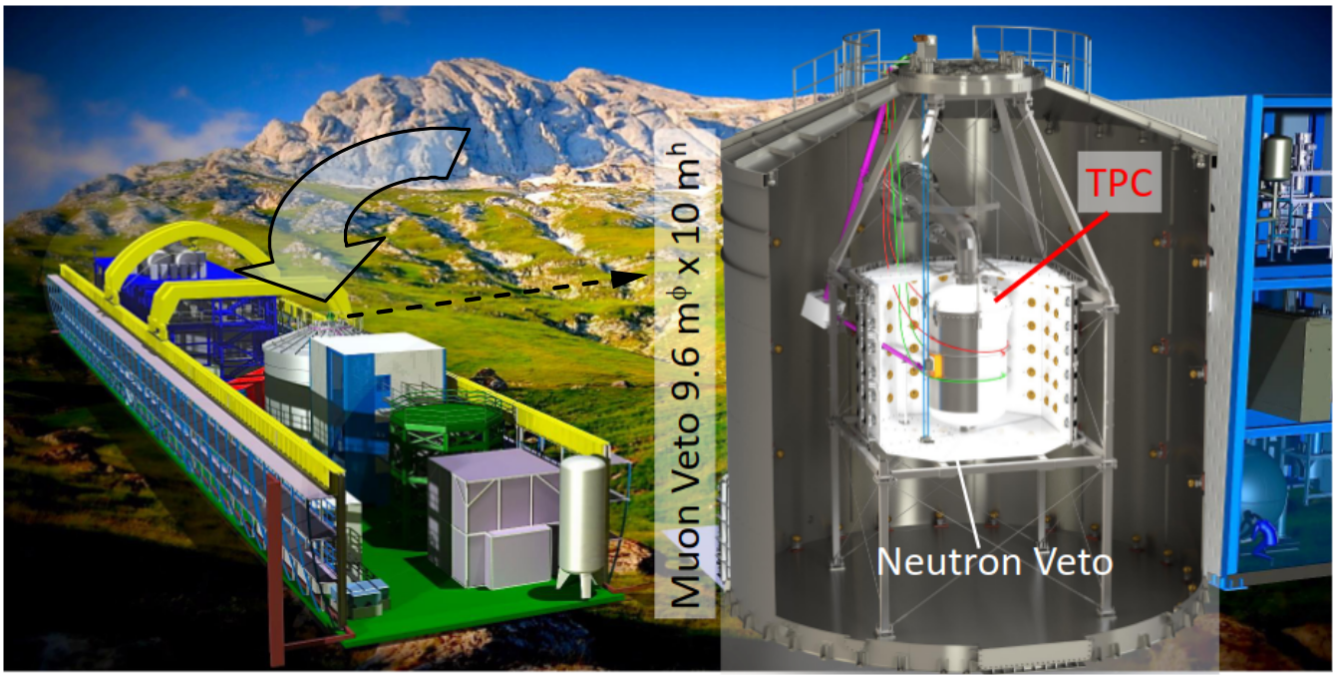

Figure 3.18: Location and 3D model of XENONnT experiment. Figure modified with the original from [345]

XENONnT TPC employs the dual phase working principle, using drift field and a liquid/gas interface. When a particle interacts with the LXe atoms, it produces prompt scintillation light called S1, which may be captured by the top (253) and bottom (241) arrays of Hamamatsu R11410-21 3 inch PMTs [346]. A drift field operating at $23^{+0.4}_{-0.3}$ V/cm drives the ionized electrons to the liquid/gas interface, where an extraction field between 2.9 and 3.7 kV/cm (depending on the radial position due to the sagging of the electrode plane) accelerates them, producing a secondary scintillation signal named S2 in the gas phase [344]. Three electrode grids generate the electric drift and extraction fields: the cathode at the bottom of the cylindrical cylinder; the gate at the top, right below the liquid/gas interface; the anode in the gas phase, 8 mm above the gate. The geometry allows for efficient fiducial volume cuts near walls (along the height axis), allowing for event rejection near the walls.

3.3.2 LXe as a target detection volume

WIMPs coherently scattering with Xe nuclei can be found directly detected. As previously stated for neutrinos, LXe, compared to other nuclei used in the field, increases the cross-section of coherent scattering for WIMPs, with a spin-independent interaction cross-section with its high atomic number $\propto A^2$[348]. On the other hand, spin-dependent (SD) WIMP-Xe coherent scattering interactions can also be considered. Unpaired neutrons present in 45.6% of the LXe isotopes (see the table in **figure 3.20**) allow the XENONnT experiment to be sensitive SD interactions [349, 350, 351]. Furthermore, its relatively high mass of $\sim$ 122.3 GeV maximizes the energy transfer in elastic collisions with WIMPs as their masses are typically predicted to be in a similar range of a few GeV up to a few TeV [348].

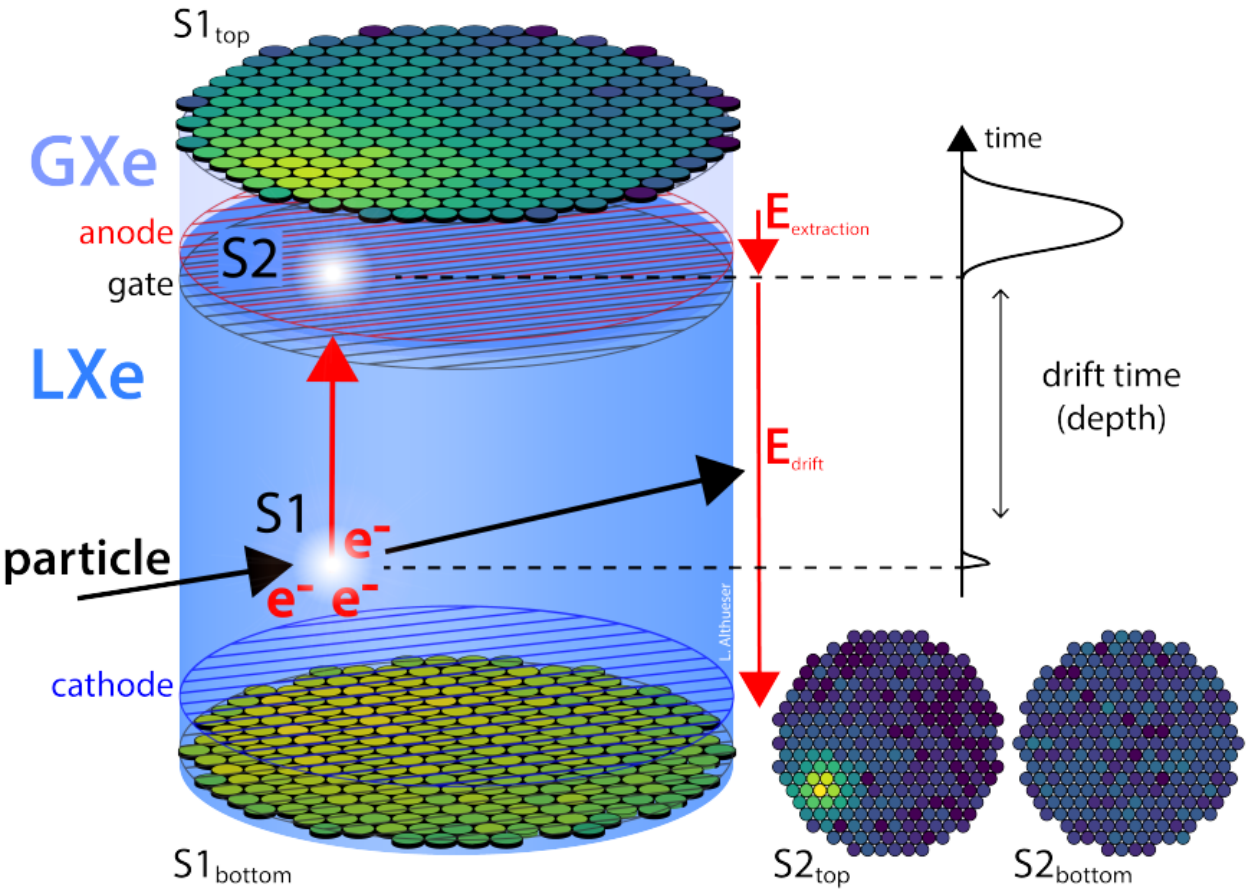

Figure 3.19: Working principle of a dual-phase time projection chamber. Prompt scintillation signal (S1) and secondary scintillation (S2) are represented in the LXe and the GXe respectively. Drift field and extraction field directions are represented by red arrows [347].

There are two Xe isotopes, ^{134}Xe and ^{136}Xe, that are unstable but exhibit long decays via two-neutrino emission, known as neutrino double beta decay [353]. While the decay of ^{134}Xe is still out of reach, ^{136}Xe has a shorter half-life, of 2.165 $\times 10^{21}$ years. The XENON1T experiment studied the neutrino-less double beta decay of the ^{136}Xe isotope [354]. XENON1T observed as well the double electron capture of the ^{124}Xe isotope, a rare event that, with its half-life length of 1.8 $\times 10^{22}$ years, represents the longest half-life ever measured directly [355, 354]. The greater density of LXe compared to LAr reduces the attenuation length for neutrons and gammas, which are the main sources of background inside the TPC. This minimizes the amount of sensitive volume loss when fiducial cuts are done along the cylinder walls, which is typically $\mathcal{O}$(10 cm). Low-energy gammas producing electron recoil inside the TPC are the main source of background. **Figure 3.22** shows the stopping power, or attenuation length, of LXe for gammas as a function of their energy. Radioactive sources producing directly or indirectly a gamma emission in the range between a few eV and a few MeV are summarized in [343]. In detector components, ^{232}Th, ^{238}U, ^{235}U, ^{40}K and their progeny, as well as ^{60}Co and ^{137}Cs, are the main sources of gamma background [343]. Also, the ^{222}Rn

Isotope	Abundance (%)
^{124}Xe	0.09
^{126}Xe	0.09
^{128}Xe	1.92
^{129}Xe	26.44
^{130}Xe	4.08
^{131}Xe	21.18
^{132}Xe	26.89
^{134}Xe	10.44
^{136}Xe	8.87

Figure 3.20: Natural abundance of LXe isotopes used in GEANT4 simulations, and in the following calculations for WIMPs and neutrinos interactions in this work. The values are given by the Geant4 internal material database (NIST)[352]

emanation rate, present in all the materials near the active volume is important [356]. If ^{222}Rn is released into the LXe, further decays can induce low-energy ER background events throughout the sensitive volume [357]. The table in **figure 3.21** summarizes the radioactivity level for XENONnT components associated with the mentioned radioactive isotopes contributing to the low-energy background.

As shown in **figure 3.22**, photoelectric effect dominates < 0.1MeV, while Compton scattering in the 0.1-1 MeV range. Between 1-10 MeV, the gamma pair production rate competes with the previous processes. The electronic recoils creating signals similar to WIMP nuclear recoils $\mathcal{O}$(keV) are due to the Compton scattering of these $\mathcal{O}$(MeV) gammas. At a separate level, low-energy gammas from metal and LXe impurities cause the photoionization of a single or a few electrons, which mostly affects the S2 signal. Furthermore, Compton scattering may yield single-electron signals. This is one of the outcomes of the very efficient S2 signal amplification in LXe, resulting in the sensitivity of a single electron signal [358, 359].

These electron recoils are able to excited xenon atoms, producing a pair of S1 and S2 signals. The discrimination between nuclear and electronic recoil, crucial in order to reduce the background for the search for WIMP, can be approached using the different weights of S1 and S2 signals for each type of recoil. LXe TPCs cannot use pulse shape discrimination based on the S1 signal as in LAr, because the decays between their two excited states are too close, within $\mathcal{O}$(10 ns). As a consequence, both S1 and S2 are needed for this discrimination. In LXe, the photon/electron ratio is expected to be different between a nuclear and an electronic recoil. The LXe microphysics that lead to signal reconstruction and enable this discrimination will be discussed in the following section.

3.3.3 Microphysics in Xe dual phase TPC: observables S1 and S2

Deposition of energy for an interacting particle can be translated as a form of detectable *quanta*, namely scintillation photons or ionization electrons. Nuclear recoils transfer their energy as well into heat, but they

Component	Mass	Activity [mBq/kg]							
	[kg]	^{238}U	^{235}U	^{226}Ra	^{232}Th	^{228}Th	^{60}Co	^{40}K	^{137}Cs
Cryostat vessels	1120	3.2 (9)	0.37 (13)	0.37 (5)	0.29 (7)	0.45 (5)	2.5 (5)	2.1 (3)	$<$0.41
Cryostat flanges	730	1.4 (4)	0.06 (2)	$<$4	0.21 (6)	4.5 (6)	14.1 (9)	$<$5.6	$<$1.5
Bell and electrodes[(1)]	190	3.2 (7)	0.57 (10)	0.62 (10)	0.36 (14)	0.46 (9)	0.78 (11)	1.6 (6)	$<$0.17
PTFE[(2)]	128	0.12 (5)	$<$0.06	0.10 (2)	0.11 (5)	$<$0.06	$<$0.053	2.4 (3)	$<$0.038
Copper[(3)]	355	$<$0.69	$<$0.28	0.033 (5)	$<$0.027	$<$0.023	0.11 (2)	$<$0.29	$<$0.016
PMTs and bases[(4)]	98	53 (15)	2.2 (7)	4.6 (10)	3.5 (12)	4.2 (8)	7.1 (9)	73 (18)	0.9 (3)

Figure 3.21: Radioactivity levels of the XENONnT detector components that generate electronic recoils in the ROI for WIMP detection. Values in parentheses correspond to uncertainties. [(1)]Stainless steel (SS) diving bell and SS frames of the electrodes. [(2)]TPC pillars, blocking and sliding reflector panels, and PMT holders. [(3)]Support structure of the PMT arrays, support rings of the TPC, inner and outer field shaping rings. [(4)]The total mass corresponds to 494 PMTs and PMT bases. Table from [351].

.

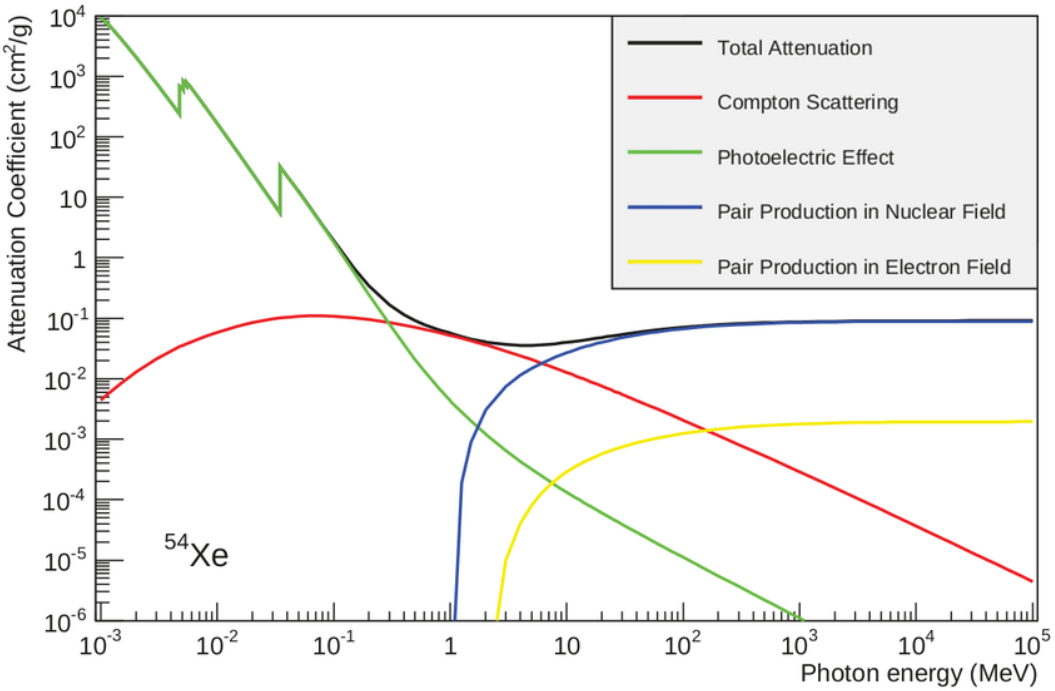

Figure 3.22: Photon Attenuation length in LXe as a function of Photon Energy, for the main process produced in the liquid.

are not exploitable by noble liquid TPCs. Heat depositions are the primary distinction between electronic and nuclear recoil energy losses in LXe. The excitation of LXe atoms results in states known as *excimers*. These excitations can be directly created by the interacting particle producing prompt scintillation light S1 or by further recombination of the ionized electrons producing a recombination S1 signal. **Figure 3.23** represents the process of LXe excitation leading to the *singlet* and *triplet* excimeric states that will decay to the ground state, producing the detectable VUV scintillation light with a peak at 177.6 nm [360].

Plaztmann equation summarizes this incident particle energy deposition for a single interaction as follows

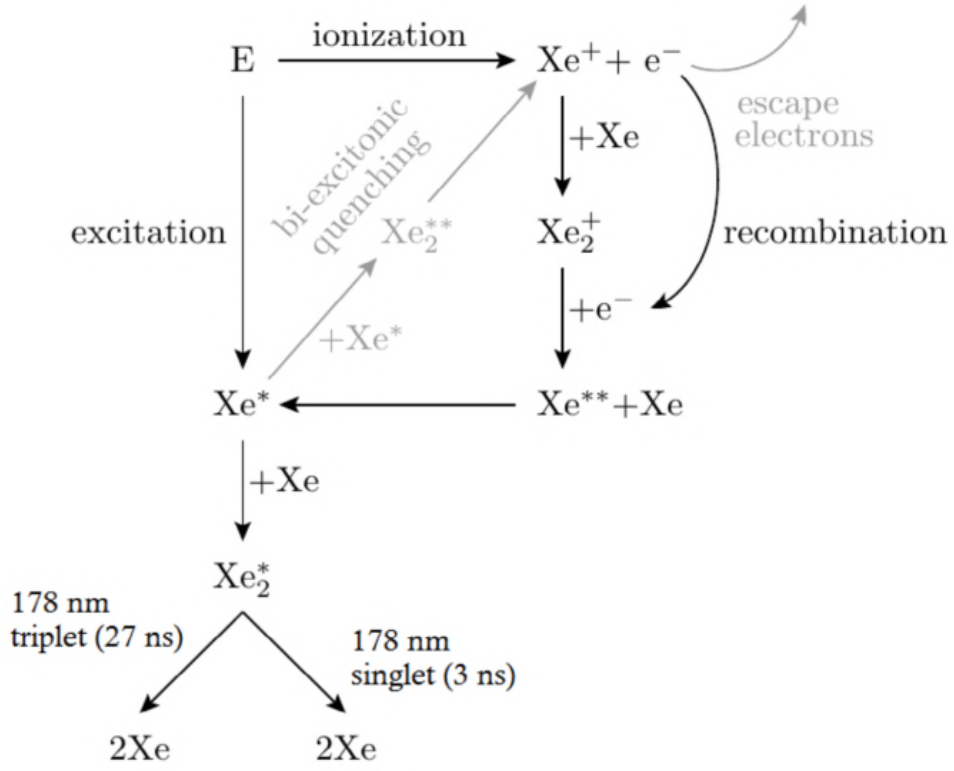

Figure 3.23: Description of the path leading to LXe excited states decay in scintillation light, direct excitation and recombination. Image taken from[361]

[362]:

$$E = N_i E_i + N_{ex} E_{ex} + N_i \epsilon, \tag{3.2}$$

with N_i the number of electron-ion pairs created, N_{ex} the number of exited atoms, E_i and E_{ex} the average energy needed for the creation of these electron-ion pairs and excited atoms, respectively. Also, free electrons with average kinetic energy ϵ, which is lower than the first excited atomic level are accounted for [363]. Neglecting the last term, we can write the relation between the quanta excitons and ions $\alpha = N_{ex}/N_i$ and describe the total average energy to create an electron-ion pair W_i:

$$E = N_i(E_i + \alpha E_{ex}), \qquad N_i = \frac{E}{(E_i + \alpha E_{ex})}, \qquad W_i = \frac{E}{N_i} = (E_i + \alpha E_{ex}). \tag{3.3}$$

The $\alpha(\rho, E)$ parameter depends on the energy deposition E and the LXe density ρ [364]. In this section, we are interested in the observables; the number of photons and the number of electrons, to quantify the discrimination capabilities based on LXe microphysics. The number of photons N_{ph} is the sum of the prompt and the recombination scintillation. Considering the latter, a recombination probability r can be used, and the number of photons and the number of electrons N_e can be written as [365, 364]:

$$N_{ph} = N_{ex} + N_i r, \qquad N_e = N_i(1-r) \tag{3.4}$$

This recombination probability r(ρ, E, F$_D$) depends on the LXe density, energy deposition E and the electric drift field F$_D$. The first dependence parameter relies on the stopping power (as the length of the track of electrons leading to recombination also depends on it), the differential $\frac{dE}{dx}$, scaled by the density from the linear energy transfer (LET). If the last track is greater than the mean ion-electron thermalization distance, r(ρ, E, F$_D$) can be adjusted as [366]:

$$r = \frac{A\frac{dE}{dx}}{1 + B\frac{dE}{dx}} + C, \qquad C = 1 - \frac{A}{B}. \tag{3.5}$$

The C parameter accounts for ionized electron recombination with parent ions, known as the Onsagers recombination parameter [367]. On the other hand, for small tracks related to this thermalization distance, the so-called Thomas-Imel box model is used instead as an alternative, more accurate description of the ionization process [368]:

$$\langle r \rangle = 1 - \frac{ln(1 + \frac{N_i\phi}{4})}{\frac{N_i\phi}{4}}. \tag{3.6}$$

Where the ϕ parameter depends on the drift field and follows a power law fitted to the empirical parameters ω and δ as $\phi = \omega F_D^{-\delta}$ [369]. On the other hand, ER recombination cannot be modeled by equation (3.6). Measurements at lower recoils than 3 keV and greater than 10 keV conclude that corrections for the recombination factor from equation (3.6) are necessary, as detailed in [358].

At this point, knowing the dependence of the microphysics on electric field and LXe properties, the two characteristic values related to the number of photons, the light yield $L_y = \frac{N_{ph}}{E}$, and the number of electrons, the charge yield $Q_y = \frac{N_e}{E}$, per unit of deposited energy, may be defined. As well as the number of quanta $N_q = N_e + N_{ph}$ and the mean work to produce one as $W_q = \frac{E}{N_q}$ (W_q=(13.7±0.2) eV [347]). The value of W_q reported here is one of the many measured by several experiments, often in tension to each other; a detailed review of this parameter is out of the scope of this manuscript. In case of ER, the number of quanta N_q is not affected by the dissipation into heat of the deposited energy. However, for NR, the motion of excited atoms that leads to non-detectable heat transfer to LXe reduces the number of quanta to $N_q^{NR} > N_q$. According to the Lindhard theory [370], the Lindhard factor L accounts for this *quenching*. It is defined as:

$$L = \frac{kg(\epsilon)}{1 + kg(\epsilon)}, \qquad L = \frac{W_q N_q^{NR}}{E}, \tag{3.7}$$

with k a constant depending on the recoil momentum and $g(\epsilon)$ depending on the energy and proportional to the ratio of the electronic to the nuclear stopping power [371]. Also, $\epsilon(E)$ is an energy-dependent dimensionless quantity associated with the Z number of protons, as detailed in [307].

In order to evaluate fluctuations due to the heat dissipation, a binomial distribution can be used, renaming the absolute *quenching* L as a probability f_{NR} to associate it with nuclear recoil. These fluctuations can be approached for a given drift electric field F_D and recoil energy (E) as detailed in [318].

$$N_q^{NR} = Binomial(N_q, f_{NR}), \qquad f_{NR} = \frac{\langle N_q^{NR} \rangle}{\langle N_q \rangle} \tag{3.8}$$

Averaging over the recoil energies, $f_{NR} \sim 0.166$ [364].

For ER, L = 1, hence the heat dissipation can be neglected, and so $\langle N_q \rangle = \frac{E}{W_q}$ [318]. By extension of equation (3.8), we can define a probability f_{ph}, different for ER and NR, and define N_{ph} and N_e [86]:

$$N_{ph}^{NR,ER} = Binomial(N_q, f_{ph}), \qquad f_{ph}^{NR} = \frac{\langle N_{ph}^{NR} \rangle}{\langle N_q^{NR} \rangle} = \frac{\langle N_{ph}^{NR} \rangle}{\langle N_q \rangle f_{NR}}, \qquad f_{ph}^{ER} = \frac{\langle N_{ph}^{ER} \rangle}{\langle N_q \rangle}, \tag{3.9}$$

$$N_e^{NR} = N_q^{NR} - N_{ph}^{NR}, \qquad N_e^{ER} = N_q - N_{ph}^{ER}. \tag{3.10}$$

Differences regarding recombination and quanta reduction to heat dissipation lead to different Q_y and L_y for ER and NR, for a given drift field F_D and recoil energy E. These values can be written using equations (3.8), (3.9) and (3.10):

$$Q_y^{NR} = f_{NR} W_q (1 - f_{ph}^{NR}), \qquad Q_y^{ER} = W_q (1 - f_{ph}^{ER}), \tag{3.11}$$

$$L_y^{NR} = W_q \frac{f_{ph}^{NR}}{f_{NR}}, \qquad L_y^{ER} = W_q f_{ph}^{ER}. \tag{3.12}$$

The LXe microphysics can be simulated by the Noble Element Simulation Technique (NEST) model [365], which was one of the tools used to simulate interactions in XENON1T, and also in XENONnT. This model features a *python package* called *nestpy* that performs calculations in LXe of the light and charge yields for several particles inducing recoils. **Figure 3.24** presents the charge and light yields for different drift electric field values, based on NEST simulations for LXe. This yield is calculated for NR and ER induced by gamma-rays, and accounts for recombination and *quenching* factors explained above. Some parameters used in NEST are based on measurements from these experiments, implementing the NEST model with empirical data. Particularly, NEST which includes default detector parameters, such as XENON10 [350] and LUX [372], can also, in this sense, account for geometries, corrections, and efficiencies specific to each detector.

The charge and light yields from expressions (3.11, 3.12) are shown in **figure 3.24**, and are quantified for a single interaction. They depend on intrinsic proprieties of LXe, such as recombination, — which also depends on the drift field—, and quenching. But other effects related to the detector geometry, photomultipliers, and impurities lead to corrections and reduction in the number of electrons and photons finally observed.

3.3.4 Observables and corrections: cS1 and cS2

The detector response for the S1 and S2 signals is not spatially uniform. These differences necessitate fixing the signal reconstruction to match the expected average response of the detector, which is dependent on the spatial coordinates of the interaction. The S1 signal necessitates these spatial corrections due to its inhomogeneous photon collection, which, even with the use of reflectors, still depends on the

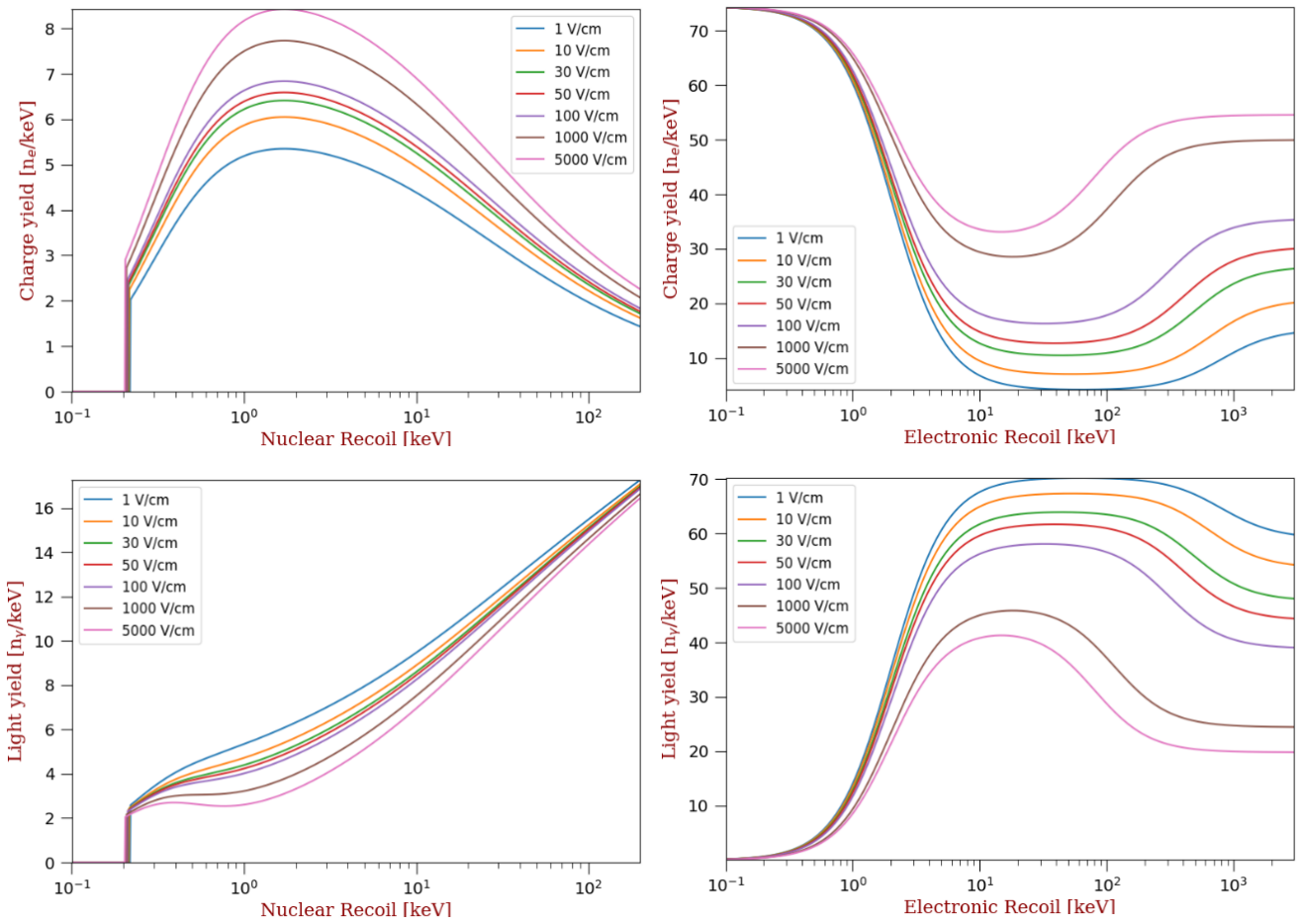

Figure 3.24: Charge and light yields for NR (Left) and ER (Right) from the NEST model [365], for several values of the drift field. The electronic recoils are induced by gamma rays.

photon path length because of Rayleigh scattering and absorption. In this sense, light collection efficiency (LCE) accounts for this spatial dependence, and the light yield will be impacted and depends on spatial coordinates, leading to a mapping of the latter. Furthermore, the spatial dependence of the drift field has also to be taken into account. Finally, the XENONnT detectors are PMTs. The photocathode absorption efficiency of PMTs depends on both the wavelength of the light and the surface of the PMTs. The average value of all the PMT absorption wavelength spectra is used and referred to as *quantum efficiency* (QE). Cylindrical coordinates $\vec{r}(R,\theta,z)$ are appropriate to describe the S1 signal at a given energy E:

$$S1(R,z,\theta,E_d,E) = L_{c_y}(R,z,\theta,E_d,E)E. \tag{3.13}$$

The light yield L_{c_y} needs to be evaluated for each channel i [318, 301]:

$$L^i_{c_y}(R,z,\theta,E_d,E) = \frac{\overbrace{\epsilon^{S1}_{LCE}(R,z,\theta) \times L_y(E_d(R,z,\theta),E)}^{N^i_{PE}/E} \times QE^i \times (1+p_{DPE})}{N^i_{hits}/E} \tag{3.14}$$

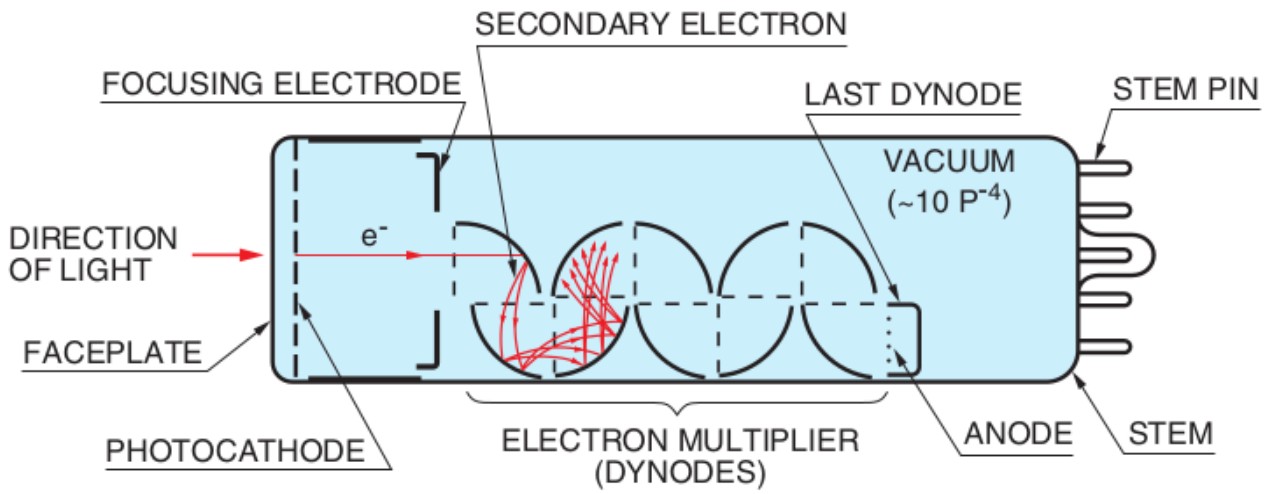

Figure 3.25: A photon crosses the PMT glass window, entering the vacuum tube. The photon excites an electron in the photocathode, and a photoelectron is emitted into the vacuum by photoelectric effect. This photoelectron is accelerated and focused by the focusing electrode and impinges on the first dynode, where it is multiplied by means of secondary electron emission. The signal is amplified in the rest of dynodes by repeating the process. Finally, electrons reach the anode, multiplied up to 10^6 to 10^7 times. Figure from [374].

where ϵ^{S1}_{LCE} is the light collection efficiency. The term p_{DPE} is added in order to include a small probability in which one absorbed photon creates two electrons instead of one (see **figure 3.25**). At this point, the observables are not more the number of photons, but photoelectrons (PE) converted from electrical pulses in the PMTs. In expression (3.14), the notion of number of PMT hits ($N_{PMThits}$) is introduced [3]. This 'PMThits' notion will help us to understand the simulation chain for the CCSN neutrinos in the water tank, separating the physics of what is happening in the interaction target volume (water) and the sensitive PMTs. However, this is not useful for the TPC signal simulation because the NEST-based waveform simulator, WFsim [373], gives the corrected S1 and S2 in PEs, including all the above-mentioned corrections.

The microphysics of the S1 signal described so far allows to represent how a scintillation signal is finally translated to an observable represented in PE; however, data driven corrections are needed to account for uncertainties due to the photon attenuation in LXe and PMT efficiencies. Second order corrections also address the inhomogeneities of the field, which ultimately influence the recombination of ionized electron. For all these corrections, regular TPC calibrations are performed with ^{83m}Kr. The two decay states of ^{83m}Kr (at 32.1 keV and 9.4 keV in a 154 ns interval) are combined to map the LCE, leading to a correction factor for S1s. The idea is to divide the detector volume into voxels and attribute to them a S1, so that it is possible to calculate (for a given energy deposition E_{kr}=41.5 keV which corresponds to the sum of the two ^{83m}Kr decays states) the S1 as a function of position, as well the average $\langle S1 \rangle$, by integrating the signal on all voxels. The light yield $L^i_{c_y}$ can then be measured experimentally as its fraction $C^i_{L_y}$ with respect to the

[3] Not the same N_{hits} defined in [301]. In the last reference, $N_{hits} \equiv N_{PE}$

average over all channels. In terms of probability, a new representation of the light yield per unit energy can be introduced, $f_{PE}(R, z, \theta, E_d, E)$, together with its volume-integrated mean f_{PE} [86, 301, 347]:

$$C^i_{L_y}(R, z, \theta)|_{E=E_{kr}} = \frac{L^i_{c_y}(R, z, \theta, E_d, E)}{\langle L^i_{c_y}(E_d, E)\rangle}$$
$$= \frac{\epsilon^{S1}_{LCE}(R, z, \theta) L_y(E_d(R, z, \theta), E) QE^i}{\langle \epsilon^{S1}_{LCE}(R, z, \theta) L_y(E_d(R, z, \theta), E)\rangle \langle QE^i\rangle} = \frac{f_{PE}(R, z, \theta, E_d, E)}{f_{PE}}. \tag{3.15}$$

The f_{PE} factor, that can be also refereed as the gain for each PMT channel, plays an important role to put in relation the number of photons N_{ph} with the number of detected photoelectrons N_{PE} as defined in reference [86]:

$$N^{S1}_{PE} = Binomial(N_{ph}, f_{PE}), \qquad \langle S1\rangle = \langle N_{ph}\rangle f_{PE}. \tag{3.16}$$

LUX and XENON1T measurements lead to a value of $f_{PE} \sim 0.12$. Finally, the relation between the corrected S1 (cS1) and S1 becomes:

$$\frac{cS1}{S1} = \frac{f_{PE}}{f_{PE}(R, z, \theta, E_d, E)} \tag{3.17}$$

The corrections for the S2 signal are strongly dependent on the drifted electron surviving probability until the liquid/gas interface. Electron losses are related to the concentration in electronegative impurities in the detector that are not necessarily uniformly distributed in the LXe volume, as well as on the length of their path, i.e., the height of the interaction (z) relative to the liquid/gas interface Δz. The survival probability of the electron can be approximated as:

$$p_{sur} = e^{-\frac{\Delta z}{v_d \tau}} \tag{3.18}$$

with v_d the drift velocity of electrons depending on the electric field, and τ, the average electron survival time. The XENONnT TPC has a liquid/gas interface, which also leads to an interface between the drift and the extraction fields. The fraction of the number of electrons that are finally extracted can be accounted for by the extraction efficiency $\epsilon_e(E_e)$, depending on the extraction field. The number of photons produced per extracted electron and arriving at PMTs is described by a gain factor $g_{ph}(\theta, R)$ that does not depend on z but only on polar coordinates on the plane of the liquid/gas interface. Analogous to the corrections of the S1 signal, a charge yield can be defined to look for the fraction of surviving electrons that are finally extracted, producing photons that will reach the PMTs, $N_{PMThits}$, some of which will lead to a detectable number of PEs, N_{PE}:

$$Q^i_{c_y}(R, z, \theta, E_d, E_e, E) = \overbrace{\underbrace{\epsilon^{S2}_{LCE}(R, \theta) g_{ph}(\theta, R) \epsilon_e(E_e) Q_y(E_d(R, z, \theta), E)}_{N^i_{PMThits}/E} \times QE^i (1 + p_{DPE})}^{N^i_{PE}/E} \tag{3.19}$$

Also in this case, the calibration source ^{83m}Kr has been used to perform data driven corrections. Including these effects, the averaged fraction of final detected S2 photoelectron is [364, 347]:

$$C^i_{Q_y}(R,z,\theta)|_{E=E^m_{kr}} = \frac{Q^i_{c_y}(R,z,\theta,E_d,E_e,E)}{\langle Q^i_{c_y}(E_d,E_e,E)\rangle} = \frac{\epsilon^{S2}_{LCE}(R,z,\theta)g_{ph}(\theta,R)\epsilon_e(E_e)Q_y(E_d(R,z,\theta),E)QE^i}{\langle \epsilon^{S2}_{LCE}(R,z,\theta)\epsilon_e(E_e)g_{ph}(\theta,R)\rangle\langle QE^i\rangle} = \frac{g_{PE}(R,z,\theta,E_d,E_e,E)p_{sur}(E_d,z)}{g_{PE}}. \quad (3.20)$$

Finally, we have the relation between the number of drifted electrons (N_e) and the number of S2 PE (N_{PE}) [301, 358]:

$$N^{ex}_e = Binomial(N_e, p_{sur}\epsilon_e), \qquad N^{S2}_{PE} \equiv Binomial(g_{ph}N^{ex}_e, g_{PE}). \quad (3.21)$$

As well, we can find the relation between the corrected S2 (cS2) and S2:

$$\frac{cS2}{S2} = \frac{g_{PE}}{g_{PE}(R,z,\theta,E_d,E_e,E)\times p_{sur}(E_d,z}. \quad (3.22)$$

Finally, we can summarize the total energy reconstruction as a linear combination of cS1 and cS2 with the following expression [301, 318]:

$$E = W_q(\frac{cS1}{f_{PE}} + \frac{cS2}{g_{PE}}). \quad (3.23)$$

3.4 Coherent elastic neutrino-nucleus scattering

The coherent neutrino nucleus scattering (CEνSN) is a process predicted in the standard model, with a well known cross-section. It is the dominant interaction of neutrinos with matter at $\mathcal{O}$(MeV) [375, 376], amplified in high neutron density regions, such as many categories of star cores. The CEνSN signal has already been observed by the COHERENT experiment [377, 378, 379, 380] using a spallation neutron source. The role of CEνSN trapping neutrinos forming the named *neutrino-sphere* during the *neutronization phase* has been already emphasized in **Chapter 1** and **Chapter 2**. This interaction, which depends quadratically on the energy of the neutrino E_ν (it will be shown in equation 3.28), results in the pinched spectrum of CCSN neutrinos, suppressing its high energy tail.

Coherent scattering of neutrinos on nuclei occurs through the weak interaction and charge exchange via Z boson emission (see **figure 3.26**). Its coherence results in a recoil of the entire nucleus, where all nucleons act as one body which does not suffer structural changes. This coherence happens at low recoils energy, when the momentum transfer q is at the scale of the atom radius ($q \sim R_N$). The Helm form factor and its related parameters depict decoherence through CEνNS interaction. This is the same form factor as the WIMP-nucleus interaction, and it accounts for the fraction of nucleons involved in the scattering. The de Broglie wavelength that parametrizes this decoherence, connected to the momentum transfer q, is

directly proportional to the scattered neutrino energy E'_ν, as the low mass of the neutrinos ($\mathcal{O}$(eV)) are not significant for the nucleus recoil.

Furthermore, the squared dependence in the amount of nucleons increases the cross-section; nevertheless, strength coupling from protons and nucleons is not equal. As a result, the nucleon cross-section cannot be scaled as A^2, but can be approximated by the number of neutrons N^2, as scattering with protons in the nucleus is reduced by a factor of $1 - 4sin^2\theta\omega$ (see equation 3.28). The three-level hypercharge Q_w in equation (3.28) handles this coupling.

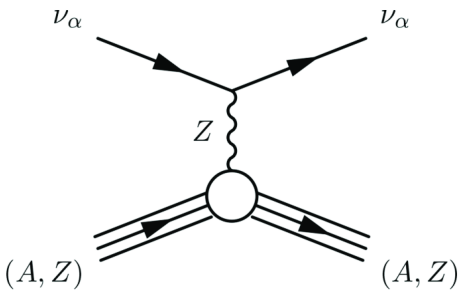

Figure 3.26: Feynman diagram of a CEνNS process. The neutrino scatters, through the exchange of a Z boson, on a nucleus with a given atomic number A.

3.4.1 CNNS cross-section

From the kinematics of the CEνNS detailed in **Appendix C.1.1**, the minimal neutrino energy $E_{v_{min}}$ to produce a nuclear recoil in the lab frame for a given energy recoil E_R can be defined as:

$$E_{\nu_{min}} = \frac{1}{2}(E_R + \sqrt{E_R(E_R + 2m_N)}). \tag{3.24}$$

This value bounds the integration for lower neutrino energies. Concerning the maximum neutrino energy, usually an upper limit due to the presence of the neutrino fog $E_\nu \leq 1$ GeV can be set, however, as the final interest is to evaluate CCSN neutrino signal in the TPC, this value can be set as $E_{\nu_{max}}$= 100 MeV, which is where the CCSN neutrino spectra falls down as shown in **figure 2.6**. In this case, $E_{\nu_{max}} << m_N$. This can be used to re-write the equation 3.24 in the limit $E_R/m_N \to 0$:

$$E_{\nu_{min}} = \sqrt{\frac{m_N E_R}{2}} \tag{3.25}$$

It is useful to define the equation that relates the recoil energy with the energy of the incoming neutrino:

$$E_R = \frac{2E_\nu^2 m_N cos^2\theta}{(m_N + E_\nu)^2 - E_\nu^2 cos^2\theta}. \tag{3.26}$$

The recoil energy E_R ranges in the interval [0,$E_{R_{max}}$] where:

$$E_{R_{max}} = \frac{2E_\nu^2}{m_N + 2E_\nu} \tag{3.27}$$

The reader could be interested on looking at the **figure C.1** from **Appendix C.1**, that illustrates the correlation between the values of $E_{\nu_{min}}$ and $E_{R_{max}}$ within the range of interest.

The differential cross-section of the CEνNS through the emission of a Z boson depends on the neutrino energy E_ν and the recoil energy of the nucleus E_R, once integrated through the scattering angle θ, assuming that this recoil direction is isotropic for the considered neutrino energy [381]:

$$\frac{d\sigma(E_\nu, E_R)}{dE_R} = \frac{G_f^2 Q_w^2 m_N}{4\pi}[1 - \frac{m_N E_R}{2E_v^2}]F^2(E_R) \tag{3.28}$$

where G_F is the Fermi constant, $Q_\omega = \mathrm{N} - (1 - 4\mathrm{sin}^2\theta_\omega)\mathrm{Z}$ the weak hypercharge, N and Z the number of neutrons and protons respectively, θ_ω the Weinberg or weak mixing angle with $sin^2\theta_\omega(q^2 = 0) = 0.23867 \pm 0.00016$ [382] and $F(E_R)$ the form factor established in equation (C.5 **Appendix C.1.2**). This equation shows that the rate increases as the neutrino energy increases. At the same time, for a given neutrino energy, the rate decreases with decreasing nucleus recoil energy. If $q \sim R_N$, the coherence is expected to be maintained. However, for $E_R \geq 10$ keV, the decoherence becomes significant, as seen in the evolution of the form factor (black dashed line) in **figure 3.27** (right). This figure displays the expected decoherence and recoil spectrum for various neutrino energies, representatives of the neutrino fog energy range. The 5 MeV, 12 MeV, and 50 MeV lines, in particular, indicate that recoils from CCSN supernova neutrinos range in energy from 0.5 to 15 keV. Finally, decoherence is projected to affect the high energy tail of the CCSN neutrino spectrum, resulting in a drop in rate at these energies, notably for the ν_x flavor, whose spectrum is broader than $\bar{\nu}_e$ and ν_e. The left panel of **figure: 3.27** depicts the integrated differential cross-section for the natural isotopes of LXe. To find this value in cm^2, the differential cross-section from equation (3.28) has been integrated using the integration limit defined by equation (3.27):

$$\sigma(E_\nu) = \int^{E_{R_{max}}} \frac{d\sigma(E_\nu, E_R)}{dE_R} \tag{3.29}$$

3.4.2 Energy dependent neutrino rate

With the derivation of the CEνNS cross-section, together with the knowledge of the incoming neutrino flux presented in the previous sections, everything is now set to derive the spectrum of the recoil energy on LXe induced by SN neutrinos. A definition of the rate for a non-time-dependent neutrino flux is introduced in this section. By applying the convolution of the neutrino energy differential neutrino flux, $\frac{dN}{dE_\nu}(E_\nu)$ and the differential cross-section $\frac{d\sigma}{dE_R}(E_\nu, E_R)$, we obtain the rate of interacting neutrinos:

$$\frac{dR\,(E_R)}{dE_R} = T \times \sum_i N_{Xe_i}(f_i) \int_{E_{\nu_{min}}} dE_\nu \frac{dN}{dE_\nu}(E_\nu)\frac{d\sigma(E_\nu, E_R)}{dE_R}. \tag{3.30}$$

where N_{Xe_i} is the number of LXe atoms per ton for each isotope i (which can be approximated as $\mathrm{N}_{Xe_i} = \frac{10^3}{A_i m_p}$, with the mass of the proton $m_p = 1.6605402{\times}10^{-27}$ kg), A_i the atomic mass of the isotope and T the exposure time of a year in seconds.

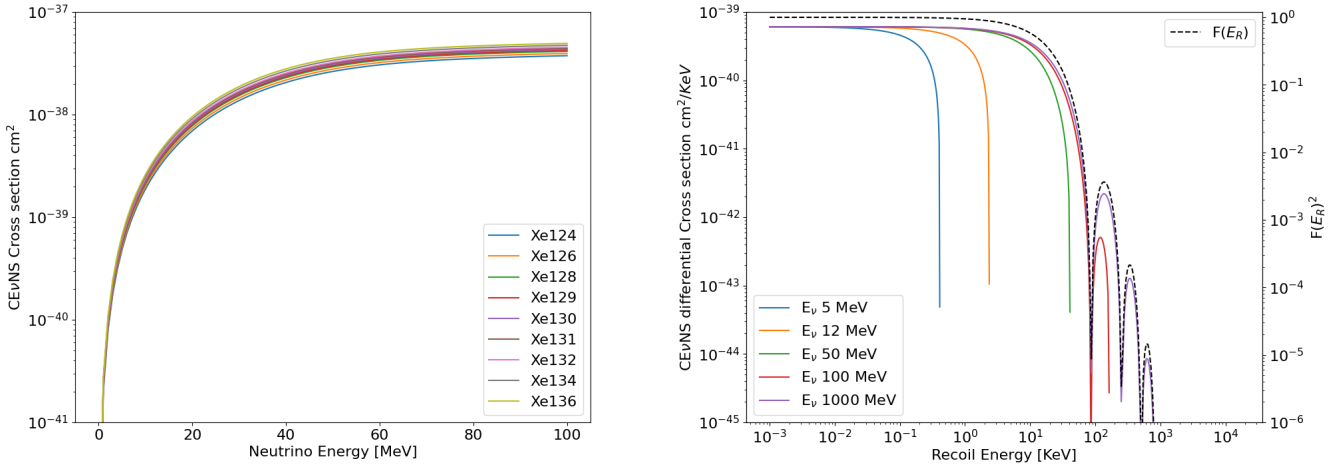

Figure 3.27: **Left**. CEνNS cross-section from equation (3.28) for the xenon isotopes described in **table 3.20** . **Right** CEνNS cross-section vs. differential recoil energy for several neutrino energies. Those energies spawn over the range of the neutrino fog for dark matter search.

The final number of events per ton per year can be obtained by integrating the equation (3.30) over the recoil energy and the neutrino energy, in the bounds $E_{R_{max}}$ and $E_{\nu_{min}}$:

$$\begin{aligned} R &= T \times \sum_i N_{Xe_i}(f_i) \int_0^\infty dE_\nu \frac{dN}{dE_\nu}(E_\nu) \int_0^{E_{R_{max}}} dE_R \frac{d\sigma(E_\nu, E_R)}{dE_R} \\ &= T \times \sum_i N_{Xe_i}(f_i) \int_0^\infty dE_R \int_{E_{\nu_{min}}} dE_\nu \frac{dN}{dE_\nu}(E_\nu) \frac{d\sigma(E_\nu, E_R)}{dE_R}. \end{aligned} \tag{3.31}$$

It is however more interesting with respect to the background rejection to calculate the rate for a given recoil energy threshold $E_{R_{th}}$. This is a common practice also for many analyses looking for light dark matter, where the energy threshold plays a crucial role. As a consequence, the integrations bounds will be impacted, as well as the effective $E_{\nu_{min}}$:

$$R = T \times \sum_i N_{Xe_i}(f_i) \int_{E_{R_{th}}}^\infty dE_R \int_{E_{\nu_{min}}} dE_{\nu_\beta} \frac{dN}{dE_{\nu_\beta}}(E_{\nu_\beta}) \frac{d\sigma(E_{\nu_\beta}, E_R)}{dE_R} \tag{3.32}$$

Figure 3.28 illustrates the recoil rates for the neutrino fog sources, as well as WIMP scattering for masses of 6 GeV/c^2 and 100 GeV/c^2 highlighting their resemblance. It is noticeable that a low energy threshold will benefit the number of detected events. For an idealistic 0 keV threshold, $\sim$ 2100 ^{8}B neutrino events per ton per year are expected while for a 0.7 keV threshold it drops to $\sim$ 500 events per ton per year. For a 4 keV threshold, no events no events are expected, but this threshold is too high for low energy WIMP detection at $\mathcal{O}$(GeV).

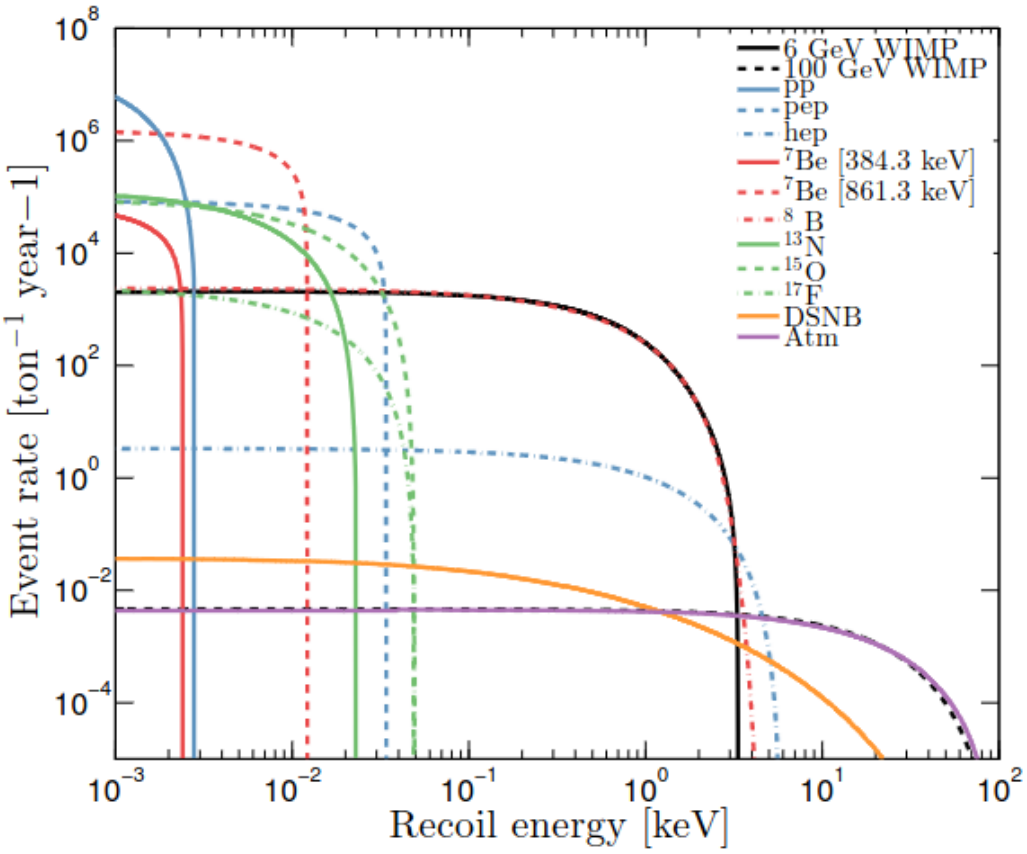

Figure 3.28: Rate of neutrino fog sources as a function of the recoil energy threshold. WIMP masses of 6 GeV/c^2 and 100 GeV/c^2 rates for spin independent coherent scattering with σ_n 10^{-45} cm^2 are compared to the ^{8}B and atmospheric neutrinos respectively. Figure from [383].

3.5 CCSN Neutrinos in the XENONnT TPC

This thesis includes a study of the CEνSN signal in the TPC from CCSN neutrinos. First, the expected CCSN recoil rates and their evolution over time will be discussed. The latter will be used to study the S2-only response based on NEST simulation results and finally go through the expected sensitivities as a function of the CCSN distance. This work will use the previously stated paper (reference [86]) as a guide, but with a different technique for signal treatment over time. The principal motivation for this TPC study is to combine the obtained sensitivity with the one from the CCSN IBD signal in the water tank and extend the latter results to a future underground direct DM search LXe detector, such as DARWIN [384] or XLZD. Furthermore, LZ, PANDA-4X, and XENONnT share a similar design: an LXe TPC surrounded by an ultra-pure water volume acting as a veto for cosmic background and/or radiogenic neutron background, and this strategy will likely be maintained in the next generation of DM detectors. The mentioned water volume in XENONnT will be described in **Chapter 4**.

3.5.1 CCSN neutrino rates in the LXe TPC

The same scattering process that trapped neutrinos in the SN core allows their detection in LXe TPC. Comparing the equations (3.30) and (3.32), the CCSN neutrino flux convolution with the CEνNS cross-section is a 2D-dimensional operation, resulting, for each neutrino flavor β, in:

$$\frac{dN_{\nu_\beta}}{dtdE_R} = \sum_i N_{Xe_i}(f_i)\frac{1}{4\pi d^2}\int_{E_{min}} \frac{dN}{dE_{\nu_\beta}dt}\frac{d\sigma(E,E_R)}{dE_R}dE. \tag{3.33}$$

To simplify the notation, we might define $\frac{dN}{dE_\nu dt} \equiv \frac{dN}{dE_{\nu_e}dt} + \frac{dN}{dE_{\bar{\nu}_e}dt} + 4\frac{dN}{dE_{\nu_x}dt}$. Furthermore, because the CEνNS rate is not affected by neutrino flavor oscillations, $\frac{dN}{dE_\nu dt} \equiv \frac{dN}{dE_\nu dt}_\oplus$ (see equation (2.63)) corresponds to the resulting rate from an unoscillated CCSN neutrino spectrum.

Figure 3.29 depicts the evolution of the rate for a representative time of the three neutrino burst phases, neutronization (0.01 s), accretion just before the explosion (0.3 s), and cooling (5 s) for two different progenitors of 11 $M_\odot$ and 27 $M_\odot$ at 10 kpc. During the neutronization phase, the spectrum has a distinct shape due to the ν_e burst, resulting in a lower mean energy ($\sim$ 12 MeV) compared to heavy flavors that will later contribute to the interaction rate. In addition, this spectrum shape results from the *pinched* initial spectra of electron neutrino flavors, where coherent scattering with nuclei suppresses the high energy tail. During the accretion phase, the mean energy increases as all flavors contribute, and the range of recoils in the spectrum becomes larger. The recoil rate of the cooling phase at 5 seconds after the core bounce is impacted by the decline in mean energy, which approaches mean values close to that of the neutronization phase. However, the overall (all neutrino flavors) spectrum at 5 seconds is less constrained than the neutronization spectrum, extending to high energies. Finally, the recoil rate spectrum is comparable to that of the accretion phase, albeit less intense. **Figures 2.5** and **2.1** of **Section 2.3** show the initial CCSN energy spectra and mean energy evolution over time. Integrated in time, the differential recoil energy rate appears as:

$$\frac{dN_\nu}{dE_R} = \sum_i N_{Xe_i}(f_i)\int_{t_1}^{t_2}\frac{1}{4\pi d^2}\int_{E_{min}} \frac{dN}{dE_\nu dt}\frac{d\sigma(E,E_R)}{dE_R}dEdt. \tag{3.34}$$

The time integration bounds vary depending on the model, but the entire duration of the burst is expected to be 10 seconds, which was approximately the case with SN1987. However, it is important to notice that several CCSN time duration were obtained from each of the three detectors involved [8, 3, 2]. They were all around $\mathcal{O}$(10 s), but with the presence of a 7.304 s gap with no events for Kamiokande-II. These duration values suggest important uncertainties, that were re-examinated in reference [385]. It has to be taken into account that this duration depends on the detector specificities (threshold, volume, optical coverage, etc.) and that only $\bar{\nu}_e$ flavor was observed. The choice of the reference model should entail constraining the burst time to its bin time simulation resolution. This time resolution has been taken into account as a model selection criteria (see **Section 2.4**). For the *Bollig 2016*, the interval for background and signal studies is fixed at 10 seconds.

The equation (3.32) integrates the CCSN number of occurrences at a particular energy recoil threshold to yield:

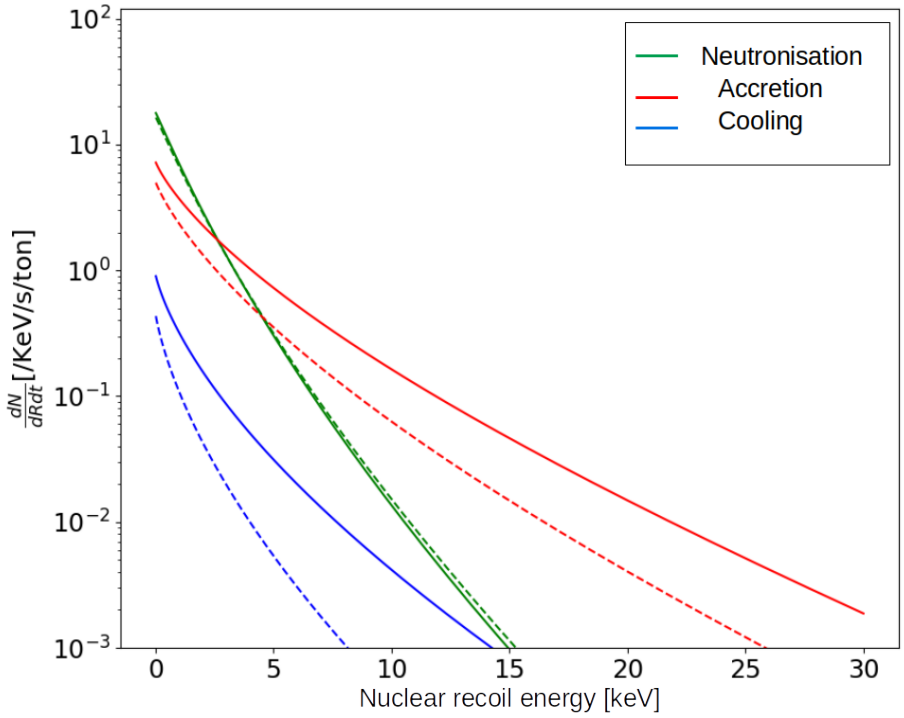

Figure 3.29: CCSN CEνNS recoil rates from equation (3.37) for different times representing the neutrino burst phases; neutronization (0.01 s) in green, accretion before explosion (0.3 s) in red and cooling (5 s) in blue, for two different progenitors of 11 $M_\odot$ (dashed lines) and 27 $M_\odot$ (solid lines) at 10 kpc.

$$N_{th} = \sum_i N_{Xe_i}(f_i) \frac{1}{4\pi d^2} \int_{t_1}^{t_2} \int_{E_{min}} \int_{E_{R_{th}}}^{E_{R_{max}}} \frac{dN}{dE_\nu dt} \frac{d\sigma(E_\nu, E_R)}{dE_R} dE_\nu dE_R dt. \tag{3.35}$$

Figure 3.30 draws equations (3.34) and (3.35), for the same models. As well, **figure 3.29** illustrates the CEνNS rates and number of interactions for a given energy recoil threshold at 10 kpc. The number of interactions results in 22 and 12 events at 0.5 keV for 27 $M_\odot$ and 11 $M_\odot$ respectively, decreasing exponentially for higher thresholds.

In some analyses performed by XENON, to reduce the energy threshold and being more sensitive to light dark matter candidates, it is dropped the requirement of the S1 signal, so that only S2 signal is considered. For those S2-only analyses, the S2/S1 ratio cannot be used to discriminate NR from ER-based background. Also for CCSN we might use the same approach of using the S2-only signal, however in our case the loss of the S2/S1 discrimination power is less critical, since it is used the characteristic rate evolution in time as main discrimination tool. Background is then expected to be assimilated to a Poissonian signal in the considered 10 seconds time window. For a given energy threshold, the evolution of the rate can be obtained with:

$$\frac{dN_{\nu_\beta}}{dt} = N_{Xe} \frac{1}{4\pi d^2} \int_{E_{R_{th}}}^{E_{R_{max}}} \int_{E_{min}} \frac{dN}{dE_{\nu_\beta} dt} \frac{d\sigma(E_{\nu_\beta}, E_R)}{dE_R} dE_{\nu_\beta} dE_R. \tag{3.36}$$

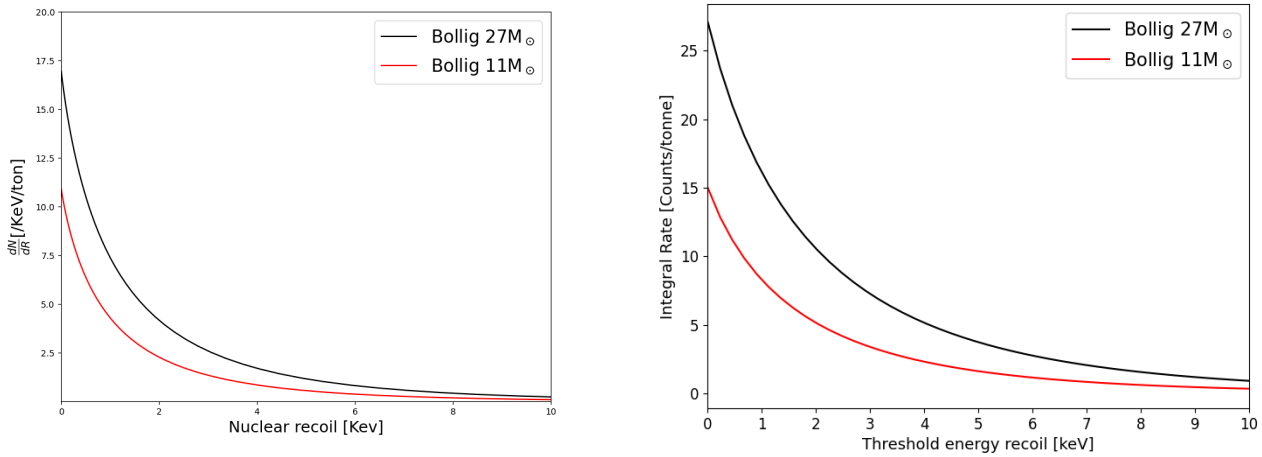

Figure 3.30: (Left) Recoil energy spectrum and (Right) number of interactions for a given threshold of CEνNS, from the equations (3.34) and (3.35) respectively, for the same models used in **figure 3.29** at 10 kpc.

Figure 3.31 depicts the time evolution described in the last equation, for the two progenitors at 10 kpc. Noticing a difference between the two progenitor rates during the accretion phase after the explosion $\sim$ 200 ms, which could be used for an eventual model discrimination. CEνNS nuclear recoil interactions do not provide a priori information about the flavor composition of the CCSN neutrino flux, at least do not provide high enough statistics to allow for the detection of the time development of the recoil rate, particularly in the first tens of milliseconds during the neutronization burst. Even before the core bounces, pre-neutrino emission is dominated by ν_e created via EC. This dominance persists until $\sim$ 0.05 seconds, signaling the conclusion of the neutronization phase, as the $\bar{\nu}_e$ contribution becomes significant and similar to ν_e. The left panel of **figure 3.32** displays the number of interactions per ton of xenon at a recoil energy threshold of 0 keV in various neutrino burst phases. As already expected by the total CCSN neutrino emission for each phase (see **table 2.1**), most of the interactions will occur within 1-10 seconds, but 45% in the first second; in which time just $\sim$5% of the interactions are expected to happen during the neutronization burst. In the case of the XENONnT TPC detection volume, only 6 and 4 interactions are expected between 0 and 0.05 seconds respectively for the two selected progenitors of 27 $M_\odot$ and 11 $M_\odot$ from the Bollig model at 10 kpc. The total number of expected interactions for the two aforementioned progenitors are 166 and 92, respectively. As shown in **figure 3.32**, the frequency of interactions increases dramatically throughout the neutronization phase. These frequencies are an important aspect for distinguishing the signal from the background. The shape of this frequency rate changes abruptly, with the characteristic high rate of the first tens of milliseconds acting as a trigger to check for a CCSN signal in the data captured over the next ten seconds. The ν_e peak of the *Bollig 2016* model, which corresponds to the neutronization burst, has a narrower width in time of roughly 10 ms. The latter corresponds to the first column of mean rates presented in **figure 3.32**.

Nevertheless, it is useful to enlarge the time step to not constrain the analysis of the CCSN signal

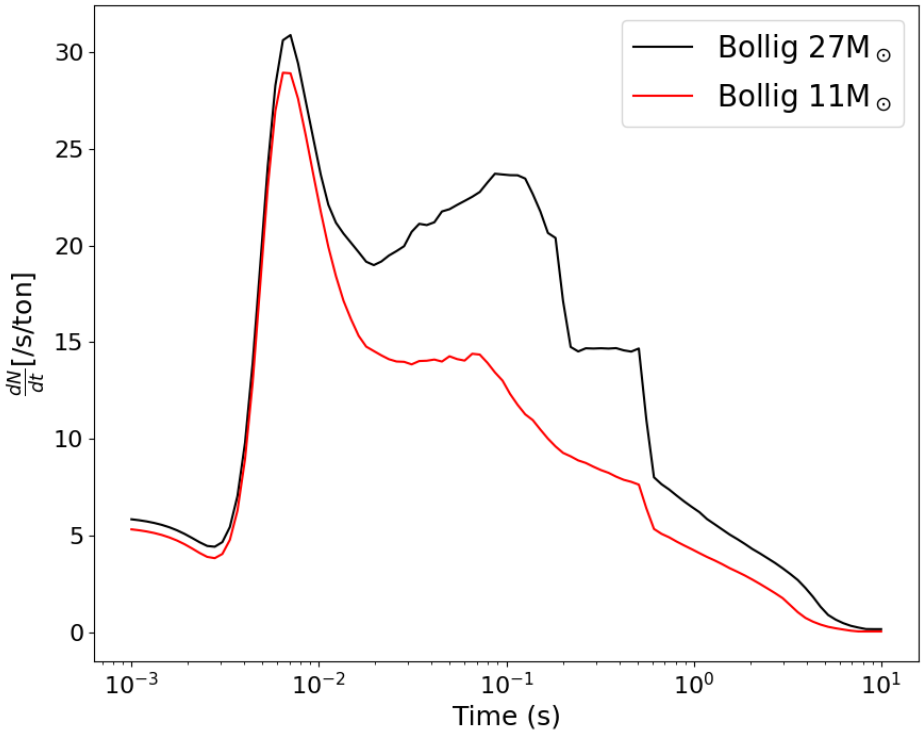

Figure 3.31: Time evolution of the rate, for recoil integrated 2D spectrum as described in equation (3.36) at 10 kpc for the Bollig $27M_{\odot}$ (black) and $11M_{\odot}$ (red) progenitors.

to the time uncertainties of the neutronization burst. By increasing the binning time, for example to 1 second, an evolution of the signal based on the mean rates can be established to check how the background discrimination would become more efficient. Another method for exproring the rate evolution is to roll a window over the entire neutrino burst, looking back at a 1 second window for each recorded potential event. The term "event" refers to an observed signal that results from an interaction in the LXe. The total values reported in **figures (3.32)**, and **(3.30)** have no ultimate implications for the detected CCSN signal, as no detector uncertainty is yet accounted for. First, a Monte Carlo (MC) method is desired to simulate CEνNS events, extracting its timing, incoming neutrino energy, and Xe atom recoil to obtain CCSN time evolution (equation (3.36)) and final spectrum (equation (3.34)) in terms of observables cS1 and cS2.

3.5.2 CCSN CEνNS simulation in dual-phase Xe TPC

The goal of this section is to simulate a significant number of CCSN neutrino bursts to obtain the response of LXe from the microphysics described in **Section 3.3.3**, leading to a characteristic cS2 and cS1 spectrum. After the evaluation of the potential detection thresholds, a rolling window is rolled over each simulated

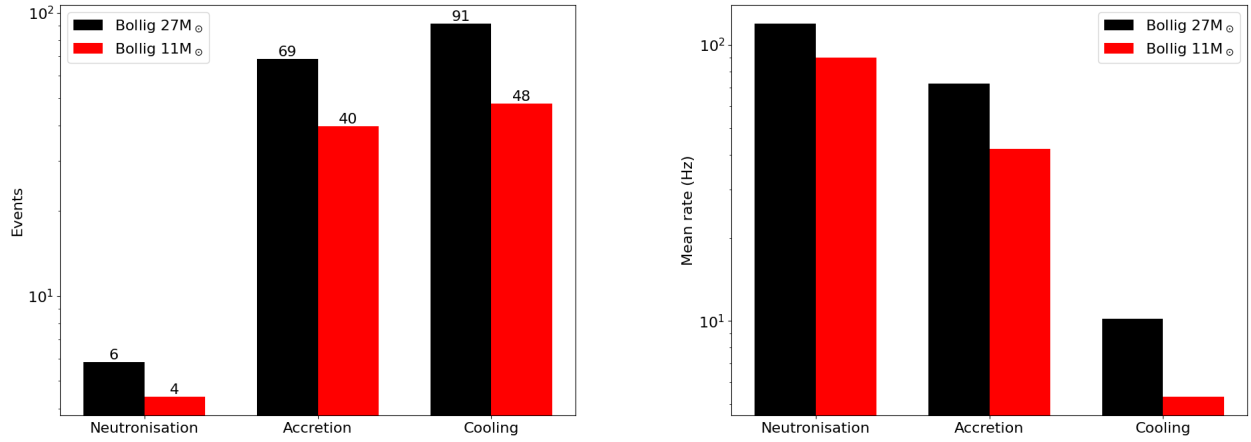

Figure 3.32: Number of events (left) and mean rates associated (right) for each CCSN burst phase at 10 kpc for the Bollig 27M$_\odot$ (black) and 11M$_\odot$ (red) progenitors.

CCSN, extracting the corresponding distribution of its maximum values. First, neutrino events require time and energy to be sampled. This can be done through a simple toy MC, using the recoil integrated time rate to obtain primarily event time (equation (3.36)). Secondly, sampled time can be inserted in the 2D CCSN recoil rate from equation (3.37) to extract the recoil energy. Finally, the neutrino energy can also be recovered, differencing again the following equation:

$$\eta(E_\nu, t, E_R) = \sum_i N_{Xe_i}(f_i) \frac{1}{4\pi d^2} \frac{dN}{dE_\nu dt} \frac{d\sigma(E, E_R)}{dE_R} \tag{3.37}$$

To account for the CCSN neutrino flux uncertainties, the number of interactions is let to fluctuate according to a Poisson function, whose mean is the number of expected total interactions N_{th} for the integration of time differential spectra (3.32) with $t_1 = 0$ and $t_2 = 10$:

$$N_{SN_i} = P(\mu = N_{th}) \tag{3.38}$$

In this case, the applied threshold is $E_{th} = 0$.

This toy MC will be important to describe the expected range of the final detected spectrum and a threshold in terms of neutrino energy for CEνNS detection. The MC neutrino energy simulated spectrum and isotope distribution are illustrated in **figure 3.34**.

3.5.2.1 CEνNS CCSN S1 and S2 distributions

The modelization of the NR recoils leading to the observables S1 (cS1) and S2 (cs2) from NEST includes specific parameters for the XENONnT detector, such as its geometry, drift, and extraction field values, as well as experimental parameters, measured from the science run 0 (SR0), such as the electron lifetime (τ_e=15 ms). The final value influences the quantity of electrons that eventually reach the gas phase and

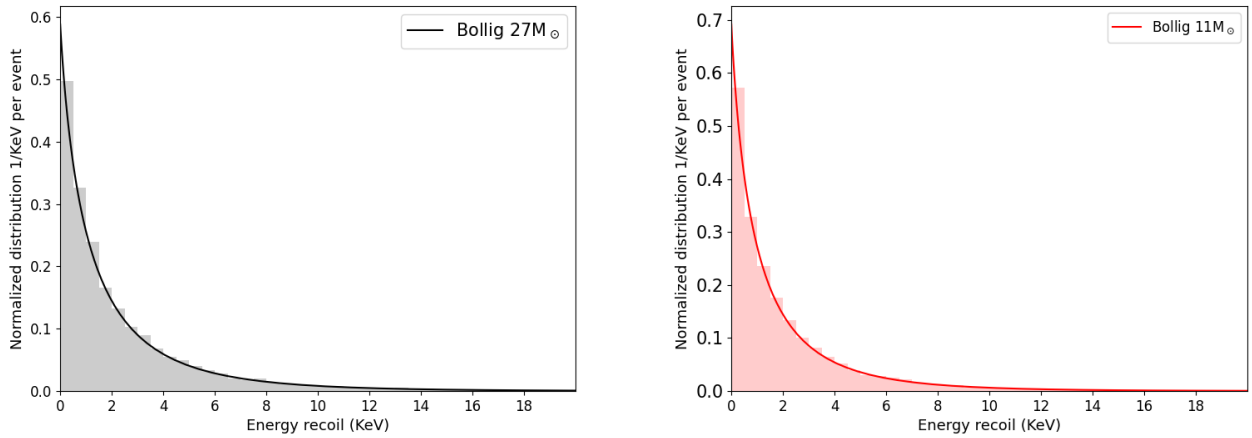

Figure 3.33: Normalized MC toy simulated recoil energy spectra. Recoil energy spectra per keV per simulated event, for the same models used for **figure 3.29** at 10 kpc. Solid lines correspond to their respective expected recoil spectra, described in equation (3.34).

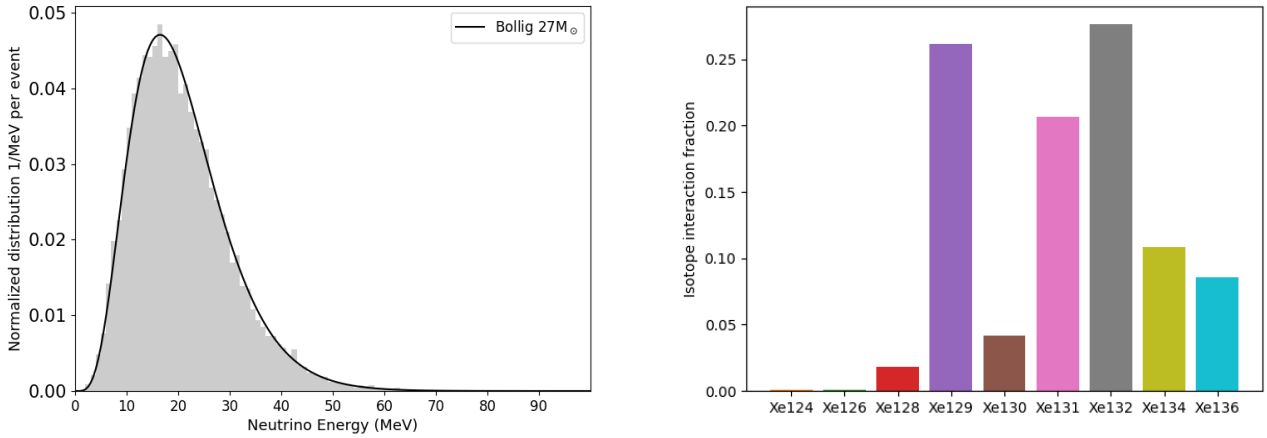

Figure 3.34: **Left.** Toy MC neutrino energy spectrum for the same models used for **figure 3.29** at 10 kpc. **Right.** Fraction of toy MC CEνNS interactions in each isotope present in LXe (see **table 3.20)**

is directly dependent on the level of LXe purity, which was highly increased by XENONnT compared to XENON1T. **Table 3.2** summarizes additional simulation inputs and SR0 settings used in this study. Some of these settings were already explained in **Section 3.3**. The reader can find the file with detector geometry, sensitive detector volume parameters, and the rest of the simulation inputs in reference [386].

Gas E.field [keV/cm]	Drift field [eV/cm]	e^- lifetime [ms]	Drift time max [ms]	g_1	g_1(gas)	g2	$S2_{th}$ [PE]	LXe dens. [g/cm^3]
6.8903	23	15	2.14	0.1252	0.1533	13.705	40	2.881

Table 3.2: Relevant parameters for the XENONnT SR0 NEST simulation

Another parameter in NEST simulation is the maximum drift time, which constrains the pairing of S1 and S2 signals to form what the XENONnT data structure refers to as an "event". To be more precise, in the XENONnT data structure jargon, "event" refers to a level of study of the signal which includes ionization and scintillation, used to reconstruct interaction parameters such as 3D position, energy of the recoil and type of the recoil (ER or NR). **Figure 3.35** depicts a time reconstruction scheme for a NR combining S1 and S2, highlighting the maximum drift-time. The PMT distribution in the top PMT array of the S2 signal reconstructs the position of the interaction in the horizontal plane of the TPC cylinder (x, y). The time between the S1 and the S2 is used to determine the z position.

The XENONnT data structure has several subcategories of "event". A complete discussion of this structure, is available with the STRAXEN plugin detailed in reference [387]. In this work, the TPC signal analysis is intended to be preliminary, and the NEST output time for each photon arriving to a PMT will be used to calculate some cut parameters for background rejection, but not to reprocess the full chain from these photon hits to generate events. However, only the S2 signal from this S1 and S2 pair will be used in this study. This decision stems from the fact that the S2 signal enhances detection efficiency as a function of recoil energy, allowing for a lower threshold than with the S1 signal. In XENONnT data processing, the S2 signal is the sum of many peaks. These S2-peaks are merged following the signal processing within a temporal window of no more than $50\mu s$. Merged peaks make up the final S2 peak signal. The final paired S2 peaks correspond to the value produced from the NEST simulation of the S2, whose distribution will be shown in this section. It is worth noting that the S2 peaks width is bound by the maximum (2.2 ms) and minimum (0.2132 ms) drift times.

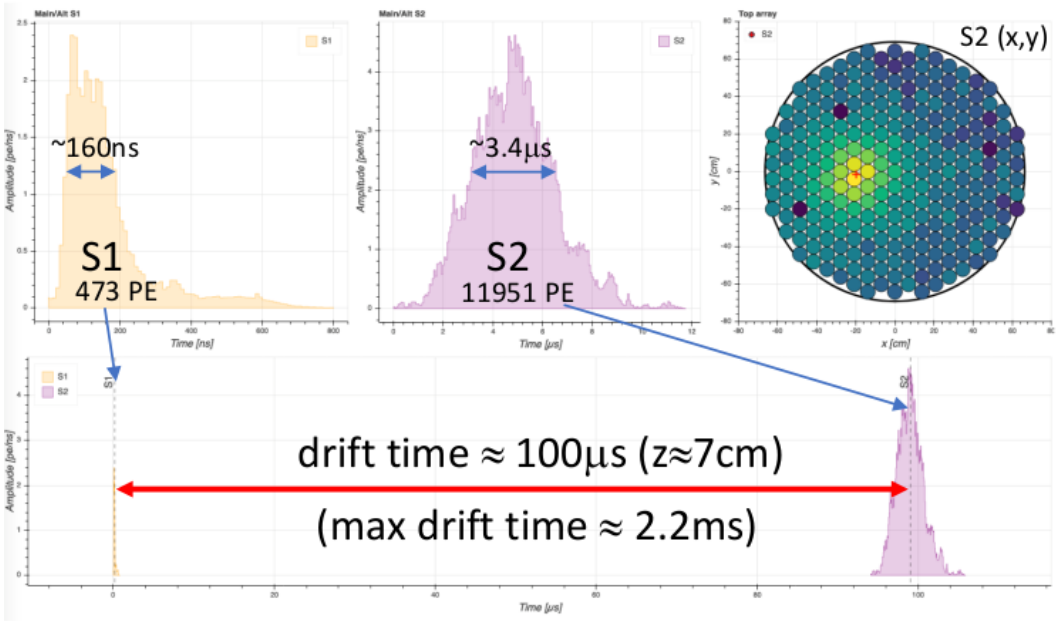

Figure 3.35: Schéma of the Z and XY position reconstruction combinining S1 and S2 signals from a random NR event in the TPC

By looking deeper at the XENONnT data structure, it is important to distinguish between the three levels of recorded signals in the TPC: "hits", "peaks" and "events", where "hits" corresponds to the lowest and "events" to the highest level of reconstruction. The first are the "PMThits" specified in **Section 3.3.4** that survive the pre-trigger conditions associated with the "record" level from the trigger-less "raw" level. These two levels correspond to the two first bubbles (orange and red) depicted in the data structure schema of **figure 3.36**. Data acquisition (DAQ) is triggerless, with the raw data ("raw_records") for the three detectors: TPC, Muon, and Neutron Vetoes. After an offline trigger selection, new "hits" are time-clustered into "peaklets". Some of them are considered "lone hits" because they are not part of a peaklet. Peaklets are classified as S1, S2, or "unknown" based on their shape and the distribution of hits in the top and bottom PMT arrays. The differentiation between S1 and S2 is based on recognizing the peaklets after applying trigger conditions. The "peaklet" S1 trigger serves primarily to prevent the inclusion of accidental coincidences from dark noise and S2 signals from single electrons. All remaining "peaklets" that are not classed as S1 and have hits from at least four different PMTs are classified as S2. The NEST simulation used for this work incorporates both conditions. Finally, "S2 peaklets" are merged, obtaining a large width S2 peak. In principle, the S1 peak is excluded from its process or merging. However, the "S1 peak" trigger requires three different PMTs, contributing to a tight coincidence time window between hits of 50 ns related to the center of the integrated waveform of the peak.

A higher data level of peaks (events) is obtained once peaks are built and classified as S1 or S2. Position reconstruction in 3D is possible, allowing for geometric corrections according to cS1 and cS2. S1 and S2 pairs produce an event if an S2 peak has an area of at least 100 PE (although this study reduces this criterion to 40 PE) and a maximum of eight competing nearby peaks with 50% of the triggering peak area in a ±10 ms window. The event window spans the interval [-2450 μs, 250 μs] from the triggering S2 peak. During this time frame, the principal pair of S1 and S2 within the event is determined. At this step in the processing, an alternative S1-S2 pair is recorded. This is critical for identifying multi-scatter occurrences caused mostly by neutron scattering.

This work focuses on the CEνNS analysis at the "event" level, without requiring any condition on the S1 signal. An analysis at the "peak level" will require more sophisticated background cuts to evaluate the sensitivity on detecting CCSN neutrinos. The NEST simulation simply extracts the main S1 and S2 pairs with the described trigger conditions. However, it also extracts hit times that contribute to the S2 signal and can be identified using a clustering algorithm, applying the mentioned trigger conditions. This time information is provided to obtain specific properties about the S2 signal crucial for background cuts, which will be detailed in **Section 3.5.3**. One of these properties is the center time, that can be defined as the mean time regarding all the photon PMT hits weighted by the PMThit area, relative to the first hit is recorded time t_0:

$$S2_{cc} = \frac{1}{\sum_i^{N_{hits}} AreaPE_{Hit_i}} \sum_i^{N_{hits}} (t_{Hit_i} - t_0) \times AreaPE_{Hit_i}. \tag{3.39}$$

This value, when combined with the interaction time and the S2 peak width, can be used to evaluate

the potential impact of the event pile up, which can be significant due to the large width of the S2 signal and the high frequency of the CEνNS CCSN interaction rate, particularly during the neutronization phase.

Finally, the interaction position is not explicitly extracted in the current simulation because the interactions of CCSN neutrinos are predicted to be homogeneously distributed across the TPC volume. Nonetheless, these location parameters must be considered and accounted for in NEST in order to produce corrected cS1 and cS2. The latter are the consequence of a gaussian smearing assuming a spatially uniform electric field, which is not exactly the case, as described in **Section 3.3.4**, and some deviations are predicted from the XENONnT data peak building. These differences also significantly affect S1 corrections, which are done using ^{83m}Kr calibration data to map the detector response. The individual PMT channel information is not recovered; it is simply the integral number of "PMThits" for each S1 and S2 signal. The quantum efficiency (QE) and the light collection efficiency (LCE) are applied based on the position of the simulated interaction, which, as mentioned, is sampled uniformly in the LXe cylinder volume. The LCE is based on the GEANT4 simulation results. The MC part handled by NEST includes

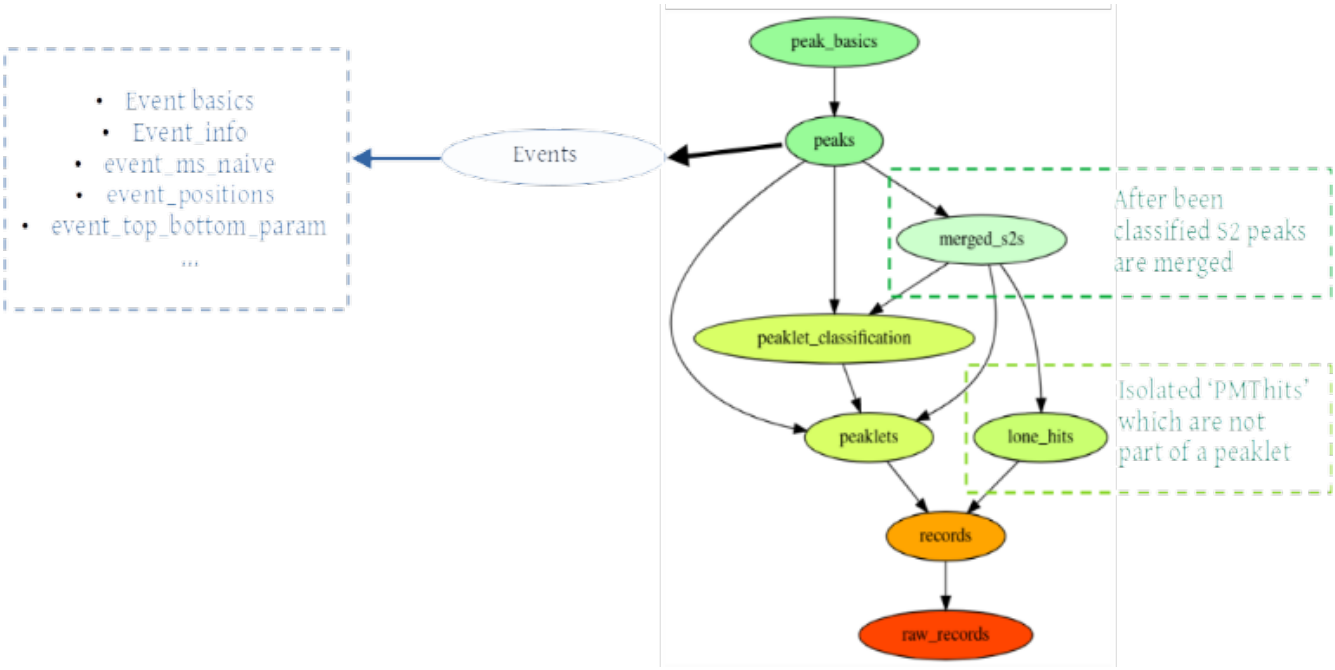

Figure 3.36: Schema of the data structure from the STRAXEN software. Raw data are on the bottom, named "raw_records", corresponding to the lowest level of the XENONnT data structure. The reconstruction chain follows the arrows up to the highest level ("events").

the microphysics described in **Section 3.3.3**, adding the mentioned S1 peak trigger conditions, S2 peak threshold, and geometry to obtain the corrected cS1 and cS2 signals, which are enough for the purpose of evaluating the signal at the event level in the S2-only scenario.

Because the primary goal of this work is to understand the potential response of the detector when a CCSN signal is observed and forecast its eventual uncertainty, each of the 100 CCSN toy MC simulations is also simulated into NEST 100 times to increase their statistics. The CEνNS findings for the 100 $\times$ 100

simulations of the chosen progenitors combining toy MC and NEST may now be reported in terms of the S1 and S2 observables. **Figure 3.37** depicts the total S1 and S2 distributions, with corrected signals shown in a dotted line. It is clear that the modifications applied to the S2 signal have a considerable impact on the S2 distribution, hence increasing the signal width. The GARFIELD software handles electron drift and extraction, taking into account electric field fluctuations in both processes. Electric drift field fluctuations result in substantially lower deviations in S1 LCE when compared to the corrections performed on S2. For the latter, the extraction efficiency at the liquid gas interface is more impacted by electric field variations and the presence of the wires compounding the extraction field (see **Section 3.3.4** for more details).

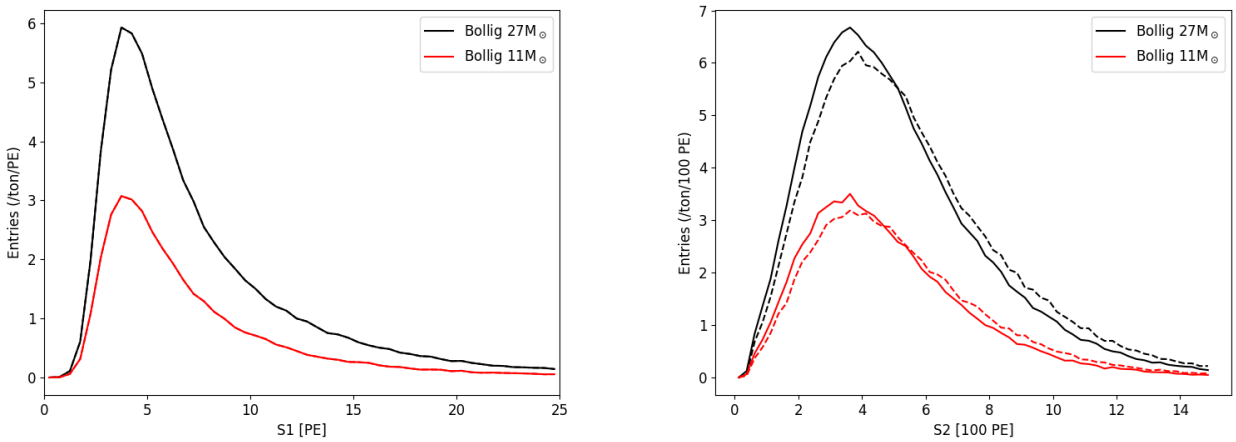

Figure 3.37: S1 (left) and S2 (right) distributions obtained from NEST using XENONnT SR0 detector for the *Bollig 2016* Model 11 $M_\odot$ (red) and 27 $M_\odot$ (black) progenitors at 10 kpc. In dashed lines, the corresponding corrected cS1 (which are not significant) and cS2 are also represented.

Table 3.3 summarizes the mean values of these distributions. In addition, the fraction of surviving S1 and S2 peaks after the trigger conditions and thresholds are shown, as well as the ROI. The S1 signal looks to be ten times less than S2 and has a poor survival fraction, indicating that the investigation should focus solely on the S2 peak, which is also likely to lower the energy threshold. In this regard, no threshold for S1 peaks will be required. **Figure 3.38** shows the correlation between cS1 and cS2 signals for two distinct progenitors at 10 kpc. As a result, an ROI can be created to include both progenitors at this distance. For S2 peaks, the signal is expected to occur in the interval $S2_{th} = [40\ ,\ 1500]$ PE.

Progenitor	$\langle S1^* \rangle$	$\langle cS1^* \rangle$	$\langle S2^* \rangle$	$\langle cS2^* \rangle$	$f_{S1_{sur}}$	$f_{S2_{sur}}$	S1 ROI	S2 ROI
$27M_\odot$	8.23 PE	8.23 PE	294.3 PE	318 PE	0.23	0.70	[2,25]	[40,1500]
$11M_\odot$	7.58 PE	7.58 PE	270 PE	292 PE	0.20	0.67	[2,20]	[40,1400]

Table 3.3: Results of toy MC + NEST simulations for 100 ($\times$ 100) CCSN of two different progenitors from Bollig Model at 10 kpc. Only S1 $\geq$ 0 or S2 $\geq$ 40 are accounted for to calculate the mean for each model, as well as the corrected signals.

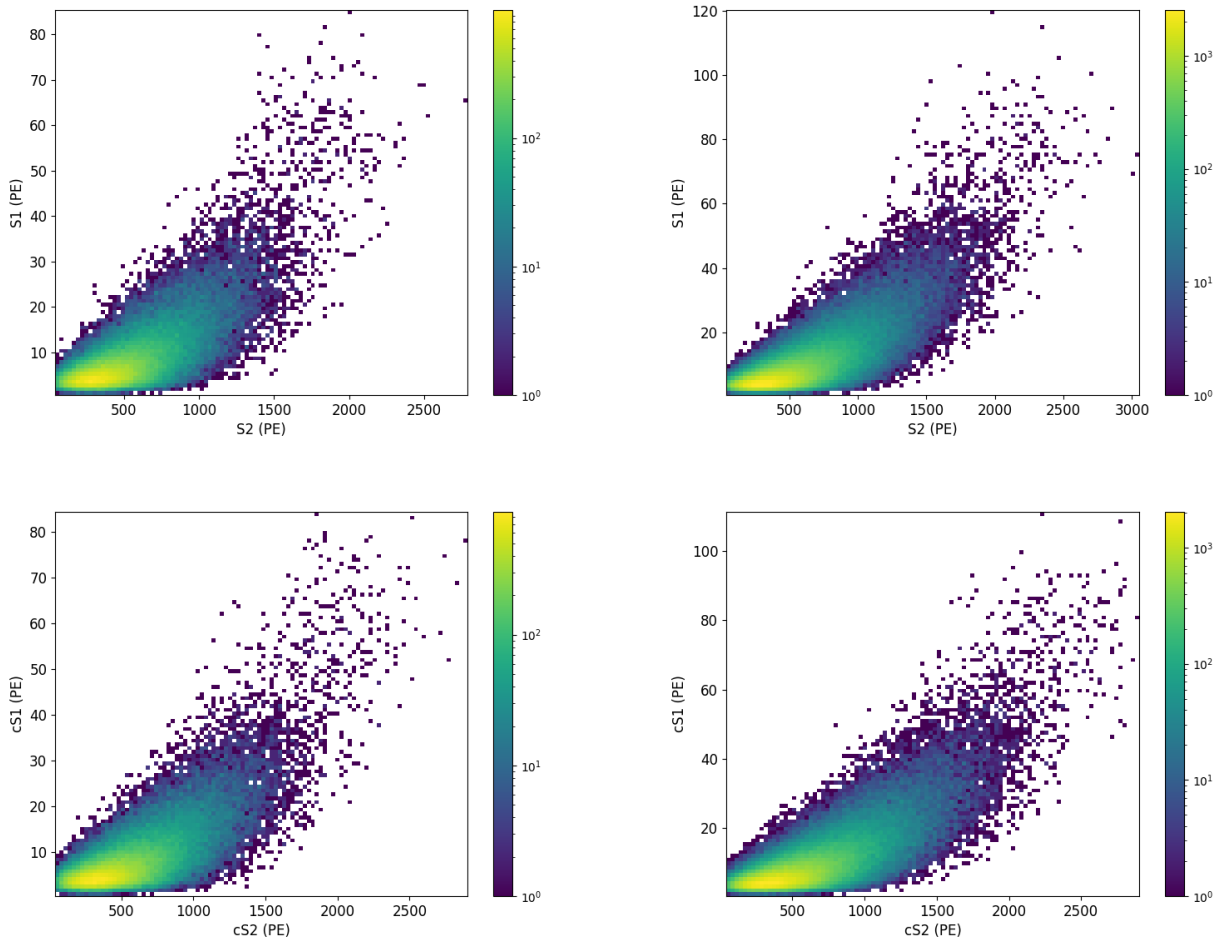

Figure 3.38: **Top**. S1 vs S2 area distributions obtained from NEST using XENONnT SR0 detector configuration for the *Bollig 2016* Model 11 $M_\odot$ (left) and 27 $M_\odot$ (right) progenitors at 10 kpc. **Bottom**. The corresponding corrected cS1 vs cS2 distributions for the same progenitors.

The main purpose of this CEνNS CCSN study is to obtain the detection efficiency for the signal as a function of the recoil energy. This detection efficiency can be defined only in terms of S2 peaks, as the fraction between the number of S2 peaks in a given recoil energy bin above the selected S2 threshold $S2_{th}$:

$$\epsilon_{S2_{th}}(E_R) = \frac{N(S2 \geq S2_{th}|E_R)}{N(E_R)}. \tag{3.40}$$

The latter value can be calculated using NEST for the described XENONnT SR0 detector parameters. The blue solid line in **figure 3.39** represents the former, utilizing only the S2 peaks (not requiring either S1>0 PE) and a threshold $S2_{th}$ of 40 PE. This is similar to assuming that the recoil energy threshold of 0.5 keV does not provide a null signal, although with a detection efficiency ∼50%, which appears quite optimistic. A more realistic S2 threshold can be 100 PE, which is comparable to the same detection efficiency, but for 1 keV energy threshold. The resulting differential rate from the convolution of the CEνNS cross-section with the arriving neutrino flux now include the detection efficiency. The result is

a recoil energy function that can be used to determine the number of events for a specific threshold, as follows:

$$N_{S2_{th}} = \sum_{\nu_\beta}^{\nu_e,\bar{\nu}_e,\nu_x} \int_{E_{th}} \frac{dN}{dE_R} \epsilon_{S2_{th}}(E_R) dE_R \tag{3.41}$$

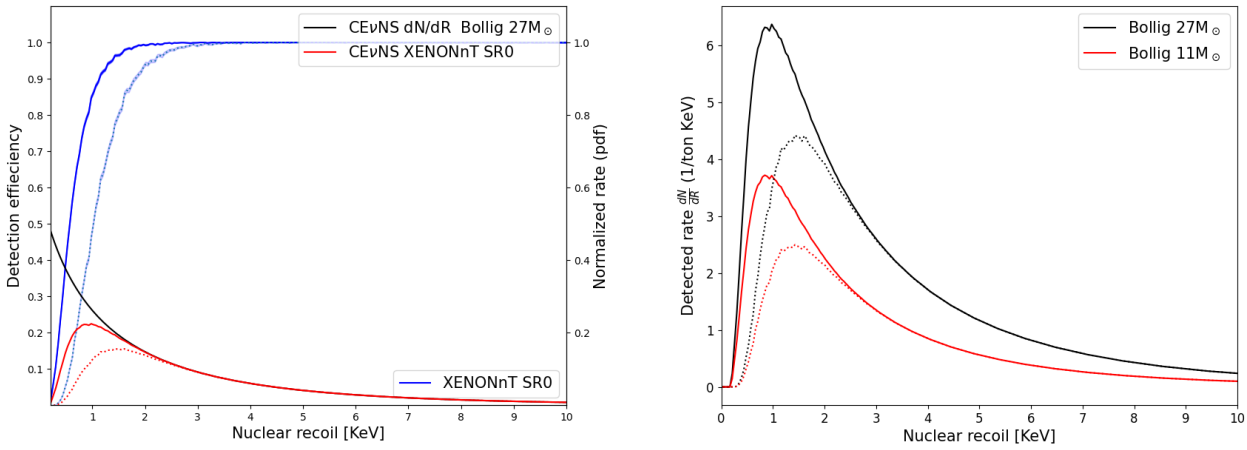

Figure 3.39: **Left**. Detection efficiencies for CEνNS CCSN S2 signal as a function of the nuclear recoil energy. In blue, the detection efficiency obtained from NEST. In black, the normalized CEνNS recoil spectra from *Bollig 2016* Model of 27M$_\odot$ progenitor. In red dashed line, the convolution between detection efficiency and the CEνNS recoil spectra. These results are constrained by the S2$_{th}$ of 40 PE. Bayesian errors are accounted for in the width of the blue line calculated as in the reference [388]. **Right**. Convolution of the detection efficiency defined in equation (3.40) and differential recoil rate spectrum (equation (3.34)) for the two different progenitors. Solid and dashed lines represent the $S2_{th}$=40PE and $S2_{th}$=100PE.

Finally, the resulting expected number of S2 peaks for a CCSN CEνNS signal are presented in **table 3.4**. This result clearly illustrates the difficulty of observing low NR events <2 keV, where most of the CCSN CEνNS interactions are expected to happen. Maximum detection efficiency is attempted around $\sim$ 1 keV for S2$_{th}$=40 PE and around 3 keV for S2$_{th}$=100 PE. However, the number of observed events is considerably reduced to $\sim$ 40% of expected interactions, and it can be deduced that XENONnT may be more sensitive to the high-energy part of the spectrum. The detector uncertainties on the neutrino energy spectrum rate can be extracted with the MC-TOY results, injecting energy recoil efficiency in the integration of the differential neutrino energy flux of expression (3.37):

$$\frac{dN}{dE_\nu}_{S2_{th}} = \int \int_{E_{R_{th}}} \epsilon_{S2_{th}}(E_R) \eta(E_\nu, t, E_R) dt dE_R. \tag{3.42}$$

Figure 3.40 depicts the detected neutrino energy spectrum for the two S2 thresholds (right panel), as well as the detection efficiency as a function of the CCSN neutrino energy. Unlike large Cerenkov water detectors, XENONnT has acceptable detection efficiencies ($\sim$ 25%) at 10 MeV. Furthermore, 70% and

Progenitor	Interactions/tonne E_{th}=0	Mean S2 peaks/tonne $S2_{th}$=40PE	Mean S2 peaks/tonne $S2_{th}$=100PE
$27M_{\odot}$	28.3	19.23	15.61
$11M_{\odot}$	15.6	10.18	8.06

Table 3.4: Expected number of S1 and S2 peaks for two different S2 thresholds of 40 PE and 100 PE. The mean number of expected S2 peaks/tonne is calculated following the equation (3.41).

60% efficiency are achieved around CCSN neutrino mean energy ($\sim$ 16 MeV) for the $S2_{th}$ of 100 and 40 PE, respectively. The shape of the visible neutrino differential rate in the right panel suggests a detection threshold of 5-6 MeV, which is much lower than that of large Water Cerenkov detectors and huge LAr TPCs, $\mathcal{O}$(15 MeV).

These are the results from the generated TPC recoils, which lead to estimations of detection efficiency as a function of recoil energy and incoming neutrino energies. The formers predict the ultimate number of expected S2-only events for a given threshold, as shown in **table 3.4**. In the section that follows, the rate evolution over time will be used to discriminate between signal and background.

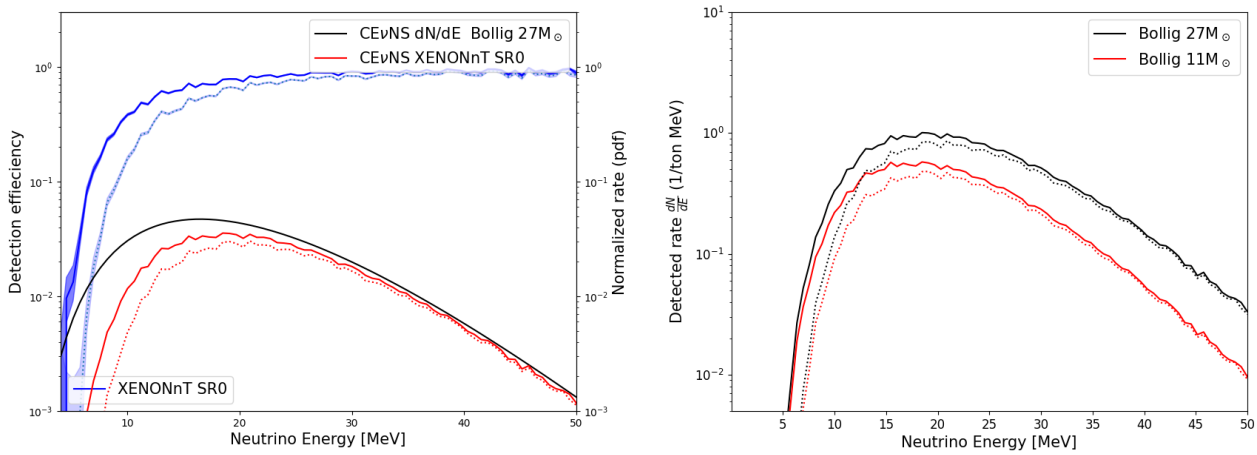

Figure 3.40: **Left**. Detection efficiencies for CEνNS CCSN S2 signal as a function of the incoming neutrino energy. In blue, the detection efficiency obtained from NEST. In black, the normalized CEνNS neutrino energy spectra from *Bollig 2016* Model of $27M_{\odot}$ progenitor. In red dashed line, the convolution between detection efficiency and the CEνNS energy spectra. These results are constrained by the $S2_{th}$ of 40 PE. Bayesian errors are accounted for in the width of the blue line. **Right**. Convolution of the detection efficiency and differential neutrino energy rate spectrum presented in equation (3.42) for the two different progenitors. Solid and dashed lines represent the $S2_{th}$=40PE and $S2_{th}$=100PE.

3.5.3 CCSN TPC Background

The S2/S1 ratio cannot be used to distinguish between CEνNS NR and the ER background in an S2-only study. The peculiar time evolution of the CCSN signal can be employed for this purpose, as the ROI background is predicted to behave differently, preferably as a Poissonian signal or, at the very least, as a compound of numerous Poissonian functions, implying time periodicity. Using a rolling window can accentuate the unique form of the CCSN CEνNS temporal evolution. This involves counting back from the time the number of events recorded in a specific time step of each observed event, e.g. over one second. **Figure 3.31** depicts the rolling window rate evolution in a time step of 1 second from the stated toy MC of 100 CCSN simulations of the 11 $M_\odot$ and 27 $M_\odot$ CCSN progenitors at 10 kpc. The narrow red line is the median of these values, more representative of the central point than the mean due to the presence of outsider points that are not mitigated by a high statistical context, as only 100 CCSN are simulated. In this situation, the bands represent the mean absolute deviation (MAD) [4]. These bands serve merely to evaluate the dispersion of each point. Similar orders of magnitude $\mathcal{O}$(10 Hz) of accretion mean rates are found, with a peak around $\sim$ 1s which indeed results from the neutronization plus accretion peaks, expected to produce together 44 and 75 interactions for 11 $M_\odot$ and 27 $M_\odot$ progenitors, respectively. This result can seem trivial as it does not include any detector uncertainty, but it illustrates how the rolling window maximizes the rate around the first second after the core bounce, when $\sim$45% of the interactions are expected to happen, exploiting the time evolution of CCSN flux.

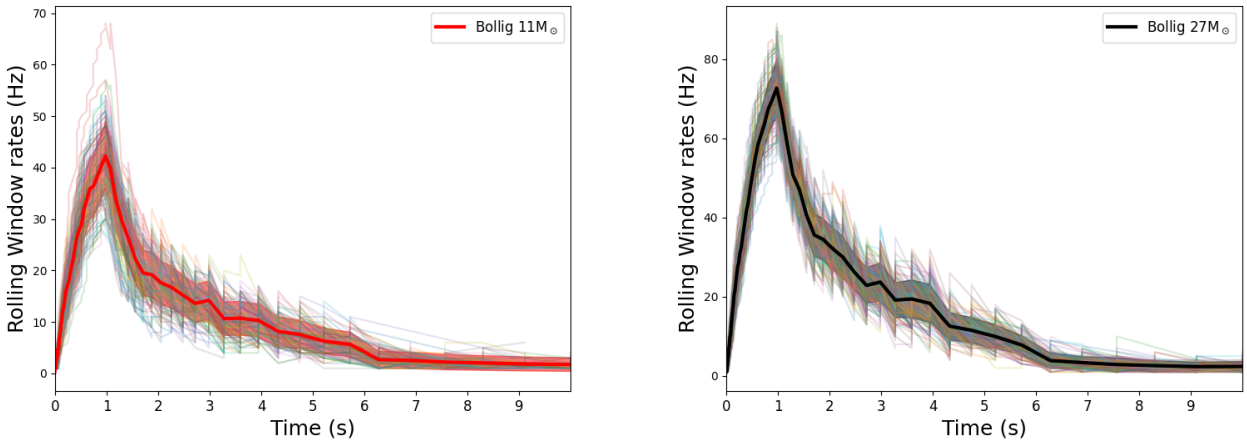

Figure 3.41: Rolling window rates using a 1 second step for 100 CCSN CEνNS interactions for 11 $M_\odot$ (left) and 27 $M_\odot$ (right). The narrow red line is the resulting median for the 100 CCSN, and the bands represent the standard deviation.

From these curves, the value of interest will be the maximum rate obtained for each simulation. As the rate of time evolution depends on the CCSN physics of collapse explained in **Chapter 2**, the maximum rate distribution will not be approximated by any parametric function. In this sense, each CCSN maximum

[4] MAD can estimate the dispersion of X values as $\sigma = \sqrt{\sum_i (X_i - m(X))^2}/\mathrm{N}$, where N is the number of values in a sample. The median is the central point of a random X sample.

rolling window will be used to calculate significance, instead of using a distribution of the later value. These maximum values, which can be deduced from **figure 3.41**, are illustrated in **figure 3.42**. The bands correspond to the MAD, and the median is drawn by the dot-dashed line. The last median value is very close to the mentioned mean rate in the first second from the neutronization and accretion expected interactions, with 73.92 Hz and 42.14 Hz maximum rates for the 27 $M_\odot$ and 11 $M_\odot$ progenitors respectively. This emphasizes the contribution of these two phases to the high rate of the CCSN signal. Notice that differences between the mean rates and the maximum rolling window rates in the first second are justified by the Poissonian uncertainty in the number of interactions used in the toy MC, whose dispersion cannot be attenuated due to the low number of simulated CCSN.

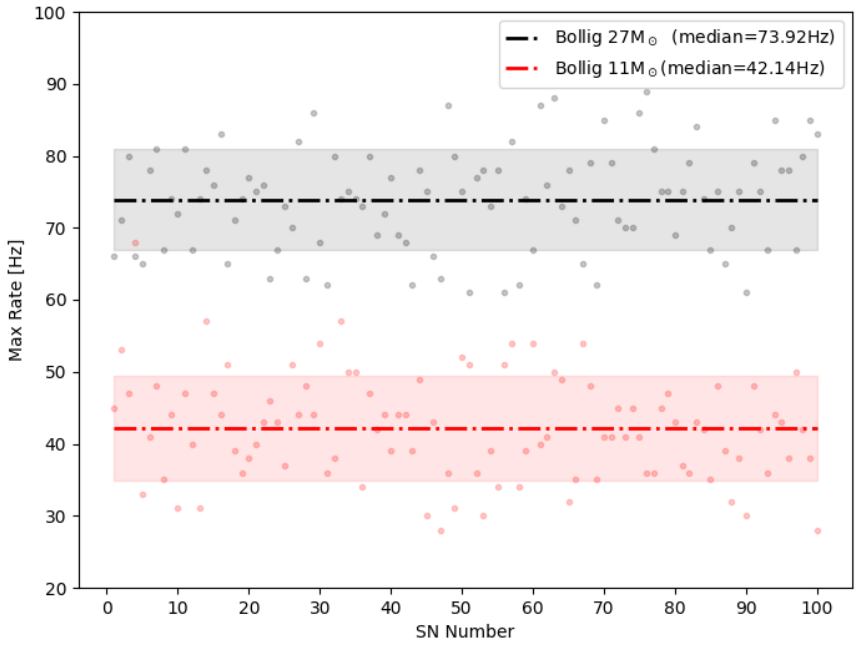

Figure 3.42: Maximum rolling windows rate for each CCSN toy MC simulated for a time step of 1 second, for the two progenitors 27 $M_\odot$ (black) and 11$M_\odot$ (red) at 10 kpc. The median is represented by the dot-dashed lines and the bands corresponds to the MAD.

The same exercise of rolling a window has been done for the SR1 background, looking into the "event info" data applying same selection criteria than the simulation. In the ROI, at the event level, background rates are expected to be low. **Figure 3.43** illustrates more than six minutes of the selected SR1 background, from a total of 40 days of data taking, divided in 10 seconds independent bins in which a rolling window of 1 second step is rolled. Independent bins are required to avoid the correlation between the data, as the final goal is to extract a distribution of the maximum rate in these 10 seconds bins. The first thing that is worth noticing is that the background is not affected by the two selected thresholds, contrarily to the NR detection efficiency. In this short period of a few minutes, the background rolling

rates fluctuate between 2 and 1 event for each second step. Another aspect that can be noticed is that at least one event of the background survives in each rolling window, which gives statistical uniformity to the further distribution.

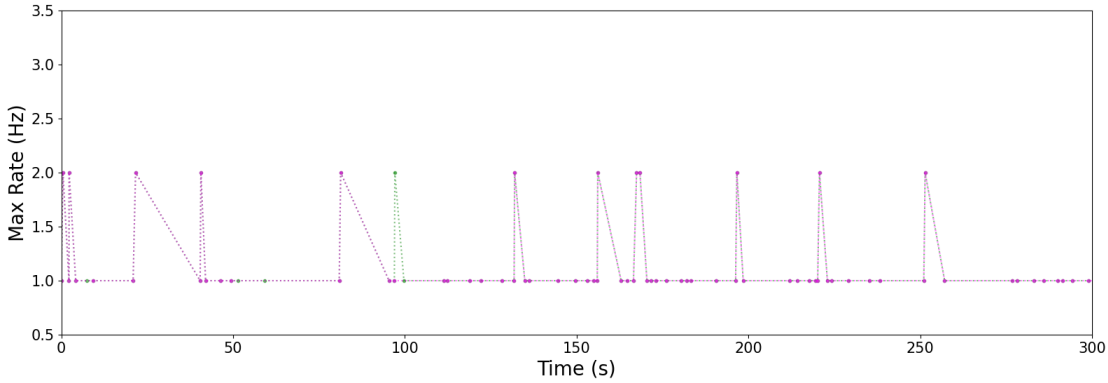

Figure 3.43: Rolling window rates in a 1 second step for the 10 seconds bins in 5 minutes representatives of the SR1 background runs. In green, a $S2_{th}$=40 PE is required, and the magenta points correspond to $S2_{th}$=100 PE.

Background and CCSN signal are expected to behave differently in time. Rolling window and mean rates for the background are anticipated to be similar if the background is stable. However, some fluctuations can appear, enhancing the maximum rolling window rate resulting in similar values to the CCSN signal. After applying the threshold for a 5.9 tons of LXe for the latter, the mean rates become 11 (6) Hz and 9.4 (4.8) Hz for the respective 40 and 100 PE threshold and the 27 (11) $M_{\odot}$ progenitors regarding values of **table 3.4**. These values imply that the mean is expected to be 5 times lower than the maximum rates (see **figure 3.42**). **Figure 3.44** illustrates the mean distribution rates and their distribution approximated through a Gaussian, as a *Poissonian-like* background is expected to dominate the ROI, composed mainly by accidental coincidences and single electron signals. Only the $S2_{th}$=40 PE will be shown, as no significant differences from between $S2_{th}$=100 PE are found (see **figure 3.43**). The same proportion of CCSN signal results from the mean and maximum rolling window rates in the SR1 background ROI. However, the shape of the CCSN is completely different, as the maximum rates happen in the first second and are softly decaying until the end of the burst. The tentative to approximate the mean and the maximum rates through a Gaussian and a skewed Gaussian (3.43) respectively, are presented to show the different shape of both and to account for the fluctuations in background through this distributions. No statistical test values are shown, as they are not relevant for the goal to establish an approximate background model. Additionally, the character of the rolling window produces a number of events in 1 step of time, i.e. an integer leading to a few points when values are distributed, which is a challenge for fitting purposes.

In order to improve the reduction of the background rate, cuts in the ROI can be applied, not presenting a significant reduction in the signal rate. The NEST simulation outputs constrains cut parameters, but some of them are sufficiently representative of the CCSN signal. Three parameters will be used: the fraction of the S2 area in the top PMT array, the time width of the 50% S2 peak area, and the time width for the

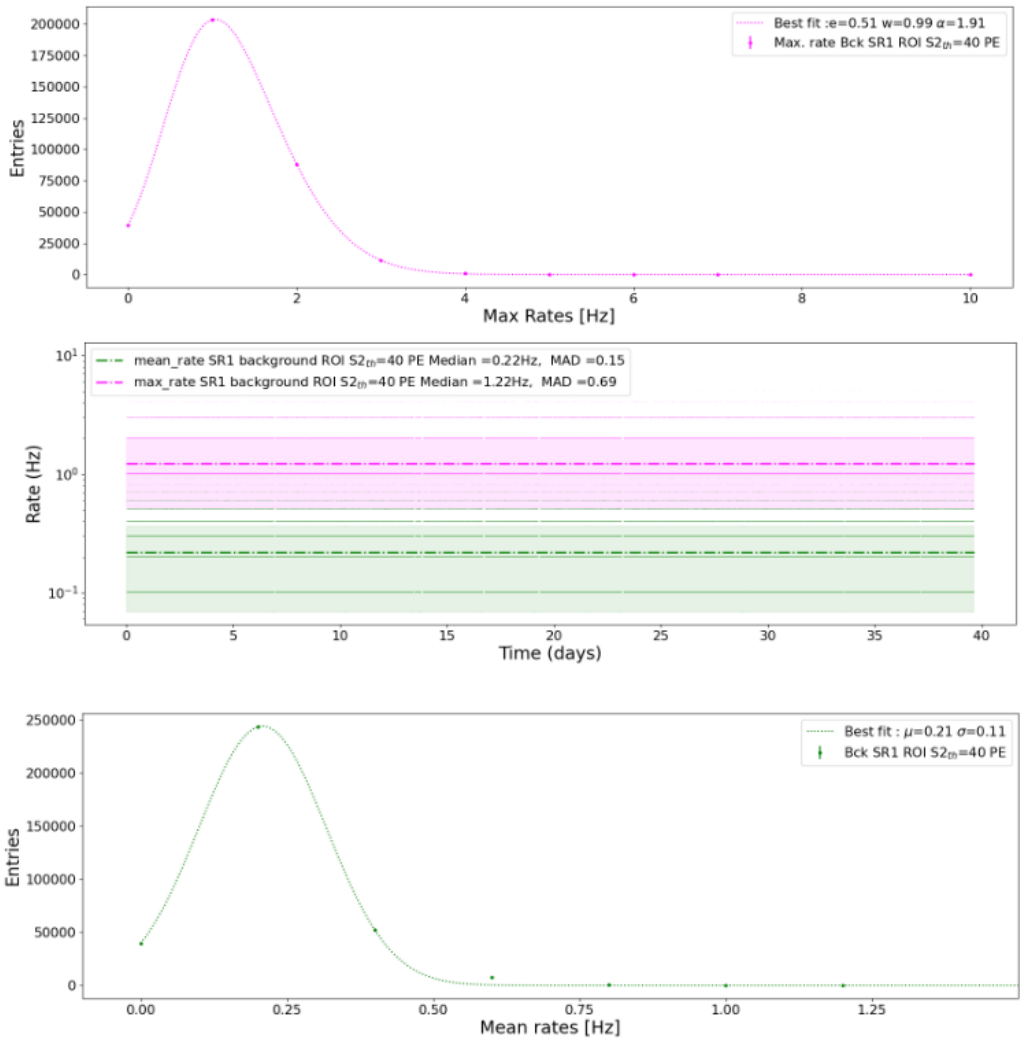

Figure 3.44: Distribution of the mean (green) and maximum (magenta) rates in 10 seconds independent bins of the SR1 background in the ROI for $S2_{th}$=100 PE. On the top, the approximated max rate distributions to a skewed Gaussian. On the bottom approximation of the mean rate distribution with a gaussian. Statistic test value is not indicated as they are not relevant for the analysis.

corresponding 90% of this area. The first parameter, related to the top fraction contributing to the S2 area, is expected to be higher from a NR recoil S2 peak than for the background. Accidental coincidences, wall events and lone hits are expected to present smaller fractions of the top array contribution. This discrimination is shown in **figure 3.45** left panel. It can be noticed that the top fraction of CEνNS signal to the S2 area is not less than 50%, and it is stretched when a 100 PE threshold is imposed. The mean fraction can be approximated around 75%. In the right panel, the center time distributions are illustrated, from the CEνNS calculated following the equation (3.39).

The extraction of these values from the simulation output is done at a hit level: PE and arriving

time to the PMTs for each hit is a part of the NEST output. A clustering algorithm, DBSCAN[5], is used to recognize the main peak identified in a window of 50 ms, as the XENONnT processing requires. In addition, at least 20 neighboring hits in this time window are imposed to determine the cluster center hit (this number is adapted to the 40 PE threshold required for the S2 peak). To discriminate the main peak from other alternative peaks, the S2 area of the main event is ultimately compared to that obtained from the clustered peak, with a precision of 1%. Results of this matching are shown in **figure C.2** of the **Appendix C.2.1**. On the other hand, the other two parameter, the S2 50% and 90% time width, are

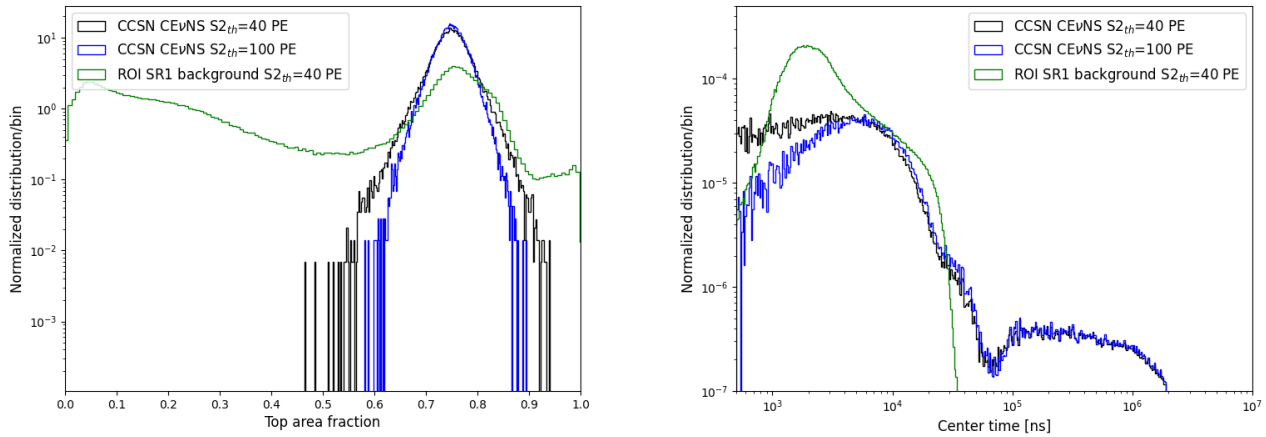

Figure 3.45: **Left.** Top PMT array area S2 fraction for the CEνNS of S2$_{th}$ 40 PE (black) and 100 PE (blue) and the SR1 ROI background for a S2$_{th}$ = 40 PE (green). **Right.** Center time distributions for the same CEνNS simulation and SR1 data than left panel. The center time is calculated following the equation (3.39)

related to the time of the peak to reach the 50% and the 90% of the total S2 area respectively, starting to count from the first hit time contributing to the peak. A cumulative function for the area and the hit time can be used to calculate this when the required percentage is reached. **Figure 3.46** illustrates the distributions for these two parameters using the CEνNS simulation results, compared to the SR1 background distributions in the ROI. A clear discrimination can be noticed between the signal and the background regarding the S2 50% time width. The background presents smaller widths around 2000 ns, while the signal present a more flatten distribution with a mean value around 8000 ns. Regarding the results of the S2 90% signal and background competed in the region $<$ 8000 ns, and losses in the signal acceptance are expected if cuts are applied to this parameter.

Regarding these distributions, cuts can be applied to enhance the signal relative to the background. Implications of these cuts in terms of acceptance of the signal and background after their application are summarized in **table 3.5**. Conservative cuts regarding signal are applied, however S2 top fraction is very efficient, cutting around 50% of the background. In addition, the S2 50% time width turns out also to be

[5]Density-based spatial clustering of applications with noise (DBSCAN), is used to cluster a group of correlated data based on the densitiy, mainly when a noise is present. The latter algorithm can also be used if the time window of the cluster-group is known. More details can be found in reference [389]

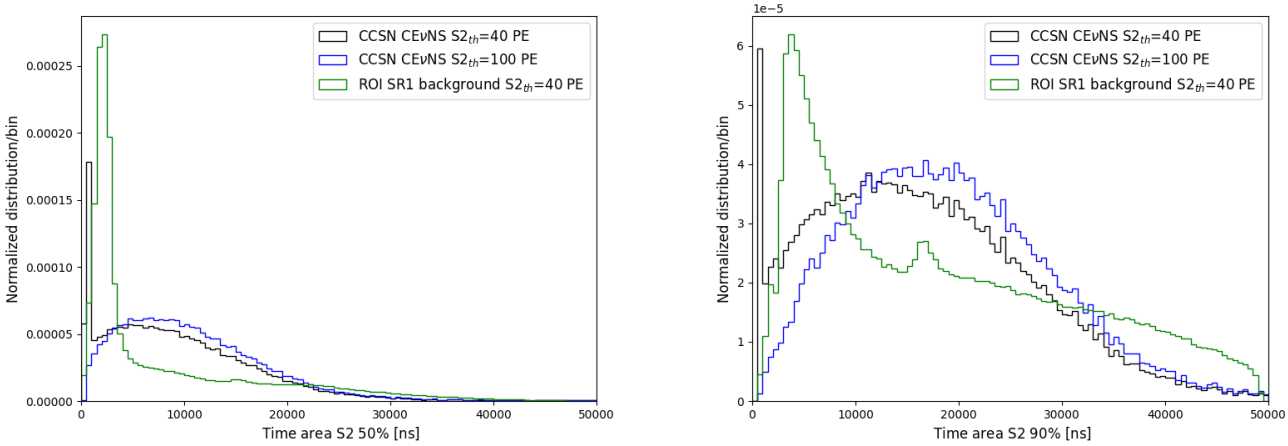

Figure 3.46: **Left.** Time range of the 50% of S2 area for the for the CEνNS of S2$_{th}$ 40 PE(black) and 100 PE (blue) and the SR1 ROI background for a S2$_{th}$ = 40 PE (green). **Right.**Time range of the 90% of S2 area for the same simulation and data as the left panel.

effective when a S2$_{th}$=100 PE is required. Finally, the S2 90% is not effective when S2$_{th}$=40 PE is chosen and not significant for the S2$_{th}$=100 PE, while presenting signal acceptances losses in both cases. Note that the presented acceptances are the result when a S2$_{th}$ is applied and normalized using this threshold. Regarding the results of this table for the S2$_{th}$=40 PE case, only the S2 top fraction may be applied, leading to maintain the signal acceptance and reducing the background in 48.7%. On the contrary, for the S2$_{th}$=100 PE results, the S2 area 50% can be added to the S2 top fraction cut achieving a signal acceptance of 89% and a background acceptance of 43.3%. However, the last acceptance is not enough to compensate for the decrease of the number of expected interactions applying the S2$_{th}$=100 PE. Therefore, it will be convenient to focus on the S2$_{th}$=40 PE case, and study the significance before and after applying the cuts, which will be the purpose of the next section.

Parameter	Cut range	CEνNS S2$_{th}$=40PE	SR1 bck. S2$_{th}$=40PE	CEνNS S2$_{th}$=100PE	SR1 bck. S2$_{th}$=100PE
S2 top fraction	[0.5,1]	0.999	0.523	0.999	0.531
S2 area 50% width	[3000,50000]	0.778	0.551	0.891	0.554
S2 area 90% width	[8000,50000]	0.75	0.723	0.845	0.729

Table 3.5: Expected acceptances for CEνNS signal and background for the S2$_{th}$ of 40 and 100 PE. The column named "Cut range" presents the upper and lower bounds of the cut.

3.5.4 CCSN CEνNS Sensitivity Study

The NEST simulation results for the observed S2 peaks for a given S2$_{th}$ for each 100($\times$ 100) CCSN can be used to roll over a rolling window and derive the associated time evolution after applying the final cuts.

The purpose of this is to obtain the maximum rolling window rate for each of the 100 CCSN simulations using the median of the corresponding 100 NEST simulations for each one. The maximum rates of these curves will be utilized to distinguish background and a potential CCSN signal. To validate this hypothesis sensitivities based on the maximum rates of rolling window will be calculated. Furthermore, the significance of the mean rate in a 10 second window will be compared to the ones obtained with the maximum rates. After applying the cuts and the S2 thresholds to 40 and 100 PE in the 100(×100) CCSN simulations, the rolling windows over the two progenitors should show reduced rates. **Figure 3.47** shows the updated rate evolution for two distinct thresholds, indicating that the number of events surviving the cuts decreased. However, below one second, the maximum rolling window appears to be the same as before applying cuts. Remark that results showed in **figures 3.47** and **3.48** are finally related to the S2 area top fraction parameter for each threshold presented in **table 3.5**, not including the cut on the S2 area 50% width time for the $S2_{th}$=100 case. For simplicity, only the $27M_{\odot}$ results will be used to demonstrate the procedure, and as mentioned before the $S2_{th}$=40 PE case. In **figure 3.48** each cluster of points is associated to a

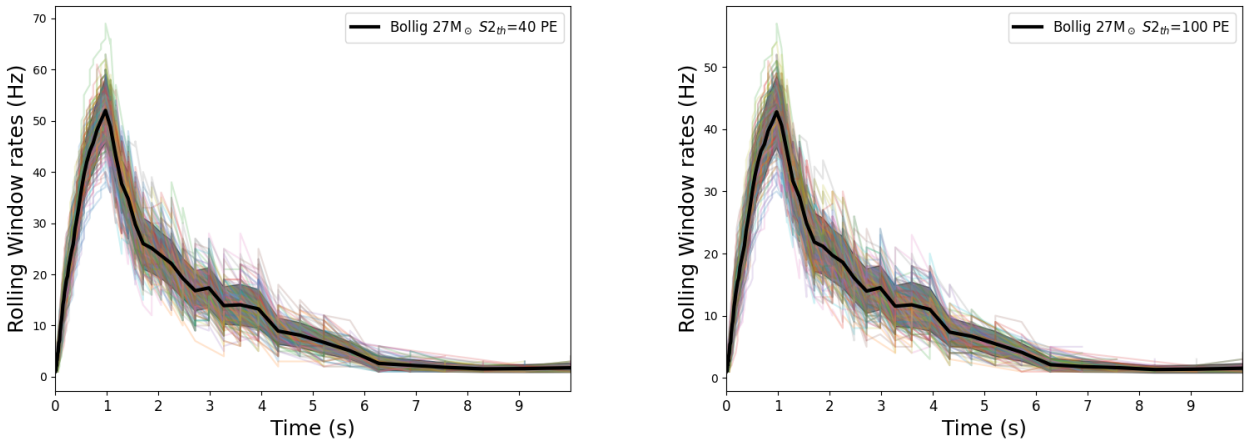

Figure 3.47: Rolling window rates using a 1 second step for 100 CCSN CEνNS observations for $27M_{\odot}$ (left) for different S2 thresholds of 40 PE (left) and 100 PE (right). Each point for each CCSN represent the median resulting from the 100 NEST simulations. As well the narrow black line is the resulting median for the 100 CCSN, and the bands represent the standard deviation

CCSN MC Toy simulation, and the points composing each cluster correspond to the 100 NEST simulations for this CCSN MC toy. Bands corresponds to the mean absolute deviation and as well the median is drawn by the dot-dashed line. Using this median as a reference, the maximum rates anticipate a decrease from 53.01 Hz to 43.51 Hz when 100 PE threshold is applied, instead of 40 PE.

Results after applying cuts to the SR1 background are illustrated in **figure 3.49**. Maximum (magenta) and mean (green) rates are significantly reduced, in regard to the results presented in the middle of this figure, showing their respective distributions in 40 days of data taking. The bottom panel illustrates the distribution of the mean rates fitted with a Gaussian centered in the mean value of ~ 0.15 Hz, which in this case is identical to the median value presented in the middle panel. Only a few points are obtained

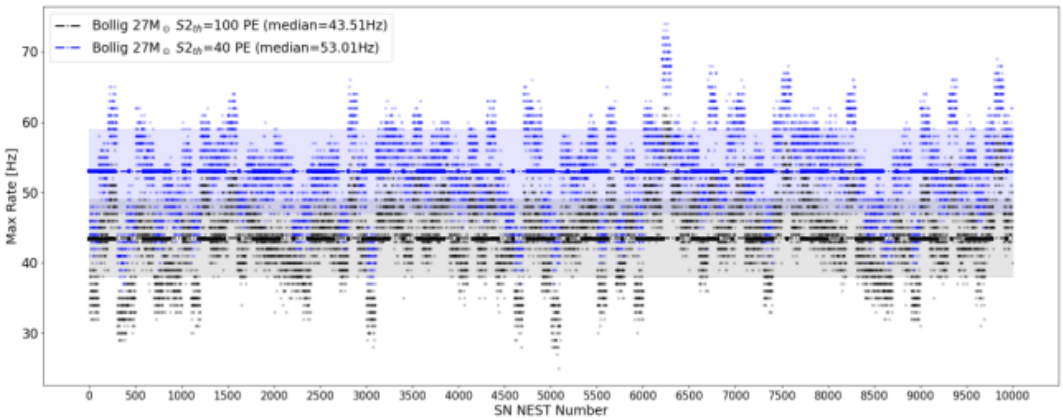

Figure 3.48: Maximum rates results from the 100 (×100) MC Toy + NEST for the 27M$_\odot$ progenitor at 10 kpc for the two selected thresholds. In blue and black the results from the S2$_{th}$=40 and S2$_{th}$=100. The median is represented by the dot-dashed lines and the bands corresponds to the MAD.

from the histogram, as the rate after cuts is extremely low, making their fit strongly challenging. On the side of the maximum rates, also a few points are obtained as expected by the results before cuts in the ROI, explained in **Section 3.5.3**. A skewed Gaussian is used to approximate the distribution in order to include the fluctuations of the data, that are enhanced into higher rates, producing an asymmetry into the Gaussian. At this point, this skewed Gaussian function parameters may be detailed, because there will be important for the calculation of the significance values, as it will be shown in the next paragraphs. The normalized skewed Gaussian can be defined as the convolution of the probability density function (PDF) $\phi(t)$ and the cumulative distribution function (CDF) $\Phi(t)$ as:

$$SkewGauss(x, \alpha, \omega, e) = \frac{2}{\omega} \times \phi(t) \times \Phi(\alpha t), \qquad t = \frac{(x-e)}{\omega} \tag{3.43}$$

Where the location parameter is represented by e, the scale parameter is ω and the α parameter related to the absolute skewness of the Gaussian, in which a normal distribution occurs when $\alpha = 0$. Respectively, the probability and cumulative density functions are correlated as:

$$\phi(t) = \frac{1}{\sqrt{2\pi}} e^{\frac{-t^2}{2}}, \qquad \Phi(t) = \int_{-\infty}^{t} \phi(t')dt' \tag{3.44}$$

Gaussian normal distribution and skewed Gaussian are strongly correlated. The typical mean (μ) and standard deviation (σ) values can be also obtained to the following relation:

$$\mu = e + \omega\delta\sqrt{\frac{2}{\pi}}, \qquad \delta = \frac{\alpha}{\sqrt{1+\alpha^2}}. \tag{3.45}$$

These values will be particularly important to obtain significances when the signal and the background are far from each other. This can happen, for example, in the case of a CCSN closer than 10 kpc. The p-value integration, that will be introduced in the next paragraphs, becomes computationally difficult. In

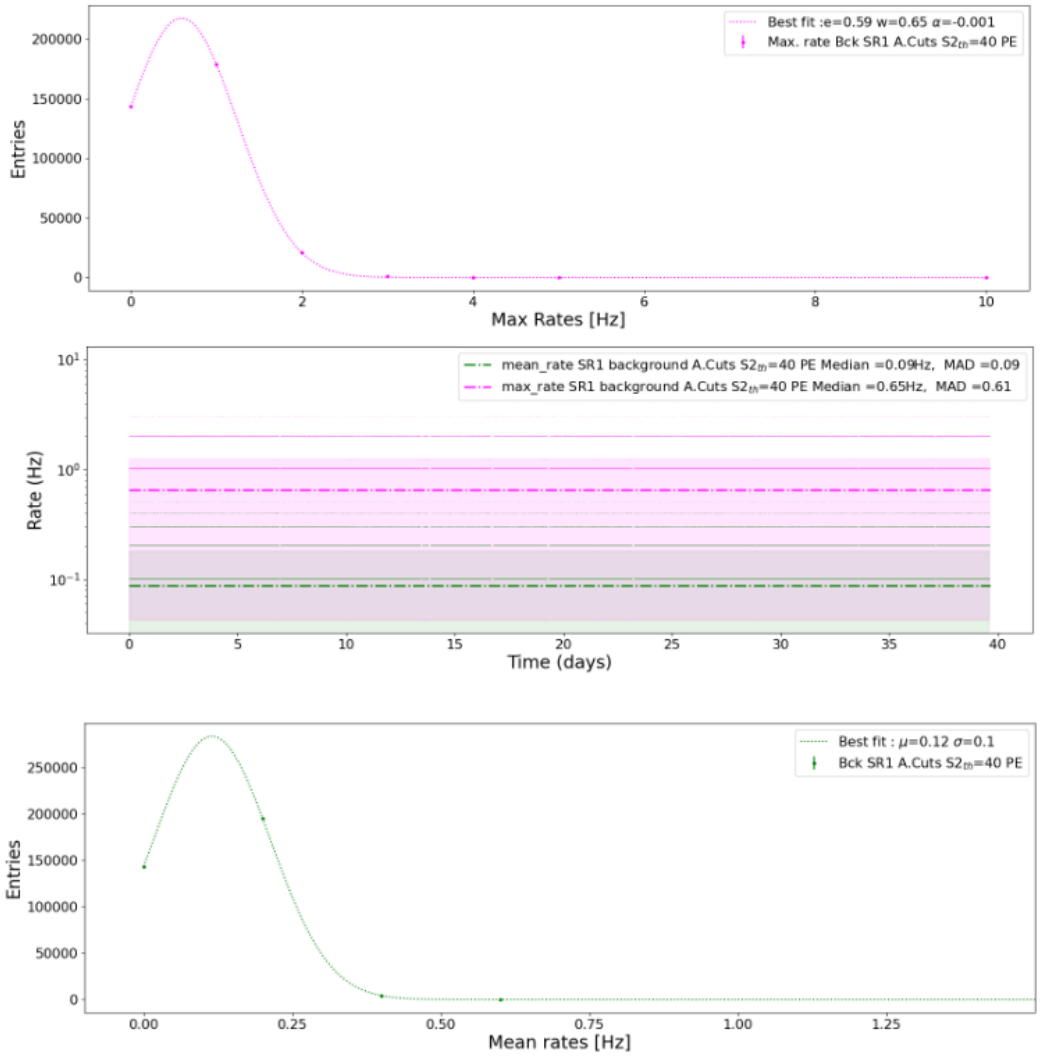

Figure 3.49: Distribution of the mean (green) and maximum(magenta) rates in 10 seconds independent bins of the SR1 background after applying the cuts for $S2_{th}$=40 PE. On the top the approximated maximum rate distributions to a skewed Gaussian. On the bottom approximation of the mean rate distribution with a Gaussian.

addition, the mean and standard deviation of the maximum rates from equation (3.45) are $\mu = 0.59$ Hz and $\sigma = 0.65$ Hz which results into the range of the median 0.41 (Hz) highlighted in the middle panel of **figure 3.49**. In a non-rigorous manner, it can validate the fit of the latter values through a skewed Gaussian.

Once the distribution of the background is determined, the statistical analysis can be performed, in order to estimate the discovery of the CCSN signal. The null hypothesis H_0 describes the 'known physics' which is represented by the background and will be compared to the background plus signal hypothesis, often designed as H_1 in literature. The compatibility between the observed CCSN data in the ROI and the background can be evaluated with the p-value, obtained from the background distribution of upper

panel of **figure 3.49**. This value estimates the probability, under the assumption of a hypothesis, of finding data of equal or greater incompatibility with the predictions of the former assumed hypothesis [390]. The p-value will be obtained to calculate the final significance with the most optimistic threshold of $S2_{th} = 40$ PE. This incompatibility of the CCSN signal with the background is often expressed through the significance Z in terms of standard deviations σ as:

$$Z = \Phi^{-1}(1 - p), \tag{3.46}$$

where Φ^{-1} is the inverse of a cumulative function of a standard normal distribution as described in expression (3.44). The discovery of the CCSN signal can be evaluated with the method of the likelihood ratio. The expectation value of the maximum rolling window R_i[6] can be expressed through the inclusion of the strength parameter ζ:

$$E(R_i) = \zeta s_i + b. \tag{3.47}$$

The case of background only is now represented by ζ=0 and the nominal value of the signal by ζ =1. Discovery can be estimated through the rejection of the ζ=0 hypothesis. The obtained maximum rolling window rates, can be evaluated for this hypothesis, in which the signal does not contribute. In this scenario, these rates will be denoted as R_0 as the variable to test. The p-value can be calculated, integrating the normalized skewed Gaussian for the background distribution of equation (3.43) $f_{bck}(R_0)$ in the interval $[R_{0_i},\infty)$, being i the corresponding index for each CCSN, corresponding to the rolling window maximum values represented in **figure 3.48**:

$$p(\zeta = 0)_i = \int_{R_{0_i}}^{\infty} f_{bck}(R_0) dR_0 \tag{3.48}$$

To obtain the significance of the CCSN signal (in this case at 10 kpc) the p-value can be obtained through the integration of this skewed Gaussian in the interval $(R_{max_i},\infty]$, being R_{max_i} the maximum rolling rate value for a i CCSN simulated represented in **figure 3.48**. These values will be scaled by the distance as $\propto \frac{1}{d^2}$. Nevertheless, instead of this scaling, in future studies a more convenient approach will be to simulate CCSN at several distances larger than 10 kpc, where significant uncertainties are anticipated to appear as not all the CCSN simulated will survive (i.e contribute at least with one event in a 10 seconds rolling window, which is expected to be the case <20 kpc for the selected *Bollig 2016* progenitors). It worth to notice that the background is inserted at a event level, after the rolling window is rolled over the background + CCSN signal. Strictly these should be done at a peak level and after the pairing of the event building should be performed and rolling the window over these events. Nevertheless, the low rate of the background supports this approximation, and signal and background can be considered independently at an event level.

This surviving property is a key point and has to be pointed out regarding the background. After the cuts are applied to the background, not all the 10 seconds time independent bins contribute with at least

[6]The same exercise can be done to obtain significance from the mean rate of the 10 seconds bins, replacing R_i by the mean value.

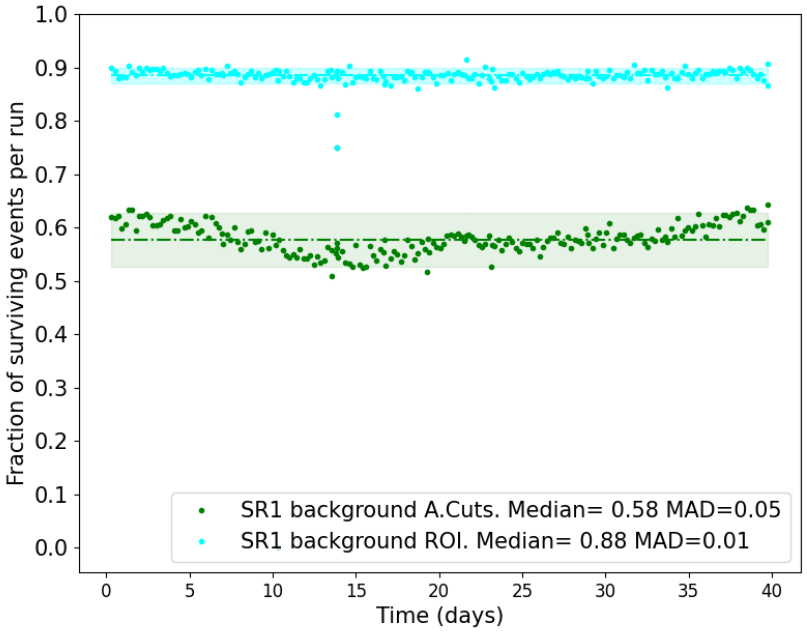

Figure 3.50: Surviving fraction per run of SR1 background in the ROI (cyan) and after cuts (green). The surviving criteria is counted by the number of

one event. Before the cuts surviving fraction in the ROI is $\sim 88\%$ which can be assumed as stable, to approximate the final distributions of the background with this data. However, after applying the cuts, this fraction drops to $\sim 58\%$. **Figure 3.50** shows the surviving fraction for each SR1 background run, represented by its time (starting to count from the first run), in the ROI in cyan before cuts and after cuts in green. Each point is calculated as the number of surviving 10 second bins contributing with at least one event $N(>1)_i$ divided by the number of bins in the run N_i:

$$f_{sur} = \frac{\sum_i^{n=\text{Number of bins}} N(>1)_i}{N_i} \tag{3.49}$$

In order to not underestimate the signal significance with regard to the background, the 10s time window bins with any background event are included in their distribution. The division of the bins is arbitrary, it starts when the first run event is recorded, dividing the run duration in 10 second intervals. Normalizing the rate distribution only with the fraction of surviving events, will attenuate the presence of high rate bins, which are the most intriguing ones in terms of compatibility with a CCSN signal. For example, if a bin has no events, but the next bin has three, cannot simply use a mean of 1.5 mean. Instead of this, this null bins have to be included in the maximum rate rolling window and mean rates distributions, as contributing with 0 value in both cases. This explains the points at 0 Hz in the distributions presented in **figures 3.44** and **3.49**. The inclusion of these points enhances the uncertainties of the background distribution, σ and w values for the Gaussian and the skewed Gaussian respectively, making the latter

left-skewed (α<0).

Finally, the significance results can be presented. **Figure 3.51** shows the obtained significances in the ROI, before the cuts (left) and after applying the cuts (right) for a $S2_{th}$=40 PE threshold. The bands represent the fluctuations in the CCSN simulated rolling window maximum rates presented in **figure 3.48**. The significance is high at the typical distance 10 kpc > 74 σ before cuts. Applying cuts turns out to not be relevant at this distance, as significance values attempted in the ROI are very optimistic. Beyond the MW edge, at 30 kpc, performance of the cuts is noticeable, obtaining >8σ and >4σ for the 27$M_\odot$ and 11 $M_\odot$ progenitors respectively. **Table 3.5.4** summarize the results before cuts (B.C.) and after cuts (A.C.) for both progenitors. On the other hand, these results can be compared to the obtained significances

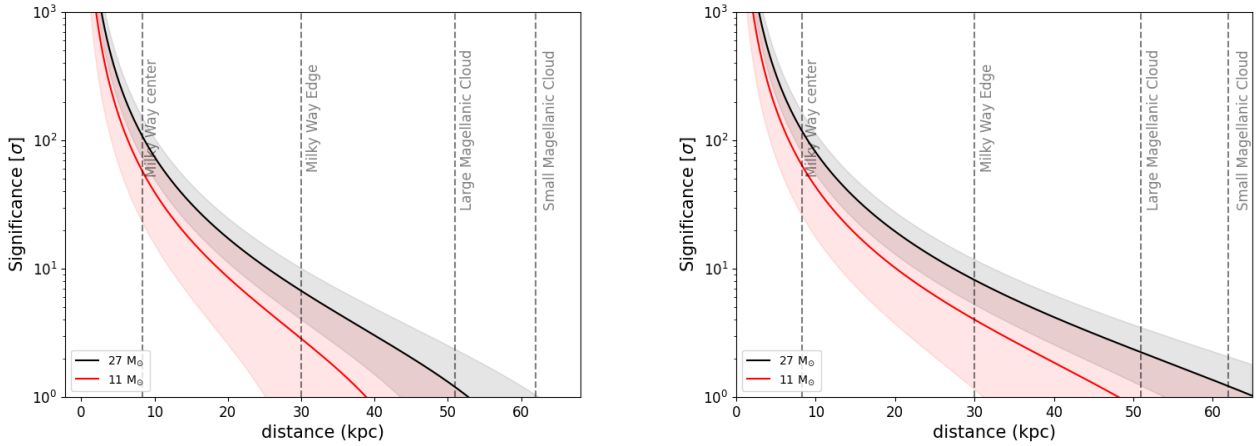

Figure 3.51: Significances using maximum rolling window rate distributions as a function of the CCSN progenitor distances, for the 27 $M_\odot$ (black) and 11 $M_\odot$ (red) progenitors requiring a $S2_{th}$=40 PE before (left) and after the cuts (right). The bands account for the fluctuations in the maximum rolling window rates. The distances of the Milky Way Center (8.3 kpc), Milky Way Edge (30 kpc), Large Magellanic cloud and Small Magellanic cloud at 51.6 and 62.3 kpc are indicated.

	27 $M_\odot$			11 $M_\odot$		
Distance	Events	Z(σ) BC	Z(σ) AC	Events	Z(σ) BC	Z(σ) AC
10 kpc	110	>74 σ	>80 σ	60	>43 σ	>39 σ
MW Edge	13	>6 σ	> 8 σ	6	>3 σ	> 4 σ
LMS	4	>1 σ	> 2 σ	2	-	>1 σ

Table 3.6: Summary of the sensitivity study results for the 27$M_\odot$ and 11$M_\odot$ progenitors with a $S2_{th}$=40 PE. The number of events and significance Z(σ) before (BC) and after cuts (AC) as a function of the selected distances: CCSN typical distance (10 kpc), MW Edge (30 kpc) and Large Magellanic cloud (51.6 kpc)

using the mean rates. These are represented in **figure 3.52**, showing that values before cuts in the ROI are slightly lower at 10 kpc than using maximum rates. However, at 10 kpc the CCSN signal before cuts

present a significance >72 σ and > 38 σ for the 27 $M_\odot$ and 11 $M_\odot$ progenitor respectively. On the contrary, applying the cuts turns very effective, increasing substantially the significance. After these cuts the sensitivity limit is attempted beyond the Small Magellanic Cloud (SMC) at 62.3 kpc, at this distance the significance is >2 σ for the 27 $M_\odot$. For the 11 $M_\odot$ progenitor, the limit is attempted after the Large Magellanic Cloud at 51.6 kpc (LMC) with a significance of 1.5 σ. However, at this distance beyond the MW edged, the probability of detecting a CCSN is very low, as only a few events are expected as **table 3.5.4** shows.

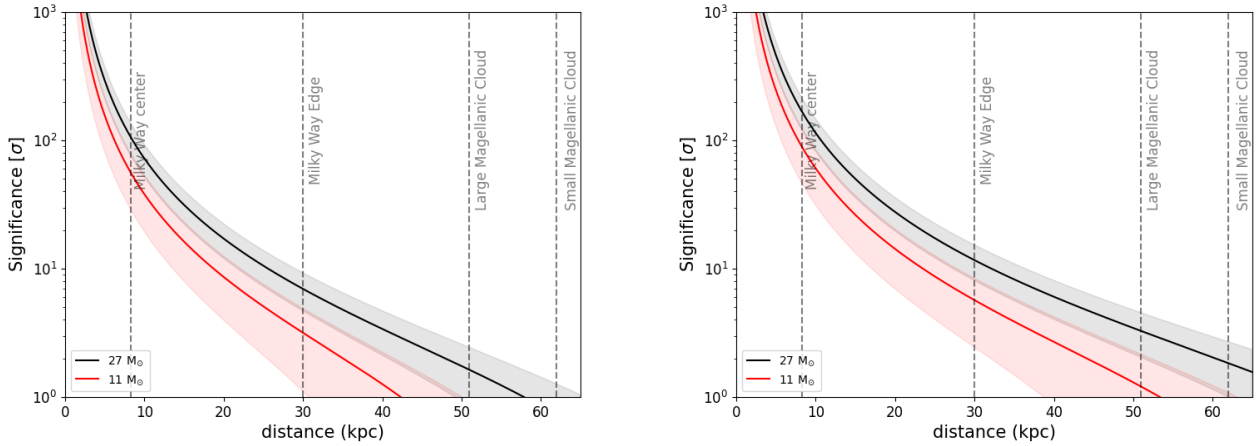

Figure 3.52: Significances using mean rate distributions as a function of the CCSN progenitor distances, for the 27 $M_\odot$ (black) and 11 $M_\odot$ (red) progenitors requiring a $S2_{th}$=40 PE before (left) and after the cuts (right). The bands account for the fluctuations in the maximum rolling window rates. The distances of the Milky Way Center (8.3 kpc), Milky Way Edge (30 kpc), Large Magellanic cloud and Small Magellanic cloud at 51.6 and 62.3 kpc are highlighted.

	27 $M_\odot$			11 $M_\odot$		
Distance	Events	Z(σ) BC	Z(σ) AC	Events	Z(σ) BC	Z(σ) AC
10 kpc	110	>72σ	114 σ	60	>38 σ	>60 σ
MW Edge	13	> 6 σ	> 11 σ	6	>3 σ	>5 σ
LMS	4	> 1 σ	> 3 σ	2	-	>1 σ

Table 3.7: Summary of the sensitivity study results using mean rates for the 27$M_\odot$ and 11$M_\odot$ progenitors with a $S2_{th}$=40 PE. The number of events and significance Z(σ) before (BC) and after cuts (AC) as a function of the selected distances: CCSN typical distance (10 kpc), MW Edge (30 kpc) and Large Magellanic cloud (51.6 kpc)

As a conclusion of this CCSN sensitivity study, it can be said that the strategy of using maximum rates, instead of mean rates, in the 10 s independent bins of SR1 data, turns out to be effective before the cuts in the ROI. This is particularly intriguing for an online analysis of the CCSN signal in real time, for example to send a CCSN alert to SNEWS. However, after the selected cuts, the increase of the significance

is not relevant. Several learning points regarding this fact can be highlighted. The first is that the rolling window maximizes the rates of the background for the selected cuts, implying that the rolling window time step of 1 s lead to background rate fluctuations. These are enhanced using a rolling window. A deeper analysis will be necessary to understand the implications of the choice of the rolling window step on the significance. Secondly, the cuts are preliminary and selected in order to affect minimally (not at all) the signal, rather than avoid these rate fluctuations. A more complete study of the cut parameters is needed to present robust conclusions for the maximum rates significance study. On the other hand, using mean rates the applied cuts applied are performant, obtaining a high significance at 10 kpc, improved regarding the ones obtained before the cuts. Furthermore, in this mean rate mode, a CCSN is expected to be detected with 3σ beyond LMS. In general, the results before applying the cuts to the background, utilizing maximum or mean rates, with a simple analysis of the data, testify that if a CCSN happens at 10 kpc from Earth CEνNS induced interaction will be potentially observed in XENONnT with a high significance ($>70\sigma$).

3.6 Summary

In this chapter, the different neutrino detection experiments which are relevant to the CCSN burst were described in **Section 3.1**. These are mainly divided into large water (or doped water) Cerenkov detectors and large liquid scintillators. Direct dark matter detectors using time projection chambers, such as XENONnT, are sensitive to CCSN neutrino bursts, being sensitive to all neutrino flavors in the low energy region <10 MeV contrarily to other mentioned detectors. After an introduction (**Section 3.2**) of the SuperNova Early Warning System (SNEWS), in **Section 3.3**, the TPC of XENONnT, the principal sensitive volume to neutrinos, was explained, including the properties of LXe and the microphysics of NR detection leading to the S1 and S2 observables, which are used in the CCSN neutrino event simulation. In **Section 3.4**, the implications of neutrino background signals in direct DM were introduced, focusing on their role regarding the sensitivity limits represented by the neutrino fog. This latter section serves as an introduction to address the CCSN neutrino detection in XENONnT TPC in **Section 3.5**. Coherent scattering interactions with Xe atoms allow for the observation of all neutrino flavors while avoiding flavor transformation uncertainties. In addition, the neutron rich LXe isotopes increase the CEνNS rate, as the cross-section is proportional to N^2. This section also includes the calculation of differential recoil rates and their time evolution. CEνNS interactions are characterized by low-energy recoils, and the detection threshold is predicted to play a role in the final number of observed events. To decrease the threshold, only the S2 signal (S2-only), can be utilized, and as a consequence, instead of the S2/S1 ratio, the time evolution and intensity of the CCSN neutrino burst can be employed for background discrimination. Regarding time evolution, differential spectra showed that during the first second around a half of the CCSN events are expected to be detected.

To test this method, the CCSN CEνNS simulation was done. First, a toy MC based on the calculated CCSN CEνNS time and recoil rates was used to proceed with the simulation of 100 CCSN for the 11

and 27 $M_\odot$ *Bollig 2016* progenitors at 10 kpc, to get the expected time and energy recoil, as well as the incoming neutrino energy for each interaction. Second, to better understand the detector response in terms of S1 and S2 signals, the NEST simulation tool, which includes the XENONnT setup and experimental parameters for SR0, was used to sample each toy MC CCSN 100 times to improve statistics. This yielded the region of interest in terms of S1 and S2, as well as the detection efficiency as a function of recoil energy and neutrino energy. Those efficiencies can determine the number of final observed occurrences for a given $S2_{th}$. In this scenario, there are two alternative thresholds: 40 and 100 PE.

One of the aims of this **Chapter 3** was to estimate the sensitivity of the CCSN CEνNS signal as a function of progenitor distance. To do this, the background throughout the SR1 phase of XENONnT data collection was examined. The goal of this study was to first determine the time uniformity of the background using the mean rate distribution, by dividing the data into independent bins with a CCSN burst duration of 10s. Secondly, a rolling window was rolled over the same time bins to maximize background rates, as done for the CCSN CEνNS simulations. This section shows that preliminary cuts are expected to improve the CCSN CEνNS detection sensitivity. It was determined that the fraction of the top PMT array contributing to the S2 signal, which lowers the background acceptance by approximately 50%, is the most effective parameter for the subsequent cuts. The analysis of sensitivity is focused on the $S2_{th}$ =40 PE as there are no relevant benefits as background reduction for higher thresholds does not compensate for the diminution of the number of CCSN events after applying them. The sensitivity study was performed using results before and after cuts were applied. The statistical strategy for conducting the sensitivity study was given. The same procedure will be used in the subsequent investigation of the CCSN signal in the water tank. Significances using the mean rate of the signal and the maximum of the rolling window rates were compared. Both cases show high significance ($>70\sigma$) at 10 kpc. The maximum rate strategy leads to similar sensitivities before and after cuts, pointing out that the choice of the rolling window step and the selected cuts have to be optimized in future studies. On the other hand, mean rate mode presents excellent results after the cuts, and with this method, the significances in the Milky Way edge and LMC are $>11\sigma$ and $>3\sigma$ for the 27 $M_\odot$. This allows us to be very optimistic for an online analysis of the CCSN signal and the contribution of XENONnT in SNEWS. Prospects for detecting a CCSN signal in the Milky Way by CEνNS are quite positive, since preliminary cuts achieve a significance of $>2\sigma$ in the Milky Way edge at 30 kpc.

In the next chapter, we will approach the description of the IBD detection microphysics in the water tank, as well as the IBD cross-section and neutron and positron rates, and their respective detection observables.

Chapter 4

CCSN Neutrino in the XENONnT Water Tank

Introduction

In the XENONnT water tank, the muon and neutron vetoes are sensitive to the CCSN neutrino burst. The primary purpose of this study is to investigate the neutrino signal in those two water volumes. The primary detection channel is expected to be the inverse beta decay (IBD), which is induced by $\bar{\nu}_e$ and emits a positron carrying almost all the $\bar{\nu}_e$ energy ($\sim$ $E_{\bar{\nu}_e}$ - 1.2 MeV) and a $\mathcal{O}$(0.01 - 1 MeV) neutron. More than 90% of these interactions are expected to occur in the muon veto. This chapter begins with a description of the mentioned water volumes in **Section 4.1**. This first section also includes a characterization of the muon veto background (**Section 4.1.1**), particularly emphasizing the low-energy region (**Section 4.1.2**). This region, comprising gammas and radiogenic neutrons, is the dominant one in the neutron veto, which was designed to tag both signals. The microphysics of neutron rejection, through the Cerenkov signal induced by its capture of gamma-ray, are also introduced (**Section 4.1.3**). In **Section 4.2**, the neutron veto is described, including the AmBe calibrations that enable the rejection of these neutrons and gammas (**Section 4.2.1**). The same calibration can be used to test the simulation of $\bar{\nu}_e$-IBD neutron capture in water. Background and AmBe calibration studies can predict the detector response to IBD-neutron capture. This section is extended to approach the microphysics of the IBD positron signal, which is the principal target signal for CCSN neutrino detection. To study this Cerenkov microphysics in the XENONnT water tank, a GEANT4 simulation was performed, concerning neutron, gammas and positrons energy depositions in this geometry. The recent addition of Gd salt[1] to the water modifies neutron microphysics, as its capture in the Gd nucleus releases a cascade of $\sim$ 8 MeV photons instead of the 2.2 MeV line when the neutron is captured in water. The CCSN $\bar{\nu}_e$ flux is projected to generate a considerable number of events in the neutron and the muon vetoes, interacting via IBD in the XENONnT water tank. **Section 4.3** provides an introduction to the cross-section, kinematics, and

[1] Gd salt refers to Gadolinium sulfate octahydrate, $Gd_2(SO_4)_3 \cdot 8H_2O$.

predicted antineutrino, positron, and neutron spectra used to simulate the CCSN IBD signal (that will be treated in the next chapter). However, electron scattering (ES) must also be considered. There are a considerable number of ES events in the muon veto volume, not enough to consider it a target signal, but it is important to evaluate its impact in the IBD positron energy spectrum reconstruction. **Section** 4.4 will cover the rate and distribution of the ES signal.

4.1 XENONnT muon Veto

A ten-meter column of ultra-pure water already surrounded the XENON1T experiment. Its performance in detecting cosmic muons was well known when the XENONnT cryostat was finally built [391, 392, 393]. The water tank, which houses the XENONnT TPC, is a modular stainless steel tank with a 9-meter-high cylinder and a 1.55-meter high frustum of a cone on top, for a total height of 10.55 m and a diameter of 9.6 m. This volume results in ten-meter tall column, yielding 700 tonnes of water. The muon veto volume accounts for 92% of this volume ($\sim$ 655 tons), while the neutron veto makes up the remainder.

Figure 4.1 displays the array of 84 waterproof Hamamatsu R5912ASSY 8-inch PMTs mounted to the cylinder walls. More than half of the PMTs are in the top (24) and bottom (24) arrays. This is the best way to model the zenith angle distribution and local LNGS specificities of the muon flux coming at the XENON1T experiment [391]. This PMT coverage is sufficient to detect cosmic muons with outstanding efficiency, thanks to the specular reflection of the polymeric 206 μm film covering the cylinder walls, the DF2000MA foil [394]. This foil also functions as a wavelength shifter, adding a small boost to the muon veto optical efficiency regarding these re-emitted photons [392]. An octogonal structure with high reflectivity of expanded PTFE (ePTFE) panels on the inside (facing the cryostat) and outside (facing the muon veto PMTs) separates the muon and neutron veto detection volumes. **Figure 4.1** shows the reflector panels in transparent turquoise. The foil and ePTFE panels cover practically the whole detection volume of the muon veto.

The muon veto is designed to allow for the rejection of cosmic muons, as well as neutrons produced by spallation muons, which are an important background for WIMP study. The high-energy ($>$ 200GeV [395, 396]) part of the muon spectrum is more likely to survive through $\sim$ 1.5 km of rock. Up to a few TeV, muons can trigger hadronic showers in the rock, producing fast neutrons (1 MeV to 1 GeV) that may enter the TPC [397, 398]. By tagging the Cerenkov light of the transiting muon or their secondary shower, these occurrences can be rejected. High-energy neutrons may be released from the rock and they may interact with other atoms before being trapped by nuclei, resulting in excited states and subsequent de-excitation with gamma emission. This is known as neutron activation, which can also occur in detector components, which is a significant source of background regarding the detection of neutrinoless double beta decay. The low-energy background in the muon veto is compounded by the neutrons and gamma rays from natural radioactivity, and the radiogenic neutrons. **Figure 4.2** depicts the survival fraction of this low-energy background based on water depth. The shortest path from this background to the cryostat containing the Xe TPC is $\sim$ 4 m. According to this assumption, only a small proportion, $\sim$ 1%, of muon-induced

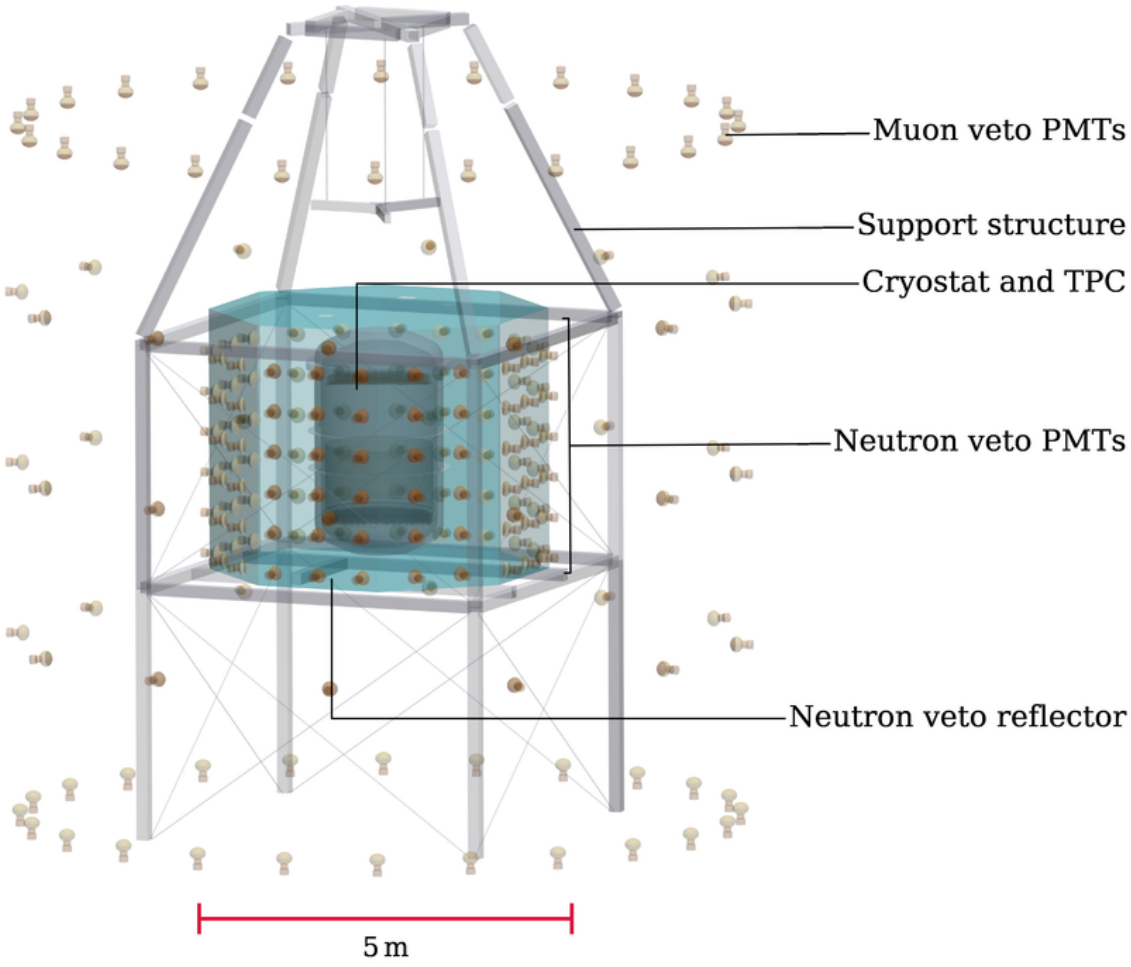

Figure 4.1: GEANT4 rendering of the three nested detectors, including the muon and neutron vetoes. The water tank walls, which support the muon veto PMTs, the neutron veto support structure, and other components (e.g. calibration systems) are omitted for clarity. Reflector panels, which optically separate the neutron and muon vetoes, are shown as transparent turquoise surfaces. The neutron veto PMT windows face the neutron veto region through openings in the panels. Figure from reference [317]

neutrons survives, while the rest are stopped and deposit all their kinetic energy in the water. Observing this low-energy background is challenging for the muon veto due to its poor PMT coverage, and because it is expected to yield similar signatures as the emitted neutron from IBD CCSN neutrinos. In this sense, even if muons are expected to cause an EM shower in the water, resulting in many detected Cerenkov photons, the low PMT coverage of the water tank requires the performance of the foils and reflector panels in order to maintain the photon collection efficiency. **Figure 4.3** illustrates the reflection performance of the ePTFE panels and the specular reflection foil. The left side of this figure depicts the manufacturer's (Hamamatsu) quantum efficiency. These reflectivity values are derived from the parameters used in the GEANT4 model of XENONnT regarding Cerenkov photons in the energy range 1–5 eV. A significant

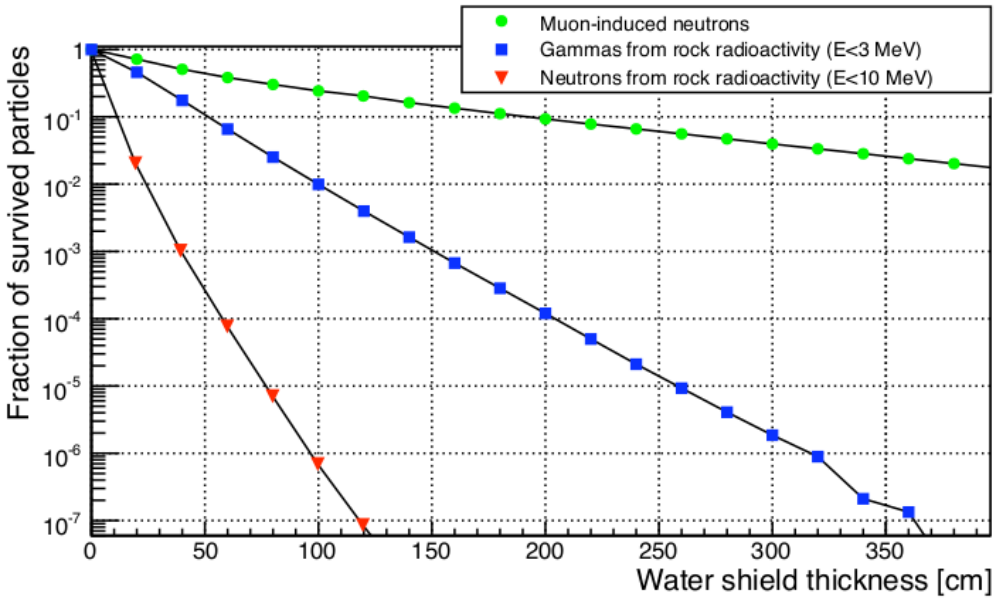

Figure 4.2: Fraction of surviving particles as a function of the thickness of the water shield surrounding the detector. Circles are used for the muon-induced neutrons, squares for the gammas from rock radioactivity and triangules for neutrons from rock radioactivity.

part of the CCSN IBD simulation is done using GEANT4. In this sense, it is necessary to note that this simulation accounts for the physics of reflection, including the foil and ePFTE panels. **Figure 4.3** shows that for a wavelength of $\lambda > 380$ nm, the foil reflectivity is more than 95%, noticing that at this wavelength, the QE is maximal, at 33%. In contrast, ePTFE exhibits 99% reflectivity across the whole Cerenkov photon spectrum. The reduction of ∼2.5-4% of the reflectivity performed by the foil (>380nm) can be assumed due to the difficulties of mounting ePTFE panels around a cylindrical surface.

4.1.1 Muon background

The interaction of cosmic radiation with particles in the upper atmosphere produces muons. Particularly, primary particles arriving at the Earth from cosmic events, high energy protons and nucleons, interact with atmospheric nuclei, causing hadronic showers that contribute to the creation of muon pairs. $\mu^{+/-}$ is commonly associated with pion ($\pi^{+/-}$) decays or, in a smaller percentage ($\sim$ 10%), kaons $K^{+/-}$ decays [78, 400]:

$$\pi^{+/(-)}, K^{+/(-)} \rightarrow \mu^{+/(-)} + \nu_{\mu}(\bar{\nu}_{\mu}). \tag{4.1}$$

The cosmic ray flux that enters the atmosphere can be considered isotropic; nevertheless, the muon flux is a subsequent result of hadronic shower of charged particles. The thickness of the atmospheric layer that cosmic rays cross, which relies on their zenith angle, influences the altitude where these showers are generated. Once produced, muons have a mean life of $\tau = 2.1969811 \pm 0.000002\ \mu s$ [78], and their survival relies on the length of their journey to the Earth's surface, which is also zenith angular dependent [401].

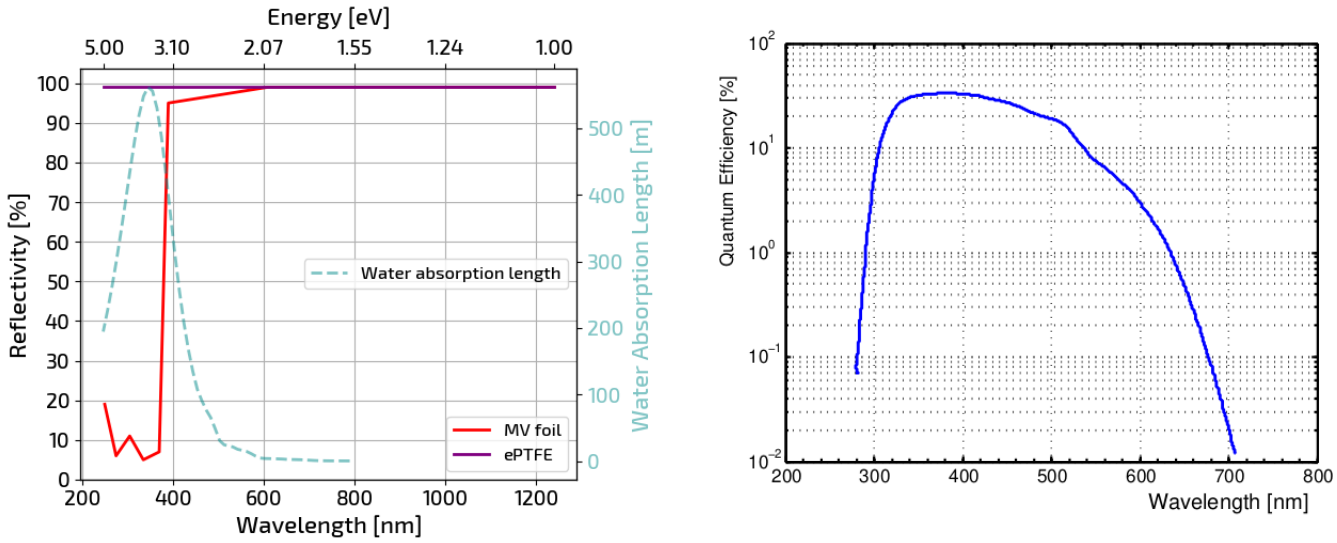

Figure 4.3: **Left:** Reflectivity performance for the DF2000MA foil (red) and ePTFE (purple) panels from the simulation of incident photons [1-5 eV] in GEANT4 for the XENONnT geometry. These photons represent the range of Cerenkov spectrum. The water absorption length is represented by the dashed cyan line. **Rigth:** Quantum efficiency for the muon veto PMTs as a function of the wavelength provided by Hamamatsu [399].

Their survival is also dependent on energy. Only >1 GeV of muon flux reaches sea level, measured at 1 muon per cm^2 per minute and with a 4 GeV mean energy [402]. The geomagnetic field, which causes the renowned east-west effect, also influences the angular distribution of muon at 1 GeV [403]. Finally, the profile of the LNGS rock has an impact on the final spectrum, altering transit for a specific event muon direction.

Figure 4.4 illustrates the muon flux energy spectrum at several underground laboratories (left), including LNGS, and the cosinus zenith angle distribution (right) measured by two experiments at LNGS. The zenith angle distributions justify the fact that the bottom and top of the muon veto account for more than half of total PMT coverage, as muons are projected to arrive from either the top or the bottom of the water tank cylinder. The predicted total rate arriving at the LNGS is $(3.432 \pm 0.003) \times 10^{-8}$ cm^{-2} s^{-1} [404], with a mean energy of 320 ± 4 GeV [396].

Monte Carlo simulations using GEANT4 modeling were used to optimize the final design of the XENON1T muon veto. Muons with energies ranging from 1 GeV to TeV, representing the expected LNGS muon energy spectrum as calculated in reference [405], were simulated in the water tank, as detailed in reference [391]. Several configurations of PMTs and trigger conditions were tested to optimize the muon detection, resulting in the currently used design. Based on a threshold associated with the number of PMTs in coincidence, 4-fold coincidence is projected to achieve 99.78% trigger efficiency, assuming one PE in a 300 ns integration time window. The XENONnT trigger for SR0 and SR1 assumes these two trigger conditions, but requires at least 5 PMTs in coincidence, averaging in a trigger efficiency even closer to 100%. The effect of increasing the number of PMT coincidences is to reject accidental coincidences as well as low energy background events.

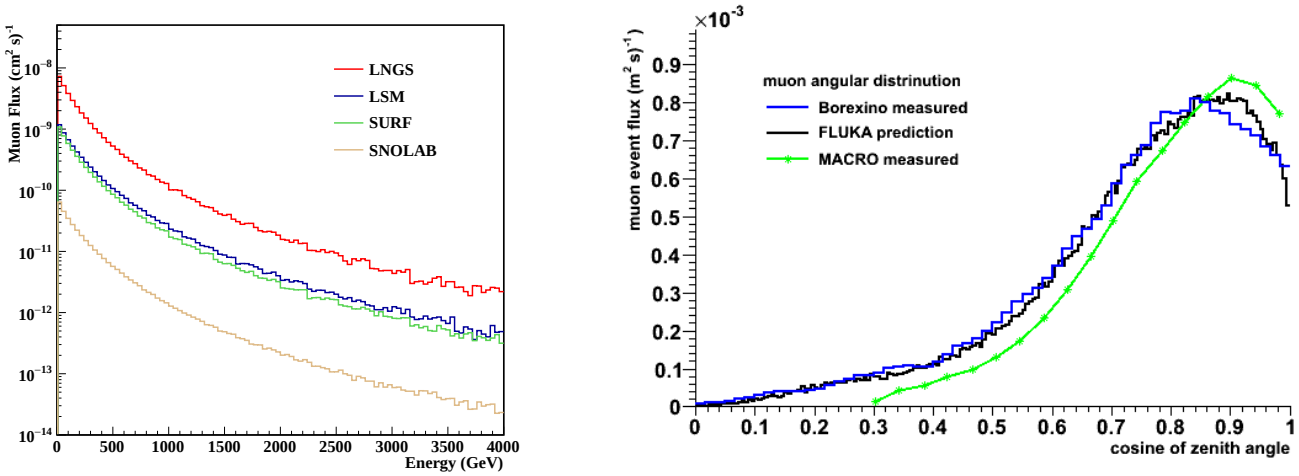

Figure 4.4: **Left:** Muon flux as a function of energy for several underground laboratories: LNGS (Gran Sasso, Italy), LSM (Modane, France), SURF (Lead, USA) and SNOLAB (Sudbury, Canada). The calculations are done with the model MUSUN [405]. **Right:** Cosmic muon zenith angle distributions at LNGS. Comparison from FLUKA model (black) [406], data from Borexino (blue) [269], and MACRO (green) [407].

As seen in **figure 4.5**, the rate of detected muons is approximately two per minute, or 120 per hour. In addition to the low rate relative to the expected CCSN, the muon signal appears to be distant from the CCSN IBD signal's ROI. Muons deposit almost 100 times more energy than positrons, resulting in $\mathcal{O}(100)$ more Cerenkov photons. In this sense, muon signals are expected to be easily distinguished from the latter. In the next section, the low-energy background, which is in the ROI of IBD positron, will be described. This background region is mainly composed of gamma-rays, in the energy range of those which are expected to produce during the $\bar{\nu}_e$ IBD interactions, after the IBD neutron capture.

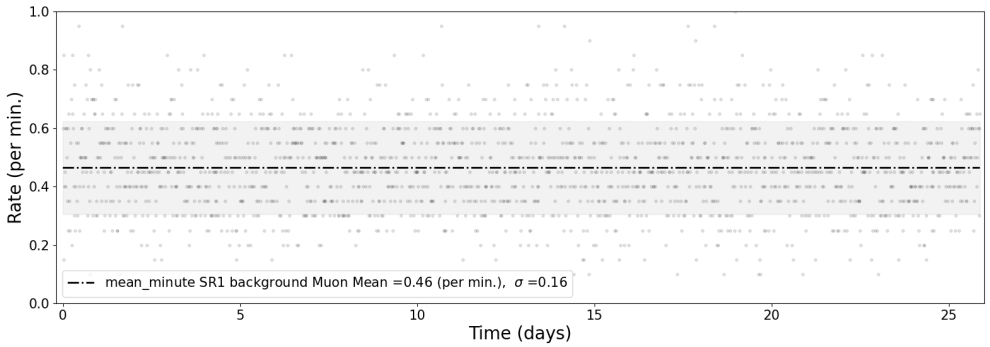

Figure 4.5: Muon mean rates for the SR1 in time bins of 10 minutes for one month of data taken. The band represents the standard deviation and the dot-dashed line corresponds to the mean.

4.1.2 Low-energy background

The low energy component of the background lies in the ROI for the anticipated CCSN neutrino signal in the muon veto volume, where the majority of IBD positrons are likely to be observed. The secondary generation of charged particles will generate Cerenkov light in the presence of neutrons and gamma radiation. The background neutrons are expected to engage in stochastic scattering with atomic nuclei in water, depositing energy through this multi-scattering until they thermalize at water temperature, which implies that they lose kinetic energy until they have less than ~ 0.025 eV [408]. For neutrons of energy $\mathcal{O}$(MeV), their brownian motion endures 10μs. The path length of neutrons varies depending on their initial energy; for $\mathcal{O}$(MeV), it is a few tens of cm, as shown in **figure 4.6 (left)**. Far above the upper bound

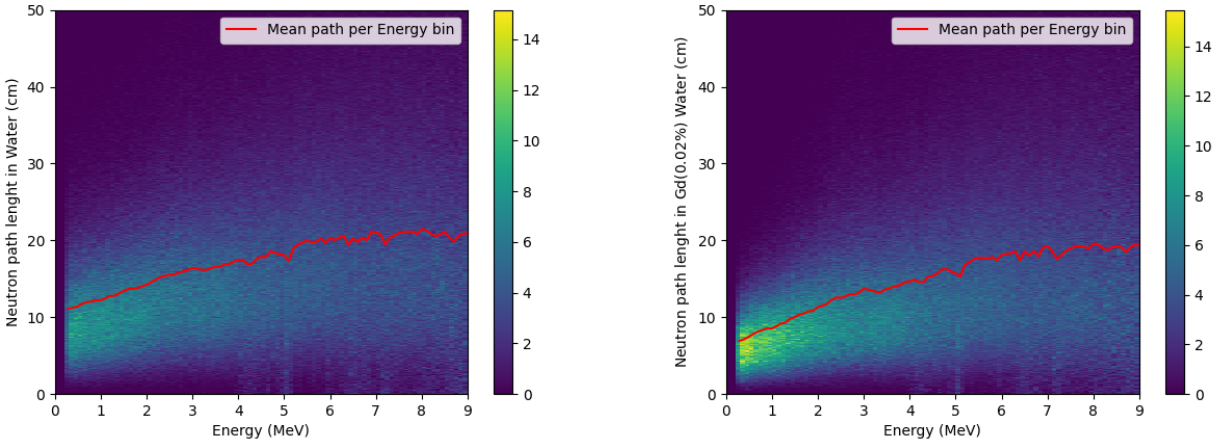

Figure 4.6: AmBe (1 to 9 MeV) neutron path in water from GEANT4 simulation in the two configurations: pure Water (left) and GdWater (right) as a function of the neutron energy. The AmBe spectrum has been normalized to present equiprobable energy bins.

of thermalization energies $\mathcal{O}$ (10^{-5} eV), neutron absorption cross-section substantially dominates beyond other scattering processes, raising to the values shown in figure **figure 4.7**. The neutron is captured by hydrogen in a high proportion rather than in oxygen nuclei, creating deuterium atoms and producing a 2.22 MeV gamma-ray in 100% of the cases [410], emitted after a characteristic time of 200 μs after thermalization [411]:

$$n + p \longrightarrow d + \gamma \quad (2.22 \text{ MeV}) \tag{4.2}$$

Some neutrons can also be trapped in metal components, resulting in nuclear excitation and consequently de-exitation with the emission of gamma rays.

Taking into account the great volume of water and the mean free path of neutrons represented in **figure 4.6**, neutron capture is merely a question of time, and nearly 100% of the neutrons are captured before entering the TPC. The muon veto is quite effective in stopping neutrons, but is expected to be less effective in its detection.

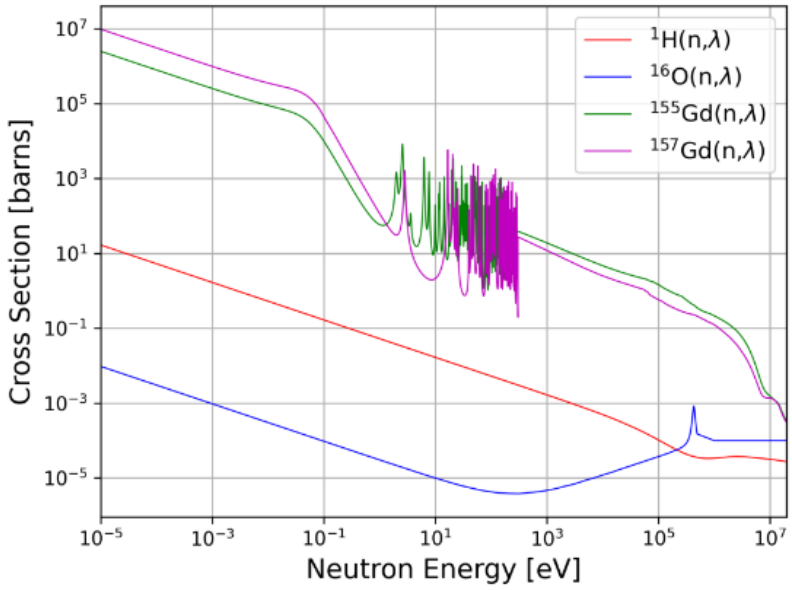

Figure 4.7: Neutron absorption cross section in water and Gd-doped water for hydrogen, oxygen, and the two principal isotopes of natural Gd. Figure from [409].

The study of IBD interactions from CCSN $\bar{\nu}_e$ includes the emitted neutron signal. The investigation of the background in the muon veto is a major opportunity to calibrate the response of the detector to this signal. The next paragraphs introduce the muon and neutron veto capabilities to detect neutrons, which are very different from each other. As shown in **figure 4.7**, the detectable signal of a neutron in water is not determined by its kinetic energy, but rather by the nuclei involved in its capture. At this $\mathcal{O}$(MeV) energy, the neutron path length in water is not relevant for detection purposes in larger volumes, such as the muon veto. Gamma rays emitted during nuclear de-excitation form the observable signal. The path length of gamma-rays in water for the 2.22 MeV neutron capture and the 4.44 MeV gamma-ray from the ^{12}C lines (the latter is released during AmBe calibrations, see **Section 4.2.1** for additional details) are indicated in **figure 4.8**. These values are computed using the mass attenuation coefficient for gamma-rays from the different processes described in **figure 3.22**. These values are modified in this case for a pure water density 0.99802 g/cm^3 at 21 degrees [412]. In the MeV-range of interest for neutron capture in water, including gammas from background radioactivity, and further neutron capture in Gd-lines as shown in **figure 4.20**, gamma-rays are expected to deposit their energy through a path of a few tens of centimeters. Neutron capture gamma rays will deposit energy through compton scattering. Ionized electrons that have gained kinetic energy beyond the Cerenkov threshold from expression (3.1) ($E_{kin} > 261$ keV) will produce Cerenkov photons in the VUV. The amount of energy transferred to the compton-scattered electron is crucial. This momentum transfer has to not only be beyond the Cerenkov threshold but must also produce a large aperture of the Cerenkov cone (see 3.1) due to the modest coverage of muon veto PMTs. The

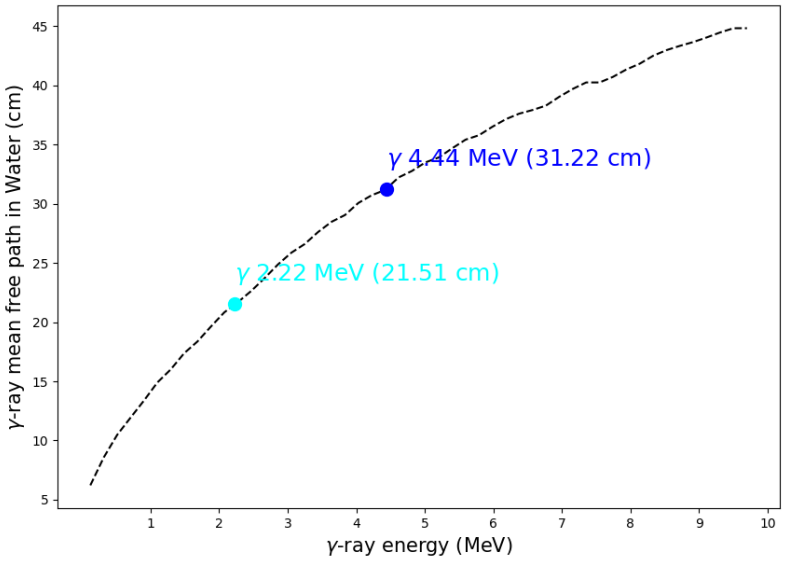

Figure 4.8: Mean free path of gamma-rays as a function of their energy in MeV. This values are calculated used the attenuation coefficients in water adapted from values of **figure3.22** to water density. Figure from [414]

maximun gamma energy transferred through compton scattering to a free electron can be written as [413]:

$$E_{e_{max}} = E_\gamma \frac{(1 - cos\theta_{max})\frac{E_\gamma}{m_e c^2}}{1 + (1 - cos\theta_{max})\frac{E_\gamma}{m_e c^2}} = E_\gamma \frac{2\frac{E_\gamma}{m_e c^2}}{1 + 2\frac{E_\gamma}{m_e c^2}}, \tag{4.3}$$

with m_e the mass of the electron (511 keV [78]) and θ the scattering angle between the scattered electron and the resulting gamma. In this energy range, the electron emission presents peaks, named in literature as compton edges [415]. The latter are represented in **Appendix figure D.1 (left)**.

For a 2.22 MeV gamma scattering in water, the maximum energy transfer to this electron is $\sim$ 1.97 MeV, which in this case leads to a cone aperture angle of $\sim$ 40 degrees according to equation (3.1). But this assumes that the incident photon is scattered backwards and that energy transfer losses due to the bounded electrons have been neglected [416]. In reality, there is a strong scattering-angle dependence in the compton effect[2] which can be evaluated using the Klein–Nishina cross-section [418] for MeV gamma energy (See **Appendix figure D.1 (right)**). At this MeV gamma energy range, the electrons are mostly scattered forward, reducing the energy transfer significantly, close to the values of the Cerenkov threshold [419, 408]. As well, the aperture of the Cerenkov cone is reduced by $\sim$ 15 degrees. In this sense, it can be deduced that reflection, and as a consequence, water transparency, will play a crucial role in the detection of Cerenkov photons. **Figure 4.9** shows the number of Cerenkov photons per deposited gamma ray energy, from the results of the GEANT4 simulation of gamma-rays in the energy range $\sim$ 0.1 to 4.5 MeV, in which Compton scattering is expected to be the major interaction for energy deposition (see **figure**

[2]Compton effect refers to the wavelength shift of the gamma as a result of the compton scattering with an electron [417].

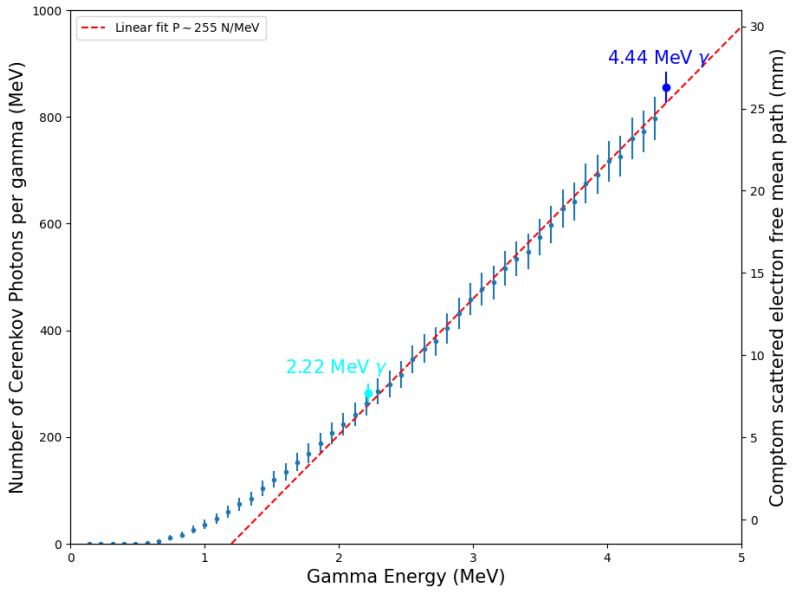

Figure 4.9: Number of Cerenkov photons per gamma ray as a function of gamma energy. The figure is made with the results of GEANT4 simulation 10^6 mono-energetic gamma-rays, homogeneously distributed in the Water tank in the range where Compton scattering dominates 0.1 to 4.5 MeV in steps of 10 keV.

3.22). Gamma-ray energy transfer to electrons is more effective when performed via a single scatter, but can also happen through multiple scatters, diminishing the probability to be seen by muon veto PMTs. The number of photons presents a quasi-linear relation as a function of gamma-ray energy, as most of their production is due to scattered electrons — also, photoelectric effect and pair production contribute to the energy deposition process. In this scenario, the number of produced Cerenkov photons per unit length (dN/dx) is directly correlated to the kinetic energy of the particle, as provided by the Frank-Tamm formula [420]:

$$\frac{dN}{dx} = 2\pi\alpha z^2 \int_{\beta n>1} (1 - \frac{1}{(\beta n(\lambda))^2}) \frac{1}{\lambda^2} d\lambda, \tag{4.4}$$

where α is the fine structure constant [3] $\sim \frac{1}{137}$, z is the charge of the particle, β is the velocity of the particle relative to the speed of light in the medium in natural units, and n is the refractive index of the medium which depends on the emitted Cerenkov photon wavelength λ (1.3336 in the range of interest in water). The term based on β represents the Cerenkov threshold (equation (3.1)). The equation (4.4) is ultimately related to the mean path of the dispersed electron in water. To understand the implications of the mentioned energy depositions into the detection of these gamma rays, the involved microphysics needs to be introduced.

[3] Explicitly the fine structure constant is defined as $\alpha = \frac{e^2}{2\epsilon_0 hc}$, with e the elementary charge in coloumbs C ($1.602176634\times10^{-19}$ C), h is the Planck constant in Joules J/Hz (6.62607015×10^{-34} J Hz^{-1}), c the speed of light (299792458 m s^{-1}), ϵ_0 is the dielectric constant ($8.8541878128\times10^{-12}$ F m^{-1}).

4.1.3 Cerenkov microphysics

MeV electrons are minimum ionizing particles (MIPs), as are cosmic muons. This implies that at this energy they achieve their minimum mean energy loss in matter through ionization, as **figure 4.10** shows. This occurs when particle kinetic energy leads to $\beta\gamma \sim 3 - 3.5$ when the medium's Z is between 7 and 100. These particles have a mean path that is connected to the stopping power $\frac{dE}{dx}$ and the density of the ionizing medium ρ. This is called linear stopping power (LST)[78]. At these energies for electrons and positrons, ionization is the dominant mechanism for energy deposition, while Bremsthralung dominates at few tens of MeV. The energy deposition per unit length can be determined by the Bethe-Bloch formula [78]:

$$\left\langle \frac{dE}{dx} \right\rangle = \frac{KZ}{2A\beta^2}\Big(ln\frac{m_e c^2 \beta 2\gamma^2 (m_e c^2(\gamma-1)/2)}{I^2} + (1-\beta^2) - \frac{2\gamma-1}{\gamma^2} ln2 + \frac{1}{8}\frac{(1-\gamma)^2}{\gamma} - \delta\Big), \tag{4.5}$$

where Z and A are respectively the number of electrons and the atomic number of the absorber medium, the coefficient $K = 4\pi N_A r_e^2 m_e c^2 = 0.307075$ MeV mol^{-1} cm^3 [78] (with r_e the classical atomic radius of electrons $e^2/4\pi\epsilon_0 m_e c^2$) and δ the density correction to ionization losses $\sqrt{\rho Z/A}\times$ 28.816 eV. Understanding the electron energy deposition in water of MIPs is particularly interesting for CCSN detection. **Figure 4.10** illustrates the referred stopping power described by the Bethe-Bloch formula (equation (4.5)) for an electron (or a positron) of 1 MeV. The blue band corresponds to the dominance energy range of ionization. Positrons emitted from CCSN $\bar{\nu}_e$ IBD are also MIPs, interacting with matter as electrons do, because electromagnetic interaction makes no distinction between both. In this sense, MeV positrons deposit energy like electrons, but can be distinguished by the pair annihilation signature of the first with the second ($e^- + e^+ \longrightarrow 2\gamma$ (1022 keV)), after depositing most of their kinetic energy in less than 1 ns [421]. On the other hand, energy depositions through Cerenkov radiation are small and significantly less effective than through ionization. This is presented in **figure 4.10** by the green line, covering the radiative stopping power, in front of the ionization one represented by the red dashed line. For a MIP, the rate of energy loss per unit path length due to Cerenkov emission is about 0.1% of that due to ionization [422]. This ratio becomes smaller with the increase of the electron energy at 100 MeV; the ratio between the Bremsstrahlung signal and the Cerenkov signal in the visible range $\lambda \sim$ 400 - 500 nm is of the order of 10^{-5} [238].

Figure 4.11, left panel, displays the number of electrons per unit length as a function of kinetic energy. The Cerenkov threshold and the convergence of the number of photons emitted when $\beta \longrightarrow 1$ ($\sim$ 55 photons/mm) are highlighted. Values are obtained by integrating equation (4.4) in the wavelength of interest (250 – 800 nm). The maximum energy transfer from a 2.22 MeV gamma to an electron provides $E_e \sim 2$ MeV and $\beta \sim 0.98$, resulting in a Cerenkov emission per unit length of $\sim$ 51.75 photons/mm. Assuming that only the events in which gamma Compton scattering produce Cerenkov light are shown in **figure 4.11**, this approximation[4] implies that the convolution between Monte Carlo GEANT4 results

[4]This is just a first order approximation, indeed is impossible to known for the vetoes how many times a gamma had scattered before producing Cerenkov light and being detected by PMTs. It is worth to notice that multi-scattering is a substantial part of the Compton spectra [423]

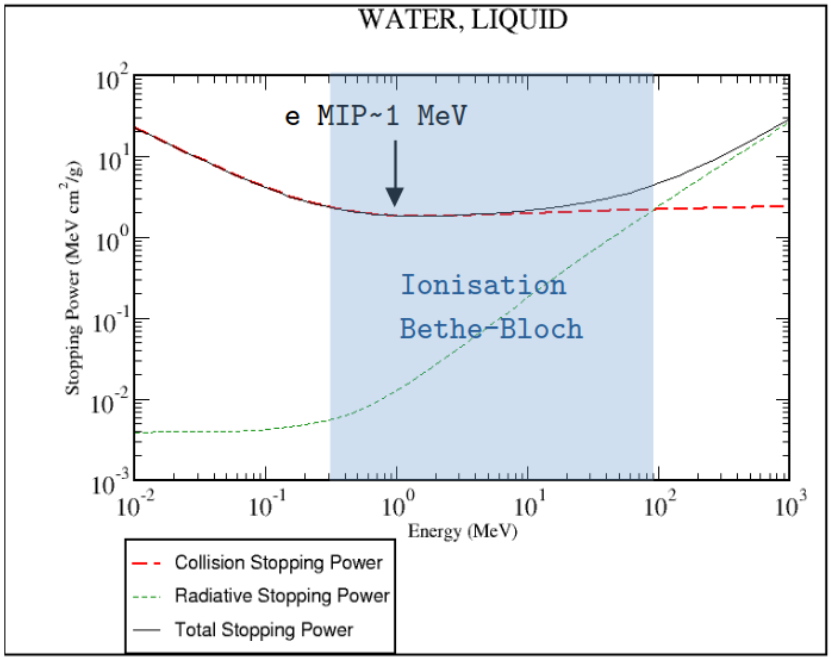

Figure 4.10: Stopping power for electrons and positrons in water as a function of their energy. Energy deposition mechanism related to this stopping power are divided in radiation stopping power (green) which is dominated by Bremsstrahlung radiation, and includes also Cerenkov radiation, and collision stopping power dominated by ionization (red). The figure is generated with the values from [352].

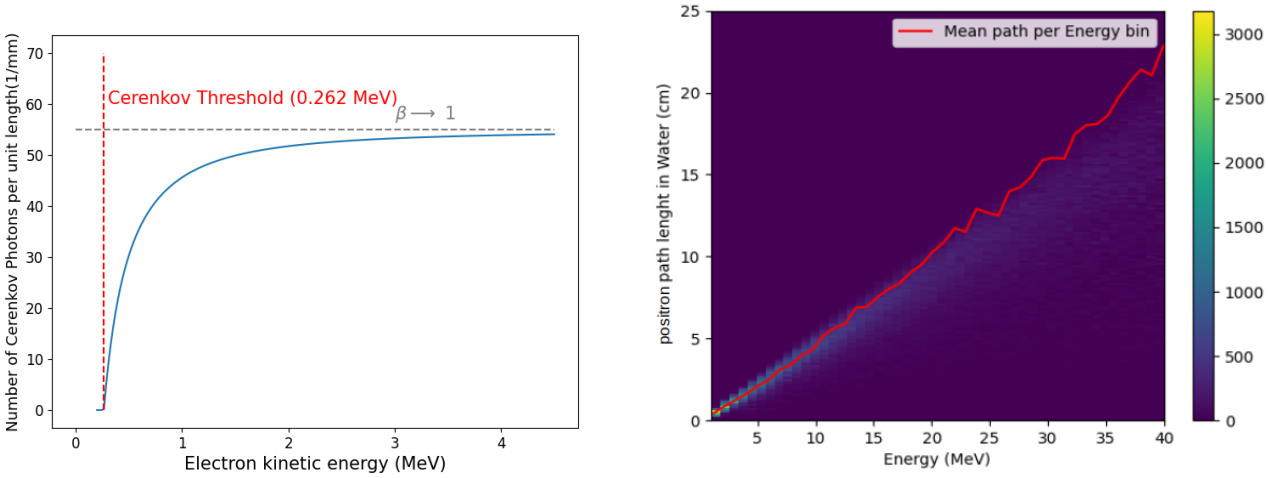

Figure 4.11: **Left:** Number of electrons per unit length as a function of the kinetic energy. The Cerenkov threshold (red dashed line) and the convergence of the number of photons emitted when $\beta \longrightarrow 1$ ($\sim$ 55 photons/mm) in grey dashed line are highlighted. Values are obtained integrating equation (4.4) in the wavelength of interest 250 - 800 nm. **Right:** Positron path length from GEANT4 simulation as a function of the energy.

of the number of photons per gamma energy and the predicted $\frac{dN}{dx}$ gives the estimation of the free mean path of scattered electrons as a function of energy, shown in the left Y-axis of this figure. Compared to

gammas or neutrons, $\mathcal{O}$(MeV) electrons are a point-like signal, with a path in water that is one order of magnitude shorter. The average of Cerenkov photons is estimated to be ~ 250 per gamma-ray per MeV, as stated in **figure4.9**. However, this is expected to change when higher energy electrons or positrons $\mathcal{O}$(10 MeV) enter in water. For positrons, the survival time in the medium, still in the same order of magnitude ($<$ 1ns) (see left panel of **figure D.6** in **Appendix D.2.2**), they create an electromagnetic shower from ionization. Regarding the left panel of **figure 4.11**, when $\beta \to 1$, the number of Cerenkov photons only depends on the path of the positron, which depends on its energy. Nevertheless, at expected CCSN IBD positron energies (few MeV to 100 MeV) their path length is approximately from few cm to a few tens of cm as **figure 4.11** right panel shows. Also in **Appendix D.2.2**, **figure D.6** right panel, a 20 MeV positron Cerenkov emission is tracked until its annihilation. Each red point present a Cerenkov emission, for a total of 5016 photons, the cross symbol presents the annihilation coordinates and the triangle the initial position when the positron is emitted.

On the other hand, only Cerenkov photons arriving at the PMTs can create a signal once QE and trigger selection criteria are applied. The latter represents a small fraction of the total cerenkov photons produced. These photons hitting the PMTs will be referred as "VPMThits". In **Section 3.3.4**, the number of PMT hits ($N_{PMThits}$) describes the number of optical photons (optical from the point of view of the PMT absorption spectrum) that eventually impact the PMTs. This magnitude accounts for photon losses from the medium (LXe or GXe), the electric field impact, reflection, and other geometric effects. In the muon and neutron vetoes, no such effects are present, but absorption and reflection, depicted in **figure 4.3**, and geometric uncertainty amplified in the muon veto by the low coverage of PMT, are the key values determining the Cerenkov photon losses. In this regard, "VPMThits", which are comparable to TPC magnitudes, might be defined as the number of Cerenkov photons arriving at PMTs. This name is just the GEANT4 XENONnT jargon, with a 'V' as prefix to distinguish it from the TPC PMT hits.

As mentioned, the primary variable influencing Cerenkov photon losses in a water tank is water transparency, which is dependent on the photon wavelength. To present the impact on photon absorption, panel reflection performance and geometry effects, a GEANT4 simulation was performed. Results of this simulation are shown in **figure 4.12**, with the neutron capture gamma-ray line of 2.22 MeV in cyan, the ^{12}C line from AmBe calibrations (or Gd capture gamma lines) 4.44 MeV, and a 20 MeV positron (expected mean energy value for CCSN IBD emitted ones). To prospect the impact of the mentioned uncertainties on the detection, the figure presents for the selected particles: the number of emitted Cerenkov photons (solid lines); the number of Cerenkov photons arriving at the PMTs (dashed lines) already defined as VPMThits; and finally, QE is applied to the VPMThits, depicted by dotted lines. These values are expressed as a function of the photon wavelength. The latter two magnitudes are also represented as a fraction relative to the number of Cerenkov photons along the left Y-axis in gray and black for 2.22 MeV black and 4.44 MeV gamma rays respectively, and magenta for 20 MeV positrons. Dot-dashed and solid lines show, respectively, the VPMThits and the VPMThits+QE fractions. As well, integral values, in the range of wavelengths of 250 - 650 nm, are summarized in **table 4.1**.

The effects of the foil reflection are significant, resulting in dramatic reduction of Cerenkov photons

with wavelengths ranging from 250 to 380 nm. As seen in **figure 4.3** right panel, PMT photocathode reflection leads to a drop in large wavelengths, over 600 nm. On the side of gamma-lines, illustrated in the left panel, only $\sim 2\%$ of Cerenkov photons generated in the region of 250 - 650 nm arrive at the PMTs and are detected; when the QE is applied, this number lowers to $\sim 0.45\%$. The number of Cerenkov photons is ~ 750 and ~ 268 per event for the 4.4 MeV and n capture, respectively. Finally, the positron signal is expected to be higher, with 5025 Cerenkov photons per event (see **table 4.1**). The right panel of **figure 4.12** shows that the fraction of VPMThits is slightly lower $\sim 1.5\%$ and 0.33% when QE is applied. Regarding these results, it can be assumed that only a few VPMThits per gamma-ray are expected to

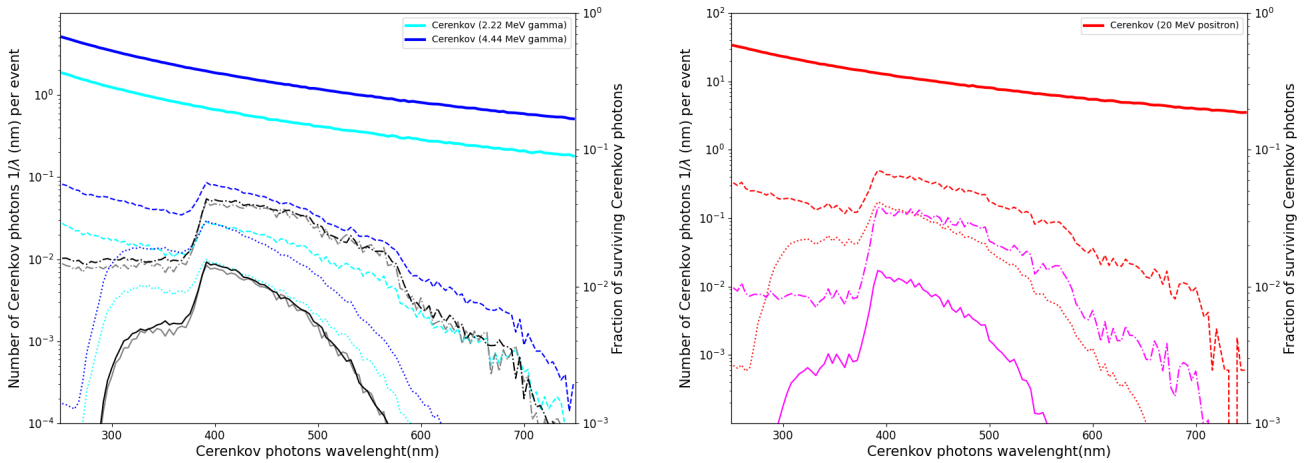

Figure 4.12: Cerenkov photon emission as a function of the wavelenght from GEANT simulation of two gamma-ray lines 2.22 MeV (cyan) and 4.44 MeV (blue) in **left panel**, and 20 MeV positron (red) in **right panel** in the muon veto. The hierarchy of the lines is: solid lines, number of Cerenkov photons; dashed lines, number of VPMThits; and dotted lines VPMThits applying QE. In grey (2.22 MeV gamma), black (4.4 MeV gamma) and pink (20 MeV positron) the fraction of the number of Cerenkov photons becoming VPMThits (dot dashed line) and the fraction after applying QE (solid line).

arrive to the muon veto PMTs. For example, the number of Cerenkov photons for 2.22 MeV is around 268 per event, and only roughly 1 will survive once QE is applied. For the 4.44 MeV gammas-rays in the same wavelength range, the number of Cerenkov photons per event after QE is ~ 3, which predicts that the detection efficiency of neutron can be enhanced with the addition of Gd, and lowering the number of PMT (N-PMT) threshold. In comparison, the from the positron ~ 16 VMPThits are expected to survive after the application of QE.

Detecting neutron capture requires a lower threshold, below the 3-PMT muon veto coincidence. The trigger condition in the muon veto is 5-PMT in a window of 300 ns, expecting a considerable amount of gamma-ray events to be lost, as shown in **figure 4.13**. Notice that in this figure, only the VPMThits surviving prior to the application of the QE is represented. This fraction is projected to be reduced in $\sim$30% because of the QE. Nevertheless, this small fraction of Cerenkov photons reaching PMTs would be much lower, if the reflector panels and foil were not there to compensate for the low PMT coverage. The

Values per event $\lambda \in$ [250,650 nm]	20 MeV e+	4.44 MeV gamma	n Capture (2.2 MeV gamma)
N. Cerenkov photons	5029.5	750.5	268.2
VPMThits	75.05 (1.5%)	15.8 (2.1%)	5.25 (1.95%)
VPMThits (+QE)	16 (0.33%)	3.4 (0.45%)	1.125 (0.42%)

Table 4.1: Summary of results for the GEANT4 simulation in water tank represented in **figure 4.12** for the neutron capture and 4.44 MeV gamma lines, and 20 MeV positrons in the muon veto. Integral values per event in the range of $\lambda \in$ [250, 650 nm] are presented, and its fraction relative to the number of Cerenkov photons in parentheses. The VPMThits are relative to the muon veto PMT array.

eventual detection of a neutron from the CCSN neutrino IBD in the Gd-water configuration, as well as the positron, will depend on the transparency of the water volume. The fraction of reflected Cerenkov photons arriving at the PMTs can be roughly estimated, thanks to the reflection properties of the foil, in the range of photon wavelength where the average reflection is projected to be ∼10% and the water absorption length reaches its maximum (see **figure 4.3**). In this range (∼ 350 nm), the majority of photons contributing to the detection should come from those that reach directly to the PMTs or after being reflected in the ePTFE panels (99.35%) on the exterior walls of the neutron veto. The detection fraction results in ∼ 0.4% for gamma lines and ∼0.7% for positrons regarding **figure 4.12** distributions. The latter number is more appropriate for evaluating Cerenkov photon collection since the aperture of the Cerenkov cone is maximum for 20 MeV positrons. The fraction is low enough to conclude that the contribution of Cerenkov photons arriving directly at PMTs is negligible, and the absorption length in water becomes important as the path length of the Cerenkov photons is enhanced by reflection. To delve deeper into this phenomenon, it will be necessary to track optical photons to determine the mean length of the path and the number of reflections before reaching the PMTs.

Furthermore, CCSN IBD interactions are expected to be homogeneously distributed in the water tank, without any distinction of muon or neutron vetoes. Interactions happening in the frontier of both detectors can lead to the generation of cerenkov photons in both volumes. This implies that neutron PMTs can detect cerenkov photons from interactions generated initially in the muon veto and vice versa. The distribution of the VPMThits fractions of cerenkov photons detected by neutron PMTs and muon veto PMTs, for events generated in this volumes, for 4.4 MeV gamma and 20 MeV positron are presented in **Appendix D.2, figures D.4** and **D.2**. At this point, it can be said that these results represent an averaged geometric uncertainty, as the gamma lines of 2.22 MeV and 4.44 MeV, and the positron are simulated following an homogeneous distribution in water muon veto volume.

As a conclusion the muon veto should detect positron signals with the nominal threshold conditions but present very low detection efficiency for neutron capture, the latter expected to be better with Gd. The objective of the muon veto is not to detect these low energy events as gamma and neutron, but to attenuate them so that they do not enter the TPC, which it does, according to the results reported. Also,

the main background will be high energy gammas > 4 MeV, as with the actual trigger conditions of 5 PMTs, the surviving fraction of PMThits is $\sim 90\%$ as shown in **figure 4.13**, which predicts a considerable detection efficiency but significantly lower compared to the surviving fraction as QE and the rest of threshold conditions are not applied yet.

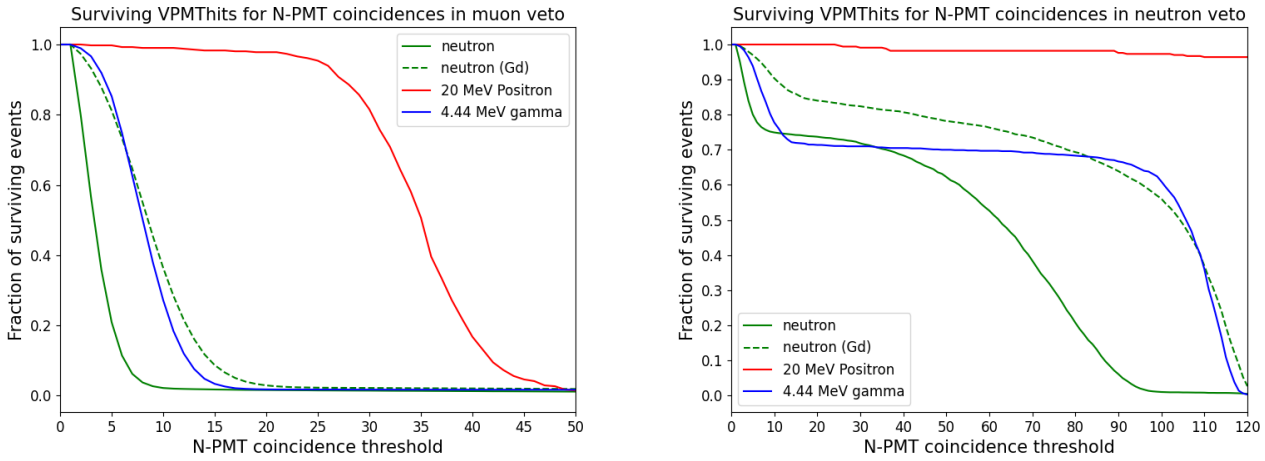

Figure 4.13: Fraction of surviving Cerenkov hits arriving to the PMTs as a function of the number of PMTs coincidence required

4.2 The XENONnT Neutron Veto

The majority of the microphysics concepts discussed in the previous section regarding low-energy background detection, i.e., radiogenic neutrons and gammas (neutrons from muon spallation are irrelevant), are applicable to the neutron veto detection volume. In this volume, low-energy background detection is projected to be substantially more efficient, and the addition of Gd salt to the water is expected to improve it. The neutron veto hosts 8% of the total amount of water. It has an approximate octagonal structure, covered with ePTFE reflector panels in which an array of 120 waterproof Hamamatsu R5912 100-10 PMTs is installed, resulting in a PMT array coverage ten times denser than that of the muon veto (see **figure 4.14**). A reflecting foil with identical optical properties as the ePTFE reflector panels covers the cryostat, which is located in the center of the volume. Neutron background discrimination from WIMP nuclear recoils remains a challenge and can only be somewhat alleviated with fiducial volume cuts and the multi-scattering signature of neutrons. Given the poor neutron capture detection performance of the muon veto, it becomes necessary to create a new volume to successfully reject neutrons penetrating into the immediate surrounding volume of TPC. What was learned from the muon veto during the XENON1T operations has been applied with this new geometry: increased PMT coverage, improved reflection on the walls, and a lower threshold in the trigger conditions. To compare the performance of both detectors for gamma-ray and positron detection, an identical exercise using Cerenkov distributions from the GEANT4 simulation was performed, shown in **figure 4.15**. The first observation is that the reflection efficiency of

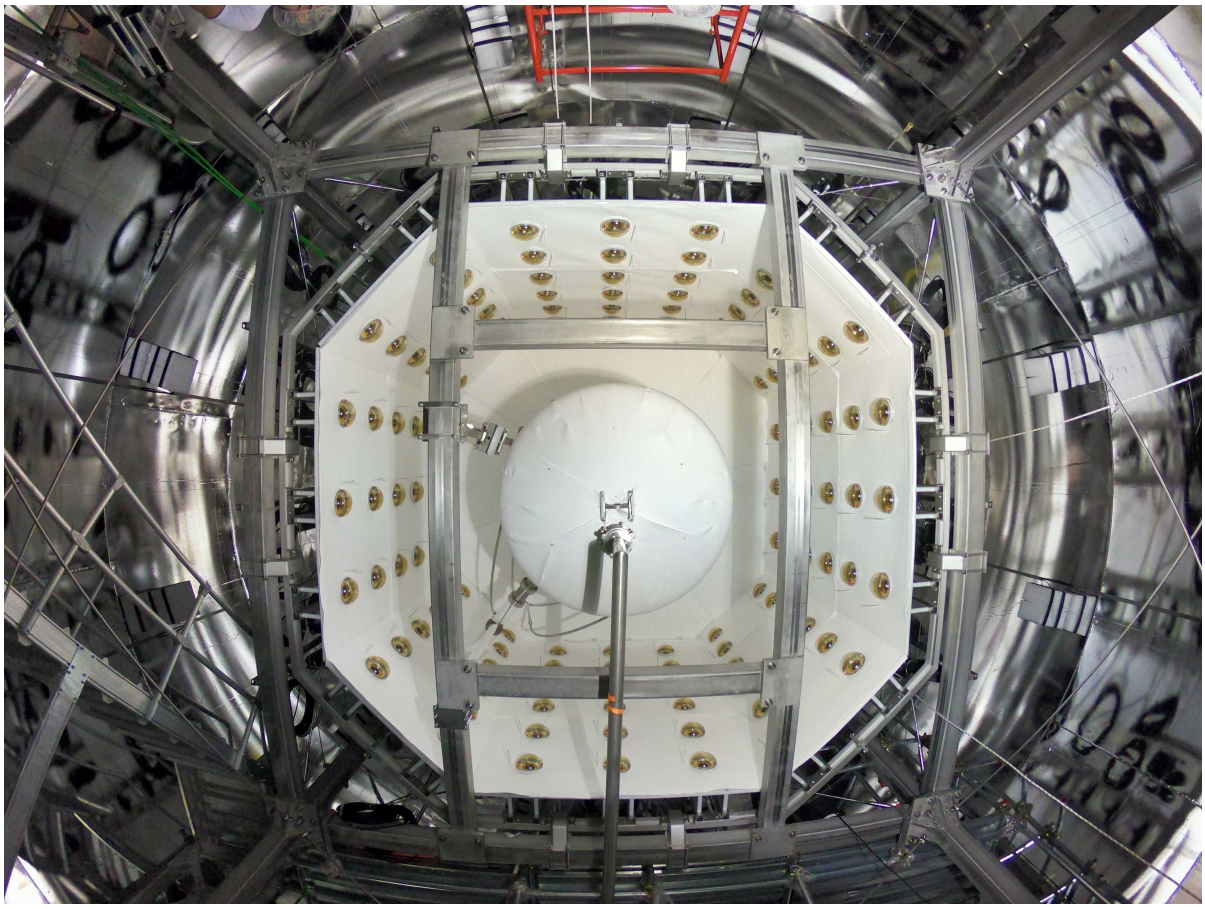

Figure 4.14: Photography from the bottom of the water tank of the neutron veto container, looking up. In the center, covered by a reflective foil, is the cryostat hosting the TPC. The reflectors panel where the 120 PMT arrays are located compound the octagonal structure of neutron veto. Credit: XENON Collaboration.

the ePTFE panels allows for the contribution of wavelengths lower than 350 nm with no dip in unlike in muon veto (see **figure 4.12**). This is critically important because the QE remains high at these wavelengths. For the 2.2 and 4.4 MeV gamma rays, the neutron veto is expected to improve the detection efficiency. This means that more than 30% of the produced Cerenkov photons will reach the PMTs, and more than 6% will be detected as VPMThits in the 250 – 650 nm range after applying the QE. **Table 4.2** summarizes the results of the GEANT4 simulation. The positron detection efficiency has also been improved, with approximately 46% of Cerenkov photons reaching the PMTs, and over 9% in the same region of interest. This result suggests that the light collection efficiency (LCE) of the neutron veto can be estimated 30 times better than the muon veto for CCSN IBD.

As shown in **figure 4.11**, beyond 2 MeV, the number of Cerenkov photons depends on the electron (or positron) path length, which increases with energy linearly as **figure D.6** of **Appendix D.2.2** illustrates. This means that the number of Cerenkov photons increase with energy. In an infinite detection volume with an infinite array of PMT (with full coverage), only the absorption length and reflection efficiency would play a role, and the number of VMPThits from Cerenkov photons arriving to PMTs would also increase.

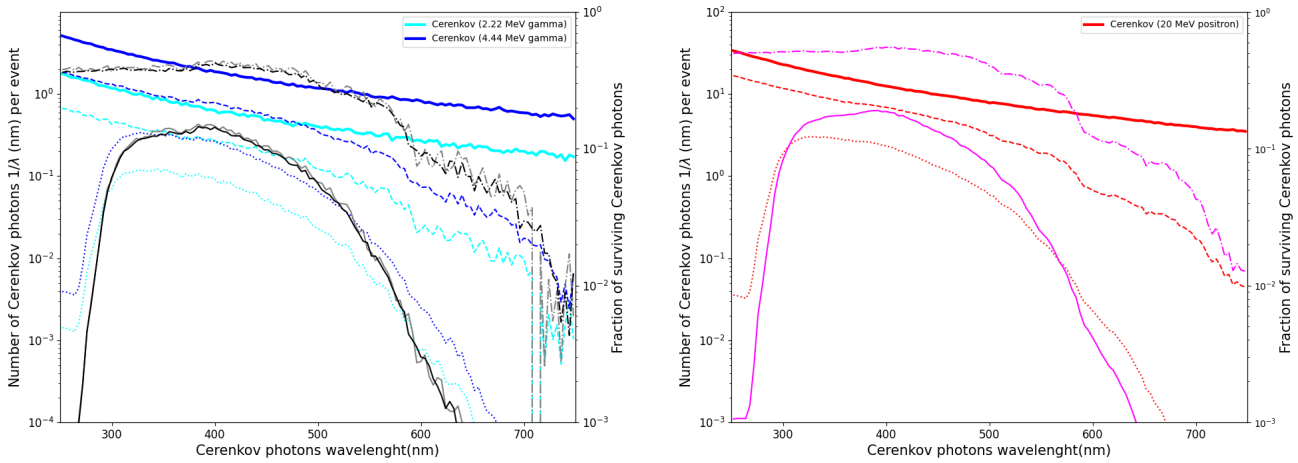

Figure 4.15: Cerenkov photon emission in the neutron veto as a function of the wavelength from GEANT4 simulation of two gamma-ray lines 2.22 MeV(cyan) and 4.44 MeV(blue) in **left panel**, and 20 MeV positron (red) in the **right panel**. Solid lines show the number of Cerenkov photons; dashed lines the number of VPMThits; dotted lines the VPMThits applying QE. Using the y-axis on the right side of the plots, in grey (2.22 MeV gamma), black (4.4 MeV gamma) and pink (20 MeV positron) the fraction of the number of Cerenkov photons becoming VPMThits (dot dashed line) and the fraction after applying QE (solid line).

The reality is that the neutron veto is a small finite volume, and when a certain positron energy is released, for higher energies the number of Cerenkov photons still increases, but a non-negligible amount of them are absorbed and a phenomena of saturation in the number of detected photons happens. In addition, the neutron scattering can lead to a path out of the neutron veto volume, being captured in the muon veto, or in other volumes, such as the cryostat, reflector panels, calibration tubes or other components presenting for example Ni and Fe isotopes than can be potentially capture these neutrons [424]. The evolution of the number of Cerenkov photons and VMPThits in the neutron veto as a function of energy is depicted in **figure D.5** of **Appendix D.2.1**. Around 10 MeV, the fraction of Cerenkov photons that are created out of the neutron veto volume increases. These photons can be detected by the muon veto. The fraction of the number of VPMThits detected by muon veto PMTs from events generated in the neutron veto volume is $\sim$ 2.1%, similar to the gamma rays with a fraction estimated at 2.6%. These values are extracted from the distributions shown in **Appendix D.2 figure (D.2)** and (**D.4**). Nevertheless, these results have to be evaluated, accounting for the fact that the number of Cerenkov photons arriving at the muon veto PMTs — from those photons generated in the muon veto volume — is only $\sim$ 1.5%, as reported in **table 4.1**. De-convoluting this 2.1% of VPMThits from events created in the neutron veto detected by the muon veto PMTs, the number of Cerenkov photons generated out of the volume is significant in the wavelength range of 250-650 nm (see **figure D.5**), representing $\sim$ 10% of the Cerenkov photons created in the neutron veto. Due to the low efficiency of muon veto detection, most of the later photons will be lost due to absorption process.

As mentioned before, these geometric effects and the detection performances are expected to vary

depending on the position of the interaction, due to the huge LCE difference between both vetoes.

Even with these small losses, the detection efficiency of positrons is expected to be extremely high, involving all the PMT array in neutron veto. **Figure 4.13** right panel shows the surviving VPMThits per event as a function of the required number of PMT involved. More than 96% of the events involved 120 PMTs.

Values per event $\lambda \in$ [250,650 nm]	20 MeV e+	4.44 MeV gamma	n Capture (2.2 MeV gamma)
N. Cerenkov photons	5014	751	255
VPMThits	2312 (46%)	254 (34.1%)	91 (35.55%)
VPMThits (+QE)	452.7 (9%)	50 (6.65%)	18 (6.92%)

Table 4.2: Summary of results for GEANT4 simulation in water tank represented in **figure 4.12** for the neutron capture and 4.44 MeV gamma lines and 20 MeV positrons, from IBD events generated in the neutron veto. Integrals values per event in the range of $\lambda \in$ [250, 650 nm] are presented, and its fraction relative to the number of Cerenkov photons in parentheses. The VPMThits are relative to the neutron veto PMT array.

4.2.1 AmBe Calibrations

The AmBe calibration source replicates the expected background signals for WIMP detection, primarily gammas and neutrons in the MeV range. During the disintegration of the ^{241}Am isotope, the AmBe source first emits α particles. These alpha particles should interact with ^{7}Be atoms to create an excited ^{12}C* state or a ^{12}C ground state with a neutron emission, as shown in **figure 4.16**. The de-excitation of ^{12}C* states results in a neutron or a neutron and a 4438 keV gamma. Later, de-excitation is likely to occur in $\sim 50\%$ of the cases (0.46 ± 0.07 [303]). The created ^{12}C(*) states produce a neutron spectrum ranging from a few

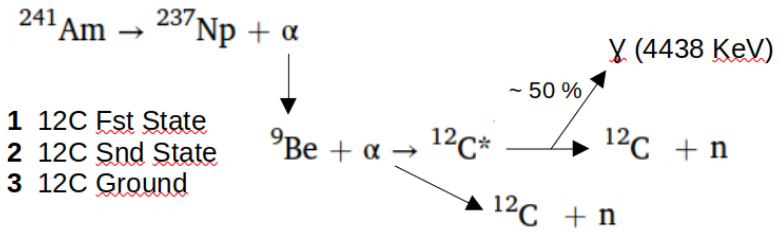

Figure 4.16: Schema of the AmBe source chain disintegration leading to the emission of the ^{12}C gamma lines and the neutron.

eV to 11 MeV, as seen in **figure 4.17**. The first state ^{12}C* is represented by number 1 and accounts for the low energy part. The second excited state is represented by number 2 and is related to the gamma-ray emission. Finally, beyond 6 MeV, the ground state accounts for the high energy part. The CCSN IBD neutron energy spectrum corresponds to neutrons emitted during the first carbon-excited state. **Section**

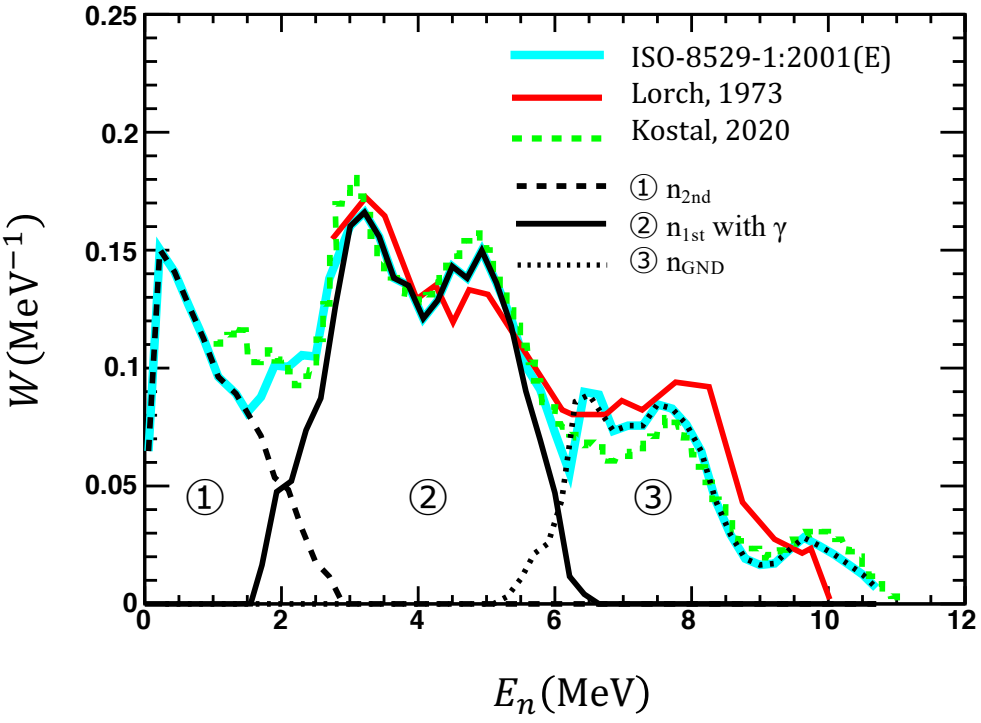

Figure 4.17: Measured neutron energy spectrum of the AmBe source based on ISO 852912001(E) [425], Lorch, 1973 [426], and the recent Kostal [427], without considering the excited states of C. The partial neutron spectrum is added using the predictions of Malaroda [428] in black lines. Associated to the first state $^{12}C^{*}$ (1) in dashed lines, second excited state with gamma emission (2) in solid line and ground state in dotted line (3).

4.3.2.2 will provide more information on this topic. The AmBe NR calibration is used to produce recoil signal with neutrons in the TPC to distinguish the latter from ER. The neutrons entering the TPC are tagged by coincidence with the emitted 4.44 MeV gamma ray signal in the neutron veto. More specifically, a narrow window of approximately 400 ns occurs between the S1 generated by the neutron NR and the Cerenkov photons emitted during the gamma-ray energy deposition in the neutron veto. This coincidence aids in pairing the aforementioned S1 with the expected S2 from the neutron NR, reducing the chances of accidental coincidence and ER from the background. As noted, this gamma emission is projected to happen half of the time; however, this proportion is meaningless because the AmBe source has a high activity with 157±6 ^{241}AmBe disintegrations per second.

AmBe calibrations, on the other hand, aim to examine the rejection capability of neutron veto in relation to neutron NR background in the TPC by using signal coincidence between the two detectors. The addition of neutron capture gamma rays to the 4.44 MeV gamma and neutron NR S1 coincidence signal expands the time coincidence window of the three signals to 600 μs. The temporal window begins with single-scatter neutron occurrences in the TPC; as previously stated, neutrons have multi-scattering fingerprints that may allow distinguishing them from WIMPs or neutrinos NR. The tagging efficiency is expected to be 67.5± 2.9 % with at least 5 PMTs contributing to the neutron veto within the time

coincidence window [347]. However, the large time frame for coincidence is related to the fact that the typical time of neutron capture is 200 μs, decreasing the efficiency of the tagging, as background from accidental coincidences becomes important. Adding Gd salt reduces the typical time for neutron capture in the Gd nucleus to 30 μs. The recent inclusion of Gd (0.02% or $Gd(SO_4)_3$ salt 500 ppm) is expected to boost neutron tagging efficiency. **Figure 4.18** compares neutron tagging efficiencies in ultrapure water with the specified Gd concentration, as a function of the event area PE threshold. Those efficiencies are obtained with 5 PMT coincidences in a time range of 250 μs. This Gd concentration improves tagging efficiency from $54.1 \pm 1.0\%$ to $76.9 \pm 1.5\%$. The temporal window remains large, but it minimizes background and AC while increasing the number of Gd neutron captures that occur within it. The next section will provide a quick discussion of Gd addition status in order to comprehend its implications for the CCSN IBD signal analysis.

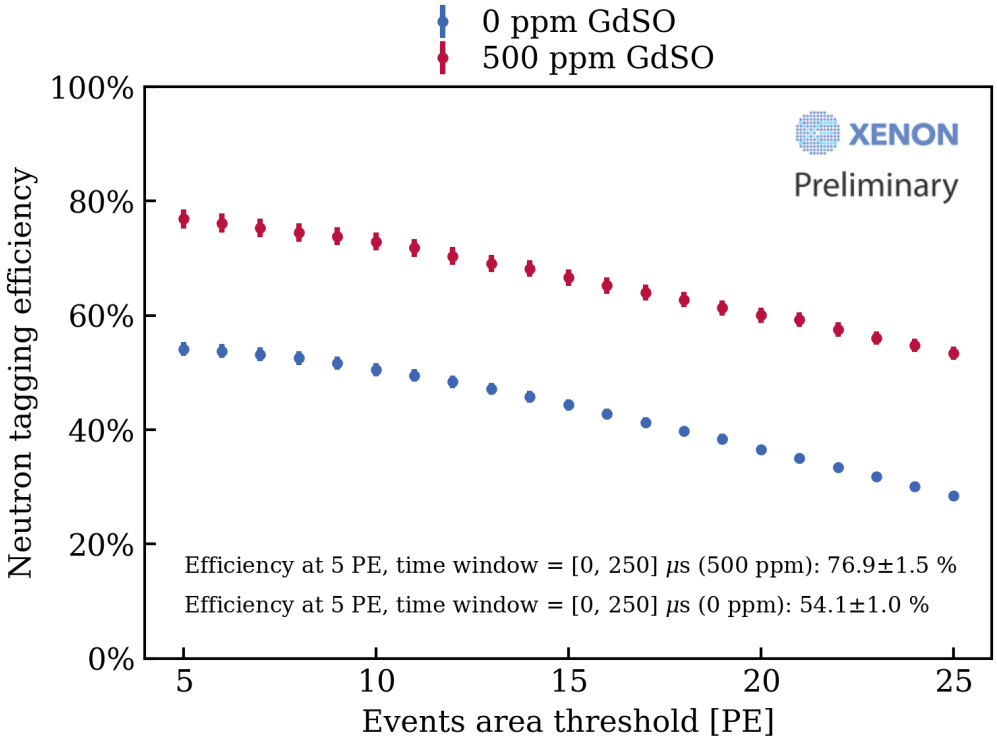

Figure 4.18: Neutron tagging efficiency of neutron veto during AmBe calibrations as a function of the required event area threshold. In blue the ultrapure water configuration and in red the $Gd(SO_4)_3$ salt 500 ppm. Both results require 5 PMT coincidences in a time window of 250 μs. Credit: XENON Collaboration.

4.2.2 Gadolinium configuration

The injection of Gd salt in the water tank began in May 2023, with 1.5 kg of GDSO (more precisely, $Gd(SO_4)_3$), gradually increasing the bulk injected, as **figure 4.19** shows. After three months, the concentration of Gd salt in the water tank was constant and evenly distributed at 0.05% (equivalent to 500 ppm). Improved neutron capture efficiency with this concentration is expected to be $\sim$ 70% [429], pro-

viding better background rejection along with increasing the rate of background identified in neutron and muon vetoes. As previously noted, neutron capture in Gd will be faster after thermalization of the neutron $\sim 30\ \mu$s, generating a cascade of gamma rays with a total energy ~ 8 MeV [430]. This can be written for the two main isotopes found in Gd salt as follows:

$$\begin{aligned} n + {}^{155}\mathrm{Gd} &\longrightarrow {}^{156}\mathrm{Gd}^{*} \longrightarrow {}^{156}\mathrm{Gd} + \mathrm{N}_{\gamma} \quad (8.536\ \mathrm{MeV\ total}), \\ n + {}^{157}\mathrm{Gd} &\longrightarrow {}^{158}\mathrm{Gd}^{*} \longrightarrow {}^{156}\mathrm{Gd} + \mathrm{N}_{\gamma} \quad (7.937\ \mathrm{MeV\ total}). \end{aligned} \tag{4.6}$$

Notice that often the concentrations are refereed as Gd 0.02% regarding Gd-isotope concentration, and the $Gd(SO_4)_3$, or Gd salt, with its equivalent of 0.05% (500 ppm).

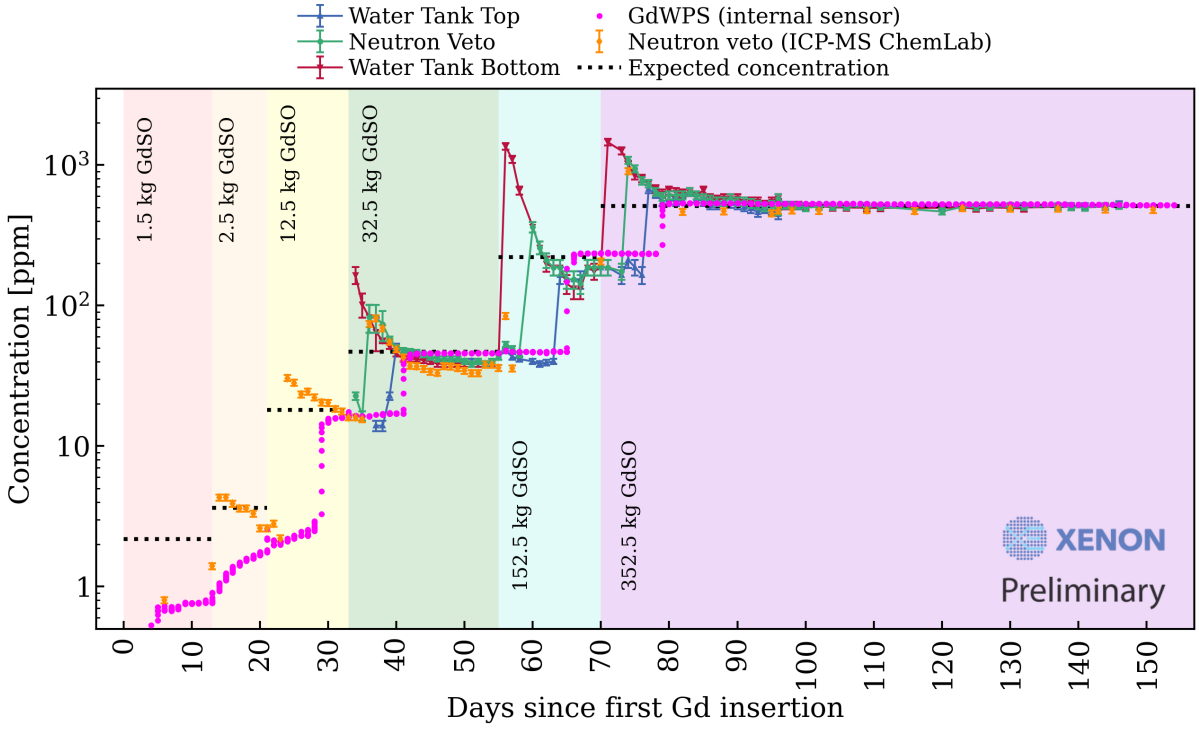

Figure 4.19: GdSO concentration evolution over time in ppm, for the process of Gd injection in the XENONnT water tank. The measurements of the concentration were taken in situ daily with conductivity measurements at different positions of the water tank: top (blue), bottom (red) and neutron veto (green), as well as chemistry lab analysis performed twice a week (orange). Credit: XENON Collaboration.

The same described process during water neutron capture after gamma emission results in Cerenkov photon generation, with a significant increase in their quantity. However, the Gd-cascade spectrum (see **figure 4.20**) is dominated by a significant non-detectable amount of gamma lines: some low-energy gamma lines in the cascade will convert their momentum to electrons via Compton scattering while remaining below the Cerenkov threshold, producing no Cerenkov light. For such gamma spectra, the observable energy transfer is estimated to start around 1 MeV. In this situation, again, the detection of Cerenkov photons is dependent on transparency, which appears to decrease with the addition of Gd salt.

Isotope	Abundance [%]	Cross section [b]
^{152}Gd	0.200	735
^{154}Gd	2.18	85
^{155}Gd	**4.80**	**60 900**
^{156}Gd	20.47	1.8
^{157}Gd	**15.65**	**254 000**
^{158}Gd	24.84	2.2
^{160}Gd	21.86	1.4

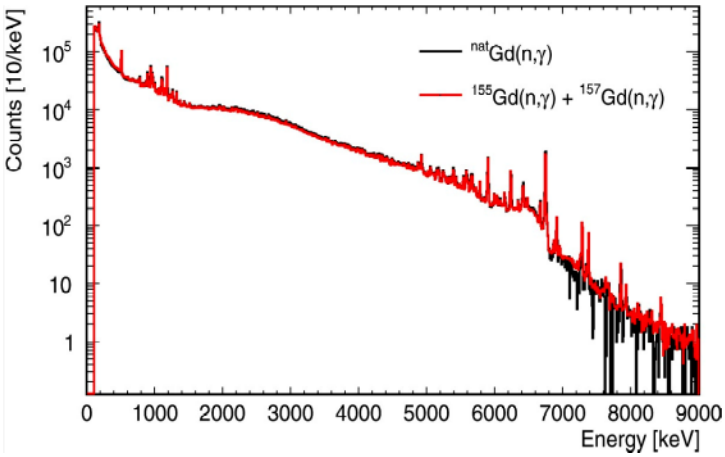

Figure 4.20: **Left:** Abundances of natural gadolinium salt and respective capture cross-section in barns (1 barn $= 10^{-24}\,\mathrm{cm}^2$ when the neutron is thermalized. **Right:** Neutron Gd Capture gamma ray cascade spectrum lines. Natural gadolinium is in red and ^{155}Gd + ^{157}Gd spectrum in green. Both figures are from [430]

Figure 4.21 depicts the evolution of the center time, which was previously defined in equation **3.39** of **Section 3.3.4**, during the Gd injection procedure. This evolution diminishes as the Gd mass concentration increases. The center time provides information on the transparency of the medium and reflection, as well as the geometry effects of the detector. Therefore, the center time value can be read as the typical travel time for a Cerenkov photon before being absorbed by the PMT photocathode, resulting in a detectable signal. Starting to count from the first VPMThit time, the time distribution of the VPMThits is expected to follow an exponential pattern, scaled by three different contributions: τ_{geo} for geometric uncertainties; τ_{att} for the attenuation process, i.e., scattering and absorption; and τ_{ref} for reflection in ePTFE and foil panels:

$$VPMThit_t(t) = e^{-(t/\tau_{geo} + t/\tau_{att} + t/\tau_{ref})}. \tag{4.7}$$

This distribution applies to "real" physics events such as neutron capture, but it differs from background processes such as PMT dark noise or AC, serving as an effective distinguishing parameter between the two. It is also expected to differ from neutrons and positrons, as shown in the right panel of **figure 4.22**. In this respect, the center time will be one of the parameters that define the ROI for the CCSN IBD signal. Assuming the exponential distribution of the VPMThit times, the center time is expected to lead to a Gaussian and may be stated using equation (4.7) and t_0 the reference VPMThit time as:

$$VPMThit_{CC} = \frac{1}{N}\sum_i VPMThit_t(t_i) - t_0, \tag{4.8}$$

where N represents the number of VPMThits used for normalization. The 20 MeV positron GEANT4 VPMThit times distribution is fitted by an exponential distribution in **figure 4.22** using the equation (4.7). The total τ accounts for the aforementioned effects regarding transparency and geometry: $\frac{1}{\tau} = \frac{1}{\tau_{geo}} + \frac{1}{\tau_{att}} + \frac{1}{\tau_{ref}}$ yields a value of 58.27 ns, which is very close to the median (58.38 ns) of the center time distribution (equation (4.8)), as shown in the right panel of **figure 4.22**.

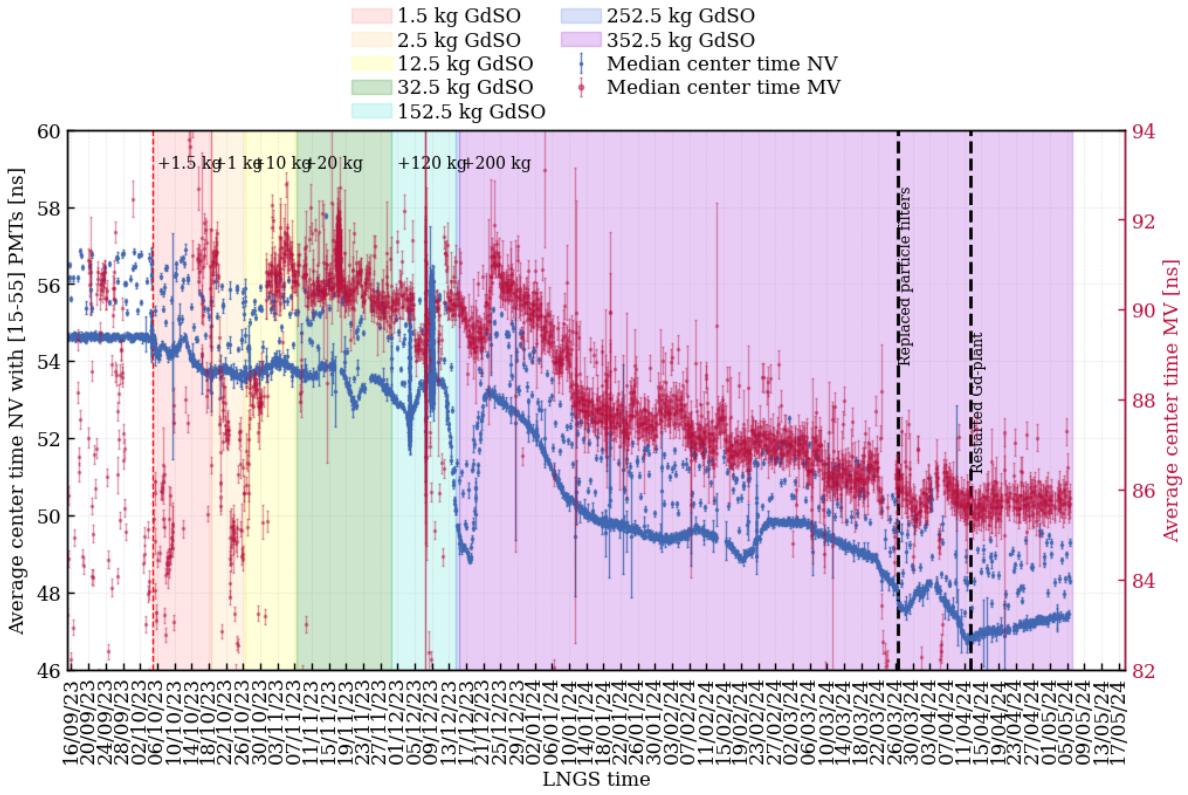

Figure 4.21: Center time evolution during the insertion of Gd in the water tank. On the left y-axis, the values of center time in the neutron veto (blue). On the right y-axis, the values concerning the muon veto (red). Credit XENON Collaboration.

The definition of center time (equation (3.39)) for the XENONnT data structure is different. The data structure for neutron and muon vetoes is simpler than the TPC one, shown in **Section: 5.3**. However, the center time is defined in the same way as the equation (3.39), resulting in the mean VPMThit time from the reference VPMThit time t_0, weighted by the VPMThit area. In equation (4.8), the weights are handled by the τ parameter, which dependends on the wavelength of the Cerenkov photon. The latter is correlated with the creation of a PE, as the QE is also wavelength dependent. In addition, once the Cerenkov photons are absorbed by the photocathode, the initial dynode electron (or, more rarely, the double electrons) is generated, participating in the charge amplification dynode chain inside the PMT, with a probability that varies depending on the incident photon wavelength [431]. The cited work evaluates wavelength dependency for the scenario of double photoelectron DPE generation (see **Section 3.3.3**). The findings of this study on global pulse area distributions as a function of wavelength (including single photoelectron (SPE)) are shown in **figure D.8** of **Appendix D.2.4**.

The addition of Gd salt does not affect the contributions of τ_{geo} and τ_{ref}, therefore any changes in the center time distributions are predicted to come from the transparency term τ_{att}. The value of the τ parameter has been determined from GEANT4 simulation. This simulation accurately accounts for the τ_{geo}. The transparency is also included in the GEANT4 physics list and the reflection parameters of panels

are the input described in **figure 4.3**. However, the genuine contribution of absorption and reflection must be determined using data from AmBe calibrations, investigating the center time distributions. The mean can be approximated to the τ of the exponential distribution of incoming VPMThit times, as previously indicated. Nonetheless, the MC result distributions above are sufficient to point out that the decrease in the center time shown in **figure 4.21** can be related to an increase of the τ_{att} induced by the addition of the Gd. In addition, because the three parameters are associated in the final τ, they can be influenced in a second order. The τ_{ref} is likely to vary due to the absorption or wavelength shift of Cerenkov photons, which might affect the reflection efficiency. Additionally, if there are spatial uniformities in the Gd concentration, the τ_{geo} can be modified. In **Section ??**, the CCSN simulation chain will be tested with AmBe calibration data and it will be the occasion to optimize the center time fit parameters.

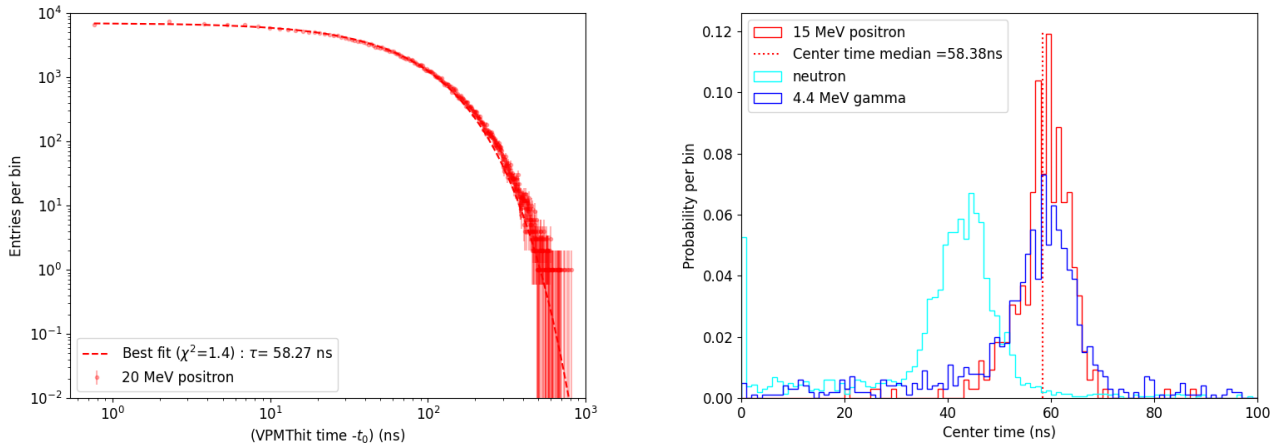

Figure 4.22: **Left:** Time distribution of the VMPThits in the neutron veto for the 20 MeV positron simulation, fitted with an exponential function to obtain the τ value. **Right:** Center time distributions for the same positron simulation in (red), the neutron (cyan) and the 4.44 MeV gamma line (blue).

Transparency losses have the opposite effect to Gd water dopage: they reduce the background rate. **Figure 4.23** compares the mean rates in a 10-second window for SR1 (pure water) and SR2 (Gd-water) in the expected IBD ROI for the muon veto. This region of interest will be accurately described in **Chapter 5**. However, the later region can be deduced from the results of the fraction of surviving PMTs as a function of the N of PMT in coincidence, $N_{PMT} < 20$. This condition is sufficient to distinguish the ROI from the muon region ($N_{PMT} > 50$). In this region, the rate drops from 13.26 Hz to 10.23 Hz. This decrease in transparency is likely to impact the IBD signal as well. Given that the muon veto background in the ROI is mostly composed of gammas and neutrons, it is projected that it will be even more difficult to observe neutron capture in Gd than in water configuration due to this transparency loss. The neutron veto detection lies less in water transparency than the muon veto, the increased PMT coverage and the efficiency of ePTFE reflection panels can compensate for this transparency loss, leading to significantly weaker absorption effects. In addition, the geometric effect leads to a smaller photon path before arriving to PMTs in the neutron veto. Even though the center time decreased throughout the

addition of Gd in the neutron veto, it appears to have stabilized, recovering values before Gd. The rate in the IBD ROI of the neutron veto, as seen in **figure 4.24** slightly increased. This might imply that the transparency is recovering the SR0 (water only) proprieties, and is increasing as expected with the Gd addition. Regarding the neutron detection, the tagging efficiency of the neutron has risen, as illustrated by **figure 4.18**. Nevertheless, no diagnosis of the causes of transparency loss has been completed, for this a monitoring of the rate is currently being performed in muon and neutron veto. With the actual conditions, it will be shown in **Section 5.3** that the neutron Gd capture region resulted from AmBe calibrations is far from the background region, producing more PE per event, enhancing the neutron detection efficiency.

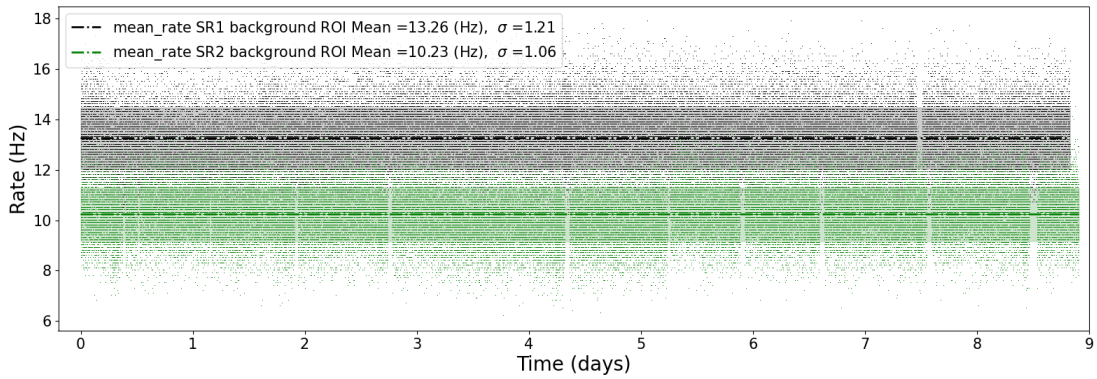

Figure 4.23: Mean rates for the SR1 (black) and SR2 (green) in the ROI in a time window of 10 seconds for the muon veto. The bands correspond to the 1σ of the best fit through a Gaussian distribution for both science runs (SR1 and SR2).

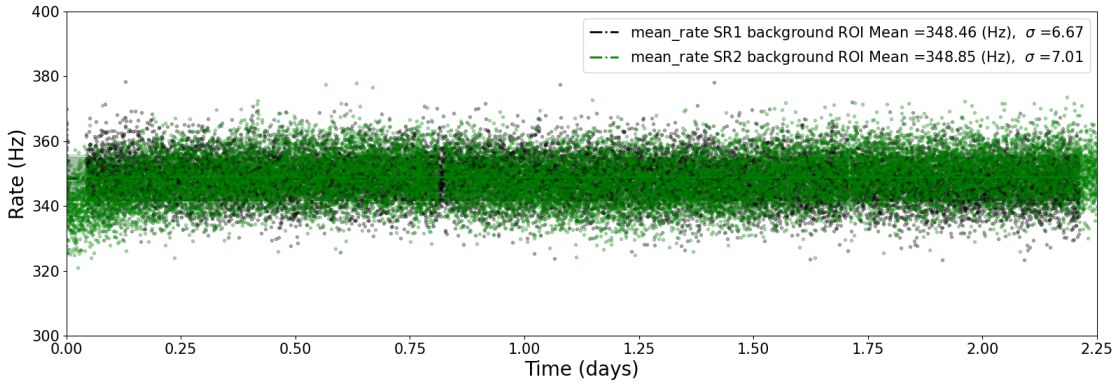

Figure 4.24: Mean rates for the SR1 (black) and SR2 (green) in the ROI in a time window of 10 seconds for the neutron veto. The bands correspond to the 1σ of the best fit through a Gaussian distribution for both science runs (SR1 and SR2).

4.3 CCSN Neutrino Inverse Beta Decay

The IBD is a weak interaction nuclear process involving free, or quasi free, protons not bounded in a nucleus and an electron antineutrino, analogous to the electron capture [432], which is the dominant mechanism of antineutrino scattering at energies below a few tens of MeV [433]. In 1956, Reines and Cowan observed IBD from reactor neutrinos interacting with hydrogen atoms of a liquid scintillator by employing the delayed signals from positron annihilation and neutron capture in Cd ($\sim$ 9 MeV gamma rays) dissolved in the scintillator [434]. Its cross-section is well known, its uncertainties have been estimated using experimental data [432, 433, 435, 436], leading to accurate measurements of reactor neutrino flux [437]. IBD in heavy water (D_2O) was one of the channels used by the SNO experiment to show the evidence of the ^8B solar neutrino flavor transformation [178]. Similarly, this channel was used by Super-K to detect the reactor neutrino flux [438]. In addition, geo-neutrinos were observed by the Borexino experiment also using IBD [439].

In the water medium, $\bar{\nu}_e$ interaction with a proton in water, will change one of the up quarks (u) to a down quark (d) through the exchange of a W^+ as described by the Feynman diagram of **figure 4.25**. Only the two hydrogen protons that are not bounded by a nucleus as the oxygen ones will contribute to the reaction, finally forming a deuterium atom. The microphysics description is essential for predicting the ROI and the likelihood of detecting the CCSN $\bar{\nu}_e$ signal for each IBD product, i.e., positron and neutron. The positron's IBD mean energy was used to understand the detector response using the GEANT4 simulation for a given positron energy. However, the goal is to simulate the IBD signal using the whole energy spectra of positrons and neutrons (including the Gd configuration). For the latter, only its capture is predicted to be observed, as neutron scattering with water atoms at the neutron IBD energies (see **Section 4.3.2.2**) is not expected to create any detectable Cerenkov light. This section will go over the IBD rates for neutrons and positrons, as well as the angular distribution of their emissions.

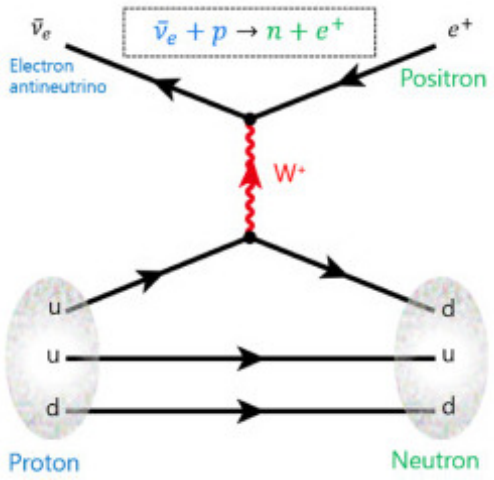

Figure 4.25: Feynman diagram of the IBD. Figure from reference [440]

4.3.1 IBD cross-section

The IBD cross-section on water is $\mathcal{O}(100)$ lower than that of CEνNS on Xe. Furthermore, IBD interaction only affects the $\bar{\nu}_e$ flavor, which accounts for $\sim$1/6 of the total CCSN ν flux. Nonetheless, the enormous volume of water (700 tonnes) compensates for the 5.9 tonnes of LXe, and similar rates as the CEνNS in the TPC are expected for the IBD interactions in the water tank. In **figure 4.26**, the IBD cross-section is compared to that of the CEνNS and the ES, the other process that will be included for the CCSN investigation. The IBD cross-section for CCSN $\bar{\nu}_e$ energies $\sim$ 5 - 100 MeV differs from that of accelerator neutrinos ($>$ GeV) and requires the addition of disregarded terms at these high energies, as well as radioactive corrections [246]. In elastic scattering, the cross-section of the figure represents the total incorporating all neutrino flavors [441]: charged and neutral current ES for ν_e and $\bar{\nu}_e$, plus neutral current ES for ν_x. **Section 4.4** will provide more information on these interactions. The IBD interaction

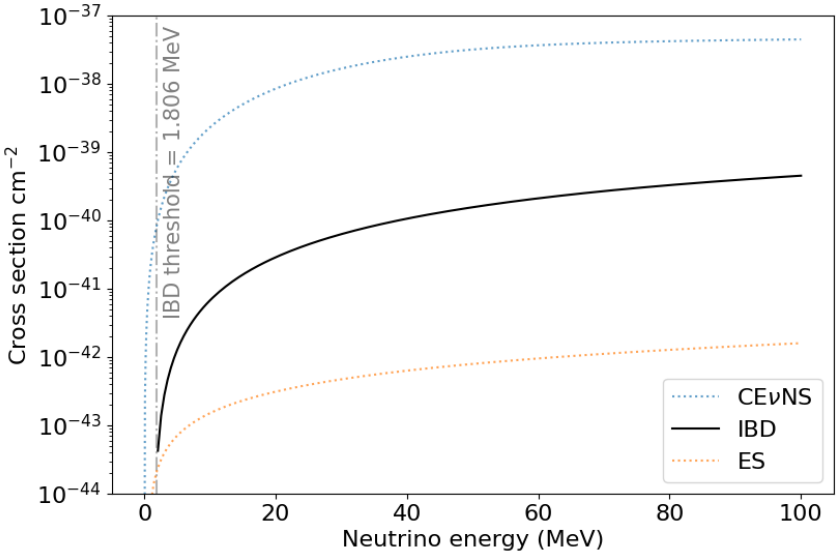

Figure 4.26: Inverse beta decay cross-section as a function of $\bar{\nu}_e$ incoming energy from [246]. Neutrino energy threshold 1.806 MeV is highlighted. In blue dotted line the CEνNS cross section and in orange dotted line the ES cross-section are represented.

is characterized by a neutrino energy threshold of 1.806 MeV, which corresponds to the mass difference between the proton and neutron plus the positron. In the lab reference frame with the proton at rest, the neutrino minimum energy results in:

$$E_{\nu_{th}} = m_n + m_e - m_p, \tag{4.9}$$

where the mass of the neutron is m_n= 939.5654133$\pm$0.0000058 MeV, the mass of the proton is m_p =938.272046 MeV and the electron mass is m_e= 0.51099892 MeV [78].

However, anticipating the impact on the rate of the positron Cerenkov threshold in water, $E_{e_{th}}$ = 772 keV, the antineutrino energy spectrum can be reduced in order to account for the latter. This results

in a rewritten expression (4.9) as:

$$E_{\bar{\nu}_{e_{c_{th}}}} = m_n + E_{e_{th}} - m_p. \tag{4.10}$$

Finally, the minimum energy for an antineutrino to produce a positron Cerenkov signal is $E_{\bar{\nu}_{e_{c_{th}}}} = 2.0684\,\text{MeV}$. However, these values are far below the antineutrino CCSN flux mean energy $\langle E_{\bar{\nu}_e} \rangle \sim 15$ MeV and are not expected to alter the rate.

The cross-section can be defined in terms of neutron or positron energy. It is frequently used in literature as a function of the latter due to its quasi-linearity with neutrino energy. The reader can find the explicit expression of the cross-section, in reference [246]. The positron differential cross-section can be reproduced as a function of the Mandelstam[5] variable t (specified in **Appendix D.3**, equations (D.3)) and the Jacobian member $\partial t/\partial E_e$ as:

$$\frac{d\sigma(E_{\bar{\nu}_e}, E_e)}{dE_e} = \frac{\partial t}{\partial E_e}\left(\frac{d\sigma}{dt}\right) \qquad t = m_n^2 + m_p^2 - 2m_p(E_{\bar{\nu}_e} - E_e) \qquad \text{and} \qquad \frac{\partial t}{\partial E_e} = 2m_p. \tag{4.11}$$

The cross-section in **figure 4.26** is the integration of equation (4.11) in the range of the positron energy boundaries for a given antineutrino energy $E_{\bar{\nu}_e} \in [E_{\bar{\nu}_{e_{c_{th}}}}, E_{max}]$. It is worth noting that E_{max} can be fixed at 100 MeV.

$$\sigma(E_{\bar{\nu}_e}) = \int_{E_{e_1}}^{E_{e_2}} \frac{d\sigma(E_{\bar{\nu}_e}, E_e)}{dE_e} dE_e. \tag{4.12}$$

These bounds can be defined as [246]:

$$E_{e_{1,2}} = E_{\bar{\nu}_e} - \delta - \frac{1}{m_p} E^{\text{CM}}_{\bar{\nu}_e}(E^{\text{CM}}_e \pm p^{\text{CM}}_e), \qquad \text{with} \qquad \delta \equiv \frac{m_n^2 - m_p^2 - m_e^2}{2m_p}. \tag{4.13}$$

The indexed CM values relate to the central mass of **Appendix D.3**, equations (D.4).

4.3.2 IBD rates

Regarding the expression of the cross-section (4.12), the differential neutrino energy spectrum $\frac{dR}{dtdE_{\bar{\nu}_e}}$ is obtained through its convolution with the 2D-CCSN neutrino spectrum $\bar{\nu}_e$ flux $\frac{dN}{dtdE_{\bar{\nu}_e}}$ arriving at the Earth (already defined in equation (2.63) of **Section 2.6**). Neutrino flavor oscillations must be accounted for, and the mass ordering (MO) is likely to influence the rate. For a given mass ordering i (NMO or IMO), the differential rate can be expressed as:

$$\frac{dR_i}{dtdE_{\bar{\nu}_e}} = N_w \times f_p \times \frac{1}{4\pi d^2} \times \frac{dN_i}{dtdE_{\bar{\nu}_e}} \times \sigma(E_{\bar{\nu}_e}), \tag{4.14}$$

[5]Mandelstam variables are Lorentz-invariant variables describing the kinematics of particle reactions, using 4-momentum conservation. This variable was introduced by S. Mandelstam in 1958 [442].

where N_w is the number of water atoms ($N_w = (1/(18\times1.67\times10^{-30}))$) and f_p is the proportion of free protons per water molecule contributing to the interaction, which is equal to 2 [443] exclusively for hydrogen. The neutrino flavor oscillated spectra used for the convolution accounts for the adiabatic flavor transformation induced by the MSW effect [202] (see **Section 2.5.2**) in the CCSN medium, as well as vacuum oscillation during neutrino travel to Earth.

Integrating the (4.14) over time across the 10 seconds of the neutrino burst yields the differential antineutrino energy rate:

$$\frac{dR_i}{dE_{\bar{\nu}_e}} = \int_{t_0}^{t_1} \frac{dR_i}{dt dE_{\bar{\nu}_e}} dt. \tag{4.15}$$

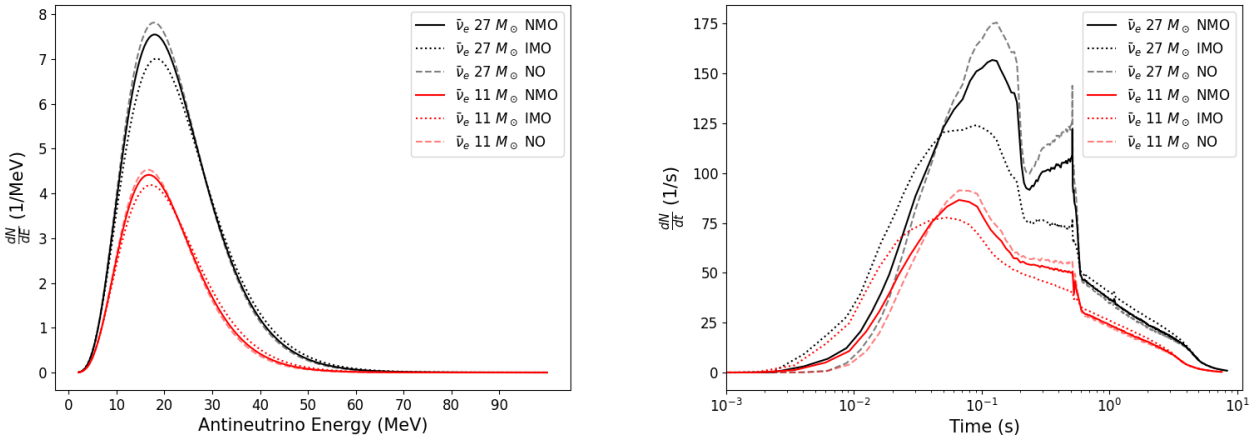

Figure 4.27: **Left:** IBD rates as a function of the incoming $\bar{\nu}_e$ energy (from equation 4.15) for the two chosen *Bollig 2016* model progenitors of $27M_\odot$ and $11M_\odot$ at 10 kpc for the NMO and IMO instances. As comparison, dashed lines show the spectrum neglecting any flavor oscillation. **Right:** Similarly, IBD rates as a function of the time (from equation 4.16)

The **figure 4.27 (left)** displays the IBD rates as a function of the incoming $\bar{\nu}_e$ energy for the two chosen *Bollig 2016* model progenitors of $27M_\odot$ and $11M_\odot$ at 10 kpc for the NMO and IMO instances. The spectrum, neglecting any flavor oscillation, is represented by the dashed lines in order to compare the impact of neutrino flavor oscillations. Shown in **Section 2.6**, flavor transformations, mainly $\bar{\nu}_e \rightarrow \bar{\nu}_x$, produce a less pinched spectrum, the high energy tail being less affected by coherent scattering suppression (see **Section 2.3**). Moreover, the IMO $\bar{\nu}_e$ spectra are less pinched than the NMO cases since the high energy tails are less suppressed, leading to an increase of the spectra in this region. The $11M_\odot$ spectra have a somewhat lower mean energy (21.25 MeV) compared to the $27M_\odot$ spectra (22.34 MeV) for the NMO mass ordering. This fact may have an impact on the final observed number of events when the interaction spectrum is convolved with the neutrino detection efficiencies, which are expected to increase with positron energy.

The rate evolution can also be determined with the neutrino energy integration of the equation (4.14), taking into consideration the specified IBD energy threshold:

$$\frac{dR_i}{dt} = \int_{E_{\bar{\nu}_e c_{th}}} \frac{dR_i}{dt dE_{\bar{\nu}_e}} dE_{\bar{\nu}_e}. \tag{4.16}$$

Neutrino flavor transformations also influence the rate over time. This has a major impact during the accretion phase, as shown in **figure 4.27 (right)**. Again, the unoscillated spectra are depicted by dashed lines for both progenitors. These are reduced when oscillations are considered, for both NMO and IMO scenarios, while their rates are enhanced during the neutronisation and cooling phases, particularly in the IMO case. Regarding the 27 $M_\odot$ progenitor, the increase in the rate expected after the explosion, $\sim$ 250 ms, is flattened for the IMO, significantly reducing the rate. On the contrary, during the cooling phase, rates are higher in the IMO scenario than in the NMO. **Table 4.3** summarizes the expected number of interactions during the several CCSN neutrino burst phases.

One interesting point regarding the different expected performances from the muon and neutron rates regarding the IBD signal detection reported in the **Section 4.1.3** and **Section 4.2** is the number of interactions that are predicted to happen in the neutron veto volume, and finally being detected by neutron veto PMTs, or on the contrary by the muon veto PMT channels. It was stated that about 10% of Cerenkov photons *escape* (are finally generated out of the volume) for positron of 20 MeV, which definitely makes this geometric effect a source of uncertainty, regarding the number of events that can be detected in the neutron veto. The values presented in **table 4.3** represent the sum of interactions in the 700 tons of water, including the neutron and muon veto volumes. The numbers in parentheses are the expected interactions in the neutron veto volume, not necessarily the ones observed by the PMTs in the former. It can be concluded that less than one event[6] is expected during the neutronisation phase in the neutron veto. Furthermore, only 13 and 7 CCSN IBD interactions are expected to happen during the burst for the $27M_\odot$ and $11M_\odot$ progenitors, respectively.

CCSN Phase	27 $M_\odot$ (NMO)	27 $M_\odot$ (IMO)	11 $M_\odot$ (NMO)	11 $M_\odot$ (IMO)
Neutronisation (0 - 0.05 s)	3 (0 *)	4 (0)	2(0)	3 (0)
Accretion (0.05 - 1 s)	77 (6)	64 (5)	42 (3)	38 (3)
Cooling (1 - 10 s)	84 (7)	92 (7)	43 (3)	47 (4)
Total (0 - 10 s)	**164 (13)**	**160 (13)**	**87 (7)**	**88 (7)**

Table 4.3: Summary of the expected IBD interactions in each phase of the CCSN neutrino burst for the two progenitors $27M_\odot$ and $11M_\odot$ at 10 kpc in the NMO and IMO cases. The values are for the 700 tonnes of water: neutron veto plus muon veto volumes. In parenthesis the number of expected events in the neutron veto volume

Another interesting feature is related to the temporal evolution, namely the detection of the maximum rate. **Figure 4.28** depicts the expected rates of the muon (left panel) and the neutron (right panel) vetoes during each CCSN burst phase. The greatest rate is expected to be observed within the first second of the burst, similarly to the TPC for CEνNS interaction. In addition, in the first second, a similar fraction of IBD

[6]The number of events is an integer by definition; the 0 values indicate that less than 1 interaction is expected. Some of the values are rounded using one decimal precision, anticipating CCSN flux uncertainties that can lead to these values.

interactions is expected: 49% and 51% in the NMO case for the 27 $M_\odot$ and 11 $M_\odot$ progenitors, respectively. However, in the IMO scenario, these fractions reduce to 40% and 47% for the same progenitors, noting that the large progenitor is more influenced than the lightest one regarding mass ordering. The muon veto exhibits the maximum rates in the first second, with 74.45 Hz (66.5 Hz) and 42.15 Hz (52.43 Hz) for the 27 $M_\odot$ and 11 $M_\odot$ for the NMO (IMO), respectively. These are suggestive values for the expected maximum ones when a rolling window will be rolled over the IBD rate. The resulting maximum rates are greater than the values of mean rates in the 10-second time window in the ROI muon veto background represented in **figure 4.23**. According to the previous findings regarding the maximum rolling window rates of the TPC background, the former should be higher than the mean rates. Nonetheless, the mean rates of IBD in the 10-second burst may be inferred from **table 4.3**, resulting in $\sim$ 16 Hz and $\sim$ 8 Hz, for each progenitor respectively which are close to the values of the muon veto background in ROI.

On the side of the neutron veto, the maximum rates are lower: 6.4 Hz (5.78 Hz) and 3.66 Hz (4.55 Hz) for the 27 $M_\odot$ and 11 $M_\odot$ for the NMO (IMO). These values are substantially lower than for the ROI rates shown in **figure 4.24**. The lower threshold for the number of PMTs required — three PMTs in the neutron veto trigger — to detect a neutron capture signal, results in a considerable background, which is dominated by PMT dark noise and AC. However, the ROI can be optimized, including other event data parameters, and background cuts can be applied to discriminate between the positron signal and background, as will be shown in **Section 5.5.1**.

The spectra of the CCSN antineutrinos draw the big lines in terms of their rate and time evolution. However, as anticipated, the CCSN detection in the water tank is based on the neutron and positron signals, particularly the latter. In the following section, the IBD rate products will be investigated through their energy and angular spectra in order to use the formers in the first step of the simulation chain.

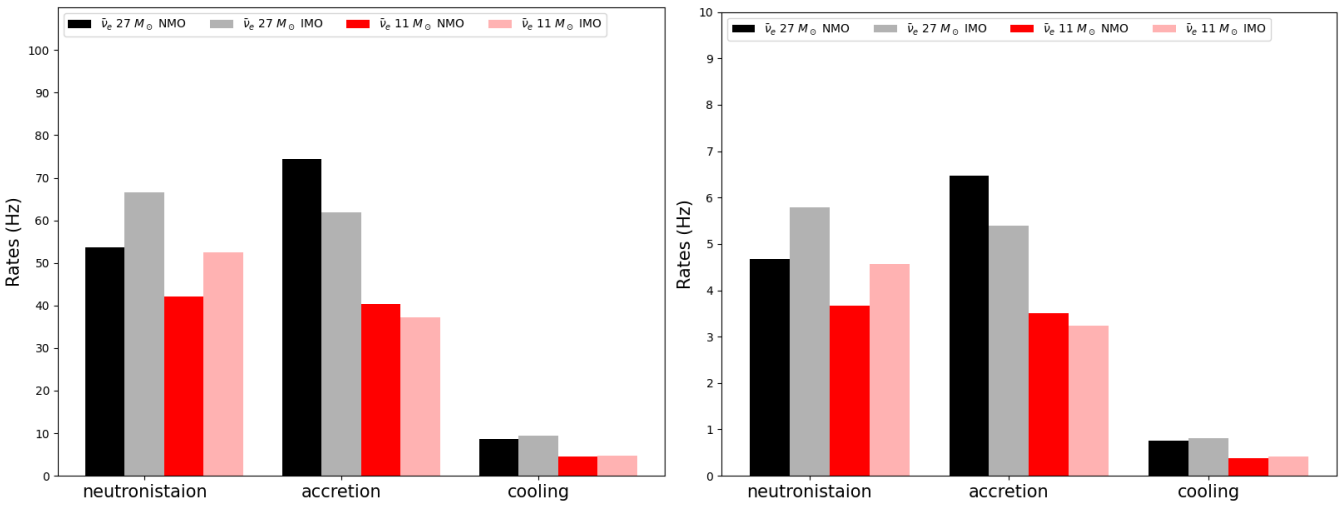

Figure 4.28: **Left:** Mean positron interaction rates for each phase of the CCSN burst in the muon veto . **Right:** Same rates in the neutron veto

4.3.2.1 CCSN IBD Positron

As expected, most of the kinetic energy of the $\bar{\nu}_e$ is transferred to the positron. The shape of the positron energy spectrum will be similar to that of the antineutrino, but its mean energy will be ~ 1.2 MeV lower [443, 444]. The positron energy spectrum can be calculated using equation (4.11) as follows:

$$\frac{dR_i}{dE_e dt} = N_w \times f_p \times \frac{1}{4\pi d^2} \int_{E_{min}}^{E_{max}} \frac{dN_i}{dt dE_{\bar{\nu}_e}} \frac{d\sigma(E_{\bar{\nu}_e}, E_e)}{dE_e} dE_{\bar{\nu}_e}$$
$$E_{min} = E_e + \delta, \qquad E_{max} = \frac{E_{min}}{(1 - 2\frac{E_{min}}{m_p})}. \tag{4.17}$$

The same impact on the $\bar{\nu}_e$ as for flavor oscillation is observed in the positron spectrum. The mean energies for $27M_\odot$ and $11M_\odot$ NMO (IMO) are 20.5 (21.05) MeV and 18.8 (19.45) MeV, respectively. The spectrum of the lightest progenitor has low energy values, as was the case for the $\bar{\nu}_e$. These similarities correspond to the previously reported approximation ($\langle E_e \rangle \sim \langle E_{\bar{\nu}_e} \rangle + 1.2$ MeV) based on obtained values from the $\bar{\nu}_e$ spectrum.

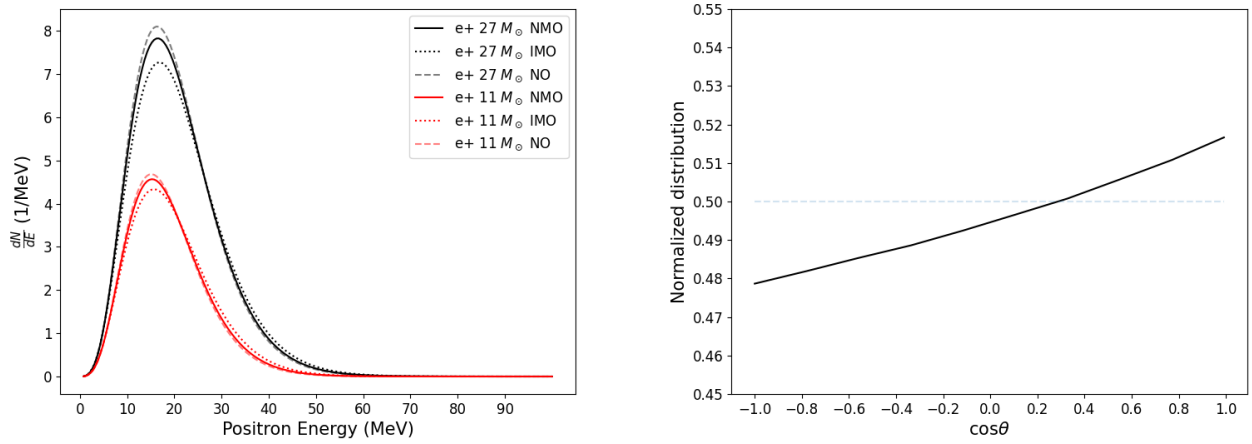

Figure 4.29: **Left:** IBD positron energy spectrum rate for the *Bollig 2016* 27 $M_\odot$(black) and 11 $M_\odot$(red) progenitors at 10 kpc. The NMO is represented by solid lines and IMO by dotted ones. **Rigth:** IBD positron normalized angular distribution depending on the cosinus of scattering angle between $\bar{\nu}_e$ and e^+ for the *Bollig 2016* 27 $M_\odot$ (NMO).

Because the positron signal will be the primary target signal, it is important to understand the consequences of the IBD cross-section uncertainty at CCSN $\bar{\nu}_e$ energies. With the approach used to calculate the rates in this thesis, the cross-section of the expression (4.11) is affected by an overall predicted uncertainty of 0.4%[246]. This implies that those uncertainties are relevant only when the number of events is $\mathcal{O}(10^4)$, corresponding to the case of larger detectors such as Super-K or JUNO. A recent study (2022) suggests that the total uncertainty in the few of MeV to 100 MeV range is slightly larger, between 0.52 and 0.94 % [435]. It can be estimated in terms of positron energy:

$$\sigma(E_e) = 1.27\sqrt{\frac{E_e}{10\ MeV}} + \frac{E_e}{10\ MeV}. \tag{4.18}$$

Nonetheless, these new uncertainties remain still enough small for being relevant for this study, given the number of projected events in the water tank. Furthermore, IBD uncertainties are low in comparison to the expected ones from CCSN flux.

The angular distribution of the positron spectrum is an important aspect to consider in simulations. At GeV antineutrino energies, the IBD positron spectrum is emitted forward, with a preferred direction near the one of the entering antineutrino. This property helps to obtain directional information from the neutrino flux angular spectrum [266]. At CCSN IBD positron energies, this is not the case, and positron emission is approximately isotropic, resulting in a loss of directionality. The kinematics of the positron and its angular distribution are detailed in **Appendix D.3.2**. **Figure 4.29 (right)** illustrates the $\cos\theta$ distribution, normalizing equation (D.10), demonstrating that this approximation is sufficiently accurate. Based on the reported data, it can be inferred that the isotropic approximation (shown by the pale blue dashed line) can be used to model the positron emission with an overall uncertainty of 0.45%, which can be assumed for detection purposes. **Figure 4.30** shows the GEANT4 simulation results

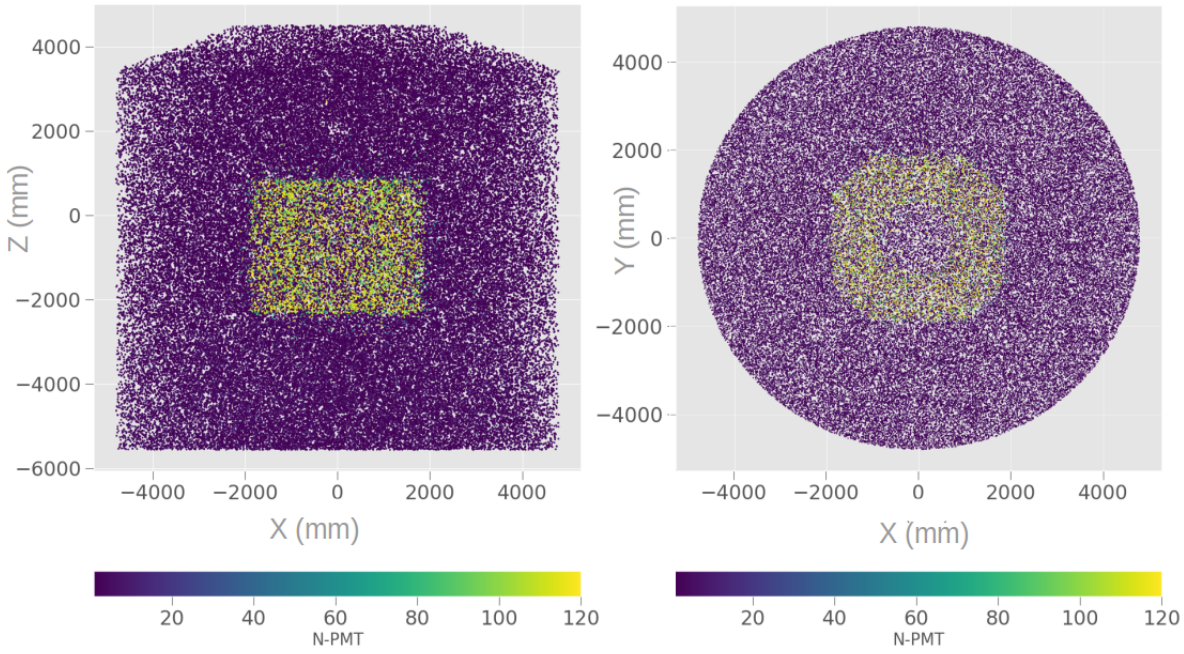

Figure 4.30: Spatial distribution for the IBD positron events from the GEANT4 simulation of the CCSN IBD using $\bar{\nu}_e$ *Bollig 2016* model $27\,M_\odot$ progenitor in NMO.

for CCSN IBD positrons as a function of the number of PMT coincidences in a time frame of $1\mu s$. The simulation sampled isotropically emitted positrons with homogeneously distributed energies from the calculated energy spectrum (4.17) in a water tank. The performance, and hence volume, of both vetoes

can be plainly distinguished, with the neutron veto having the greater number of PMT coincidences in the center of the water tank. The decrease in the number of PMTs allows to deduce the volume of the TPC in the middle of the neutron veto. The figure aims to depict the geometry of the water tank, highlighting the detection efficiencies of both volumes already reported in **Sections 4.1** and **4.2**.

4.3.2.2 CCSN IBD neutron

The neutron kinetic energy is roughly equal to the difference between the positron and the antineutrino energy, minus the mass difference between proton and neutron. This is projected to be $\mathcal{O}$(keV), which corresponds to the energy range of fast neutrons, meaning that several scatterings in water are expected before the neutron thermalization at room temperature. In the lab frame, the neutron kinetic energy is represented as:

$$T_n = E_{\bar{\nu}_e} - E_e + \Delta_m, \qquad E_n = m_n + T_n, \qquad \Delta_m = m_p - m_n. \tag{4.19}$$

At these energies, the efficiency of neutron detection is determined by the sensitivity of the detector to its capture in water, or Gd-doped water, rather than its energy or angular distribution. The CCSN IBD neutron observation not depends on its energy. Nonetheless, the reader can find a detailed description of the neutron energy and angular spectra, needed for accurately simulating the CCSN IBD neutron in GEANT4 as done in this work in **Appendixes D.3.3** and **D.3.4**. **Figure 4.31** presents the spatial distribution (x-y plane) of IBD neutron events from the GEANT4 simulation for an IBD neutron following the energy and angular distributions detailed above for the water (left) and Gd-water (right) configurations in the case of the $27\,\mathrm{M}_\odot$ progenitor in NMO. The neutron events are weighted by the number of PMT coincidences between the events. It is worth noting that adding Gd to water improves a priori neutron detection efficiency, leaving aside its impact on water transparency discussed in **Section 4.2.2**. The figure exposes the low expectations for observing neutron capture in water.

4.4 CCSN Neutrino Electron scattering ES

The second interaction to examine is neutrino-electron scattering (ES). The scattered electron is predicted to produce Cerenkov photons, but as will be demonstrated, a significant part of the energies are below the Cerenkov threshold. As a result, ES will be relevant for determining the significance of the CCSN IBD signal rather than for its detection. The number of projected ES events would be insufficient to project its detection through it, but enough to evaluate the former signal as a possible background. At CCSN neutrino energy, only electron-flavored neutrinos interact via charge current (CC), whereas neutral current (NC) ES includes all flavors:

$$\begin{aligned} \text{CC/NC} \qquad & \nu_\mathrm{e}(\bar{\nu}_\mathrm{e}) + \mathrm{e}^- \longrightarrow \nu_\mathrm{e}(\bar{\nu}_\mathrm{e}) + \mathrm{e}^-, \\ \text{NC} \qquad & \nu(\bar{\nu}) + \mathrm{e}^- \longrightarrow \nu(\bar{\nu}) + \mathrm{e}^-. \end{aligned} \tag{4.20}$$

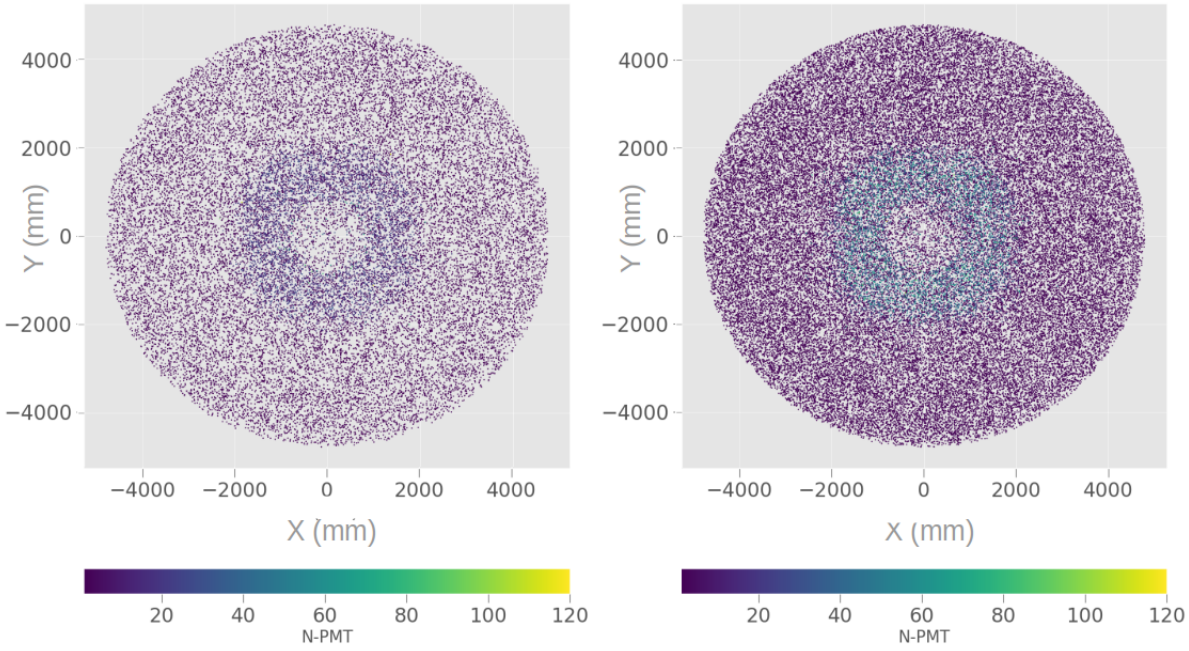

Figure 4.31: Spatial distribution of the IBD neutron events resulting from the GEANT4 simulation of the CCSN IBD, using $\bar{\nu}_e$ *Bollig 2016* model $27\,M_\odot$ progenitor in NMO, in water (**left**) and Gd-doped water (**right**).

The Feynman diagrams of **figure 4.32** describe the mentioned CC (1) and NC (2) channels for ES.

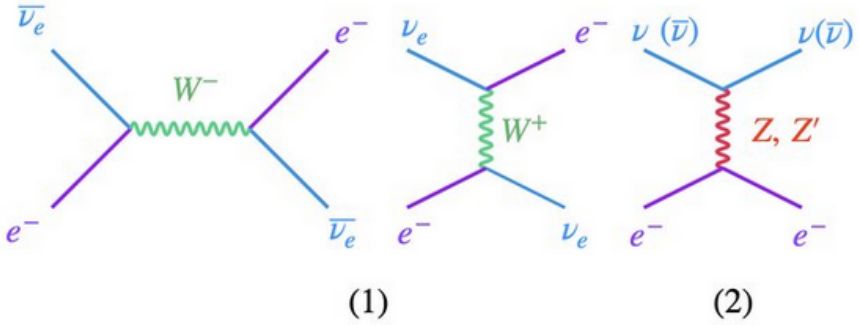

Figure 4.32: Feynman diagrams for the expected process involving CCSN neutrino ES [445]

Because the number of events is expected to be low, the value of interest will be the total number of ES over both channels. The cross-section will be the sum of the two, with the first only accounting for $\sim 1/3$ of the flux involving the $\nu_e, \bar{\nu}_e$ flavors. This work implements elastic scattering using the cross-section from reference [446] and includes one-loop electroweak and QCD adjustments, as well as QED radiative corrections from reference [447]. The two components of the differential cross-section connected to the kinetic electron energy can be expressed for all the flavors related to the axial vectors g_R and g_L, which

are different for $\nu_e, \bar{\nu}_e, \nu_x$ and $\bar{\nu}_x$:

$$\frac{d\sigma(E_{\nu_\beta}, E_e)}{dT_e} = 2m_e \frac{G_F^2}{\pi} \times (g_L^2(1 + \frac{\alpha}{\pi} f_1) + g_R^2((1 - Z)^2 + \frac{\alpha}{\pi} f_2) - g_R g_L \frac{m_e}{E_\nu} Z(1 + \frac{\alpha}{\pi} f_3)). \tag{4.21}$$

The QED radiative corrections are handled by the f_1, f_2, and f_3 parameters (Appendix B from reference [447]), α is the fine structure constant (1/137.035999084 [78]), and the G_F the Fermi coupling constant (1.1663787×10^{-5} GeV^{-2} [78]). The axial vector values for each flavor are associated with g_1 and g_2:

$$\begin{aligned} g1 = \rho_{NC}(\frac{1}{2} - ksin^2\theta_w) \quad , \quad g2 = -\rho_{NC} ksin^2\theta_w \\ \nu_e : gL = g1 - 1, \quad gR = g2 \qquad \bar{\nu}_e : gL = g2, \quad gR = g1 - 1 \\ \nu_x : gL = g1, \quad gR = g2 \qquad \bar{\nu}_x : gL = g2, \quad gR = g1\nu_e, \end{aligned} \tag{4.22}$$

where ρ_{NC} and k are the numerical factors described in Appendix A from reference [447] and the $\sin^2\theta_w$ from the weak mixing angle 0.23122 [78].

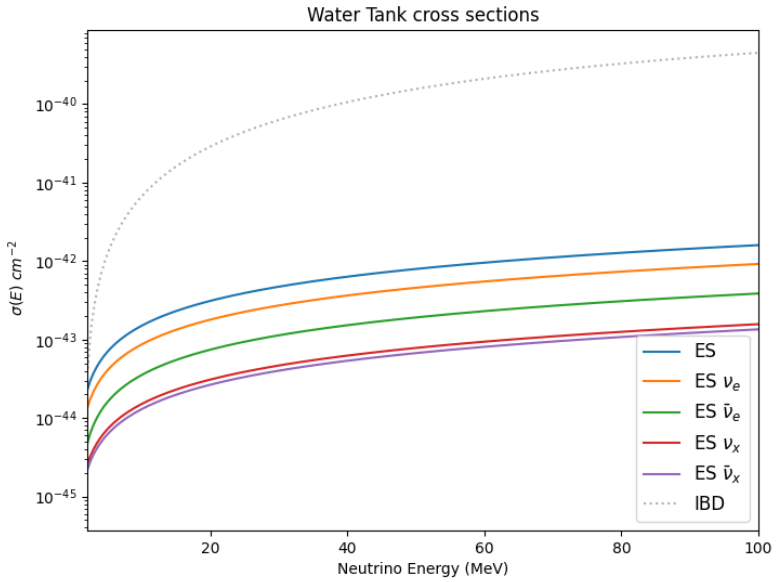

Figure 4.33: ES cross-section for the several neutrino flavors of the CCSN from equation (4.21). To highlight the weakness of the ES compared to IBD, the cross-section of the latter appears in dotted black line.

Regarding the two different components of the cross-section the rate of ES interaction is anticipated to be affected by the flavor transformations $\nu_e(\bar{\nu}_e) \leftrightarrow \nu_x(\bar{\nu}_x)$. Using equations (4.21) and (4.22), the total differential energy rate can be written for a given MO i:

$$\frac{dR_i}{dT_e} = N_w \times f_{p_{ES}} \times \frac{1}{4\pi d^2} \sum_{\beta}^{\nu_e, \bar{\nu}_e, \nu_x, \bar{\nu}_x} \int_{t1}^{t2} \int_{E_{\beta_{min}}}^{E_{\beta max}} \frac{dN_i}{dE_{\nu_\beta} dt} \frac{d\sigma(E_{\nu_\beta}, T_e)}{dT_e} dE_{\nu_\beta} dt \tag{4.23}$$

The f_{pES} factor represents the number of external layer electrons in water, which are stated to be 10, as well, the kinetic energy of the electron is defined as T_e = E_e - m_e. **Figure 4.34** represents the ES total spectrum as a function of electron kinetic energy, for the selected progenitors and the two mass orderings at 10 kpc.

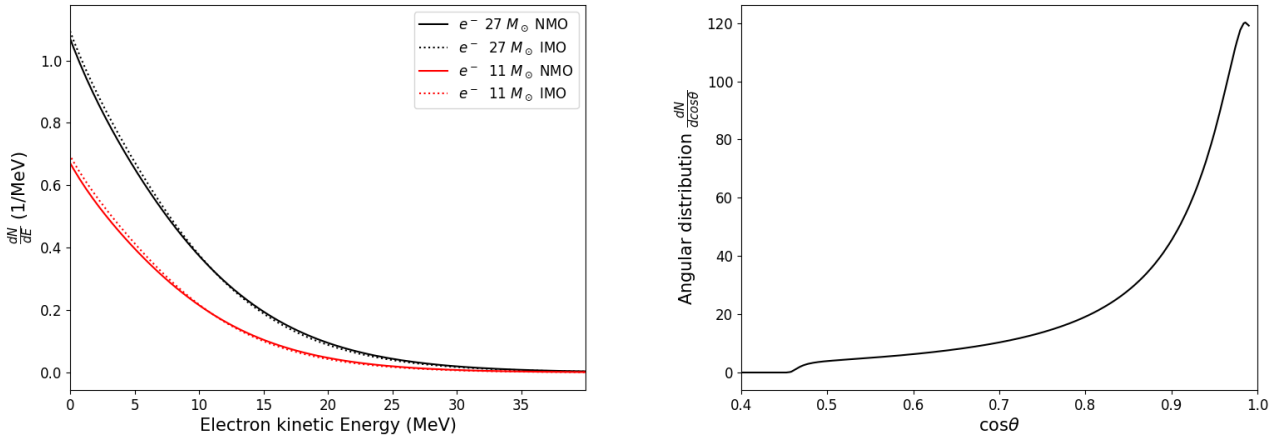

Figure 4.34: **Left:** ES rate as a function of the electron kinetic energy for the *Bollig 2016* 27 $M_\odot$ (black) and 11 $M_\odot$ (red) progenitors at 10 kpc. The NMO is represented by solid lines and IMO by dotted ones. **Right:** ES scattered electron angular distribution in terms of the cosinus of scattering angle between the neutron and electron $\cos\theta_n$ for the 27 $M_\odot$ progenitor (NMO).

The ES angular distribution is substantially peaked forward relative to the neutrino flow, as shown in the right panel of **figure 4.34**. This property is useful for locating Supernova progenitors. To achieve appropriate pointing precision, a greater number of events and denser PMT coverage will be required than that of the neutron and muon vetoes. Finally, **table 4.4** summarizes the expected number of events in the water tank, highlighting in parenthesis the number of events expected in the neutron veto. This number in the neutron veto is less than one event at 10 kpc, it has to be considered for CCSN progenitors at a lower distance, for example, at 8.3 kpc in the MW center, in order to include enough statistics to its evaluation. That is why these values are not rounded, but just reported from rate integration.

CCSN Progenitor	27 $M_\odot$ (NMO)	27 $M_\odot$ (IMO)	11 $M_\odot$ (NMO)	11 $M_\odot$ (IMO)
Total at 10 kpc	12 (0.96)	12 (0.91)	7 (0.56)	7 (0.5)
Total in the MW center	17 (1.4)	17 (1.4)	10 (0.81)	10 (0.73)

Table 4.4: Summary of the expected ES interactions in each phase of the CCSN neutrino burst for the two progenitors 27 $M_\odot$ and 11 $M_\odot$ at 10 kpc and in the MW center at 8.3 kpc in the NMO and IMO cases. The values are for the 700 tonnes of water: neutron veto plus muon veto volumes. Number of expected events in the neutron veto appears in parentheses.

4.5 Summary

In this chapter, the two sensitive volumes regarding the detection of the CCSN neutrinos in water were described, highlighting the differences between them, which can be summarized as: large volume (92% of 700 tonnes of water) and modest PMT coverage (84 PMTs) for the muon veto; and small volume (56 tonnes of water) and a denser PMT coverage (120 PMTs) for the neutron veto. Also, the reflector foil of the muon veto presents a low reflecting efficiency in the 250 - 380 nm range, resulting in a loss in collection efficiency in this Cerenkov radiation wavelength range. Cerenkov microphysics emphasizes the differences between both vetoes regarding the principal CCSN detection channel, IBD neutron and positron signals, and its potential background.

Regarding the muon veto, an a priori neutron signal via water capture is unlikely to be observed under actual trigger conditions, even with the inclusion of Gd. Lowering the trigger threshold to 3 or 2 PMTs does not result in a considerable improvement, and detecting neutron capture signals remains difficult. In contrast, the positron signal anticipated greater detection efficiency and hence serves as the target signal for CCSN neutrino detection in muon veto. Finally, high energy gamma rays > 4 MeV provide a potential background for the positron signal, whereas muons are far from the ROI and have modest rates (1 or 2 per minute). The GEANT4 simulation results for the IBD mean energy positron are given in **table 4.1**, with 5020 Cerenkov photons and 75 VPMThits, only 16 of which create a PMT signal after applying the QE. This is indicative of the low collection efficiency of the positron Cerenkov signal.

The neutron veto is sensitive to neutron capture, which is projected to improve the detection efficiency with the addition of Gd. The lower trigger threshold in terms of PMT coincidences (3) and the denser PMT array result in excellent detection efficiency, as confirmed by AmBe calibrations, as it will be shown in detail in the following chapter. As for the positron, the collection efficiency is improved, resulting in very optimistic values summarized in **table 4.2**, potentially detecting each IBD positron created inside the neutron veto. To compare with the muon veto expectations, the number of VPMThits is projected to be 2310 (for 20 MeV positrons), with 450 of those generating a signal after applying the QE. This indicates an increase in collection and detection efficiency of roughly ~ 28 times.

The doping of water with Gd improves the neutron background rejection but reduces the optical transparency of the water. The latter attribute is critical in the muon veto because Cerenkov photons travel a longer path before arriving at the PMTs after being reflected by ePTFE and foil. XENONnT data from SR2 with Gd is compared to SR1 (only water) during a 10-second window, revealing that this rate drops in the ROI for the muon veto, but remains stable in the neutron veto. It is difficult to assess the potential influence of absorption for positron Cerenkov photons at this time because no calibration was performed in the muon veto, but it will undoubtedly be clarified in future studies to resolve this transparency degradation.

Anticipating the simulation of the CCSN IBD signal in water, the expected energy spectrum of $\bar{\nu}_e$, e^+, and n and its time evolution are presented. As IBD is sensitive to the $\bar{\nu}_e$ component of the CCSN flux, flavor oscillations have to be taken into account. It was concluded that the rate will be mainly affected by

the neutrino mass ordering (MO), and as a consequence, normal NMO and inverted IMO are considered. The IBD present similar rates to CEνNS in the TPC, which are summarized in **table 4.3**, as a well similar time evolution. At 10 kpc, the number of interactions are $\sim$ 164 (160) and 87 (88) for 27 $M_\odot$ and 11 $M_\odot$ for NMO (IMO) respectively. This implies that the mean rate in the mean of the burst is in the same order as the mean rates in the 10-second window of the muon veto background in the ROI, and $\mathcal{O}(10)$ times lower than the background ones in the neutron veto. Also, the expected maximum rates are expected to happen in the first second after the bounce of the progenitor core.

In the next chapter we will approach the full chain simulation of the IBD neutron and positron in water and Gd-water scenarios, in order to obtain the observables that lead to the same signal format of science run data SR0 and SR2 for the neutron veto, and SR1 and SR2 for the muon veto. The results of these simulations will be used to perform a sensitivity study, as done in **Chapter 3** (**Section 3.5.4**) for CEνNS in the TPC, as a function of the CCSN progenitor distance.

Chapter 5

CCSN neutrino simulation in water Tank

Introduction

This last chapter is dedicated to the simulation of the CCSN IBD signal in the water tank. Results of this simulation will lead to CCSN neutrino sensitivity studies for the neutron and muon vetoes. The simulation chain, described in the first section, is divided in two main parts: the GEANT4 simulation, which has already been used to derive the geometric uncertainties and the water transparency affecting vetoes detection capabilities in **Chapter 4, Section 4.1.3**, and the digitization of the PMT information extracted from the GEANT4 simulations. The physics list used in GEANT4 includes the neutrino interaction with water molecules. However, the IBD cross-section (see **Section 4.3.1**) is small, and it requires the simulation of a neutrino flux equivalent to that of the CCSN $\mathcal{O}(10^{14}$ cm^{-2} s$^{-1})$. This is not feasible with our computing capabilities. Instead, the IBD positrons and neutrons are directly simulated using a generator based on incoming neutrino energy, both particle energy spectra described in **Sections 4.3.2.1** and **4.3.2.2**. This IBD generator will be described in **Section 5.2**. The data digitization of the GEANT4 output is an original work of this thesis and will be discussed in **Section 5.3**. It requires the PMTs calibration (that the experiment performs weekly with the help of LED light), particularly the single photo-electron (SPE) distribution for each PMT channel, crucial to sample the charge in PE of the VPMThits signal. The PMT response of the neutron and the muon vetoes are different, the associated SPE for charge sampling will be treated separately for the muon and neutron vetoes in **Appendix E.1.3** and **E.1.2**. However, the structure of the hitlet simulator is identical for both vetoes, as they share the same data structure. This allows to compare the neutron veto AmBe calibration data with the GEANT4 AmBe simulations in this volume to test the digitization, then the validity of the simulation can be extrapolated to the muon veto digitization. The results of this data-MC comparison from AmBe will be presented in **Section 5.4**. The outcome of the CCSN simulation is presented in **Section 5.5**.

The sensitivity study of the CCSN neutrinos in the XENONnT water tank based on the IBD positron signal will be discussed in **Section 5.6**. A background model has been performed in order to include IBD neutrons, ES and main background of muon (**Section 5.6.1**) and neutron (**Section 5.6.2**) vetoes, for the two different configurations: ultrapure and Gd-doped water. With this background model, the IBD

positron sensitivity is calculated separately in a first instance, then the combination of neutron and muon vetoes sensitivity will be discussed in **Section 5.7**.

Finally, at the end of this chapter, the TPC, neutron and muon veto sensitivities will be all combined, in order to derive the full XENONnT sensitivity to the next CCSN neutrino burst. This corresponds to the final outcome of this work.

5.1 Simulation chain

The challenge of simulating IBD induced from CCSN $\bar{\nu}_e$ is not only due to the three body decay nature of the interaction and its weak cross-section, but also to the time dependence of the CCSN flux. The simulation chain (schematized in **figure 5.1**) is divided in two parts. At the top can be distinguished the

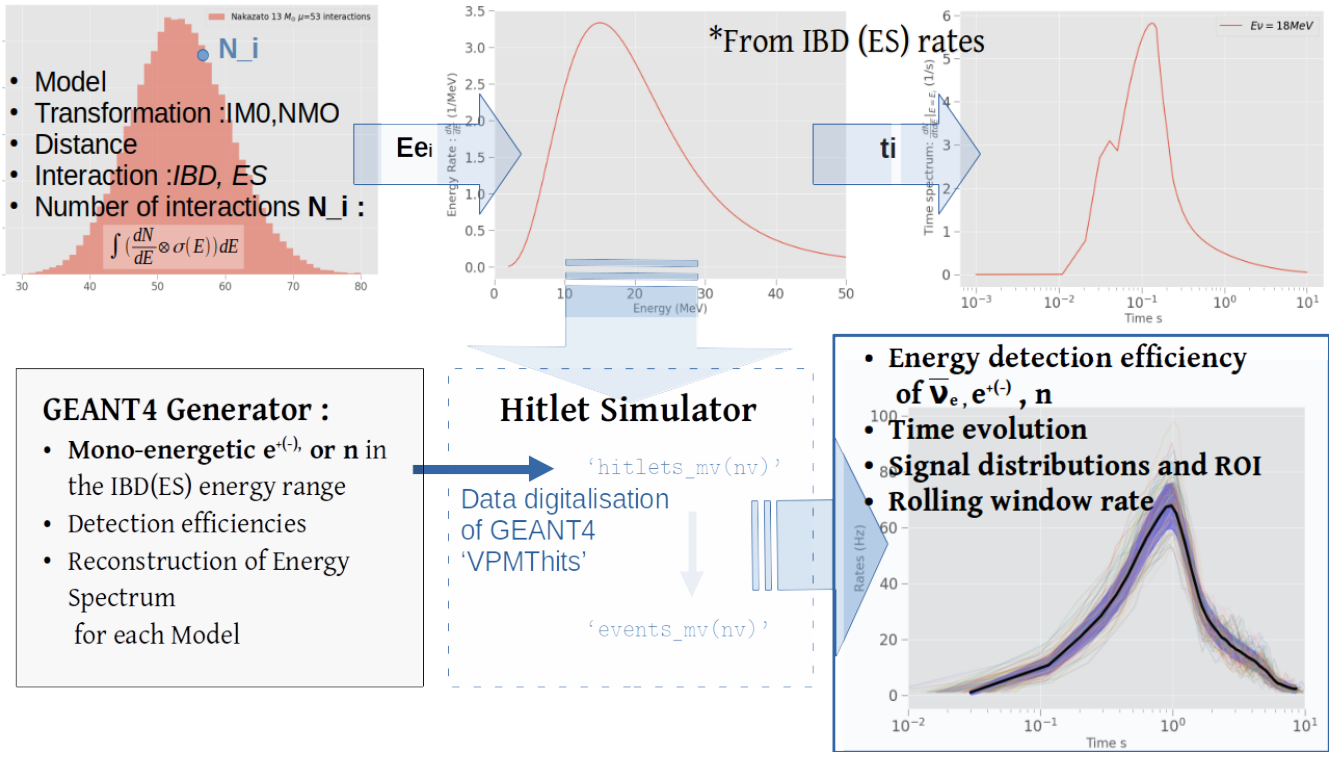

Figure 5.1: Reconstruction of the CCSN IBD simulation chain.

MC simulation which delivers, for the CCSN $\bar{\nu}_e$, the total energy spectra from equations (4.15) and (4.14). The number of interactions, as done for the CEνNS TPC simulation, follows a Poisson distribution, with the number of expected interactions N as the mean value, in order to account for potential uncertainties of the CCSN neutrino flux:

$$N_{SN_i} = P(\mu = N_i), \qquad N_i = \int_{E_{\bar{\nu}_e th}} \frac{dR_i}{dE_{\bar{\nu}_e}} dE_{\bar{\nu}_e}. \tag{5.1}$$

Once the number of interactions is sampled, the $\bar{\nu}_e$ energy is selected from the normalized spectra,

i.e. probability $P_i(E_{\bar{\nu}_e})$ and secondly the time from an analogous normalized 2D spectra for this given E^S, $P_i(t,E^S)$. For a given mass ordering i (i = NMO, IMO), these probabilities can be written as:

$$P_i(E_{\bar{\nu}_e}) = \int_{E_{\bar{\nu}_e}^{c_{th}}} \frac{1}{\frac{dR_i}{dE_{\bar{\nu}_e}}} dE_{\bar{\nu}_e} \frac{dR}{dE_{\bar{\nu}_e}} \quad \longrightarrow \quad P_i(t, E^S) = \int_{t_0}^{t_1} \frac{1}{\frac{dR_i}{dtdE_{\bar{\nu}_e}}|_{E_{\bar{\nu}_e}=E^S}} dt \quad \frac{dR_i}{dtdE_{\bar{\nu}_e}|_{E_{\bar{\nu}_e}=E^S}} \tag{5.2}$$

This allows for the simulation of positrons and neutrons in the water tank, recovering the information of the incoming antineutrino. Once the energy and time after the core bounce of the $\bar{\nu}_e$ is chosen, kinematics described in **Appendix D.3.1,D.3.2** and **D.3.4** can be used to calculate positron and neutron momenta. For this purpose, the GEANT4 simulation includes an CCSN IBD generator. In the next section, the bottom left part of the **figure 5.1**, corresponding to the GEANT4 IBD event simulation, will be described.

5.2 GEANT4 IBD event generator

The GEANT4 simulation has two main purposes: obtaining the detection efficiencies as a function of the IBD positron (hence, the antineutrino) energy; and gathering the e^+ + n production time information, characterized by the difference between a fast energy deposition of the positron ($\mathcal{O}(10ns)$) and the neutron capture ($\mathcal{O}(100\mu s)$ in water and $\mathcal{O}(10\mu s)$ in Gd). Positrons and neutrons are simulated in GEANT4 for given antineutrino energies, which are selected according to an external MC simulation, as it will be explained. Both MC will be so connected by this generator.

In order to collect enough statistics for each energy of the $\bar{\nu}_e$ spectrum, 10 000 mono-energetic $\bar{\nu}_e$ in the CCSN IBD range [$E_{\bar{\nu}_e}^{c_{th}}$, 100 MeV] divided in 200 bins are simulated. This implies 2 000 000 of $\bar{\nu}_e$ in this energy range, in each neutron and muon veto volumes. The direction of the $\bar{\nu}_e$, considering the proton at rest in the lab frame, became necessary. The CCSN neutrino source is far enough to neglect the $\bar{\nu}_e$ flux momentum dispersion, approximating the incoming neutrinos direction through the same vector. The selected direction of $\bar{\nu}_e$ is arbitrary, having no implications into simulation results. Once the energy and direction of the incoming antineutrino are known, taking advantage of the isotropic positron emission approximation (see **Section 4.3.2.1**), the value of the scattering angle between $\bar{\nu}_e$ and e^+ can be obtained. From equation (D.11) the positron energy is calculated. Finally, knowing positron and antineutrino momentum, the neutron emission momentum, following the relations detailed in **Appendix D.3.1**, is set. **Figure 5.2** shows the scheme of the vertex simulation in GEANT4 for a given antineutrino energy and the fixed direction of the incoming CCSN flux. The IBD vertex are distributed uniformly in the water tank, as showed in **figures** 4.30 and 4.31 of **Chapter 4**. The final neutron (bottom) and positron (top) GEANT4 spectra are compared to the theoretical ones presented in **figures 4.3.2.1** and D.9, showing an accurate matching of the MC vs the analytical integration performed to obtain these spectra.

The last point is to extract information of the GEANT4 VPMThits, coming from positron energy depositions and neutron capture, separately. Due to the XENONnT MC code design, a priori it is not possible to save information of the tracking of each particle, without a prohibitive computing cost. The

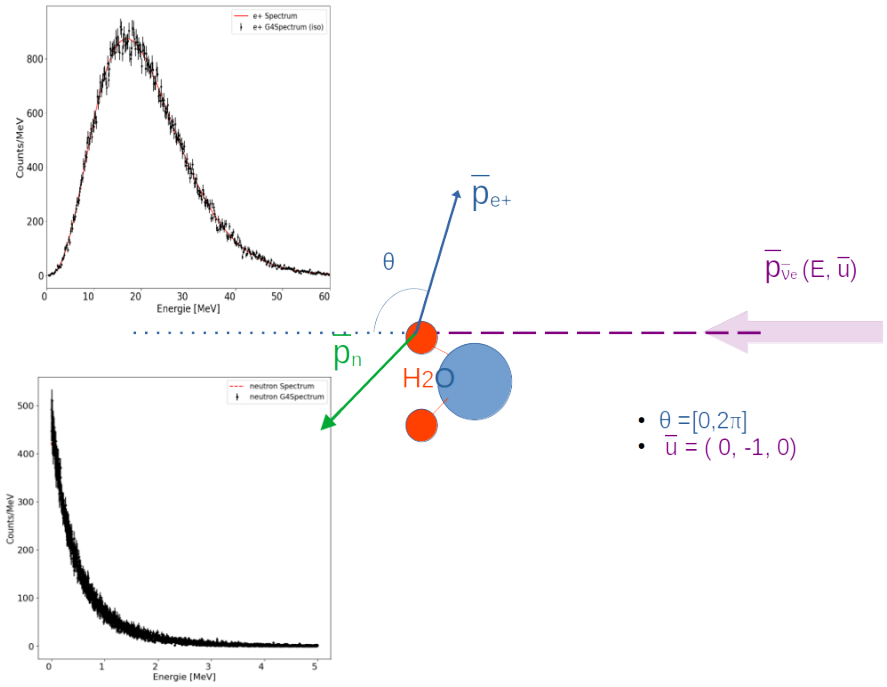

Figure 5.2: Scheme of the GEANT4 generator IBD vertex. The incoming $\bar{\nu}_e$ direction is set to [0, -1, 0] and the positron is emitted isotropically in the full range of θ ([0, 2π]. Both final positron (top) and neutron (bottom) spectra are represented.

GEANT4 output only recovers information per simulated vertex, labelling each IBD event simulated with an 'eventid'. However, the VPMThits coming from positron should arrive far before the ones induced by the neutron capture, even if the latter comes from the Gd nucleus, as showed by the VPMThit time distributions of **figure D.7** in **Appendix D.2.3**. In this sense, some time cuts regarding VPMThits time can be applied to discriminate positrons and neutrons. It is worth to notice that GEANT4 starts counting when the vertex is created (not in the earlier VMPThit generating a signal) and it switches again the counting to zero for the next event simulated, making each the IBD event time independent.

A typical n-e^+ discrimination time can be found from GEANT4 VMPThits arriving times, based on separate simulations of 20 MeV positions (representing the CCSN IBD mean energy of positrons, see **Section 4.3.2.1**) and neutrons in ultrapure and Gd-doped water configurations. **Figure 5.3** presents the results of the surviving fractions of VMPThits from this independent simulations in the muon (left) and neutron (right) vetoes, as a function of the time-cut applied. These fractions are obtained applying the time cuts t_{cut} to the positron, whose surviving VPMThits arrive before this time, and on the contrary, to the neutron in which corresponding VPMThits are expected to arrive latter as:

$$f_{e^+} = \frac{\text{VPMThits}_{e^+} <= t_{cut}}{\text{Total VPMThits}_{e^+}} \quad , \quad f_n = \frac{\text{VPMThits}_n >= t_{cut}}{\text{Total VPMThits}_n} \tag{5.3}$$

For the both volumes, a value of 800 ns can be adopted as t_{cut} resulting in a 100% of surviving VPMThits for positron, and 99.45%(99.5%) for neutrons in the muon veto and 99.32%(99.5%) in the

neutron veto in water(Gd-water) configuration. This efficiencies can be assumed and should not affect the final positron or neutron detection efficiencies.

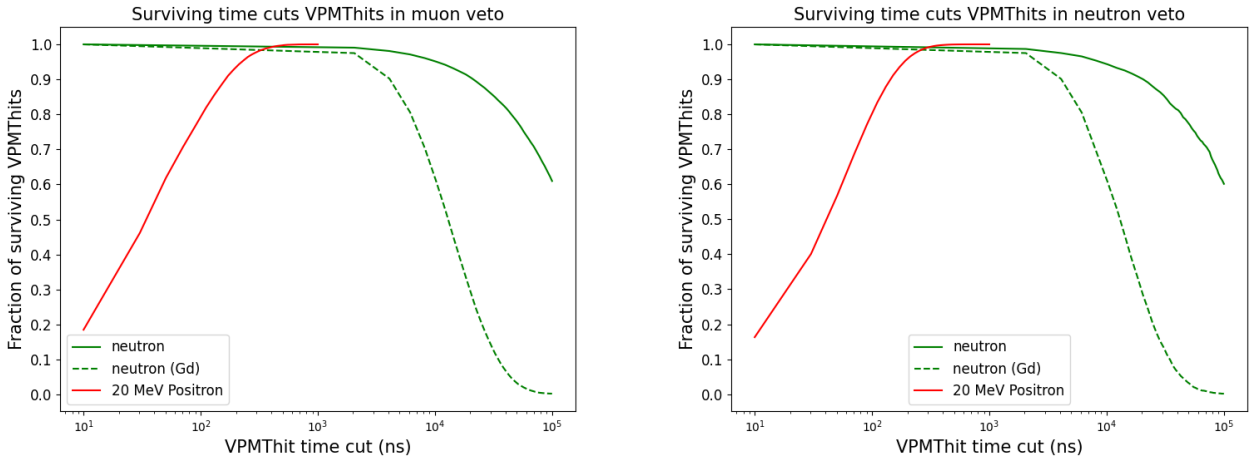

Figure 5.3: **Left:** Fraction of VPMThits surviving after the arriving time cuts applied for positron (red) VPMThits and neutron (green) VPMThits in muon veto. **Right:** Fraction of VPMThits surviving after the arriving time cuts applied for positron (red) VPMThits and neutron (green) VPMThits in neutron veto. The dashed green line represents the result in the Gd-water configuration.

The value of interest to perform the simulation chain from each IBD event for the positron and the neutron are the information regarding their respective VPMThits. From the latter VPMThits output, the last step is to include time information of the simulated $\bar{\nu}_e$, to conclude the 2D CCSN IBD simulation. Finally, the digitization of the MC (+ GEANT4) output will be performed from the following VPMThits values:

- 'VPMThitID': ID for the PMT channel identification.

- 'VPMThitTime': time of the arriving photon since the GEANT4 vertex is generated. For this time, the one from the MC simulation corresponding to the incoming $\bar{\nu}_e$ is added as :
  t = $t_{\bar{\nu}_e}$ + 'VPMThitTime'

- 'VPMThitEnergy': energy of the photon which is transformed into its wavelength $\lambda = E$h, necessary to apply the QE of the channel.

The next step, the data digitalization, will transform this VPMThits into 'hitlets' which are the ones that finally generate a recorded signal, surviving trigger conditions for each veto. This process is performed thanks to a 'hitlet simulator' which will include the specific and individual response of PMT channels, as well a trigger and signal processing conditions.

5.3 The Hitlet Simulator

What is called 'hitlet' is the signal of a VPMThit fulfilling specific trigger conditions, and it corresponds to the final layer of the XENONnT vetoes data structure before creating a fully reconstructed event. To help using an analogy, while in the Xe TPC an event (typically an interaction occurring in liquid xenon) is obtained by clustered peaks that we label S1 and S2 (to distinguish scintillation vs ionization signals), in the two vetoes the events are named 'eventnv' or 'eventmv' and are obtained by clusters of 'hitlets' arriving in a precise time window, observed by a certain number of PMTs (number that is different in the two vetoes). In this sense, the "hitlet" handles the signal data for each single PMT channel level, while the "event" is built with the information of all the PMTs involved, mainly using those quantities: pulse area [PE], number of contributing PMTs, and center time. This section is extremely technical, and it has the purpose to provide to future XENON Collaboration members a complete summary of the detailed work done on the data digitization on the vetoes.

The data structure of muon and neutron veto is identical, but trigger conditions are different, as explained in **Chapter 4**. The muon veto is strongly affected by background, being the first layer of shielding after the Gran Sasso mountain chain rock. This contamination has been classified in **Section 4.1.2** as coming from the low energy background of the experiment, mainly neutrons and gammas. In order to avoid this component and focus on the rejection of muons, the trigger conditions are exigent in the number of PMTs, which has been set to 5 PMTs in a time window of 300 ns. On the neutron veto, the VPMThits should arrive before, hence this time window has been reduced to 200 ns, which reduces the accidental coincidence rate. The number of required PMTs for the event cluster is 3 PMTs. For low energy detection purpose, as the neutron capture signal, a good compromise between the window time length and the low number of PMT threshold required is important to avoid accidental coincidences. These are the global trigger conditions that should be accounted by the hitlet simulator in order to create a final event in the muon and neutron veto, but individual PMT requirements can be adopted in order to avoid well known PMTs dark noise signals. This will be explained latter, concerning the VMPThit PE area sampling, which depends on the individual PMTs SPE distribution extracted from LED calibration, and this threshold to avoid PMTs noise will be handled by an acceptance parameter.

Figure 5.4 shows the basic structure of processing for both vetoes, from the trigger-less raw data ('raw-record' level) up to a fully reconstructed event ('events' level). The only difference between both is the recording of lone hits, which are not included in any coincidence window, for monitoring purposes in the neutron veto, presented by the grey bubble of the scheme. It is worth to notice that the hitlet simulator is a simplified, and minimal, version of the data processing, and only including the last step. In reality, before data processing arrives to the hitlet level, the signal is based on the waveform pulse data analysis, which is much more complex. The recorded pulse signal is digitized in samples, through analog-to-digital converters (ADCs). The neutron veto digitizer (CAEN V1730 which has a higher sampling rate of 500 MHz, i.e. 2ns sample width) is different for that of muon veto (CAEN V1724, which have a sampling rate of 100 MHz and a 14 bit resolution, i.e. 10 ns sample width). At this point, in the first 2 steps (or 3 for

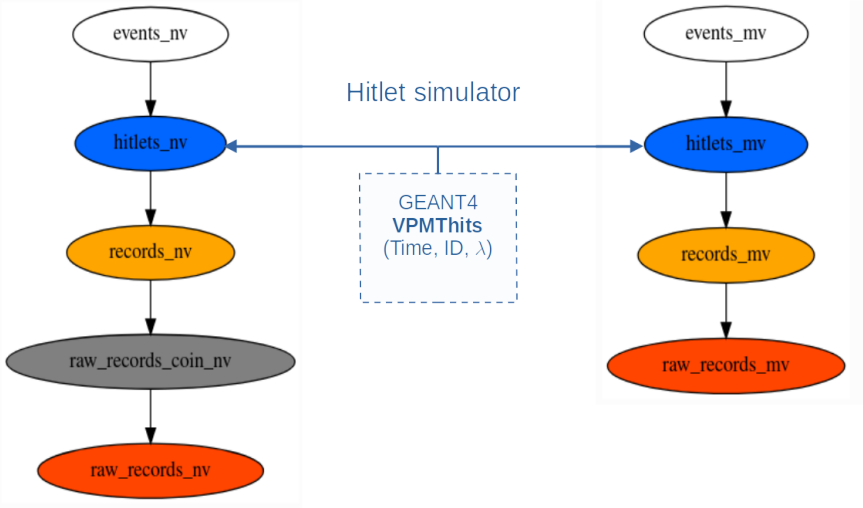

Figure 5.4: Scheme of the neutron veto data structure, identical to the muon veto one replacing the 'nv' with 'mv'.

.

neutron veto) including the name 'records' represented in the **figure 5.4**, the signal pulses are recorded in ADC counts.

Figure 5.5 shows an example of a 'raw records' triggerless entry in which the channel baseline has been calculated (left). The final ADC pulse amplitudes generating a hitlet (baseline corrected and flipped) in each channel is shown on the right. It can be seen that it is above the required 15 ADC counts threshold (other channels presenting high dark count rates require at least 20 ADC counts). At this level, a VPMThit-finder algorithm is used to detect the pulses above the threshold. In the neutron and muon veto, 110 samples are recorded at raw record level. In the first detector, the baseline is calculated in the first 26 samples (52 ns).

In the next step from records to hitlets, VPMThit finder is applied again, extending the VPMThits 3 samples from the left and 20 from the right, converting them with this extension into hitlets. But hitlet processing not ends here. Overlapping hitlets are merged into one, constrained by the sample resolution of the digitizer and the width of the pulse, a single waveform is created per PMT channel. At this point, the amplitude of the signal is converted from ADC counts/sample to PE/sample. The conversion factors are based on the gain estimated from the weekly LED calibrations, accounting for the actual conditions of the detector. Finally, a splitting algorithm is used to check which hitlets can be split into two (or more). No more details of this preliminary data processing steps will be given, to focus on the hitlet simulation from GEANT4 VMPThits, nevertheless the reader should find a more extensive work here [347] and in the open source documentation of the straxen plugins- [1].

The time resolution of the hitlet separation is a key factor that could affect the acceptance of the

[1] `https://straxen.readthedocs.io/en/latest/reference/datastructure_nv_nT.html`

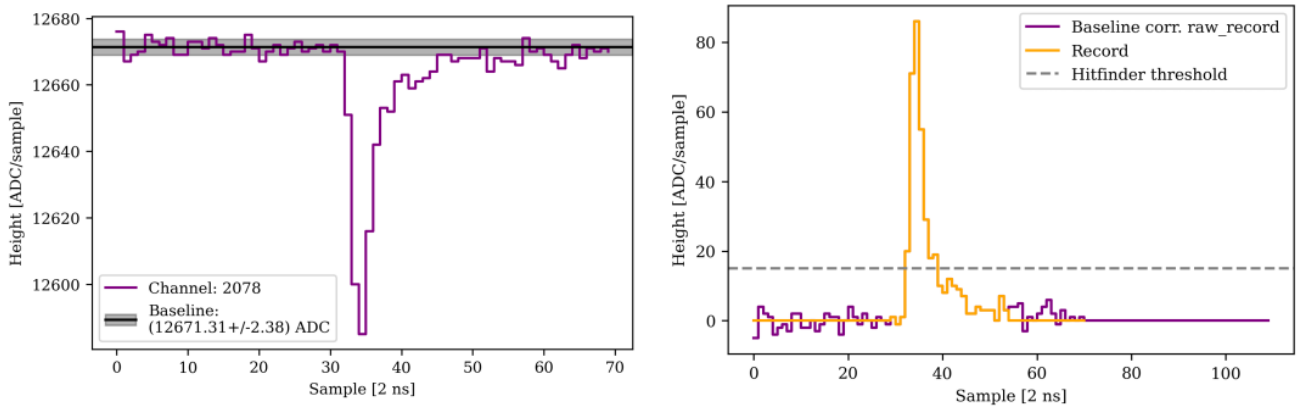

Figure 5.5: Illustration of a "raw record" (left) and "record" (right) of a single NV PMT pulse. The left figure shows the raw pulse returned by the DAQReader plugin. The baseline mean and RMS is shown as a black line and gray shaded region. Only the non-zero padded part of the waveform is plotted. The plot on the right side shows the baseline corrected and flipped raw record in purple, including the zero padded buffer for samples larger than 70. The orange graph shows the resulting "record". The grey dashed line indicates the channel-dependent hit-finder threshold. Figure from [347].

IBD positron hitlets as a significant number of photons is expected to arrive in a few nanoseconds. It implies that if two Cerenkov photons arrive at the same PMT channel, being absorbed by the photocathode, within an interval of a few ns for the neutron veto (and a few tens for the muon as each sample correspond to 10 ns) probably they will be merged into one, implying that by definition the acceptance of these 'stacked hitlets' has to be total, and no more related to the SPE estimations. In order to obtain a minimum delta time δt for muon and neutron vetoes, equivalent to a real time resolution of the hitlets waveform, a random run with enough statistics can be used to select the hitlets arriving at the same channel, and look to their δt time interval distribution. These distributions are shown in **figure5.6** for muon (left) and neutron (right) random runs. As expected, the better time resolution of the neutron veto digitizer allows separating hitlets in a few ns, while the muon veto starts being more efficient in splitting the peaks around 100 ns (10 samples). Conservative values for this δt can be adopted for neutron veto as 8 ns and for muon veto to 80 ns. This implies that two GEANT4 VPMThits arriving in this coincidence window in the same channel will be merged by the hitlet simulator, and will have an acceptance of 100% once QE is applied.

For both neutron and muon vetoes, the schema of the hitlet simulator, also graphically represented in **figure5.7**, is based on the following steps:

1. Applying QE scaled by the effective collection efficiency eCE
2. Including possible stacked hitlets (2 or more hitlets processed like one), happening in a close time window $\mathcal{O}$(ns) in the same channel
3. Sample the hitlet in PE, taking into account also the previous step of "stacked hitlets"

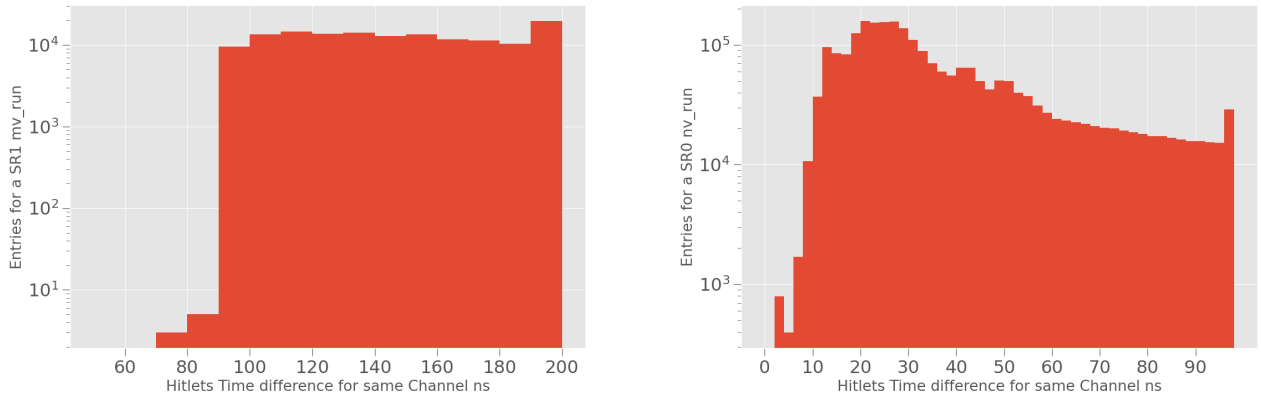

Figure 5.6: **Left:** Delta time δt distribution for hitlets arriving to the same PMT muon veto channel for a random run of SR1. **Right:** Delta time δt distribution for hitlets arriving to the same PMT neutron veto channel for a random run of SR0.

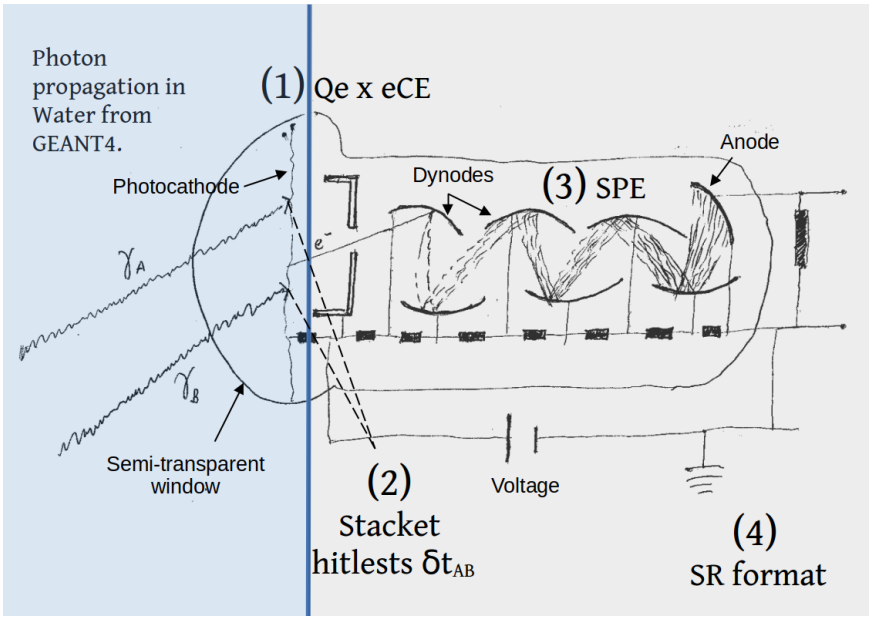

Figure 5.7: Scheme of the signal production in a veto PMT, from the incoming photon to the electric pulse.

4. Formatting the "hitlets" output with the same data format used for real data

Those steps are quite complex to be detailed and contain microphysics of the generation of a signal in PMTs. While their detailed description is a very valuable source of information for a young XENON member, detailing it in this section has been judged too heavy to read for a general reader. Hence, the full description has been put in **Appendix E.1.1**.

5.4 Validation of the hitlet simulator with AmBe calibrations

The next sections will present the results of the first CCSN simulation, which are based on the actual trigger conditions in the muon and neutron veto. But first, in order to understand the matching between the simulation and the data, and subsequently the future corrections and optimizations needed in the hitlet simulator chain, all the algorithms presented so far will be tested with the help of AmBe calibrations, which have been acquired during SR0 (in ultrapure water) and SR2 (after adding Gd in water).

The AmBe simulations performed with the described GEANT4 + hitlet simulator chain were tested in the two configurations SR0 (water only) and SR2 (Gd 0.02% concentration), i.e., using the SPE distributions and acceptances obtained for the respective data collection period. The AmBe source used in XENONnT calibrations has an expected rate of 160 neutrons/s; this could cause small variations for each source. This activity is related to the neutron emission, while the number of AmBe events produced and potentially recorded is indeed ~ 1.5 times more due to the ^{12}C 4.44 MeV gamma contribution in the $\sim 50\%$ of the cases. This fraction also can vary for each source. For the MC AmBe simulation, neutron and gamma will be simulated separately, making the gamma fraction a free parameter that will be extracted from AmBe data results.

Two different contributions are expected to be distinguished in the event PE area distributions, as the energy deposition from the 2.2 MeV from neutron capture in water — plus the gamma cascade of ~ 8 MeV from capture in Gd — , and the 4.44 MeV from ^{12}C will create a different amount of cerenkov photons. Anticipated performances for these gamma energy depositions in neutron vetoes have been discussed in **Section 4.1.3**. AmBe calibration results, show that PE area distributions for these contributions can be a priori approximated through a gaussian distribution. However, the threshold that the neutron trigger imposes leads to an asymmetry in the distribution of the neutron capture in water, in which some events are close to the threshold region. The latter contribution will be approximated by a skewed Gaussina to account for this effect. The results for 60 30-minute runs are shown in **figure 5.8**. The AmBe source was placed at the bottom of the neutron veto (CW6d0 position), which can be seen in **figure E.7** of **Appendix E.2.2**.

In this position, the detection efficiency of the neutron capture is higher, close to the bottom PMT array and the bottom surface of the neutron detection volume, which is covered by reflector panels. Before discussing the results shown in the right panel of **figure 5.8** it is worth pointing out that the subtraction of the background is done in a cumulative manner in terms of the δPE bin rate, more details about background subtraction are given in **Appendix E.2.3**. Background is different from SR0 and SR2 periods, particularly for the latter the former is higher in the [0,10] PE event area range. As a consequence two different thresholds are required for the analysis of the AmBe results: SR0 6 PE, and for the SR2 10 PE. The function used to approximate the background subtracted, imposes firstly a threshold of 6 PE per event, as not all the background in the low event area region can be subtracted. Particularly, this threshold is required to reduce the accidental coincidence (AC) rate. The function is compounded by the combination of two gaussians for the neutron capture, an skewed one, and the gamma, plus two others

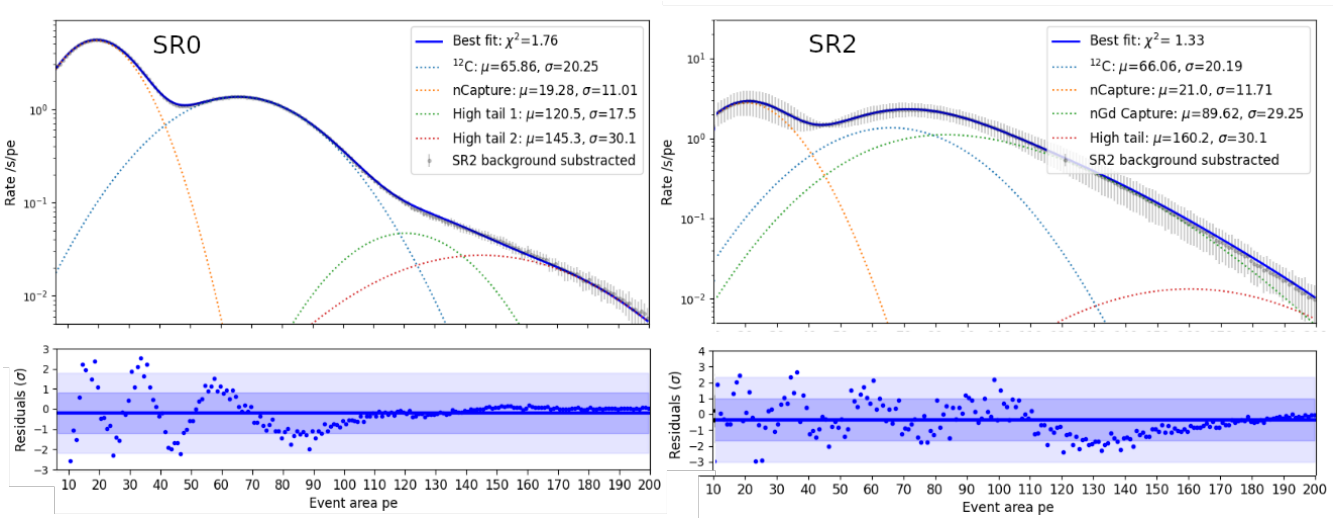

Figure 5.8: Event area distributions from calibration SR0 (left) and SR2 (right) in the bottom source position CW6d0.The errors bars of the AmBe substracted backgrounds correspond to the standard deviation for each obtained from the analysis of the 60 runs. Fit of the obtained background subtracted distributions with the function described in equation 5.4 accounting for the neutron capture in hydrogen (orange dotted line), the ^{12}C 4.44MeV gamma line (blue dotted line) and the Gd capture for SR2 (green dotted line). Two high energy tails for captures happening in other nuclei for SR0 (green and red dotted lines) and one for SR2 (red dotted line) are also included.

that handle the high energy tail contributions from neutron captures in oxygen [448], or not happening in water but rather in the detector components nuclei isotopes such as ^{54,56,57}Fe and ^{58,62,63} Ni generating high energy gamma ray's [424]. In the SR0 case the event area distribution can be described as:

$$\frac{dN}{dtdPE}^{SR0}_{sub}(PE) = A_1 \times SkGauss^{\text{nCapture}}(\mu,\sigma) + A_2 \times Gauss^{^{12}C}(\mu,\sigma) + A_3 \times Gauss^{\text{High tail1}}(\mu,\sigma) + A_4 \times Gauss^{\text{High tail2}}(\mu,\sigma) \quad (5.4)$$

On the other hand, the SR2 spectra include Gd neutron capture gamma lines compounding the $\sim$ 8 MeV cascade. These lines are spread in a large range, varying to a few hundred of keVs to 10 MeV (see **figure 4.19** of **Section 4.2.2** illustrates). A significant part of gamma's from neutron captures not happening in hydrogen, described by the SR0 high tails, are absorbed by the Gd-capture contribution. To account for this fact, a skewed Gaussian adjustment is applied to this Gd neutron capture distribution. However, a contribution for the second high energy tail remains. The SR2 AmBe spectrum will be fitted with the following functions:

$$\frac{dN}{dtdPE}^{SR2}_{sub}(PE) = A_1 \times SkGauss^{\text{nCapture}}(\mu,\sigma) + A_2 \times Gauss^{^{12}C}(\mu,\sigma) + A_3 \times SkGauss^{\text{nGd capture}}(\mu,\sigma) + A_4 \times Gauss^{\text{High tail}}(\mu,\sigma) \quad (5.5)$$

Regarding the neutron capture distribution from **figure 5.8** SR0 (left) and SR2 (right), the skewed gaussian fit function approximating its contribution (orange dotted line) is centered around 19 PE, while

the ^{12}C gamma line is at $\sim$ 65 PE, which is more than 3 times more, being this proportion consistent with the number of expected cerenkov photons for each line 255 and 751 respectively (see **table 4.2**). The Gd neutron capture gamma cascade, fitted with a skeweed gaussian, is centered at 89.62 PE while the SR2 ^{12}C gamma at 66 PE resulting in a higher contribution for the first one, accounting the fact that some energy tail events are included in the former.

One estimation that can be done regarding the obtained distributions for each component is the fraction of gamma's detected, which is expected to be close to the real emitted one as its distribution is less affected by the background, as the left panel of **figure 5.8** shows. This fraction can be obtained from the integration of neutron capture distributions, including ones not happening in hydrogen, for SR0 and SR2 as:

$$F^{\gamma} = \frac{\int_{th} Gauss^{^{12}C}(\mu,\sigma)dPE}{\text{Total cap.}} \sim 0.48$$

$$\text{Total cap.}^{SR0} = \int_{th} SkGauss^{\text{nCapture}}(\mu,\sigma) + Gauss^{\text{High tail1}}(\mu,\sigma) + Gauss^{\text{High tail2}}(\mu,\sigma)dPE$$

$$\text{Total cap.}^{SR2} = \int_{th} Gauss^{\text{nCapture}}(\mu,\sigma) + SkGauss^{\text{nGd capture}}(\mu,\sigma) + Gauss^{\text{High tail}}(\mu,\sigma)dPE \quad (5.6)$$

As **figure 5.8** illustrates the threshold impacts the neutron capture in H distribution rather more than the ^{12} C gamma, affecting the calculated fraction of gamma's for the SR0 and SR2 summarized in **table 5.4**. On the other hand, the neutron capture from another AmBe interaction can also contribute to the gamma peak. Neutron and gamma's not coincide in the same recorded event, being separated enough in time as the neutron capture is $\sim 200\mu s$ in water and $\sim 30\mu$ s in Gd (far from the period of the source τ_{AmBe} 6.25 ms), while the ^{12}C gamma is emitted within the neutron, and its energy deposition happens in the next 100 ns. Inclusion of neutron capture VMPThits from precedent events will enhance the estimated gamma fraction. Anyway, the gamma fraction obtained values 0.464 for SR0 and 0.436 for SR2 are coherent with the obtained from recent measurements (0.46 $\pm$ 0.07 [303]). As mentioned before, the fraction is anticipated to vary with the position of the source. In the estimation of equation (5.6) no uncertainty related to the position is given because only one source position will be studied for comparison purposes with MC simulation.

To perform MC vs data comparison instead applying additional cuts to diminish the background, with the risk of losing information about the neutron capture distribution, the background is inserted in to the MC simulation at a hitlet level. The hitlets from neutron and gamma are merged with this background at a hitlet level, contributing with a fraction of 0.48 (different from the fit data estimations) resulting this value from the best fit between data and MC. The hitlet times are given to each hit counting from the GEANT4 time (i.e. starting to count when the particle is generated), as well as accounting for the rate of 160 neutrons/s to each simulation. This background plus AmBe hitlets will be processed using the event plugin, leading to a MC AmBe + background event area distribution. After this, the obtained distribution rates will be submitted to the background subtraction, in order to be compared with the AmBe background subtracted data depicted in **figure 5.8** in equivalent conditions. This procedure is more rigorous than compare both without inclusion of the background, however, it was noticed that the impact of background injection is residual and can be neglected.

Figure E.9 of **appendix** section **E.2.4** illustrates the two distributions, SR0 (left) and SR2 (right) subtracted background (black points) versus the MC AmBe by a red solid line. Before analyzing the result, a discrepancy that is not due to the hitlet simulator or other uncertainties but to an issue in the GEANT4 physics list regarding neutron capture process simulation, affecting the high energy tail rate, has to be pointed out. This problem is known and has been already reported[2]. Its final impact consisting in the apparition of extra gamma lines, leads to an increment of the total energy released during neutron capture in some nuclei isotopes present in detector components, which is significantly higher than the predicted energy value of the reaction. This results in a rate for this high energy tail contribution of 7.04 Hz higher in front of the 3.93 Hz obtained from the data fit in the SR0 case. This should not affect the further analysis of CCSN IBD neutron simulation, as this tail can be eventually corrected with the one obtained with the data. Furthermore, its rate is not significant representing less than 3% of the total rate.

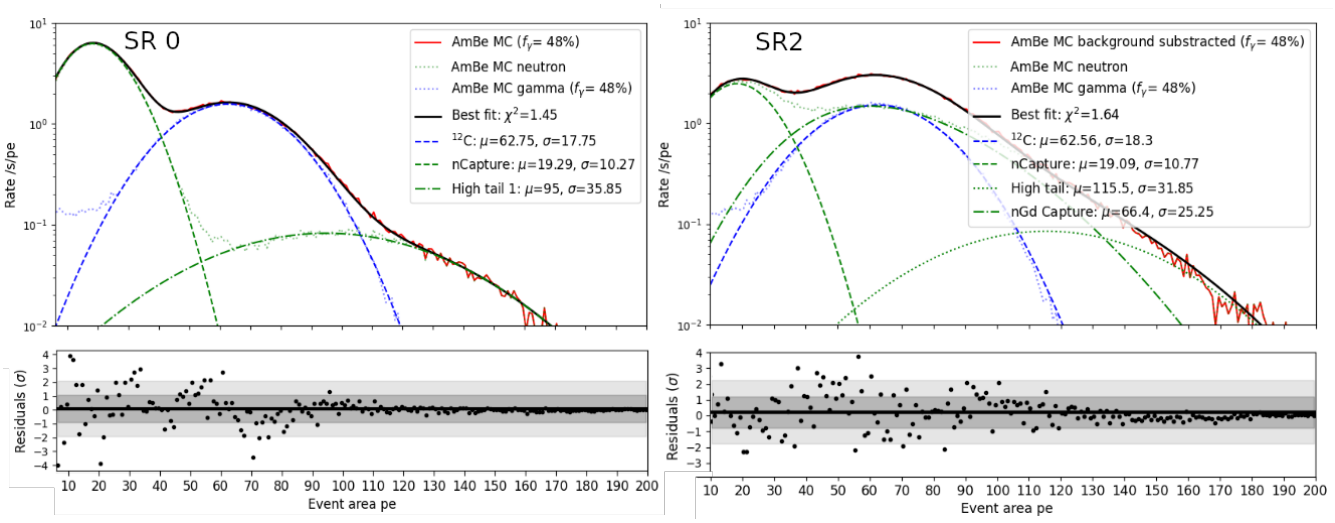

Figure 5.9: **Left**.Comparison of the event area distribution obtained in using GEANT + hitlet simulator versus the SR0 background substracted in the bottom source position CW6d0. As explained in the text an insertion of the background at a hitlet level into the MC AmBe hitlet preced the substraction of background. The errors bars of the AmBe SR0 substracted backgrounds correspond to the standard deviation for each obtained from the analysis of the 60 runs.**Right**. Fit of the obtained distributions with the function described in equation 5.4 accounting for the neutron capture in hydrogen (orange dotted line), the ^{12}C 4.44MeV gamma line (blue dotted line) and the high energy tails for captures happening in other nuclei (green and red dotted lines).

Figure 5.9 depicts the SR0 and SR2 MC simulation gamma results, illustrating each contribution from neutron captures and ^{12}C gamma as described in equations (5.4) and (5.5). Despite the high energy

[2]This issue affects mainly neutron capture on isotopes of Ni and Fe responsible for the high energy tails and has been discussed in the GEANT4 forum by John Mcfee `https://geant4-forum.web.cern.ch/t/thermal-neutron-capture-gamma-spectra-give-major-disagreement-with-nndc-data-base-for-some-isotopes/6504`. GEANT4 generates additional gamma rays when a cascade is simulated to sustain the momentum conservation. The reader can find an extended study of how these cascades are generated here [449]

tail, the approximation of the MC distributions is done using the same functions corresponding to the same contributions: skewed gaussians for neutron capture in H and Gd, a gaussian for the ^{12}C gamma, and other gaussians to handle the high energy tail for neutron captures not happening in H or Gd. Regarding the peaks corresponding to the neutron capture and the ^{12}C gamma lines, values close to the calibration data have been founded at 19.29 PE (19.28 PE) and 62.75 PE (65.86 PE) respectively (data in values in parenthesis) for the SR0. **Table 5.4** summarizes the results for the AmBe calibration data vs. MC in SR0 and SR2 configurations. The obtained gamma fraction 0.46087% from fit is equivalent to the one extracted from the data fit. Nevertheless, this fraction should be higher, but it is reduced due to the enhancement of the high energy tail. Indeed, with the obtained high tail rates from the data, the gamma fractions are ∼47% very close to the simulated one (48%). Another discrepancy is the rate of neutron capture in hydrogen, which is 149.89 Hz, representing 93.68% of the generated neutrons in front of 144.02 Hz from the data leading to an equivalent fraction of 90.07%. This value is the one of interest regarding CCSN IBD simulation.

The MC chain resembles accurately the data, exhibiting close values in terms of the mean PE per neutron capture (H) event, with a precision of 0.05%. The resolution of this peak is better from MC chain, appearing its distribution more pinched than in comparison with data, but, again, this difference is small $\sim$ 3%. Finally, the reproduction of the gamma peak is the most significant difference. This discrepancy does not belong to the incursion of high energy tail, as independent contributions of gamma and neutron depicted by the blue dotted line and the green dotted line in the right panel of **figure 5.9** shows. One factor that impacts this distribution is the fraction of simulated gamma. The former is estimated, making the choice, even finding a shifted distribution, to reproduce a similar total rate for the gamma contribution. This optimization is shown by the results of the rates in trigger conditions and requiring a threshold of 6PE depicted in **table 5.4**. As reported, the subtraction of the background is effective regarding the integral of the rate rather than in the shape of event area distributions. However, in the low energy event area region [0,10] PE some bins present high rates after the background subtraction, supporting the threshold of 6PE and its inclusion into the MC vs. data rate comparison. Results of the event area distributions of MC vs AmBe calibration data for several gamma fractions are shown in **figure E.6** of **Appendix E.2.1**, but any fraction is able to reproduce accurately its shape, particularly the large sigma of the fitted data gaussian.

Conversely, the uncertainty in the neutron capture peak, which represents the peak resolution, has spread to the gamma one. In the case of the neutron capture peak, this uncertainty is evaluated by the standard deviation of the skewed gaussian, and its propagation will lead to equivalent values founded in the data fit[3]. This should be related to the uncertainties from water transparency, reflector performances,

[3]Central limit theorem can be used to calculate the propagation of the event area PE gaussian distribution uncertainty to different mean values [450]. This method assumes the same detector conditions and approximates the detector response, or its PE resolution, as a linear correlation between the two mean values. In this sense, for a N$\mu_{nCapture}$ this leads to $\sigma = \sqrt{N}\sigma_{nCapture}$, finding for the gamma contribution a value of $\sigma_{^{12}C}$=20.4 PE very close to the obtained from fit. Indeed, the detector resolution is not infinity-small as a base resolution. σ_{base} should be adopted, leading to re-defining $\sigma^2_{nCapture}$= $\sigma^2_{base} + \sigma^2$, and as well, $\sigma^2_{^{12}C} = \sigma^2_{base}$ + N σ^2, as highlighted in the legend of **figure 5.8**

PMT response, and SPE distribution, among other ones, that cannot be accounted for in the MC chain. The propagation of these uncertainties is also noticeable in the high energy region; however, it is difficult to dictate a more detailed conclusion about reproducibility by the simulation chain due to the mentioned discrepancies.

On the other hand, a similar exercise can be done to discuss the AmBe calibration results with the addition of Gd salt. **Figure 5.9** left panel shows the calibration results, background and background subtracted as done for SR0, corresponding to the SR2 period. The same gamma fraction obtained from the SR0 is assumed for the SR2 based on the optimization of the AmBe rate (see **table 5.4**). This is supported by the fact that uncertainties of SR2 calibration are significant regarding a re-estimation via a comparison with MC, which presents an important mismatch in the gamma region of the event area distribution (see **figure 5.9**). Concerning the subtracted distribution, the neutron capture contribution is diminished compared to the SR0 period as a fraction of neutron capture happened in Gd nuclei, representing only a fraction of 46.75% of the total captures. The obtained gamma distribution is similar to the one obtained from SR0 calibration as anticipated, but its rate is diminished, finding a fraction of 43.6% from the fit results. This reduction can be due to the AmBe source, or, on the contrary, propitiated from the transparency looses. The second idea is backed up by gamma fractions obtained from MC, shown in **table 5.4**, which stay the same at 45.65% in the water configuration with no Gd in SR0. The GEANT4 simulation in Gd configuration accounts for the small modification of transparency, but its impact of is not significant and can be neglected, while the important reduction of transparency shown by background data during Gd insertion (see **figure 4.21**) cannot be accounted yet by the MC chain. The Gd capture distribution is centered around 90 PE, but it is skewed to high PE area regions, this should lead to an increase in the neutron capture efficiency, as a significant fraction should happen in Gd. This fraction is estimated to a 50.1%. In SR0 calibration results the contribution of the high tails was $\sim$ 3 Hz representing $\sim$2% of the total captures (for a 6 PE threshold), while in SR2 this contribution is diminished by a fraction of $\frac{1}{3}$ due to the high efficiency of Gd capture. In comparison to the SR0, the obtained uncertainties for each bin are higher, announcing that some instabilities still being present in the detector with the addition of Gd, as the error bars (corresponding to the standard deviation for each bin) of the right panel of **figure 5.8** illustrates. This is expected to govern the discrepancies between the MC and the data.

5.5 CCSN simulation results

The Hitlet simulator is employed to simulate the CCSN IBD neutron and positron signals in the energy ranges of [0,2] MeV and [0,50] MeV, respectively, based on the GEANT4 output. The aforementioned discrepancies evidenced by the AmBe MC vs. data comparison are anticipated to be present in these signals. These will result in an optimal reconstruction for the neutron capture, and for higher energies, of the positron; it will be also noticed a spectrum with a better resolution than that of data, as the energy resolution uncertainties will propagate proportionally to the number of Cerenkov photons generated, which

	SR0 ($F_\gamma = 0.48$)		SR2 ($F_\gamma = 0.48$)	
Values from Data/MC	Data	MC	Data	MC
Rate (Hz)	233.9 ± 0.82	229.86	234 ± 24	228.98
Rate$_{th=6PE}$Hz	220.7 ± 0.63	222.46	221 ± 23	223.86
Values from fit				
F_γ(γ efficiency)	0.464(96.6%)	0.4608(96.01%)	0.436(90.83%)	0.456(95%)
nCapture rate (th=6PE) Hz	147 ± 0.51 (144.02)	156.93(149.89)	156 ± 16	157.13(59.73)
F$^{\text{nGd Capture}}$(%)	–	–	50.1%	56.67%
nCapture efficiency (H_2)*	90.07%	93.68 %	46.75 % (± 4.58 %)	40.6 %
Total nCapture efficiency	91.86%	98.08%	97.51 % (± 9.56 %)	98.88 %

Table 5.1: Summary of the AmBe study results for the SR0 and the SR2 period, comparing the data and the MC simulation. The values from the fit, which is normalized with the obtained rates are represented to better understand the implications of the MC vs data corrections. The values in parenthesis corresponds to the neutron capture happening in hydrogen. * The neutron capture efficiency for MC and data is calculated based on the obtained capture rate divided by the source neutron rate of the source 160 n/s.

is greater in this case (see **Section 4.1.3**). This will lead to a ROI bounds for the positron less large, which will impact the final detection efficiencies.

5.5.1 Detection efficiencies and observed spectra

The strategy of simulating $\bar{\nu}_e$ mono-energetic lines results — due to the linearity of $\bar{\nu}_e$ and e+ spectra— in equivalent positron mono-energetic lines, obtaining the positron detection efficiency $\epsilon(E_e)$ as a function of its energy, independently of the IBD positron spectra. This efficiency, convoluted with the IBD or ES[4] rates for a given CCSN model and distance will lead to obtaining the energy spectrum and the number of observed events. The observed rates $\frac{dR_i^l(E_e)}{dE_e}$, for a given interaction l (l="IBD","ES") and a Mass Ordering i, and the corresponding number of events N_i^l (obtained by integrating the rate through the energy) can be written as it follows (using the rates from the energy spectra, equations (4.17) and (4.23)):

$$N_i^l = \int_{th} \frac{dR_i^l(E_e)}{dE_e} dE_e, \qquad \frac{dR_i^l(E_e)}{dE_e} = \epsilon(E_e) \frac{dR_i^l(E_e)}{dE_e} \tag{5.7}$$

Figure 5.10 shows the positron detection efficiency curves in the muon veto (left) and the neutron veto (right), for the 27 $M_\odot$ and 11 $M_\odot$ for NMO, and its corresponding detectable energy spectrum from equation (5.7). As expected in **Section 4.1.3**, the muon veto efficiency for detecting positrons is highest when it's close to the IBD positron mean energy at 20 MeV, exhibiting an efficiency of 94.4%. Only

[4]Positron simulation results can be used to build the ES electron scattered distributions, as the only difference between energy deposition of the electron and positron is the two annihilation gamma rays, of 511 keV, which are not expected to be observed by the detector as their energy deposition through Compton scattering will lead to electrons with an energy close to the Cerenkov threshold (261 keV).

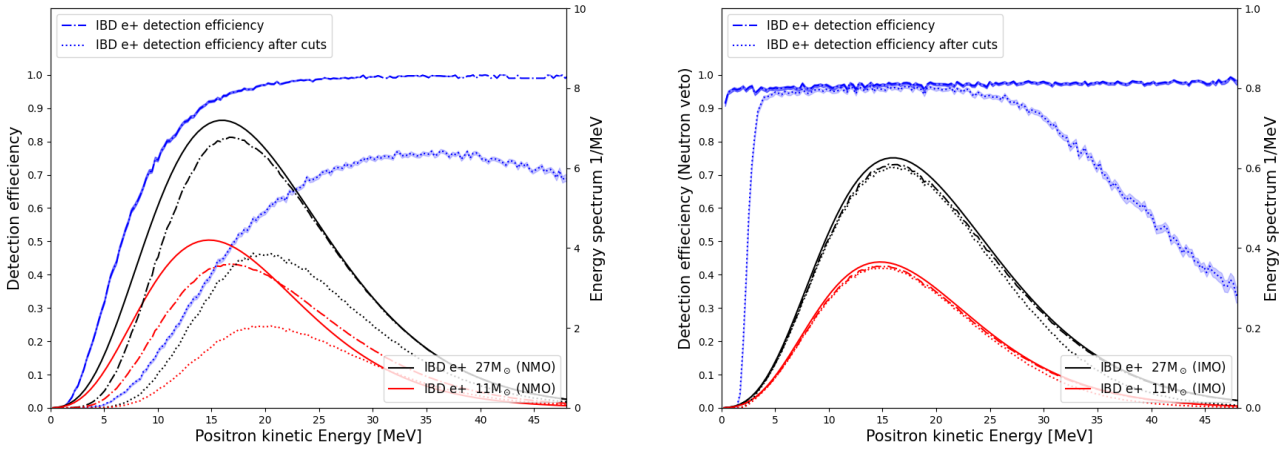

Figure 5.10: **Left:** IBD positron detection efficiency as a function of positron kinetic energy in muon veto (left axis), the corresponding efficiency after cuts is depicted in dotted lines. On the right axis the corresponding observable (solid lines), the detected (dot-dashed lines) positron energy spectrum (right axis) and the spectrum detected after the cuts in dotted lines. These values correspond to the 27 (black) and 11 (red) $M_\odot$ progenitors from *Bollig 2016* model in the NMO. **Right:** Same values for the neutron veto.

beyond 1 MeV positrons present a non-null detection efficiency, which is higher than the 261 keV Cerenkov threshold. It is comfortable to extrapolate the positron detection efficiency impact on the anti-neutrino energy spectrum via the approximation $T_e \sim 1.8$ MeV. At 6.5 MeV, the efficiency is 50% and increases at 10 MeV to more than 70%, which for the $\bar{\nu}_e$ energy corresponds to ∼8.2 MeV, and 11.7 MeV in which the CCSN spectrum becomes significant. These are values below the CCSN neutrino energy thresholds of large Cerenkov detectors, such as Super-K [262] or DUNE [297] higher than 15 MeV, but as it will be shown, the will be modified after applying background rejection cuts. On the other hand, it can be noticed that the shape of the positron spectrum is conserved, presenting a reduction in the low energy part, while the obtained mean energy; 20.88 MeV and 19.33 MeV for 27 and 11 $M_\odot$ progenitors, respectively, is close to mean energies from the observable spectra, 22.34 MeV and 21.25 MeV respectively. Concerning the neutron veto, almost all the IBD positron signals are expected to be detected, with the efficiency ∼ 94% at the Cerenkov threshold and beyond 95% in the rest of the spectrum, reaching 98% for the high energy tail values. This high efficiency leads to the conservation of the observable spectrum shape, and results in a number of detected events very close to the number of expected interactions (see **table 4.3**) as reported in **table 5.2** with 12.69 interactions against the 13 expected.

For each positron energy, the associated IBD emitted neutron is simulated. In this sense, the latter neutron energy spectrum is not independent but related to the IBD kinematics described in 4.19 and D.3.1. This implies that the GEANT4 output neutron energy bins are not uniform, but present statistics following the neutron IBD spectrum. However, enough statistics have been extracted in the range of interest [0 - 2 MeV] and normalization can be applied, to obtain the detection efficiency $\epsilon^{IBD}(E_n)$ as a function of the neutron energy independently. The respective neutron energy observed rates and number

of IBD neutron events can be calculated using equation (D.13) as:

$$N_n^{IBD} = \int_{th} \frac{dR_i^{IBD}}{dE_n} dE_n, \qquad \frac{dR_i^{IBD}(E_n)}{dE_n} = \epsilon^{IBD}(E_n) \frac{dR_i(E_n)}{dE_n}. \tag{5.8}$$

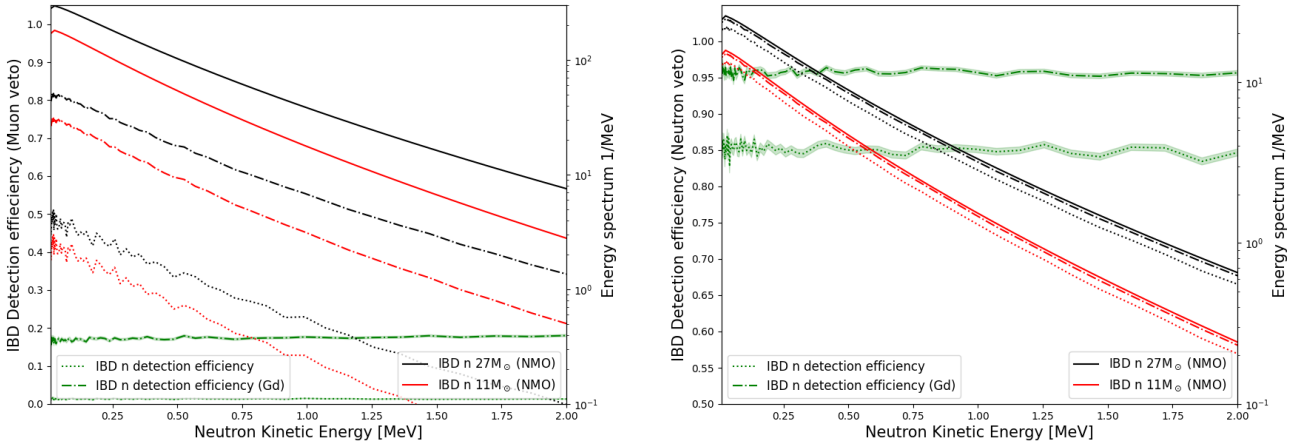

Figure 5.11: **Left:** IBD neutron detection efficiency as a function of neutron kinetic energy in muon veto (left axis), for the water (green dotted line) and (green dashed-dotted line). On the right axis, the corresponding observable (solid lines) and detected in water (dotted lines) and in Gd-water (dot-dashed lines) neutron energy spectrum. These values correspond to the 27 (black) and 11 (red) $M_\odot$ progenitors from *Bollig 2016* model in the NMO. **Right**. Same values for the neutron veto.

Figure 5.11 depicts the IBD neutron detection efficiency as a function of its kinetic energy for the 27 and $M_\odot$ in the water(SR1) and Gd-water (SR2) configurations for NMO.In the muon veto, without Gd doping, the neutron veto signal presents extremely low detection efficiencies ∼1%. This value is almost maintained during the neutron kinetic energy spectrum, as neutron detection does not depend on the former but on the gamma-ray energy deposition during its capture in water. In the SR2 configuration with Gd, the detection efficiencies increase but are still low, ∼16-18%. It is worth noting that efficiency curves are made with a logarithmic step in order to reproduce the exponential decrease of the IBD neutron spectrum, presenting fluctuations in the energy region around the maximum of the neutron spectrum ∼ 2.5 keV presented in **figure D.9**. This effect comes only from statistic, because these bins do not have enough neutron events for the step width to be uniform. Detection efficiencies for neutrons in ultrapure water and Gd-doped water are high, as expected from the results of AmBe simulations. Comparable values to the neutron capture efficiencies extracted from MC AmBe (see **table 5.4**) are founded. However, AmBe simulations represent the geometric uncertainties for a given position of the neutron emission, while in CCSN IBD simulation the neutron emission is homogeneously distributed in the volume of the water tank. This leads to a diminished neutron detection efficiency of 86% and 96% from the efficiency curve median in water and Gd-water, respectively.

Finally, the corresponding detected energy spectra for the ES interaction scattered electron can be obtained. As mentioned in the introduction of this section, the positron detection efficiency can be used to perform the convolution of the CCSN ES electron energy rate, as this efficiency is independent only related to the incoming positron (electron) energy. **Figure 5.12** illustrates the detected energy spectrum for the selected progenitors in the NMO case for muon and neutron vetoes. From the commented results of the positron energy efficiency in the muon veto, which present tiny values below 1 MeV, it can be anticipated regarding the shape of the scattered electron spectrum, represented by solid red and black lines, that it will be challenging to observe the ES signal. The maximum of the spectrum is located at energies lower than the Cerenkov threshold. In addition, the detection characteristics of the muon veto described in **Section 4.1.3** lead to the necessity of a significant amount in the number of Cerenkov productions to observe positron signals, resulting in a detection threshold $\sim$ 1 MeV. The exponential decrease of the ES spectrum leads to the fact that the spectrum is reduced in a half at $\sim$ 6.5 MeV when detection efficiency is near 50%. This low detection power anticipates 5 and 2 ES events in the muon veto at 10 kpc for the two selected progenitors 27 and 11 $M_\odot$ respectively (in front of the 12 and 6 interactions expected). On the contrary, the detection threshold of neutron veto is close to the Cerenkov threshold, and the obtained ES detected spectrum is close to the observable above Cerenkov threshold energies. However, at 10 kpc, less than one ES was expected to be observed, while more than one in the MW center, which is maintained after applying detection efficiencies.

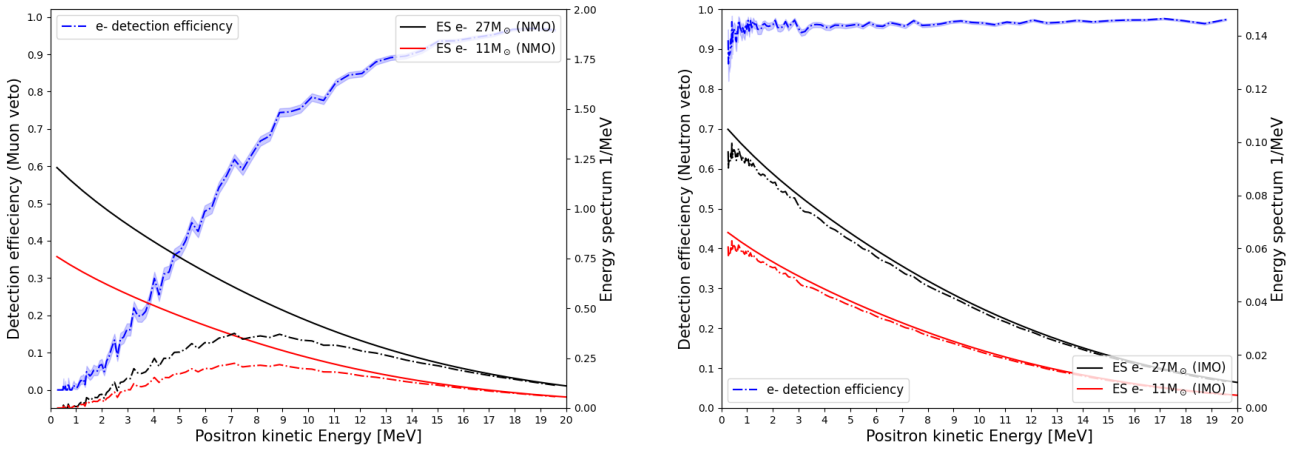

Figure 5.12: **Left:** ES positron detection efficiency as a function of the scattered electron kinetic energy in muon veto (left axis). On the right axis, the corresponding observable (solid lines) and detected in water (dotted lines) ES energy spectrum. These values correspond to the 27 (black) and 11 (red) $M_\odot$ progenitors from *Bollig 2016* model in the NMO. **Right:** Same values for the neutron veto.

Table 5.2 summarizes the detected number of events resulting from the extraction of the detection efficiencies at 10 kpc including the IMO case, for the IBD and ES interactions in the muon and the neutron. The efficiency function accounts for the detector uncertainties reproduced by the simulation chain, including the event trigger conditions. These expressions are valid for a given threshold defined by

	Number of CCSN detected events(*) at 10 kpc			
Progenitor	$27M_\odot$		$11M_\odot$	
MO	NMO	IMO	NMO	IMO
Muon veto				
IBD e+	136.71	133.2	71.41	72.15
IBD n	2.02	1.96	1.08	1.085
IBD n (Gd)	26.01	25.24	13.75	13.84
ES	5.13	5.1	2.87	2.85
Neutron veto				
IBD e+	12.67	12.3	6.75	6.71
IBD n	11.12	10.82	5.91	5.95
IBD n (Gd)	12.51	12.15	6.64	6.68
ES	<1 (0.88)	<1 (0.88)	<1 (0.51)	<1 (0.51)

Table 5.2: Summary of the number of CCSN detected events in muon and neutron veto for the IBD and ES interactions at 10 kpc. This event numbers accounts for the two progenitors 27 $M_\odot$ and $11M_\odot$ from *Bollig 2016* model, in the NMO and IMO neutrino mass ordering. * What we call "number of events" must be intended as an average number, these values are particularly useful to evaluate the impact of the detection capabilities for each volume at other CCSN distances, in which the differences between NMO and IMO will be enhanced.

one, or several, of the event parameters or special trigger conditions. When background analysis will be performed, its study and its subsequent reduction will be done using event parameter distributions, i.e. the event area, the number of PMT contributions, and the center time distributions. In order to compare signal and background in those terms, event parameters distributions are also extracted for neutron and positron. As mentioned, their simulation is CCSN model independent, as any CCSN model flux is used, but mono-energetic positrons and their associated IBD neutron. This allows to build any event parameter k distribution for different models, through the convolution of the former with the chosen model *Mod* rate energy spectra. For example, this convolution is done for the positron as:

$$\frac{dN_k^{Mod}(k)}{dk} = \int_{th} \frac{dN(E_e,k)}{dE_e dk} \frac{dR_i(E_e)}{dE_e} dE_e \tag{5.9}$$

5.5.2 Event distributions

Figure 5.13 illustrates the event area rate distribution for the IBD positron using the *Bollig 2016* spectrum for the $27M_\odot$ and $11M_\odot$ progenitors at 10 kpc in muon veto and neutron veto. Regarding the muon veto spectrum, the latter is centered around 16 PE for both progenitors (being the lightest one spectrum more skewed), which implies less than 1 PE per MeV is recorded from the positron, approximating this relation through its mean energy ($\sim$ 21 MeV). This proportion is maintained in all the spectrum, in which the positron energy (see **figure 5.10** left panel) spectrum shape is recognizable, resulting in a linear correlation between the positron energy and the number of PE. The mean number of PE per energy bin is

represented in **figure E.11** left panel, verifying this linear increasing for an approximative value of 0.65 PE/MeV. The positron event area spectrum will be impacted by the background, as gamma and neutron captures from the background will lead to a lower PE signal but close to the latter one in the region of interest (see **Section 5.6.1**). The latter region of interest (ROI) will be precised in the next paragraphs. Conversely, the positron spectrum in the neutron veto is larger, spanning a range of [0,1200] PE, with a center around 900 PE. This larger spectrum provides a better resolution, thereby promoting a greater photon collection efficiency. The average number of PE/MeV is approximately 21 PE/MeV (see **figure E.11** left panel). In addition, to the better resolution, the positron signal is not impacted by the neutron background, being the ROI far from the former as showed during the AmBe analysis (**Section 5.4**). These properties anticipate a high resolution of the positron signal in neutron veto.

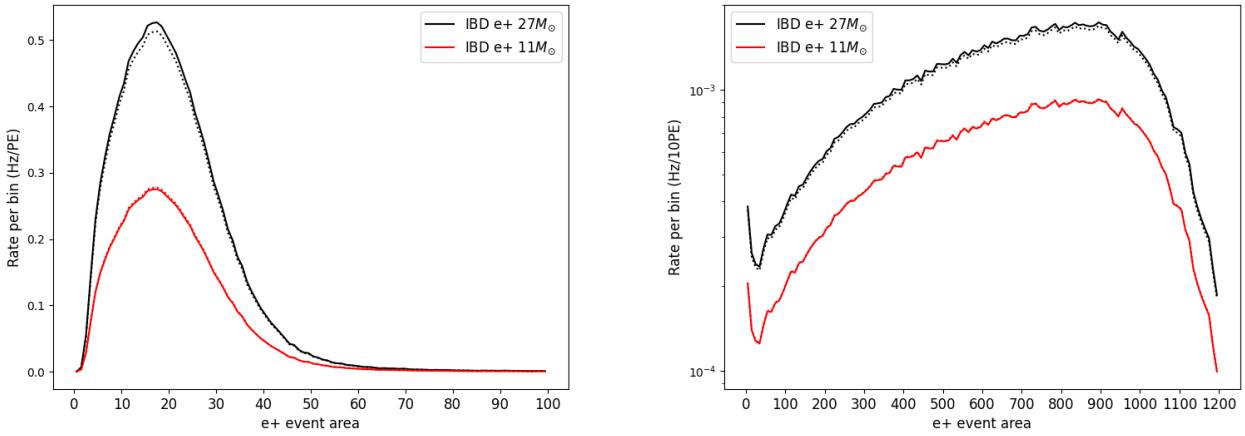

Figure 5.13: **Left**. Event area distribution for IBD positron in muon veto for the NMO (solid lines) and IMO (dotted lines), for the water (green dotted line) and (green dashed-dotted line) for the 27 $M_\odot$ (black) and 11$M_\odot$ (red) at 10 kpc. **Right**. Same values for the neutron veto.

The other event parameters, center time and number of pmt contributing (N-PMTs), can be obtained in the same way following the relation (5.9), defining as well the ROI for the IBD positron. This is illustrated by the 2D histograms in **figures 5.14** and **5.15** for the muon and neutron veto respectively. In the muon veto not more than 30 PMTs are involved in positron events, and the main ratio, or the correlation, N-PMT / PE area is close to 2, meaning that a significant part of the VPMThitlets contributing to the events will produce stacket hitlets as anticipated in **Section 5.3** (see **figure E.2**). Regarding the center time, it is shown that most of the VMPThits arrive to the channels between 10 and 100 ns. The ROI bounds are: event area [0,100] PE; center time [0,100] ns; and N-PMTs [5,30]. It is worth noting that the 5 PMT required for the muon veto trigger is applied.

Compared to the ROI of the muon veto, the neutron veto offers a more precise domain, better characterizing the positron signal compared to the background or neutron. This is due to its superior photon collection, which leads to a higher resolution. This difference is particularly represented by the center

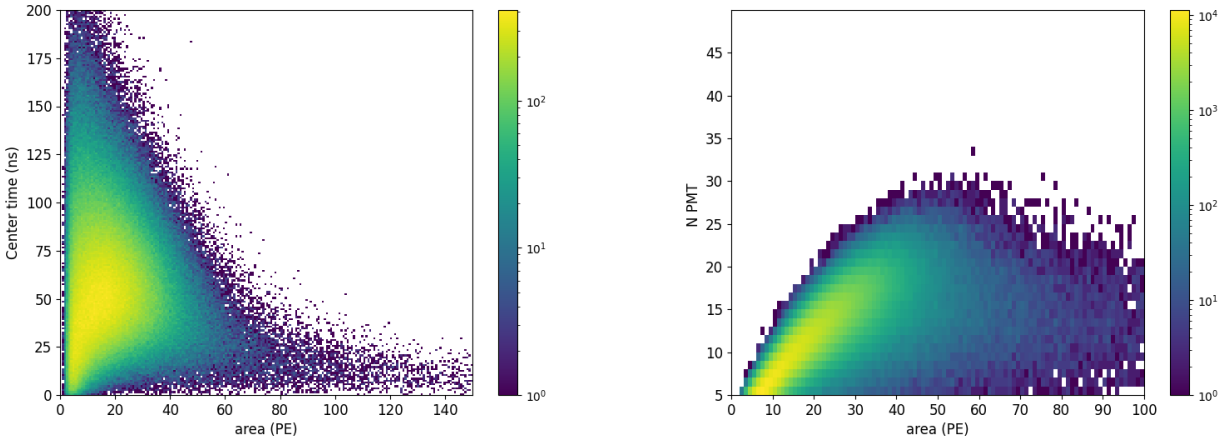

Figure 5.14: **Left**. Center time vs area distribution for the IBD positron in the muon veto. **Right**. Number of pmt contributing vs area distribution for the IBD positron in the muon veto. For this histograms the $27M_{\odot}$ progenitor is used but no substantial differences between progenitor or MO are expected.

time vs. area histogram, which is less spread and clearly defined from the side of center time between 25 and 100 ns. Also, the number of PMTs contributing (N-PMTs), presents a peculiar distribution close to a CDF (1-e^{-x}) with a saturation and main contribution at the maximum of 120 PMTs, implying that all the PMTs are contributions in the majority of the positron events. The ROI bounds for the neutron veto are: event area [2,1200] PE; center time [0,100] ns; and N-PMTs [3,120].

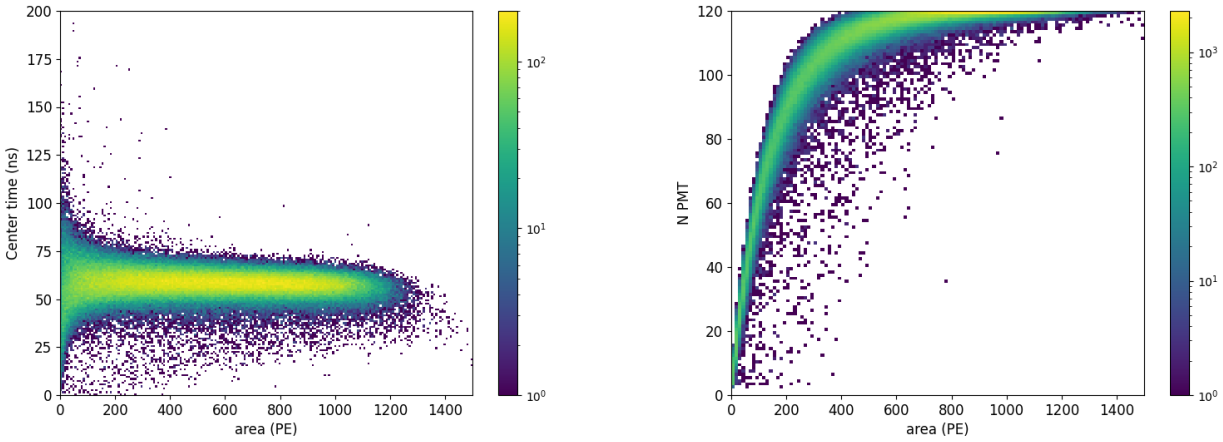

Figure 5.15: **Left**. Center time vs area distribution for the IBD positron in the neutron veto. **Right**. Number of pmt contributing vs area distribution for the IBD positron in the muon veto. For this histograms the $27M_{\odot}$ progenitor is used but no substantial differences between progenitor or MO are expected.

5.5.3 Time distributions

The latter sections are focused on the energy detected spectra and their corresponding event parameter distributions characterizing the CCSN ROI in muon and neutron vetoes, resulting from the positron signal simulation. Regarding the detected number of events reported in **table 5.2** only this signal presents enough statistics to reproduce the time evolution spectra, distinguishing the tree main phases of the CCSN burts. The simulation of the time evolution of the CCSN IBD signal is crucial for background rejection purposes, and a similar strategy used in **Chapter 3, Section 3.5.2.1** will be applied. For this purpose, 100 CCSN are simulated in the water tank. Each CCSN simulated account for IBD interaction, i.e. neutron and a positron simulation, and the ES scattered electron simulation. **Figure 5.16** depicts event time from the IBD interaction for one CCSN simulated in the SR2 (Gd-water configuration). The choice of this configuration is motivated by the fact that a maximum of 2 IBD neutron events are expected in the SR1 configuration. The number of IBD detected events, including a neutron and positron signal, represents only a fraction of ∼19%, as only a maximum of 26 events from the neutron capture in Gd-water are expected. This is the most optimistic case for a CCSN at 10 kpc — and for the selected *Bollig 2016* model progenitors— in the muon veto, in which neutron signal information can be used. Right panel of the **figure 5.16** shows the obtained time spectrum's for both particles. The dotted lines correspond to the distribution after applying the cuts for background rejection that will be explained in the next section. Before the cuts, the rate hierarchy of the three phases (*neutronisation*>*accretion*>*cooling*)is conserved, even for the neutron signal.

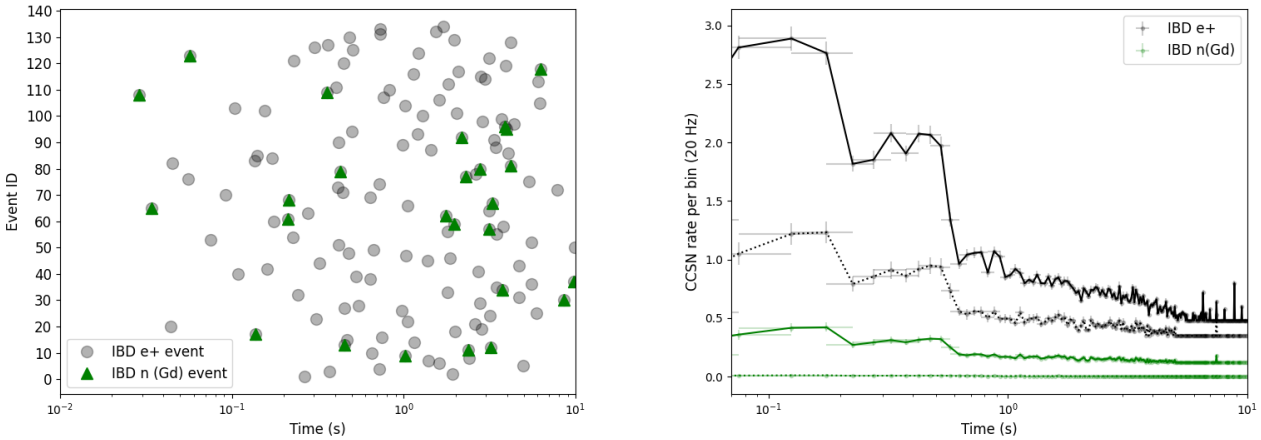

Figure 5.16: **Left**. Representation of the IBD event time recognized by its 'event ID' for one CCSN simulated in the water tank, for events recorded in the muon veto in the SR2 configuration. Green triangles represent the neutron signal, while black circles the positron events. **Right**. Time distributions obtained from the 100 CCSN simulated in the water tank fro positron (black) and neutron (green) for the $27M_{\odot}$ progenitor before (solid line) and after cuts (dotted lines). The errors bars correspond to the standard deviation for each time bin.

In the case of the neutron veto, a maximum of 12 events is expected at 10 kpc (see **table 5.2**), which a priori is not enough to reproduce accurately the shape of the time evolution of the CCSN burst. The

time reconstruction will be challenging for a CCSN at 10 kpc due to the low number of expected events, however the combination of neutron and positron signals can reinforce time information as a similar number is expected for both signals, as **figure 5.17** shows. The figure also shows the results after the cuts, presenting only a few points for the neutron, in the two configurations. Results are extracted from the events happening in the neutron veto for the 100 CCSN simulated in the water tank. Only a small fraction of these CCSN survive regarding neutron signal (i.e. presenting at least one neutron event) . Nevertheless, after the cuts 11 events from positron signal are expected, and even if themselves are not enough to accurately reconstruct the time spectrum, they can be combined with the muon veto positron ones. Results of this combination will be shown later in **Section 5.7** .

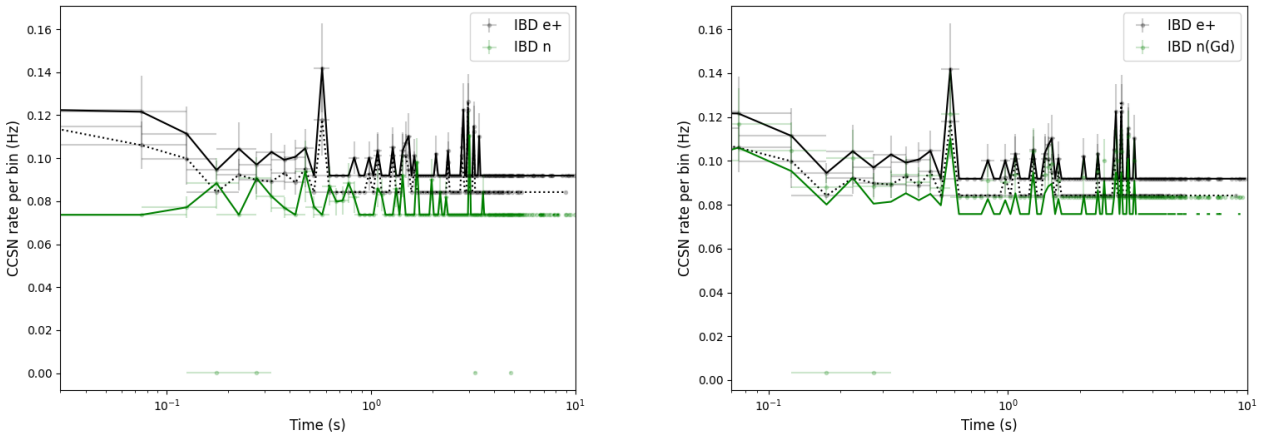

Figure 5.17: **Left**. Time distributions obtained from the 100 CCSN simulated in the water tank for positron (black) and neutron (green) for the $27M_{\odot}$ progenitor before (solid line) and after cuts (dotted lines) in the SR0 configuration. The errors bars correspond to the standard deviation for each time bin. **Right**. Same distribution for the SR2 configuration.

5.6 CCSN water tank sensitivity study

The previous sections demonstrated that multiple channels contribute to CCSN detection, with the IBD positron being the most significant in both vetoes. The former is expected to succeed in extracting time and energy spectrum information. On the other hand, ES electron and IBD neutron signals generate different responses in muon and neutron vetoes. In the largest water volume, only the neutron capture in Gd is relevant, while a maximum of 5 ES events are expected at 10 kpc. Neutron and positron signals in the neutron veto show similar rates, with the background strongly dominating the first one in SR0 configuration. Neutron and muon veto backgrounds are very different, as explained in **Sections 4.1** and **4.2**. All of these statements encourage evaluating CCSN sensitivity separately for both detectors. The implications of the background rejection cuts in the positron signal are expected to be significantly different, anticipating a more important reduction of the former amplitude in muon veto. Those cuts will

affect distinctly ES and neutron IBD signals in each veto, reducing dramatically their amplitude in both detection volumes. Then, the sensititvity studies of muon and neutron vetoes will be combined, in order to obtain the water tank sensitivity curve as a function of the progenitor distance.

5.6.1 Muon veto background study

The muon veto low energy background component is dominant in the ROI of IBD and ES signals. In addition, the amplitudes of neutron IBD and ES electron signals are not significant enough at 10 kpc, particularly in the SR1 configuration, to extract energy or time information by themselves. The muon veto's poor energy resolution in the MeV range for gamma (from neutron captures) and positron (electron) energy depositions makes it difficult to distinguish between the IBD neutron and positron signals, which in turn affects the potential reconstruction of the positron energy spectrum. Studying the discrimination of both signals through their individual event parameters can finally have a collateral impact on the reconstruction of the time spectrum. As its distinction is a priori challenging, the neutron signal from the IBD vertex will happen $\mathcal{O}(100\mu s)$ later than the positron, and in the case of the former cannot be efficiently distinguished from the latter, it will affect the information of time evolution of the CCSN burst. Consequently, after applying background rejection cuts, the neutron and ES electron signals, which are expected to be even more reduced, will be integrated as part of the background model.

SR1, SR2 background

The CCSN signal's short duration necessitates accounting for background rate fluctuations. Neutron veto calibrations, typically conducted twice a month, significantly influence the muon veto background rates within the ROI. Some of the particles produced, directly or indirectly, during calibrations can attend the muon veto volume, such as neutrons from AmBe calibrations. A selection of stable runs from background periods outside of neutron calibrations has been undertaken to manage these fluctuations. However, it is intriguing to evaluate the expected CCSN sensitivity while also accounting for these fluctuations through a long period of data collection. As a consequence, for the SR1 configuration, two different sensitivity studies are performed: one utilizing the selected runs (from 1 month of data taking); and the other with the non-selected in a long period of around 70 days of data taking. Both run collections will often be referred to as "SR1" and "SR1 (No sel.)" for the selected and the non-selected data, respectively. The background rates are studied in terms of mean rates in a ten-seconds window, and rolling a 1s step window over ten-second independent bins and obtaining the maximum rate. This procedure is identical to the one performed during the study of the background rate in the TPC.

The first two top panels of **figure 5.18** depict the time evolution of the mean and maximum rates for the selected and non-selected SR1 background runs. Significant fluctuations, which enhance the rates during the calibration periods, are present in the non-selected runs (second top panel). In addition, some fluctuations that are not relevant, are present in the first top panel, as the selection of the runs is based on the labeling applied to each run during the processing, and the immediate runs after a calibration run often present higher rates. The non-selected runs display a median mean rate of 18 Hz, whereas the selected runs

display a lower rate of 13.16 Hz. The maximum rates for the non-selected and selected runs, respectively, are 28.36 Hz and 21.79 Hz, demonstrating the same trend. In the case of the mean rates, the latter are close to the values of $27M_{\odot}$ progenitors 13.7(13.3) Hz for the NMO(IMO). In order to better evaluate the CCSN sensitivity, the distributions of mean and maximum rates can be approximated to analytical functions, i.e., gaussians and skewed gaussians already used and defined in this work (e.g., equations for AmBe studies (5.4)). The two bottom panels represent these distributions and their corresponding fit functions. For the selected runs, the mean and maximum rates are approximated via a gaussian and a skewed gaussian, respectively, while the non-selected runs, include several gaussian to deal with rate fluctuations.

The rejection of the background will necessitate cutting a significant region of the ROI, resulting in a considerable reduction of the positron amplitude. Additionally, due to the similar values of the positron signal and background mean rates, presenting the latter higher rates than the low-mass $11M_{\odot}$ progenitor signal at 10 kpc, employing the maximum rates to evaluate the sensitivity is a priori a better strategy. **Figure 5.19** depicts the 2D histogram representing the background event parameters, noticing that the former is strongly present in the ROI and only can be moderately reduced rather than being efficiently cut. Nevertheless, the right panel of the figures shows that the background exhibits a different, and inverse, correlation between the event area and the number of N-PMTs compared to the positron, approximately $\sim 1/2$. This is attributed to the strong contribution of accidental coincidences (AC) that survive to the 5 PMT threshold of the muon veto trigger.

The mean and maximum rate distributions resulting from the application of the cuts are shown in **Figure 5.20**. A significant reduction in both mean and maximum rates for the selected and non-selected run groups is noticeable. In addition, fluctuations for the data period, including neutron veto calibrations, are lessened and can be handled with the inclusion of a gaussian in order to approximate its contribution to the distribution. The evolution in time of the rates after the cuts for SR1 is depicted in **figure E.12** of **Appendix E.4**, showing the mitigation of these fluctuations. In the case of the non-selected background, the median serves as a more accurate indicator. The former is reduced to 4.08 Hz for the mean and 8.74 Hz for the maximum rates, as illustrated in the annexed figure. For the selection, the rate reduction led to 3.64 Hz and 8.04 Hz for the mean and maximum rates extracted from the fit values depicted in **figure 5.20**.

On the other hand, the same exercise can be done for the SR2 period. Transparency losses reported in **Section 4.2.2** mitigate significantly the rate fluctuations. However, studying these fluctuations appears premature, given the lack of sufficient data to assess the long-term effects. As a consequence for this SR2 period, a stable group of data is selected, and it will be used for the background study. The latter selection will consist of 12 days of recorded background data. The event parameter distributions for the SR2 data do not present significant differences for rejection purposes and are presented in **figure E.14**. The reduction this time led to similar rates than SR1 after cuts: 3.16 Hz and 7.15 Hz for the mean and the maximum rate distributions, representing the mean of the gaussian and skewed gaussian used to perform their respective approximations, as **figure 5.21** shows. These values, in terms of mean rates, are lower

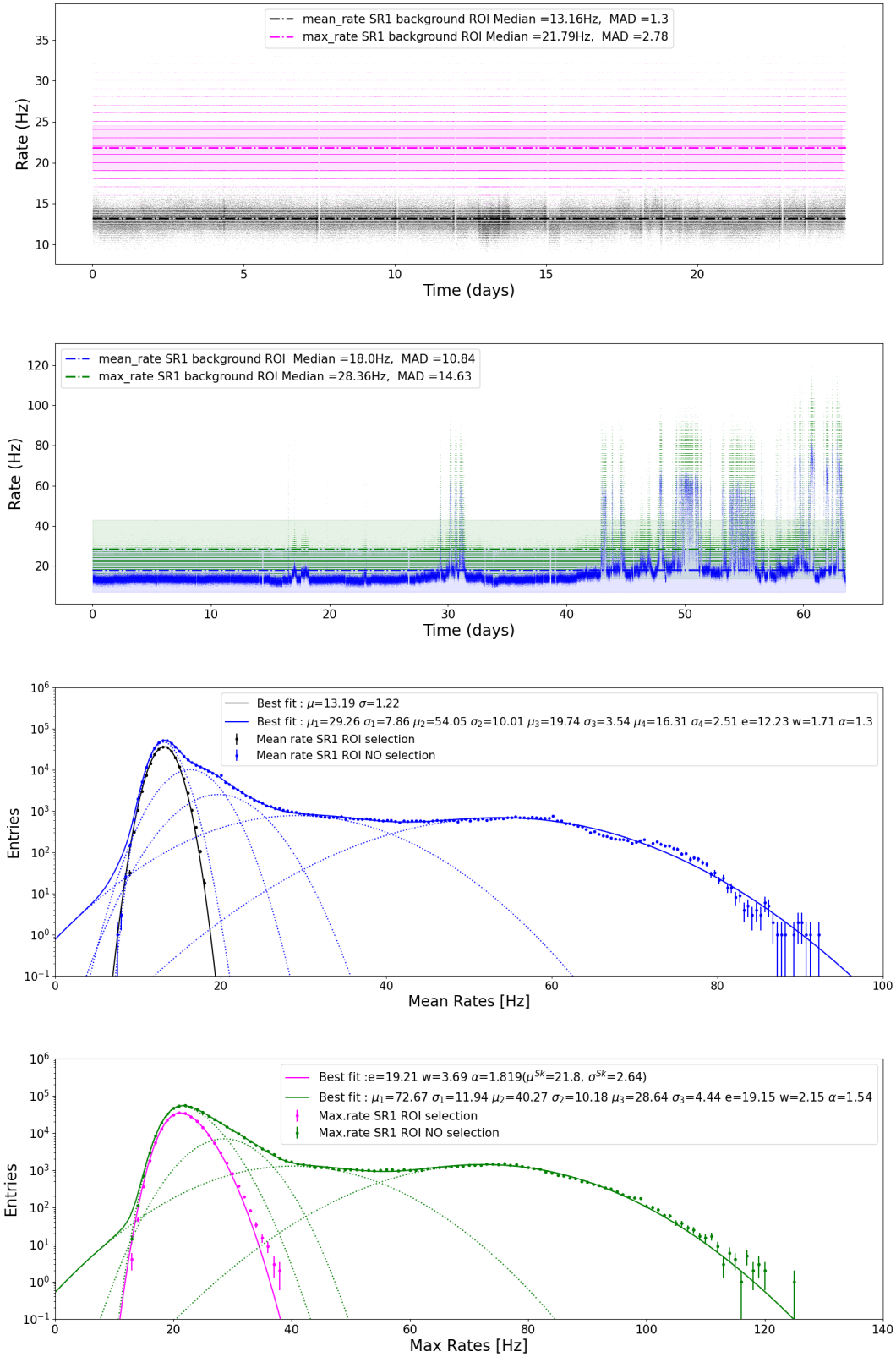

Figure 5.18: First and second upper plots present the evolution in time of the mean and maximum rates of SR1 in the ROI in the muon veto for the selected (black and magenta) and non-selected (blue and green). Their respective distributions represented in the two other bottom plots can be approximated by analytical functions skewed and, in which fit parameters appears in the legend.

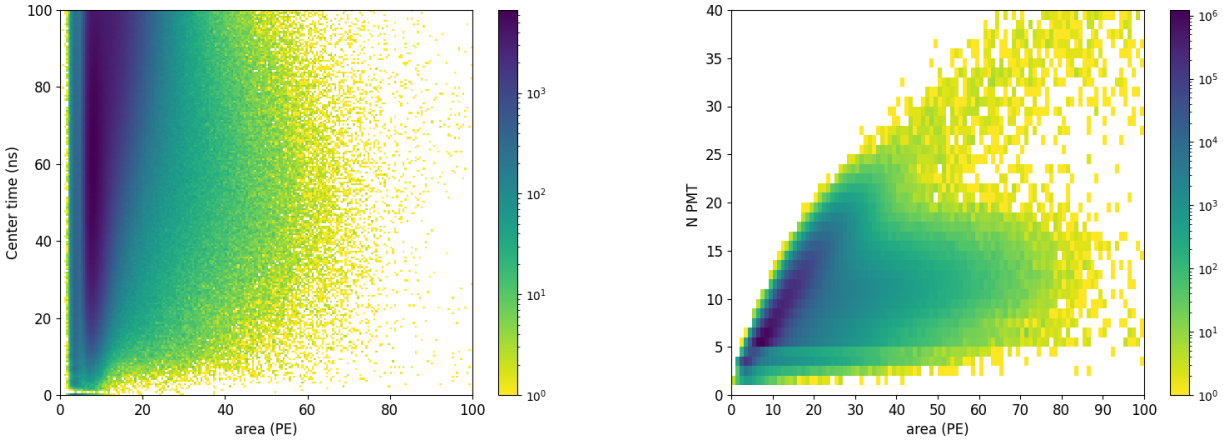

Figure 5.19: **Left**. Center time vs area distribution for the selected background data of SR1. **Right**. Number of pmt contributing vs area distribution for the same SR1 period and selection

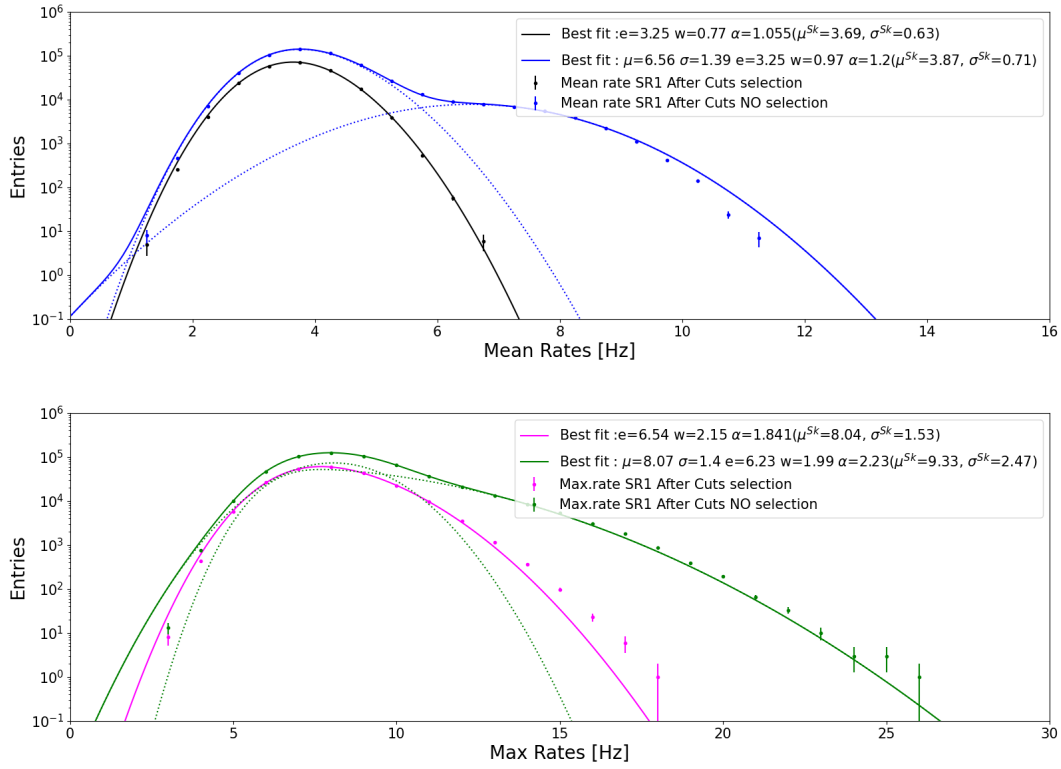

Figure 5.20: **Top**. Mean rates distributions for SR1 background selected(black) and non-selected(blue) after applying the cuts. **Bottom**. Maximum rates from the rolling window distributions for SR1 background selected(magenta) and non-selected(green) after applying the cuts.

than the CCSN obtained from simulation before applying the cuts, but as anticipated, the latter will be diminished. Furthermore, it is worth noting that the SR2 rates are lower than the SR1 ones in the ROI

due to the transparency losses related to the Gd addition. This effect cannot be handled by the MC simulation, but it is probable that it will also affect the positron signal, absorbing a part of the Cerenkov photon spectrum with the consequent diminution of its rate. In the next section, the impact on IBD and ES signals will be explored and compared to the background rates.

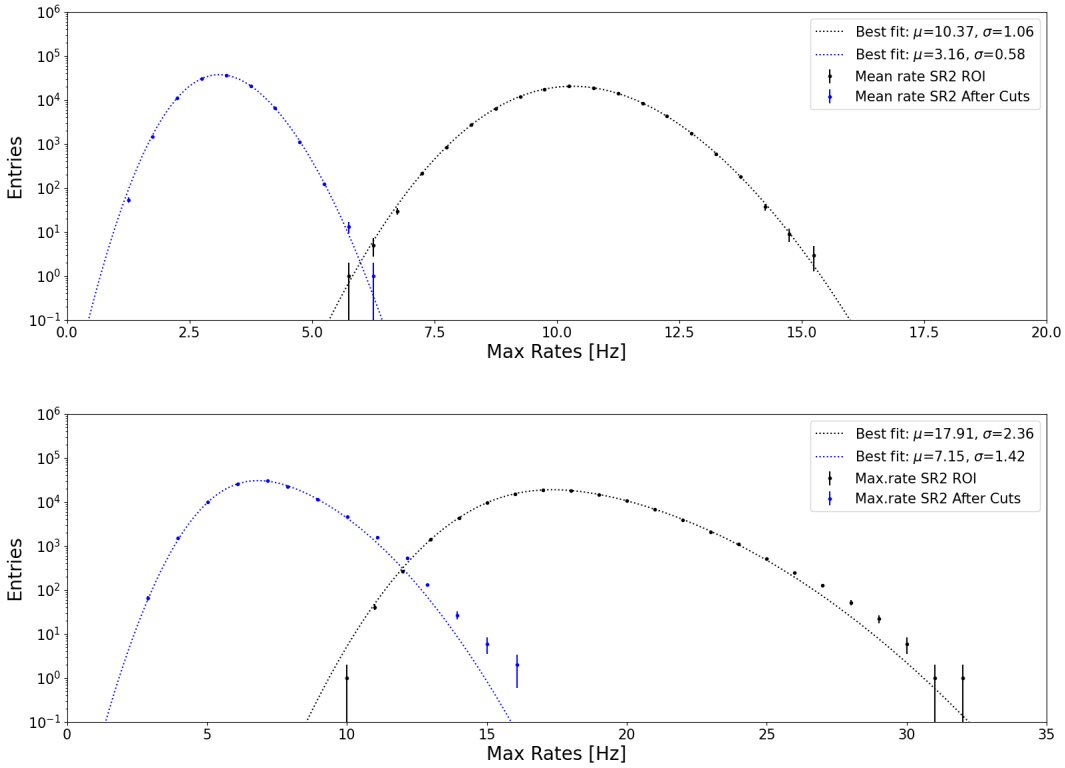

Figure 5.21: **Top**. Mean rates distributions for SR2 background before (black) and after (blue) applying the cuts. **Bottom**. Maximum rates from the rolling window distributions for SR2 background before (black) and after (blue) applying the cuts.

CCSN rates and event distributions after cuts

The **table 5.6.1** shows the total number of CCSN events at 10 kpc before and after background cuts were applied. It also shows the expected number of background events before and after the cuts in the time window of the CCSN burst. The positron values presented correspond to the 27 $M_{\odot}$, progenitor in NMO, and are not impacted by the configuration of the detector expecting 76 events after cuts in SR1 and SR2. As the SR2 presents lower rates, one can assume that the sensitivity regarding the positron signal will be enhanced, but the SR2 lowering is not due to new trigger conditions or background reduction improvement from this configuration, but to the transparency changes in water that will also impact the positron. Indeed, the most probable outcome is that the reduction in positron signal will also lead to a sensitivity decrease for the former. Consequently, SR2 sensitivity results interpretation should account for the fact that, as mentioned, it is premature to handle transparency conditions into the CCSN simulation.

	Number of CCSN(*) and background events before and after cuts in the muon veto			
Background	**SR1**		**SR2**	
	Before cuts	After cuts	Before cuts	After cuts
Selected	180(±10.85)	37(±0.63)	-	-
Non-selected	132(±1.22)	39(±0.71)	103(±1.06)	31(±0.58)
Signal	**SR1**		**SR2**	
	Before cuts	After cuts	Before cuts	After cuts
IBD e+	136.71	76.47	136.71	76.47
IBD n	2.02	<1 (0.073)	26.01	<1 (0.73)
ES	5.13	1.62	5.13	1.62

Table 5.3: Summary of the number of CCSN detected events at 10 kpc and background before and after applying the cuts in muon veto SR1 and SR2 configurations. This event numbers accounts for the 27 $M_\odot$ progenitor from *Bollig 2016* model in NMO. * The number of events are not an integer, and have no physical meaning, but these values are particularly useful to evaluate the impact of the detection capabilities for each volume at other CCSN distances. The complete impact of the cuts in the rest of progenitors and IMO is reported in **table E.4**

On the side of the neutron signal, less than one event is expected with extremely low mean rates $\mathcal{O}(10^{-3})$ Hz. In SR1, this signal is ten times lower than in SR2 after the cuts, as shown in **table 5.6.1**, but also leading to very low mean rates of ∼0.073 Hz. Finally, one event from ES interaction is expected to be detected for SR1 and SR2 configurations.

Figure 5.22 illustrates the event area rates for the IBD, ES induced by the CCSN burst of the $27M_\odot$ progenitor (NMO) in the muon veto and the corresponding to the background in SR1 and SR2 configurations, before (solid lines) and after (dotted lines) cuts. It is worth noting that the background is dominant in the low-energy region of the positron spectrum, and its rates are higher than the IBD neutron and ES ones, covering their spectrum even after applying the cuts. It is difficult to include, or reject, the IBD and ES contributions into the background model as the latter signals are scaled with the square of CCSN distance, implying, for example, that 100 ES events and 7 IBD neutron events are expected at 1 kpc (see **figure 5.24**). In this scenario, the ES signal may not be considered as background, and discrimination between the ES scattered electron and positron signals should be studied, which is still challenging regarding their similar event distributions. However, the probability of detecting a CCSN in the next decades at this distance is very small, as mentioned in the first chapter (see **Section 1.3.1**). For this first sensitivity study in the XENONnT water tank, only signals that exhibit more than one event expectation at 10 kpc will be considered. For larger volumes of water, the neutron signal should be accounted for; nevertheless, it is not yet clarified if the design of the next DM detectors (LXZD or DARWIN) will include water tank vetoes for larger volumes.

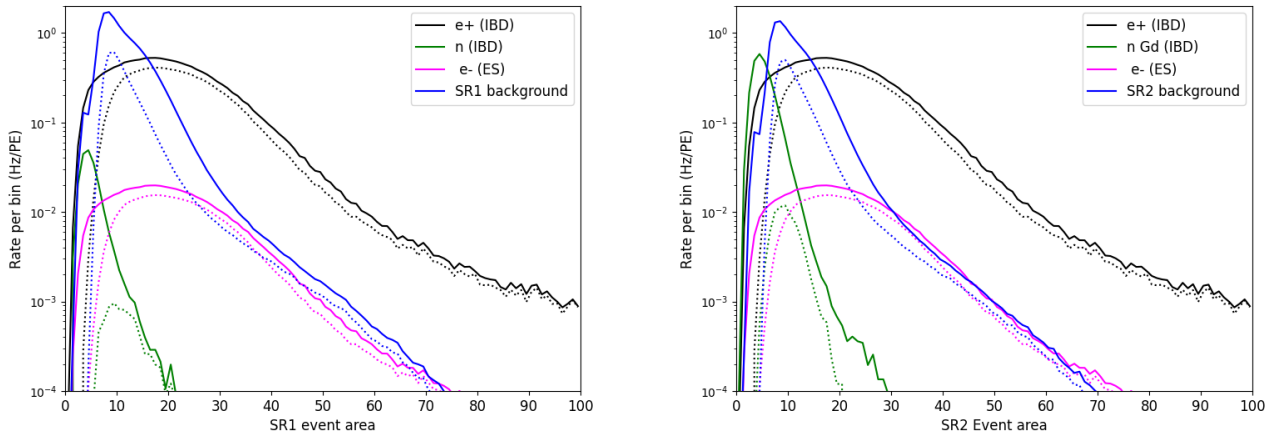

Figure 5.22: Event area distribution before (solid lines) and after (dotted) applying the cuts for the IBD positron (black), neutron (green), ES (magenta) and background (blue) for the SR1 (left) and SR2(right) periods.

Muon veto background model

The background model in the muon veto for SR1 and SR2 will account for ES plus the muon veto background. **Figure 5.24** shows the evolution of the number of ES events as a function of the CCSN distance, compared to the background, and the positron and neutron IBD signal for the non-selected runs of SR1 (left) and SR2 (right) periods before (solid lines) and after the cuts (dotted lines). Around the MW center at 8.3 kpc, the background and the positron expected events are in the same order of magnitude; as a consequence, a decrease in the sensitivity for larger distances is expected. With the applications of the cuts, this similar number of events is reached further, around 20 kpc, predicting a significant increase in the sensitivity at 10 kpc. On the other hand, after the cuts, ES scattering is the dominant contribution into the background model for distances < 2 kpc. An identical behavior is founded in the SR2, with the inclusion of the neutron contribution, which is relevant <1 kpc compared to the background. Two conclusions can be extracted from the evolution of the number of CCSN events as a function of the distance.
The first one is that the ES signal may be integrated into the background. Its contribution will be added to the SR1 and SR2 distributions depicted in **figures 5.20** and **5.21**. The latter contribution depends on the considered CCSN distance. The second conclusion, is the reinforcement that mean rates of the positron signal will present a poor sensitivity, and the maximum rates will be a better technique to explode the time evolution of the CCSN for background discrimination purposes. Sensitivity in muon veto will be studied through this value. The independent mean and rolling rates of the ES electron scattering signal for the 100 CCSN supernova simulated at 10 kpc are depicted in the figure5.23, noticing that its impact at 10 kpc is expected to increase the maximum rolling window rates in ~ 1 Hz. The combination of the ES signal with the background presents a challenge regarding the rolling window rates, as the ES signal should be inserted in the background before rolling the 1s step window. This should be done correctly at the hitlet level. Adding the ES hitlets to the background ones, and then performing the event building,

to finally roll the rolling window over these events. This will imply an enormous computing cost, and the simulation of 100 CCSN at different distances.

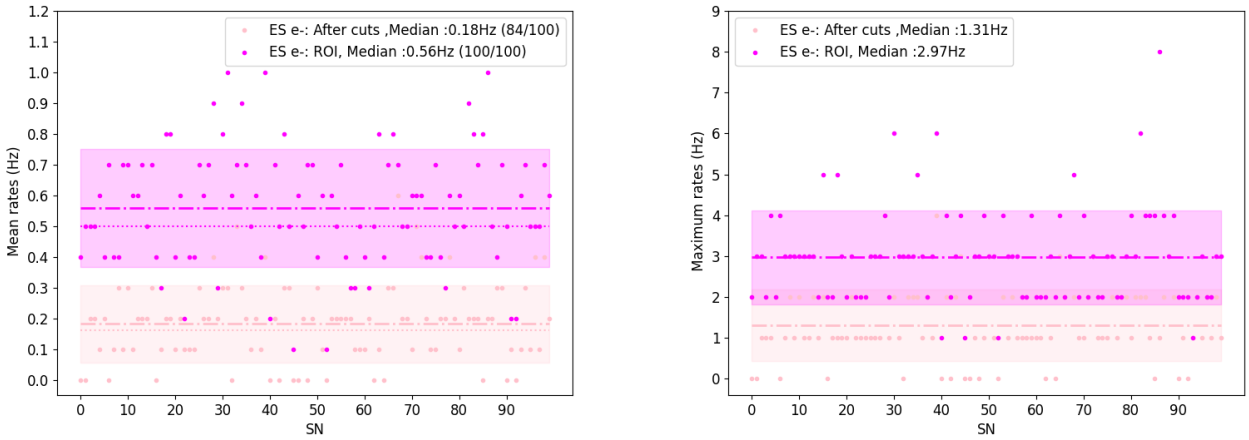

Figure 5.23: **Left**. Center time vs area distribution for the background data of SR2 in neutron veto. **Right**. Number of pmt contributing vs area distribution for the same SR2 period.

Instead, a MC toy can be used to approximate the contribution of the ES signal to the background. Using the background data at an event level and inserting a N $\propto 10^2/\mathrm{d}^2$ number of events scaled by the value at 10 kpc for a given distance d, rolling window can be used to obtain the maximum rolling window rates. At this point, it may be remembered that in the simulation of 100 CCSN ES, a poissonian uncertainty was applied to the number of interactions. The obtained mean rates of this simulation will be used to determine the number of ES events inserted, including its uncertainty (i.e., the obtained MAD, shown by the band of **figure 5.23**). It is worth noting that this mean is slightly higher, 1.81 events (0.181 Hz$\times$10s) than the obtained from the integration of the observable ES energy spectra after cuts 1.65 events (see **figure 5.12**). Another point is that the low ES rate results in a fraction of the 100 ES CCSN simulated not survive, i.e., have at least one event after cuts. The surviving fraction before and after cuts is highlighted in the label of the **figure 5.23** left panel, indicating that 84/100 survives. For this MC toy simulation, an overestimation of the signal will be assumed, accepting that this fraction is 100/100 after cuts. Finally, the ES events will be inserted, following the time ES time distribution rates described in equation (4.23).

The contribution of ES will modify the fit parameters of the background function approximations. The idea is to extract the information about the evolution of these parameters as a function of the distance accounting a priori for two discontinuities that can be anticipated at 2 kpc and 15 kpc. For CCSN closer than 2 kpc, the ES will dominate the maximum rate distributions. Its expected rate can be roughly scaled by the median of the distributions illustrated in **figure 5.23**, $\sim$32.5 Hz, which is more than four times the background contribution. At 10 kpc, on the contrary, the maximum rates from ES are expected to be $\sim$ 1.31 Hz, and its impact for further distances will decrease, being negligible at some point. At 15 kpc, less than one ES event is expected, and the background will dominate above this distance. In this case

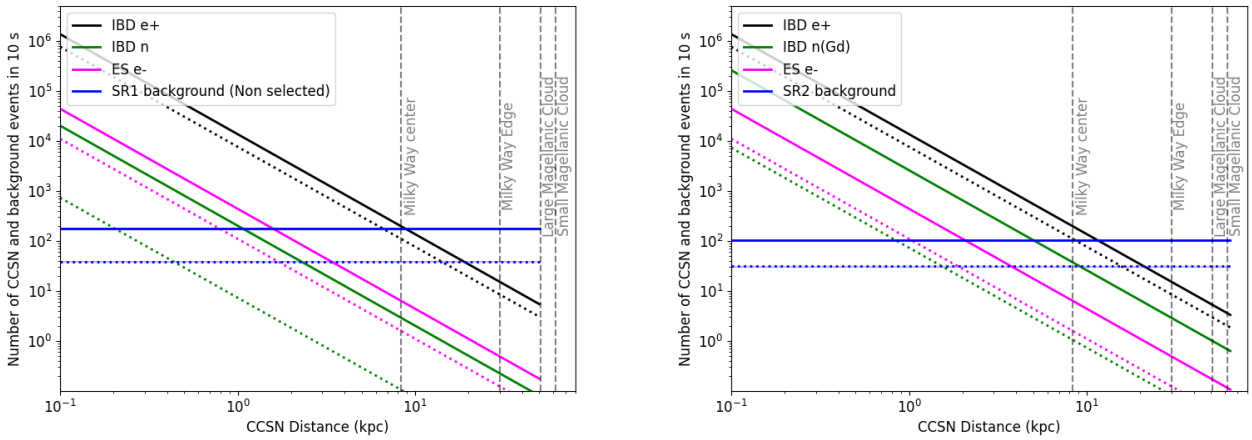

Figure 5.24: Number of events as a function of the progenitor distance before (solid lines) and after (dotted) applying the cuts for the IBD positron (black), neutron (green), ES (magenta) and background (blue) for the SR0 (left) and SR2(right) periods in the muon veto.

the background model PDF will not depend anymore on the CCSN distance. This discontinuities can be expressed for the background model PDF F(x,d) as it follows:

$$F(x,d) = \begin{cases} f(d)^{ES} & : \quad d < 2 \quad \text{kpc} \\ f(x,d)^{bck+ES} & : \quad d \in [2,15] \quad \text{kpc} \\ f(x)^{bck} & : \quad d > 15 \quad \text{kpc} \end{cases} \tag{5.10}$$

The background model probability density function can be written with the SR1 and SR2 maximum rates fit functions $f(x)^{bck}$ represented in **figure 5.20**, including the ES contribution $f(x,d)^{bck+ES}$ and the ES contribution alone f(x)^{ES} as:

$$f(x)^{bck} = \begin{cases} A \times SkGauss(x, \mu^{Sk}, \sigma^{SK}) + B \times Gauss(x, \mu, \sigma) & : \quad \text{SR1 (No sel)} \\ SkGauss(x, \mu^{Sk}, \sigma^{SK}) & : \quad \text{SR1, SR2} \end{cases} \tag{5.11}$$

$$f(x,d)^{bck+ES} = \begin{cases} SkGauss(x, \theta_i(d)) + Gauss(x, \theta_j(d)) & : \quad \text{SR1 (No sel)} \\ SkGauss(x, \theta_i) & : \quad \text{SR1, SR2} \end{cases}$$
$$\theta_i(d) = f_i^{ES}(d) \times i \quad (i = A, \mu^{SK}, \sigma^{SK}), \qquad \theta_j(d) = f_j^{ES}(d) \times j \quad (j = B, \mu, \sigma) \tag{5.12}$$

$$f(x,d)^{ES} = SkGauss(x, N(d)\mu^{10}, \sqrt{N(d)}\sigma^{10}), \qquad N = \frac{10^2}{d^2} \tag{5.13}$$

Where μ^{10} and σ^{10} are the obtained values at 10 kpc (see **figure 5.23**), and μ^{SK} and σ^{SK} are the equivalent mean and standard deviation from the original skewed gaussian parameters e,w and α defined in **Chapter 3** expression (3.45).

To complete the background model, the f_i^{ES} parameter has to be studied for the 3 considered cases: the

non-selected runs from SR1 (SR1 NO), the SR1 selection, and the SR2. For this purpose, the obtained maximum rate distributions for several CCSN distances from the insertion of the ES signal in the muon veto background will be used.

Figure 5.25 the results of the simulation of 10^6 ES events in the background rolling window for several CCSN distances. It is noticeable that the 15 kpc distribution (pink) is almost equal to the one corresponding to the background, supporting the interpolation bounds of equation (5.10) in which the ES signal is negligible. On the other hand, the distribution at 2 kpc (cyan) is dominated by the contribution of the ES; the background in this case is represented by a second gaussian function with a low probability, as shown in the figure. The interpolation parameters evolution through distance, corresponding to the fitting of the simulation ES plus background, are represented in the **figure E.15 Appendix E.4.1.1** . The significance

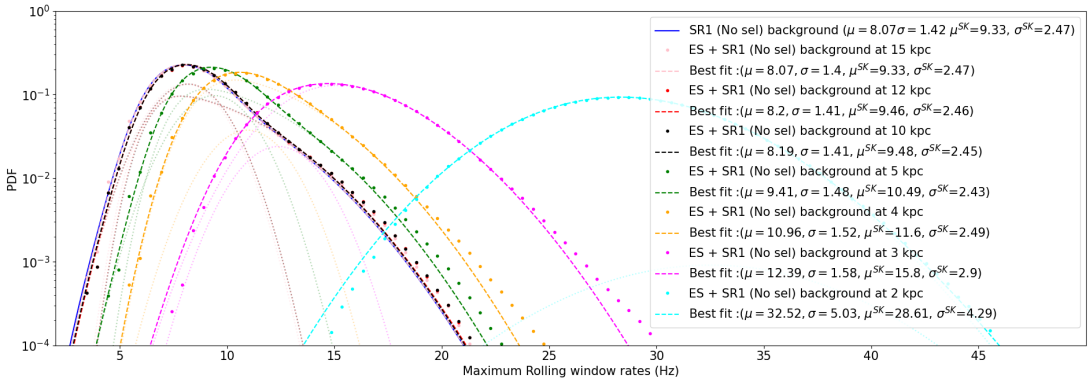

Figure 5.25: Maximum rates distribution for background model including the ES contribution, for several a CCSN distances: 2 kpc (cyan), 3kpc (magenta), 4 kpc (orange), 5 kpc (green) 10 kpc (black), 12 kpc (red) and 15 kpc (pink). The background PDF is composed by gaussian and a skewed gaussian (see E.4.1.1) which contributions are represented by the semi-transparent dotted lines. The SR1 background only contribution is represented by the blue solid line.

can be calculated from the p-value, obtained from this background model PDFs and the expected CCSN positron maximum rates for a given distance, in the background only hypothesis, as done for the CEνNS signal in the TPC (see equation (3.46) of section **Section 3.5.4**). The calculation of the p-value can be written, and remembered, in this case for the given expectation rate R_i:

$$Z(\sigma) = \Phi^{-1}(1-p), \qquad p = \int_{R_i}^{\infty} F(x,d)dx \tag{5.14}$$

The null hypothesis assumes that the observations are only due to the background, whereas the alternative hypothesis accounts for signal plus background. The null hypothesis will be evaluated through the R_i maximum and mean rates extracted from the simulation of 100 CCSN IBD positrons in which background is inserted. These rates are depicted in **figure 5.26** for the $27M_\odot$ progenitor at 10 kpc (NMO), including the background inserted for each CCSN in the time duration burst of 10 seconds.The contribution of the SN signal only from the simulation of these 100 CCSN IBD positrons is depicted in **figure E.18** in the

ROI before and after cuts for the $27M_{\odot}$ in NMO at 10 kpc. For the calculation of mean rates, a toy MC is not necessary. Using the background model PDF describing the mean rates, background events can be sampled in order to obtain the number of observations q_i for each of the 100 SN simulated. In addition, the signal from ES scattering is also inserted using the mentioned mean rates from the 100 CCSN results. For the mean rate sensitivity study, the observation rates R_i can be obtained by dividing the number of observations by the time burst, which is set to 10 seconds, to maintain the homogeneity of the time bins — as background is included, even if the CCSN signal's proper duration is lower due to the loss of some events after applying the cuts. Finally, rolling window rate maximums are extracted from the sampling of the PDFs including ES scattering, illustrated in **figure 5.27**, and will be added to the rolling window rates of the CCSN positron signal. This approximation is the most pessimistic one, assuming that the background is stable during the 1 second of the rolling window rate step and, as a consequence, stating that the ES contribution always maximizes the rate. This leads to adding both signal and background independently.

At 10 kpc, in the most pessimistic scenario: the SR1 including calibration rate fluctuations and the inclusion of ES illustrated in **figure 5.25**, the maximum rates of the signal only are significantly higher than the considered background, 36.4 Hz for the $27M_{\odot}$ and 18.48 Hz for the $11M_{\odot}$ as depicted in **figures E.18** and **E.19** (left panel). These values anticipate a high significance for the background only hypothesis. In the IMO case, similar values are obtained at 35.9 Hz and 18.16 Hz for the respective progenitors. This difference manifests in the **figure 5.26** comparing the blue solid line (background only) and the CCSN positron data simulated in black. The background is approximately six times lower than the observations from the data simulation.

On the other hand, the number of events from the IBD positron after cuts is similar to the number of background events, as **table 5.6.1** shows. This is particularly true for the $11M_{\odot}$ progenitor, in which the signal-background ratio is close to 1. The pink line in the **figure 5.26** represents the obtained background mean rates for each CCSN in SR1 and SR2 configurations, noting that the simulated positron mean rates are three times higher than the latter. This reduces in a half the relation obtained from the maximum rates. Values of the mean rates for each CCSN positron signal only are depicted in the right panel of **figure E.19**, and are 7.15 (7.12) Hz and 3.54 (3.6) Hz for the $27M_{\odot}$ and $11M_{\odot}$ progenitors for NMO(IMO). However, for distances lower or equal to 10 kpc, it is intriguing to calculate the sensitivity for an eventual combination of the former with the neutron veto or the TPC. Results for the significance obtained using the mean rates are annexed in **figures E.22** for the SR1 and SR2 periods.

Figure 5.27 shows the sensitivity curves as a function of the CCSN distance for the two progenitors, based on the rejection of the background only hypothesis, using the PDFs depending on the CCSN distance depicted in **figure 5.25**. The curves represent the mean and band standard deviation obtained from 100 observations at each distance, assuming that significance follows a gaussian distribution. At the distance of interest 10 kpc the significance Z (σ) for both progenitors is 17.3 $\pm$2.7 σ and 8.7 $\pm$1.1 σ. Beyond this distance, the low-mass progenitor significance drops down to less than 5σ at 13 kpc, with the maximum

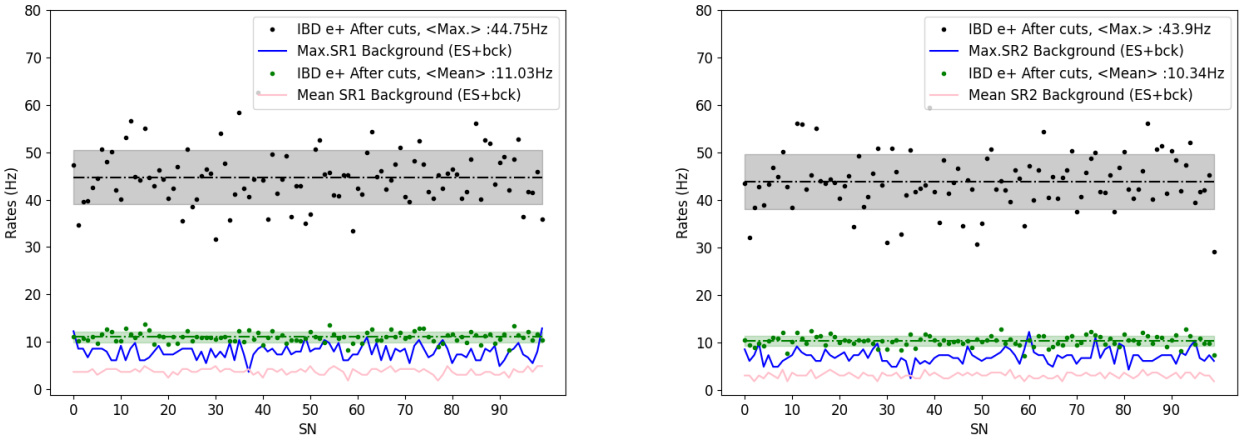

Figure 5.26: **Left**. Rolling window maximum (black) and mean (green) rates for the the CCSN IBD positron observations in the SR1 configuration, from the simulation of 100 CCSN of the $27M_{\odot}$ in the NMO. Background (SR1 selection) + ES contribution is represented by the blue line for the rolling window maximum rates and the mean by the pink line in the background only hypothesis. The thick line black line and the thick green dotted line corresponds to the median and the bands to the standard deviation. **Right**. Same representations in the SR2 configurations.

rates very close to the background ones at this distance. For the heavier progenitor, expectations of CCSN discovery at 5σ are limited by a 19 kpc distance, while CCSN evidence ($\geq 3\sigma$) will be extended to 23 kpc. In the limits of the MW, significance is 2 σ in the MW edge at 30 kpc, while the 2σ significance is reached at $\sim$ 23 kpc for the $11M_{\odot}$ progenitor. Regarding the shape of the curves, the latter are smooth in the domain in which background and ES contribute, and background only beyond 15 kpc, but some small fluctuations appear in the region where ES dominates as its rate grows up with $1/d^2$. These fluctuations impact particularly the lightest progenitor. The expectations for the sensitivity of the SR1 selection, whose rates are more stable, are optimistic, as well as for the SR2 period. The production of a similar background model for both periods incorporates the contribution of ES. In this case, the SR1 and SR2 muon veto backgrounds are approximated both with a skewed gaussian (see equation (5.11)). The distribution of the PDFs for several CCSN distances is depicted in **figure E.16**, and the evolution of their parameters as a function of the corresponding distances is described in **figure E.17**. **Figure 5.36** illustrates the sensitivity curves for the mentioned periods as a function of the CCSN distance for the $27M_{\odot}$ (black) and $11M_{\odot}$ (red) progenitors for NMO. Regarding the left panel corresponding to the SR1, the significance is improved around the distances of interest between the MW center and 12 kpc. At 10 kpc significance of $24.05 \pm 3.8\,\sigma$ and $12.05 \pm 2.36\,\sigma$ are expected for the $27M_{\odot}$ and the $11M_{\odot}$ progenitors, improving the ones of the SR1 non-selected data. In addition, excluding background fluctuations in SR1, further distances can be observed. Requiring at least 3σ the distance limits will be 28 kpc and 20.5 kpc for the respective progenitors. In the MW edge, the heaviest progenitor presents a significance of 2.67 ± 0.43 σ.
Finally, the SR2 configuration shows the better results. Remembering, that these results are conditioned

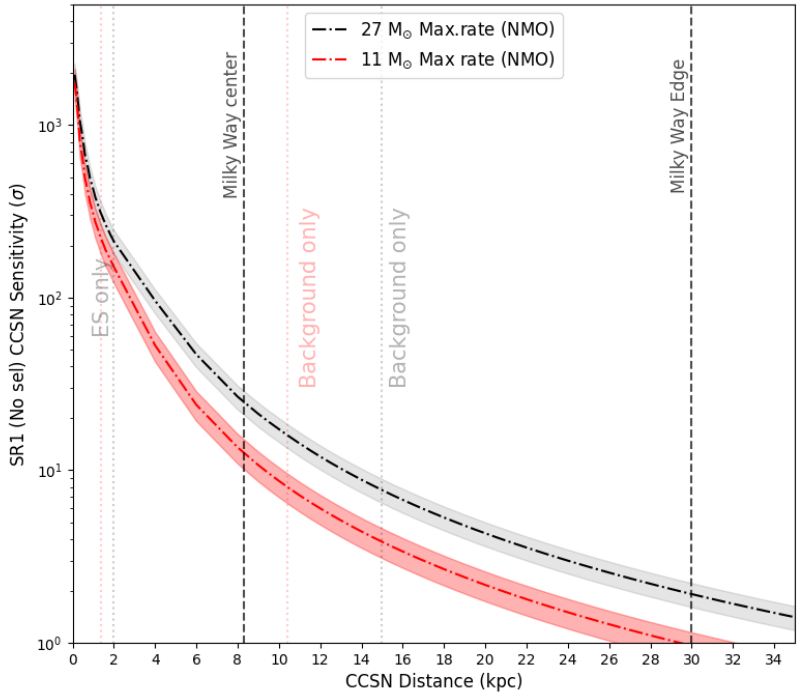

Figure 5.27: Sensitivity curves as a function of the CCSN progenitor distance in muon veto for the background model including the SR1 non-selected runs and the ES contribution. The significance is obtained from the maximun rates of the 27 $M_\odot$ (black) and the 11$M_\odot$ (red) progenitor for MNO. The dotted-dashed lines shows the significance mean and the bands the standard deviation. Regions dominated by ES and muon veto background are limited by the doted transparent lines.

by the impact on the water transparency, which also will affect positron rates. As a consequence, the results presented for SR2 have to be carefully interpreted by the reader, accounting for this. At 10 kpc values are improved in comparison to SR1 period, with significances of 25.3 $\pm 4.0\,\sigma$ and 12.8 $\pm 2.5\,\sigma$ for the 27$M_\odot$ and 11$M_\odot$ progenitors, respectively. This is a considerable improvement in comparison with SR1 non-selected data. In this SR2 configuration, the CCSN signal from the 27$M_\odot$ progenitor in the MW edge has a significance of 2.9 $\pm$ 0.5 σ.

For the IM0 case, sensitivity curves are annexed in **figure E.20** expecting slightly different values at 10 kpc. Those differences will be enhanced at closer distances. This contrast is due to the number of expected events for IMO and NMO after cuts reported in **tables 5.6.1** and **E.4**, affecting differently the 27$M_\odot$ in which sensitivity values are smaller for IMO and on the contrary for the 11$M_\odot$ progenitor. As well, the obtained sensitivities from mean rates are depicted in **figure E.22** showing the anticipated lower values at 10 kpc, particularly for the lightest progenitor.

Significance results have to be combined with the number of events, depicted as a function of the distance in **figure 5.24**. In the 2σ boundaries described for SR1 selection, 23 and 11 events are expected, and for

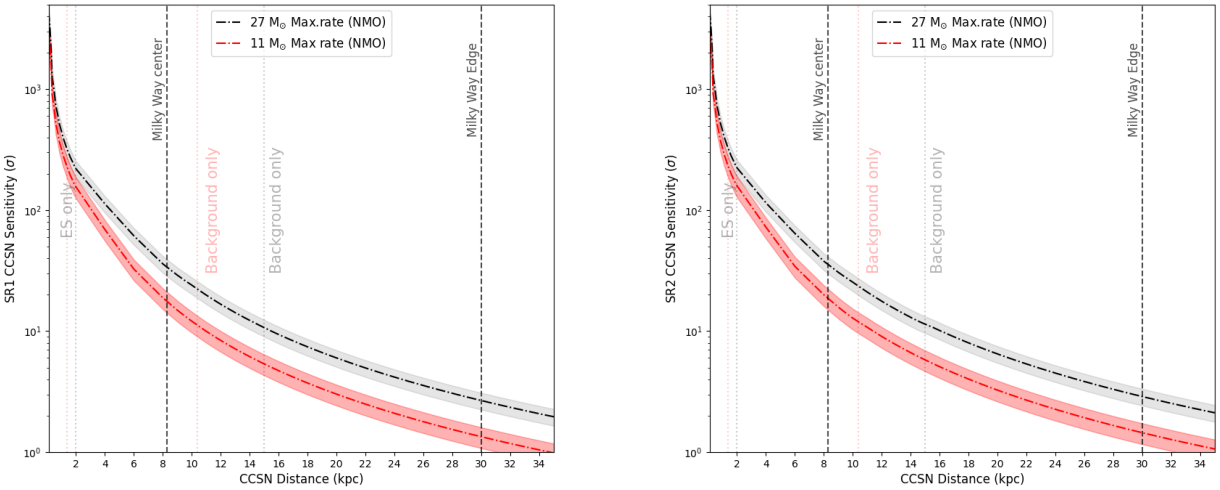

Figure 5.28: Sensitivity curves as a function of the CCSN progenitor distance in muon veto for the background model including the SR1 selected runs and the ES contribution (left) and SR2 (right). The significance is obtained from the maximun rates of the 27 $M_\odot$ (black) and the 11$M_\odot$ (red) progenitor for MNO. The dotted-dashed lines shows the significance mean and the bands the standard deviation. Regions dominated by ES and muon veto background are limited by the doted transparent lines.

SR2 20 and 11 events, for the 27$M_\odot$ and 11 $M_\odot$ respectively. In a global way, at 20 kpc, 4 times fewer events are expected, 19 and 9 for the two respective progenitors; beyond these distances, the reconstruction of the positron energy spectrum will be challenging. Values of the number of events and their respective significances at 10 kpc are summarized in **table 5.2**.

5.6.2 Neutron veto background study

The neutron background in the ROI in SR0 and SR2 is mostly the same that the already studied in **Section 5.4** during the test of the hitlet simulator with AmBe calibrations, and its event area distribution is well known. Nevertheless, the background strongly affects the CCSN signal in comparison to the AmBe, whose source rate is 10 times higher than the CCSN mean burst rate. The ROI for the positron is more extended in terms of event area than AmBe, in the [0,1200] PE range. However, any relevant background rate is expected beyond 200 PE. **Figures 5.29** depicts the event parameter distributions for the SR0 background. The corresponding ones for the SR2 are annexed in **figures E.23**, noticing that not relevant differences are present for background reduction purposes. Particularly, it will be feasible to discriminate the background using the distributions shown in the right panel for the N-PMT versus event area. Most of the positron events involve the 120 PMT array, while the background is concentrated around 5 N-PMTs, dominated by AC.

In order to study the background rates, the same analysis as described for muon veto is performed. The high rates >340 Hz obtained for the 10 second time bins in the ROI are efficiently cut, because the high

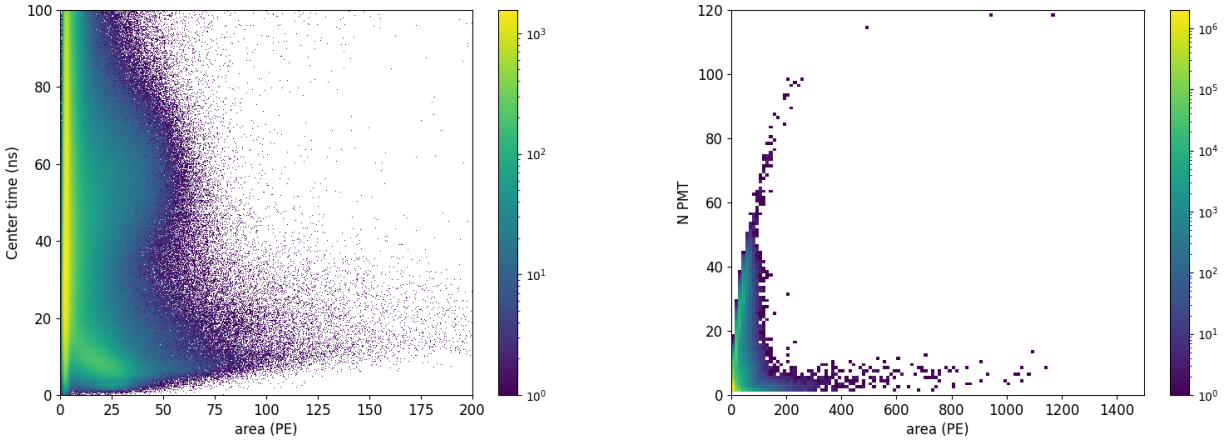

Figure 5.29: **Left**. Center time vs area distribution for the background data of SR0 in neutron veto. **Right**. Number of pmt contributing vs area distribution for the same SR0 period.

resolution of the neutron veto allows to clearly discriminate background from positron signal, presenting a significantly differentiated event parameter distribution as reported in the last paragraph. As a consequence, the background cuts will be more effective than in muon veto, in which only accidental coincidences are effectively rejected, and the selection of the cut region could be more precise. Identical distributions than for muon veto, i.e. mean and maximum rolling window rates before and after cuts are presented in **figure 5.30**. In this case, the background period without calibrations is selected, compounding a stable run selection for SR0 and SR2 data taking. The runs studied represent 10 days of effective background time data collection[5] in both cases (not disposing of more data from SR2 at this time). Regarding the results obtained, the efficiency of the cuts invites to calculate sensitivities also using the mean rates. Those are strongly reduced after applying the cuts, attending even lower values than neutron (0.027 Hz) and ES (0.03 Hz) signals, 0.004 Hz for SR0 and 0.01 Hz for SR2, in front of the 1.1 Hz mean rate anticipated for the IBD positron induced by the $27M_{\odot}$ progenitor. However, these values represent the median of this long period of 10 days. In reality, after the cuts, 98.6% (95.3%) of the surviving bins, i.e. the time bins with at least one event, only include 1 event exhibiting 0.1 Hz rates in SR0(SR2). In addition, the surviving fraction is very small after cuts, varying for SR0 and SR2 with 3% and 9%, justifying the distinct median mean rates reported after cuts in **figure 5.30**, which follow this proportion of 3 times more for SR2. The same behavior is founded for maximum rates, in which most of these surviving bins present 1 Hz rates.

The advantage of the effectiveness of the cuts also has the disadvantage of presenting inhomogeneities in the final distributions. It will be desirable that the fraction of surviving bins will be close to 100%, in order to obtain a certain stability in the window time of interest corresponding to the duration of the CCSN burst. The PDF that is planned to be used for the background only hypothesis has to be representative

[5]In reality, this presents the absolute time of data taking, and not real date-time, in which runs will appear more separated. Consequently, this 10 concentrates three weeks of data taking without calibrations.

enough of the former mean and maximum rates in this time bin.

In the TPC a similar problem was found, but the surviving fractions for each run were higher than 50%, and a non-negligible amount of the bins present more than one background event, leading to a distribution with enough points to be approximated. The solution to deal with was to use a gaussian distribution including the 0 Hz rates, which are not physical, in order to approximate the real weights of the rest of the rates. Another option, due to the low number of expected events $\lambda \ll 1$ is to present the background rates following a poisonian distribution $P(\lambda)$ with an expectation value λ equal to the mentioned mean rates (r) $r \times$t(=10 s). The p-value calculation for the background only hypothesis becomes:

$$p = \int_{R_i^{mean}}^{\infty} P(\lambda = rt, x)dx \tag{5.15}$$

This will be an approximation concerning the background mean rates. For the maximum rate of the rolling window, another alternative will be to use the median obtained from the analysis of the rate time evolution and the MAD to handle uncertainties assuming a gaussian distribution.

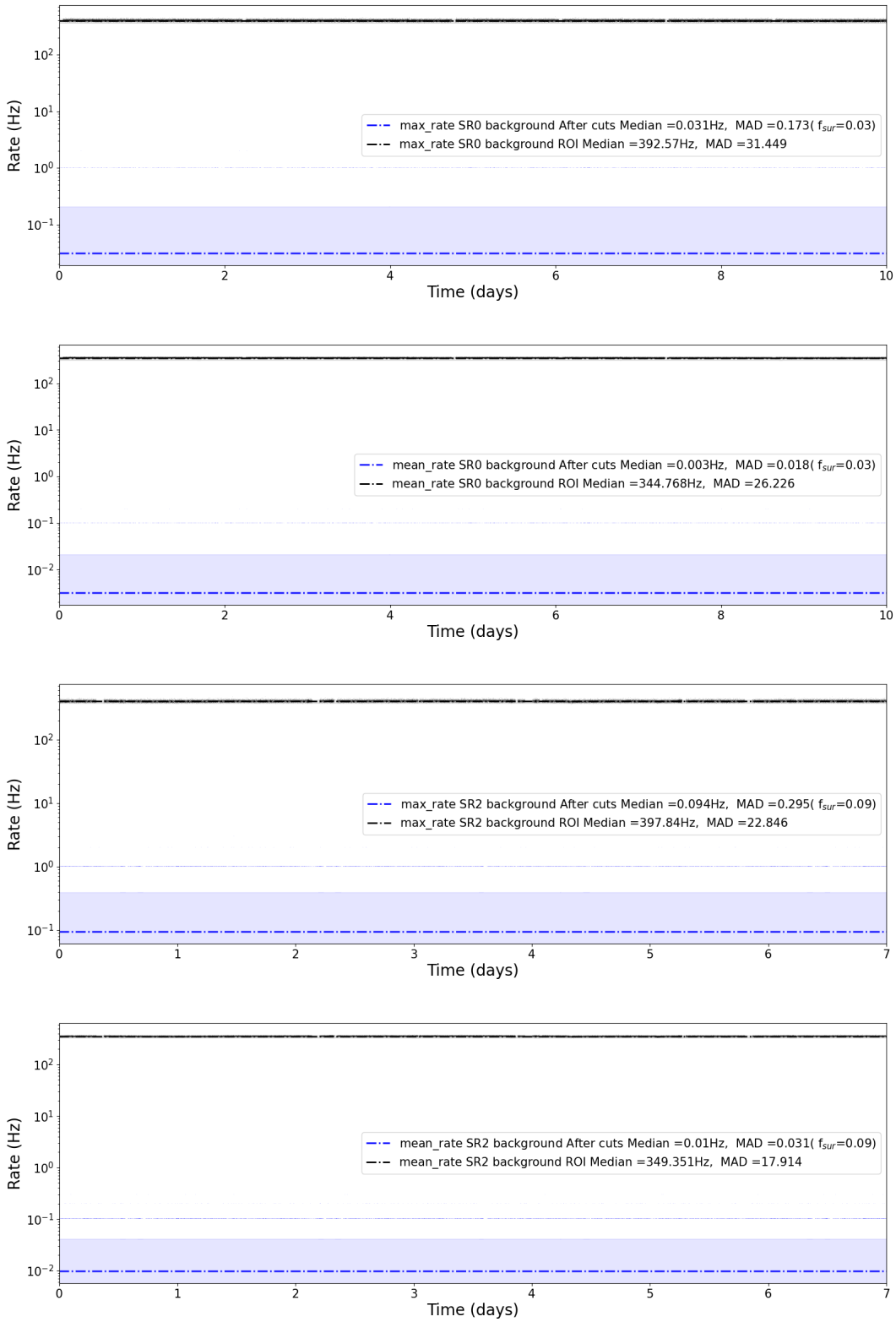

Figure 5.30: **Top**. Mean and maximum rates time evolution for SR0 background before (black) and after (blue) applying the cuts. **Bottom**. Same distribution for the SR2 period.

This is supported by the fact that the rolling window maximization of the rates cannot be associated strictly with a poissonian distribution. In this case, the p-value is calculated as:

$$p = \int_{R_i^{max}}^{\infty} Gaus(\mu, \sigma \sim \text{MAD})dx \tag{5.16}$$

This approximation is far from being perfect as most of the rates are not included at 1 σ but at 3 σ distance from the median, supporting the low probability of founding an event in a 10 s bin. However, its net effect regarding the p-value, will be close to reality. In future studies, the maximum rolling window rate evaluation of the significance has to be optimized, including a CCSN simulation inserting the background itself at a hitlet or an event level. Finally, future studies may also include the possibility of accounting for the IBD neutron signal in the SR2 configuration through an optimization of the cuts and deeper study on the neutron Gd capture and positron signals.

CCSN distributions and rates after cuts

Figure 5.31 illustrates the event area rate distributions for background and CCSN signals regarding ES and IBD interactions for SR0 and SR2 data taking. Only the positron signal remains isolated from the background's influence. The spectrum of the positron signal is significantly preserved after the cuts (dotted lines), showing a decrease around 600 event area PE in comparison to the one before the cuts (solid lines). This is due because a part of the high energy tail has been diminished, imposing the cuts on the center time, reducing its range to [25,100] ns, as well as requiring a 50 N-PMT threshold. It can be deduced from the obtained 21 PE/MeV (see **figure E.11**), that this reduction starts around 30 MeV. The dispersion of cerenkov photons, impacting the N-PMTs and center time distributions, is expected to evolve inversely with the positron energy, making the signal faster and less dispersed as the positron energy increases. The ES scattering exhibits a similar distribution as the IBD positron; however, less than one event is expected at 10 kpc. The neutron signal distributions, even with the addition of Gd, are still dominated by the background after cuts. This event area distributions are normalized in a 10-second window bin. It is clear, from the point of view of event area positron discrimination, the necessity of applying cuts for background diminution, as the latter highly dominates the low energy region of the ROI. The impact of these cuts in the background rates has already been reported, but they also include a reduction of the latter event area distribution rates, as the blue dotted line of **figure 5.31** shows.

The background cuts also have a dramatic impact on the rest of the IBD signals, mainly ES and IBD neutrons. As well as in the muon veto, the neutron and ES signals do not exhibit relevant amplitudes to combine them with positron one after applying the cuts, but particularly the ES will be difficult to discriminate from the positron as their event parameter distributions are similar. Values after the cuts at 10 kpc are summarized in **table 5.6.2**. The latter rate evolves with the distance, and 1 event is expected at 6.5 kpc. In addition, also one event is expected in the SR2 configuration for the IBD neutron at 6.5 kpc, while the neutron signal in the SR0 configuration can be ignored, expecting only 3 events at 1 kpc. The evolution of the CCSN number of events compared to the background as a function of the progenitor distance is depicted in **figure 5.32** in order to visualize their implications.

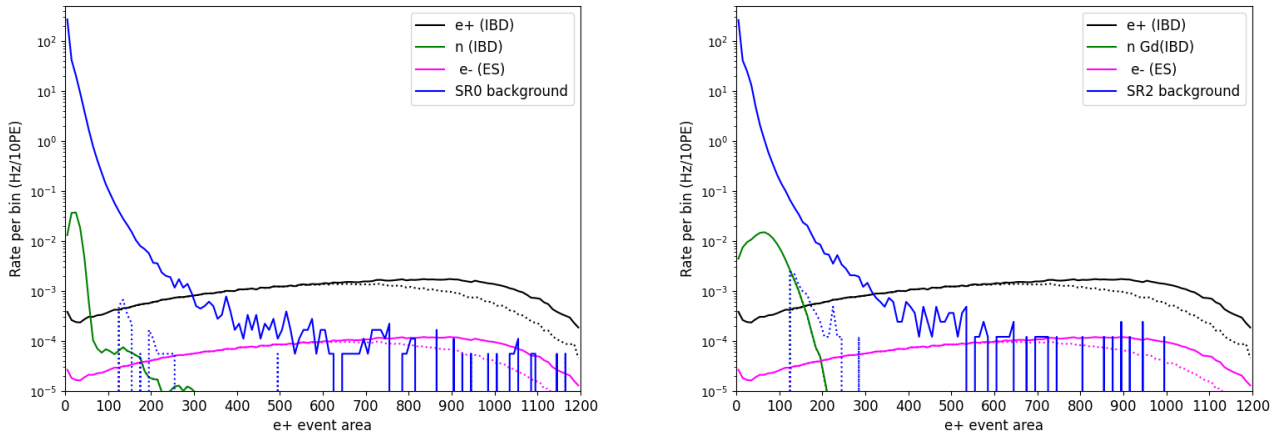

Figure 5.31: Event area distribution before (solid lines) and after (dotted) applying the cuts for the IBD positron (black), neutron (green), ES (magenta) and background (blue) for the SR0 (left) and SR2(right) periods in the neutron veto.

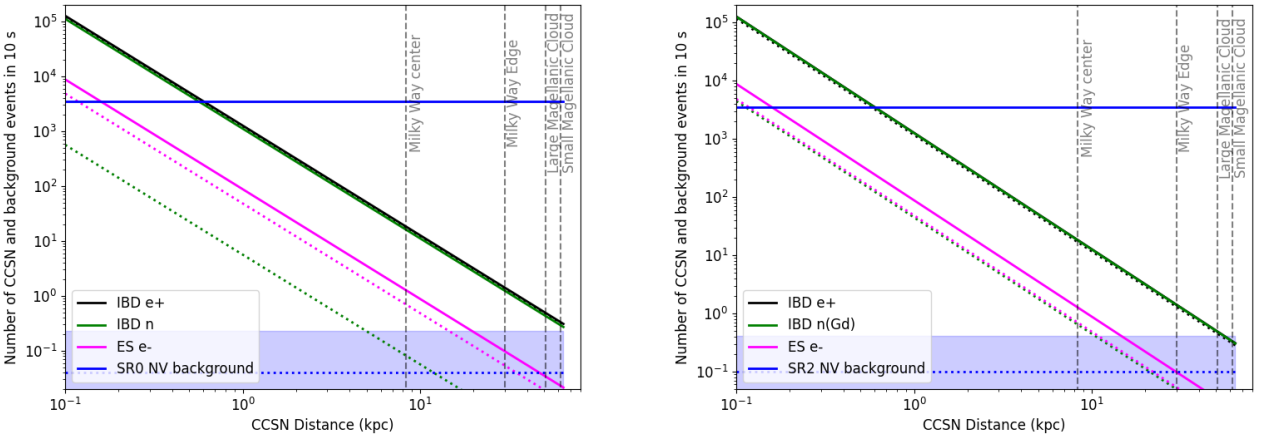

Figure 5.32: Number of events as a function of the progenitor distance before (solid lines) and after (dotted) applying the cuts for the IBD positron (black), neutron (green), ES (magenta) and background (blue) for the SR0 (left) and SR2(right) periods in the neutron veto.

Neutron veto background model and CCSN sensitivity

The same criteria of requiring at least 1 event at 10 kpc for considering other CCSN signals than IBD positron in the background model, results in accounting for only neutron veto background, which is extremely reduced after the cuts, as reported in the last sections. This creates a background model that is independent of the CCSN distance. The probability density function will be in this case represented by a poisonian distribution (see equation 5.15) for the mean rates and a gaussian, centered in the median and the MAD reported in **figure 5.30**, for maximum rolling window rates (see equation 5.16). The simulation of the CCSN data will be performed by inserting the background to the IBD positron signal simulation

	Number of CCSN and background events(*) before and after cuts in the neutron veto			
Background	**SR0**		**SR2**	
	Before cuts	After cuts	Before cuts	After cuts
	3447(±26)	<1(0.045±0.19)	3493(±18)	<1(0.1±0.3)
Signal	**SR0**		**SR2**	
	Before cuts	After cuts	Before cuts	After cuts
IBD e+	12.67	11.62	12.67	11.62
IBD n	11.12	<1 (0.055)	12.51	<1 (0.45)
ES	<1 (0.88)	<1 (0.48)	<1(0.88)	<1(0.48)

Table 5.4: Summary of the number of CCSN detected events after applying the cuts in muon and neutron veto for the IBD and ES interactions at 10 kpc. This event numbers accounts for the progenitor 27 $M_\odot$ from *Bollig 2016* model, in the NMO neutrino mass ordering. * The number of events are not an integer, and have no physical meaning, but these values are particularly useful to evaluate the impact of the detection capabilities for each volume at other CCSN distances. The complete impact of the cuts in the rest of progenitors and IMO is reported in **table E.4**

in SR0 and SR2. The surviving fractions, of the background in the 10-second time bins will be used to sample the background 3% and 9% for the SR0 and SR2, respectively. As **figure 5.33** shows, only 3 of the 100 CCSN simulated include a background contribution in SR0, increasing the mean and maximum rolling window rates. Even if this happens rarely, the increment in the mean rate is considerable, $\sim$ 8% of the 100 CCSN mean rate. Regarding the maximum rates, the latter impact is less relevant as only one event of background is expected; it has to happen in the first second of the burst to have chances to increment the rate when the rolling window rate is maximum, as shown by the **figure E.24**. The right panel of the **figure 5.33** illustrates the SR2 results; the mean and maximum are slightly higher due to the presence of background in 9 of the 100 CCSN. The sample of the background is in this sense more realistic, accounting for the real data rate increment if background events are recorded in the CCSN ROI after cuts. **Figure 5.34** depicts the obtained sensitivities for the IBD positron signal in the neutron veto from the mean rates (dashed dotted line) and maximum rolling window rates (dotted line) for the 27$M_\odot$ (NMO). Unlike the muon veto, the mean rate analysis yields a higher significance. However, both mean and maximum rate significance's are high at 10 kpc, presenting values >3 σ in the MW edge. This result appears very optimistic; nevertheless, it has to be evaluated, accounting for the number of events. Only one positron event is expected in the MW edge, making CCSN discrimination from background challenging using time evolution, i.e., maximum rolling rates. Five events, expected at 15 kpc, is a more realistic number to evaluate the results. Mean rate sensitivities will be shown separately from maximum rate ones for both periods SR0 and SR2, and both progenitors, in order to comment in more detail on these expectations for each one.

Figure 5.35 illustrates the IBD positron sensitivity curves as a function of the distance for the 27 $M_\odot$

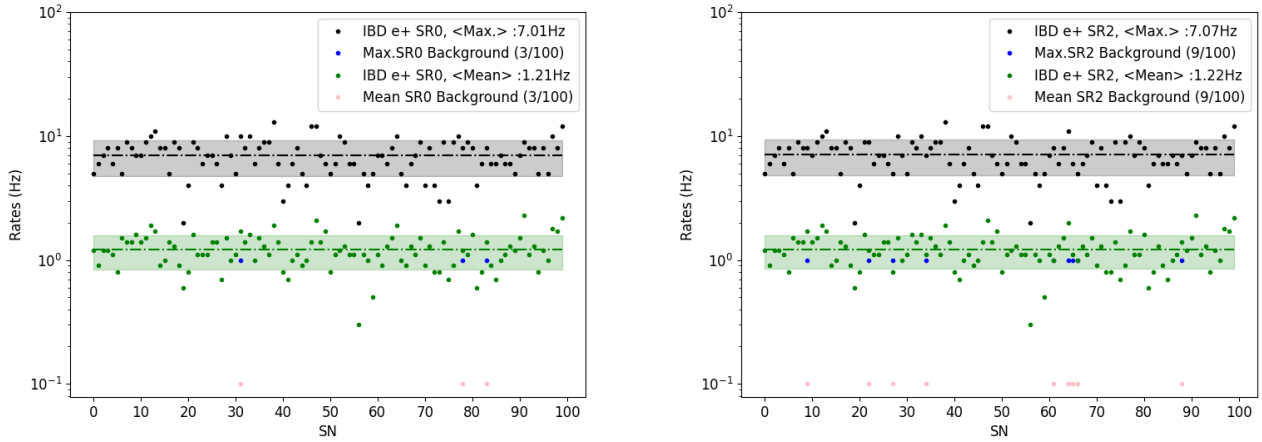

Figure 5.33: **Left**. Rolling window maximum (black) and mean (green) rates for the the CCSN IBD positron observations in the neutron veto for the SR0 configuration, from the simulation of 100 CCSN of the $27M_{\odot}$ in the NMO. SR0 Background contribution is represented by the blue line for the rolling window maximum rates and the mean by the pink line in the background only hypothesis. The thick line black line and the thick green dotted line corresponds to the median and the bands to the standard deviation. **Right**. Same representations in the SR2 configurations.

and 11 $M_{\odot}$ progenitors for NMO. On the contrary of the results from the muon veto, the SR0 is expected to exhibit better sensitivities than SR2, as the cuts applied turn out to be less effective in the former. The causes of this have to be studied in futures analysis. An hypothesis could be that cuts reveal the signal of some of the radiogenic neutrons that are more effectively captured with Gd addition. For the SR0 period illustrated in the left panel, at 10 kpc the sensitivity for both progenitors is high: $62.6\pm9.3\,\sigma$, $27\pm14\,\sigma$ for the heavier and the lightest one, respectively. These values are particularly intriguing for the $11M_{\odot}$ progenitor, whose sensitivity in the muon veto is reduced above 10 kpc. In the MW edge, the latter progenitor presents a sensitivity of $2.82\pm0.71\,\sigma$, while for the $27M_{\odot}$ the latter is $6.8\pm1.0\,\sigma$. However, these values are anecdotal due to the low number of events expected (1 and <1). Requiring 5 events, at 15 kpc for the $27M_{\odot}$ progenitor, the significance is $27.9\pm8.34\,\sigma$. High sensitivity values are obtained in the IMO case, which curves are annexed in **figure E.26**, illustrating smaller values as predicted for the number of events expected after cuts (see **table E.4**). For the neutron veto $27M_{\odot}$and $11M_{\odot}$present both lower significances in the IMO case.

For the SR2 configuration, presented in the right panel sensitivities still being high at 10 kpc: $36\pm11\,\sigma$ and $15.1\pm3.5\,\sigma$ for the two progenitors in the usual order. At 15 kpc, these values are reduced to $16.1\pm4.9\,\sigma$ and $6.7\pm 3.5\,\sigma$.

Finally, the sensitivities obtained for the maximum rates are illustrated in **figure 5.36**. As anticipated they are smaller than the obtained from the mean rates but still high at the target distances of 10 and 15 kpc for both progenitors. For the lightest one at 15 kpc, the significances are larger than 5σ in SR0 and SR2 configurations, while for the $27M_{\odot}$ progenitor significance increases up to 10σ. For the IMO

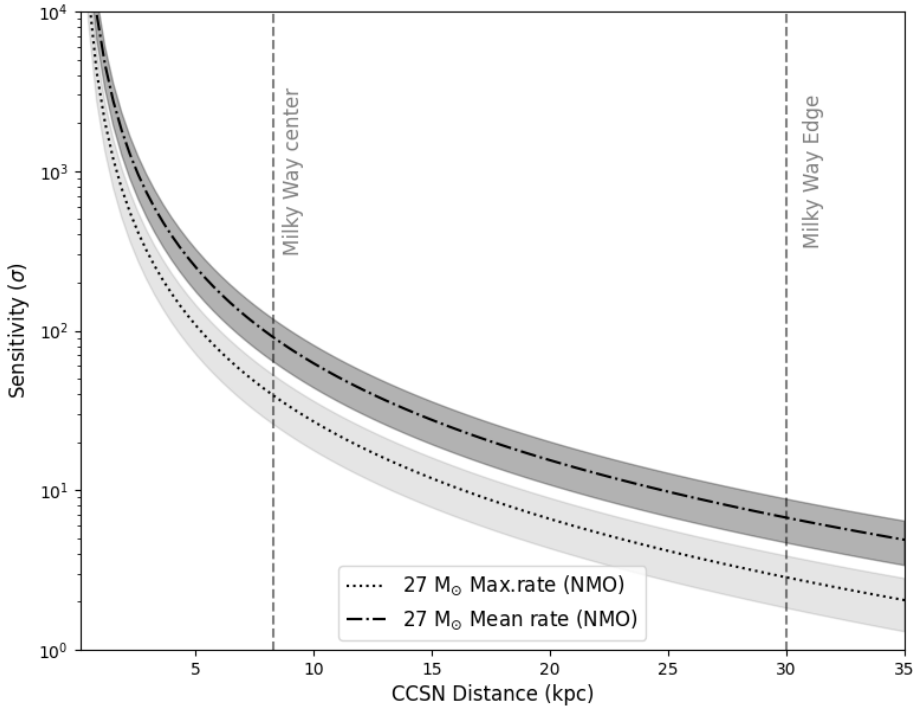

Figure 5.34: Sensitivity curves as a function of the CCSN progenitor distance in muon veto for the background model including the SR1 non-selected runs and the ES contribution. The significance is obtained from the maximun rates of the 27 $M_\odot$ (black) and the 11$M_\odot$ (red) progenitor for MNO. The dotted-dashed lines shows the significance mean and the bands the standard deviation. Regions dominated by ES and muon veto background are limited by the doted transparent lines.

case, results are reported in **figure E.25**, presenting the expected variation of both progenitors, while maintaining the significance constraints of 5σ and 10σ at 15 and 10 kpc respectively.

The significance obtained from maximum rates can be combined with the resulting ones in the muon veto, leading to a water tank CCSN sensitivity curve as a function of the progenitor distance. This combination and the resulting total positron energy and time spectrum, adding the neutron and muon veto observations after cuts, will be performed in the next section.

It is worth to emphasize, again, that the reported sensitivity values are conditioned by the lack of events at distances greater than 10 kpc, but they show that the neutron veto design exhibits an efficient balance between PMT array coverage and detection volume. In future DM detectors, this PMT array density could be extrapolated into larger volumes, but with an increased proportion to compensate for water absorption. As the volume increases, the latter effect is enhanced, and the PMT density array has to be increased in order to compensate for photon losses and maintain CE, as larger detectors such as Super-K are conceived. Nevertheless, one can wonder what will be the response of the muon veto with a PMT density array close to the one of the neutron veto.

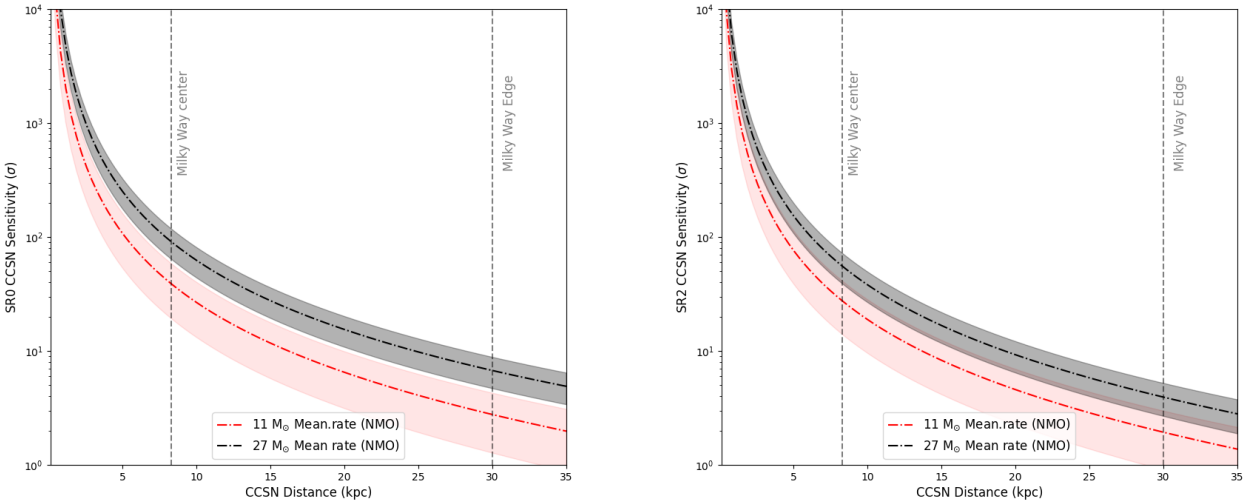

Figure 5.35: Sensitivity curves as a function of the CCSN progenitor distance in neutron veto for the mean rate background model for SR0(left) and SR2 (right). The significance is obtained from the maximun rates of the 27 $M_{\odot}$ (black) and the 11$M_{\odot}$ (red) progenitor for MNO. The dotted-dashed lines shows the significance mean and the bands the standard deviation.

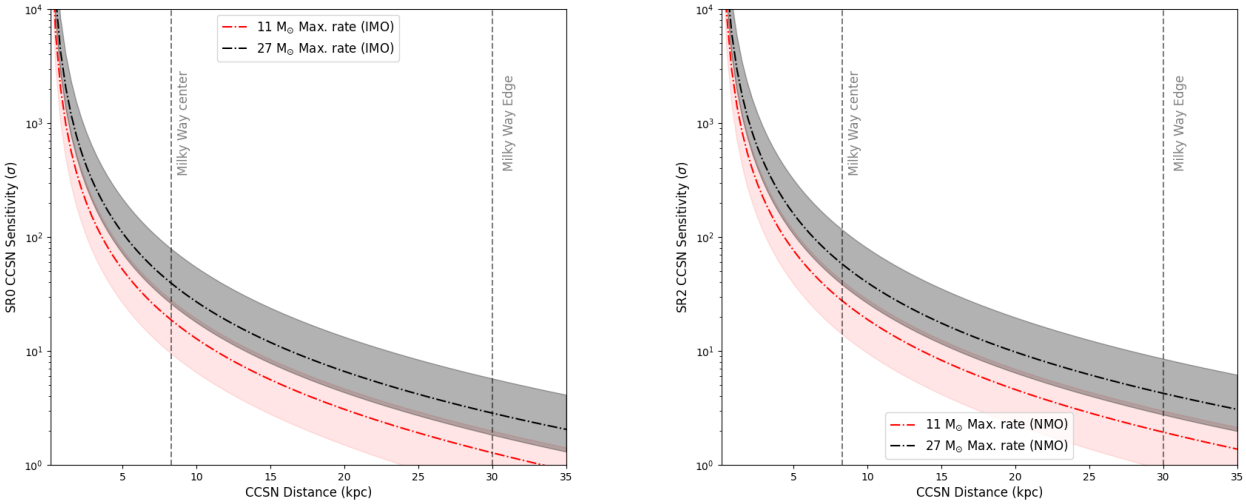

Figure 5.36: Sensitivity curves as a function of the CCSN progenitor distance in neutron veto for the maximum rate background model for SR0(left) and SR2 (right). The significance is obtained from the maximun rates of the 27 $M_{\odot}$ (black) and the 11$M_{\odot}$ (red) progenitor for MNO. The dotted-dashed lines shows the significance mean and the bands the standard deviation.

5.7 Water tank CCSN sensitivity

The combination of the two vetoes sensitivities is the last step of this work. Both sensitivities obtained independently can be linearly combined following the Stouffer's Z-score method [451, 452, 453] which leads to a weighted significance combination. This strategy is inspired by the KM3net CCSN sensitivity study combining ARCA and ORCA detectors [454]. The final significance $Z(d)$ for a given distance d from the muon veto Z^{MV} and the neutron veto Z^{NV} combination can be written as:

$$Z(d) = \frac{1}{\sqrt{2}}(Z^{MV}(d) + Z^{NV}(d)) \tag{5.17}$$

Figure 5.37 illustrates the sensitivity curves from the two vetoes combinations regarding the two progenitors at 10 kpc. This combination is performed using maximum rates, and in the case of the SR0 and SR1 combination, the background model from SR1 consists of the selected SR1 data. This is supported by the exclusion of the calibration periods in the neutron veto background model, responsible for background fluctuations in the muon veto, and the consequent selection of runs out of this period in this volume.As expected, the combination of both sensitivities increases the ones obtained in muon veto beyond 15 kpc, which is interesting because at this distance 39 events are expected in the water tank. The limit in distance to consider relevant this combination has to be interpreted in the MW edge, in which only one positron event is expected in the neutron veto. At this distance, 8 events are expected in the muon veto, for a total of 9 events, which is a value similar to the number of detected events from SN1987A by Kamiokande. At this limit, for the SR0+SR1 combination, the significance is $6.1 \pm 1.8\sigma$ for the 27 $\mathrm{M}_{\odot}$ progenitor and $2.9 \pm 1.2\ \sigma$ for the $11\mathrm{M}_{\odot}$ are obtained, while higher values are extracted from SR2 $8.3 \pm 2.5\sigma$ for the 27 $\mathrm{M}_{\odot}$ progenitor and $3.9 \pm 1.7\ \sigma$ for the respective progenitors. The values of the expected events and their corresponding significances at 10 kpc are summarized in **table 5.5** including the IMO for both progenitors. Sensitivity curves for the IM0 case show the same tendency than in neutron veto for both progenitors, i.e. also a reduction of the significance regarding $11\mathrm{M}_{\odot}$. On the contrary, on the muon veto, even if the number of expected positron events in the water for $11\mathrm{M}_{\odot}$ in IMO is higher than in NMO, as reported in **table 5.5**, the resulting significance is lower due to the contribution of the neutron veto, which governs the curve. Sensitivity curves in the water tank for IMO are annexed in **figure E.27**. The values reported in the table show a significant increase in significance at 10 kpc, which is better than the established value for neutron veto. Waiting for the future design of the muon veto, particularly the new PMT coverage, that could increase sensitivity for larger DM detectors such as DARWIN or LXZD, the combination of the two vetoes seems like a good strategy to compensate for the actual design.

It is interesting, regarding the neutron veto results for the significances based on CCSN burst mean rates reported in the last section, to combine both detectors regarding the latter value. The muon veto shows lower significance for mean rates, while in the neutron veto this analysis is the most favorable. Furthermore, in the SR1 configuration, the rate in the neutron veto is rather stable, and, as it was shown for the maximum rates, the neutron significance drives the resulting combination of both detectors. **Figure 5.38** depicts the sensitivity curves based on mean rates. For simplicity for the reader, as the

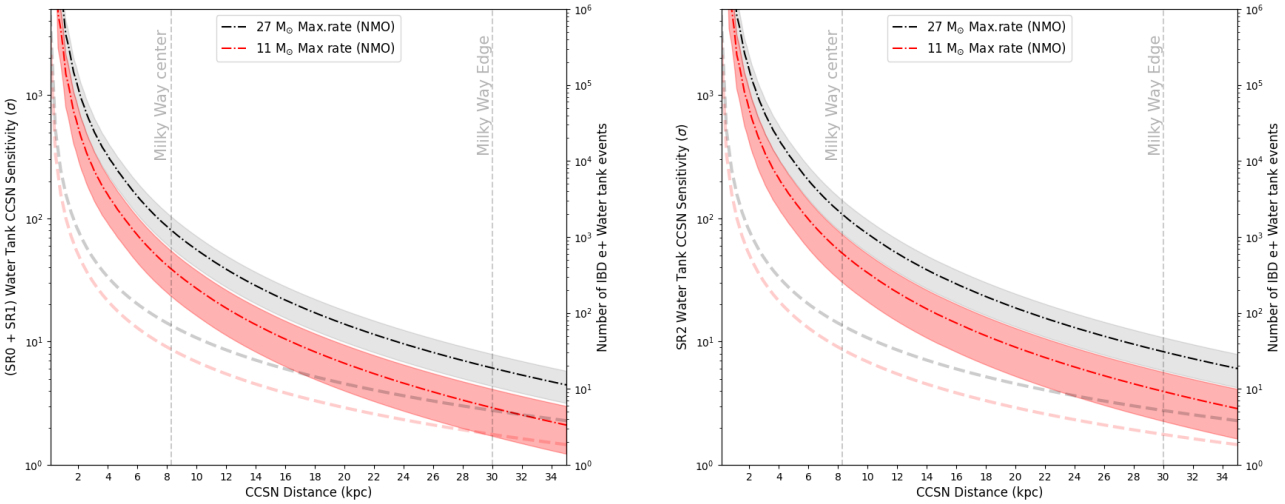

Figure 5.37: Sensitivity curves as a function of the CCSN progenitor distance in the water tank, from the combination of muon and neutron veto for the maximum rates, from the relation of equation 5.17. The significance is obtained from the maximum rates of the 27 $M_\odot$ (black) and the $11M_\odot$ (red) progenitor for MNO. The dotted-dashed lines shows the significance mean and the bands the standard deviation. As well, the number of events, represented in the right axis, for each progenitor is drawn by the semi-transparent dashed thick lines.

values at 10 kpc are summarized in **table 5.5**, only how far it can be seen with this analysis will be commented. This leads to looking at the values on the MW edge significance, which are slightly improved in comparison to the maximum rates. For the 27 $M_\odot$ and $11M_\odot$ progenitors in NMO for the SR1 + SR0 combination, the significances are $10.8\pm3.0\sigma$ and $4.6\pm2.2\sigma$. Similar but smaller values are found for IMO, whose corresponding curves are annexed in the E.28. The stability of the background plays an important role in determining the significance of this strategy. The addition of Gd increases fluctuations in the ROI. This means that, as shown in **table 5.5**, the SR2 period significances from combining both detectors are the smaller ones for the 4 possible configurations shown in the table. However, those significances are still higher, and in the MW edge present values of $6.7\pm$ 1.9 σ and $2.6\pm1.2\sigma$ for the respective progenitors in the usual order in NMO. It can be resumed that for the SR1+SR0 combination, the most favorable strategy will be the sensitivity study based on the maximum rates, as well as neutron vetoes in this period. On the contrary, for the SR2 configuration, the better approach would be to use maximum rates, as well as the muon veto during this period.

Figures 5.39 illustrate the final IBD positron energy spectrum from the combination of the observed spectra for muon veto and neutron veto after cuts depicted in **figure 5.10**. The detection threshold reported of $\sim$ 5 MeV for the positron kinetic energy is noticeable, due to the extremely low efficiency of the muon veto in this low energy region. Around the mean energy, the spectrum is shifted, in comparison to the interaction spectra, due to the increased detection efficiency for higher energies in the muon veto, which drives the shape of the spectrum in this region. However, the high detection efficiency of the neutron

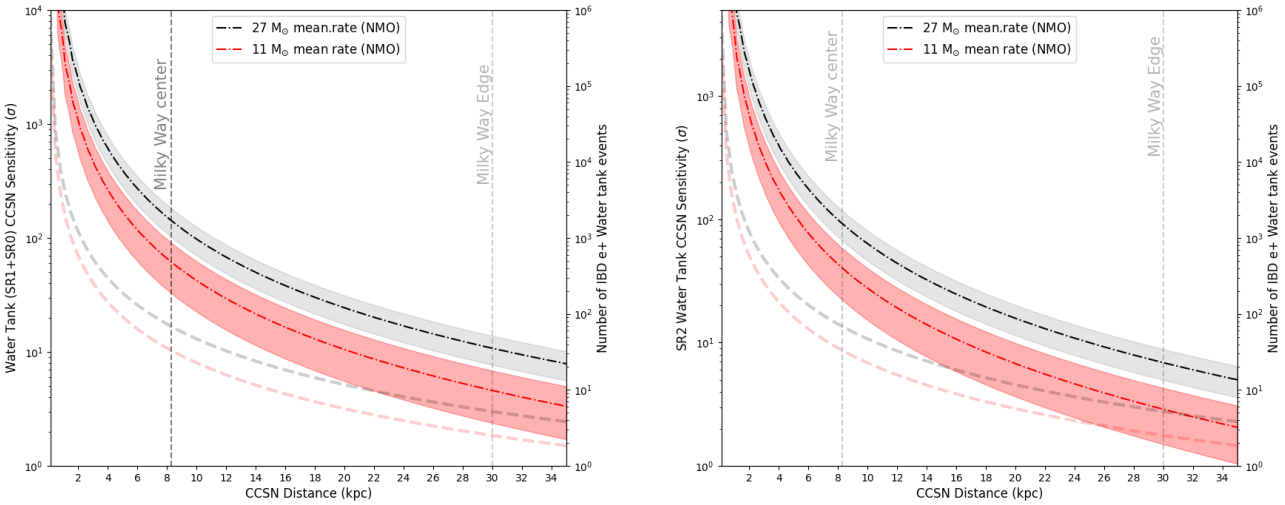

Figure 5.38: Sensitivity curves as a function of the CCSN progenitor distance in the water tank, from the combination of muon and neutron veto for the maximum rates, from the relation of equation 5.17. The significance is obtained from the maximum rates of the 27 $M_\odot$ (black) and the 11$M_\odot$ (red) progenitor for MNO. The dotted-dashed lines shows the significance mean and the bands the standard deviation. As well, the number of events, represented in the right axis, for each progenitor is drawn by the semi-transparent dashed thick lines.

Number of CCSN events and significances at 10 kpc							
	Number of events			**Significance Max. (σ)**		**Significance Mean (σ)**	
Progenitor	MV	NV	Total	SR1(SR0)	SR2	SR1(SR0)	SR2
27 $M_\odot$ (NMO)	76.5	11.6	88.1	56±16	75±22	98±28	63±17
27 $M_\odot$ (IMO)	75.53	11.21	86.74	53±15	72±22	95±28	62±17
11 $M_\odot$ (NMO)	37.87	6.25	44.12	27±11	36±15	43±20	28±12
11 $M_\odot$ (IMO)	39.07	6.22	45.29	24.0±9.1	32±12	38±17	25±11

Table 5.5: Summary of the number of CCSN detected positron events and its respective significances in the water tank from the combination of both vetoes at 10 kpc in the SR1+SR0 and SR2 configuration.

veto covering all the positron spectrum led to a small increase in the detection at low energies between 5 and 10 MeV. On the other hand, no substantial differences between the mass orderings for both progenitors are found. On the right panel of the figure, the corresponding $\bar{\nu}_e$ energy spectra calculated from the IBD simulation after the cuts, as the information of the anti-neutrino energy was saved for each IBD event. The results lead to deduce that a detection threshold around 7 MeV will be a realistic approximation for the ν_e energy detection constraints. This, indeed, appears as a shift of the positron detection efficiency $\sim$ 1.8 MeV, using the value of the latter kinetic energy. The linearity of the positron and neutrino spectrums can be exploited, resulting in very similar shapes.

Finally, the reconstruction of the time evolution of the IBD positron signal can be evaluated, combining

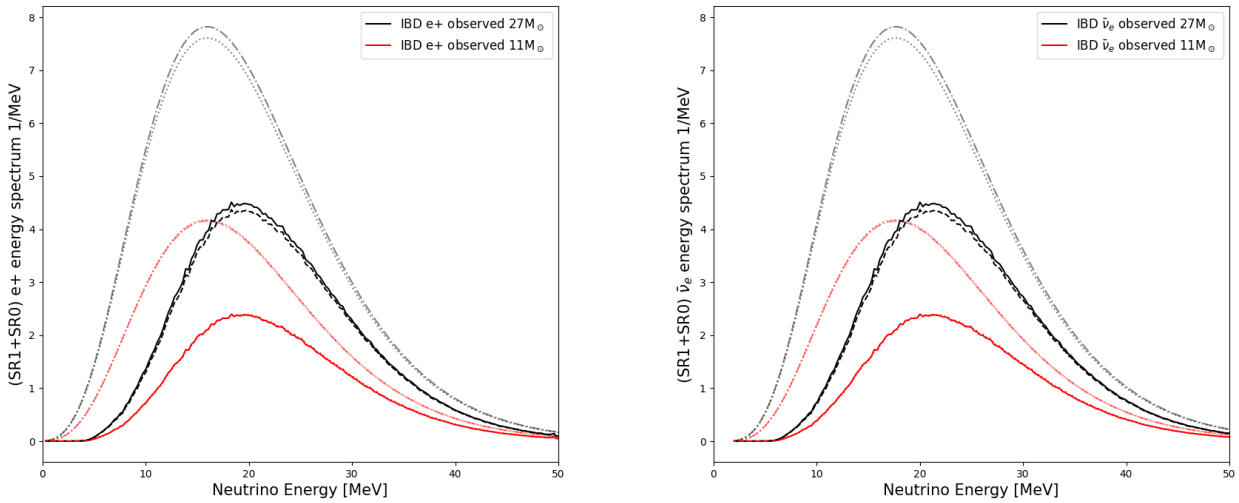

Figure 5.39: **Left:** Water tank IBD positron observed energy spectra combining neutron and muon veto observations after cuts, for the 27$M_\odot$ (black) and 11 $M_\odot$ (red) progenitors in the NMO (solid lines) and IMO (dashed lines) at 10 kpc. Semi-transparent dot-dashed lines correspond to the energy interaction spectra.

the observations of the two vetoes. **Figure 5.40** represents the evolution in time for the total events in the water tank for the two progenitors in NMO and IMO. This distribution is the result of the rates in each 50ms time bin and can be better understood using the right panel. It is relevant that during the neutronization phase only a few events are expected, making it difficult to describe the rate evolution during this neutronization burst. During the accretion phase for the heaviest progenitor, the peak of the explosion is represented, as well as the further decreasing gradually entering into the cooling in which most of the events are expected to be observed. For the 11 $M_\odot$ progenitor, the transition from the neutronization to the accretion phase is not clearly distinguished. Moreover, the cooling phase exhibits unexpected rate fluctuations, despite the representation of the rate decrease after explosion. The most interesting part of this time evolution spectra is that it is pretended to contain the MO information, as NMO and IMO present a distinct evolution, particularly relevant, during the accretion and the cooling phase. For example, for the 27$M_\odot$the number of events expected during the accretion phase is 42 and 34 for the NMO and IMO respectively. This relation is inverted during the cooling phase, in which 43 and 50 events are detected for the NMO and IMO cases. Similar differences are reported for the 11$M_\odot$.

5.8 Summary

In this final chapter, the CCSN neutrino simulation in the water tank was performed, including the IBD and ES chanels. The simulation chain is supported by the GEANT4 simulation of mono-energetic positrons in the expected IBD range [0,50] MeV. This first step was performed in two different configurations: ultrapure and Gd-doped water. The second step consisted into recovering the information of the IBD or

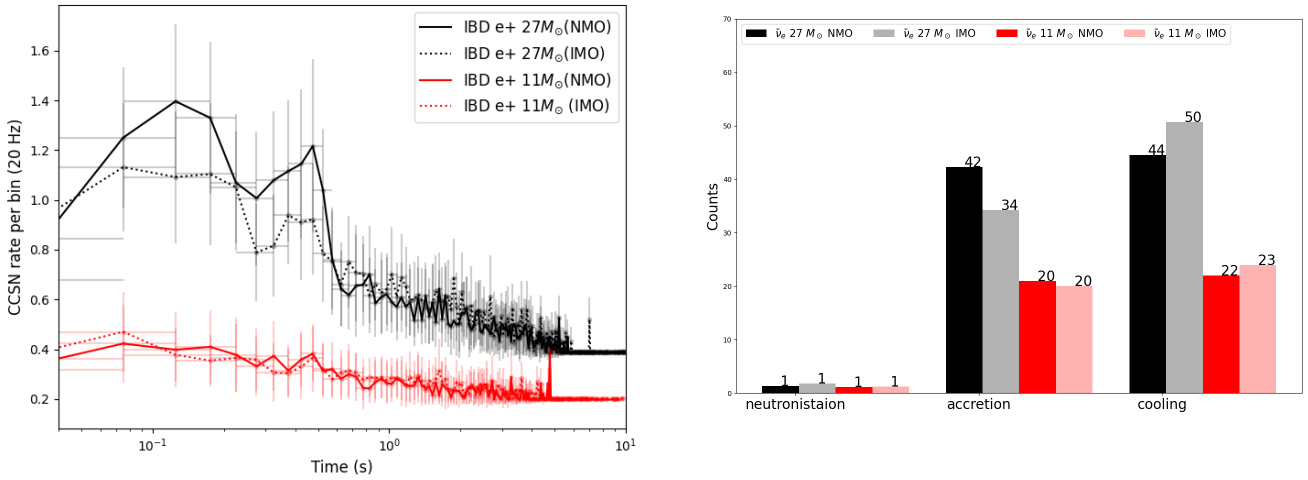

Figure 5.40: **Left:** Time distribution of the IBD positron signal combined from the observations of neutron and muon veto after cuts for the 27$M_\odot$ (black) and 11 $M_\odot$ (red) progenitors in the NMO at 10 kpc. The error bars correspond to the standard deviation obtained from the 100 CCSN IBD positron simulation for each time bin. **Right:** Number of expected observations after cuts for each phase of the CCSN for the two progenitors in NMO (black and red bars) and IMO (grey and pink bars).

ES interaction, i.e vertex generation time after the CCSN core bounce and energy of the incoming $\bar{\nu}_e$ in order to construct the corresponding rate spectrum. This part was performed by a toy MC based on the 2D IBD and ES rates described in **Sections 4.3** and **4.4**. A detailed "hitlet simulator" was included in the simulation chain, transforming the incoming optical photons hitting the vetoes PMTs (VPMThits) into photoelectron signals, using some properties of PMTs such as the Single Photoelectron (SPE) distribution, the Quantum Efficiency (QE) and Collection Efficiency (CE). This information has been collected, for each PMT, from dedicated LED calibration studies. The approaches used in the hitlet simulation depend on the specific veto and are described in detail in a dedicated appendix (**Appendix E.1.1**). The last step was to build events from the created hitlets, to obtain a simulated CCSN signal having the same format of the recorded data.

In order to justify and validate the corrections that can be made to the simulated data, the hitlet simulator has been tested with AmBe calibrations in the neutron veto, performed in two different periods during two Science Runs: the very first one SR0 and the SR2, that started after the addition of Gd salt in water. This data-simulation comparison focused on the discrepancies of the distributions of the event signals. In SR0, the simulator reproduced correctly the neutron capture from the emission of a 2.2 MeV gamma-line, however a discrepancy on the energy resolution for this peak in PE/MeV has been found. The discrepancies between simulation and data in the signal of the ^{12}C 4.44 MeV gamma line are the result of the propagation of the deduced resolutions, supporting the fact that other uncertainties have to be taken into account in the hitlet simulator (or in the GEANT4 simulation), particularly affecting the SPE distributions. In SR2, the results are less conclusive, because relevant modifications on the transparency

of water seem to happen with the presence of Gd in water. Even if the simulated spectrum of neutrons does not differ significantly from data, discrepancies appear as well with Gd (∼8 MeV) and the ^{12}C peaks. These uncertainties can also come from not having reproduced exactly the same experimental conditions. In particular, the estimation of some free parameters as the neutron/^{12}C gamma fraction, the AmBe source rate and the CE estimation, which are correlated to the background subtraction, can contribute to enhance discrepancies, particularly in the SR2. Concerning the CCSN physics, those discrepancies might lead to an increase of the uncertainties of the positron energy spectrum and on the detection efficiency in the two vetoes. This has an impact on the final choice of the ROI bounds to maximize the CCSN detection efficiency. The presented work on the hitlet simulation in the water tank allowed the validation of the full simulation chain of CCSN signal. In future studies, the SPE corrections, as well as the light transparency in GEANT4 have to be optimized.

With this simulation, the detection efficiency for each induced particle (the positron and the neutron from the IBD and the electron from ES) was obtained for each detector, in each configuration accounting for the neutrino mass ordering (MO). Results are consistent with what was anticipated in **Section 4.1.3**. Namely, in the muon veto, the golden IBD signal is the one from the positron, being the neutron signal extremely challenging to detect, even after the addition of Gd. However, the positron detection efficiency after applying the cuts is very low at energies smaller than 10 MeV, losing the information of this part of the spectrum, while it attends 60-70% for energies higher than 20 MeV, reproducing better that part of the spectrum. This results in an average of 76 expected events with a SN 10 kpc far away from Earth and with a 27M$_\odot$ progenitor mass (in the NMO case, see **table E.4**). On the other hand, an average of 1 ES event is expected in the muon veto, sharing a ROI similar to the one of the IBD positron. In the neutron veto, on the contrary, after applying the background rejection cuts, the IBD positron detection efficiency is significantly affected only below 5MeV, resulting in a total of 11 events (over the initial 12 pre-cuts events) from a 27M$_\odot$ SN at 10 kpc distance. The strong presence of the background in the neutron capture in water and Gd ROI impacts dramatically the IBD neutron channel, resulting the IBD positron channel the most interesting one for the CCSN detection. It is worth to notice that, due to the differences between NMO and IMO spectra, the cuts applied in the neutron veto have an impact on the capability to distinguish the neutrino mass order hierarchy.

In order to obtain the sensitivity curves based on the rejection of the background only hypothesis, a background model was created, resulting from the study of the background data during the periods of SR1 and SR2 for the muon veto and SR0 and SR2 for the neutron veto. With the goal of studying uniquely the implications of reconstructing the $\bar{\nu}_e$ energy spectrum from the positron signal, the ES signal is treated as a background and included in the background model. This turns to a background model dependent on the distance of the SN. In addition, in neutron veto, the background can be affected over time by the detector calibrations used to improve Dark Matter search performances. Hence, we distinguished two cases when we reproduced in the simulation the experimental conditions of SR1: a period far from calibrations, presenting extremely stable data and low background; and a period close to calibrations. Those two cases present clearly rather different sensitivity curves. Additional studies need to be performed by the

Collaboration to properly deal with time-dependent background, hence time-dependent significances in detecting a CCSN signal.

The results of the sensitivity curves are very encouraging for both detectors, and include the analysis based on the CCSN burst mean rate and maximum rolling window rate as done in **Chapter 3** for the TPC. With a SN at 10 kpc, both muon and neutron vetoes present a high discovery potential, with significances $> 10\sigma$ and >20 σ respectively. As expected, the neutron veto presents higher sensitivities but low rate, while the muon veto presents higher rates but lower sensitivities. As the background of both detectors is different, the muon veto can be made more sensitive to the CCSN signal by maximizing the rates through a rolling window, while in the neutron veto the study of the mean rate signal can be more effective for background rejection. In addition, the detector background in the SR2 configuration presents better sensitivities in muon veto, but worst in neutron veto. These results are constrained by the transparency conditions after Gd addition in SR2 and have to be carefully understood.

Finally, the combination of the sensitivities of both detectors allows excellent XENONnT performances for an evidence of a CCSN signal in the Milky Way edge.

Conclusion

The first simulation of a Core Collapse Supernova (CCSN) neutrino signal in XENONnT was accomplished in this work. Two different progenitors, $27M_\odot$ and $11M_\odot$ from *Bollig 2016* model, were used for the study of the CCSN signal. In addition, all the simulations and studies include the two hypotheses of the neutrino mass ordering: normal (NMO) and inverted (IMO). The original CEνNS simulation work in the TPC presented in **Chapter 3** is preliminary, but more extensive work has been undertaken by another XENON colleague (Kara Melhi[6]) with a specialized analysis on the CCSN neutrino signal in the TPC, including a detailed waveform simulation of nuclear recoils induced by CCSN neutrinos. Nonetheless, this simulation work takes into account a full background and signal digitalization, allowing us to study both rates during an eventual neutrino burst. The detector response to a neutrino burst is evaluated through a sensitivity study. It includes the evaluation of the CCSN detection capabilities through the background rejection in the background only hypothesis, using the CCSN burst signal mean rates, and in addition, a rolling window that maximizes the rate using the peculiar time evolution of CCSN neutrino emission. The results of the sensitivity curves as a function of the CCSN distance are encouraging, announcing a potential discovery for the next CCSN in the Milky way (MW). Significances higher than 5σ in the MW edge (at 30 kpc from Earth) are found with the technique of the "mean rate" which turns out to be the most favorable. As the probability of finding a CCSN increases when approaching to the galactic center at 8.3 kpc, the target distance used as reference along this work is 10 kpc. At this distance, the sensitivity of the Xe TPC presents high significances, $>30\sigma$, for both progenitors, with 110 and 60 events expected for the $27M_\odot$ and $11M_\odot$ progenitors respectively. The simulation methods used in the Xe TPC have been then used in the simulation in the water tank.

The simulation of the Inverse Beta Decay (IBD) in the XENONnT water tank (namely on the two vetoes systems: the neutron veto and the muon veto), presented in **Chapters 4** and **5**, consisted in an extensive simulation chain, starting with the GEANT4 software, in which the Cerenkov microphysics and an accurate modeling of the detector geometry have been included. In addition, an original work of signal digitalization from GEANT4 in the neutron and muon vetoes was accomplished. This work explored in a general way the capabilities of these vetoes on searching for CCSN neutrinos through the Cerenkov effect. The simulation chain results permit to describe the IBD positron detected energy and time spectra. In this analysis, the positron was expected to be the golden signal in both volumes and its energy spectrum is almost linearly connected to the incoming $\bar{\nu}_e$ neutrino spectrum, facilitating its reconstruction. As

[6]The reference corresponding to this ongoing work will be added as soon as this thesis is online.

expected, the neutron veto, designed for the detection of low energy signals as neutron capture in water, exhibits an energy resolution 30 times better than muon veto, conceived to reject cosmic muons, regarding positron signal. The main difference between the two detectors is the PMT coverage: the muon veto is equipped with 84 PMTs in a volume 11 times larger than that of the neutron veto, which employs 120 PMTs. This implies for the neutron veto a detection threshold of $\sim$ 1 MeV that is close to the positron Cerenkov threshold in water, 261 KeV, providing a detection efficiency greater than 95% for most of the positron spectrum. In the muon veto, the detection threshold is around 5 MeV, the detection efficiency starts being relevant for energies >10 MeV, to attend higher values ($60\% - 70\%$) beyond 20 MeV. This leads to two different shapes of positron energy spectrum, resulting in 76(74) and 36(38) events for the $27M_{\odot}$ and $11M_{\odot}$ in the NMO(IMO) at 10 kpc for the muon veto and 11(11) and 6(6) events for the neutron veto.

A similar strategy for the TPC to evaluate sensitivity was used in muon and neutron vetoes. In order to consider realistic scenarios for a future detection of CCSN, two past XENONnT configurations have been taken into consideration for the study: the one of the first two science runs SR0 and SR1, where water was ultrapure, and the latest SR2, where water was first doped with Gd. The analysis started with a separate study of the two vetoes, then the performances have been compared and combined. For the first time, the low energy background and its potential response through energy depositions in the $\mathcal{O}(10MeV)$ energy range has been analyzed in the muon veto. For SN study purposes, XENONnT can be seen as a detector with a background varying over time, since XENONnT has by time in time to perform high rate energy calibrations, that might impact the CCSN signal search. For this reason, two types of background data have been evaluated in this analysis: in absence or in presence of calibrations. Sensitivity curves for the muon veto showed a sensitivity, at the target distance of 10 kpc and using the "maximum rate" analysis approach, of $>10\sigma$ for both progenitors, but exhibits a low significance in the MW edge, 2.88 ± 0.45 σ and 1.36 ±0.32 σ for the $27M_{\odot}$ and $11M_{\odot}$. The sensitivity curves of the neutron veto are higher as the background reduction rates applying cuts is extremely efficient. This lead to even higher significance at 10 kpc and $>3\sigma$ in the MW edge for the $27M_{\odot}$ this time performing a mean rate analysis which turned out to be the most favorable for the neutron veto case. These sensitivities are also studied in the IMO case, presenting slightly smaller values for both detectors.

The two vetoes sensitivity curves have been combined to obtain a total sensitivity with the XENONnT water tank. As the neutron veto exhibits better sensitivities, for mean and maximum rates, the former will govern the combination of both. This combination allowed to increase sensitivity and extend the potential CCSN discovery to further distances. At the MW edges, >10 and >4 σ significances are obtained for the $27M_{\odot}$ and $11M_{\odot}$ in which a total of 9 and 5 positron events are expected, respectively. This combination not only increases the sensitivity and the number of events, but also enlarges the detected positron energy spectrum, providing as well a more detailed information on the time evolution of the incoming neutrinos. This turns out to be fruitful at 10 kpc where 88(86) and 44(45) CCSN events are expected. Regarding the time evolution, the combination of positron signal results to be crucial to extract information about the MO, enhancing the difference between rates exhibited by the NMO and IMO during the accretion and

cooling phases.

The study of the three XENONnT detection volumes has provided a global picture of the CCSN signal for the experiment, with a positive outlook for its future detection. The primary result from this first analysis of CCSN neutrino signal in XENONnT is that, if the next Milky Way CCSN neutrinos cross the XENONnT detection volume, they will be observed by the Xe TPC and by the two water-based vetoes independently, with at least a 5σ significance for a $27M_{\odot}$ and 3σ for a $11M_{\odot}$progenitor, even if the SN happened at the edge of the Milky Way (result obtained using *Bollig 2016* model and NMO). These neutrinos will generate enough observable events to provide information about their energy spectrum as well as time information on the burst history, notably during the accretion and cooling stages of the concerned SN. However, a more in-depth investigation is required to determine the likelihood of time rate evolution, specifically the impact of the pile-up of multiple neutrinos in the TPC-CCSN study, in particular if the S2-only analysis techniques will be applied. Furthermore, the integration of XENONnT into the SNEWS network will necessitate some hardware efforts, including the creation of a CCSN trigger. A straightforward next step will be to combine the analysis of the TPC and the vetoes for the $\bar{\nu}_e$ flavor.

The CCSN ν signal is projected to yield more statistics when it interacts with LXe atoms through CEνNS and via IBD in the water, giving about a hundred events in each detection volume with a CCSN progenitor located at 10 kpc distance. This indicates that XENONnT can compete with big scintillators-based detectors like JUNO or DUNE, as well as water Cerenkov-based experiments like Super-K, for such CCSN progenitor distances, with a detection volume that is 10 times smaller. Furthermore, XENONnT will have a lower neutrino energy threshold than other detectors, as it is sensitive to an energy spectrum with a threshold of $\sim$ 3 MeV in the TPC, $\sim$ 1 MeV in the neutron veto and $\sim$ 7 MeV in the muon veto.

These findings are encouraging for the detection capabilities of CCSN neutrinos with the next generation of dark matter detectors. The scaling to ten times bigger active volumes of these detectors as XLZD will improve in the same proportion their sensitivity, and are expected to see *far away* than XENONnT, beyond the Large Magellanic Cloud, surpassing the limit of 100 kpc. This will allow improving the sensitivity at larger distances, as the other larger detectors indicated above already do, while also decreasing the neutrino energy threshold.

Appendix A

CCSN Neutrinos

A.1 Gravitational Potential energy during H-burning process of a Star

We can approach the gravitational potential energy of the star at this early H-burning stage using an homogeneous distribution of mass into the star, assuming a linear variation of density $\rho(r)$):

$$\frac{dm}{dr} = 4\pi r^2 \rho(r) \tag{A.1}$$

The potential energy for a thick of mass dm to a point r with a accreted mass M_r can be defined as:

$$dE = \Delta E(r) - \Delta E(\infty) = -\frac{GM_r dm}{r} - 0 \tag{A.2}$$

This can be extended in later stages when the star has an onion-like structure assuming a uniform density for each layer. Integration of (A.1) for a boundary R condition give us:

$$E = -\int_0^R \frac{GM_r 4\pi r^2 \rho(r)}{r} dr \tag{A.3}$$

In this expression, note that M_r is itself an integral, since the total mass interior to the radius r requires integrating the density from the center to the point r:

$$M_r = -\int_0^r 4\pi r'^2 \rho(r') dr' \tag{A.4}$$

At this point, some of the common approximations are to set the density as a constant, but a more rigorous one is our approach of a linear variations as mass is more concentrated in the center. That said a better approximations is:

$$\rho(r) = \rho_c(1 - \frac{r}{R}) \qquad \rho_c = \frac{M_R}{\int_0^R dV} = \frac{3M_R}{4\pi R^3} \tag{A.5}$$

Applying (A.4) into (A.3) we have:

$$E = -\int_0^R \frac{16}{3} G\pi^2 r^4 (\rho_c(1 - \frac{r}{R}))^2 dr = \xi \frac{3}{5} \frac{GM_R^2}{R} \tag{A.6}$$

With $\xi \sim 1.24$.

Appendix B

CCSN Neutrino Emission

B.1 Flavor transformation due to $\nu - \nu$ interaction

B.1.1 Slow modes

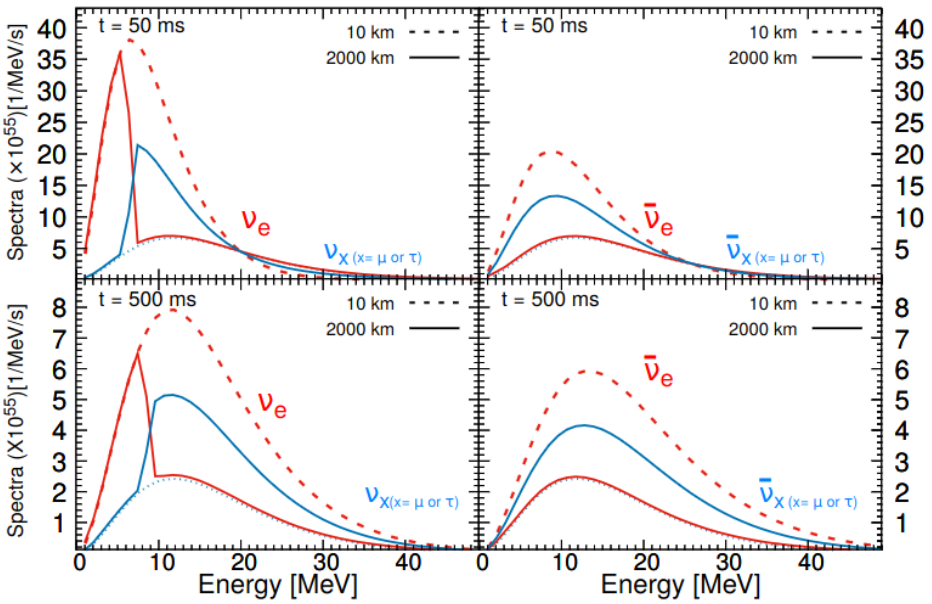

Figure B.1: Neutrino spectra at different times of the *accretion* phase before (50 ms) and after (500) ms the SN explosion. Dashed lines represent the spectrum in the PNS surface, while solid ones represent this spectrum in outer layers at 2000 km [209].

The mentioned bulb modeling of $\nu - \nu$ can result in energy 'splits' with respect to slow modes, as depicted in **figure B.1**. **Figure B.1** illustrates the influence of $\nu - \nu$ interaction on the ν_e and $\bar{\nu}_e$ spectra during the *accretion* phase for the IMO at various representatives radii for PNS and the *neutrino-sphere* surfaces.

It is observed that the low energy spectrum (less than 10 MeV) remains unaffected by this energy split and remains unchanged. Furthermore, it is worth noting that the spectrum of ν_e undergoes a sudden splitting, occurring at approximately 9 MeV. This split results in the emergence of a step-like pattern in the probability flavor transformation [176]. It is noteworthy that the split occurs more smoothly in 500 ms compared to 50 ms, since the densities of ν_e and $\bar{\nu}_e$ begin to equalize. In contrast, the $\bar{\nu}_e$ is less affected by collective oscillations as it does not exhibit spectral splits. Instead, there is a notable transition that decreases its spectra in favor of neutrino heavy flavors.

B.1.2 Fast modes

Fast modes lead to a high frequency transformations in typical times $t_F \sim \frac{2}{\mathrm{V}_{\nu\nu}}(\mathcal{O}(ns))$ [226]. This mode, in contrast to the slow mode, is not contingent on matter but just on neutrino emission rate. Flavor transformation can occur rapidly in regions where $2G_F(n_{\nu_e} - n_{\bar{\nu}_e}) \gg \frac{\Delta m_{13}}{2E}$ is satisfied. The rapid mode potential associated with this condition can be expressed as shown in [227].

$$\mathrm{V}_{\nu\nu} = \sqrt{2}\mathrm{G}_\mathrm{F} \int_0^\infty \mathrm{dE} \frac{\mathrm{E}^2}{2\pi^2} [\eta_{\nu_\mathrm{e}}(\mathrm{E}, \mathbf{v}) - \eta_{\bar{\nu}_\mathrm{e}}(\mathrm{E}, \mathbf{v})], \tag{B.1}$$

Where η_ν represent the number of neutrinos present. Regarding the expression(B.1) if $n_{\bar{\nu}_e} \geq n_{\nu_e}$, $\mathrm{V}_{\nu\nu}$ changes his sign. This can occur when the angular distribution within a certain region, or along a particular axis, is sufficiently distinct to infer an intersection into the ν_e and $\bar{\nu}_e$ trajectories. This is referred to as the *crossing* into the angular Electron Lepton number (ELN) distribution[228, 229]. When anisotropy occurs, it induces the instability necessary for fast mode conversion[230, 231].Considering the usual time frame for transformation, which is around 1 nanosecond, it is necessary to incorporate a precise temporal resolution when studying the evolution of neutrino trajectories. This is in addition to the already indicated accurate assessment of the spatial distribution of neutrino emission. This implies a challenge for CCSN simulations to account this "crossing," considering the substantial computing expense it would entail. Additional research has been conducted to enhance our comprehension and subsequently streamline the issue, leading to the occurrence of this "crossing" in CCSN simulations. This work is documented in the references:[228, 455, 456]. One of the findings of this study is that the phenomenon of *crossing* exhibits distinct behavior

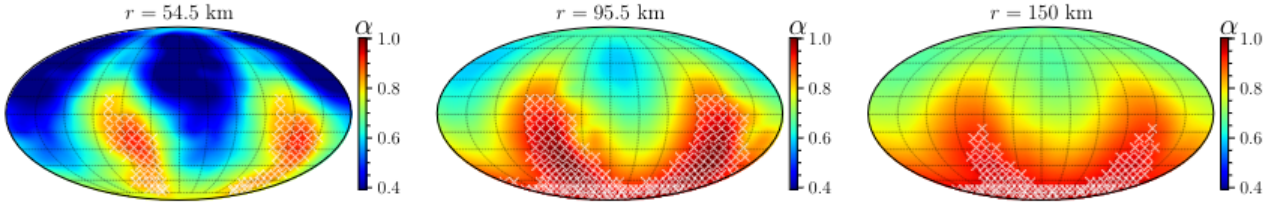

Figure B.2: Projection of α (upper panels) of the 3D 11.2$\mathrm{M}_\odot$ progenitor[457] at a time t = 200 ms for different radius r= 54.5, 95.5 and 150 km, respectively from left to the rigth.

between 2-ν and 3ν flavor mixing, as reported by [458, 459]. Furthermore, [460] demonstrates that collisions

have the capability to generate the necessary conditions for the occurrence of rapid modes, employing a modeling method based on a one-dimensional approach.Recent multi-dimensional simulations of CCSN have successfully identified fast modes. These modes have a small impact on the neutrino spectrum and exhibit a similar shape in regions where they intersect with other modes, as reported by [461]. As reported in **Section B.1.1** crossing condition depends on the evolution of the ratio between ν_e and $\bar{\nu}_e$ densities $\alpha = \frac{n_{\nu_e}}{n_{\bar{\nu}_e}}$.**Figure B.2** represents, for different radius, the α polar map at a time after the bounce t_{pb}= 200 ms. At this time, neutrinos decouple from matter around a radius of $\sim$ 50-70 km, highly depending on their flavors and energies [461].

Appendix C

CCSN Detection

C.1 Coherent elastic neutrino nucleus scattering

C.1.1 CEνNS kinematics

First from the kinematics, the 4-vector momemtum $\vec{P_i}$ in the lab frame, neglecting antineutrino mass $|p_{\bar{\nu}_e}| = E_{\bar{\nu}_e}$ can be degined as:

$$\vec{P_\nu} = E_\nu \begin{bmatrix} 1 \\ u_x \\ u_y \\ u_z \end{bmatrix}, \quad \vec{P_N} = \begin{bmatrix} m_N \\ 0 \\ 0 \\ 0 \end{bmatrix}, \quad \vec{P'}_N = \begin{bmatrix} E_R + m_N \\ q_{N_x} \\ q_{N_y} \\ q_{N_z} \end{bmatrix}, \quad \vec{P'}_\nu = E'_\nu \begin{bmatrix} 1 \\ u'_x \\ u'_y \\ u'_z \end{bmatrix} \tag{C.1}$$

Using energy and momentum conservation:

$$E_\nu - E'_\nu = E_R, \qquad (E_\nu - E'_\nu)^2 = |\vec{q_N}|^2 = R_N^2 + 2R_N m_N \tag{C.2}$$

Using (C.2) the expression of the neutrino energy can be obtained, after a few calculations:

$$E_\nu = \frac{R_N m_N(\sqrt{R_N^2 + 2R_N m_N} cos\theta + R_N)}{2m_N R_N cos\theta} = \frac{1}{2cos\theta}(R_N + \sqrt{R_N^2 + 2R_N m_N} cos\theta) \tag{C.3}$$

C.1.2 CEνNS cross section

Form factor

The form factor accounts for the decrease in coherence with higher momentum transfers. The Helm form factor [371][462] can be employed for spin-independent collisions, and is defined as:

$$|F(E_R)|^2 = \left(3\frac{j_1(\sqrt{2m_n E_R} R_0)}{\sqrt{2m_n E_R} R_0}\right)^2 e^{-2m_n E_R s^2} \tag{C.4}$$

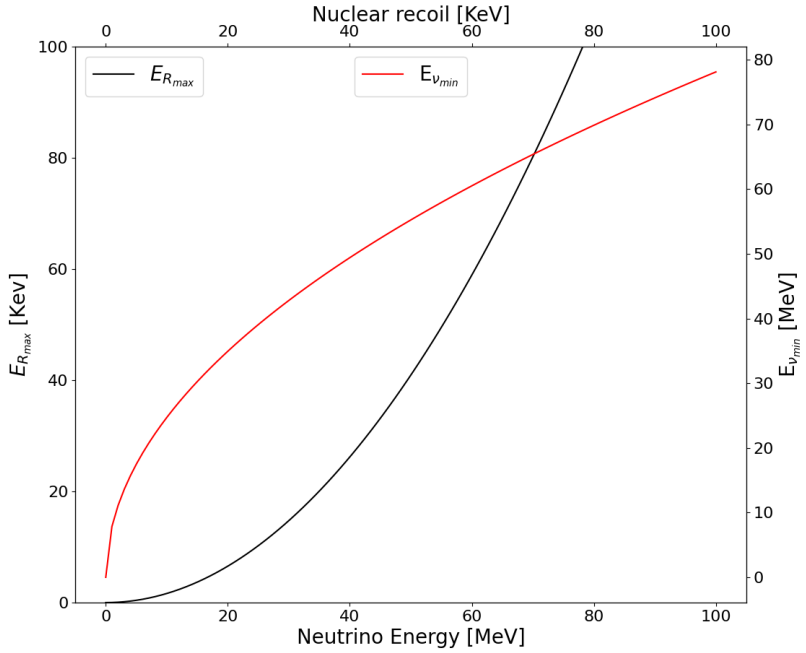

Figure C.1: E_{min} and $E_{R_{max}}$ for the ranges [0,100 MeV] and [0,100 keV] following equations (3.24) and (3.27) respectively

Where j_1 is a first order spherical Bessel function, $R_0 = 1.14A^{\frac{1}{3}}$ fm the effective radius of the nucleus and s the nucleus skin-thickness $s = 0.9$ fm [371]. Form factor can be approximated by non-dimensional parameters q_r and q_s with recoils E_R in keV and the relation already used $\hbar c \equiv 197$ MeVfm [348] :

$$|F(E_R)|^2 = \left(\frac{3(sin(q_r) - qrcos(q_r))}{q_r^3} e^{\frac{-q_s^2}{2}}\right)^2 \tag{C.5}$$

$$q_r = \frac{\sqrt{(2E_R m_n + E_R^2)} r_n}{(197 \times 10^3)} \qquad q_s = \frac{\sqrt{(2E_R m_n + E_R^2)} s}{(197 \times 10^3)} \tag{C.6}$$

Where r_n in fm it's defined as:

$$r_n = \sqrt{c^2 + (3/7) \times \pi^2 \times a^2 - 5s^2} \qquad a = 0.52 \qquad c = 1.23((A_{Xe})^{1/3}) - 0.60 \tag{C.7}$$

By definition, if the recoil energy is zero, the form factor reaches a bounded value at 1. The form depends strongly on the atomic number A, and so it will be different for each LXe isotope of **table 3.20**.

C.2 CEνNS NEST simulation

C.2.1 Event S2 peak from hit clustering

It is possible to recover the time and the PE area of scintillation photons arriving to each PMT from NEST, refereed in the text as 'PMThits'. From this PMThit times a clustering using a density algorithm DBSCAN

can be performed, to reconstruct the mean S2 peak contributing to the NEST event and compare both results. This permit the extraction of additional parameters that an standard simulation with NEST not include, such as the center time and the width of area fractions (50, 90%) that XENONnT data processing includes. This parameters can be used to make selections and cuts, to reduce the background contribution to the signal. The **figure C.2** shows the event S2 area (without corrections) distributions from NEST, corresponding to the simulation of 100 CCSN from *Bollig 2016* $11M_{\odot}$ at 10 kpc. The clustering requiring

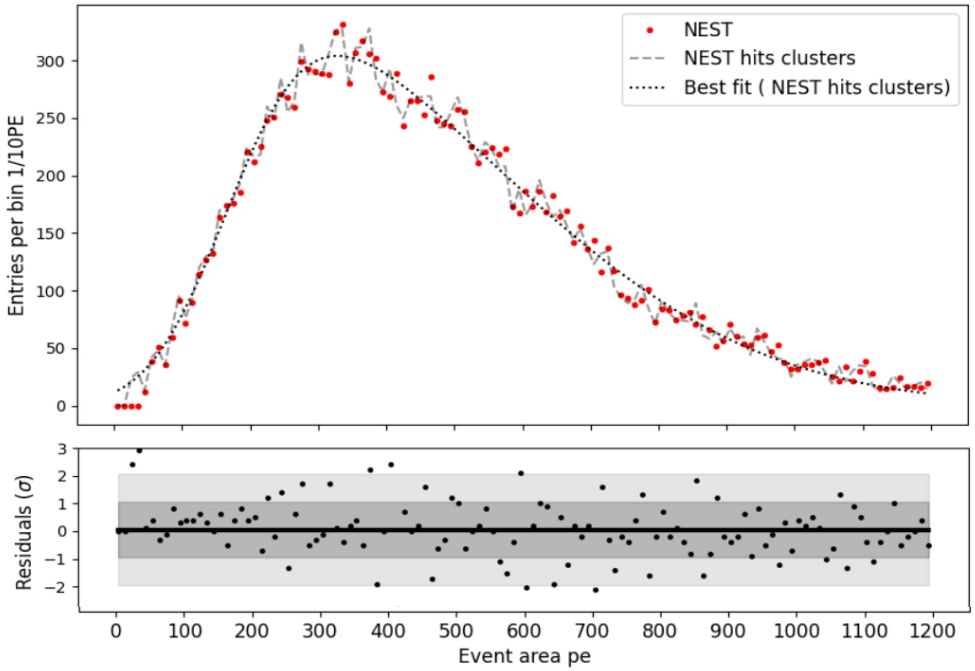

Figure C.2: S2 area distributions from NEST(red points) vs the reconstructed from the PMThit time clustering (dotted semi-transparent black line), resulting the simulation of 100 CCSN from *Bollig 2016* $11M_{\odot}$ at 10 kpc. The dashed black line correspond to the best fit of the reconstructed distribution for its better visulation as the fluctuations due to the low statistics are significant. The residuals corresponds to the difference between the two distributions.

20 hits neighbouring in a time window of 50 ms appears to be effective, regarding the results from both distributions. The mean precision for each event is 0.21% not presenting any result higher than 1%.

Appendix D

CCSN detection in XENONnT water tank

D.1 Compton Scattering

The compton scattering edges and angular distribution

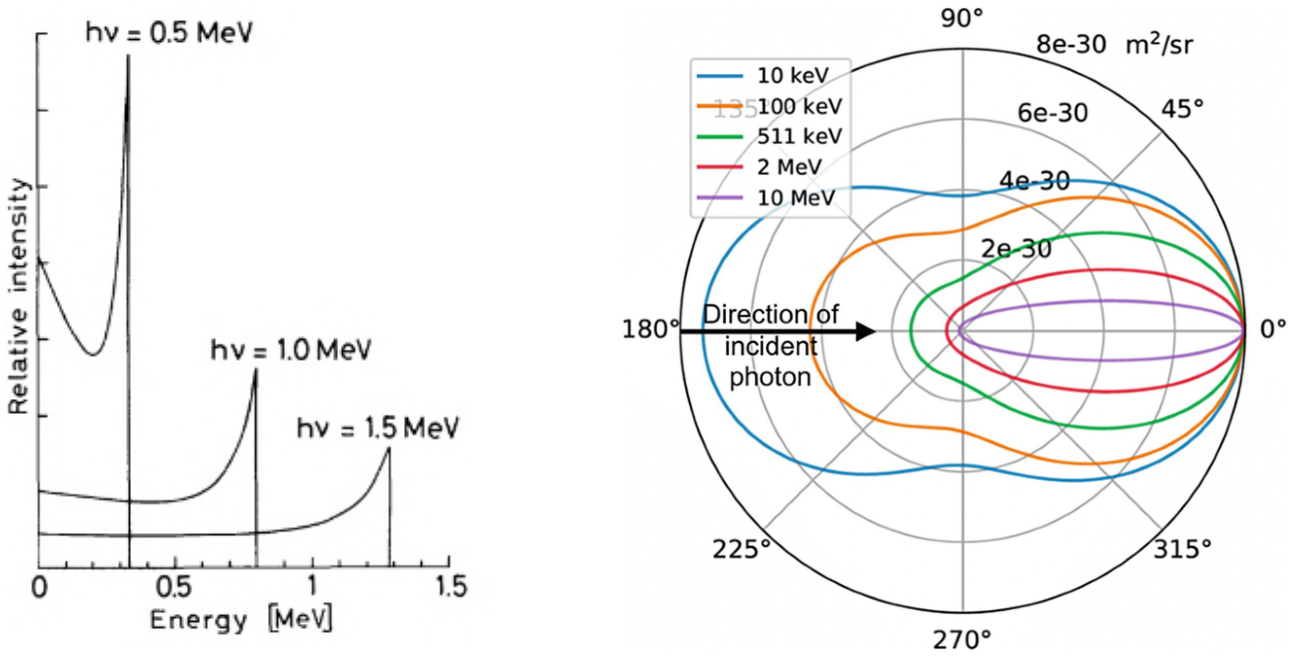

Figure D.1: **Left.**Compton maximum energy transfer from gamma scattering. The maximum electron energy for a given gamma energy, refereed as comptom edges, are obtained following expression (4.3). **Right**.Polar distribution of compton scattered electron, using the Klein-Nishima solid angle dependent cross section. Figure from [463]

D.2 Vetoes cerenkov microphysics

Fraction of PMTs in the different vetoes for 20 MeV positrons

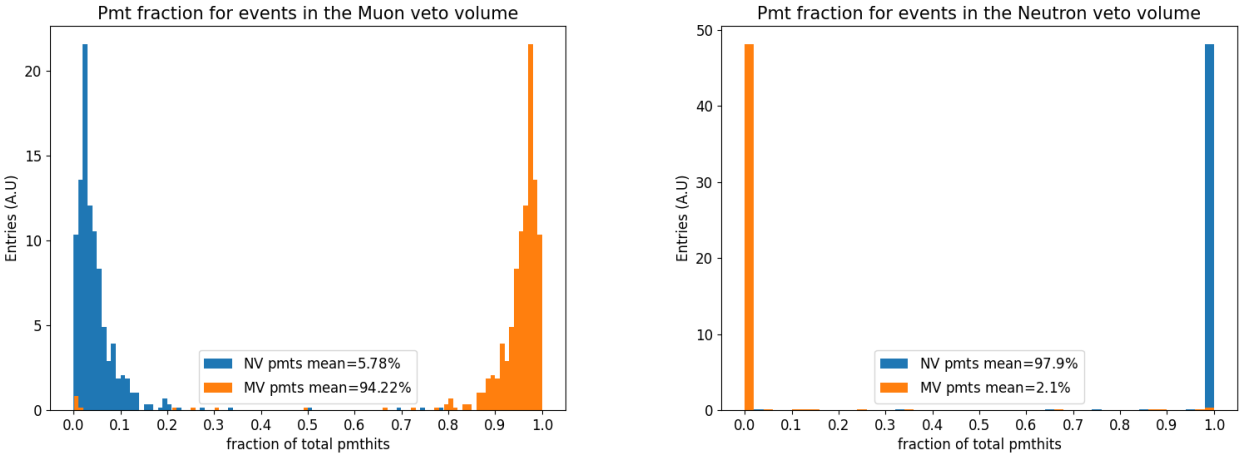

Figure D.2: **Left**. Fraction of VPMThits from 15 MeV positron events generated in the muon veto absorbed by photocathodes of neutron veto (blue) PMTs and muon veto (orange) PMTs. **Right**. Fraction of VPMThits from 15 MeV positron events generated in the neutron veto absorbed by photocathodes of neutron veto (blue) PMTs and muon veto (orange) PMTs.

Fraction of PMTs in the different vetoes for 4.44 MeV gamma

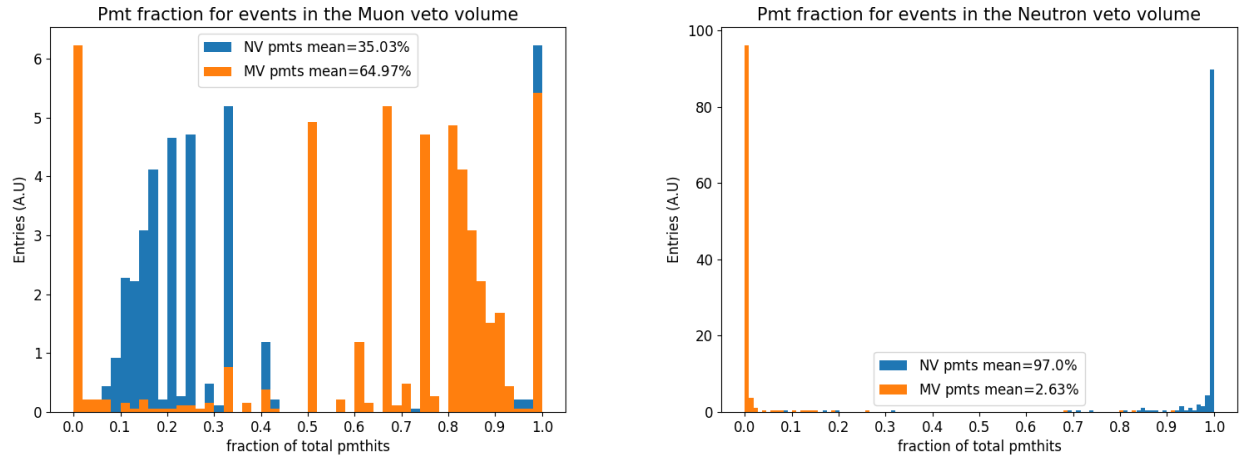

Figure D.3: **Left**. Fraction of VPMThits from 4.44 MeV gamma events generated in the muon veto absorbed by photocathodes of neutron veto (blue) PMTs and muon veto (orange) PMTs. **Right**. Fraction of VPMThits from 4.44 MeV gamma events generated in the neutron veto absorbed by photocathodes of neutron veto (blue) PMTs and muon veto (orange) PMTs.

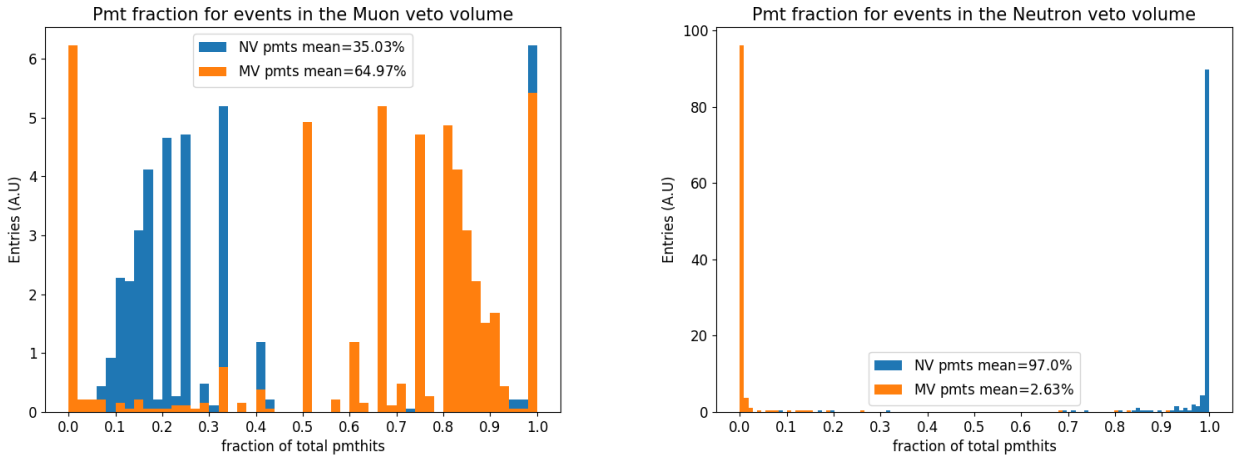

Figure D.4: **Left**. Fraction of VPMThits from 4.44 MeV gamma events generated in the muon veto absorbed by photocathodes of neutron veto (blue) PMTs and muon veto (orange) PMTs. **Right**. Fraction of VPMThits from 4.44 MeV gamma events generated in the neutron veto absorbed by photocathodes of neutron veto (blue) PMTs and muon veto (orange) PMTs.

D.2.1 Vetoes cerenkov spatial performance

The **figureD.5** shows the photon cerenkov dispersion for each veto and as a consequence the VPMThit distribution in each volume as a function of the positron energy.

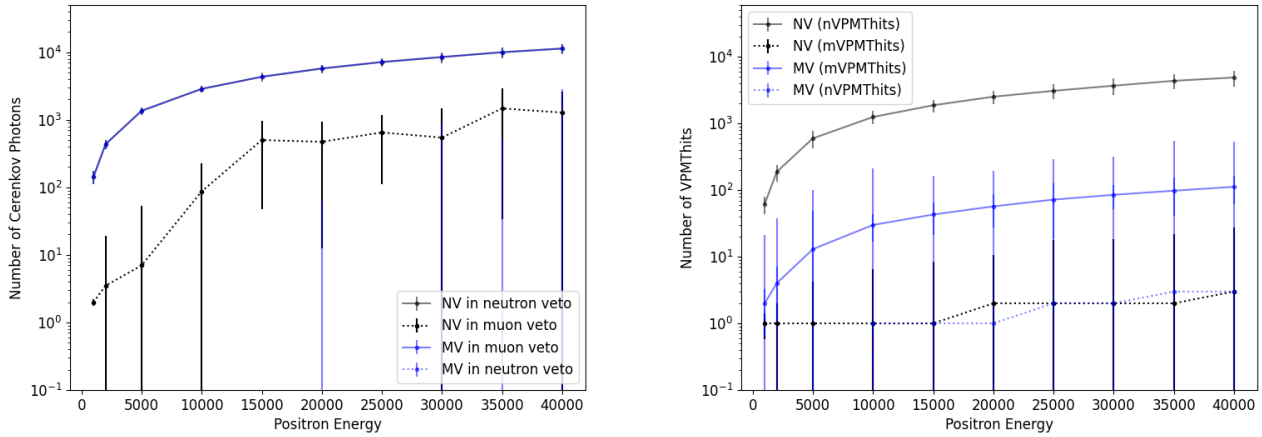

Figure D.5: **Left**. Cerenkov photons spatial volume creation as a function of the energy (in neutron veto or muon veto) for primary positron events generated in the muon veto (MV) or neutron veto (NV). The photons generated out of the volume where the event is created are represented in dotted lines. **Right**. VPMThits of in muon or neutron veto for primary positron generated in the MV or NV in the right panel. The VPMThits detected in a distinct volume of the event generation are represented by dotted lines.

D.2.2 Positron annihilation

Time distribution of 20 MeV positron annihilation for GEANT4 simulation and random event annihilation.

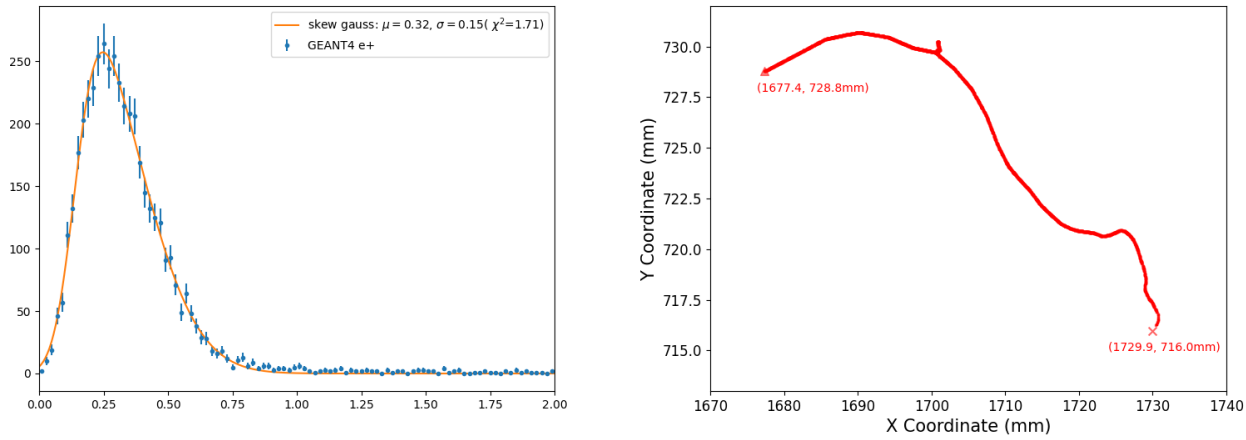

Figure D.6: **Right**. Positron annihilation time distribution in neutron veto for IBD positron energy spectrum simulated in GEANT4. The errors correspond to the standard deviation for each bin. The distribution is fitted with a Skewed gaussian obtaining a mean value of 0.32±0.15. **Left** Cerenkov emission path from GEANT4 simulation, for a random 20 MeV positron event in muon veto. The annihilation (x) and emission (triangle) position are highlighted. In this case a total of 3105 photons are emitted

D.2.3 Time distribution of VPMThits

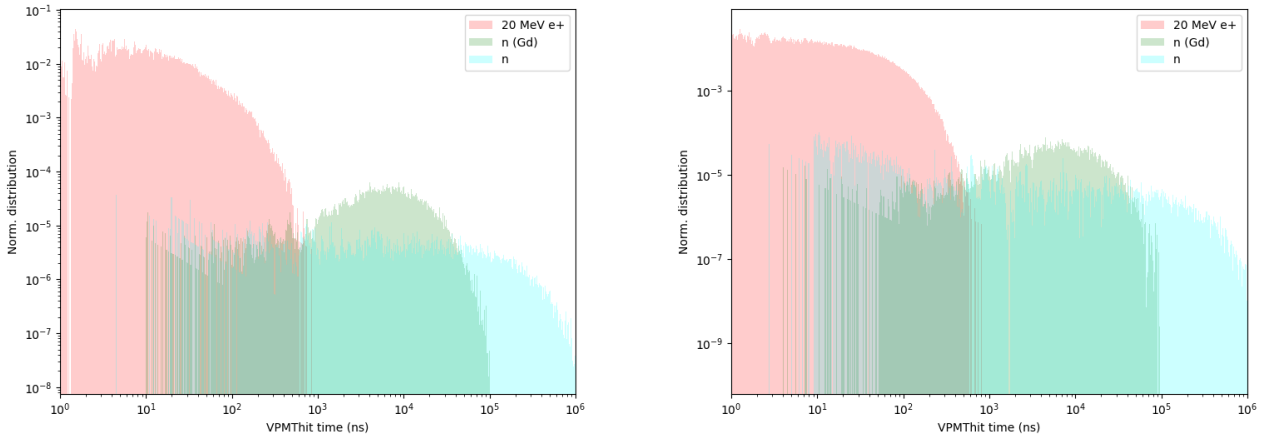

Figure D.7: **Right**.VPMThit time distribution in muon veto for IBD positron energy spectrum (red) and neutron (blue water and green in Gd configuration). **Left** .VPMThit time distribution in neutron veto for IBD positron energy spectrum (red) and neutron (blue water and green in Gd configuration)

Figure D.7 depicts the arrival time distribution for the VMPThits for the IBD 20 MeV positron and neutron, resulting for the GEANT4 simulation of those in the water tank for water and Gd water configurations. VPMThits reaching PMTs in the muon veto are represented in left panel, while the right panel present those arriving into the neutron veto PMTs. The arrival times are relative to the positron-neutron IBD vertex generation. The difference on their respective time arriving is noticeable, as the neutron has to be captured in water in $\sim 200\mu$ s ($\sim$ 30 μs in Gd), while the positron is annihilated in less than 1<ns. However, cerenkov photon propagation generated from the later, extends in time with a dispersion of around $\sim$ 100 ns in the neutron veto, while in the muon veto cerenkov photons typical time will be 200 ns. This different VPMThits time arriving will allow to discriminate positron and neutron, in a simulation context in which IBD time vertex generation is known.

D.2.4 Single and double PE distributions

Wavelenght dependence on the SPE and DPE pulses areas.

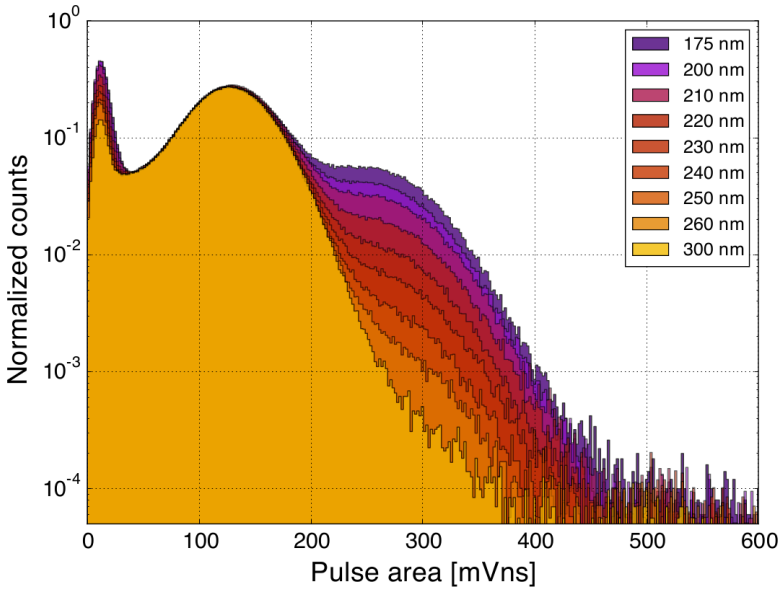

Figure D.8: Distribution of SPE pulse areas for different photon wavelenght from R11410-21 PMT [346]

D.3 IBD cross section

D.3.1 IBD kinematics

IBD Maldestan variables: u,s,t

First from the kinematics, the 4-vector momentum $\vec{P_i}$ in the lab frame, neglecting antineutrino mass $|p_{\bar{\nu}_e}| = E_{\bar{\nu}_e}$ can be defined as:

$$\vec{P}_{\bar{\nu}_e} = E_{\bar{\nu}_e} \begin{bmatrix} 1 \\ u_x \\ u_y \\ u_z \end{bmatrix}, \quad \vec{P}_p = \begin{bmatrix} m_p \\ 0 \\ 0 \\ 0 \end{bmatrix}, \quad \vec{P}_n = \begin{bmatrix} E_n \\ p_{n_x} \\ p_{n_y} \\ p_{n_z} \end{bmatrix}, \quad \vec{P}_{e^+} = \begin{bmatrix} E_e \\ p_{e_x} \\ p_{e_y} \\ p_{e_z} \end{bmatrix}, \tag{D.1}$$

s=$(\vec{P}_{\bar{\nu}_e} + \vec{P}_p)^2 = (\vec{P}_{e^+} + \vec{P}_n)^2$, t =$(\vec{P}_{\bar{\nu}_e} - \vec{P}_{e^+})^2 = (\vec{P}_p - \vec{P}_n)^2$ and u = $(\vec{P}_{\bar{\nu}_e} - \vec{P}_n)^2 = (\vec{P}_p + \vec{P}_{e^+})^2$.

Using energy and momentum conservation:

$$E_{\bar{\nu}_e} = E_n + E_e - m_p, \qquad E_{\bar{\nu}_e}\vec{u} = \vec{p_n} + \vec{p}_{e^+} \tag{D.2}$$

These relations lead to, with θ_n the scattering angle between $\bar{\nu}_e$ and n:

$$\begin{aligned} s &= 2E_{\bar{\nu}_e}m_p + m_p^2 = E_n^2 + E_e^2 + 2E_nE_e - E_{\bar{\nu}_e}^2 \\ t &= m_n^2 + m_p^2 - 2m_p(E_{\bar{\nu}_e} - E_e) = m_n^2 + m_p^2 - 2m_pE_n \\ u &= m_p^2 + m_e^2 - 2m_pE_e = m_n^2 - 2E_{\bar{\nu}_e}(E_n - p_n cos(\theta_n)) \end{aligned} \tag{D.3}$$

Finally, is also useful to define the positron and neutron variables in the mass center (CM). For this the Maldestan variable s, which is a Lorentz invariant, can be defined also in this reference frame leading to:

$$\begin{aligned} p_{e_{CM}} &= \frac{\sqrt{(s-(m_n-m_e)^2)(s-(m_n+m_e)^2)}}{2\sqrt{s}}, \qquad E_{e_{CM}} = \frac{s - m_n^2 + m_e^2}{2\sqrt{s}} \\ E_{n_{CM}} &= \frac{s + m_n^2 - m_e^2}{2\sqrt{(s)}}, \qquad p_{n_{CM}} = \sqrt{E_{n_{CM}} - m_n^2}, \qquad s = 2m_pE_{\bar{\nu}_e} + m_p^2 \end{aligned} \tag{D.4}$$

D.3.2 IBD positron angular distribution

In order to understand the angular distribution of the positron emission, using the scattering angle θ with θ varying between [0,π] in the rest lab frame. For that the t maldestan variable can be writted as:

$$t = me^2 - 2E_{\bar{\nu}_e}(E_e - p_e cos(\theta)) \tag{D.5}$$

A technique to transform the dependence of the cross section from t to $\cos\theta$ $\frac{d\sigma}{dt} \rightarrow \frac{d\sigma}{dcos\theta}$ is to use implicit functions, involving the two variables. This implicit functions $f_1(t, cos(\theta), E_e, E_{\bar{\nu}_e}) = 0$ and $f_2(t, cos\theta, E_e, E_{\bar{\nu}_e}) = 0$, as $t(E_e, E_{\bar{\nu}_e})$ and $cos\theta(E_e, E_{\bar{\nu}_e})$ are also functions of E_e and$E_{\bar{\nu}_e}$.

$$f_1 = t - (m_n^2 + m_p^2) + 2m_p(E_{\bar{\nu}_e} - E_e) = 0 \qquad f_2 = t - m_e^2 + 2E_{\bar{\nu}_e}(E_e - p_{e^+}cos\theta) = 0 \tag{D.6}$$

$$cos\theta = \frac{(m_n^2 - m_p^2 - m_e^2 + 2m_p(E_{\bar{\nu}_e} - E_e) - 2E_{\bar{\nu}_e}E_e)}{2E_{\bar{\nu}_e}p_{e^+}} \tag{D.7}$$

Using the implicit differentiation the relation between the jacobians $\frac{\partial(f_1,f_2)}{\partial(t,E_e)}$ and $\frac{\partial(f_1,f_2)}{\partial(cos(\theta),t)}$ becomes :

$$\frac{\partial cos(\theta)}{\partial E_e} = -\frac{\frac{\partial(f_1,f_2)}{\partial(t,E_e)}}{\frac{\partial(f_1,f_2)}{\partial(cos(\theta),t)}} = \frac{1+\epsilon(1-\frac{E_e}{p_e}cos(\theta))}{\epsilon p_e}, \qquad \epsilon = \frac{E_{\bar{\nu}_e}}{m_p} \tag{D.8}$$

Finally, the expression of $\frac{d\sigma(E,cos(\theta))}{dcos(\theta)}$ is obtained from $\frac{d\sigma(E,E_e)}{dE_e}$:

$$\frac{d\sigma(E,cos(\theta))}{dcos(\theta)} = \frac{d\sigma(E_\nu,\cos\theta)}{d\cos\theta} = \left(\frac{\partial cos(\theta)}{\partial E_e}\right)^{-1}\frac{d\sigma}{dE_e} = \frac{p_e\varepsilon}{1+\varepsilon(1-\frac{E_e}{p_e}\cos\theta)}\,\frac{d\sigma}{dE_e} \tag{D.9}$$

The positron rate as a function of cosθ can be written as:

$$\begin{aligned}\frac{dR_i}{dcos\theta} &= \int_{t1}^{t2} N_w \times f_p \times \frac{1}{4\pi d^2}\int_{E_{min}}^{E_{max}} \frac{dN_i}{dt dE_{\bar{\nu}_e}}\frac{d\sigma(E_{\bar{\nu}_e},cos\theta)}{d\cos\theta}dE_{\bar{\nu}_e}dt \\ \frac{d\sigma(E_{\bar{\nu}_e},\cos\theta)}{d\cos\theta} &= \frac{p_e\varepsilon}{1+\varepsilon(1-\frac{E_e}{p_e}\cos\theta)}\frac{d\sigma}{dE_e} \qquad , \qquad \epsilon = \frac{E_{\bar{\nu}_e}}{m_p},\end{aligned} \tag{D.10}$$

where the positron energy E_e depends on $E_{\bar{\nu}_e}$ and cosθ as:

$$\begin{aligned}E_e &= \frac{(E-\delta_{CM})(1+\epsilon)+\epsilon cos\theta\sqrt{((E-\delta_{CM})^2 - m_e^2\kappa)}}{\kappa}, \\ \kappa &= (1+\epsilon)^2 - (\epsilon cos\theta)^2, \qquad \delta_{CM} = \frac{(m_n^2 - m_p^2 - m_e^2)}{(2m_p)}.\end{aligned} \tag{D.11}$$

D.3.3 IBD Neutron energy spectrum

The first equation can be written using the differential positron energy cross-section presented in equation (4.11). Using the relation of the Jacobian terms $\frac{\partial t}{\partial n} = \frac{\partial t}{\partial E_e}$, the cross-section equivalence can be written as:

$$\frac{d\sigma}{dE_n}(E_{\bar{\nu}_e},E_n) = \frac{\partial t}{\partial n}\frac{d\sigma}{dt} = -2m_p\frac{d\sigma}{dt} = \frac{d\sigma}{dE_e}(E_{\bar{\nu}_e},E_e), \qquad t = m_n^2 + m_p^2 - 2m_p(E_n). \tag{D.12}$$

The kinematics of the neutron are detailed in **Appendix D.3.4**. The convolution with the CCSN antineutrino flux lead to the differential neutron energy spectrum.

$$\begin{aligned}\frac{dR_i}{dE_n} &= N_w \times f_p \times \frac{1}{4\pi d^2}\int_{t1}^{t2}\int_{E_{min}}^{E_{max}} \frac{dN_i}{dE_{\bar{\nu}_e}dt}\frac{d\sigma(E,E_n)}{dE_n}dE_{\bar{\nu}_e}dt, \\ E_{min} &= \frac{E_n+\Delta}{(1-(E_n-p_n)/m_p)}, \qquad \Delta = \frac{-m_p^2 - m_n^2 + m_e^2}{2m_p}.\end{aligned} \tag{D.13}$$

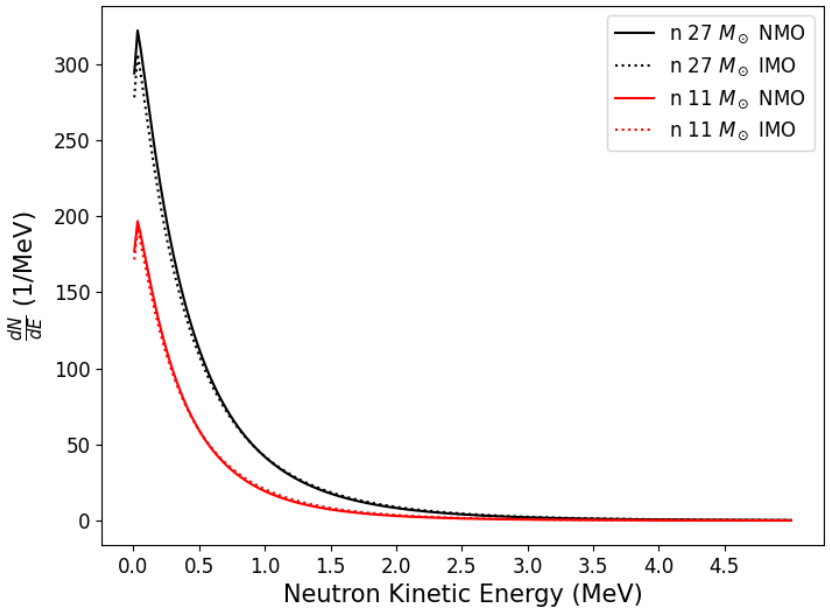

Figure D.9: IBD neutron rate for the *Bollig 2016* 27 $M_\odot$(black) and 11 $M_\odot$(red) progenitors at 10 kpc. The NMO is represented by solid lines and IMO by dotted ones.

The neutron spectrum has a distinct form in comparison to the positron and antineutrino, close to the CEνNS nuclear recoil distribution, with an exponential drop after reaching its peak at ~ 32 keV, as **figure D.9** shows. This distribution assumes that most neutrons have < 1 MeV energy; therefore, Cerenkov light from electrons created during water ionization due to neutron scattering are unlikely to be detected.

Obtaining the angular distribution of the neutron involves various calculations, that will be presented in the next section **Appendix D.3.4**.

D.3.4 IBD neutron angular distribution

As well the neutron angular distribution can be obtained. This can be done using the same technique than for positron. First, neutron energy can be defined using the scattering angle θ_n between the neutrino and the neutron as:

$$E_n = \frac{-(1+\epsilon)(\Delta - E_{\bar{\nu}_e}) + \epsilon cos\theta_n \sqrt{(\Delta - E_{\bar{\nu}_e})^2 - m_N^2 \kappa}}{\kappa}$$
$$\Delta = \frac{-m_p^2 - m_n^2 + m_e^2}{2m_p} \qquad \kappa = (1+\epsilon)^2 - (\epsilon cos\theta)^2 \tag{D.14}$$

As well the scattering angle reads as:

$$cos(\theta_N) = \frac{\Delta - (E_\nu - E_n) + \epsilon E_n}{\epsilon p_n} \tag{D.15}$$

The neutron mass is greater than the neutrino kinetic energy, so the approximation of the angle domain for positron [0,2π] is not more good, as there will be a limit in the aperture of the neutron emission. In this sense, to obtain the maximum of the cosinus is to derive the expression of $cos\theta_N$ by the neutron energy, in order to obtain the value of $E_{n_{cos\theta_{max}}}$:

$$\frac{\partial cos\theta_n}{\partial E_n} = 0 = 1 + \epsilon - \frac{\Delta + E_n(1+\epsilon) - E_{\bar{\nu}_e}}{\epsilon p_n^2} E_n \tag{D.16}$$

The solution becomes:

$$E_{n_{cos\theta_{max}}} = -\frac{(\epsilon+1)m_n^2}{(\Delta - E_{\bar{\nu}_e})} \tag{D.17}$$

The value of the neutron energy, in the expression D.14 obtaining the cos $\theta_{N_{max}}$ accurate value.

$$cos\theta_{max} = \frac{(\Delta - E_{\bar{\nu}_e})^2 - (\epsilon+1)^2 m_n^2}{(\Delta - E_{\bar{\nu}_e})\epsilon m_n \sqrt{\frac{\epsilon+1}{\Delta - E_{\bar{\nu}_e}} - 1}} \tag{D.18}$$

Once the limits of the scattering angle bounds are fixed [cos(θ_{max}),1], the bounds on neutron energy can be obtained:

$$E_{n_{1,2}} = E_\nu - \Delta - \frac{E_{\nu CM}}{m_p}(E_{n_{CM}} \quad \begin{matrix}- \\ + \end{matrix} \quad p_{n_{CM}}) \tag{D.19}$$

Regarding the cross section relative to the Maldestan variable t defined in (D.3) the following relation can be written:

$$\frac{d\sigma}{dE_e}(E_\nu, E_e) = -2m_p \frac{d\sigma}{dt} = \frac{d\sigma}{dE_n}(E_\nu, E_n) \tag{D.20}$$

The final purpose is to express the differential cross section as a function of the scattering angle of the neutrino and the neutron $cos(\theta_N)$. Defining the implicit functions $f_1(t, cos(\theta_N))$ and $f_2(t, cos(\theta_N))$ it can be derived:

$$\frac{\partial cos(\theta_N)}{\partial E_n} = -\frac{\frac{\partial (f_1, f_2)}{\partial (t, E_n)}}{\frac{(f_1, f_2)}{\partial (cos(\theta_N), t)}} = \frac{1 + \epsilon(1 - \frac{E_n}{p_n} cos(\theta_N))}{\epsilon p_N} \tag{28}$$

Finally, the expression of $\frac{d\sigma(E, cos(\theta_N))}{dcos(\theta)}$ is obtained from $\frac{d\sigma(E, E_e)}{dE_e}$:

$$\frac{d\sigma(E_\nu, cos(\theta_N))}{dcos(\theta_N)} = (\frac{\partial cos(\theta)}{\partial E_n})^{-1} \frac{d\sigma}{dE_n} = \frac{p_n \varepsilon}{1 + \varepsilon(1 - \frac{E_n}{p_n} \cos(\theta_N)} \frac{d\sigma}{dE_n} \tag{D.21}$$

Using the expression (D.21) the angular distribution of the neutron, as a function of $cos\theta_n$.

$$\begin{aligned} \frac{dR_i}{dcos\theta_n} &= N_w \times f_p \times \frac{1}{4\pi d^2} \int_{t1}^{t2} \int_{E_{min}}^{E_{max}} \frac{dN_i}{dE_{\bar{\nu}_e} dt} \frac{d\sigma(E_\nu, cos\theta_n)}{dcos\theta_n} dE_{\bar{\nu}_e} dt \\ \frac{d\sigma(E_\nu, cos\theta_n)}{dcos\theta_n} &= (\frac{\partial cos\theta_n}{\partial E_n})^{-1} \frac{d\sigma}{dE_n} = \frac{p_n \varepsilon}{1 + \varepsilon(1 - \frac{E_n}{p_n} \cos\theta_n)} \frac{d\sigma}{dE_n} \end{aligned} \tag{D.22}$$

These calculations yield the angular emission rate as a function of the cosinus of the scattering angle between neutrons and $\bar{\nu}_e$ cos θ_n.

Figure D.10 depicts the cosθ_n normalized distribution from equation (D.22). The neutron is always emitted forwards from the antineutrino incoming direction, and its distribution is bounded by a maximal

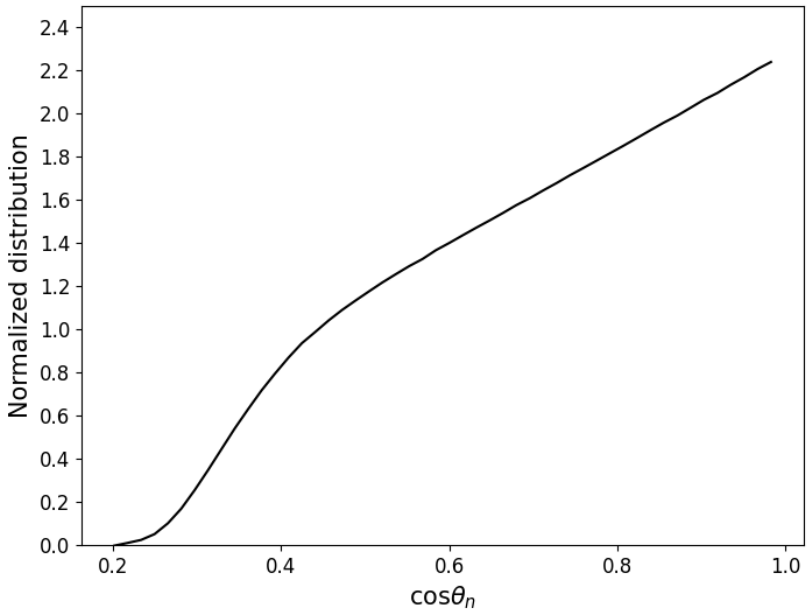

Figure D.10: IBD neutron angular distribution in terms of the cosinus of scattering angle between $\bar{\nu}_e$ and neutron $\cos\theta_n$ for the $27\,\mathrm{M}_\odot$ progenitor (NMO).

aperture emission for the neutron $\theta_{n_{max}}$, which depends on the antineutrino neutrino energy [444], and it is close to 78.4 degrees for the $27\,\mathrm{M}_\odot$ progenitor in the NMO. This maximum angle reads as:

$$cos\theta_{n_{max}} = \frac{(\Delta - E_{\bar{\nu}_e})^2 - (\epsilon+1)^2 m_n^2}{(\Delta - E_{\bar{\nu}_e})\epsilon m_n \sqrt{\frac{\epsilon+1}{\Delta - E_{\bar{\nu}_e}} - 1}}. \tag{D.23}$$

Appendix E

CCSN simulation in water tank

E.1 Hitlet simulator

E.1.1 Flow chart of the Hitlet Simulator

For both neutron and muon vetoes, the schema of the hitlet simulator, also graphically represented in **figure5.7**, is based on the following steps:

1. **Applying QE scaled by the effective collection efficiency eCE**:
   The first step consists of applying the QE to the VPMThits, depending on its wavelength. The muon veto obtains the QE efficiency distribution from HAMAMATSU. Conversely, an individual QE spectrum is obtained for each PMT from weekly calibration data. This is a more accurate approach to performing the QE in the hitlet simulator, but it should not present significant differences from the provided Hamamatsu QE. Another key point is the scaling of the QE by an effective collection efficiency eCE parameter. This parameter is needed in order to simulate the real losses of cerenkov photons finally absorbed by PMTs photocathode that cannot be handled by the GEANT4 mentioned uncertainties, i.e., geometry and transparency (including data-driven corrections). The eCE parameter absorbs uncertainties associated with the PMTs, ensuring their appropriate collection efficiency. In this sense, collection efficiency in a detector volume is usually related to geometric uncertainties, the PMTs also have different responses as a function of the angle and the location of the photon collected, particularly between the photo-cathode surface and the first dynode [464]. This is a parameter that is extremely difficult to measure and for which no standardized methods have been defined [465, 466, 467]. However, the former can be estimated with the comparison of MC GEANT4 results and data, with the best fit obtained between both. The later fit as it will be shown in **Section 5.4** presents some differences that have to be understood.

   $$P_{sur}(\lambda) = Binomial(1, QE(\lambda) \times eCE) \tag{E.1}$$

   The best fit comparing AmBe calibration vs MC GEANT4 + hitlet simulator, results in a value of eCE = 78% (see cumulative event area comparison of MC vs SR0 AmBe data of **figure E.1** right

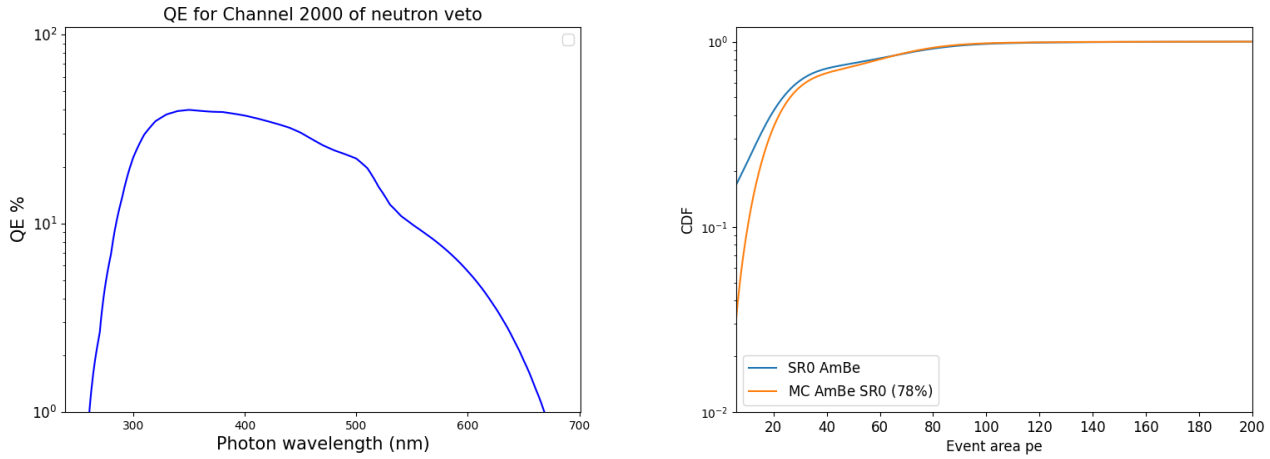

Figure E.1: **Left.** Quantum efficiency as a function of the photon wavelenght for the channel with ID 2000 of neutron veto. **Right.** Event area cumulative distribution function comparison regargind AmBe SR0 calibration data and MC using a eCE=78% and a gamma fraction of 48%.

panel) . As no calibration is performed in muon veto, this parameter cannot be deduced in the same way. Nevertheless, being the PMTs very similar, being the main difference the digitiser as mentioned before, the eCE in the muon veto can be for instance approximated with the value of the neutron one.

2. **stacked hitlets(2 or more hitlets processed like one) happening in a close time window $\mathcal{O}$(ns) in the same PMT channel**:
   With the surviving hits after applying the $QE \times eCE$ factor, the hitlet simulator finds the 'stacked' hitlets mentioned before. This is done by building clusters of photons arriving at the same PMT channel using a density algorithm, DBSCAN[389], as done for the clustering of S2 in the TPC CEνNS simulation (see **chapter 3 section 3.5.2.1**).From the results shown in **figure 5.6** the window for the clustering will be fixed to four digitiser samples for the neutron veto, i.e., 8 ns, and ten samples (80 ns) for the mVeto, requiring at least two hitlets in the coincidence window.
   The impact of the stacked hitlets is expected to be particularly significant in the neutron veto, because the dispersion of the Cerenkov photons is lower, as stated in **Section 4.1.3**, and so the likelihood of finding photons that arrive in the save PMT in a short interval is higher than in muon veto. In the latter volume, on the contrary, a spread in their arrival is anticipated. Values of the center time in both vetoes, which are larger in the muon veto, are also an indication of this different photon arriving (see **figure 4.21**).
   Figure E.2 presents the fraction of hitlets for muon (left) and the neutron veto (right) from IBD simulated neutron (including Gd configuration) and positron as a function of the number of stacked hitlets. It is noticeable that more than 65% of the neutron positron hitlets are stacked with 2 hitlets into the clusters. For the neutron signal, this fraction is lower, and this phenomenon has been neglected in the preceding AmBe analysis of the XENON collaboration. Around 10 % of the

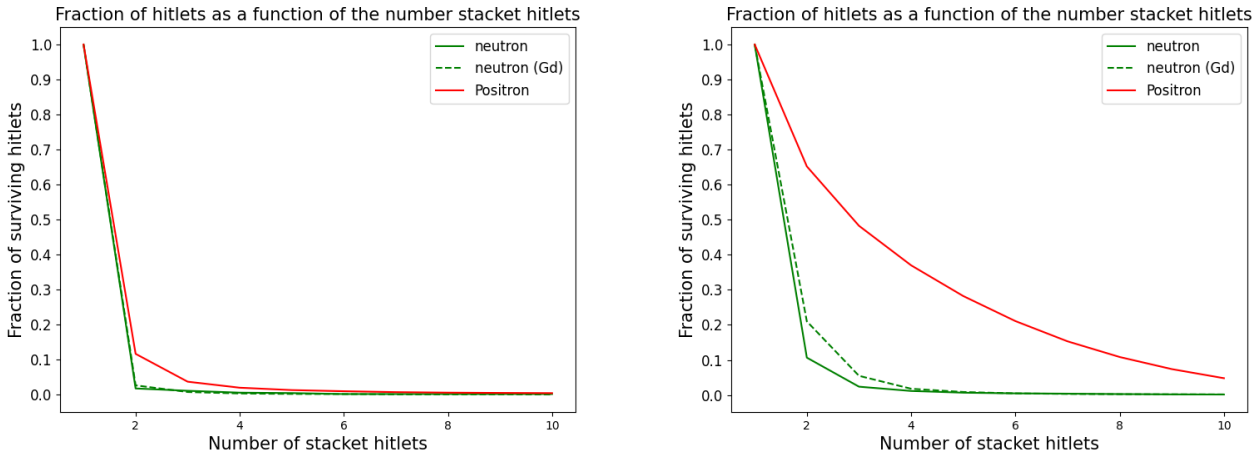

Figure E.2: **Left**. Quantum efficiency as a function of the photon wavelenght for the channel with ID 2000 of neutron veto. **Right**.Cumulative distribution of the event area for SR0 AmBe calibrations (blue) and MC AmBe (GEANT4 + hitlet simulator).

neutron hitlets present 2 stacked hitlets and more than 20% with Gd in water. On the contrary, in the muon veto, the surviving fractions are even lower. For the neutron, the fraction of hitlets with more than 2 stacked hitlets is $\sim$ 1%, while for the positron, it is more significant with more than 10%.

First, the impact of these stacked hitlets will increase the total acceptance, as two or more photons in these short-time cluster windows are expected to produce a signal significantly far from the PMT noise, above the individual PMT threshold, which implies total acceptance for the formers. Secondly, the PE values of the resulting merged hitlet from these stacked hitlets should also be higher in the distribution domain of the double photo-electron DPE distribution. The sampling of PE values of hitlets will be discussed in the next point.

3. **Sample the hitlet PE** :

   This is a critical aspect of the hitlet simulator. The final signal in PE from a hitlet should, in principle, depend on the wavelength of the absorbed photon (see **figure D.8**). However, this information is not provided by the performed LED calibrations, as monochromatic LED is used (HLMP-Cx1A/1B/2A/2B/3A/3B) and only blue wavelength (470nm)[468] is provided. This wavelength aligns with the expected maximum QE of most PMTs in the neutron veto. The idea behind this calibration is to provide the PE distribution of a single photon in a given PMT channel, known as the SPE distribution. That means that the LED pulse has to be low, in this case 8000 mHz, to send the photons one by one.

   The information regarding the individual channel SPE is more comprehensive for the neutron veto than for the muon veto, as the latter not requires an accurate SPE information for muon rejection purposes.

E.1.2 Neutron veto SPE

The SPE distribution obtained with LED calibrations during the SR0 data taking for channel 2000 is shown in **Figure E.4**. The calibrations produce the PE distribution, which combines several functions to describe different processes during signal recording. The electronic and thermionic (dark) noise PMT compounding the baseline lead to the pedestial function represented by the cyan dashed lines, which is the sum of two gaussian distributions, each one describing one of the processes. This background part of the distribution is the one that imposes the PMT threshold leading to the final acceptance (see right panel of **figure E.4**), and will be excluded from the SPE that will be used for the sampling of the PE charge, [1] as the latter only includes the 'real' signal from an energy deposition in the detector volume. Secondly, a simil-box probability function handles the looses due to the inelastic scattering in the first dynode, producing what is often called in literature, sub-amplified components, as the charge multiplication is not so efficient, leading to a lower amplification [466]. Indeed, for each dynode surface, two main sources of secondary electron emission can contribute to the gain from the primary electron arriving at a certain dynode: the mentioned inelastic back-scattered electrons, compounding the sub-amplified spectrum, and 'true secondary electrons', electrons emitted with high angles, as the multiplication chain efficiency has an angular dependence on the incoming direction of the precedent electron [469]. The 'true electrons' should be described through a poisonian distribution centered around 1PE, the former is presented by the orange dashed line.

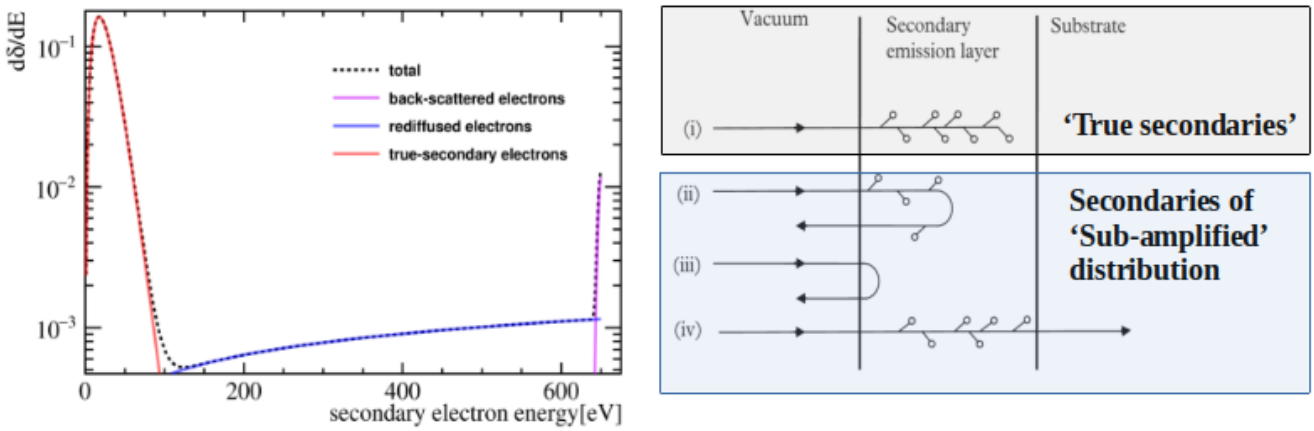

Figure E.3: **Left. Energy spectrum of secondary emission. True secondaries are represented by the red dashed line,** [470] **Right**.Schéma from an incoming primary electron interacting with an electron emissive layer. The i,ii,iii, and iv points are detailed the text. The figure has been modified from the original from [466]

To understand these two components, it is worth introducing the secondary emission process and, as a result, the final gain produced in a PMT. Each dynode is provided with a positive monotonic

[1] It is possible that sometimes PE values are referred to as PE charge in analogy of the final voltage released at the end of the dynode chain, transformed in ADC counts

potential sequence, adding a potential ϵ_p between each step. This sequence extends from the first dynode to the last, accelerating the extraction of secondary electrons from the dynode surface in each inter-dynode space. The electrons transfer their kinetic energy to the dynode surfaces, which then extract another secondary bunch. This process multiplies the number of electrons at each dynode, resulting in an amplified gain that is dependent on the number of secondary electrons. This gain depends on the voltage initially applied, the nature of the dynode surface (metal, semiconductor, or isolant), and its geometry. Dynodes are often composed of a thin active metallic surface supported by a substrate with insulation, or at least non-magnetic, characteristics [399]. In the electron primary[2] kinetic energy transfer, secondary emission spectrum can be described as distinguishing tree regions as **figure E.3** shows. The true secondaries (red line) compounding the low spectrum part represents 70-80% of the total emission, while around 30% came from the primary electrons suffering at some point of the chain an inelastic scattering. Some of them, after generating a few secondaries, are back-scattered after depositing a part of this energy (redifused electrons, in blued line), and others are back-scattered without depositing any kinetic energy. Those are represented by the magenta line, keeping all the ϵ_p; in this case, ϵ_p= 650 eV [470]. A Schema of the mentioned process is displayed in the right panel of **figure E.3**: (i) refers to the primary electrons creating a number of secondaries, some of which escape the dynoded surface, becoming 'true secondaries'; (ii, iii) refers to the inelastic scattering, including the case of no energy deposition; (iii), in the case of some of the secondaries produced escape, their number should be lower than the expected from the (i) case, and the gain is lower being the resulting signal sub-amplified; and finally (iv) accounts for primary electrons that have enough energy to leave the emitting surface layer entering in the substrate, in which secondary emission is strongly diminished [466]. The last case can also be resolved as a sub-amplified signal.Among this, other processes are responsible for SPE gain, such as the transparency of the photocathode and trapping of secondaryelectrons in dynode material, and the already mentioned collection efficiency. Inelastic scattering probability is correlated to the probability of one, or n, secondary electrons to be generated in the first dynode, which can be described by a Poisonian distribution. For a single electron, convolution between the simil-box from sub-amplified components and the 1PE gaussian leads to the SPE distribution described by the red dashed line. Finally, a gaussian function centering around 2PE (black dashed line) describes the case of double photo-electron production. The precise mathematical expressions of these functions are described in **Appendix E.1.4**, particularly focusing on the sub-amplified approximation distribution.

Regarding the PE sampling, the DPE has not been included. Considering its distance from noise, its acceptance should be around 100%. However, its contribution is negligible and easily overlooked. If it is incorporated into the charge sampling, the acceptance process should differ from that of the SPE. In the hitlet simulator, SPE only includes sub-amplified components and 1PE distributions. The noise region only impacts the sub-amplified component of the SPE, anticipating a high acceptance

[2]Primary not correspond to the first electron emitted from a photon interaction in the photocathode, but an incoming electron arriving at any dynode.

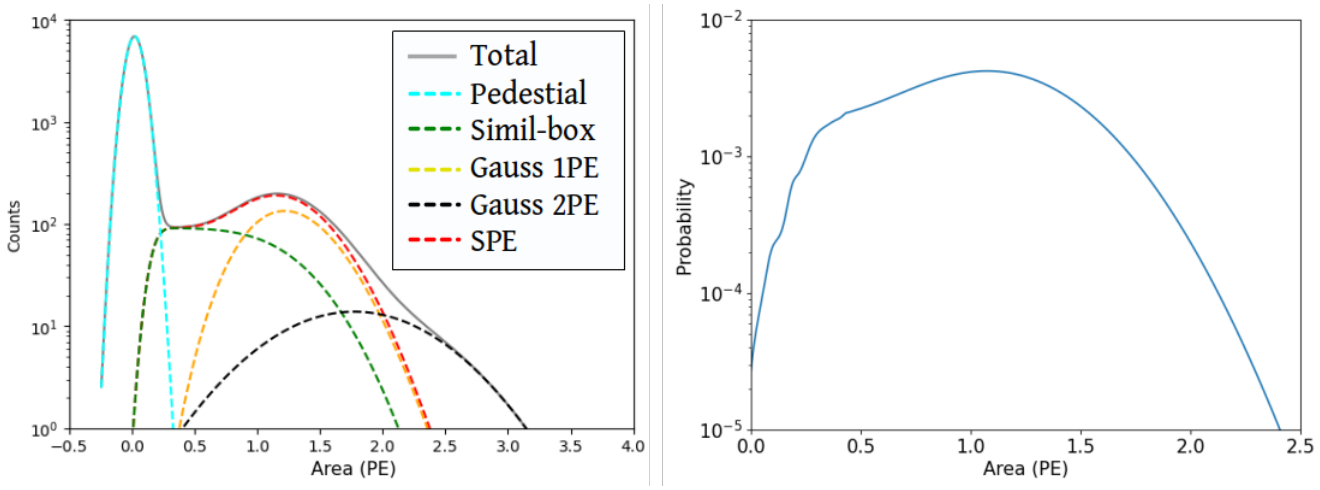

Figure E.4: **Left**. Single photo-electron distribution for the channel 2000 for the SR0 data taking. The different contributions of the pedestial describing PMT noise (cyan), 'simil-box' (green) for sub-amplified components, 1PE(orange) and 2PE (black) gaussians . **Right**. Normalized SPE distribution, applying the acceptance from cumulative distribution.

that results in 94-99% depending on the channel for SR0. The final SPE probability is normalized using the acceptance as shown in **figure E.4** (right panel). The surviving fraction P_{sur}, after QE, includes the application again of the acceptance, which is applied as a cumulative parameter, distinguishing the case of stacked hitlets as:

$$P_{sur} = \frac{\text{hitlet} \times Binonmial(\text{Acceptance}) + \text{stacked hitlets} \times 1}{\text{Total hitlets}} \tag{E.2}$$

Once the acceptance is applied, the PE sampling can be performed. Hitelts PE are sampled using the SPE for each PMT, and accounting for the stacked hitlets, which are sampled separately using the SPE and after summed: $PE_{stacked(i)} = \Sigma^i$ PE. The stacked hitlets can be after merged, saving the time of the earlier hitlet arriving and the total PE.

E.1.3 Muon veto SPE

Regarding the muon veto, the SPE will be approximated by a gaussian distribution related to LED calibrations similar to neutron veto ones, but not weekly performed. Information per channel will be the related mean μ and the σ of this gaussian, and a deeper analysis into the SPE components is needed. This adds a non-negligible uncertainty to the SPE, absorbed by a large sigma in most of the PMT channels, as **figure E.5** shows. This is due because this gaussian encloses the contributions of sub-amplified 1PE and 2PE. There exists some noticeable dispersion of a few channels presenting a narrower distribution, but in general, the SPE gaussian is centered around $\langle\mu\rangle \sim 1.25$ PE, with a large sigma $\langle\sigma\rangle \sim 0.7$, as the median of the distribution (black line) represents. This can lead to a global increment of the sampled PE values, as the 2PE and sub-amplified risk are overestimated if

they are compared to the neutron veto results shown before.

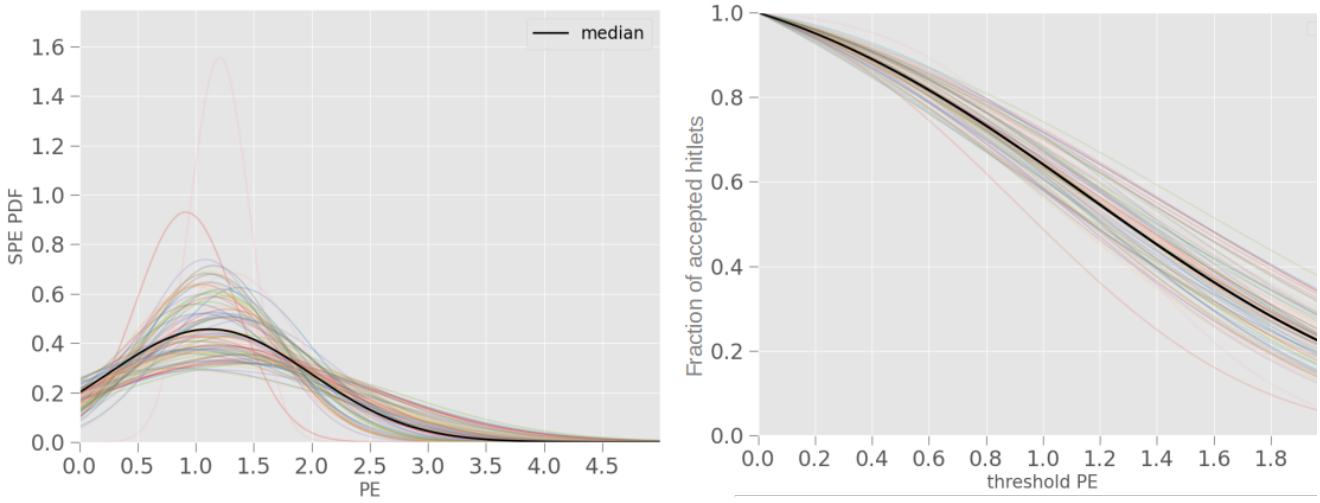

Figure E.5: **Left**. Single photo-electron distribution for the 84 PMT muon veto channels (1000-1083 IDs) for the SR1 data taking, approximated through a gaussian distribution. The median is represented by the black line. **Right**. Acceptances for the muon veto PMTs for a given PE threshold per channel.

On the other hand, the background component has been subtracted for these distributions, but no information about the acceptance is disposable, which is an aspect to perform in future studies. In this sense, the application of the acceptance will be based on a general threshold of 0.25 PE, as a preliminary approach in which acceptances per channel are between 92 and 95%, as the left panel shows. It makes no sense to perform an individual study as LED calibration analysis has to be deeply understood, in the same way as for neutron vetoes PMTs. Similar to the neutron veto, the charge sampling will account for the stacked hitlets, and it must be performed before imposing the threshold relative to the acceptance. The surviving fraction in this case will be:

$$P_{sur} = \frac{\text{hitlet} > 0.25 \text{ PE}}{\text{Total hitlets}} \tag{E.3}$$

4. **' Formatting 'hitlets' to 'events'**

   The CCSN signal simulation study will be conducted at the event level. For that, it is necessary to cluster the succeeding hitlets, which will produce what's called an 'event' in the vetoes data structure. This can be done using the same existing software plugin for the XENONnT data processing. As a consequence, the last step of the hitlet simulator is to transform the hitlet output into the same Science Run data format in order to use this plugin. There is no need to mention any coding details, as this is a trivial process. However, the event clustering trigger conditions can be mentioned (or remenbered, as some have already been mentioned in **chapter 4**). Events in the neutron veto 'events nv' (see **figure 5.4**) consist of a coincidence window of 200 ns and 3 PMT contributing. The former conditions are not expected to affect detection efficiencies for the IBD positron, nor neutron ones. On the contrary, for the muon veto, the time coincidence window is larger, 300 ns,

but a 5-fold PMT is required. This will strongly impact the detection of the neutron as shown in **Section 4.1.3**, particularly emphasized in the results of the low surviving VPMThit fractions presented in **figure 4.13** at this PMT threshold. This requirement will also impact the positron low energy spectrum detection efficiency. However, these trigger conditions are only 'hardware/software' arrangements that can be optimized, creating a kind of CCSN triggering, which will also require studying background rejection, particularly accidental coincidences if the threshold is lowered. The main values characterizing an event for the neutron and the muon vetoes, that will determine the region of interest ROI are:

(a) The event area ($\sum_i^{N_{hitlets}} PE_i$) (the integral of the area of the hitlets contributing in PE);

(b) the center time (already defined in **Section 4.1.3** from expression (3.39));

(c) and the number of PMT channels contributing (N-PMTs).

E.1.4 Neutron veto SPE distribution contribution

The SPE is the convolution of the sub-amplified component and the 'true' secondary electron distribution, resulting from a discrete Poissonian process at the first dynode convoluted with the response of the remaining dynodes. It depends on the gain G_1 of the first dynode of the PMT, the gain of the remaining dynode chain f (in ADC counts) as well as its fluctuations Σ, and finally on σ_{PED}:

$$P(x) = \rho \frac{e^{-\mu\rho}(\mu\rho)^{x\rho}}{\Gamma(1+x\rho)} \tag{E.4}$$

where $\mu = G_1 \cdot f$ represents the mean of the distribution in ADC counts, and $\rho = \frac{G_1,f}{G_1,f^2+\sigma^2_{\text{PED}}+G_1,\Sigma^2}$ is the scaling factor. The point is to understand how this convolution is propagated into the amplification dynode chain. This can be done using two smothed step functions:

$$P'(x) = \frac{\left[1+\text{Erf}\left(\frac{x-\mu_L}{\sqrt{2}\sigma_L}\right)\right]\left[1-\text{Erf}\left(\frac{x-\mu_R}{\sqrt{2}\sigma_R}\right)\right]}{4(\mu_R-\mu_L)} \tag{E.5}$$

The parameters μ_L and μ_R represent the central left and right positions of the distribution shoulders, and there are correlated to f and G_1, $\mu_L = f/2.25$ and $\mu_R = (G_1+0.375)\cdot f$. Theses left and rigth parameters are data driven, based on calibration results. On the other hand, the corresponding σ_L and σ_R parameters describe the smoothing of the left and right step functions:

$$\sigma_L = \alpha\sqrt{G_1 f^2 + G_1\Sigma^2 + \sigma^2_{\text{base}}}, \qquad \sigma_R = \alpha\sqrt{\Sigma^2+\sigma^2_{\text{base}}} \tag{E.6}$$

Where α is a scaling factor close to unity determined from simulation.
Another important parameter that can be calculated from the fit is the SPE acceptance ε; it characterizes the ability to detect weak signals in the presence of a hardware acquisition threshold, as in the case of the self-trigger DAQ of the NV, and it is calculated from data as follows:

$$\varepsilon = \frac{N - \int[\mathcal{F}_{2PE}(x)+\mathcal{F}_{3PE}(x)]dx}{\int \mathcal{F}_{1PE}(x)dx} \tag{E.7}$$

where N is the total number of events after applying the trigger threshold offline, and $\mathcal{F}_{nPE}(x)$ representing the n-photo-electron contributions of the fit function.

E.2 Residuals calculation

The residuals are calculated in order to evaluate the data fit quality from the analytical function of equations (5.4) and (5.5). There are defined as the difference between the observed values from the data and the independent model of the fit f. The mean of the residuals is calculated as the arithmetic mean $\sum R_i/\mathrm{N}$, with N the number of bins.

$$\sigma_R = \sqrt{(\sum_i^N R_i - \bar{R})^2/N}, \qquad R_i = Data_i - f_i \tag{E.8}$$

Residuals give a more explicit information than χ^2 for the quality of the fit, and are particular important for regression analysis. The reader can extended discussion on the topic of residual errors in the following work [471]. In the mentioned figures the residuals are presented as a function of the standard deviation as they are expected to follow a Gaussian distribution. Is oftenly used the studentzed residuals, as the standard deviation of each event area bin σ_i has been calculated. This gives bin:

$$R_i^S = \frac{Data_i - f_i}{\sigma_i} \tag{E.9}$$

E.2.1 Gamma fraction

Several gamma fractions can be used to compare the calibration with the results from MC. A priori the fraction present a non-negligible uncertainty from the source 0.46±0.07 [303]. **Figure E.6** top panel

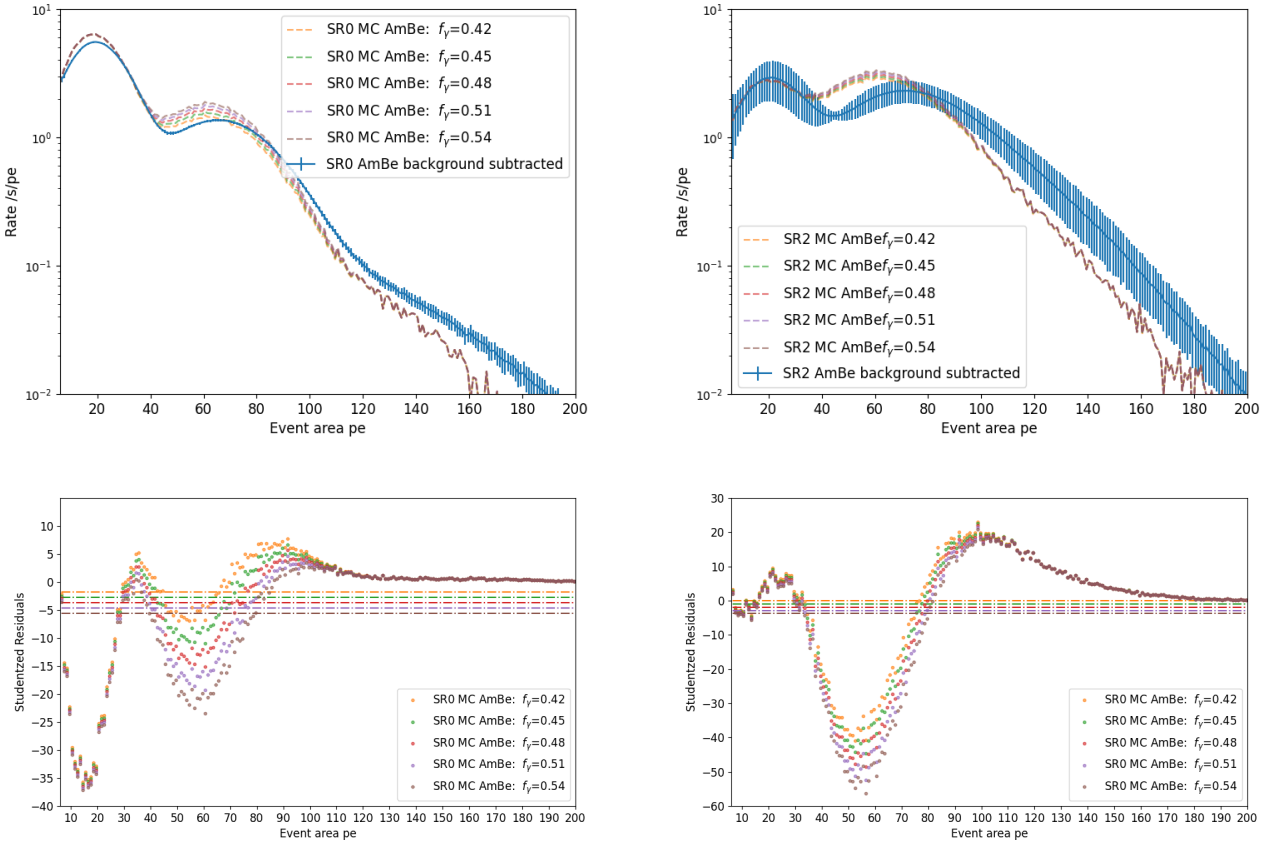

Figure E.6: **Top**. S1 vs S2 area distributions obtained from NEST using XENONnT SR0 detector configuration for the *Bollig 2016* Model 11 $M_\odot$ (left) and 27 $M_\odot$ (right) progenitors at 10 kpc. **Bottom**. The corresponding corrected cS1 vs cS2 distributions for the same progenitors.

shows the total spectrum assuming different gamma fractions compared to the SR0 (left) and SR2 (right) AmBe calibrations, noticing that any of those fractions is able to fit accurately the data. Nevertheless, in the range of gamma distribution [20,100] PE, the better compromise is the 0.48 fraction. This could seem not coherent with the studentzed residuals (E.9) results for each gamma fraction presented in the bottom panel of the **figure E.6**, in which the smallest fraction of 0.42 is the most optimal. However, it can be anticipated that GEANT4 + hitlet simulator MC chain cannot take into account all the neutron veto detection uncertainties, particularly the real transparency conditions and the background from AC during the data recording. The calibration detection efficiencies for neutron capture and ^{12} C gamma are expected to be lower than the resulting from the MC simulation. This has to be accounted for the choice of gamma fraction to perform the MC vs data comparison. Furthermore, the expected rate of the gamma fraction is known as mentioned before. Another point, is the match of the total (neutron + gamma) rate

obtained with the selected threshold to reduce the influence of the background at 6 PE. This is a more objective values as the subtraction of the background is effective in the integral rate, and not in the shape of the event area distribution.

E.2.2 AmBe source position

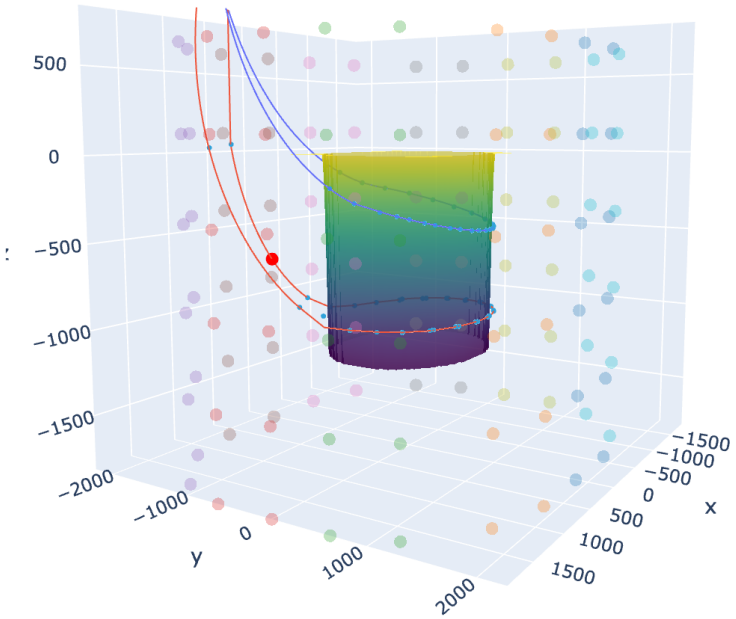

Figure E.7: Position of the AmBe source (red point) in the bottom of neutron veto volume, used for the AmBe calibration analysis in this work. Credit XENON.

E.2.3 AmBe Data

Figure E.9 depicts data, background subtracted data and background in order to understand. Background subtraction is done in a cumulative manner, i.e., $\frac{dN}{dtdPE}_{sub} = \frac{dN}{dtdPE}_{data}$ - $\frac{dN}{dtdPE}_{background}$. The solid blue line in the left panel of this figure also represents the background event area rate distribution from the days before and after these calibrations, spanning 500 runs of 2 to 5 hours duration. The green solid line displays the distribution after subtracting the background. The last will be used for the fit through an analytical function. This also implies to treat independently the data and the background, which do not correspond to the real recording signal proceeding. Even if both process, background, and signal are strictly independent, background hitlets are expected to contribute in a significant fraction of recorded AmBe neutron or gamma signal events, shifting the event area distribution to high values. Considering a

poisonian background for each event area bin and also for the AmBe data, there is a coincidence probability of both periodic phenomena in the 200 ns event window, which is dependent of both periods, or typical times, τ^i_{bck} and τ^i_{data} for each bin i. For the purpose of studying the detector response and evaluating the hitlet simulator, the analysis of the impact of this fraction of events contaminated by the background is not necessary. The reader can find a simple approach to studying the former case in the following work [472]. Nevertheless, the background subtracted data can be used to estimate the number of AmBe events and the contribution of the neutron capture and ^{12}C gammas.

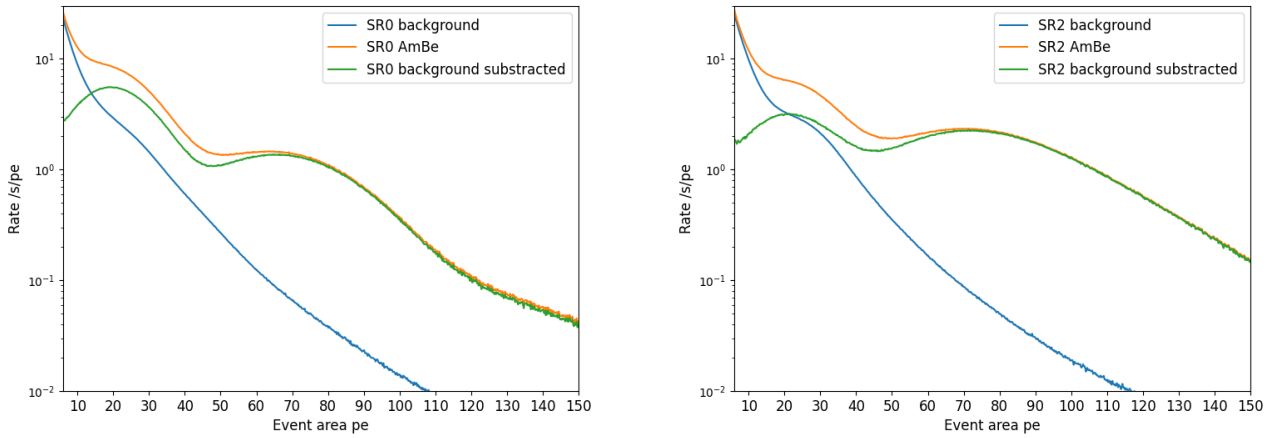

Figure E.8: Event area distributions for AmBe calibration data (orange), background (blue) and AmBe background subtracted (green) for SR0 (left) and SR2 (right).

E.2.4 AmBe MC vs Data

Figure E.9 illustrates the comparison between MC vs AmBe data for SR0 (left) and SR2 (right) periods. The reproduction of the neutron capture in H is remarkable, in the [0,30] range, while discrepancies appear for high energy depositions resulting in a shifted spectrum towards the ^{12} C gamma line (see left panel $\sim$ 65 PE peak) and neutron capture in Gd which event area distribution overlaps with the ^{12} C (see right panel [30, 150] PE range). It can be deduced that the simulation chain requires corrections in order to match data energy resolution. Regarding CCSN detection, IBD positron spectrum from MC simulation is expected to exhibit better energy resolution. For the latter it can be anticipated that its final recorded spectra will be shifted to higher energies in comparison to MC, being approximated by a wide-ranging gaussian. In principle it should be simple to apply this uncertainties using a propagation therm in PE/MeV assuming a gaussina distribution for the positron spectrum.

E.2.5 AmBe SR0 and SR2 center time distributions

Before starting the study of the CCSN simulation results, including in the chain the hitlet simulator, a parenthesis can be done in regards to exploring the center time distribution in SR0 and SR2. As

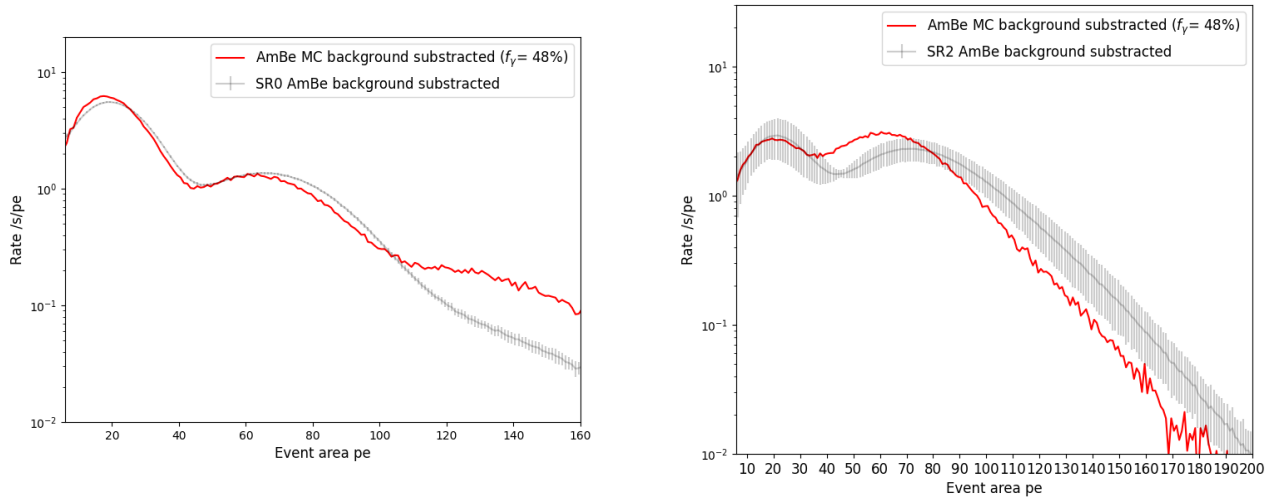

Figure E.9: Comparison of the event area distribution obtained in using GEANT + hitlet simulator (red) versus the SR0 (left) and SR2 (right) background subtracted in the bottom source position CW6d0 (grey). As explained in the text an insertion of the background at a hitlet level into the MC AmBe hitlet precede the subtraction of background. The errors bars of the AmBe subtracted backgrounds correspond to the standard deviation for each obtained from the analysis of the 60 runs.

mentioned in **Section 4.2.2** its implications in the water transparency are strongly correlated, being an excellent indicator of the latter modifications. For this purpose, the AmBe neutron capture in water signal, background subtracted, can be isolated in a region [0, 30] PE and compared in both configurations. **Figure** illustrates the center time distributions corresponding for the two periods, noticing that a different shape corresponds to each data taking period. The distributions are approximated with a skewed gaussian distribution as some background events are still present after the subtraction, particularly in the low center time values, corresponding to AC. The SR2 distribution centers around 4 ns less than the SR0 distribution, exhibiting a more rounded shape. It can be deduced that a decrease in the τ of the exponential time evolution expected from cerenkov photon arrival to the PMTs (see equation 4.7) is shifted by a similar value, enhancing the absorption of part of the cerenkov optical photon spectra in comparison to the SR0. This only confirms that the data used for the AmBe SR2 comparison with simulation present transparency modifications in comparison to SR0 that cannot be handeled yet impose some correction to the MC obtained spectra. At this point, a deeper study will be necessary to understand the transparency modification implication for the CCSN detection, which will not be performed in this work but will be desirable in future studies.

E.3 CCSN simulation results

Energy resolution of neutron and muon vetoes for positron signal

Figures E.11 left panel illustrates the event area mean in PE for each energy bin of positron simulated

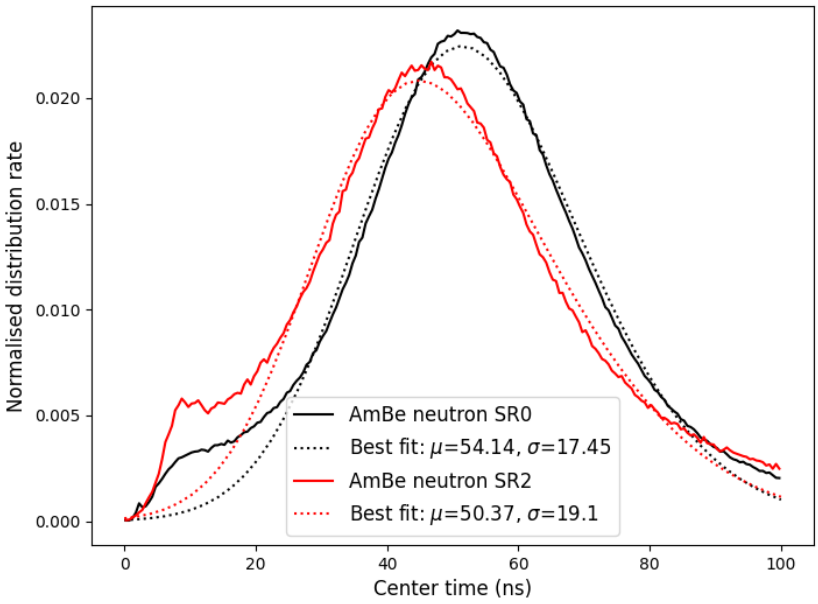

Figure E.10: Center time distribution for the neutron capture 2.22 MeV gamma line from AmBe calibration data in the CW6d0 positron for SR0 (black) and SR2 (red) periods. The distributions are approximated with an skewed gaussian distribution as some background still presente after the subtraction.

energy in the muon veto. The size of each bin 0.1 MeV is normalized in order to represent this mean in PE/MeV. The best linear approximation fits correctly the data beyond 10 MeV in which the detection efficiency as a function of positron energy is $> 50\%$ (see **figure 5.10**) for the muon veto. This results in a low energy resolution around 0.65/MeV. On the side of the neutron veto, the resolution is presented in the right panel, showing a linear evolution in energy. For energies above the cerenkov threshol (222 KeV) the detection efficiency is already $\sim 95\%$, as **figure 5.10** right panel shows, leading to a resolution of 21 PE /MeV which is more than 30 times the muon veto one.

E.4 Sensitivity study in water tank

E.4.1 Muon veto background

Figure E.12 depicts the time evolution of mean and maximum rolling window rates for selected SR1(top) and non-selected SR1 (bottom) in the muon veto after applying the cuts in the ROI.
Figure E.13 illustrates the time evolution of mean (top) and maximum rolling window (bottom) rates for selected SR2(top) before (black.) and after applying the cuts (blue).
Finally, the 2D event parameters distributions corresponding to the SR2 period are represented in **figure E.14** in the IBD positron region of interest. Event area vs center time is depicted in the left panel and event area vs the number of pmts contributing (N-pmts) in the right panel. No substantial differences,

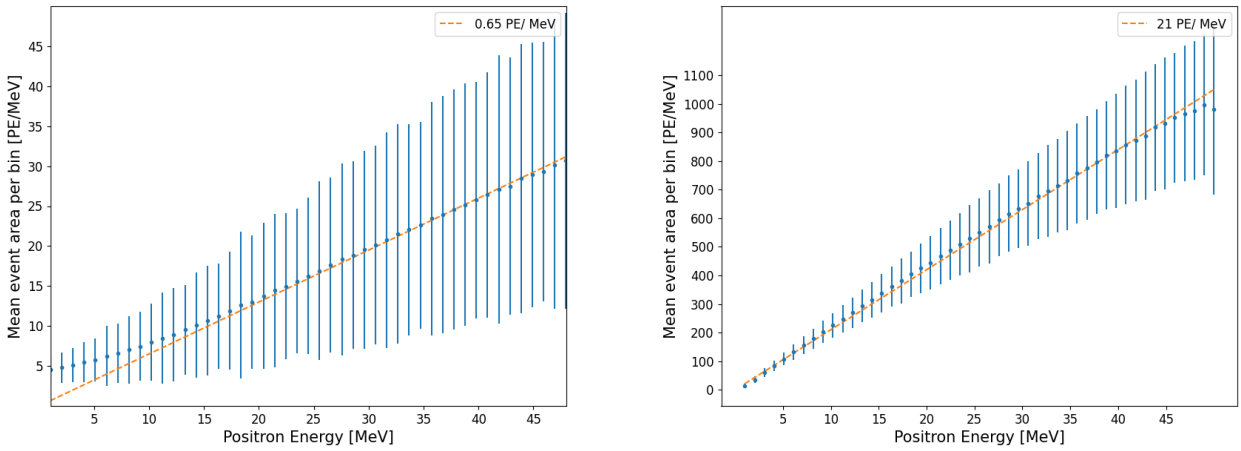

Figure E.11: Average number of detected PE per positron energy bin from MC simulation in the muon veto (left) and the neutron veto (right)

Signal	**Number of CCSN detected events(*) at 10 kpc after cuts**			
Progenitor	$27M_{\odot}$		$11M_{\odot}$	
MO	NMO	IMO	NMO	IMO
Muon veto				
IBD e+	76.47	75.53	37.87	39.07
IBD n	<1 (0.073)	<1 (0.071)	<1 (0.039)	<1 (0.038)
IBD n (Gd)	<1 (0.73)	<1 (0.71)	<1 (0.39)	<1 (0.39)
ES	1	1	<1 (0.61)	<1 (0.605)
Neutron veto				
IBD e+	11.62	11.21	6.25	6.22
IBD n	<1 (0.056)	<1 (0.054)	1< (0.03)	1< (0.032)
IBD n (Gd)	<1 (0.45)	<1 (0.45)	<1 (0.23)	<1 (0.24)
ES	<1 (0.48)	<1 (0.48)	<1 (0.27)	<1 (0.27)

Table E.1: Summary of the number of CCSN detected events after applying the cuts in muon and neutron veto for the IBD and ES interactions at 10 kpc. This event numbers accounts for the two progenitors 27 $M_{\odot}$ and $11M_{\odot}$ from *Bollig 2016* model, in the NMO and IMO neutrino mass orderings. * The number of events are not an integer, and have no physical meaning, but these values are particularly useful to evaluate the impact of the detection capabilities for each volume at other CCSN distances.

among the center time reduction due to the SR2 transparency loos already reported in **Section 4.2.2**, are found in comparison to SR1, that will impact the cut selection. SR2 muon veto event parameters distributions in the ROI.

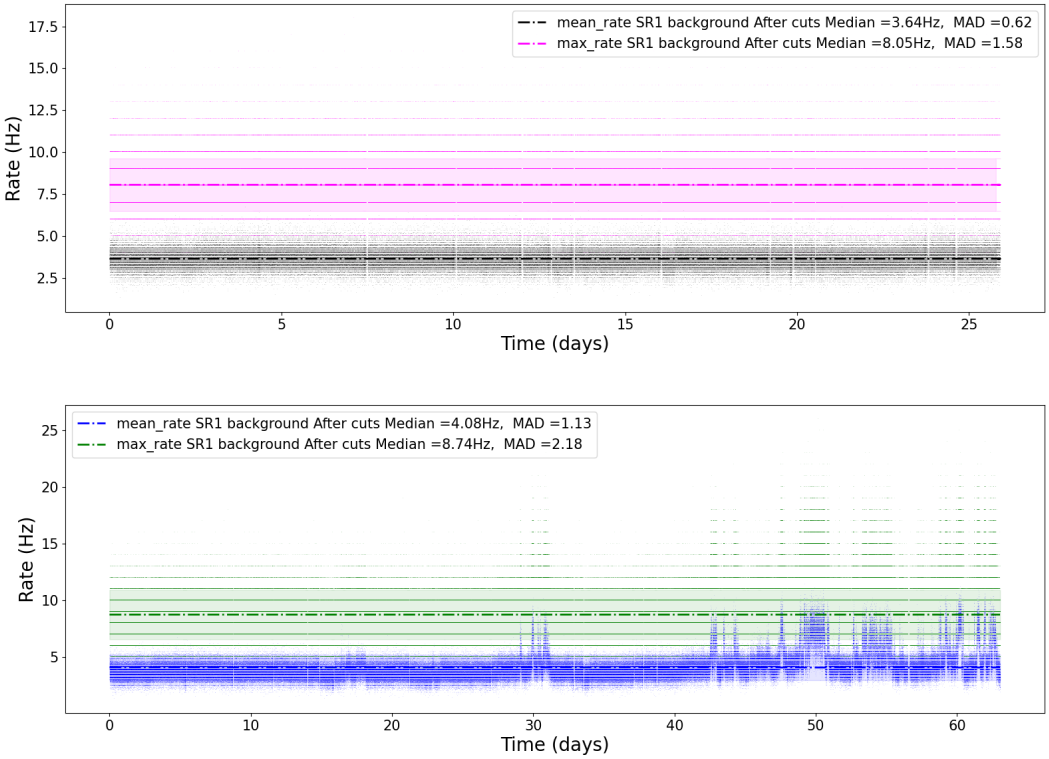

Figure E.12: First and second upper plots present the evolution in time of the mean and maximum rates of SR2 in the ROI in the muon veto for the selected (black and magenta) and non-selected (blue and green). Their respective distributions represented in the two other bottom plots can be approximated by analytical functions skewed and, in which fit parameters appears in the legend.

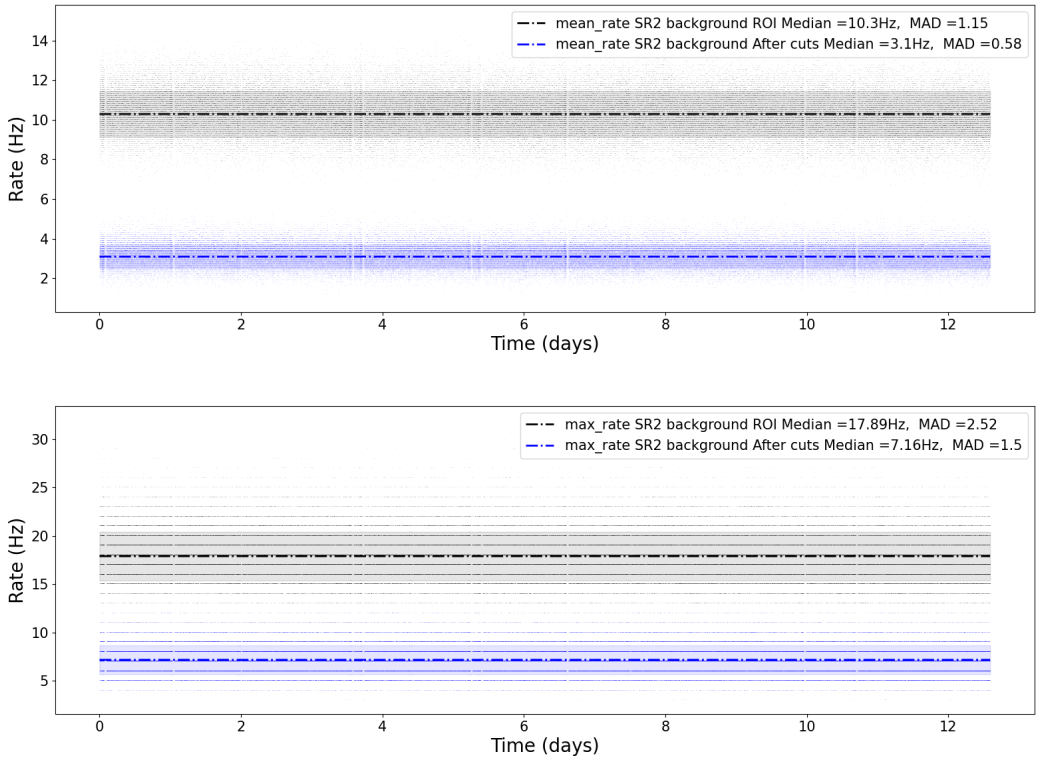

Figure E.13: First and second upper plots present the evolution in time of the mean and maximum rates of SR2 in the ROI in the muon veto for the selected (black and magenta) and non-selected (blue and green). Their respective distributions represented in the two other bottom plots can be approximated by analytical functions skewed and, in which fit parameters appears in the legend.

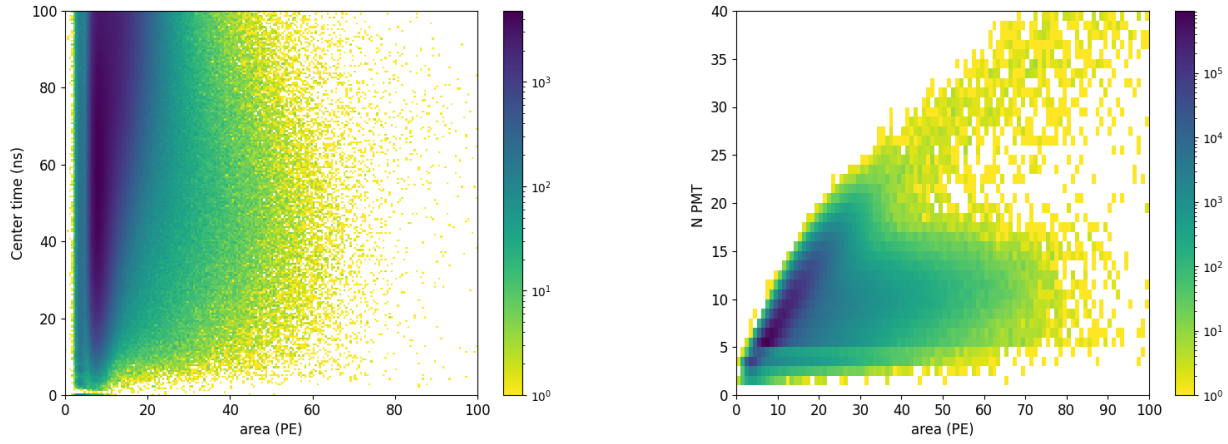

Figure E.14: **Left**. Center time vs area distribution for the background data of SR2 in muon veto. **Right**. Number of pmt contributing vs area distribution for the same SR2 period.

E.4.1.1 Muon veto background model

Parameters from ES contribution.

For a given parameter $\theta_{i,j}$ following the notation for SR1 (NO) + ES background model of equation

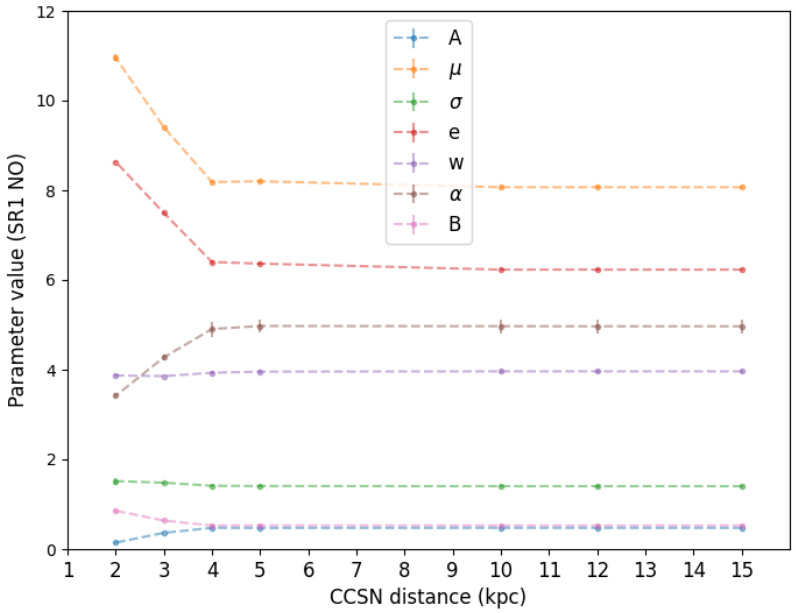

Figure E.15: Evolution as a function of the CCSN of the fit parameters corresponding to the background model of the SR1 non-selected runs including ES contribution from expression (5.12), obtained from the approximation of the ES signal simulation + background maximum rolling window distributions depicted in **figure 5.25**. The errors correspond to the standard deviation extracted from the covariance values extracted from the fit as equation (E.10)
.

(5.12) the standard deviation from the covariance matrix can be obtained as:

$$\sigma_{\theta_{i,j}} = \sqrt{diag[CoV_{\theta_{i,j}}]} \tag{E.10}$$

The covariance matrix $CoV_{\theta_{i,j}}$ from the fit parameter correlation is obtained from the equations (2.1) and (2.2) described in the following work [473].

For the SR1 and the SR2 background models the inclusion of the ES signal has been performed in the same way than for the non selected SR1 runs. The approximation of the PDFs for several distances is less challenging, as muon veto background in this two periods is approximated via a skewed gaussian, which parameters are impacted via the inclusion of the ES signal, and as a consequence varying with the distance, as **figure E.17** shows. The PDFs for several distances corresponding to the SR1 and SR2 background model are illustrated in **figure E.16**.

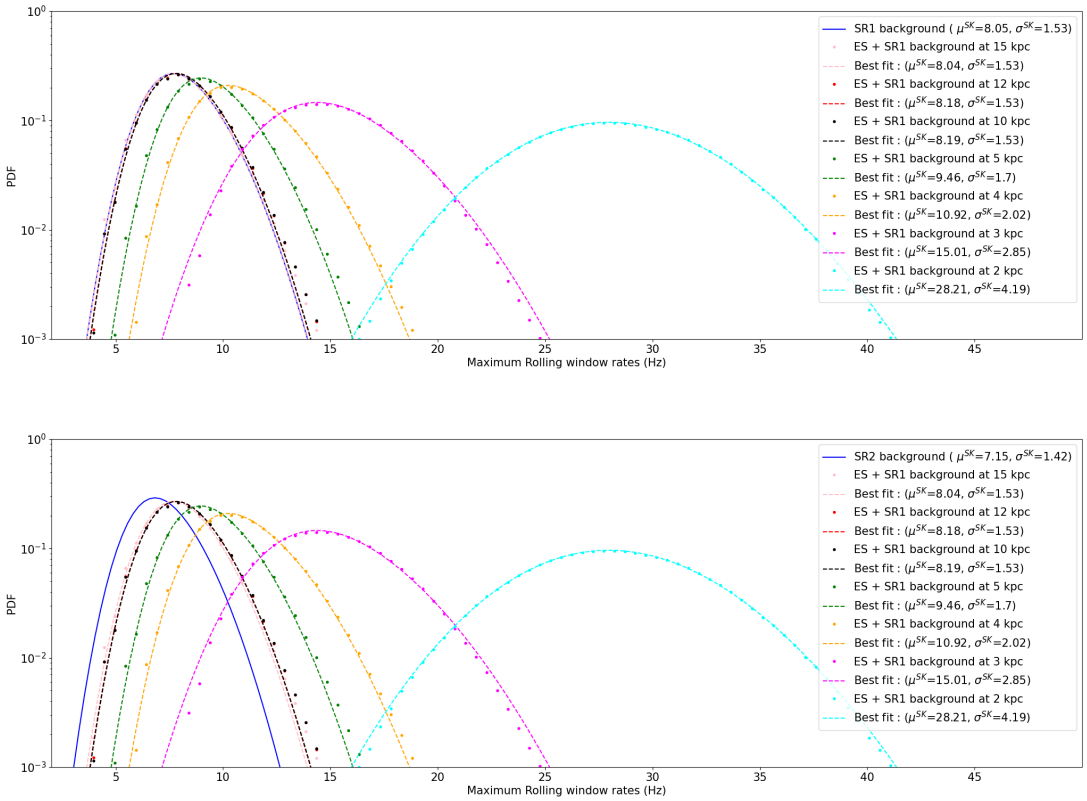

Figure E.16: Maximum rates distribution for SR1 selected runs (top) and the SR2 (bottom) background model including the ES contribution, for several a CCSN distances: 2 kpc (cyan), 3kpc (magenta), 4 kpc (orange), 5 kpc (green) 10 kpc (black), 12 kpc (red) and 15 kpc (pink). The background PDF is composed by gaussian and a skewed gaussian (see 5.12) which contributions are represented by the semi-transparent dotted lines. The SR1 background only contribution is represented by the blue solid line.

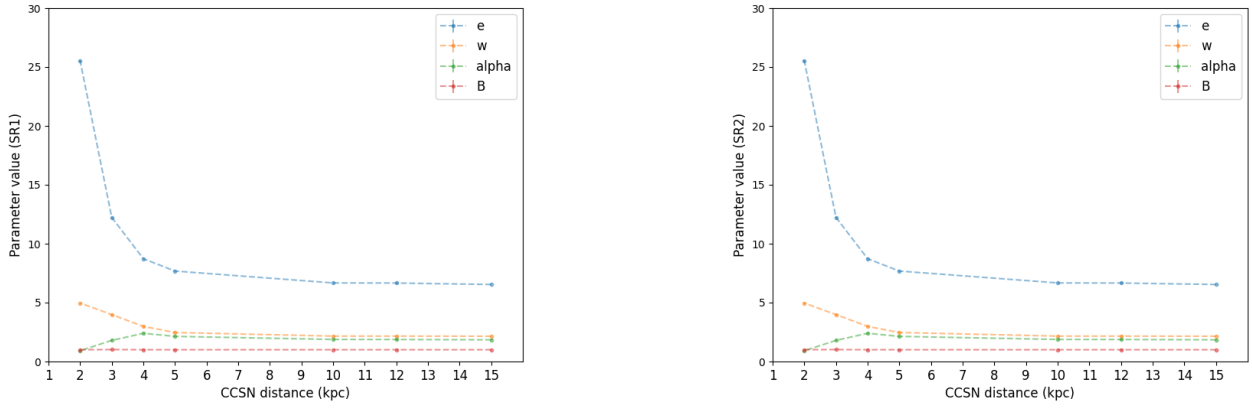

Figure E.17: Evolution as a function of the CCSN of the fit parameters corresponding to the background model of the SR1 (selected) and SR2 periods including ES contribution from expression (5.12), obtained from the approximation of the ES signal simulation + background maximum rolling window distributions depicted in **figure E.16**. The errors correspond to the standard deviation extracted from the covariance values extracted from the fit as equation (E.10)

E.4.1.2 CCSN IBD simulation rate distributions

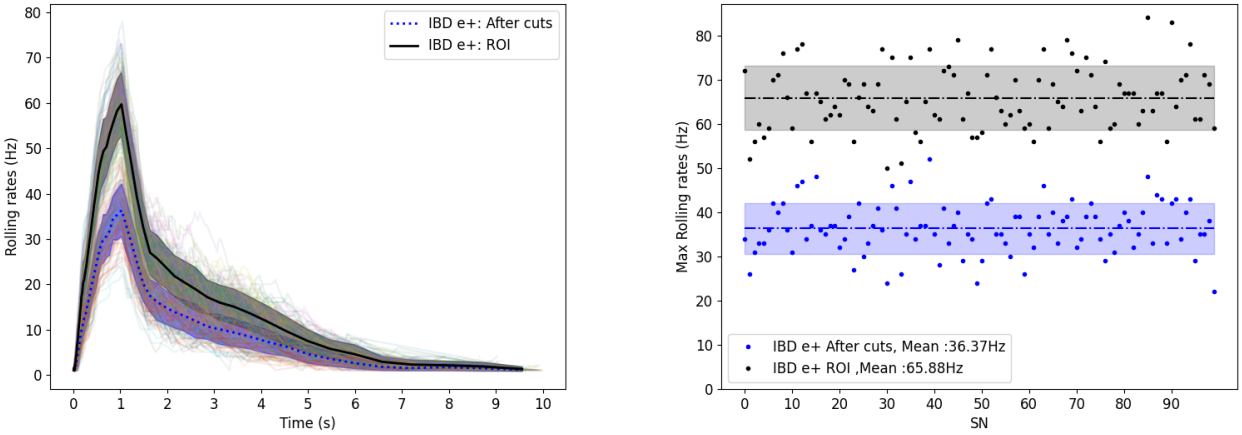

Figure E.18: **Left**. Rolling window rates time evolution for the CCSN IBD positron from the simulation of 100 CCSN of the $27M_{\odot}$ in the NMO, before (black) and after (blue) the applying the cuts. The thick line black line and the thick blue dotted line corresponds to the median and the bands to the standard deviation. **Right**. Maximum rates for the corresponding rolling windows represented in the left panel for each CCSN . The median of this maximum and the MAD bands are also represented.

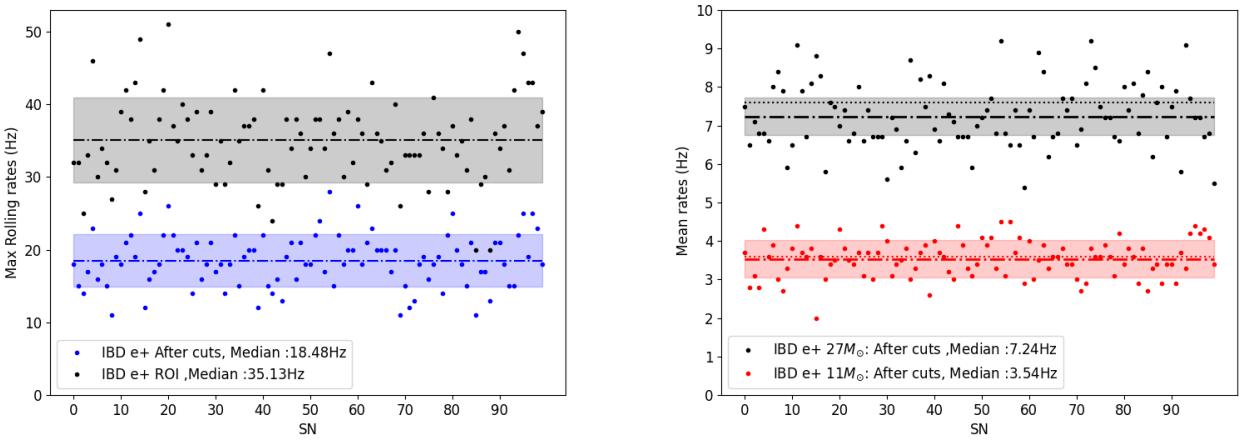

Figure E.19: **Left**. Center time vs area distribution for the background data of SR2 in muon veto. **Right**. Number of pmt contributing vs area distribution for the same SR2 period.

E.4.1.3 Sensitivity from CCSN max rates distributions IMO

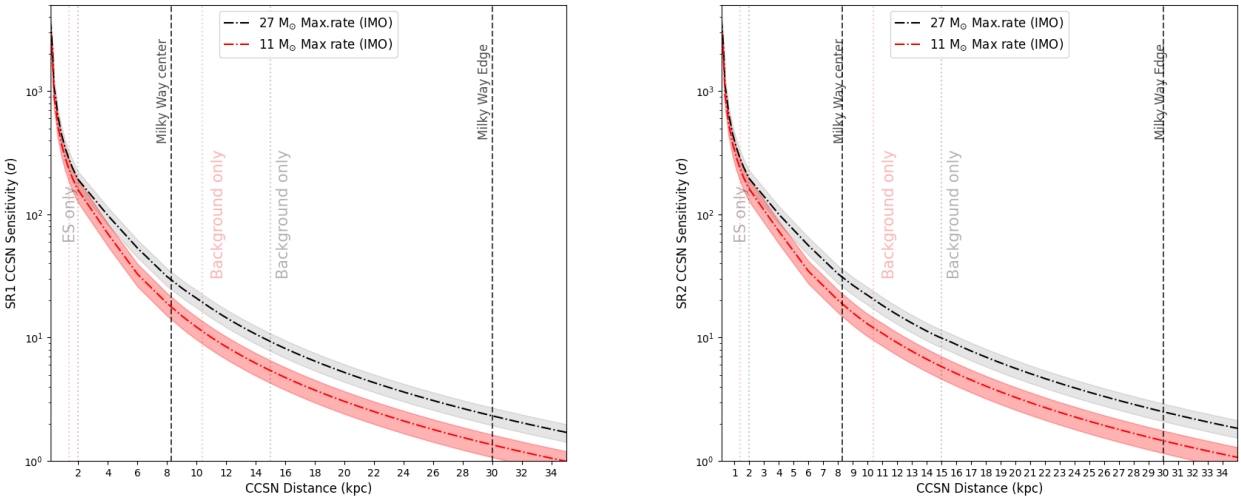

Figure E.20: Sensitivity curves as a function of the CCSN progenitor distance in muon veto for the background model including the SR1 selected runs (left), and the SR2 (right), and the ES contribution. The significance is obtained from the maximun rates of the 27 $M_\odot$ (black) and the 11$M_\odot$ (red) progenitor for IMO. The dotted-dashed lines shows the significance mean and the bands the standard deviation. Regions dominated by ES and muon veto background are limited by the doted transparent lines.

E.4.1.4 Mean and rolling window maximum rates for ES

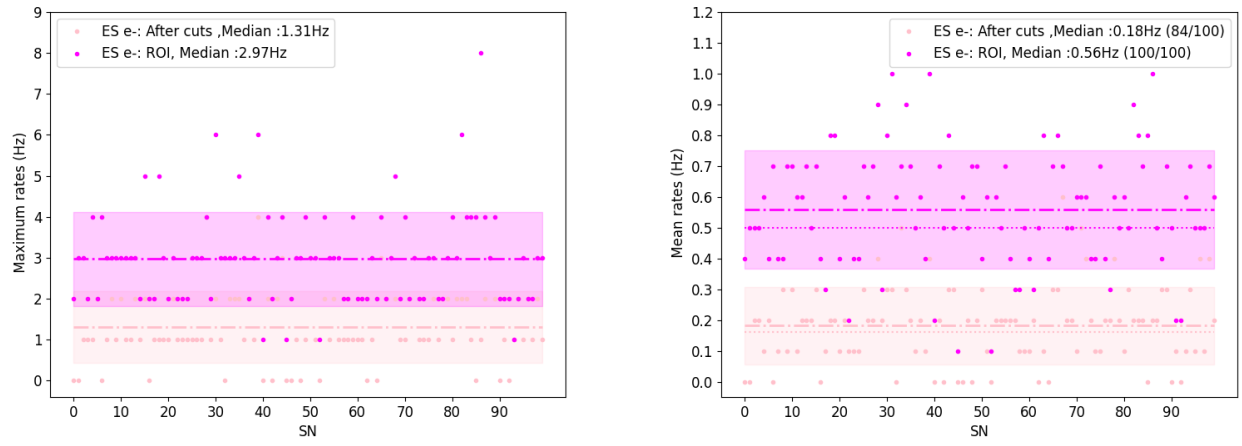

Figure E.21: **Left**. Center time vs area distribution for the background data of SR2 in neutron veto. **Right**. Number of pmt contributing vs area distribution for the same SR2 period.

E.4.1.5 Sensitivity from CCSN mean rates distributions

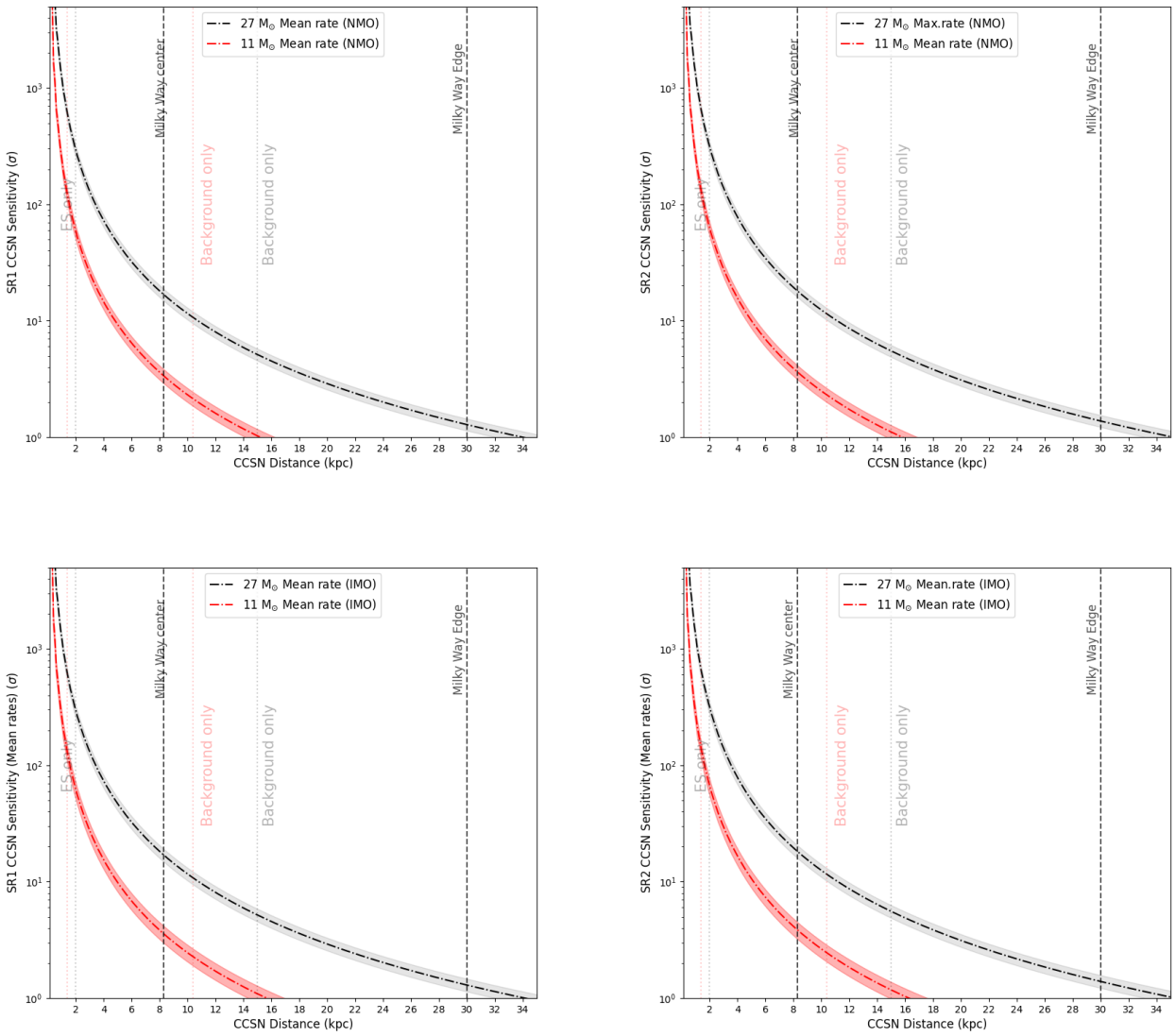

Figure E.22: Sensitivity curves as a function of the CCSN progenitor distance in muon veto for the background model including the SR1 selected runs (left), and the SR2 (right), and the ES contribution. The significance is obtained from the maximun (top panels) and mean (bottom panels) rates of the 27 $M_\odot$ (black) and the 11$M_\odot$ (red) progenitor for IMO. The dotted-dashed lines shows the significance mean and the bands the standard deviation. Regions dominated by ES and muon veto background are limited by the doted transparent lines.

E.4.2 Neutron veto background

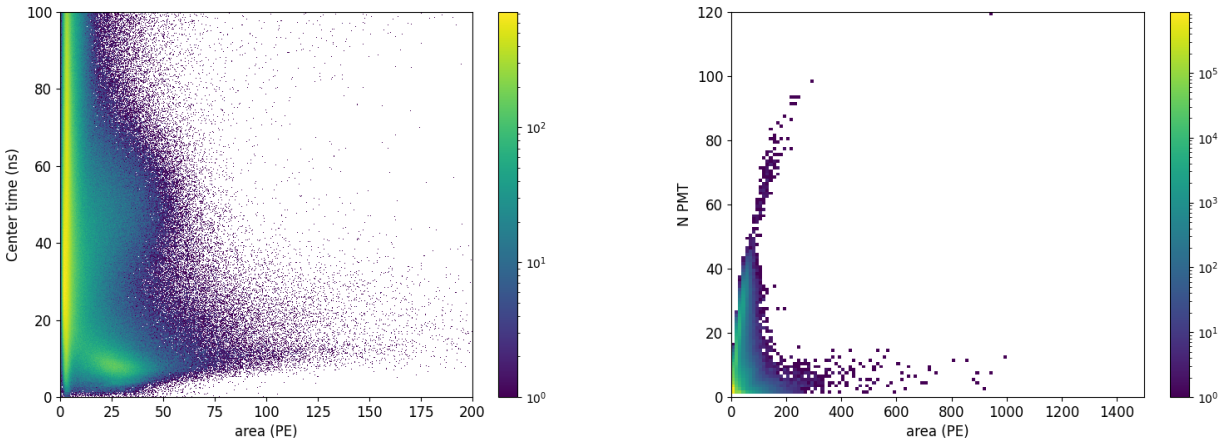

Figure E.23: **Left**. Center time vs area distribution for the background data of SR2 in neutron veto. **Right**. Number of pmt contributing vs area distribution for the same SR2 period.

SR0 background ROI event parameters distributions in the neutron veto. The **figure** depicts the same 2D distributions than **figure 5.29**. As well, the corresponding event parameters distributions for SR2 period are depicted in **figure E.23**.

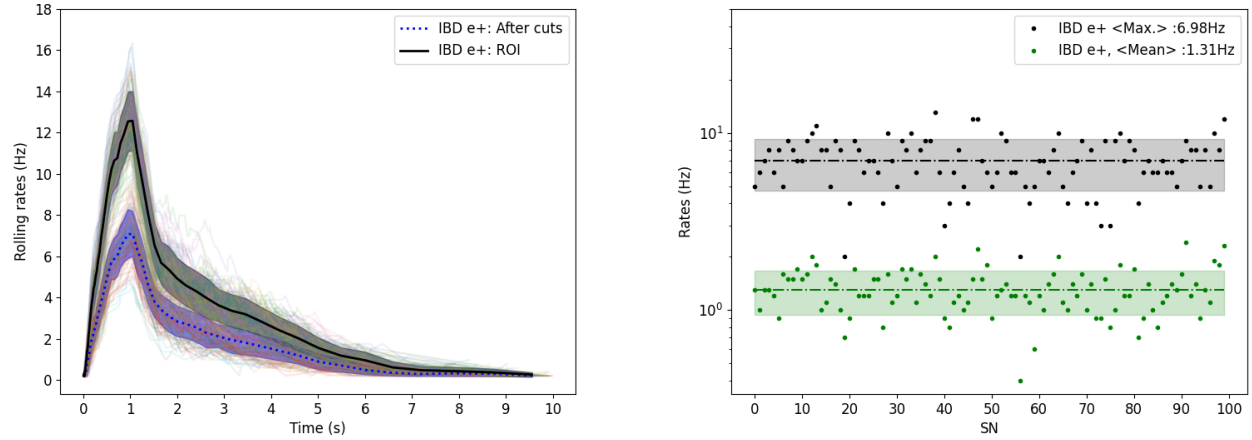

Figure E.24: **Left**. Rolling window rates time evolution for the CCSN IBD positron in the neutron veto obtained from the simulation of 100 CCSN of the $27M_{\odot}$ in the NMO, before (black) and after (blue) the applying the cuts. The thick line black line and the thick blue dotted line corresponds to the median and the bands to the standard deviation. **Right**. Maximum rates for the corresponding rolling windows after cuts represented in the left panel for each CCSN. The median of this maximum and the MAD bands are also represented. In green the mean rates for each CCSN burst similated after the cuts. As well, the median and the MAD bands are represented.

E.4.2.1 Sensitivity from CCSN rates distributions IMO

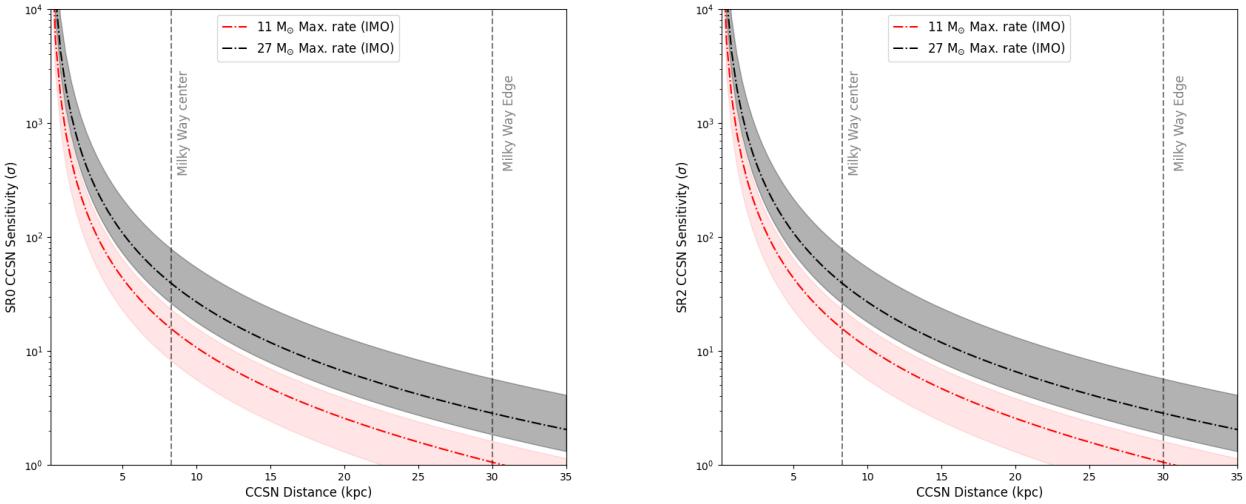

Figure E.25: Sensitivity curves as a function of the CCSN progenitor distance in neutron veto for the background model for the SR0 (left), and the SR2 (right). The significance is obtained from the maximum rates of the 27 $M_\odot$ (black) and the 11$M_\odot$ (red) progenitor for IMO. The dotted-dashed lines shows the significance mean and the bands the standard deviation.

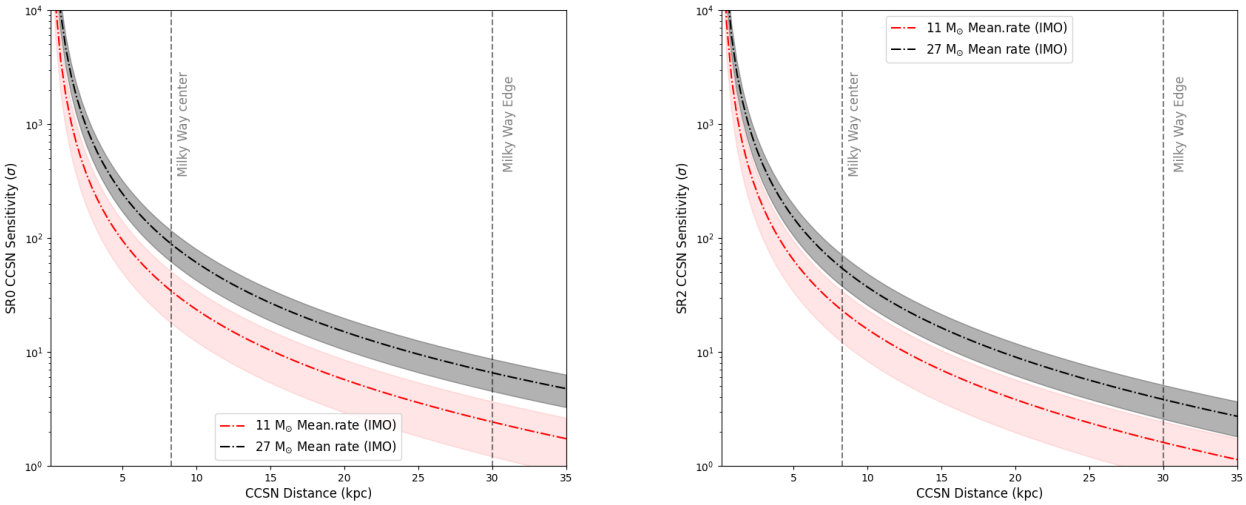

Figure E.26: Sensitivity curves as a function of the CCSN progenitor distance in neutron veto for the background model for the SRO (left), and the SR2 (right), and the ES contribution. The significance is obtained from the mean rates of the 27 $M_\odot$ (black) and the 11$M_\odot$ (red) progenitor for IMO. The dotted-dashed lines shows the significance mean and the bands the standard deviation.

E.4.3 Neutron and muon veto combined sensitivities

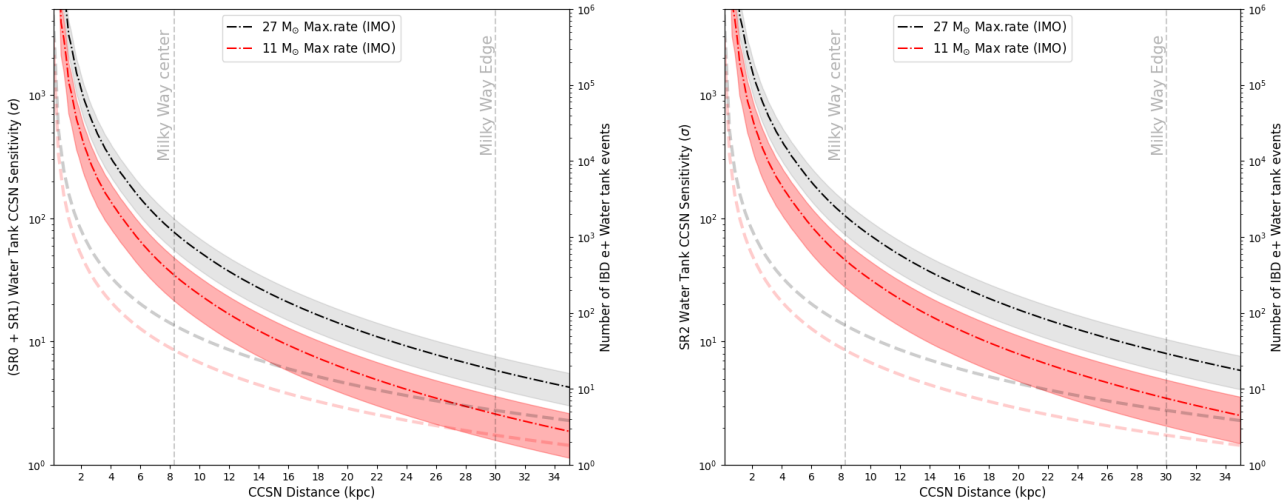

Figure E.27: Sensitivity curves as a function of the CCSN progenitor distance in the water tank, from the combination of muon and neutron veto for the maximum rates, from the relation of equation 5.17. The significance is obtained from the maximum rates of the 27 $M_\odot$ (black) and the 11$M_\odot$ (red) progenitor for IMO. The dotted-dashed lines shows the significance mean and the bands the standard deviation. As well the number of events, represented in the right axis, for each progenitor is drawn by the semi-transparent dashed thick lines.

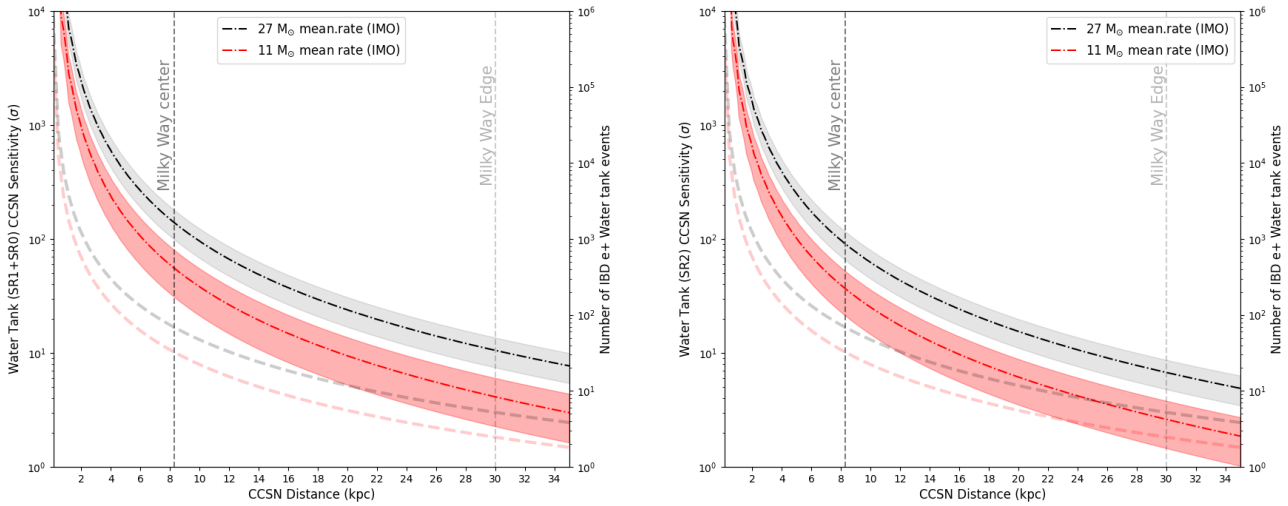

Figure E.28: Sensitivity curves as a function of the CCSN progenitor distance in the water tank, from the combination of muon and neutron veto for the mean rates, from the relation of equation 5.17. The significance is obtained from the mean rates of the 27 $M_\odot$ (black) and the 11$M_\odot$ (red) progenitor for IMO. The dotted-dashed lines shows the significance mean and the bands the standard deviation. As well the number of events, represented in the right axis, for each progenitor is drawn by the semi-transparent dashed thick lines.

Bibliography

[1] K. et al. Hirata. Observation of a neutrino burst from the supernova sn1987a. *Phys. Rev. Lett.*, 58:1490–1493, Apr 1987.

[2] R. M. et al. Bionta. Observation of a neutrino burst in coincidence with supernova 1987a in the large magellanic cloud. *Phys. Rev. Lett.*, 58:1494–1496, Apr 1987.

[3] E. N. et al. Alekseev. Possible Detection of a Neutrino Signal on 23 February 1987 at the Baksan Underground Scintillation Telescope of the Institute of Nuclear Research. *JETP Lett.*, 45:589–592, 1987.

[4] Alexei V. Filippenko. Supernovae and their massive star progenitors, 2004.

[5] Kool et al. Sn 2020bqj: A type ibn supernova with a long-lasting peak plateau. *Astronomy amp; Astrophysics*, 652:A136, August 2021.

[6] Kuncarayakti et al. The broad-lined type-ic supernova sn 2022xxf and its extraordinary two-humped light curves: I. signatures of h/he-free interaction in the first four months. *Astronomy amp; Astrophysics*, 678:A209, October 2023.

[7] Alexei V. Filippenko, Thomas Matheson, and Luis C. Ho. The "Type IIb" Supernova 1993J in M81: A Close Relative of Type Ib Supernovae. , 415:L103, October 1993.

[8] Alexei V. Filippenko. Supernova 1987K: Type II in Youth, Type Ib in Old Age. *Astr. Journ.*, 96:1941, December 1988.

[9] Tanja Nymark. X-ray emission from supernova shock waves. 01 2007.

[10] F. K. Röpke and W. Hillebrandt. The case against the progenitor's carbon-to-oxygen ratio as a source of peak luminosity variations in type ia supernovae. *Astronomy amp; Astrophysics*, 420(1):L1–L4, May 2004.

[11] Paolo A. Mazzali, Friedrich K. Ropke, Stefano Benetti, and Wolfgang Hillebrandt. A common explosion mechanism for type ia supernovae. *Science*, 315(5813):825–828, feb 2007.

[12] Satoru Katsuda, Tomoya Takiwaki, Nozomu Tominaga, Takashi J. Moriya, and Ko Nakamura. Progenitor mass distribution of core-collapse supernova remnants in our galaxy and magellanic clouds based on elemental abundances. *The Astrophysical Journal*, 863(2):127, aug 2018.

[13] UK K Zuber Denys Wilkinson Laboratory, University of Oxford. Neutrino physics. *Series in High Energy Physics, Cosmology and Gravitation*, 2004.

[14] Warren P. et al. Wright. Neutrinos from type ia supernovae: The gravitationally confined detonation scenario. *Physical Review D*, 95(4), February 2017.

[15] Takashi Kunugise and Koichi Iwamoto. Neutrino Emission from Type Ia Supernovae. *Publications of the Astronomical Society of Japan*, 59(6):L57–L61, 12 2007.

[16] Shigenori Maruyama, Toshiaki Ebisuzaki, and Ken Kurokawa. Origin and Evolution of Earth and Life: Towards the Establishment of Astrobiology from Universe to Genome. *PoS*, FRAPWS2018:071, 2019.

[17] Gerald North, F. Zhang, and J. Pyle. *Encyclopedia of Atmospheric Sciences: Second Edition.* 01 2014.

[18] Q. He, Z. Fang, O. Shoshanim, S. S. Brown, and Y. Rudich. Scattering and absorption cross sections of atmospheric gases in the ultraviolet–visible wavelength range (307–725 nm). *Atmospheric Chemistry and Physics*, 21(19):14927–14940, 2021.

[19] Christopher M Sorensen. Rayleigh scattering. In *Light Scattering and Absorption by Particles*, 2053-2563, pages 6–1 to 6–17. IOP Publishing, 2022.

[20] Garry McCracken and Peter Stott. Chapter 3 - fusion in the sun and stars. In Garry McCracken and Peter Stott, editors, *Fusion (Second Edition)*, pages 15–29. Academic Press, Boston, second edition edition, 2013.

[21] K. Grotz and H.V. Klapdor. The weak interaction in nuclear, particle and astrophysics. *S.S. Wilson, Trans.; 1st ed.*, 07 1990.

[22] Axel V. Nielsen. Contributions to the history of the hertzsprung-russell diagram. *Centaurus*, 9(4):219–253, 1964.

[23] Arkaprabha Sarangi, Mikako Matsuura, and Elisabetta Micelotta. Dust in supernovae and supernova remnants i: Formation scenarios. *Space Science Reviews*, 214, 03 2018.

[24] Adelberger et al. Solar fusion cross sections. ii. the pp chain and cno cycles. *Reviews of Modern Physics*, 83(1):195–245, April 2011.

[25] Hao Wang, Chunhua Zhu, Helei Liu, Sufen Guo, and Guoliang Lü. Evolutionary tracks of massive stars with different rotation and metallicity in neutrino h-r diagram, 2023.

[26] Ebraheem Farag, F. X. Timmes, Morgan Taylor, Kelly M. Patton, and R. Farmer. On Stellar Evolution in a Neutrino Hertzsprung-Russell Diagram. , 893(2):133, April 2020.

[27] J.N. Bahcall. *Neutrino Astrophysics*. Cambridge University Press, 1989.

[28] M. W. GuidryA. Pp and cno-cycle nucleosynthesis: Kinetics and numerical modeling of competitive fusion processes. 2018.

[29] A. Heger, C. L. Fryer, S. E. Woosley, N. Langer, and D. H. Hartmann. How massive single stars end their life. *The Astrophysical Journal*, 591(1):288–300, July 2003.

[30] Grotz K. and Klapdor H.V. The weak interaction in nuclear, particle and astrophysics. *United Kingdom: Adam Hilger*, 1990.

[31] Yang Shi et al. Neutrino luminosity of stars with different masses. *Research in Astronomy and Astrophysics*, 20(1):005, jan 2020.

[32] H JANKA, K LANGANKE, A MAREK, G MARTINEZPINEDO, and B MULLER. Theory of core-collapse supernovae. *Physics Reports*, 442(1-6):38–74, apr 2007.

[33] S. Chandrasekhar. *An Introduction to the Study of Stellar Structure*. Astrophysical monographs. University of Chicago Press, 1939.

[34] S. Chandrasekhar. The Highly Collapsed Configurations of a Stellar Mass. (Second Paper.). *Monthly Notices of the Royal Astronomical Society*, 95(3):207–225, 01 1935.

[35] E. Baron, J. Cooperstein, and S. Kahana. Type ii supernovae in $12m_{cirdot}$ and $15m_{cirdot}$ stars: The equation of state and general relativity. *Phys. Rev. Lett.*, 55:126–129, Jul 1985.

[36] Kei Kotake, Katsuhiko Sato, and Keitaro Takahashi. Explosion mechanism, neutrino burst and gravitational wave in core-collapse supernovae. *Reports on Progress in Physics*, 69(4):971–1143, mar 2006.

[37] Michael A. Sandoval et al. Three-dimensional core-collapse supernova simulations with 160 isotopic species evolved to shock breakout. *The Astrophysical Journal*, 921(2):113, nov 2021.

[38] Hiroki Nagakura, Adam Burrows, David Radice, and David Vartanyan. Towards an understanding of the resolution dependence of Core-Collapse Supernova simulations. *Monthly Notices of the Royal Astronomical Society*, 490(4):4622–4637, 10 2019.

[39] Schulz, C., Pflamm-Altenburg, J., and Kroupa, P. Mass distributions of star clusters for different star formation histories in a galaxy cluster environment. *A and A*, 582:A93, 2015.

[40] C. Schulz, J. Pflamm-Altenburg, and P. Kroupa. Mass distributions of star clusters for different star formation histories in a galaxy cluster environment. *Astronomy and Astrophysics*, 582:A93, October 2015.

[41] David Radice, Adam Burrows, David Vartanyan, M. Aaron Skinner, and Joshua C. Dolence. Electron-capture and low-mass iron-core-collapse supernovae: New neutrino-radiation-hydrodynamics simulations. *The Astrophysical Journal*, 850(1):43, nov 2017.

[42] Jones, S., Röpke, F. K., Pakmor, R., Seitenzahl, I. R., Ohlmann, S. T., and Edelmann, P. V. F. Do electron-capture supernovae make neutron stars? - first multidimensional hydrodynamic simulations of the oxygen deflagration. *A&A*, 593:A72, 2016.

[43] Shuai Zha, Shing-Chi Leung, Toshio Suzuki, and Ken'ichi Nomoto. Evolution of ONeMg core in super-AGB stars toward electron-capture supernovae: Effects of updated electron-capture rate. *The Astrophysical Journal*, 886(1):22, nov 2019.

[44] S. Wanajo, K. Nomoto, H. T. Janka, F. S. Kitaura, and B. Müller. Nucleosynthesis in Electron Capture Supernovae of Asymptotic Giant Branch Stars. , 695(1):208–220, April 2009.

[45] A. J. T. Poelarends, F. Herwig, N. Langer, and A. Heger. The supernova channel of super-agb stars. *The Astrophysical Journal*, 675(1):614, mar 2008.

[46] David Radice, Adam Burrows, David Vartanyan, M. Aaron Skinner, and Joshua C. Dolence. Electron-capture and low-mass iron-core-collapse supernovae: New neutrino-radiation-hydrodynamics simulations. *The Astrophysical Journal*, 850(1):43, nov 2017.

[47] C. Kato, K. Ishidoshiro, and T. Yoshida. Theoretical prediction of presupernova neutrinos and their detection. *Annual Review of Nuclear and Particle Science*, 70(1):121–145, October 2020.

[48] Masaaki et al. Hashimoto. Type II Supernovae from 8–10 M_{sun} Asymptotic Giant Branch Stars. , 414:L105, September 1993.

[49] Wanajo et al. Nucleosynthesis in the innermost ejecta of neutrino-driven supernova explosions in two dimensions. *The Astrophysical Journal*, 852(1):40, January 2018.

[50] Sukhbold Tuguldur et al. Core-collapse Supernovae from 9 to 120 Solar Masses Based on Neutrino-powered Explosions. , 821(1):38, April 2016.

[51] Zidu Lin and C. J. Horowitz. Neutrino scattering in supernovae and the universal spin correlations of a unitary gas. *Phys. Rev. C*, 96:055804, Nov 2017.

[52] Drozda, P., Belczynski, K., O'Shaughnessy, R., Bulik, T., and Fryer, C. L. Black hole–neutron star mergers: The first mass gap and kilonovae. *A and A*, 667:A126, 2022.

[53] Strobel, K. and Weigel, M. K. On the minimum and maximum mass of neutron stars and the delayed collapse. *A and A*, 367(2):582–587, 2001.

[54] Weiqun Zhang, S. E. Woosley, and A. Heger. Fallback and black hole production in massive stars. *The Astrophysical Journal*, 679(1):639–654, May 2008.

[55] Evan O'Connor and Christian D. Ott. Black hole formation in failing core-collapse supernovae. *The Astrophysical Journal*, 730(2):70, mar 2011.

[56] Conrad Chan, Bernhard Müller, Alexander Heger, Rüdiger Pakmor, and Volker Springel. Black Hole Formation and Fallback during the Supernova Explosion of a 40 M $_\odot$ Star. , 852(1):L19, January 2018.

[57] Kei Kotake, Katsuhiko Sato, and Keitaro Takahashi. Explosion mechanism, neutrino burst and gravitational wave in core-collapse supernovae. *Reports on Progress in Physics*, 69(4):971–1143, March 2006.

[58] Daniel Kresse, Thomas Ertl, and Hans-Thomas Janka. Stellar collapse diversity and the diffuse supernova neutrino background. *The Astrophysical Journal*, 909(2):169, mar 2021.

[59] Evan O'Connor. An open-source neutrino radiation hydrodynamics code for core-collapse supernovae. *The Astrophysical Journal Supplement Series*, 219(2):24, aug 2015.

[60] Samuel Gullin, Evan P. O'Connor, Jia-Shian Wang, and Jeff Tseng. Neutrino echos following black hole formation in core-collapse supernovae. *The Astrophysical Journal*, 926(2):212, feb 2022.

[61] Evan O'Connor. An open-source neutrino radiation hydrodynamics code for core-collapse supernovae. *The Astrophysical Journal Supplement Series*, 219(2):24, August 2015.

[62] S.E. Woosley and J.S. Bloom. The supernova–gamma-ray burst connection. *Annual Review of Astronomy and Astrophysics*, 44(1):507–556, September 2006.

[63] S. E. Woosley, A. Heger, and T. A. Weaver. The evolution and explosion of massive stars. *Rev. Mod. Phys.*, 74:1015–1071, Nov 2002.

[64] Diaz-Rodriguez et al. Progenitor mass distribution for 22 historic core-collapse supernovae. *Monthly Notices of the Royal Astronomical Society*, 506(1):781–790, 06 2021.

[65] Giulio Magli and Juan Antonio Belmonte. Archaeoastronomy and the alleged «stonehenge calendar», 2022.

[66] K. et al. Rozwadowska. On the rate of core collapse supernovae in the milky way. *New Astronomy*, 83:101498, February 2021.

[67] S. Al Dallal and W.J Azzam. A brief review of his- torical supernovae. *International Journal of Astronomy and Astrophysics*, 11:73–86, November 2021.

[68] Robert A. et al. Fesen. The expansion asymmetry and age of the cassiopeia a supernova remnant. *The Astrophysical Journal*, 645(1):283–292, July 2006.

[69] Ravi Gupta. The evolution of sn-observations 1885-2019. 2019.

[70] Kwang-Chang Lai, C. S. Jason Leung, and Guey-Lin Lin. Testing msw effect in supernova explosion with neutrino event rates, 2020.

[71] Kwang-Chang Lai, Fei-Fan Lee, Feng-Shiuh Lee, Guey-Lin Lin, Tsung-Che Liu, and Yi Yang. Probing neutrino mass hierarchy by comparing the charged-current and neutral-current interaction rates of supernova neutrinos. *Journal of Cosmology and Astroparticle Physics*, 2016(07):039–039, July 2016.

[72] Sudip Jana, Yago Porto-Silva, and Manibrata Sen. Exploiting a future galactic supernova to probe neutrino magnetic moments. *Journal of Cosmology and Astroparticle Physics*, 2022:079, 09 2022.

[73] Scott M. et al. Adams. Observing the next galactic supernova. *The Astrophysical Journal*, 778(2):164, November 2013.

[74] A. T. et al. Gallego-Calvente. Radio observations of massive stars in the galactic centre: The arches cluster. *A and A*, 647:A110, 2021.

[75] *La Rivista del Nuovo Cimento*, 39(102):1–112, Feb 2016.

[76] S. Karushi et al. Snews 2.0: A next-generation supernova early warning system for multi-messenger astronomy. *New Journal of Physics*, 23, 03 2021.

[77] Brendan Reed and C. J. Horowitz. Total energy in supernova neutrinos and the tidal deformability and binding energy of neutron stars. *Phys. Rev. D*, 102:103011, Nov 2020.

[78] Particle Data Group. Review of Particle Physics. *Progress of Theoretical and Experimental Physics*, 2020(8):083C01, 08 2020.

[79] Hideyuki Suzuki. Neutrinos from Core-Collapse Supernova Explosions. *Progress of Theoretical and Experimental Physics*, 2024(5):05B101, 04 2024.

[80] Hans-Thomas Janka. Explosion mechanisms of core-collapse supernovae. *Annual Review of Nuclear and Particle Science*, 62(1):407–451, November 2012.

[81] Chinami Kato et al. Pre-supernova neutrino emission from massive stars and their detection. *Journal of Physics: Conference Series*, 1468(1):012173, feb 2020.

[82] Couch SM. The mechanism(s) of core-collapse supernovae. *Annual Review of Nuclear and Particle Science*, 2017.

[83] Sebastian Baum, Francesco Capozzi, and Shunsaku Horiuchi. Rocks, water, and noble liquids: Unfolding the flavor contents of supernova neutrinos. *Phys. Rev. D*, 106(12):123008, 2022.

[84] Zahra Tabrizi and Shunsaku Horiuchi. Flavor triangle of the diffuse supernova neutrino background. , 2021(5):011, May 2021.

[85] Hiroki Nagakura. Roles of fast neutrino-flavor conversion on the neutrino-heating mechanism of core-collapse supernova. *Physical Review Letters*, 130(21), May 2023.

[86] Rafael F. Lang, Christopher McCabe, Shayne Reichard, Marco Selvi, and Irene Tamborra. Supernova neutrino physics with xenon dark matter detectors: A timely perspective. *Physical Review D*, 94(10), nov 2016.

[87] B. Müller. Neutrino emission as diagnostics of core-collapse supernovae. *Annual Review of Nuclear and Particle Science*, 69(1):253–278, Oct 2019.

[88] H. T. Janka and E. Mueller. Neutrino heating, convection, and the mechanism of Type-II supernova explosions. , 306:167, February 1996.

[89] T. Foglizzo, P. Galletti, L. Scheck, and H. Th. Janka. Instability of a Stalled Accretion Shock: Evidence for the Advective-Acoustic Cycle. , 654(2):1006–1021, January 2007.

[90] John M. Blondin, Anthony Mezzacappa, and Christine DeMarino. Stability of Standing Accretion Shocks, with an Eye toward Core-Collapse Supernovae. , 584(2):971–980, February 2003.

[91] Rodrigo Fernández and Christopher Thompson. Stability of a spherical accretion shock with nuclear dissociation. *The Astrophysical Journal*, 697(2):1827, may 2009.

[92] Hans-Thomas Janka. *Neutrino Emission from Supernovae*, page 1575–1604. Springer International Publishing, 2017.

[93] Irene Tamborra, Bernhard Müller, Lorenz Hüdepohl, Hans-Thomas Janka, and Georg Raffelt. High-resolution supernova neutrino spectra represented by a simple fit. *Physical Review D*, 86(12), December 2012.

[94] Ken'ichiro Nakazato, Kohsuke Sumiyoshi, and Hajime Togashi. Numerical study of stellar core collapse and neutrino emission using the nuclear equation of state obtained by the variational method. *Publications of the Astronomical Society of Japan*, 73(3):639–651, May 2021.

[95] Mathias Th. Keil, Georg G. Raffelt, and Hans-Thomas Janka. Monte carlo study of supernova neutrino spectra formation. *The Astrophysical Journal*, 590(2):971–991, June 2003.

[96] GEORG G. RAFFELT, MATHIAS TH. KEIL, ROBERT BURAS, HANS-THOMAS JANKA, and MARKUS RAMPP. Supernova neutrinos: Flavor-dependent fluxes and spectra. In *Neutrino Oscillations and Their Origin*. WORLD SCIENTIFIC, May 2004.

[97] Xu-Run Huang, Chuan-Le Sun, Lie-Wen Chen, and Jun Gao. Bayesian inference of supernova neutrino spectra with multiple detectors, 2023.

[98] Hasan Yüksel and John F. Beacom. Neutrino spectrum from sn 1987a and from cosmic supernovae. *Physical Review D*, 76(8), oct 2007.

[99] Takashi Yoshida, Toshitaka Kajino, and Dieter H. Hartmann. Constraining the spectrum of supernova neutrinos from ν-process induced light element synthesis. *Physical Review Letters*, 94(23), June 2005.

[100] Hui-Ling Li, Xin Huang, Yu-Feng Li, Liang-Jian Wen, and Shun Zhou. Model-independent approach to the reconstruction of multiflavor supernova neutrino energy spectra. *Phys. Rev. D*, 99:123009, Jun 2019.

[101] Masamitsu et al. Mori. Developing an end-to-end simulation framework of supernova neutrino detection. *Progress of Theoretical and Experimental Physics*, 2021(2), December 2020.

[102] Takami Kuroda. Impact of a magnetic field on neutrino–matter interactions in core-collapse supernovae. *The Astrophysical Journal*, 906(2):128, jan 2021.

[103] Shuai Zha, Evan P. O'Connor, and André da Silva Schneider. Progenitor dependence of hadron-quark phase transition in failing core-collapse supernovae. *The Astrophysical Journal*, 911(2):74, apr 2021.

[104] Laurie Walk, Irene Tamborra, Hans-Thomas Janka, Alexander Summa, and Daniel Kresse. Neutrino emission characteristics of black hole formation in three-dimensional simulations of stellar collapse. *Phys. Rev. D*, 101:123013, Jun 2020.

[105] James M. Lattimer and Douglas F. Swesty. A generalized equation of state for hot, dense matter. , 535(2):331–376, December 1991.

[106] David Cerdeño, Marina Cermeño, and Yasaman Farzan. Constraints from the duration of supernova neutrino burst on on-shell light gauge boson production by neutrinos. *Physical Review D*, 107(12), June 2023.

[107] H. T. Janka and W. Hillebrandt. Neutrino emission from type II supernovae : an analysis of the spectra. , 224:49–56, October 1989.

[108] Hisakazu Minakata, Hiroshi Nunokawa, Ricard Tomas Bayo, and Jose Valle. Parameter degeneracy in flavor-dependent reconstruction of supernova neutrino fluxes. *Journal of Cosmology and Astroparticle Physics*, 2008, 02 2008.

[109] Robert Bollig, Naveen Yadav, Daniel Kresse, Hans-Thomas Janka, Bernhard Müller, and Alexander Heger. Self-consistent 3d supernova models from 7 minutes to +7 s: A 1-bethe explosion of a 19 m progenitor. *The Astrophysical Journal*, 915(1):28, June 2021.

[110] Supernova neutrino database - nakazato 2013. `http://asphwww.ph.noda.tus.ac.jp/snn/`.

[111] Ken'ichiro et al. Nakazato. Supernova neutrino light curves and spectra for various progenitor stars: From core collapse to proto-neutron star cooling. *The Astrophysical Journal Supplement Series*, 205(1):2, February 2013.

[112] K. Sumiyoshi, S. Yamada, H. Suzuki, H. Shen, S. Chiba, and H. Toki. Postbounce Evolution of Core-Collapse Supernovae: Long-Term Effects of the Equation of State. , 629(2):922–932, August 2005.

[113] M. Rampp and H.-T. Janka. Radiation hydrodynamics with neutrinos: Variable eddington factor method for core-collapse supernova simulations. *Astronomy amp; Astrophysics*, 396(1):361–392, November 2002.

[114] L. F. Roberts, G. Shen, V. Cirigliano, J. A. Pons, S. Reddy, and S. E. Woosley. Protoneutron star cooling with convection: The effect of the symmetry energy. *Physical Review Letters*, 108(6), February 2012.

[115] Ken'ichiro Nakazato and Hideyuki Suzuki. Supernova neutrinos in the proto-neutron star cooling phase and nuclear matter. *J. Phys. Conf. Ser.*, 1468(1):012089, 2020.

[116] Garching Group. Max planck university. `https://wwwmpa.mpa-garching.mpg.de/ccsnarchive`.

[117] Amanda L. Baxter et al. Snewpy: A data pipeline from supernova simulations to neutrino signals. `https://github.com/SNEWS2`, 2021.

[118] Hans-Thomas Janka, Florian Hanke, Lorenz Hüdepohl, Andreas Marek, Bernhard Müller, and Martin Obergaulinger. Core-collapse supernovae: Reflections and directions. *Progress of Theoretical and Experimental Physics*, 2012(1):01A309, December 2012.

[119] Bernhard Müller, Hans-Thomas Janka, and Alexander Heger. New Two-dimensional Models of Supernova Explosions by the Neutrino-heating Mechanism: Evidence for Different Instability Regimes in Collapsing Stellar Cores. , 761(1):72, December 2012.

[120] Shinya Wanajo, Hans-Thomas Janka, and Bernhard Müller. Electron-capture Supernovae as Sources of ^{60}Fe. , 774(1):L6, September 2013.

[121] R. D. Hoffman, B. Müller, and H. T. Janka. Nucleosynthesis in O-Ne-Mg Supernovae. , 676(2):L127, April 2008.

[122] David Vartanyan, Adam Burrows, David Radice, M Aaron Skinner, and Joshua Dolence. A successful 3D core-collapse supernova explosion model. *Monthly Notices of the Royal Astronomical Society*, 482(1):351–369, 09 2018.

[123] Tobias Melson, Hans-Thomas Janka, Robert Bollig, Florian Hanke, Andreas Marek, and Bernhard Müller. Neutrino-driven Explosion of a 20 Solar-mass Star in Three Dimensions Enabled by Strange-quark Contributions to Neutrino-Nucleon Scattering. , 808(2):L42, August 2015.

[124] B. Müller. The status of multi-dimensional core-collapse supernova models. *Publications of the Astronomical Society of Australia*, 33, 2016.

[125] M. Aaron Skinner, Joshua C. Dolence, Adam Burrows, David Radice, and David Vartanyan. Fornax: A flexible code for multiphysics astrophysical simulations. *The Astrophysical Journal Supplement Series*, 241(1):7, feb 2019.

[126] Bernhard Müller, Tobias Melson, Alexander Heger, and Hans-Thomas Janka. Supernova simulations from a 3D progenitor model - Impact of perturbations and evolution of explosion properties. , 472(1):491–513, November 2017.

[127] O Just, R Bollig, H-Th Janka, M Obergaulinger, R Glas, and S Nagataki. Core-collapse supernova simulations in one and two dimensions: comparison of codes and approximations. *Monthly Notices of the Royal Astronomical Society*, 481(4):4786–4814, 09 2018.

[128] Adam Burrows and John Goshy. A Theory of Supernova Explosions. , 416:L75, October 1993.

[129] Rodrigo Fernández. Three-dimensional simulations of SASI- and convection-dominated core-collapse supernovae. , 452(2):2071–2086, September 2015.

[130] Tuguldur Sukhbold, T. Ertl, S. E. Woosley, Justin M. Brown, and H.-T. Janka. Core-collapse supernovae from 9 to 120 solar masses based on neutrino-powered explosions. *The Astrophysical Journal*, 821(1):38, apr 2016.

[131] Luca Boccioli, Grant J. Mathews, and Evan P. O'Connor. General relativistic neutrino-driven turbulence in one-dimensional core-collapse supernovae. *The Astrophysical Journal*, 912(1):29, apr 2021.

[132] R. Daniel Murphy, Alejandro Casallas-Lagos, Anthony Mezzacappa, Michele Zanolin, Ryan E. Landfield, Eric J. Lentz, Pedro Marronetti, Javier M. Antelis, and Claudia Moreno. Dependence of the reconstructed core-collapse supernova gravitational wave high-frequency feature on the nuclear equation of state in real interferometric data. *Phys. Rev. D*, 110(8):083006, 2024.

[133] Cabezón, Rubén M., Pan, Kuo-Chuan, Liebendörfer, Matthias, Kuroda, Takami, Ebinger, Kevin, Heinimann, Oliver, Perego, Albino, and Thielemann, Friedrich-Karl. Core-collapse supernovae in the hall of mirrors - a three-dimensional code-comparison project. *A and A*, 619:A118, 2018.

[134] A. Burrows and D. Vartanyan. Core-collapse supernova explosion theory. *Nature*, 589(7840):29–39, January 2021.

[135] Tuguldur Sukhbold, S. E. Woosley, and Alexander Heger. A High-resolution Study of Presupernova Core Structure. , 860(2):93, June 2018.

[136] David Radice and Sebastiano Bernuzzi. Ab-initio general-relativistic neutrino-radiation hydrodynamics simulations of long-lived neutron star merger remnants to neutrino cooling timescales. *The Astrophysical Journal*, 959(1):46, December 2023.

[137] Shota Shibagaki, Takami Kuroda, Kei Kotake, Tomoya Takiwaki, and Tobias Fischer. Three-dimensional grmhd simulations of rapidly rotating stellar core-collapse, 2023.

[138] Rodrigo Fernández, Bernhard Müller, Thierry Foglizzo, and Hans-Thomas Janka. Characterizing SASI- and convection-dominated core-collapse supernova explosions in two dimensions. , 440(3):2763–2780, May 2014.

[139] Janka, H.-Th. Conditions for shock revival by neutrino heating in core-collapse supernovae. *A and AA*, 368(2):527–560, 2001.

[140] Irene Tamborra. Supernova neutrinos: Theory, 2016.

[141] MacKenzie L. Warren, Sean M. Couch, Evan P. O'Connor, and Viktoriya Morozova. Constraining properties of the next nearby core-collapse supernova with multimessenger signals. *The Astrophysical Journal*, 898(2):139, July 2020.

[142] Adam Burrows, Sanjay Reddy, and Todd A. Thompson. Neutrino opacities in nuclear matter. *Nuclear Physics A*, 777:356–394, October 2006.

[143] Adam Burrows, David Vartanyan, Joshua Dolence, M. Skinner, and David Radice. Crucial physical dependencies of the core-collapse supernova mechanism. *Space Science Reviews*, 214, 01 2018.

[144] Evan O'Connor, C. J. Horowitz, Zidu Lin, and Sean Couch. Core-collapse supernova simulations including neutrino interactions from the virial eos. *Proceedings of the International Astronomical Union*, 12(S331):107–112, February 2017.

[145] Tobias Melson, Hans-Thomas Janka, Robert Bollig, Florian Hanke, Andreas Marek, and Bernhard Müller. Neutrino-driven Explosion of a 20 Solar-mass Star in Three Dimensions Enabled by Strange-quark Contributions to Neutrino-Nucleon Scattering. , 808(2):L42, August 2015.

[146] A. et al. Airapetian. Precise determination of the spin structure function g_1 of the proton, deuteron, and neutron. , 75(1):012007, January 2007.

[147] Tobias Fischer. The role of medium modifications for neutrino-pair processes from nucleon-nucleon bremsstrahlung: Impact on the protoneutron star deleptonization. *Astronomy amp; Astrophysics*, 593:A103, September 2016.

[148] Robert Buras, Hans-Thomas Janka, Mathias Th. Keil, Georg G. Raffelt, and Markus Rampp. Electron neutrino pair annihilation: A new source for muon and tau neutrinos in supernovae. *The Astrophysical Journal*, 587(1):320–326, April 2003.

[149] Po-Wen Chang, Ivan Esteban, John F. Beacom, Todd A. Thompson, and Christopher M. Hirata. Toward powerful probes of neutrino self-interactions in supernovae. *Physical Review Letters*, 131(7), August 2023.

[150] Bernhard Müller, Thomas M. Tauris, Alexander Heger, Projjwal Banerjee, Yong-Zhong Qian, Jade Powell, Conrad Chan, Daniel W. Gay, and Norbert Langer. Three-dimensional simulations of neutrino-driven core-collapse supernovae from low-mass single and binary star progenitors. , 484(3):3307–3324, April 2019.

[151] Ko Nakamura, Tomoya Takiwaki, and Kei Kotake. Long-term simulations of multi-dimensional core-collapse supernovae: Implications for neutron star kicks. , 71(5):98, October 2019.

[152] Dong Lai. Neutron star kicks and asymmetric supernovae, 2000.

[153] Christian D. Ott, Adam Burrows, Todd A. Thompson, Eli Livne, and Rolf Walder. The spin periods and rotational profiles of neutron stars at birth. *The Astrophysical Journal Supplement Series*, 164(1):130–155, May 2006.

[154] Christian D. Ott, Luke F. Roberts, André da Silva Schneider, Joseph M. Fedrow, Roland Haas, and Erik Schnetter. The Progenitor Dependence of Core-collapse Supernovae from Three-dimensional Simulations with Progenitor Models of 12-40 M $_\odot$. , 855(1):L3, March 2018.

[155] Hiroki Nagakura, Kohsuke Sumiyoshi, and Shoichi Yamada. Possible Early Linear Acceleration of Proto-neutron Stars via Asymmetric Neutrino Emission in Core-collapse Supernovae. , 880(2):L28, August 2019.

[156] Laurie Walk, Irene Tamborra, Hans-Thomas Janka, and Alexander Summa. Identifying rotation in sasi-dominated core-collapse supernovae with a neutrino gyroscope. *Physical Review D*, 98(12), December 2018.

[157] Irene Tamborra, Georg Raffelt, Florian Hanke, Hans-Thomas Janka, and Bernhard Müller. Neutrino emission characteristics and detection opportunities based on three-dimensional supernova simulations. *Physical Review D*, 90(4), August 2014.

[158] Bernhard Müller and Hans-Thomas Janka. A new multi-dimensional general relativistic neutrino hydrodynamics code for core-collapse supernovae. iv. the neutrino signal. *The Astrophysical Journal*, 788(1):82, May 2014.

[159] Tina Lund, Andreas Marek, Cecilia Lunardini, Hans-Thomas Janka, and Georg Raffelt. Fast time variations of supernova neutrino fluxes and their detectability. *Physical Review D*, 82(6), September 2010.

[160] A. Wongwathanarat, H. Th. Janka, and E. Müller. Three-dimensional neutrino-driven supernovae: Neutron star kicks, spins, and asymmetric ejection of nucleosynthesis products. , 552:A126, April 2013.

[161] C. J. Horowitz and Gang Li. Cumulative Parity Violation in Supernovae. , 80(17):3694–3697, April 1998.

[162] E. Mueller and W. Hillebrandt. A magnetohydrodynamical supernova model. , 80:147–154, December 1979.

[163] G. S. Bisnovatyi-Kogan. The Explosion of a Rotating Star As a Supernova Mechanism. , 47:813, August 1970.

[164] M Obergaulinger and M Á Aloy. Magnetorotational core collapse of possible grb progenitors – iii. three-dimensional models. *Monthly Notices of the Royal Astronomical Society*, 503(4):4942–4963, February 2021.

[165] J Matsumoto, Y Asahina, T Takiwaki, K Kotake, and H R Takahashi. Magnetic support for neutrino-driven explosion of 3D non-rotating core-collapse supernova models. *Monthly Notices of the Royal Astronomical Society*, 516(2):1752–1767, 08 2022.

[166] M. Reichert, M. Bugli, J. Guilet, M. Obergaulinger, M. Á. Aloy, and A. Arcones. Nucleosynthesis in magnetorotational supernovae: impact of the magnetic field configuration, 2024.

[167] J. M. LeBlanc and J. R. Wilson. A Numerical Example of the Collapse of a Rotating Magnetized Star. , 161:541, August 1970.

[168] D. L. Meier, R. I. Epstein, W. D. Arnett, and D. N. Schramm. Magnetohydrodynamic phenomena in collapsing stellar cores. , 204:869–878, March 1976.

[169] Ken'ichi Nomoto, Nozomu Tominaga, Hideyuki Umeda, Chiaki Kobayashi, and Keiichi Maeda. Nucleosynthesis yields of core-collapse supernovae and hypernovae, and galactic chemical evolution. , 777:424–458, October 2006.

[170] B. D. Metzger, D. Giannios, T. A. Thompson, N. Bucciantini, and E. Quataert. The protomagnetar model for gamma-ray bursts. , 413(3):2031–2056, May 2011.

[171] Pawan Kumar and Bing Zhang. The physics of gamma-ray bursts & relativistic jets. , 561:1–109, February 2015.

[172] Ph. Podsiadlowski, P. A. Mazzali, K. Nomoto, D. Lazzati, and E. Cappellaro. The rates of hypernovae and gamma-ray bursts: Implications for their progenitors. *The Astrophysical Journal*, 607(1):L17–L20, April 2004.

[173] A Y Smirnov. The mikheyev-smirnov-wolfenstein (msw) effect, 2019.

[174] Gianluigi Fogli, Eligio Lisi, Antonio Marrone, and Alessandro Mirizzi. Neutrinos self interactions in supernovae, 2008.

[175] S. Hannestad, G. G. Raffelt, G. Sigl, and Y. Y. Y. Wong. Self-induced conversion in dense neutrino gases: Pendulum in flavour space, 2007.

[176] Huaiyu Duan, George M. Fuller, and Yong-Zhong Qian. Collective neutrino oscillations. *Annual Review of Nuclear and Particle Science*, 60(1):569–594, 2010.

[177] Damiano F. G. Fiorillo, Georg G. Raffelt, and Günter Sigl. Collective neutrino-antineutrino oscillations in dense neutrino environments?, 2024.

[178] Q. R. et al. Ahmad. Direct evidence for neutrino flavor transformation from neutral-current interactions in the sudbury neutrino observatory. *Physical Review Letters*, 89(1), June 2002.

[179] G. Battistoni, A. Ferrari, T. Montaruli, and P.R. Sala. The fluka atmospheric neutrino flux calculation. *Astroparticle Physics*, 19(2):269–290, May 2003.

[180] Arnon Dar and Giora Shaviv. The solar neutrino problem – an update. *Physics Reports*, 311(3–5):115–141, April 1999.

[181] Raymond Davis, Don S. Harmer, and Kenneth C. Hoffman. Search for neutrinos from the sun. *Phys. Rev. Lett.*, 20:1205–1209, May 1968.

[182] Y. et Al. Fukuda. Evidence for oscillation of atmospheric neutrinos. *Physical Review Letters*, 81(8):1562–1567, August 1998.

[183] Pralay Chakraborty, Manash Dey, and Subhankar Roy. Constrained neutrino mass matrix and majorana phases. *Journal of Physics G: Nuclear and Particle Physics*, 51(1):015003, December 2023.

[184] Ara Ioannisian and Stefan Pokorski. Three neutrino oscillations in matter. *Physics Letters B*, 782:641–645, July 2018.

[185] Jun Iizuka, Teruyuki Kitabayashi, Yuki Minagawa, and Masaki Yasuè. Parametrization of pontecorvo–maki–nakagawa–sakata mixing matrix based on cp-violating bipair neutrino mixing. *Modern Physics Letters A*, 30(05):1550019, February 2015.

[186] Ivan Esteban, M.C. Gonzalez-Garcia, Michele Maltoni, Thomas Schwetz, and Albert Zhou. The fate of hints: updated global analysis of three-flavor neutrino oscillations. *Journal of High Energy Physics*, 2020(9), September 2020.

[187] Nu-fit. `http://www.nu-fit.org/`, 2020.

[188] Ali Rida Khalifeh and Raul Jimenez. Using neutrino oscillations to measure h0. *Physics of the Dark Universe*, 37:101063, September 2022.

[189] Yasaman Farzan and Alexei Yu. Smirnov. Coherence and oscillations of cosmic neutrinos. *Nuclear Physics B*, 805(1–2):356–376, December 2008.

[190] M. Cristina Volpe. Neutrinos from dense environments : Flavor mechanisms, theoretical approaches, observations, and new directions, 2024.

[191] James P. Kneller and Gail C. McLaughlin. Three flavor neutrino oscillations in matter: Flavor diagonal potentials, the adiabatic basis, and the cp phase. *Physical Review D*, 80(5), September 2009.

[192] R. Bollig, H.-T. Janka, A. Lohs, G. Martínez-Pinedo, C.J. Horowitz, and T. Melson. Muon creation in supernova matter facilitates neutrino-driven explosions. *Physical Review Letters*, 119(24), December 2017.

[193] Tobias Fischer, Gang Guo, Gabriel Martínez-Pinedo, Matthias Liebendörfer, and Anthony Mezzacappa. Muonization of supernova matter. *Phys. Rev. D*, 102:123001, Dec 2020.

[194] Cristina Volpe, Daavid Väänänen, and Catalina Espinoza. Extended evolution equations for neutrino propagation in astrophysical and cosmological environments. *Phys. Rev. D*, 87(11):113010, 2013.

[195] Julien Serreau and Cristina Volpe. Neutrino-antineutrino correlations in dense anisotropic media. *Phys. Rev. D*, 90(12):125040, 2014.

[196] Shu Luo. Neutrino oscillation in dense matter. *Physical Review D*, 101(3), February 2020.

[197] L. Wolfenstein. Neutrino oscillations in matter. *Phys. Rev. D*, 17:2369–2374, May 1978.

[198] L. Wolfenstein. Neutrino oscillations and stellar collapse. *Phys. Rev. D*, 20:2634–2635, Nov 1979.

[199] S. P. Mikheyev and A. Yu. Smirnov. Resonance Amplification of Oscillations in Matter and Spectroscopy of Solar Neutrinos. *Sov. J. Nucl. Phys.*, 42:913–917, 1985.

[200] S. P. Mikheev and A. Yu. Smirnov. Resonant amplification of neutrino oscillations in matter and solar neutrino spectroscopy. *Nuovo Cim. C*, 9:17–26, 1986.

[201] Stanislav P Mikheev and A Yu Smirnov. Neutrino oscillations in a medium with variable density. *Soviet Physics Uspekhi*, 29(12):1155, dec 1986.

[202] A. Yu. Smirnov. The msw effect and solar neutrinos, 2003.

[203] A Yu Smirnov. The msw effect and matter effects in neutrino oscillations. *Physica Scripta*, 2005(T121):57, jan 2005.

[204] Carlo Giunti and Chung W. Kim. *Fundamentals of Neutrino Physics and Astrophysics*. 2007.

[205] Amol S. Dighe and Alexei Yu. Smirnov. Identifying the neutrino mass spectrum from a supernova neutrino burst. *Physical Review D*, 62(3), July 2000.

[206] R Tomàs, M Kachelrieß, G Raffelt, A Dighe, H-T Janka, and L Scheck. Neutrino signatures of supernova forward and reverse shock propagation. *Journal of Cosmology and Astroparticle Physics*, 2004(09):015–015, October 2004.

[207] A. Esteban-Pretel, Ricard Tomas Bayo, and Jose Valle. Probing nonstandard neutrino interactions with supernova neutrinos. *Phys. Rev. D*, 76, 05 2007.

[208] Y. Pehlivan, A. B. Balantekin, Toshitaka Kajino, and Takashi Yoshida. Invariants of collective neutrino oscillations. *Physical Review D*, 84(6), September 2011.

[209] Heamin et al. Ko. Neutrino process in core-collapse supernovae with neutrino self-interaction and msw effects. *The Astrophysical Journal Letters*, 891(1):L24, March 2020.

[210] Sovan Chakraborty, Tobias Fischer, Alessandro Mirizzi, Ninetta Saviano, and Ricard Tomàs. No collective neutrino flavor conversions during the supernova accretion phase. *Physical Review Letters*, 107(15), October 2011.

[211] G. L. Fogli, E. Lisi, A. Mirizzi, and D. Montanino. Analysis of energy and time dependence of supernova shock effects on neutrino crossing probabilities. *Physical Review D*, 68(3), August 2003.

[212] T. K. Kuo and James Pantaleone. Neutrino oscillations in matter. *Rev. Mod. Phys.*, 61:937–979, Oct 1989.

[213] G. L. Fogli, E. Lisi, D. Montanino, and A. Palazzo. Supernova neutrino oscillations: A simple analytical approach. *Phys. Rev. D*, 65:073008, Mar 2002.

[214] S. H. Chiu, C.-C. Huang, and K.-C. Lai. Signatures of the neutrino mass hierarchy in supernova neutrinos. *Progress of Theoretical and Experimental Physics*, 2015(6):63B01–0, June 2015.

[215] Shunsaku Horiuchi and James P Kneller. What can be learned from a future supernova neutrino detection? *Journal of Physics G: Nuclear and Particle Physics*, 45(4):043002, mar 2018.

[216] Richard C. Schirato and George M. Fuller. Connection between supernova shocks, flavor transformation, and the neutrino signal, 2002.

[217] Jérôme Gava, James Kneller, Cristina Volpe, and G. C. McLaughlin. Dynamical collective calculation of supernova neutrino signals. *Physical Review Letters*, 103(7), August 2009.

[218] Ricard Tomas. Identifying the neutrino mass hierarchy with supernova neutrinos. *Journal of Physics: Conference Series*, 39(1):297, may 2006.

[219] James P. Kneller and Alex W. Mauney. Consequences of large theta 13 for the turbulence signatures in supernova neutrinos. *Physical Review D*, 88(2), July 2013.

[220] Berryman et al. Neutrino self-interactions: A white paper. *Physics of the Dark Universe*, 42:101267, December 2023.

[221] Cecilia Lunardini and Irene Tamborra. Diffuse supernova neutrinos: oscillation effects, stellar cooling and progenitor mass dependence. *Journal of Cosmology and Astroparticle Physics*, 2012(07):012–012, July 2012.

[222] John F. Cherry, George M. Fuller, J. Carlson, Huaiyu Duan, and Yong-Zhong Qian. Multiangle simulation of flavor evolution in the neutronization neutrino burst from an o-ne-mg core-collapse supernova. *Physical Review D*, 82(8), October 2010.

[223] Huaiyu Duan, George M. Fuller, J. Carlson, and Yong-Zhong Qian. Simulation of coherent nonlinear neutrino flavor transformation in the supernova environment: Correlated neutrino trajectories. *Physical Review D*, 74(10), November 2006.

[224] R. F. Sawyer. Speed-up of neutrino transformations in a supernova environment. *Phys. Rev. D*, 72:045003, Aug 2005.

[225] Steen Hannestad, Georg G. Raffelt, Günter Sigl, and Yvonne Y. Y. Wong. Self-induced conversion in dense neutrino gases: Pendulum in flavor space. *Phys. Rev. D*, 74:105010, Nov 2006.

[226] R. F. Sawyer. Multiangle instability in dense neutrino systems. *Physical Review D*, 79(10), May 2009.

[227] Ignacio Izaguirre, Georg Raffelt, and Irene Tamborra. Fast pairwise conversion of supernova neutrinos: A dispersion relation approach. *Physical Review Letters*, 118(2), January 2017.

[228] R.F. Sawyer. Neutrino cloud instabilities just above the neutrino sphere of a supernova. *Physical Review Letters*, 116(8), February 2016.

[229] Basudeb Dasgupta, Alessandro Mirizzi, and Manibrata Sen. Fast neutrino flavor conversions near the supernova core with realistic flavor-dependent angular distributions. *Journal of Cosmology and Astroparticle Physics*, 2017(02):019–019, February 2017.

[230] Taiki Morinaga. Fast neutrino flavor instability and neutrino flavor lepton number crossings. *Physical Review D*, 105(10), May 2022.

[231] Damiano F.G. Fiorillo and Georg G. Raffelt. Flavor solitons in dense neutrino gases. *Physical Review D*, 107(12), June 2023.

[232] Sajad Abbar, Huaiyu Duan, Kohsuke Sumiyoshi, Tomoya Takiwaki, and Maria Cristina Volpe. On the occurrence of fast neutrino flavor conversions in multidimensional supernova models. *Physical Review D*, 100(4), August 2019.

[233] Sajad Abbar, Akira Harada, and Hiroki Nagakura. Machine learning-based detection of non-axisymmetric fast neutrino flavor instabilities in core-collapse supernovae, 2024.

[234] Jakob Ehring, Sajad Abbar, Hans-Thomas Janka, Georg Raffelt, and Irene Tamborra. Fast neutrino flavor conversions can help and hinder neutrino-driven explosions. *Physical Review Letters*, 131(6), August 2023.

[235] Sandhya Choubey, Basudeb Dasgupta, Amol Dighe, and Alessandro Mirizzi. Signatures of collective and matter effects on supernova neutrinos at large detectors, 2010.

[236] Ankur Nath and Ng. K. Francis. Detection techniques and investigation of different neutrino experiments. *International Journal of Modern Physics A*, 36(13):2130008, April 2021.

[237] M.V. Diwan, V. Galymov, X. Qian, and A. Rubbia. Long-baseline neutrino experiments. *Annual Review of Nuclear and Particle Science*, 66(1):47–71, October 2016.

[238] Esther Ciarrocchi and Nicola Belcari. Cerenkov luminescence imaging: physics principles and potential applications in biomedical sciences. *EJNMMI Physics*, 4, 03 2017.

[239] Kate Scholberg. Supernova neutrino detection in water Cherenkov detectors. *J. Phys. Conf. Ser.*, 309:012028, 2011.

[240] Iwata City Hamamatsu Photonics KK. Photomultiplier tubes hamamatsu and photomultupliers tubes photonics. basics and applications. 2007.

[241] M.F. L'Annunziata. *Radionuclide Tracers: Their Detection and Measurement.* Academic Press, 1987.

[242] M. L'Annunziata. *Handbook of Radioactivity Analysis, 3rd Edition.* 09 2012.

[243] D.R. Lide. *CRC Handbook of Chemistry and Physics, 84th Edition.* Taylor & Francis, 2003.

[244] K. et al. Abe. First gadolinium loading to super-kamiokande. *Nuclear Instruments and Methods in Physics Research Section A: Accelerators, Spectrometers, Detectors and Associated Equipment*, 1027:166248, mar 2022.

[245] E. Kolbe, K. Langanke, and P. Vogel. Estimates of weak and electromagnetic nuclear decay signatures for neutrino reactions in super-kamiokande. *Phys. Rev. D*, 66:013007, Jul 2002.

[246] Alessandro Strumia and Francesco Vissani. Precise quasielastic neutrino/nucleon cross-section. *Physics Letters B*, 564(1):42–54, 2003.

[247] John N. Bahcall, Marc Kamionkowski, and Alberto Sirlin. Solar neutrinos: Radiative corrections in neutrino-electron scattering experiments. *Phys. Rev. D*, 51:6146–6158, Jun 1995.

[248] K. Langanke, P. Vogel, and E. Kolbe. Signal for supernova ν_μ and ν_τ neutrinos in water Čerenkov detectors. *Phys. Rev. Lett.*, 76:2629–2632, Apr 1996.

[249] Christopher W. Walter. *The Super-Kamiokande Experiment*, page 19–43. WORLD SCIENTIFIC, March 2008.

[250] Yoichiro Suzuki. The super-kamiokande experiment. *The European Physical Journal C*, 79, 04 2019.

[251] Katsushige et al. Abe. Real-time supernova neutrino burst monitor at super-kamiokande. *Astroparticle Physics*, 81, 01 2016.

[252] L. Kneale. Supernova spotting in super-kamiokande gd, 2024.

[253] A. Bellerive, J.R. Klein, A.B. McDonald, A.J. Noble, and A.W.P. Poon. The sudbury neutrino observatory. *Nuclear Physics B*, 908:30–51, July 2016.

[254] J. N. Bahcall. The Solar Neutrino Problem. *Solar Physics*, 100:53, October 1985.

[255] Robert Cross, Alexander Fritz, and Spencer Griswold. Eleven year search for supernovae with the icecube neutrino observatory, 2019.

[256] M. et al. Ageron. Antares: The first undersea neutrino telescope. *Nuclear Instruments and Methods in Physics Research Section A: Accelerators, Spectrometers, Detectors and Associated Equipment*, 656(1):11–38, November 2011.

[257] V. Kulikovskiy. Supernova neutrino detection in the ANTARES neutrino telescope. In *32nd International Cosmic Ray Conference*, volume 7, page 204, 2011.

[258] S Adrián-Martínez et al. Letter of intent for km3net 2.0. *Journal of Physics G: Nuclear and Particle Physics*, 43(8):084001, jun 2016.

[259] F. Halzen, J. E. Jacobsen, and E. Zas. Ultratransparent antarctic ice as a supernova detector. *Phys. Rev. D*, 53:7359–7361, Jun 1996.

[260] The IceCube Collaboration. The icecube collaboration: contributions to the 30th international cosmic ray conference (icrc 2007), 2007.

[261] The IceCube Collaboration and Abbasi, R. et al. Icecube sensitivity for low-energy neutrinos from nearby supernovae. *A&A*, 535:A109, 2011.

[262] D. Guetta, Aurora Langella, Silvia Gagliardini, and Massimo Della Valle. Low- and high-energy neutrinos from sn 2023ixf in m101. *The Astrophysical Journal Letters*, 955:L9, 09 2023.

[263] S. et al. Aiello. The km3net potential for the next core-collapse supernova observation with neutrinos: Km3net collaboration. *The European Physical Journal C*, 81(5), May 2021.

[264] G. Knoll. *Radiation Detection and Measurement*. 01 2000.

[265] Simon R. Cherry, James A. Sorenson, and Michael E. Phelps. chapter 7 - radiation detectors. In Simon R. Cherry et al., editor, *Physics in Nuclear Medicine (Fourth Edition)*, pages 87–106. W.B. Saunders, Philadelphia, fourth edition edition, 2012.

[266] Kate Scholberg. Supernova neutrino detection. *Annual Review of Nuclear and Particle Science*, 62(1):81–103, nov 2012.

[267] E. N. Alexeyev and L. N. Alexeyeva. Twenty years of galactic observations in searching for bursts of collapse neutrinos with the baksan underground scintillation telescope. *Journal of Experimental and Theoretical Physics*, 95(1):5–10, July 2002.

[268] M. Aglietta et al. The most powerful scintillator supernovae detector: Lvd. *La Rivista del Nuovo Cimento*, 105(12):1793–1804, December 1992.

[269] Alimonti et al. The borexino detector at the laboratori nazionali del gran sasso. *Nuclear Instruments and Methods in Physics Research Section A: Accelerators, Spectrometers, Detectors and Associated Equipment*, 600(3):568–593, March 2009.

[270] Atsuto Suzuki. Antineutrino science in kamland. *The European Physical Journal C*, 74, 09 2014.

[271] Aguilar-Arevalo et al. Search for core-collapse supernovae using the miniboone neutrino detector. *Physical Review D*, 81(3), feb 2010.

[272] S. et al. Mufson. Liquid scintillator production for the nova experiment. *Nuclear Instruments and Methods in Physics Research Section A: Accelerators, Spectrometers, Detectors and Associated Equipment*, 799:1–9, November 2015.

[273] R.B. Patterson. The nova experiment: status and outlook. *Nuclear Physics B - Proceedings Supplements*, 235–236:151–157, February 2013.

[274] The NOvA Collaboration and D. Ayres. Nova proposal to build a 30 kiloton off-axis detector to study neutrino oscillations in the fermilab numi beamline, 2005.

[275] Andringa et al. Current status and future prospects of the sno+ experiment. *Advances in High Energy Physics*, 2016:1–21, 2016.

[276] Ranjan Laha, John F. Beacom, and Sanjib Kumar Agarwalla. New power to measure supernova ν_e with large liquid scintillator detectors, 2014.

[277] Juno physics and detector. *Progress in Particle and Nuclear Physics*, 123:103927, March 2022.

[278] Daya Bay and JUNO collaborations. Optimization of the juno liquid scintillator composition using a daya bay antineutrino detector, 2020.

[279] Jia-Shu Lu, Yu-Feng Li, and Shun Zhou. Getting the most from the detection of galactic supernova neutrinos in future large liquid-scintillator detectors. *Physical Review D*, 94(2), July 2016.

[280] et al. An. Neutrino physics with juno. *Journal of Physics G: Nuclear and Particle Physics*, 43(3):030401, February 2016.

[281] Yufeng Li. Supernova Neutrinos in Future Liquid-Scintillator Detectors. *PoS*, NOW2016:046, 2017.

[282] Angel Abusleme et al. Real-time monitoring for the next core-collapse supernova in juno, 2023.

[283] Bhavesh Chauhan, Basudeb Dasgupta, and Vivek Datar. A deuterated liquid scintillator for supernova neutrino detection. *Journal of Cosmology and Astroparticle Physics*, 2021(11):005, November 2021.

[284] L.J. et al. Bignell. Characterization and modeling of a water-based liquid scintillator. *Journal of Instrumentation*, 10(12):P12009–P12009, December 2015.

[285] Julia Sawatzki, Michael Wurm, and Daniel Kresse. Detecting the diffuse supernova neutrino background in the future water-based liquid scintillator detector theia. *Physical Review D*, 103(2), January 2021.

[286] M. et al. Askins. Theia: an advanced optical neutrino detector. *The European Physical Journal C*, 80(5), May 2020.

[287] Cao et al. Measurement of scintillation and ionization yield and scintillation pulse shape from nuclear recoils in liquid argon. *Physical Review D*, 91(9), May 2015.

[288] C.M.B. Monteiro, J.A.M. Lopes, J.F.C.A. Veloso, and J.M.F. dos Santos. Secondary scintillation yield in pure argon. *Physics Letters B*, 668(3):167–170, 2008.

[289] Leigh Howard Whitehead. Status of single phase and dual phase DUNE prototype detectors at CERN. *PoS*, ICHEP2018:300, 2019.

[290] Krishanu Majumdar and Konstantinos Mavrokoridis. Review of liquid argon detector technologies in the neutrino sector. *Applied Sciences*, 11:2455, 03 2021.

[291] Dario Autiero. Charge readout and dual-phase readout technology for large scale cryogenic liquid detectors. *AIDA2020 WP8 wiki pages*, 11 2019.

[292] A. Bueno, I. Gil-Botella, and A. Rubbia. Supernova neutrino detection in a liquid argon tpc, 2003.

[293] R. et al. Obousy. Project icarus: Progress report on technical developments and design considerations. *Journal of the British Interplanetary Society*, 64:358, 11 2011.

[294] R. Acciarri et al. Long-baseline neutrino facility (lbnf) and deep underground neutrino experiment (dune) conceptual design report volume 1: The lbnf and dune projects, 2016.

[295] B. Abi et al. Deep underground neutrino experiment (dune), far detector technical design report, volume i: Introduction to dune, 2020.

[296] DUNE Collaboration et al. Long-baseline neutrino facility (lbnf) and deep underground neutrino experiment (dune) conceptual design report volume 2: The physics program for dune at lbnf, 2016.

[297] Amanda Weinstein and for theDUNE Collaboration. Supernova neutrinos at the dune experiment. *Journal of Physics: Conference Series*, 1342(1):012052, jan 2020.

[298] D. Yu. Akimov et al. Observation of delayed electron emission in a two-phase liquid xenon detector. *JINST*, 11(03):C03007, 2016.

[299] P. Agnes et al. Low-mass dark matter search with the darkside-50 experiment. *Physical Review Letters*, 121(8), Aug 2018.

[300] E. Aprile et al. Response of the xenon100 dark matter detector to nuclear recoils. *Phys. Rev. D*, 88:012006, Jul 2013.

[301] E. Aprile et al. Xenon1t dark matter data analysis: Signal and background models and statistical inference. *Physical Review D*, 99(11), June 2019.

[302] James Nikkel, Tsahi Gozani, Craig Brown, John Kwong, D. Mckinsey, Yeonjeong Shin, Charles Gary, and Murray Firestone. Liquefied noble gas detectors for detection of nuclear materials. *Journal of Instrumentation - J INSTRUM*, 7, 03 2012.

[303] Hiroshi et al. Ito. Analyzing the neutron and γ-ray emission properties of an americium–beryllium tagged neutron source. *Nuclear Instruments and Methods in Physics Research Section A: Accelerators, Spectrometers, Detectors and Associated Equipment*, 1057:168701, December 2023.

[304] G. Gallina et al. Characterization of the hamamatsu vuv4 mppcs for nexo. *Nuclear Instruments and Methods in Physics Research Section A: Accelerators, Spectrometers, Detectors and Associated Equipment*, 940:371–379, 2019.

[305] Wei Zheng, Lemin Jia, and Feng Huang. Vacuum-ultraviolet photon detections. *iScience*, 23(6):101145, 2020.

[306] C G Wahl, E P Bernard, W H Lippincott, J A Nikkel, Y Shin, and D N McKinsey. Pulse-shape discrimination and energy resolution of a liquid-argon scintillator with xenon doping. *Journal of Instrumentation*, 9(06):P06013–P06013, June 2014.

[307] Brian Lenardo, Kareem Kazkaz, Aaron Manalaysay, Jeremy Mock, Matthew Szydagis, and Mani Tripathi. A global analysis of light and charge yields in liquid xenon. *IEEE Transactions on Nuclear Science*, 62(6):3387–3396, December 2015.

[308] Elena Aprile, Aleksey E. Bolotnikov, Alexander L. Bolozdynya, and Tadayoshi Doke. *Noble Gas Detectors*. Wiley, 2008.

[309] Tadayoshi Doke, Akira Hitachi, Jun Kikuchi, Kimiaki Masuda, Hiroyuki Okada, and Eido Shibamura. Absolute scintillation yields in liquid argon and xenon for various particles. *Japanese Journal of Applied Physics*, 41(3R):1538, mar 2002.

[310] Badertscher et al. Ardm: first results from underground commissioning. *Journal of Instrumentation*, 8(09):C09005–C09005, September 2013.

[311] Aalseth C. E. et al. Darkside-20k: A 20 tonne two-phase lar tpc for direct dark matter detection at lngs. *The European Physical Journal Plus*, 133(3), March 2018.

[312] Agnes et al. Sensitivity of future liquid argon dark matter search experiments to core-collapse supernova neutrinos. *Journal of Cosmology and Astroparticle Physics*, 2021(03):043, March 2021.

[313] C. A. Duba et al. HALO: The helium and lead observatory for supernova neutrinos. *J. Phys. Conf. Ser.*, 136:042077, 2008.

[314] K. S. Abe and XMASS Collaboration. Detectability of galactic supernova neutrinos coherently scattered on xenon nuclei in xmass. *Astroparticle Physics*, 89:51–56, March 2017.

[315] Yue et al. Meng. Dark matter search results from the pandax-4t commissioning run. *Physical Review Letters*, 127(26), December 2021.

[316] D.S. et al. Akerib. The lux-zeplin (lz) experiment. *Nuclear Instruments and Methods in Physics Research Section A: Accelerators, Spectrometers, Detectors and Associated Equipment*, 953:163047, February 2020.

[317] E. Aprile et al. Projected wimp sensitivity of the xenonnt dark matter experiment. *Journal of Cosmology and Astroparticle Physics*, 2020(11):031–031, nov 2020.

[318] E. Aprile et al. Physics reach of the xenon1t dark matter experiment. *Journal of Cosmology and Astroparticle Physics*, 2016(04):027, apr 2016.

[319] D. Khaitan. Supernova neutrino detection in lz. *Journal of Instrumentation*, 13(02):C02024–C02024, February 2018.

[320] Sovan Chakraborty, Pijushpani Bhattacharjee, and Kamales Kar. Observing supernova neutrino light curve in future dark matter detectors. *Physical Review D*, 89(1), January 2014.

[321] Binyu Pang et al. Detecting neutrinos from supernova bursts in pandax-4t, 2024.

[322] Gary J. Feldman and Robert D. Cousins. Unified approach to the classical statistical analysis of small signals. *Phys. Rev. D*, 57:3873–3889, Apr 1998.

[323] Ko Nakamura et al. Multimessenger signals of long-term core-collapse supernova simulations: synergetic observation strategies. *Monthly Notices of the Royal Astronomical Society*, 461(3):3296–3313, 06 2016.

[324] Antonioli et al. Snews: the supernova early warning system. *New Journal of Physics*, 6:114–114, September 2004.

[325] J. Ahrens et al. Search for supernova neutrino bursts with the amanda detector. *Astroparticle Physics*, 16(4):345–359, 2002.

[326] P.F. Smith. Omnis—an improved low-cost detector to measure mass and mixing of mu/tau neutrinos from a galactic supernova. *Astroparticle Physics*, 8(1):27–42, 1997.

[327] Gergely Dálya, Sibe Bleuzé, Bence Bécsy, Rafael S. de Souza, and Tamás Szalai. Constraining supernova physics through gravitational-wave observations, 2023.

[328] Barry Pointon. HALO-1kT - Helium And Lead Observatory for Supernova Neutrinos with High Sensitivity to ν_e. In *XXVIII International Conference on Neutrino Physics and Astrophysics*, page 165, June 2018.

[329] M.G. Boulay. *DEAP-3600 Dark Matter Search at SNOLAB*. Phys. Rev. Lett. 109, 181301, 2012.

[330] Agnes P. et al. Calibration of the liquid argon ionization response to low energy electronic and nuclear recoils with darkside-50. *Physical Review D*, 104(8), October 2021.

[331] S. Rosswog and M. Liebendörfer. High-resolution calculations of merging neutron stars — II. Neutrino emission. *Monthly Notices of the Royal Astronomical Society*, 342(3):673–689, 07 2003.

[332] O. L. Caballero, G. C. McLaughlin, and R. Surman. Detecting neutrinos from black hole-neutron star mergers. *Phys. Rev. D*, 80:123004, Dec 2009.

[333] Viktoriya Morozova, David Radice, Adam Burrows, and David Vartanyan. The gravitational wave signal from core-collapse supernovae. *The Astrophysical Journal*, 861(1):10, jun 2018.

[334] Ernazar Abdikamalov, Giulia Pagliaroli, and David Radice. *Gravitational Waves from Core-Collapse Supernovae*, page 1–37. Springer Singapore, 2021.

[335] David Vartanyan, Adam Burrows, Tianshu Wang, Matthew S. B. Coleman, and Christopher J. White. The gravitational-wave signature of core-collapse supernovae, 2023.

[336] M. Aker et al. Direct neutrino-mass measurement with sub-electronvolt sensitivity. *Nature Phys.*, 18(2):160–166, 2022.

[337] D. Fargion. Time delay between gravitational waves and neutrino burst from a supernova explosion: a test for the neutrino mass, 2001.

[338] K. Abe et al. Real-time supernova neutrino burst monitor at super-kamiokande. *Astroparticle Physics*, 81:39–48, 2016.

[339] R. Tomàs, D. Semikoz, G. G. Raffelt, M. Kachelrieß, and A. S. Dighe. Supernova pointing with low- and high-energy neutrino detectors. *Phys. Rev. D*, 68:093013, Nov 2003.

[340] J. F. Beacom and P. Vogel. Can a supernova be located by its neutrinos? *Phys. Rev. D*, 60:033007, Jul 1999.

[341] K. et al. Abe. Atmospheric neutrino oscillation analysis with external constraints in super-kamiokande i-iv. *Physical Review D*, 97(7), April 2018.

[342] J.L. Autran, D. Munteanu, T. Saad Saoud, and S. Moindjie. Characterization of atmospheric muons at sea level using a cosmic ray telescope. *Nuclear Instruments and Methods in Physics Research Section A: Accelerators, Spectrometers, Detectors and Associated Equipment*, 903:77–84, 2018.

[343] Material radiopurity control in the xenonnt experiment. *The European Physical Journal C*, 82(7), July 2022.

[344] XENON Collaboration and E. Aprile. The xenonnt dark matter experiment, 2024.

[345] XENON Collaboration Bui T. Khai. Status of the neutron veto system of xenonnt. *The University of Tokyo, Kavli IPMU*, 2021.

[346] V.C. Antochi et al. Improved quality tests of r11410-21 photomultiplier tubes for the xenonnt experiment. *Journal of Instrumentation*, 16(08):P08033, aug 2021.

[347] Daniel Wenz. *Commissioning of the world's first water Cherenkov neutron veto and first WIMP dark matter search results of the XENONnT experiment.* PhD thesis, Mainz U., 2023.

[348] Marc Schumann. Direct detection of wimp dark matter: concepts and status. *Journal of Physics G: Nuclear and Particle Physics*, 46(10):103003, August 2019.

[349] M. Cannoni, J. D. Vergados, and M. E. Gómez. Scheme for the extraction of wimp-nucleon scattering cross sections from total event rates. *Physical Review D*, 83(7), April 2011.

[350] J. Angle and E. Aprile et al. First results from the xenon10 dark matter experiment at the gran sasso national laboratory. *Physical Review Letters*, 100(2), January 2008.

[351] E. Aprile et al. Constraining the spin-dependent wimp-nucleon cross sections with xenon1t. *Physical Review Letters*, 122(14), April 2019.

[352] Reader J. Kramida A., Ralchenko Yu. and NIST ASD Team. Nist atomic spectra database (version 5.11). *National Institute of Standards and Technology, Gaithersburg, MD*, 84, 01 2023.

[353] T. Tomoda. Double beta decay. *Rept. Prog. Phys.*, 54:53–126, 1991.

[354] E. Aprile et al. Double-weak decays of ^{124}Xe and ^{136}Xe in the xenon1t and xenonnt experiments. *Phys. Rev. C*, 106:024328, Aug 2022.

[355] Observation of two-neutrino double electron capture in 124xe with xenon1t. *Nature*, 568(7753):532–535, April 2019.

[356] Wolfango Plastino and Fatin Bella. Radon groundwater monitoring at underground laboratories of gran sasso (italy). *Geophysical Research Letters - GEOPHYS RES LETT*, 28:2675–2678, 07 2001.

[357] E. Aprile et al. 222rn emanation measurements for the xenon1t experiment. *The European Physical Journal C*, 81(4), April 2021.

[358] Jean-Philippe Zopounidis. *Search for leptonically interacting dark matter with the XENON1T electronic recoil data*. Theses, Sorbonne Université, September 2020.

[359] Sid El Moctar Ahmed Maouloud. *Search for dark matter using XENONnT electron recoil data*. Theses, Sorbonne Université, October 2022.

[360] Joshua Jortner, Lothar Meyer, Stuart A. Rice, and E. G. Wilson. Localized Excitations in Condensed Ne, Ar, Kr, and Xe. *The Journal of Chemical Physics*, 42(12):4250–4253, 06 1965.

[361] Plante Guillaume. *The XENON100 Dark Matter Experiment: Design, Construction, Calibration and 2010 Search Results with Improved Measurement of the Scintillation Response of Liquid Xenon to Low-Energy Nuclear Recoils*. PhD thesis, 01 2012.

[362] R.L. Platzman. Total ionization in gases by high-energy particles: An appraisal of our understanding. *The International Journal of Applied Radiation and Isotopes*, 10(2):116–127, 1961.

[363] Shinzou Kubota, Masahiko Hishida, Masayo Suzuki, and Jian-zhi Ruan(Gen). Dynamical behavior of free electrons in the recombination process in liquid argon, krypton, and xenon. *Phys. Rev. B*, 20:3486–3496, Oct 1979.

[364] M. Szydagis et al. A review of nest models, and their application to improvement of particle identification in liquid xenon experiments, 2023.

[365] M Szydagis, N Barry, K Kazkaz, J Mock, D Stolp, M Sweany, M Tripathi, S Uvarov, N Walsh, and M Woods. Nest: a comprehensive model for scintillation yield in liquid xenon. *Journal of Instrumentation*, 6(10):P10002–P10002, October 2011.

[366] Tadayoshi Doke, Henry J. Crawford, Akira Hitachi, Jun Kikuchi, Peter J. Lindstrom, Kimiaki Masuda, Eido Shibamura, and Tan Takahashi. Let dependence of scintillation yields in liquid argon. *Nuclear Instruments and Methods in Physics Research Section A: Accelerators, Spectrometers, Detectors and Associated Equipment*, 269(1):291–296, 1988.

[367] Lars Onsager. Initial recombination of ions. *Physical Review*, 54:554–557, 1938.

[368] J. Thomas and D. A. Imel. Recombination of electron-ion pairs in liquid argon and liquid xenon. *Phys. Rev. A*, 36:614–616, Jul 1987.

[369] Brian Lenardo, Kareem Kazkaz, Aaron Manalaysay, Jeremy Mock, Matthew Szydagis, and Mani Tripathi. A global analysis of light and charge yields in liquid xenon. *IEEE Transactions on Nuclear Science*, 62(6):3387–3396, 2015.

[370] J Lindhard, M Scharff, and H E Schioett. Range concepts and heavy ion ranges (notes on atomic collisions, ii). *Kgl. Danske Videnskab. Selskab. Mat. Fys. Medd.*, Vol: 33: No. 14, 1 1963.

[371] P.F.Smith J.D.Lewin. Review of mathematics, numerical factors, and corrections for dark matter experiments based on elastic nuclear recoil. 1996.

[372] First results from the lux dark matter experiment at the sanford underground research facility. *Physical Review Letters*, 112(9), March 2014.

[373] Peter Gaemers, tianyu zhu, Joran R. Angevaare, and Diego Ramírez García. Xenonnt/wfsim: v1.0.2. oct 2022.

[374] Yoni Sher. *Low Intensity LIDAR using Compressed Sensing and a Photon Counting Detector*. PhD thesis, 05 2018.

[375] M. Abdullah et al. Coherent elastic neutrino-nucleus scattering: Terrestrial and astrophysical applications, 2022.

[376] Thomas Rink. Coherent elastic neutrino-nucleus scattering – first constraints/observations and future potential, 2023.

[377] D. Akimov et al. and COHERENT Collaboration. Observation of coherent elastic neutrino-nucleus scattering. *Science*, 357(6356):1123–1126, 2017.

[378] D. et al. Akimov. First measurement of coherent elastic neutrino-nucleus scattering on argon. *Phys. Rev. Lett.*, 126:012002, Jan 2021.

[379] Bjorn Jorg Scholz. *First Observation of Coherent Elastic Neutrino-Nucleus Scattering*. PhD thesis, Chicago U., 2017.

[380] D. et al. Akimov. First measurement of coherent elastic neutrino-nucleus scattering on argon. *Physical Review Letters*, 126(1), jan 2021.

[381] J. Billard, E. Figueroa-Feliciano, and L. Strigari. Implication of neutrino backgrounds on the reach of next generation dark matter direct detection experiments. *Physical Review D*, 89(2), January 2014.

[382] Jens Erler and Michael Ramsey-Musolf. Weak mixing angle at low energies. *Physical Review D*, 72, 09 2004.

[383] Ciaran A.J. O'Hare. Dark matter astrophysical uncertainties and the neutrino floor. *Physical Review D*, 94(6), September 2016.

[384] J. et al. Aalbers. Darwin: towards the ultimate dark matter detector. *Journal of Cosmology and Astroparticle Physics*, 2016(11):017–017, November 2016.

[385] Yuichi Oyama. Re-examination of the time structure of the sn1987a neutrino burst data in kamiokande-ii. *The Astrophysical Journal*, 922(2):223, December 2021.

[386] NEST. Xenonnt sro detector nest implementation. 2022.

[387] STRAXEN plugin. Straxen. 2024.

[388] Marc Paterno. Calculating efficiencies and their uncertainties. 12 2004.

[389] Martin Ester, Hans-Peter Kriegel, Jörg Sander, and Xiaowei Xu. A density-based algorithm for discovering clusters in large spatial databases with noise. In *Knowledge Discovery and Data Mining*, 1996.

[390] Glen Cowan, Kyle Cranmer, Eilam Gross, and Ofer Vitells. Asymptotic formulae for likelihood-based tests of new physics. *The European Physical Journal C*, 71(2), February 2011.

[391] Aprile E. et al. Conceptual design and simulation of a water cherenkov muon veto for the xenon1t experiment. *Journal of Instrumentation*, 9(11):P11006–P11006, November 2014.

[392] Christopher Werner Geis. *The XENON1T water Cherenkov muon veto system and commissioning of the XENON1T Dark Matter experiment.* PhD thesis, Mainz U., 2018.

[393] Marco Selvi. Study of the performances of the shield and muon veto of the xenon1t experiment. *PoS*, 2010, 01 2010.

[394] Digikey Electronics. 3m specular film df2000ma. `https://www.digikey.de/htmldatasheets/production/1639507/0/0/1/df2000ma-specular-film-datasheet.html`, 2013.

[395] Adams C et al. Sensitivity of a tonne-scale next detector for neutrinoless double-beta decay searches. *Journal of High Energy Physics*, 2021, 08 2021.

[396] Ambrosio et al. Measurement of the energy spectrum of underground muons at gran sasso with a transition radiation detector. *Astroparticle Physics*, 10(1):11–20, January 1999.

[397] A. Empl, R. Jasim, E. Hungerford, and P. Mosteiro. Study of Cosmogenic Neutron Backgrounds at LNGS. 10 2012.

[398] E. Aguayo, R. T. Kouzes, and E. R. Siciliano. Neutron spallation measurements and impacts on low-background experiments. *Phys. Rev. C*, 90:034607, Sep 2014.

[399] HAMAMATSU-Photonics. Related documents | photomultiplier tubes (pmts). 2024.

[400] Thomas K. Gaisser. Spectrum of cosmic-ray nucleons, kaon production, and the atmospheric muon charge ratio. *Astroparticle Physics*, 35(12):801–806, July 2012.

[401] Junghyun Bae and Stylianos Chatzidakis. A new semi-empirical model for cosmic ray muon flux estimation, 2022.

[402] J.L. Autran, D. Munteanu, T. Saad Saoud, and S. Moindjie. Characterization of atmospheric muons at sea level using a cosmic ray telescope. *Nuclear Instruments and Methods in Physics Research Section A: Accelerators, Spectrometers, Detectors and Associated Equipment*, 903:77–84, 2018.

[403] Mehmet Bektasoglu and Halil Arslan. Estimation of the effects of the earth's electric and magnetic fields on cosmic muons at sea level by geant4. *Journal of Atmospheric and Solar-Terrestrial Physics*, 74:212–216, 2012.

[404] Agostini et al. Modulations of the cosmic muon signal in ten years of borexino data. *Journal of Cosmology and Astroparticle Physics*, 2019(02):046–046, February 2019.

[405] V.A. Kudryavtsev. Muon simulation codes music and musun for underground physics. *Computer Physics Communications*, 180(3):339–346, March 2009.

[406] Giuseppe Battistoni, Annarita Margiotta, Silvia Muraro, and Maximiliano Sioli. Fluka as a new high energy cosmic ray generator. *Nuclear Instruments and Methods in Physics Research Section A: Accelerators, Spectrometers, Detectors and Associated Equipment*, 626-627:S191–S192, 2011.

[407] S. P. Ahlen et al. Muon astronomy with the MACRO detector. *Astrophys. J.*, 412:301–311, 1993.

[408] Watanabe et al. First study of neutron tagging with a water cherenkov detector. *Astroparticle Physics*, 31(4):320–328, May 2009.

[409] Nahid Bhuiyan. Characterising Neutrons for Neutrino Experiments. *King's College London*, 06 2023.

[410] Ll. Marti et al. Evaluation of gadolinium's action on water cherenkov detector systems with egads. *Nuclear Instruments and Methods in Physics Research Section A: Accelerators, Spectrometers, Detectors and Associated Equipment*, 959:163549, 2020.

[411] I. Israelashvili, Marco Cortesi, David Vartsky, L. Arazi, Damian Bar, E. Caspi, and Amos Breskin. A comprehensive simulation study of a liquid-xe detector for contraband detection. *Journal of Instrumentation*, 10, 12 2014.

[412] J. Fierro and E.K. Nyer. *The Water Encyclopedia: Hydrologic Data and Internet Resources*. CRC Press, 2007.

[413] Francisco A. Scannavino and Paulo E. Cruvinel. A graphical tool for an analytical approach of scattering photons by the compton effect. *Nuclear Instruments and Methods in Physics Research Section A: Accelerators, Spectrometers, Detectors and Associated Equipment*, 674:28–38, 2012.

[414] P. et al Peplowski. Characterizing near-surface elemental layering on mars using gamma-ray spectroscopy: A proof-of-principle experiment. *Nuclear Instruments and Methods in Physics Research Section B: Beam Interactions with Materials and Atoms*, 415:89–99, 01 2018.

[415] W. R. Leo. *Techniques for Nuclear and Particle Physics Experiments: A How to Approach*. 1987.

[416] Max et al. Kircher. Kinematically complete experimental study of compton scattering at helium atoms near the threshold. *Nature Physics*, 16(7):756–760, April 2020.

[417] Arthur H. Compton. A quantum theory of the scattering of x-rays by light elements. *Phys. Rev.*, 21:483–502, May 1923.

[418] O. Klein and T. Nishina. Über die Streuung von Strahlung durch freie Elektronen nach der neuen relativistischen Quantendynamik von Dirac. *Zeitschrift fur Physik*, 52(11-12):853–868, November 1929.

[419] In Leonard L. Gunderson and Joel E. Tepper, editors, *Clinical Radiation Oncology (Fourth Edition)*, page iii. Elsevier, Philadelphia, fourth edition edition, 2016.

[420] Richard Clinton Fernow. *Introduction to Experimental Particle Physics*. Oxford University Press, 1986.

[421] V.T. Adonkin, B.M. Gorelov, D.V. Morozovskay, and V.M. Ogenko. Effect of water adsorption on positron annihilation lifetimes in barium oxide and barium peroxide. *Colloids and Surfaces A: Physicochemical and Engineering Aspects*, 101(2):233–237, 1995. Chemistry at Interfaces.

[422] J V Jelley. Cerenkov radiation and its applications. *British Journal of Applied Physics*, 6(7):227, jul 1955.

[423] Lorenz Kuger and Gaël Rigaud. On multiple scattering in compton scattering tomography and its impact on fan-beam ct. *Inverse Problems and Imaging*, 16(5):1359, 2022.

[424] Claudia Lederer. Neutron-induced reactions for the s-process, and the case of Fe and Ni isotopes. *PoS*, NIC XII:023, 2013.

[425] J.W. Marsh, D.J. Thomas, and M. Burke. High resolution measurements of neutron energy spectra from ambe and ambe neutron sources. *Nuclear Instruments and Methods in Physics Research Section A: Accelerators, Spectrometers, Detectors and Associated Equipment*, 366(2):340–348, 1995.

[426] Edgar A. Lorch. Neutron spectra of 214am/b, 241am/be, 241am/f, 242cm/be, 238pu/13c and 252cf isotopic neutron sources. *The International Journal of Applied Radiation and Isotopes*, 24(10):585–591, 1973.

[427] Kostal, Michal, Schulc, Martin, Novak, Evzen, Czakoj, Tomas, Matej, Zdenek, Cvachovec, Frantisek, Mravec, Filip, Jansky, Bohumil, and Leal, Luiz. Validation of heavy water cross section using ambe neutron source. *EPJ Web Conf.*, 239:18008, 2020.

[428] F. De Guarrini and R. Malaroda. Two different technique measurements of the neutron spectrum of an ambe source. *Nuclear Instruments and Methods*, 92(2):277–284, 1971.

[429] Hiroyuki Sekiya. Supernova neutrinos in sk-gd and other experiments. *Journal of Physics: Conference Series*, 888(1):012041, sep 2017.

[430] Tanaka et al. Gamma-ray spectra from thermal neutron capture on gadolinium-155 and natural gadolinium. *Progress of Theoretical and Experimental Physics*, 2020(4):043D02, 04 2020.

[431] C.H. Faham, V.M. Gehman, A. Currie, A. Dobi, P. Sorensen, and R.J. Gaitskell. Measurements of wavelength-dependent double photoelectron emission from single photons in vuv-sensitive photomultiplier tubes. *Journal of Instrumentation*, 10(09):P09010–P09010, September 2015.

[432] A Oralbaev, M Skorokhvatov, and O Titov. The inverse beta decay: a study of cross section. *Journal of Physics: Conference Series*, 675(1):012003, jan 2016.

[433] Artur M Ankowski. Improved estimate of the cross section for inverse beta decay. *Journal of Physics: Conference Series*, 1216(1):012015, apr 2019.

[434] C. L. Cowan, F. Reines, F. B. Harrison, H. W. Kruse, and A. D. McGuire. Detection of the free neutrino: A Confirmation. *Science*, 124:103–104, 1956.

[435] Giulia Ricciardi, Natascia Vignaroli, and Francesco Vissani. An accurate evaluation of electron (anti-)neutrino scattering on nucleons. *Journal of High Energy Physics*, 2022(8), August 2022.

[436] William J Marciano and Zohreh Parsa. Neutrino–electron scattering theory. *Journal of Physics G: Nuclear and Particle Physics*, 29(11):2629–2645, October 2003.

[437] Daya Bay Collaboration. Measurement of the reactor antineutrino flux and spectrum at daya bay. *Physical Review Letters*, 116(6), 2016.

[438] Y. Ashie and et al. Hosaka. Evidence for an oscillatory signature in atmospheric neutrino oscillations. *Physical Review Letters*, 93(10), September 2004.

[439] G. Bellini and Benziger et al. Observation of geo-neutrinos. *Physics Letters B*, 687(4–5):299–304, April 2010.

[440] Ji Young Choi, Kyung Kwang Joo, Hyun-Gi Lee, and Sang Yong Kim. Organic liquid scintillation detectors for reactor neutrino experiments: Toward precision neutrino physics. *Current Applied Physics*, 59:182–196, 2024.

[441] William J Marciano and Zohreh Parsa. Neutrino–electron scattering theory. *Journal of Physics G: Nuclear and Particle Physics*, 29(11):2629–2645, October 2003.

[442] S. Mandelstam. Determination of the pion-nucleon scattering amplitude from dispersion relations and unitarity. general theory. *Phys. Rev.*, 112:1344–1360, Nov 1958.

[443] G. Fiorentini, M. Moretti, and F.L. Villante. Superkamiokande and solar antineutrinos. *Physics Letters B*, 413(3–4):378–381, November 1997.

[444] P. Vogel and J. F. Beacom. Angular distribution of neutron inverse beta decay,<mml:math xmlns:mml="http://www.w3.org/1998/math/mathml" display="inline"><mml:mrow><mml:msub><mml:mover><mml:mrow><mml:mi></mml:mi></mml:mrow> *Physical Review D*, 60(5), July 1999.

[445] Kaustav Chakraborty, Arindam Das, Srubabati Goswami, and Samiran Roy. Constraining general u(1) interactions from neutrino-electron scattering measurements at dune near detector. *Journal of High Energy Physics*, 2022(4), April 2022.

[446] G.'t Hooft. Prediction for neutrino-electron cross-sections in weinberg's model of weak interactions. *Physics Letters B*, 37(2):195–196, 1971.

[447] John N. Bahcall, Marc Kamionkowski, and Alberto Sirlin. Solar neutrinos: Radiative corrections in neutrino-electron scattering experiments. *Physical Review D*, 51(11):6146–6158, June 1995.

[448] T. Horai and for theE525 Collaboration. The measurement of gamma rays from neutron-oxygen interactions. *Journal of Physics: Conference Series*, 1468(1):012183, feb 2020.

[449] E. Mendoza, Daniel Ott, J.L. Tain, and Alejandro Algora. Nudex: A new nuclear gamma ray cascades generator. *EPJ Web of Conferences*, 239:17006, 01 2020.

[450] Eric W. Weisstein. "central limit theorem." from mathworld. *A Wolfram Web Resource*, 239:17006, 08 2024.

[451] I. J. Good. On the Weighted Combination of Significance Tests. *Journal of the Royal Statistical Society: Series B (Methodological)*, 17(2):264–265, 12 2018.

[452] Robert D. Cousins. Annotated bibliography of some papers on combining significances or p-values, 2008.

[453] N. J. Demerath. The American Soldier: Volume I, Adjustment During Army Life. By S. A. Stouffer et al. *Social Forces*, 28(1):87–90, 10 1949.

[454] Damien Dornic, Donzaud Corinne, Sonia Hedri, Vladimir Kulikovskiy, and Godefroy Vannoye. Implementation of the km3net online core-collapse supernova neutrino search. page 1223, 07 2023.

[455] Irene Tamborra and Shashank Shalgar. New developments in flavor evolution of a dense neutrino gas. *Annual Review of Nuclear and Particle Science*, 71(1):165–188, September 2021.

[456] Ian Padilla-Gay, Shashank Shalgar, and Irene Tamborra. Multi-dimensional solution of fast neutrino conversions in binary neutron star merger remnants. *Journal of Cosmology and Astroparticle Physics*, 2021(01):017–017, January 2021.

[457] Tomoya Takiwaki, Kei Kotake, and Yudai Suwa. Three-dimensional hydrodynamic core-collapse supernova simulations for an 11.2mstar with spectral neutrino transport. *The Astrophysical Journal*, 749(2):98, March 2012.

[458] Madhurima Chakraborty and Sovan Chakraborty. Three flavor neutrino conversions in supernovae: slow amp; fast instabilities. *Journal of Cosmology and Astroparticle Physics*, 2020(01):005–005, January 2020.

[459] Francesco Capozzi, Madhurima Chakraborty, Sovan Chakraborty, and Manibrata Sen. Mu-tau neutrinos: Influencing fast flavor conversions in supernovae. *Physical Review Letters*, 125(25), December 2020.

[460] Francesco Capozzi, Basudeb Dasgupta, Alessandro Mirizzi, Manibrata Sen, and Günter Sigl. Collisional triggering of fast flavor conversions of supernova neutrinos. *Physical Review Letters*, 122(9), March 2019.

[461] Sajad Abbar, Huaiyu Duan, Kohsuke Sumiyoshi, Tomoya Takiwaki, and Maria Cristina Volpe. Fast neutrino flavor conversion modes in multidimensional core-collapse supernova models: The role of the asymmetric neutrino distributions. *Physical Review D*, 101(4), February 2020.

[462] Richard H. Helm. Inelastic and elastic scattering of 187-mev electrons from selected even-even nuclei. 1956.

[463] Carolyn Kierans, Tadayuki Takahashi, and Gottfried Kanbach. *Compton Telescopes for Gamma-Ray Astrophysics*. Springer Nature Singapore, Singapore, 2022.

[464] Photonis. Photomultiplier tube basics. *University of Chicago*, 2024.

[465] Johan de Haas and Pieter Dorenbos. Methods for accurate measurement of the response of photomultiplier tubes and intensity of light pulses. *IEEE Transactions on Nuclear Science*, 58, 06 2011.

[466] A. G. Wright. 410Collection and counting efficiency. In *The Photomultiplier Handbook*. Oxford University Press, 06 2017.

[467] P. Besson, Ph. Bourgeois, P. Garganne, J.P. Robert, L. Giry, and Y. Vitel. Measurement of photomultiplier quantum efficiency. *Nuclear Instruments and Methods in Physics Research Section A: Accelerators, Spectrometers, Detectors and Associated Equipment*, 344(2):435–437, 1994.

[468] Avago technology. Led hlmp-cx1a/1b/2a/2b/3a/3b. *Avago technology*, 2024.

[469] The Photomultiplier Handbook. University of Chicago.

[470] Jun Weng, Aiqiang Zhang, Qi Wu, Lishuang Ma, Benda Xu, Sen Qian, Zhe Wang, and Shaomin Chen. Single electron charge spectra of 8-inch high-collection-efficiency mcp-pmts, 2024.

[471] Stephen D Webb. Residual analysis as a technique for specifying and optimizing predictive models. *Social Science Research*, 2(1):31–40, 1973.

[472] Paul I. Richards. Probability of Coincidence for Two Periodically Recurring Events. *The Annals of Mathematical Statistics*, 19(1):16 – 29, 1948.

[473] Alessandra Fumagalli, Matteo Biagetti, Alex Saro, Emiliano Sefusatti, Anže Slosar, Pierluigi Monaco, and Alfonso Veropalumbo. Fitting covariance matrix models to simulations. *Journal of Cosmology and Astroparticle Physics*, 2022(12):022, December 2022.